Quantitative description & computational modelling of the BRI1 response module controlling root cell elongation growth – from organ-scale to nanodomains

Dissertation

der Mathematisch-Naturwissenschaftlichen Fakultät
der Eberhard Karls Universität Tübingen
zur Erlangung des Grades eines
Doktors der Naturwissenschaften
(Dr. rer. nat.)

vorgelegt von
Nina Glöckner
aus Aalen

Tübingen
2019

Gedruckt mit Genehmigung der Mathematisch-Naturwissenschaftlichen Fakultät der Eberhard Karls Universität Tübingen.

Tag der mündlichen Qualifikation:	27.09.2019
Dekan:	Prof. Dr. Wolfgang Rosenstiel
1. Berichterstatter:	Prof. Dr. Klaus Harter
2. Berichterstatter:	Prof. Dr. Claudia Oecking
3. Berichterstatter:	Prof. Dr. Raimund Tenhaken

Zusammenfassung

Die Familie der Brassinosteroid-Pflanzenhormone (BR) ist an der schnellen Kontrolle des Zellstreckungswachstums beteiligt. Die Aktivierung des plasmamembran-ständigen Brassinosteroidrezeptors BRASSINOSTEROID INSENSITIVE 1 (BRI1) und seines Cofaktors BRI1-ASSOCIATED KINASE (BAK1) führt zur Dissoziation des Inhibitors BAK1-INTERACTING RECEPTOR-LIKE KINASE 3 (BIR3) und schließlich zur Aktivierung von P-Typ ATPasen (AHAs). Die aktivierung der Protonenpumpen (AHAs) führt zu einer Ansäuerung des extrazellulären Raums, einer Hyperpolarisierung der Plasmamembran und einer Lockerung der Zellwand, was schließlich zu Zellstreckungswachstum führt. Dieses Signaltransduktionsmodul ist auf Komponentenebene gut beschrieben.

Es ist jedoch noch nicht bekannt, wie diese Akteure räumlich und zeitlich zusammenwirken, um das unterschiedliche Zellstreckungswachstum als Reaktion auf BR in verschiedenen Pflanzengeweben zu vermitteln. Hier zeigen wir durch quantitative *in vivo*-Ansätze, dass sich die Proteinmenge von AHA2 in der schnell wachsenden Elongationszone von der in der weniger / nicht wachsenden meristematischen und Wurzelhaarzone in der Wurzel von *Arabidopsis thaliana* unterscheidet. Während das Proteinverhältnis von BIR3 und BRI1 entlang der Wurzelachse gleich bleibt, ist das Verhältnis von AHAs und BRI1 in der meristematischen Zone signifikant niedriger. Unter Einbeziehung der Proteinmengen in ein mathematisches Modell untersuchen wir die Regulation und Dynamik des schnellen BR-Antwortmoduls *in silico*, einschließlich der Membranhyperpolarisation und des Zellstreckungswachstums. Sowohl das Modell als auch die Experimente unterstreichen die Bedeutung der Protonenpumpen in Kombination mit dem Hormonrezeptor. Unter Berücksichtigung der unterschiedlichen Proteinspiegel kann das Modell das unterschiedliche Wachstumsverhalten entlang der Wurzelachse beschreiben, einschließlich nicht-invasiver Protonenflussmessungen und apoplastischer pH-Messungen. Wir nehmen daher an, dass das Verhältnis von AHAs zu BRI1 der entscheidende Parameter ist, der die differentielle Fähigkeit von Zellen steuert, sich als Reaktion auf BR entlang der Wurzelachse zu verlängern.

Es ist auch noch nicht geklärt, ob die Aufteilung der Komplexe in der Plasmamembran (Mikrodomänen) für die physiologische Leistung, nämlich das Zellstreckungswachstums, relevant ist. Unter Verwendung der photoaktivierten Lokalisationsmikroskopie mit Einzelpartikelverfolgung (sptPALM) fanden wir, dass die Mehrheit der BRI1-Rezeptoren in Tabakblättern (*Nicotiana benthamiana*) ein subdiffusives Verhalten zeigt. Dieses heterologe System ist jedoch vermutlich nicht gut für den Nachweis geringfügiger Änderungen der Rezeptordynamik geeignet, da weder die BR-Behandlung noch das Aufbrechen von Mikrodomänen mit Methyl-Beta-Cyclodextran (MβCD) und die Depolymerisation von Aktinfilamenten die BRI1-Rezeptordynamik signifikant veränderten. Im Gegensatz dazu, schwächt die Störung der Mikrodomänen durch MβCD in *Arabidopsis thaliana* die

Brassinosteroid-Signalübertragung in Bezug auf primäres Wurzelwachstum und Wurzelwellen ab, was darauf hinweist, dass die Integrität der PM-Mikrodomänen für die BRI1-Funktion entscheidend ist.

Es ist derzeit nicht klar, ob BRI1, BAK1 und das die Zellwandintegrität erfassende RECEPTOR LIKE PROTEIN 44 (RLP44) gleichzeitig in derselben Mikrodomäne lokalisiert sind und einen Trimerkomplex bilden. Hier liefern wir durch quantitative *in vivo* FRET-FLIM-Messungen mit drei Fluorophoren den Nachweis, dass RLP44, BRI1 und BAK1 in der Plasmamembran von *Nicotiana benthamiana*-Blattzellen in Abwesenheit von exogenem BR einen Trimerkomplex bilden, wobei der geschätzte Abstand zwischen ihnen unter 15 nm liegt. Der Immunrezeptor FLAGELLIN SENSING 2 (FLS2), der strukturell BRI1 ähnlich ist, ist nicht in einen ähnlichen Komplex mit RLP44 und BAK1 integriert. Unsere Studie belegt, dass BRI1 und FLS2 in der Plasmamembran in unterschiedlichen Nanodomänen lokalisiert sind. Darüber hinaus scheint RLP44 spezifisch für BRI1-haltige Mikrodomänen zu sein, da FRET mit FLS2 nie beobachtet wurde. Da die Fluoreszenzlebensdauer des Donors überwacht wird, umgeht unsere Methode die umfangreichen Berechnungen, die für intensitätsbasierte FRET-Interaktionstests erforderlich sind, und bietet somit eine praktikable Grundlage für die Untersuchung der Subkompartimentierung in der Plasmamembran lebender Pflanzenzellen mit einer Auflösung im Nanomaßstab.

Zuletzt zeigen wir, wie FRET-FLIM-Interaktionsstudien dazu beitragen können, die zugrunde liegenden molekularen Mechanismen in verschiedenen biologischen Umgebungen aufzudecken.

Summary

The brassinosteroid plant hormone family (BR) is involved the fast control of cell elongation growth. The activation of the plasma membrane-resident brassinosteroid receptor BRASSINOSTEROID INSENSITIVE 1 (BRI1) and its cofactor BRI1-ASSOCIATED KINASE (BAK1) leads to the dissociation of the inhibitor BAK1-INTERACTING RECEPTOR-LIKE KINASE 3 (BIR3) and eventually to the activation of P-type ATPases (AHAs). This causes the acidification of the extracellular space, hyperpolarization of the PM and wall loosening, eventually leading to cell elongation. This signalling module is well described at constituent level. However, it is not yet understood, how these players act collectively in space and time to mediate differential cell elongation in response to BR in various plant tissues.

Here we show by quantitative *in vivo* approaches that the protein amount of AHA2 differs in the fast-growing elongation zone compared to that in the less/non-growing meristematic and root hair zone in *Arabidopsis thaliana* roots. While the protein ratio of BIR3 and BRI1 stays the same along the root axis, the ratio of AHAs and BRI1 is significantly lower in the meristematic zone. Including the protein amounts in a computational model, we evaluate the regulation and dynamics of the fast BR response module *in silico* including membrane hyperpolarization and cell elongation growth. Both the model and experiments underline the importance of the proton pumps in combination with the hormone receptor. Accounting for the varying protein levels, the model is able to describe the differential growth behaviour along the root axis, including non-invasive proton flux measurements and apoplastic pH measurements. We, therefore, hypothesize that the ratio of AHA to BRI1 is the crucial parameter that controls the differential competence of cells to elongate in response to BR along the root axis.

It is also not yet understood, whether the partitioning of the complexes in the plasma membrane (microdomains) is relevant for the physiological output, namely cell elongation. By using single-particle tracking photoactivated localization microscopy (spt-PALM), we found that the majority of BRI1 receptors show subdiffusive behaviour in *Nicotiana benthamiana* leaves. However, this heterologous system is probably not well suited for the detection of minor changes in receptor dynamics, as neither BR treatment, the disruption of microdomains with methyl-beta-cyclodextran (MβCD) and actin filament depolymerization significantly altered the BRI1 receptor dynamics. In contrast, the disturbance of microdomains by MβCD in *Arabidopsis thaliana* attenuates brassinosteroid signalling with respect to primary root growth and root waving indicating that the integrity of PM microdomains is crucial for BRI1 function.

It is currently not clear, whether BRI1, BAK1 and the cell wall integrity sensing RECEPTOR LIKE PROTEIN 44 (RLP44) are located together at the same time in the same microdomain, forming a trimeric complex.

Here we provide evidence by quantitative *in vivo* three-fluorophore FRET-FLIM measurements, that RLP44, BRI1 and BAK1 form a trimeric complex in the plasma membrane of *Nicotiana benthamiana* leaf cells in the absence of exogenous BL, with an estimated distance between them below 15 nm. The immune receptor FLAGELLIN SENSING 2 (FLS2), which is also a receptor-like kinase like BRI1, is not integrated in a similar complex with RLP44 and BAK1. Our study supports, that BRI1 and FLS2 are localized in distinct nanodomains in the plasma membrane. Furthermore, RLP44 appears to be specific for BRI1 containing microdomains, as FRET was never observed with FLS2. As the fluorescence lifetime of the donor is monitored, our method circumvents the extensive calculations necessitated by intensity-based FRET interaction assays and thus provides a feasible base for studying the sub-compartmentalization in the plasma membrane of living plant cells with a nanoscale resolution.

Lastly, we show, how FRET-FLIM interaction studies can help to unravel underlying molecular mechanisms in diverse biological settings.

Table of Contents

1 Introduction

1.1 The *Arabidopsis thaliana* root as model system for cell elongation growth

The precise integration of signalling cues is essential for the survival of any living organism. This holds especially true for plants, as they cannot run from unfavourable conditions. Both internal and external factors have to be balanced: The internal growth and developmental program on the one hand, leading to reproduction and the survival of a species. On the other hand, unfavourable external conditions such as pathogens (biotic) or cold stress, drought, anoxic conditions and many other (abiotic) stresses have to be considered. Thus, only with a fine-tuned response in space (e.g. on tissue level, organ level or whole plant) and in time (e.g. fast immune response or initiation of flowering), the reproductive state may be reached. The root of the model plant *Arabidopsis thaliana* (*A. thaliana*) is an ideal system to study signalling integration, as its anatomy and developmental program is well studied.

Along the horizontal axis, the root of *A. thaliana* seedlings is divided into specific tissue layers. The outermost cell layer is the epidermis, which can be divided into root-hair producing cells, the trichoblasts and non-root-hair cells, the atrichoblasts. Below, a single layer of cortex cells is produced. The endodermis with the median deposition of lignin (casparian strip) functions as control gate for nutrient uptake as it disrupts apoplastic water flow (Lee et al. 2013; Naseer et al. 2012). The pericycle initiates lateral root formation and is the outermost cell layer of the root stele, which in turn contains the vasculature (Casimiro et al. 2003; Sussex et al. 1995). In the vasculature, the xylem conducts water and nutrients from the root to the shoot and the phloem transports products of photosynthesis, including sucrose, from source tissues like mature leaves to sink tissues such as roots (Dinney and Yanofsky, 2004)

Along the longitudinal root axis, the root can be separated into four functional domains: The root cap protects the root tip and mediates gravitropic responses. The meristematic zone comprises a set of initial cells (stem cells) that surround the quiescent centre, a group of less mitotically active cells with major regulatory function (Petricka et al. 2012; Shishkova et al. 2008). Cells migrating out of the stem cell niche in turn divide multiple times and thus generate a pool of cells that will elongate. Elongating cells grow first slowly by triplicating their size in 10 h while undergoing diverse adaptations such as centralizing their vacuole, polarization of the cytoskeleton and remodelling of the cell walls (Verbelen et al. 2006) and only then enter fast elongation growth by becoming four-times their former size in only 2 h (Verbelen et al. 2006).

At the moment, no unified definition exists, where the elongation zone starts (Ishikawa and Evans 1995; Fasano et al. 2001; Dünser et al. 2019). A clearly visible boundary is the first cell in the cortex, that is twice as long as thick (Dünser et al. 2019). Articles that address how the boundary between the meristem and elongation zone is determined, additionally specify a transition zone (Baluška et al. 2001; Baluska et al. 1997; Baluska et al. 1996; Pacifici et al. 2018; Vermeer et al. 2014). Lastly, the cells acquire their specific characteristics and functions in the differentiation zone. Fully differentiated tissue is called mature zone, which in turn is characterized by fully developed trichoblasts and is thus also called root hair zone. Root hairs are important for nutrient uptake, as they increase the root surface and their length is regulated by nutrient availability (e.g. external phosphate) (Bhosale at al. 2018).

Several factors determine the initiation of cell elongation growth. The boundary between the elongation zone and meristem is balanced by the phytohormones auxin and the antagonistic cytokinin (Pacifici et al. 2018; Vos et al. 2014). The structure and properties of the cell wall provides another layer of regulation: Firstly, the barrel-like, transverse configuration of the cellulose microfibrils determines the cells' growth direction. This special orientation is mediated by transverse oriented microtubules that guide the cellulose synthase (Bichet et al. 2001; Burk et al. 2001). Secondly, the balance between the cell wall rigidity and the intracellular turgor governs cell elongation growth (Barbez et al. 2017; Dünser et al. 2019; Marowa et al. 2016; McQueen-Mason and Cosgrove 1994; Sede et al. 2018; Draeger et al. 2015).
The extracellular (apoplastic) pH strongly influences the rigidity of the cell wall. Already in 1934, 'acidic growth' was described (Bonner 1934; Hager et al. 1971) and the description of directional growth by differential cell elongation dates even back to Charles Darwin with his botanist son Francis (Darwin 1880). On the cellular level, plasma membrane resident P-type proton pumps are activated, leading to an acidification of the extracellular space, which in turn weakens the interaction between cell wall components (Phyo et al. 2019). This induces cell wall swelling and finally, expansins mediate a pH-dependent, non-enzymatic polymer creep (McQueen-Mason and Cosgrove 1994; Cosgrove 2000). Indeed, the apoplastic pH decreases in the elongation zone in response to auxin (Barbez et al. 2017; Fasano et al. 2001) and the alkalinisation of the apoplast instantly inhibits elongation growth (Staal et al. 2011; Campos et al. 2018).

Brassinosteroid hormone signalling is essential for cell elongation growth, as its disruption generates miniature versions of plants (Zhang et al. 2018; Noguchi et al. 1999). Concordantly, brassinosteroid signalling leads to the fast activation of P-type proton pumps and cell wall swelling 20-30 minutes after hormone treatment (Elgass et al. 2009; Caesar et al. 2011; Witthöft et al. 2011), enabling cell elongation growth. This short time of their activation precludes signalling involving transcriptional and translational regulation (Moore et al. 2018; Goda et al. 2008), indicating the existence of a fast brassinosteroid response module.

1.2 Brassinosteroid hormone signalling

Brassinosteroid (BR) hormones are a class of phytohormones with similar chemical structure as the mammalian oestradiol and testosterone hormone or the insect steroid hormone ecdysone (Bishop and Koncz 2002). The most active form of brassinosteroid hormones in plants is brassinolide (BL) (Yokota 1999). Its recognition and signal transduction belongs to the best understood pathways in plants. It is recognized and mediated by the plasma membrane-resident receptor BRASSINOSTEROID INSENSITIVE 1 (BRI1). The extracellular domain of BRI1 comprises 24 leucin-rich repeat (LRR) domains and has an island domain, to which BR hormones bind (Wang et al. 2001). The extracellular domain is connected by a single trans-membrane domain with an intracellular kinase domain (Wang et al. 2014). Thus, the receptor is classified as an LRR receptor-like kinase (LRR-RLK). It interacts with BRI1-ASSOCIATED KINASE 1 (BAK1), also a LRR-RLK that is required for full activation of hormone signalling and thus functions as co-receptor (Clouse et al. 1996; Li and Chory 1997; Nam and Li 2002; Friedrichsen et al. 2000). Large populations of BRI1 and BAK1 form heterodimers in Arabidopsis, independently of BR (Bücherl et al. 2013; Nam and Li 2002; Wang et al. 2005b; Yun et al. 2009; Wang et al. 2005a; Hutten et al. 2017).

In the absence of BR, the activation by trans-phosphorylation events between the cytoplasmic kinase domains is inhibited by the auto-inhibitory C-terminal tail of BRI1, the cytoplasmic BRI1 KINASE INHIBITOR 1 (BKI1) protein, and a LRR-RLK named BAK1-INTERACTING RECEPTOR-LIKE KINASE 3 (BIR3) (Figure 1) (Wang and Chory 2006; Wang et al. 2014; Imkampe et al. 2017). BIR3 seems to keep BAK1 and the receptor in close proximity, and, at the same time, inhibits signalling in the absence of the hormone (Imkampe et al. 2017; Großeholz et al. 2019). Binding of BR to the extracellular island domain of the receptor acts as 'molecular glue' between BRI1 and BAK1 and enhances their interaction (Hothorn et al. 2011; Santiago et al. 2013; Wang et al. 2005a; Sun et al. 2013).

This leads to the auto- and trans-phosphorylation of the Ser/Thr-kinase domains, the dissociation of BKI1 from the plasma membrane (PM) (Jaillais et al. 2011; Friedrichsen et al. 2000; Oh et al. 2000; Wang et al. 2005a; Wang et al. 2008b) and the partial release of BIR3 (Imkampe et al. 2017; Großeholz et al. 2018). In consequence, increased interaction, colocalization and hetero-oligomerization is observed (Wang et al. 2005a; Bücherl et al. 2013). These events at the PM then lead to the activation or repression of BR-responsive genes by a signalling cascade mediated by several cytoplasmic proteins (Yin et al. 2005; Vert and Chory 2006; Mora-García et al. 2004; Zhu et al. 2017). Simultaneously, this leads to the fast activation of P-type proton pumps, hyperpolarization of the membrane potential (E_m), the acidification of the extracellular space, cell wall swelling and thus cell elongation growth as described earlier (Elgass et al. 2009; Caesar et al. 2011; Witthöft et al. 2014). Also, BR signalling is involved in normal vascular differentiation (Caño-Delgado et al. 2004) such as the protophloem differentiation (Fàbregas et al. 2013; Kang et al. 2017; Planas-Riverola et al. 2019).

In summary, the brassinosteroid hormone signalling pathway is very well described at a constitutive level.

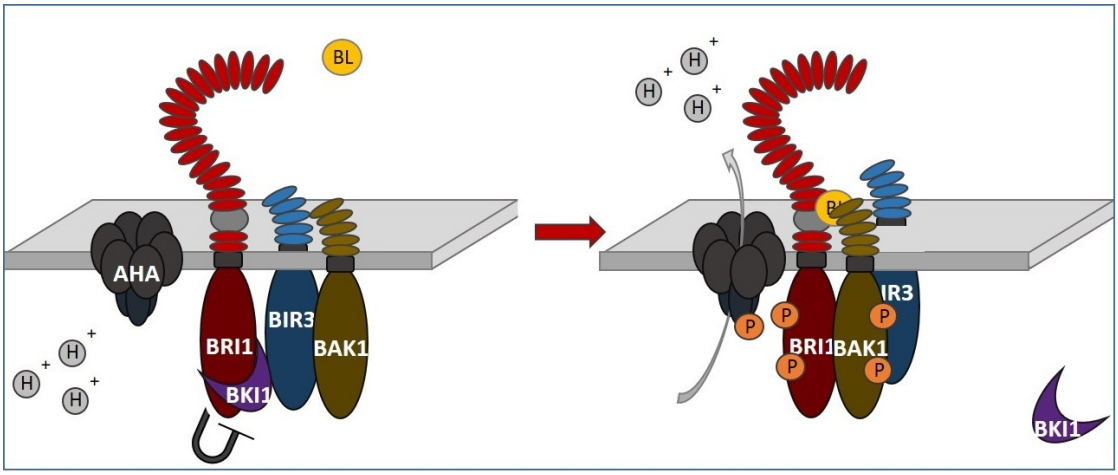

Figure 1: Components of the brassinosteroid response module in the abscence of hormone (left) and signalling activation upon hormone treatment (right)

(left) The brassinosteroid hormone receptor BRI1 (red) is inhibited by its own C-terminal as well as by BIR3 (blue) and the cytoplasmic BKI1 (purple). Signalling activation is inhibited, since BAK1 (brown) associates more tightly with BIR3 than with BRI1. (right) Addition of a brassinosteroid hormone, such as the most active form brassinolide (BL, yellow) increases the affinity of the extracellular domains, which effectively brings the kinase domains in a favourable position, leading to transphosphorylation, party dissociation of BIR3 and to the phosphorylation and thus activation of P-type proton pumps (AHA) (grey). The active proton pump transports H+ into the extracellular space, leading to cell wall acidification, decreased wall stiffness and ultimately, cell elongation growth.

However, it is not clear, how the same set of proteins mediate a differential growth regulation on tissue level (in space) and at what time scale (in time). Open questions are for example, where exactly is the apoplastic pH decreased, for how long after BR hormone signalling does this effect remain and what are the underlying molecular mechanisms for differential growth regulation in response to BR.

1.2.1 Dynamics and organization of the signalling components

The plasma membrane is a heterogeneous lipid bilayer which comprises diverse subdomains that may serve as hotspots for for signal transduction (Konrad and Ott, 2015). The complex formation of the signalling components may facilitate the fast and effective signal transduction or the removal from the plasma membrane to terminate signal transduction. Indeed, the pool of plasma membrane-localized BRI1 and BAK1 is relevant for signalling output, as the endocytosis of BRI1 attenuates BR signalling (Russinova et al., 2004; Irani et al., 2012; Di Rubbo et al., 2013; Wen et al., 2014; Martins et al., 2015; Liang et al., 2016; Peng et al., 2018). Several details on the distribution and interaction of BRI1 support, that a BRI1/BR response module exists. BRI1 can frequently form homodimers (Wang et al. 2005b), it interacts with BAK1 without external hormone application (Bücherl et al., 2013; Wang et al., 2005b, Hutten et al., 2017) In the course of signalling transduction, homo-oligomerisation is involved (Wang et al., 2005a; Bücherl et al., 2013). These observations rely on biochemical protein-protein interaction studies such as co-immunoprecipitations (CO-IP) or spectroscopic interaction tests such as Förster resonance energy transfer (FRET) or FRET by fluorescence lifetime imaging (FRET-FLIM), fluorescence cross-correlation spectroscopy (FCCS) or tests in heterologous systems such as the mating-based split-ubiquitin in yeast (mbSUS).

While biochemical interaction studies represent the average found in the plant or in a specific organ (e.g. leaf, root, flower), optical spectroscopic methods can provide *in vivo* information in space and in time. Nonetheless, a higher resolution is highly desirable, as it provides information on how subpopulations of receptors behave within a single cell, leading to a better understanding of signal transduction processes *in vivo*. First tests on the BRI1 dynamics were performed recently, using GREEN FLUORESCENT PROTEIN (GFP) fusions (Wang et al., 2015; Hutten et al., 2017). However, when observing the fluorescence emission of fluorophores such as the GFP (Cormack et al., 1996; Heim and Tsien, 1996; Tsien, 1998), originally found in the luminous jellyfish *Aequorea victoria* (Shimomura et al., 1962), or colour-shifted derivates (Campbell et al., 2002; Ai et al., 2007; Shaner et al., 2008; Day and Davidson, 2009) it is not possible to resolve single molecules with conventional microscopes.

Super-resolution microscopy

The diffraction limit prevents the resolution of two fluorescent proteins closer than approximately 200 µm (Abbe, 1873; Turkowyd et al., 2016). In 2014, the nobel prize in chemistry was jointly awarded to Eric Betzig, Stefan W. Hell and William E. Moerner "*for the development of super-resolved fluorescence microscopy*" (https://www. nobel-

prize.org/prizes/chemistry/2014/summary). Two major approaches to super-resolved imaging currently exist.
Stimulated emission depletion (STED) microscopy utilizes an activation laser line that is surrounded by a donut-shaped emission depletion laser line which quenches the fluorescence (Hell and Wichmann, 1994; Klar et al., 2000). After scanning pixel-by-pixel, the signal of each scan is combined into a single image. Thus, in an axial intensity profile, the full width half maximum (FWHM) of the point-spread function of a single emitting fluorophore is reduced from 490 nm down to 97 nm (5.1-fold) (Klar et al., 2000), even reaching down to 50 nm (Turkowyd et al., 2016). For plants, however, this method may be challenging, as high intensities of a pulsed laser are needed (Rust et al., 2006) which may cause phototoxic effects as they possess light harvesting complexes (Dixit and Cyr, 2003; Turkowyd et al., 2016; Wangenheim et al., 2017; Komis et al., 2018).
Photoactivated localization microscopy (PALM) exploits the possibility to activate a small subset of fluorophores at different time points (Betzig, 1995; Dickson et al., 1997; Betzig et al., 2006). This was first enabled by the demonstration that single molecules can be detected (Moerner and Kador, 1989). By repeating cycles of photoactivation, imaging and bleaching or deactivation, detected single molecules are combined in one image (Betzig et al., 2006) until even and sufficient sampling is reached (Nyquist-Shannon sampling) (Nyquist, 1928; Shannon, 1949; Thompson et al., 2012). Additionally, the resolution is increased by using the FWHM of a single emitter, thus enabling the resolution of two single emitters down to 20 nm (Turkowyd et al., 2016).

Later in the year of the description of PALM, two more methods using this pointillistic approach were published, the stochastic optical reconstruction microscopy STORM (Rust et al., 2006) and the fluorescence-PALM (fPALM) (Hess et al., 2006) and many further forms of super-resolved microscopy currently exist (Voie et al., 1993; Gustafsson, 2000; Dertinger et al., 2010). A method to further increase the contrast of super-resolution microscopy techniques (Hosy et al., 2015) and conventional microscopy (Li et al., 2011) is the total internal reflection (TIRF) microscopy, where the excitation laser is totally reflected at the coverslip-water boundary, thus generating a thin evanescent field with a depth of 100 nm (Ambrose, 1961; Axelrod, 1981; Axelrod, 2001; Hedde and Nienhaus, 2014; Johnson and Vert, 2017). However, when labelling the plasma membrane with a fluorescent protein in *A. thaliana* plants, the apparent cell wall has a FWHM thickness between 0.4 and 1.8 µm (Elgass et al., 2009). Thus, for the imaging in plants (Bücherl et al., 2013; Hutten et al., 2017), the angle of the excitation laser has to be varied to increase the depth of the evanescent field and is hence called variable-angle TIRF (VA-TIRF) (Stock et al., 2003) or variable angle epifluorescence microscopy (VAEM) (Konopka and Bednarek, 2008).

With this super-resolved microscopy techniques, now, observations of single molecules *in vivo* in plant tissue are possible (Hosy et al., 2015). Thus, the previously observed dynamics of brassinosteroid hormone signalling can newly and more precisely be addressed. Open questions are for example, whether the BRI1 receptor changes its dynamics upon hormone perception as e.g. in the course of signal transduction the co-receptor associates more tightly, or inhibitors dissociate. The picket-fence theory postulates, that actin fil-

aments in the cytoplasm below the plasma membrane restrict the lateral movement of plasma membrane-resident proteins (van Zanten and Mayor, 2015). Furthermore, sterol-enriched microdomains (and other mechanisms favouring complex formation) are thought to be relevant for the formation of signalling hotspots (Konrad and Ott, 2015; Ott, 2017; Cheng and Smith, 2019). Thus, another question is, whether the mobility of BRI1 is restricted by sterol-dependent microdomains or the actin cytoskeleton and whether this actually is relevant for the effective signal transduction in the plant.

1.2.2 Signalling integration with cell wall integrity sensing and phytosulfokine signalling

Brassinosteroid hormone signalling not only features fast elongation growth. BR signalling is involved in normal vascular patterning (Caño-Delgado et al., 2004; Ibañes et al., 2009). It also induces the transcription of many cell-wall related genes (Sun et al., 2010a) which in turn may stabilize the stretching cell wall. The plant primary cell wall is composed of cellulose microfibrils and the interconnecting matrix polysaccharides hemicellulose and pectin microfibrils (Cosgrove, 2005, 2018). A main component of pectin is homogalacturonan (HG) (besides rhamnogalacturonan-I and II) (Willats et al., 2001), which may form load-bearing Ca^{2+} crosslinks upon demethylesterification by PECTIN METHYLESTERASE (PME) (Wolf et al., 2012).

An impressive demonstration on the importance of feed-back signalling from the cell wall provides the strong induction of an PME inhibitor, which effectively reduces the number of pectin cross-links and thus leads to cell rupture in the root tip (Wolf et al., 2012). Interestingly, interfering with PME activity with the chemical epigallocatechin gallate (EGCG) leads to the activation of BR signalling and root waving, with BR mutants being hypersensitive to EGCG treatment which even leads to cell rupture (Wolf et al., 2012).

This indicates, that BR signalling is involved in a regulatory feedback signalling from the cell wall to modifying the root growth. Indeed, a LRR-receptor like protein named RECEPTOR LIKE PROTEIN 44 (RLP44) was found to be involved in the responses to cell wall damage by pectin modification (Wolf et al., 2012; Wolf et al., 2014). On the extracellular side, RLP44 comprises four LRRs, followed by a transmembrane domain and a short cytoplasmic tail. RLP44 can directly interact with BAK1 (Wolf et al., 2014) and at least in presence of BAK1, RLP44 can also interact with BRI1 (Wolf et al., 2014). Thus, RLP44 is involved in cell wall integrity sensing via manipulation of brassinosteroid signalling (Wolf et al., 2014).

Phytosulfokine hormone signalling mediates protoplast swelling (Stührwohldt et al., 2011; Ladwig et al., 2015), and is thus another integral part of cell elongation growth. PSK-α is a disulfated penta-peptide hormone, that is activated by cleavage and sulfation from a precursor peptide and sensed by different LRR-RLK receptors, e.g. PHYTOSULFOKINE RECEPTOR 1 (PSKR1) (Matsubayashi and Sakagami, 1996; Yang et al.,

2000; Lorbiecke and Sauter, 2002; Matsubayashi et al., 2002; Amano et al., 2007; Komori et al., 2009; Stührwohldt et al., 2011).

The receptor PSKR1 is structurally similar to BRI1 and its interaction with BAK1 is necessary for protoplast swelling (Ladwig et al., 2015). Remarkably, signal transduction is not restricted to phosphorylation events (Hartmann et al., 2014; Ladwig et al., 2015) and the interaction of PSKR1 with P-type proton pumps was shown (Ladwig et al., 2015). It also has both *in vivo* and *in vitro* GC activity, creating the second messenger cGMP (Kwezi et al., 2011), which in turn may activate the cation channel CYCLIC NUCLEOTIDE-GATED CHANNEL17 (CNGC17), thus leading to cell swelling (Ladwig et al., 2015). Additionally, the calcium-binding calmodulin can bind to PSKR1 (Hartmann et al., 2014), adding yet another layer of regulation. Consequently, down-stream signalling of the PSKR1 receptor is currently not well understood.

PSK hormone signalling also plays an important role in developmental processes. Already at nanomolar concentrations, PSK (together with auxin and cytokinin) induces plant cells to dedifferentiate and re-enter the cell cycle (Matsubayashi and Sakagami, 1996; Matsubayashi et al., 1999; Matsubayashi et al., 2002; Holzwart et al., 2018). The determination of the cell fate in the root vasculature of *A. thaliana* is important for water and nutrient uptake and is tightly regulated (Iyer-Pascuzzi and Benfey, 2009).

Currently, the precise interplay between brassinosteroid signalling, cell wall integrity sensing and phytosulfokine signalling is not well understood. A mechanism for signalling integration between those different pathways, however, seems likely, as they act concordantly during cell elongation growth, with BRI1 causing cell wall loosening, PSK for cell swelling and RLP44 for cell wall integrity signalling. Both the interconnectability of cell walls as well as PSKR1 receptor activity is modulated by calcium ions. Moreover, during the highly regulated root vasculature development, a precise signalling integration is necessary, with PSK mediating the re-entery into the cell cycle (Matsubayashi et al., 1999) and BR in the vascular differentiation of the shoot (Caño-Delgado et al., 2004; Ibañes et al., 2009). Importantly, both BRI1 and PSKR1 interact with BAK1, and BAK1 in turn interacts with RLP44. Therefore, questions on the specificity and the function of RLP44 arises.

Protein-protein interaction by FRET-FLIM

Protein-protein interaction studies provide an important tool for a better understanding of signal transduction pathways.

The spectroscopic method of Förster resonance energy transfer (FRET) by fluorescence lifetime imaging (FRET-FLIM) has the advantage, that the interaction of two proteins can be tested *in vivo* with high spatial and temporal resolution (Medintz and Hildebrandt, 2014; Somssich et al., 2015), resolving even transient interactions.

FRET describes the energy transfer, without emission of a photon, from a donor-fluorophore (D) to an acceptor fluorophore (A) (Förster, 1948; Medintz and Hildebrandt, 2014). This is only possible for fluorophore pairs with spectral overlap (between donor

emission and acceptor absorbance) and at small distances between them, typically below 10 nm. The Förster distance (R_0) describes the distance between D and A, where 50% of the maximally possible energy transfer (FRET efficiency) occurs. However, additionally the relative orientation of the respective dipoles of A and D strongly influence the FRET efficiency (Medintz and Hildebrandt, 2014).

If A drains energy from D, then the fluorescence intensity of D decreases, while A can then emit photons itself, noticeable as an increased fluorescence intensity at a higher wavelength compared to the donor. This effect is measured in intensity-based FRET assays.

FRET also influences the fluorophore's excited state life time (FLT), i.e. the time the fluorophore stays in the excited state undergoing vibrational relaxation/internal conversion before emitting a photon. The alternative relaxation path from D to A provided by FRET consequently decreases the radiative decay rate of the donor, quantifiable as an apparently reduced FLT, which is the basis for FRET-FLIM experiments (Noomnarm and Clegg, 2009; Medintz and Hildebrandt, 2014). However, for FRET-FLIM interaction studies, a donor fluorophore with specific physico-chemical characteristics (e.g. monoexponential decay) has to be fused to the protein of interest.

FRET-FLIM measurements thus provide a spectroscopic method, to test whether two proteins are in close spatial proximity *in vivo*, but how close exactly can rarely be precisely determined, especially in live-cell imaging. Provided, the physico-chemical environment of the fluorophore did not change (e.g. temperature), a decrease of the fluorescence lifetime means they are in close spatial proximity (interact). However, the absence of FRET does not necessarily mean they do not interact, as the relative orientation of the two fluorophores, and thus the dipole orientation factor, may be unfavourable. FRET-FLIM has become a well-established method.

However, it is currently limited to test the interaction of two proteins *in vivo* in plants. But many signalling transduction processes involve the interaction of three proteins, e.g. as earlier described for BRI1, BIR3 and BAK1 (Imkampe et al., 2017; Großeholz et al., 2019). Especially for BAK1 the question arises, whether it is located together with BRI1 and RLP44 at the same time in the same spot, or only at different points in time. Thus, a test for trimeric protein interaction may help to elucidate the spatial organization of proteins in the plasma membrane (e.g. distinct nanodomains for specific signalling processes).

1.3 Signalling integration of other pathways

Proteins may modulate the state of the DNA (e.g. methylation, acetylation), the number of mRNA copies (e.g. transcription, splicing, degradation), the state of other proteins (involved e.g. in signal transduction, ion fluxes, metabolism, degradation) and may even sense intracellular (e.g. hormones, damage) and extracellular cues (e.g. light, pathogen associated molecular patterns) . Consequently, protein-protein interaction studies may be relevant in many different biological settings.

The timely transition from the vegetative to the reproductive state is an important step for the survival of a plant species, as it synchronizes flowering, ensures the attendance of pollinators and the seed maturation during favourable environmental conditions (Arongaus et al., 2018). The model plant *Arabidopsis thaliana* is a facultative long-day plant, meaning that it flowers early under long-day conditions, but will also flower later under short-day conditions (Arongaus et al., 2018).
The expression profile of CONSTANS (CO) is under circadian control, with its mRNA level peaking 16 hours after the light was switched on, independent of the prevailing current light regime (Suárez-López et al., 2001; Mathieu, 2009). At the same time, CO protein is proteasomal degraded in darkness by an E3 ubiquitin ligase CONSTITUTIVELY PHOTOMORPHOGENIC 1 (COP1) (Laubinger et al., 2004; Jang et al., 2008; Liu et al., 2008).

Consequently, significant CO protein levels can only accumulate under long-day conditions. Then, CO mediates the transcription of FLOWERING LOCUS T (FT) which acts systemically and moves from the leaves to shoots (Wigge et al., 2005; Corbesier et al., 2007; Jaeger and Wigge, 2007; Mathieu et al., 2007; Turck et al., 2008; Song et al., 2015; Arongaus et al., 2018). Thus, the formerly vegetative programme of the shoot apical meristem is reprogrammed to reproductive, terminated growth (flowers). Another central integrator, besides FT (and others), for this transition is LEAFY (LFY) (Kobayashi and Weigel, 2007). The expression of LFY precedes the expression of homeotic genes such as AGAMOUS and APETALA3, which specify organ identity within the flower (ABC model) (Weigel et al., 1992; Kobayashi and Weigel, 2007; Bowman et al., 2012).

Currently, the specific UV-dependent regulation of flowering induction is hardly studied, as the light in growth chambers rarely includes UV-B light (Arongaus et al., 2018). The UV-B receptor UV RESISTANCE LOCUS 8 (UVR8) monomerizes upon UV-B absorption, interacts with COP1 and can be deactivated by re-homodimerization mediated by REPRESSOR OF UV-B PHOTOMORPHOGENESIS 1 (RUP1) or RUP2 (Favory et al., 2009; Gruber et al., 2010; Rizzini et al., 2011; Cloix et al., 2012; Heijde and Ulm, 2013; Yin et al., 2015; Jenkins, 2017; Arongaus et al., 2018; Podolec and Ulm, 2018). However, the precise molecular mechanism of how the repression of flowering is released under inductive photoperiods by UV-B, and the precise role of RUP1 and RUP2, is currently not well understood.

Remarkably, pathogens have developed diverse strategies to manipulate plant hormones, such as auxin (and cytokinin), in order to induce plant architecture changes that are beneficial for pathogenesis and colonization (e.g. *Agrobacterium tumefaciens*, truffels, *Taphrina spp.*,) (Sziraki et al., 1975; Splivallo et al., 2009; Spaepen and Vanderleyden, 2011; Aryal et al., 2019). In the root of *Arabidopsis thaliana*, transporters fulfil many different functions, such as primary active and secondary active transport of nutrients/ions as well as transport of hormones (Gaedeke et al., 2001; Noh et al., 2001; Luschnig, 2002; Blakeslee et al., 2005; Masclaux-Daubresse et al., 2010).

The pleiotropic drug resistance-type ATP BINDING CASETTE type G (ABCG) transporter, ABCG36 (aka. PDR8 or PEN3), is thought to mediate the export of a

few structurally unrelated substrates, including indole-3-butyric acid (IBA), an auxin or auxin precursor (Aryal et al., 2019; Jasiński et al., 2001; Ludwig-Müller, 2007; Bednarek et al., 2009; Krattinger et al., 2009; Strader and Bartel, 2009, 2011; Bienert et al., 2012; Lu et al., 2015).

Mutant alleles of ABCG36 show altered responses to pathogens and in response to flagellin 22 (flg22), a pathogen-derived molecule (Aryal et al., 2019; Kobae et al., 2006; Stein et al., 2006; Bednarek et al., 2009; Clay et al., 2009; Jelenska et al., 2017). But it was also identified in screens for hypersensitivity toward auxin transport inhibitors and auxinic compounds, such as IBA, which alters the root morphology inducing more lateral roots (Aryal et al., 2019; Strader and Bartel, 2009, 2011).

Currently, the underlying molecular mechanism of how ABCG36 is involved in both auxin signalling and immune responses is not well understood. Also, the precise substrate is enigmatic as well as the activation mechanism of the channel.

2 Aim of this work

The brassinosteroid hormone signalling pathway is very well described at a constitutive level. However, it is not clear, how the same set of proteins mediate a differential growth regulation on tissue level (in space) and at what time scale (in time) they act. My studies therefore aim to elucidate the underlying molecular mechanisms that are responsible for differential growth regulation, to spatially resolve the apoplastic pH changes in response to brassinosteroid (BR) signalling, and to gain first insights on the downregulation of signalling by several approaches. Namely, with physiological measurements together with computational modelling. Computational models provide a powerful tool to predict new features of well-established pathways (Pacifici et al., 2018). Therefore, the ordinary differential equation (ODE)-based model of the BR signalling-related elongation growth, established by Ruth Großeholz from the research group Kummer at the BioQuant Heidelberg, should be refined, as the interplay between simulations from models and the experimental testing was expected to lead to a better understanding of the complex BR signalling network.

Also, the spatial organisation of the BR receptor together with its signalling partners (e.g. co-receptor) in the plasma membrane is currently not well understood. Hence, I aim to elucidate in cooperation with Sven zur Oven-Krockhaus from the Institute of Physical and Theoretical Chemistry at the University of Tübingen, how the dynamics of the BRI1 receptor behaves in the plasma membrane regarding its lateral movement with super-resolved single-particle tracking (sptPALM) in *Arabidopsis thaliana* and *Nicotiana benthamiana*. If its lateral mobility is restricted, the underlying molecular mechanism (e.g. involvement of actin microfilaments or sterol-rich microdomains) should be examined more closely. Currently, only few experimental evidences for a functional relationship between the spatiotemporal organisation of proteins in the plasma membrane and the signalling output is available. Therefore, I aim to elucidate, by performing physiological root measurements whether the disruption of sterol-rich microdomains impairs BR signalling and responses.

The RLP44, which is involved in cell wall integrity control, interacts with the co-receptor BAK1, and BAK1 in turn interacts with the BR receptor BRI1. However, it is not clear yet, whether the three proteins are located together at the same time and in the same domain in the plasma membrane, thus forming a hetero-trimeric complex. To this end, I aim to develop and establish a FRET-FLIM-based trimeric interaction approach *in vivo* in *Nicotiana benthamiana* leafs, again with the support of Sven zur Oven-Krockhaus. This method may provide a tool for the elucidation of the spatial protein organization on a nanoscale in the plasma membrane (e.g. in distinct nanodomains for specific signalling processes) for brassinosteroid signalling or other pathways.

Protein-protein interaction studies provide a powerful tool to better understand the information integration of different signalling pathways. For instance, the precise molecular mechanism, how RLP44 may be involved in brassinosteroid and phytosulfokine hormone signalling, is currently unknown. Consequently, I aim to support Eleonore Holzwart in the research group Wolf at the COS Heidelberg in her efforts to elucidate, whether RLP44 still interacts with novel mutations in the BRI1 receptor and how RLP44 may balance the two pathways. Also, I aim to support Anne Mohrholz in the research group Harter at the ZMBP Tübingen and Adriana Arongaus in the research group Ulm at the University Geneva in their efforts, to better understand the molecular mechanisms that mediate the transition from vegetative to reproductive plant growth as well as Bibek Aryal in the research group Geisler at the University of Fribourg in the efforts to elucidate the dual role of the ABCG36 transporter in auxin hormone distribution and the immune response to pathogens.

3 Results and discussion

3.1 Brassinosteroid signalling

3.1.1 Quantitative and computational description

Glöckner, N.[1]; Großeholz, R.[1]; Wanke, F.; Jaspert, N.; Shabala, L.; Shabala, S.; Kummer, U.; Harter, K. (2019) Quantitative description and computational modelling of the BRI1 response module controlling cell elongation growth. *In preparation for submission.*

[1] Authors contributed equally

Großeholz, R.; Feldman-Salit, A.; Wanke, F.; Schulze, S.; Glöckner, N.; Kemmerling, B.; Harter, K.; Kummer, U. (2018) Specifying the role of BAK1-interacting receptor like kinase 3 in brassinosteroid signaling. *Journal of Integrative Plant Biology.*

Computational modelling is a powerful tool for analysing a system of interest *in silico* and can thus decisively help to better understand biological signal transduction processes. In particular, models consisting of ordinary differential equations (ODEs) contain detailed knowledge on the kinetic parameters of a system allowing for the analysis of the dynamics and regulation of the system. Detailed information of the model structure, parameter estimation and simulations can be found in the dissertation of Ruth Großeholz. (Großeholz 2018).

We established an ODE-based computational model of the brassinosteroid signalling events in COPASI leading to proton extrusion and membrane potential (E_m) hyperpolarization. Thus, we constructed a precise representation of the currently described steps in the fast, BR/BRI1 response model leading to the activation of the P-type proton pump and thus hyperpolarisation of the plasma membrane and acidification of the extracellular space. In the absence of BR, the receptor BRI1 and the co-receptor BAK1 are inhibited by BIR3. Using computational modelling, the potential complexes between the cytoplasmic domains of BRI1, BAK1 and BIR3 were simulated (Großeholz et al., 2019). Both calculations and experimental data show, that BIR3 interacts with BAK1 and BRI1 and that the BAK1-BIR3 interaction is clearly favoured (Großeholz et al., 2019). Interestingly, BIR3 and BAK1 share the same binding site, suggesting competition between BRI1 and BIR3 for the active site, while at the same time, BRI1 can bind to an additional site on the flank of BAK1 (Großeholz et al., 2019). Thus, a simple rotation of BAK1, shifting the catalytic side to BRI1 upon increased affinity by hormone

binding, may be enough for signalling activation (Großeholz et al., 2019).

In the following, all numbers in brackets indicate a reaction in the model, leading to activation of the proton pump. Upon binding of the brassinolide (BL), a potent BR, to BRI1 the inhibitor BIR3 is released from BAK1 and BRI1 (reaction number [3], [4]). Furthermore, BL binding to BRI1 [5] leads to phosphorylation of BIK1 [7], the dissociation of BKI1 from the PM into the cytoplasm [6] and the full interaction/hetero-dimerization of BRI1 and BAK [9] which leads to Ser/Thr auto- and trans-phosphorylation [10]. In addition, the C-terminal tail of the proton pump AHA is phosphorylated [11], which in turn leads to the up-regulation of its activity, proton extrusion into the apoplast (extracellular space) [1] and $E_m$hyperpolarization. This is counter-weighted by proton leakage back across the PM [2] and probably by cation import by a transporter (not incorporated yet). Also, deactivation rates are included [d1-d7].

Thus, we were able to describe the E_m hyperpolarization in response to BL application at cellular level. Unknown model parameters were fitted to data from Caesar et al. (2011), which allowed a precise reproduction of the membrane potential over time after 10 nM BL hormone treatment. To implement the cell elongation growth, the parameters of the growth function were adjusted to describe the data by Beemster & Baskin (1998), and our strain rates of 32% h^{-1} reproduced the reported strain rate of 30% h^{-1}.

It is currently not clear, how a differential response to BR hormones is mediated along the root axis. As the measurement of BR gradients at high spatial resolution is currently not possible, we tested the hypothesis, that the relative abundance of the different proteins in the BR/BRI1 perception and response module is the cause for the differential cellular response along the root axis. Therefore, we quantified the relative protein abundance of *pBIR3*-expressed BIR3-GFP in the *bir3-2* mutant (Imkampe et al., 2017) and *pAHA2*-expressed AHA2-GFP in the *aha2-4* mutant (Fuglsang et al., 2014) by applying biochemical and cell biological approaches. As an reference, we used the *pBRI1::BRI1-GFP* line (Friedrichsen et al., 2000), in which the absolute number of BRI1-GFP receptor molecules per μm^2 of the plasma membrane had been quantified before (van Esse et al., 2011; van Esse et al., 2012).

In 5-days-old seedlings, the fluorescence of BIR3-GFP was 1.4 x that of BRI1-GFP in both the meristem and the outer cell layers 250 µm from the root tip (epidermis/cortex). The AHA2-GFP fluorescence was almost completely absent in the meristem and 0.3 x that of BRI1-GFP in the outer cell layers 250 µm from the root tip.

To assess, whether these amounts were representative for the entire root, we quantified the fusion proteins in total extracts and microsomal fractions of roots using a GFP antibody and an IR-Dye coupled secondary antibody with high linear dynamic range (Wang et al., 2007). The amount of BIR3-GFP was approx. 1.5 x the abundance of BRI1-GFP, revealing similar results as with fluorescence quantification by confocal microscopy. However, the amount of AHA2-GFP was approx. 2.8 x that of BRI1-GFP, contrasting with the results of fluorescence quantification. We tested, whether AHA2-GFP accumulation was indeed increased in mature root tissues and quantified

the fluorescence intensity of BRI1-GFP and AHA2-GFP in the root hair zone (RHZ) (middle of the root) and below the hypocotyl and found respective ratios of 5 x and 3 x.

We thus concluded, that the AHA2 expression increases with the distance from the root tip. This hypothesis was substantiated by the steady-state absolute transcript amount found on eFP browser (http://bar.utoronto.ca/efp/cgi-bin/efpWeb.cgi), which also indicated that AHA1 and AHA2 are the most important P-type proton pumps in roots with similar expression levels. Importantly, the AHAs:BRI1 ratio strongly changed along the root axis being low in the MZ and high in the EZ, whereas the BIR3:BRI1 ratio stayed constant.

We therefore were interested, whether the model could provide predictions, which parameters of the BRI1 response module might implement strong positive or negative effects on the membrane potential. In a scaled sensitivities test, a strong positive effect was consistently predicted for the activity of the proton pumps, the AHA1:AHA2 ratio, the BRI1 receptor density and the AHA2:BRI1 ratio. A consistent negative effect was found for increased proton leakage back into the cell, increased inhibition by the C-terminal tail of the AHAs, a lower affinity for the BL binding to the receptor (BRI1) and higher amounts of BIR3 in comparison to BRI1.

This prompted us to test, whether BL-triggered, spatially resolved proton extrusion and apoplast acidification can be in fact observed. With proton-specific microelectrode ion flux estimation (MIFE) measurements on 5-days-old seedlings, we indeed observed proton efflux in response to 10 nM BL only in the elongation zone (400-600 µm from the root tip) of Col-0 seedlings but not for *bri1-301* mutant plants, with a strongly impaired kinase activity of BRI1 (Zhang et al., 2018)(note: low sample numbers). Also, in the root hair zone no significant increase in proton efflux was detected. We hypothesize, that the relatively small amount of BRI1 receptors in comparison to the expression level of the P-type proton pumps is too small, to induce a significant efflux. Also, it has to be assumed, that the proton pumps are active to mediate primary active transport to allow secondary active nutrient and ion uptake. As method complementary to MIFE, we measured the apoplastic pH by ratiometric confocal laser scanning microscopy after staining the roots with 8-hydroxypyrene-1,3,6-trisulfonicacid-trisodiumsalt (HPTS) (Barbez et al., 2017). The presence of both 0.1 nM and 1 nM BL for 1 h resulted in a decrease of the apolastic pH in the elongation zone roots compared to the elongation zone of mock-treated roots. Surprisingly, only addition of 0.1 nM BL led to a significant decrease in the ratiometric intensity in the elongation zone after 1h in two biological replicates (small sample numbers). The average pH of the mock-treated plants was 5.46 in the meristematic zone of the root tip and 5.35 in the elongation zone. The pH of the roots treated with 0.1 nM BL was 5.33 in the tip and 5.16 in the EZ.

If the prediction of the computational model is correct, apoplast acidification and membrane potential (E_m) hyperpolarization depend on the number (density) of functional BRI1 receptors. Therefore, we determined by MIFE and ratiometric HPTS measurements, whether BRI1 is important for the regulation of the apoplastic pH in the absence of exogenously applied BL. In MIFE measurements, a strong gradient of proton

fluxes from the root tip to the elongation zone, with an onset of proton efflux approximately 450 µm from the root tip were observed for the wild type. In contrast, this gradient was strongly diminished along the root axis of *bri1-301* seedlings. Comparable results were obtained by the HPTS measurements, with a less pronounced pH gradient between the meristematic zone and the elongation zone for *bri1-301* mutant seedlings compared to wild type (low sample numbers). In summary, this indicates that the presence of kinase-active BRI1 is required for the establishment of the proton flux and pH gradient along the axis of the root. Also, the predictions of the computational model on the significance of the AHA:BRI1 ratio and the BRI1 receptor density for apoplast acidification, pH-linked $E_m$hyperpolarization and elongation growth were experimentally supported by our MIFE and ratiometric HPTS measurements.

If, indeed, the AHA:BRI1 ratio establishes the competence for BL-induced apoplast acidification, $E_m$hyperpolarization and eventually elongation growth in otherwise non-responsive cells, then the overexpression of a proton-pump should induce cell elongation growth in the meristem. Therefore, we computationally modelled how the ectopic expression of AHAs in the cells of the meristematic zone would affect their elongation growth compared to meristematic cells that have wild type AHA:BRI1 ratios. In an ODE model, the application of 10 nM BL did not lead to a significant elongation response of meristematic cells expressing the wild type AHA:BRI1 ratio. However, AHA-OE in meristematic cells treated with 10 nM BL quickly started to elongate, yielding a cell length of 40 µm for AHA-OE in four hours (and 8 µm for wild type cells).

To corroborate the *in silico* results, we were able to access published data. Pacifici and colleagues (2018) had established a transgenic *Arabidopsis* line, which enables the dexamethasone (DEX) inducible overexpression of AHA2 in the root. Indeed, 20 hours after DEX treatment, cells in the meristematic zone started to swell and elongate in comparison to mock-treated roots (Pacifici et al., 2018), thus decreasing the size of the meristematic zone. This supports the prediction from our model.

In the future, it will be interesting to measure the apoplastic pH over the time in response to DEX-induced AHA2 overexpression. If indeed the AHAs:BRI1 ratio is decisive (and not the AHAs abundance alone), then loss of BRI1 should counteract this effect. It will be interesting to investigate the apoplastic pH upon DEX-treatment of *bri1-301* mutants transformed with *pUBQ::AHA2-GR* compared to the published *pUBQ::AHA2-GR* line. Alternatively, an additional shrinkage of the meristematic zone for DEX-treated seedlings transformed with both *pBRI1::BRI1-GFP* and *pUBQ10::AHA2-GR* could be tested. In summary, our data support the notion, that the AHA:BRI1 ratio determines the onset and capacity for cell elongation growth.

3.1.2 Dynamics and organization of the signalling components

Glöckner, N.[1]; zur Oven-Krockhaus, S.[1]; Meixner, A.J., Harter, K.: (2019) Single-particle tracking photoactivated localization microscopy analysis of BRASSINOSTEROID INSENSITIVE 1 receptor (BRI1) dynamics and BRI1-related microdomain functions in plants. *In preparation for submission.*

[1] Autors contributed equally

Recently, studies on the dynamics and sub-compartmentation in the plasma membrane of the BRI1 receptor employing GFP, or in combination with BAK1, employing an RFP fusion protein, have been published (Bücherl et al., 2013; Wang et al., 2015; Hutten et al., 2017). However, GFP-based variable-angle epifluorescence microscopy (VAEM) for these purposes is suboptimal, as it is restricted to discuss receptor complexes since it cannot resolve single molecules. Here, we describe the establishment of single-particle tracking VAEM combined with photoactivated localization microscopy (PALM) (spt-PALM) *in planta*. Currently, the evidence on the biological relevance of microdomains for signal transduction is scarce. Here, we provide first (preliminary) evidence, that the disruption of microdomains with the sterol-extracting agent methyl-beta-cyclodextran (MβCD) attenuates brassinosteroid signalling, giving first physiological evidence that the disruption may reduce the efficiency of signal transduction.

To test the new, custom-made VA-TIRF-PALM microscopy setup, first measurements of published *A. thaliana* plant lines expressing PIP2;1-mEOS, an aquaporin, and LTI6a-mEOS under the control of the *PIP2;1* promoter were performed (Hosy et al., 2015). Single-particle tracks were recorded (sptPALM). The average mean square displacement (MSD) analysis of all tracks yielded a higher MSD of the small, single trans-membrane protein LTI6a-mEOS than for the six trans-membrane domains spanning aquaporin PIP2;1-mEOS, thus reproducing previously published results (Hosy et al, 2015). To quantify the movement behaviour, the first ten points of the MSD were fitted to MSD $= 4D(t_{lag})^{\alpha}$ with D as diffusion coefficient, t_{lag} as lag times and α as coefficient, and classified as undergoing free diffusion for $0.9 > \alpha > 1.1$, as superdiffusive with $\alpha > 1.1$ and as subdiffusive with $\alpha < 0.9$ (Jean-Yves Tinevez). Even the small LTI6a-mEOS showed all three forms of movement behaviour, indicating that this may be a sensitive method to detect differences in movement behaviour. Previously, an apparent diffusion coefficient similar to that of lipids in the plasma membrane with 0.03-0.6 μm^2 s^{-1} was shown for LTI6a-mEOS (Dugas et al. 1989; Hosy et al. 2015). Indirect effects imposed on LTI6a may be an explanation for the prescence of subdiffusive or superdiffusive movement behaviour, so that e.g. subdiffusive microdomains temporarily affect its movement.

Next, *pUBC::BRI1-mEOS* constructs were generated to later be tested in transgenic *A. thaliana* lines. To test the usability of BRI1-mEOS for sptPALM, we performed spt-PALM measurements in epidermal leaf cells of the heterologous *N. benthamiana* system two days after transient transformation. The tracks of ten epidermis cells were classified as before for LTI6a-mEOS. The largest subpopulation, comprising 70% of BRI1-mEOS molecules, showed a subdiffusive behaviour, the second largest, comprising 20% of the

receptors, free diffusion and the smallest, with 10%, superdiffusive behaviour. Hence, the vast majority of BRI1-mEOS molecules were restricted in their free lateral movement in the PM of *N. benthamiana* cells.

The BRI1 receptor was reported to increase its interaction with BAK1 upon BR treatment, leading to hetero-oligomerization (Nam and Li, 2002; Wang et al., 2005b; Yun et al., 2009; Bücherl et al., 2013) which may lead to an altered dynamic in the PM. We therefore tested whether BRI1-mEOS shows changes in its mobility upon treatment of transiently transformed *N. benthamiana* cells with 1 nM brassinolide (BL), the most active form of the BRs, for 30 minutes. The actin cytoskeleton is located right below the PM and was proposed to separate the PM into smaller subcompartments (van Zanten and Mayor, 2015; Weinberg and Puthenveedu, 2019). We therefore assessed the diffusion coefficient of BRI1-mEOS in *N. benthamiana* leaf cells after 30 minutes of 25 µM latrunculin B (LatB) treatment. LatB inhibits actin polymerisation, and after 30 minutes treatment with 25 µM LatB, all but the largest actin filament bundles are dissolved in *N. benthamiana* leaf cells (Rocchetti et al., 2014). Lastly, we asked whether the disturbance of potential microdomains affects the dynamics of BRI1-mEOS in the PM by treatment of the cells with methyl-β-cyclodextran (MβCD) for 30 minutes. MβCD forms ring-like structures with an apolar core and is suggested to act as an acceptor compartment for sterol (Yeagle, 2016). The prolonged treatment thus disrupts the spatial organisation of the PM. After 30 minutes of treatment with 10 mM MβCD, approx. 30 % of the sterol content was depleted in *A. thaliana* roots (Li et al., 2011).
Plotting the apparent log-scaled diffusion coefficient against the occurrence of the observation revealed, that no clear bimodal separation into a mobile and immobile fraction was visible for any treatment. Thus, no reasonable separation in a mobile and immobile fraction was possible. Wang and colleagues (2015a) found by classical VA-TIRF microscopy that about 60 % of BRI1-GFP particles were immobile and showed restricted diffusion with an average "motion range" of 0.5 µm. The remaining 40 % showed long distance movement with an average "motion range" of 1 µm. However, the fitted bimodal distribution of Wang and colleagues (2015a) was essentially a unimodal distribution, indicating that their value for the diffusion coefficient of the mobile fraction may be artificial. It is questionable whether the fit of a bimodal distribution is a good method of evaluation, if the majority of single-particles shows restricted diffusion and no clear-cut second subfraction can be found. Forcing a bimodal fit may introduce artefacts instead of representing the *in vivo* situation. To my knowledge, the only instance in literature, where a clear-cut mobile fraction with a bimodal fit was found, was by Hosy and colleagues (2015) for plasmolysis of the plasma membrane from the cell wall, emphasizing the importance of the cell wall.

To extract the modal diffusion coefficient of the traces, a normal fit was applied to the log (D) distribution for each cell and the maximum of the fit was calculated. However, no statistically significant differences in the diffusion coefficient were found for any treatment compared to the two mock-treatments in three biological replicates or when combining the replicates. A mild effect was found for the osmolar control, inducing plasmolysis, supporting previous observations (Hosy et al., 2015). As the apparent diffusion

coefficient of 0.002 μm^2 s^{-1} was even lower than that of AtPIP2;1-EOS with 0.0047 μm^2 s^{-1} (Hosy et al. 2015), BRI1-mEOS in *N. benthamiana* leaves can be characterized as immobile. This supports, that BRI1 is located in distinct micro-/nanodomains in the PM of plant cells in the absence of exogenously applied hormone. The mammalian TRANSFORMING GROWTH FACTOR-BETA (TGF-β) receptor TβRI-EGFP was found to have a diffusion coefficient of 0.049 μm^2 s^{-1} (Zhao et al., 2018). Interestingly, only when coexpressing TβRII, a significant decrease to 0.015 μm^2 s^{-1} after TGF treatment was found (Zhao et al., 2018). Both BR and TGF signalling show the same signal transduction mechanism, including hetero-oligomerization (Bücherl et al. 2013; Massagué 1998; Eckardt 2005; Ehsan et al. 2005), indicating that possibly, in the heterologous system, same stoichiometries of e.g. co-receptors are necessary for significant changes in the movement behaviour.
In summary, the transient expression system in *N. benthamiana* appears not to be suitable for distinguishing potential subtle changes in the dynamics of the BRI1-mEOS receptor fusion in response to hormone treatment, depolymerization of actin filaments or microdomain disruption. This observed insensibility is in contrast to the transient expression of BRI1-GFP and the receptor FLS2-mCherry in *N. benthamiana*, which revealed different movement behaviour in kymographs of the hormone receptor from the immune receptor FLS2-GFP (Bücherl et al., 2013). Before the heterologous system in *N. benthamiana* can be used in the future, measurements whether e.g. LTI6a-mEOS and PIP2;1-mEOS yield a different apparent diffusion coefficient are necessary.

The measurements of the dynamics of the BRI1 receptor in the PM of *N. benthamiana* cells may not be representative for the dynamics in *A. thaliana* cells. Until now, no physiological evidence was provided, whether the disruption of sterol-dependent microdomains by MβCD indeed affects the physiological response to BR signalling. As a first glimpse, physiological measurements of the root length were performed. Therefore, 5-days-old seedlings of wild type Col-0, *bri1-301* mutants with a reduced kinase activity (Zhang et al., 2018) and the mild BRI1-GFP overexpressor (*pBRI1::BRI1-GFP*) (Friedrichsen et al., 2000) were transferred to plates containing 0.1 mM MβCD plates supplemented with and without 1 nM BL. The treatment with 1 nM BL significantly reduced the normalized root growth of the BRI1-GFP line compared to that of *bri1-301* and Col-0 seedlings, as inhibitory levels are reached for BRI1-GFP (González-García et al., 2011).

Most importantly, the presence of MβCD attenuated the inhibitory effect of 1 nM BL in the BRI1-GFP seedlings, indicating that MβCD attenuates brassinosteroid signalling. A second effect of enhanced BL signalling is the appearance of root waving (González-García et al., 2011). The quantification of root waving revealed, that the increased root-waving of BRI1-GFP on 1 nM BL (compared to *bri1-301* and Col-0) was abolished for the combined treatment of the BRI1-GFP seedlings with 0.1 mM MβCD and 1 nM BL and no statistical difference to the control group was detected anymore. This indicates, that sterol-dependent microdomains are important for the effective brassinosteroid hormone signalling transduction, as their disruption attenuated hormone signalling. To our knowledge, only one study has provided similar physiological evidence (Xue et al.,

2018), where dark-grown seedlings irradiated with blue light had a reduced bending angle after sterol depletion.

In the future, it will be interesting to observe the dynamics of BRI1-mEOS in *A. thaliana* seedlings in response to hormone treatment, actin depolymerization and the disruption of sterol-microdomains as well as plasmolysis. If even in *A. thaliana* no bimodal distribution is visible, the mode of evaluation by Jean-Yves Tinevez may be an option. Also, more detailed studies on the physiological effect of MβCD treatments on the effect of brassinosteroid hormone signalling including the measurement of the apolastic pH will help to better understand the importance of the spatial distribution of the BRI1/BR response module. The precise mode of action of MβCD is not clear (Kierszniowska et al., 2009; Fantini and J. Barrantes, 2018) and experimental controls for the receptor levels have to be included.

3.1.3 Three-fluorophore FRET-FLIM

Glöckner, N., zur Oven-Krockhaus, S.; Wackenhut, F.; Burmeister, M.; Wanke, F.; Holzwart, E.; Wolf, S.; Harter, K. (2019) Three-fluorophore FRET-FLIM enables the study of trimeric protein interactions and complex formation with nanoscale resolution in living plant cells. *In preparation for submission.*

To study protein-protein interactions, Förster resonance energy transfer (FRET) with fluorescence lifetime imaging microscopy (FLIM) has become a frequently used method. However, it is limited to protein pairs, which is regrettable, as many signal transduction processes require the interplay of three or more proteins at the same time. Here, we describe the establishment of three-fluorophore FRET-FLIM *in vivo* in *N. benthamiana* leaves on the example of RLP44, BRI1 and BAK1, showing that they, indeed, form a trimeric complex with less than 15 nm between them.

First, considerations on the dynamic range of our chosen fluorophores help for the interpretation of the obtained data and exemplary dimensions of the plasma membrane-resident proteins are shown. In an arduous procedure, we show in spectra, that FRET for interacting protein is detectable, and that indeed, an intermediate fluorophore increases the dynamic range. The more elegant way, however, provides the measurement of the donor fluorescence lifetime to assess trimeric complex formation, as no corrections for spectral bleed-through and cross-excitation are then necessary. To my knowledge, three-fluorophore FRET-FLIM was never shown in plants before and in the mammalian field, none has used donor fluorescence lifetime imaging, even though a wide range of three-fluorophore-sets are published (Haustein et al., 2003; Galperin et al., 2004; Hohng et al., 2004; He et al., 2005; Shyu et al., 2008; Seidel et al., 2010; Sun et al., 2010b; Pauker et al., 2012; Fábián et al., 2013; Hoppe et al., 2013; Wallrabe et al., 2013; Fried et al., 2014; Scott and Hoppe, 2015; Kuo et al., 2018). Also, of the current three-fluorophoreFRET applications, only few have considered the impact of different stoichiometries and spatial

arrangements (e.g. in a plasma membrane setting).

As the physico-chemical parameters of the fluorophores are important for FLIM measurements (e.g. a monoexponential decay) and fast maturation rates are beneficial (Hoppe et al., 2013), mTurquoise 2 (mTRQ2) was chosen as donor fluorophore (D), mVenus (mVEN) as intermediate fluorophore (A1) and mRFP as second acceptor fluorophore (A2). For the expression of D and A1, the 2in1 vector system was used to ensure similar expression levels (Grefen and Blatt, 2012; Hecker et al., 2015; Lin et al., 2018). To elucidate, between which fluorophore pairs Förster resonance energy transfer (FRET) is possible, we plotted the absorption and emission spectra in one graph. Energy transfer was possible between D-A1, A1-A2 and D-A2 and calculation of the Förster distances assuming a refractive index of 1.4 and a dipole orientation factor of 2/3 (Hink et al., 2002) yielded values of respectively 5.7 nm, 5.1 nm and 4.6 nm. Thus, highest FRET efficiency was obtained between D-A1 and lowest between D-A2.

For large distances between D and A2, however, no direct FRET is possible. At large distances, the introduction of an intermediate acceptor A1 should increase the dynamic range between D-A2. To estimate this long-range effect, an effective R_0 ('adjusted R_0') between D and A2 was calculated with the intermediate acceptor A1 between them (Haustein et al., 2003), which resulted in an increase from 4.6 nm to 9.2 nm. Of course, there is one Förster distance - the 'adjusted R_0' was only taken as an estimate on the effect of the dynamic range. Haustein and colleagues (2003) had fixed distances between the fluorophores, whereas an *in vivo* setting allows free movement of the fluorophores. Therefore, the average FRET efficiency for all possible positions of A1 between the D and A2 was calculated separately for each distance between D-A2. This resulted in a reduced apparent Förster distance for D-A2 with A1 positioned between them ('adjusted R_0') from 9.2 nm to 6.8 nm. Lastly, the effect of FRET-favouring fluorophore stoichiometries and the influence of a changed dipole orientation factor for plasma membrane-resident proteins was estimated with an 'adjusted R_0' as proposed (Bunt and Wouters, 2017).

A projection of the D-A2 FRET efficiency with variable position of A1 to a stoichiometry of 1:5 in a planar system (Bunt and Wouters, 2017) showed, that 10% FRET would occur at distances below 15 nm. Hence, in an *in vivo* setting with favourable stoichiometries of plasma membrane-resident proteins, long-range FRET can roughly span up to 15 nm. Even though many variations of three-fluorophore FRET are published in the mammalian field (see references earlier), only few have tried to estimate the dynamic range of their system or considered how changed spatial arrangements or donor-to-acceptor ratios may affect the dynamic range. Another study estimated the impact of stoichiometry to be even more severe, so that with multiple acceptors (n) proximal to a single donor fluorophore, the operational R_0 becomes n-times R_0 (Jares-Erijman and Jovin 2003; Müller et al. 2013). Until now, no study circumvented the direct FRET between D-A2 for genetically encoded fluorophores (He et al., 2005; Sun et al., 2010b; Pauker et al., 2012; Hoppe et al., 2013; Wallrabe et al., 2013; Kuo et al., 2018). Future studies may consider using mCherry instead of mRFP. Especially, since mCherry only weakly oligomerizes even under harsh oxidizing environments such as in the lumen of the ER

and Golgi stacks (Costantini et al., 2015).

In an arduous procedure, we demonstrated that FRET from D-A1 and D-A2 can be detected in spectra specifically for interacting RLP44-BRI1 and RLP44-BAK1 in comparison to the negative-control FLAGELLIN SENSING 2 (FLS2) and that indeed an intermediate A1 fluorophore is necessary for a detectable A2 intensity peak if the three fusion proteins are expressed. More importantly, also in FRET-FLIM measurements, energy transfer was detectable specifically for interacting D-A1, D-A2 in comparison the negative control (decrease in the fluorescence lifetime (FLT)). As the expression of interacting D-A1-A2 (RLP44–BRI1–BAK1, with the sequence indicating the fused fluorophore) led to a significant reduction in the fluorescence lifetime in comparison to RLP44–BRI1–FLS2, RLP44–BRI1– and RLP44– –BAK1. This indicates that the three proteins are at the same time in close spatial proximity *in vivo*, demonstrating the existence of a trimeric complex in *N. benthamiana*:

This measured additional decrease is only possible, if hetero-trimers with an estimated distance of less than 15 nm between D and A2 are present. If only heterodimers are formed, then the measured FLT of RLP44–BRI1–BAK1 would be the average of RLP44–BRI1 and RLP44– –BAK1. Alternatively, the FLT would increase, as formerly existing D-A1 and D-A2 pairs would be split, as new A1-A2 pairs are formed. Only with a changed donor-to-acceptor ratio, the additional decrease in FLT could be explained with solely heterodimers. But as ratios were not significantly changed, hetero-trimeric arrangements must have been present. In summary, we could show the complex formation of RLP44, BRI1 and BAK1 *in vivo*. As no FRET to A2 was observed even for RLP44, BRI1 and FLS2, we conclude that the immune receptor must be in average more than 15 nm distanced from RLP44. Thus, our result supports the previous finding, that the BRI1 hormone receptor and the FLS2 immune receptor are located in distinct subdomains in the plasma membrane *in vivo* (Hutten et al., 2017).

In the future, it will be interesting to test, whether hetero-trimeric complexes depend on sterol-rich microdomains and possibly, the fast three-fluorophore FRET-FLIM can help to elucidate complex formation *in planta* also for other signalling pathways.

Signalling mechanisms in the plasma membrane

Since BAK1 is involved in growth and defence signalling, it has been hypothesized, that BAK1 might be the factor, that balances growth and defence output so that immune responses are inhibited during growth (Albrecht et al., 2012; Belkhadir et al., 2012; Belkhadir et al., 2014). At the same time, BAK1 and other SERKs are common coreceptors for many LRR-RKs receptors perceiving ligands (Matsubayashi and Sakagami, 1996; Chinchilla et al., 2009; Hartmann et al., 2014; Ladwig et al., 2015; Tang et al., 2017). Additionally, not only BAK1 is present in both growth-related and defence-mediating signalling complexes. BIR3 shows interaction with BAK1 and many receptors of different pathways, such as BRI1, FLS2 and other pathogen receptors (e.g. the bacterial peptide recognizing EF-Tu RECEPTOR (EFR)) (Imkampe et al., 2017). BIR3 seems to keep BAK1 and the receptor in close proximity, and at the same time acts

as an inhibitor on signalling in the absence of the respective signalling cue (Imkampe et al., 2017; Großeholz et al., 2019).

Thus, it is tempting to speculate, that BAK1 as second kinase in a receptor complex constitutively serves as fast amplification of the signal by various auto- and trans-phosphorylations and that BIR3 is a constitutive scaffold and inhibitor in the absence of the signalling cue. However, for the immune-response mediating receptor FLS2, multiparameter fluorescence imaging spectroscopy (MFIS) found FLS2 to predominantly be monomeric and to form FLS2-BAK1 heterodimers only upon flg22 sensing (Somssich et al. 2015). This proposes a signalling mechanism similar to the mammalian transmembrane receptor Tyr kinases, which include the insulin receptor (IR) and the EPIDERMAL GROWTH FACTOR RECEPTOR (EGFR) (Ward et al., 2007; De Meyts, 2008; Sun et al., 2012; Somssich et al., 2015).

For brassinosteroid hormone signalling, hetero-oligomerization was observed , which in turn would propose a similar signalling mechanism to that observed for the animal TRANSFORMING GROWTH FACTOR-BETA (TGF-β) (Massagué, 1998; Ehsan et al., 2005; Bücherl et al., 2013). In summary, both in the mammalian field and the plant field, different dynamics of plasma membrane-resident proteins was observed during signalling activation. It is noteworthy, that for BRI1 heterodimerization with BAK1 only upon BL binding was described (Jaillais et al., 2011). Possibly, the defininition of a heterodimer is just more strict in their use, meaning only activated heterodimers and not in close proximity. Also, FLS2-FLS2 homodimerization was reported (Sun et al., 2012). In the future, it will be interesting to further unravel, whether these two proposed general signalling dynamics are merely mild changes in affinity or localization, results of different experimental procedures, different intracellular hormone or microbe associated molecular pattern levels or indeed strikingly affect signalling transduction dynamics.

In contrast to BAK1 and BIR3, RLP44 is a protein that is specific to growth/development-mediating signalling compartments as in interacts with both BRI1 and PSKR1, but not with FLS2 (Glöckner et al., 2019b; Holzwart et al., 2019). It is evolutionary conserved and is, in an evolutionary tree, as basal as the stomatal development-mediating TOO MANY MOUTH (TMM) (Wang et al., 2008a). RLP44 is involved in feed-back-signalling from the cell wall in response to homogalacturonan (pectin) modifications by pectin methylesterases (PME), and interestingly, PMEs show evidence of multiple members in the early land plant that gave rise to the mosses and vascular plants (McCarthy et al., 2014). RLP44 is physically in close proximity with at least two components of the BRI1 signalling module in the heterologous expression system in *N. benthamiana* leaves (Glöckner et al., 2019a), and the localization of RLP44 is dependent on the phosphorylation status of its small, cytoplasmic tail (Garnelo Gomez et al., 2019).

Consequently, the phosphorylation state of the short cytoplasmic region in RLP44 could regulate the amount of PM-resident BRI1-BAK1 signalling complexes in the plasma membrane, e.g. in response to secondary cues such as cell wall integrity sensing. Mechanisms, similar to the model proposed for the cell wall integrity receptor FERONIA for the regulation of immune complexes (Stegmann et al., 2017) and the mechanism of

signalling attenuation by internalization of BRI1 and BAK1 in response to high glucose levels (Peng et al., 2018) are conceivable.

3.1.4 Cross-talk with phytosulfokine signalling via RLP44

Holzwart, E.; Huerta, A. I.; Glöckner, N.; Garnelo Gómez, B.; Wanke, F.; Augustin, S.; Askani, J. C.; Schürholz, A.-K.; Harter, K.; Wolf, S. (2018) BRI1 controls vascular cell fate in the *Arabidopsis* root through RLP44 and phytosulfokine signaling. *Proc. Natl. Acad. Sci. USA*.

Holzwart, E.; Glöckner, N.; Höfte, H.; Harter, K.; Wolf, S. (2019) A novel mutant allele uncouples brassinosteroid-dependent and independent functions of BRI1. *Preprint on bioRxiv 605923, doi: https://doi.org/10.1101/605923.*

Currently, a possible cross-talk between BR hormone signalling, RLP44 and PSK hormone signalling is not well understood and was thus studied especially by Eleonore Holzwart in the group of Sebastian Wolf. It was previously shown, that RLP44 interacts directly with BAK1, and in co-immunoprecipitations, both BAK1 and BRI1 were pulled down (Wolf et al., 2014).

We found, that also in mating-based split ubiquitin assays (mbSUS) and in FRET-FLIM interaction assays, RLP44 directly interacted with BRI1 (Holzwart et al., 2018), supporting a direct interaction between them. A slightly increased expression of pRLP44-expressed RLP44-GFP was found in the root vasculature in root xylem precursor cells and undifferentiated procambial cells (Holzwart et al., 2018). In a detailed developmental genetic analysis of various *bri1* and *rlp44* mutants it was shown, that RLP44 controls the xylem cell fate in a BRI1 dependent manner, but independently of brassinosteroid hormone signalling outputs (Holzwart et al., 2018; Glöckner et al., 2019).
Interestingly, RLP44 also directly interacts with the phytosulfokine hormone receptor PSKR1 both in FRET-FLIM and co-immunoprecipitation assays (Holzwart et al., 2018). Moreover, after transient expression in *N. benthamiana* leaves, higher amounts of BAK1-HA in PSKR1-GFP immunoprecipitates were found in the presence of RLP44-GFP in comparison to the absence of RLP44. In turn, also lower BAK1-HA levels in PSKR1-GFP immunoprecipitates in *rlp44* mutant plants (Holzwart et al., 2018) suggesting, that RLP44 is important for the receptor-co-receptor complex formation.

In a detailed, developmental genetic analysis it was shown, that PSK signalling likely promotes procambial identity and thus inhibits progression to xylem cell fate (Holzwart et al., 2018). In accordance with the observed promotion of PSKR1-BAK1 interaction by RLP44 (increasing signalling), both the *rlp44* mutant and the *pskr1-3 pskr2-1* double-mutant showed increased xylem cell numbers and the phenotype for *rlp44* could be rescued by addition of PSK hormone (Holzwart et al., 2018).

In summary, this suggested that both the brassinosteroid receptor BRI1 and the phytosulfokine receptor PSKR1 may compete for RLP44, balancing root vasculature development (Holzwart et al., 2018). Yet another, novel mutation in BRI1 termed *comfortably numb 4* (*bri1*^{cnu4}) supports this hypothesis. Both a mating-based split-ubiquitin (mb-

SUS) interaction assay and coimmunoprecipitation assay showed increased interaction of *BRI1*^{cnu4} with RLP44 and indeed, *bri1*^{cnu4} mutants had increased numbers of xylem cells (Holzwart et al., 2019). A mechanistical explanation would be, that the increased interaction between RLP44 and BRI1 keeps RLP44 from promoting PSK signalling, which in turn led to more cells with xylem identity. Thus, BRI1 may pose indirect effects (independent of BR signalling itself) via RLP44 on phytosulfokine signalling.

In the future, it will be interesting to test, whether RLP44, BRI1 and PSKR1 are in close spatial proximity imposing this indirect effect e.g. by localization to the same microdomain or to alternatively test, whether competition between BRI1 and PSKR1 for RLP44 can be shown. For the competition assay, however, an inducible system in *A. thaliana* would be best suited, as different stoichiometries in heterologous systems pose an additional obstacle for the interpretation (Glöckner et al., 2019a).

3.2 Signalling integration of other pathways

Arongaus, A. B.; Chen, S; Pireyre, M.; Glöckner, N.; Galvão, V. C.; Albert, A; Winkler, J. B.; Fankhauser, C; Harter, K; Ulm, R. (2018) *Arabidopsis* RUP2 represses UVR8-mediated flowering in noninductive photoperiods. *Genes and Development.*

Mohrholz, A.; Sun, H.; Gloeckner, N.; Hummel, S. Kolukisaoglu, Ü.; Schneeberger, K.; Harter, K. (2019) The striking flower-in-flower phenotype of *Arabidopsis thaliana* Nossen (No-0) is caused by a novel LEAFY allele. P*reprint on bioRxiv 535120; doi: https://doi.org/10.1101/535120.*

Aryal, B.; Huynh, J.; Hu, Z.; Schneuwly, J.; Di Donato, M.; Fukao, Y.; Lehmann, S.; Alejandro, S.; Ludwig-Muller, J.; Glöckner, N.; Hothorn, M.; Dengjel, J.; Harter, K., Martinoia, E.; Metraux, J.-P.; Geisler, M. (2019) Regulation of ABCG36/PEN3/PDR8 during Fusarium oxysporum infection involves the LRR receptor-like kinase, ALK1. *In preparation for submission.*

Protein-protein interaction assays may help to unravel the signal transduction pathway in many different settings. An advantage of FRET-FLIM is, that even fast molecular events can be shown *in vivo* (Bajar et al., 2016). Here, we describe three different biological settings, in which FRET-FLIM interaction studies helped to unravel underlying molecular mechanisms (Aryal et al., 2019; Arongaus et al., 2018; Mohrholz et al., 2019). In order to provide a frame-work, only parts of the results of the respective publication are summarized here in broad terms.

Repression of flowering induction is an important mechanism (Yant et al., 2009), as few activators suffice for this morphological transition (Mathieu, 2009) and flowering at the wrong time may be lethal for the plant. However, currently, the UV-B light

dependent repression of flowering is not well understood, and thus studied especially by Adriana Arongaus in the group of Roman Ulm.

Interestingly, functional RUP2 is important for the UV-B dependent repression of flowering under non-inductive photoperiods, as specifically both *rup2* and *rup1 rup2* mutants (but not *rup1*) showed early flowering in short day conditions with UV-B light (SD+UV) (Arongaus et al., 2018).

To better understand, how this inhibition is established, protein-protein interaction assays were performed. Both in yeast two hybrid assays and in FRET-FLIM interaction studies, RUP2 interacted with the CO protein (Arongaus et al., 2018). This interaction was associated with the formation of speckles in the nucleus of *N. benthamiana* plants (Arongaus et al., 2018), suggesting, that the activity of CO was directly repressed by RUP2. Indeed, the early flowering under SD+UV of *rup2* was abolished for *rup2 co* double mutants and FT expression level was upregulated in *rup2* (Arongaus et al., 2018). To further elucidate the signalling mechanism, the RUP2-dependent influence of CO on FT expression was investigated. An chromatin co-immunoprecipitation assay demonstrated, that CO protein was able to bind to the FT promoter region and RUP2-deficient protoplasts showed increased FT promoter activation by CO (Arongaus et al., 2018). Consequently, the interaction of RUP2 and CO may keep CO from binding to the FT promoter, thus inhibiting transcription of FT, a major activator of flowering (Arongaus et al., 2018). If RUP2 would be a general repressor of CO, delayed flowering could be expected by RUP2 overexpression (RUP2-OE) under LD-UV conditions. However, even though RUP2-OE was confirmed, no such effect was observed, indicating that RUP2 affects photoperiodic flowering very specifically for a distinct UVR8-induced CO activation mechanism (Arongaus et al., 2018).

The importance of LFY for flower patterning and organ identity is well appreciated (Weigel et al., 1992; Kobayashi and Weigel, 2007; Bowman et al., 2012). Yet, recently, a novel mutant allele of LFY was found by classical and whole-genome based mapping by Anne Mohrholz in the group of Klaus Harter. As it exhibited the outgrowth of secondary flowers from the primary flower, it was termed flower in flower (lfy^{FIF}) (Mohrholz et al., 2019). The causal cysteine to tyrosine change in the second exon of LFY^{FIF} strongly reduced its ability to act as an transcription factor, as its binding to the promoter of APETALA was almost completely abolished in an DNA-protein-interaction enzyme-linked immunosorbent assay (DPI-ELISA) (Brand et al., 2010). However, FRET-FLIM interaction studies revealed, that LFY^{FIF} still was able to form homotypic (LFY^{FIF}-LFY^{FIF}) and heterotypic (LFY^{FIF}-LFY) dimers, still locating to the nucleus and cytoplasm *in planta* (Mohrholz et al., 2019). Dimerization is not essential for DNA binding but for the biological function (Hamès et al., 2008; Siriwardana and Lamb, 2012). Thus, LFY^{FIF} may act dominant-negatively by either forming non-functional heteromers with wild-type LFY, which cannot longer bind to DNA, or by titrating out interaction partners required for LFY function (Siriwardana and Lamb, 2012; Mohrholz et al., 2019).

Currently, the precise substrate and function of the ABCG36 channel is not well understood and was thus studied by Bibek Aryal in the group of Markus Geisler. ABCG36

mediated the transport of IBA, but not IAA, over the plasma membrane, together with its close homolog ABCG37 it was involved in the polar distribution of IBA, which in turn affected lateral root formation (Aryal et al., 2019). Currently, it is not clear whether this is a primary auxinic effect of IBA itself (Ludwig-Müller, 2007) or caused by peroxisomal IBA to IAA conversion (Aryal et al., 2019; Strader and Bartel, 2011). In leaves, ABCG36 was shown to accumulate at the site of pathogen entry (Stein et al., 2006; Xin et al., 2013) but the effect of pathogen infection on its root location is currently unknown. Indeed, both the expression and polarity of ABCG36 was specifically distorted upon *F. oxysporum* root infection, which could be phenocopied by IBA treatments (Aryal et al., 2019).

Interestingly, an activator of ABCG36 was found, the LRR-RLK, AUXIN-INDUCED LRR KINASE 1 (ALK1). Both in FRET-FLIM analysis and coimmunoprecipitations, ALK1 interacted with ABCG36 (Aryal et al., 2019). Quantitative phospho-proteomics identified several potential phosphorylation sites in ABCG36 by ALK1, and S825 phosphorylation led to channel activation and was significantly down-regulated by *F. oxysporum* infection (Aryal et al., 2019). To test, whether ALK1 and ABCG36 are involved in resistance to the fungus, soil infection assays were performed. Indeed, *alk1* and *abcg36* mutants showed increased susceptibility (chlorosis/necrosis of the plant and increased fungal biomass), which could be rescued by the overexpression of the respective protein (Aryal et al., 2019).

Taken together, these data point to a common function of ABCG36 and ALK1 in disease resistance toward the root-penetrating fungus F. oxysporum. In summary, protein-protein interaction studies may help to unravel the underlying molecular mechanisms in diverse signal transduction processes on several levels of regulation, e.g. the repression of a transcriptional activator (Arongaus et al., 2018), the possible titration of functional transcription factors (or its interaction partners) by a non-functional one (Mohrholz et al., 2019) or the importance of an IBA-transporting channel during fungal pathogen infection can be found (Aryal et al., 2019).

4 References

Abbe, E. (1873). Beiträge zur Theorie des Mikroskops und der mikroskopischen Wahrnehmung. Archiv für mikroskopische Anatomie *9*, 413-418.

Ai, H.-W., Shaner, N.C., Cheng, Z., Tsien, R.Y., and Campbell, R.E. (2007). Exploration of new chromophore structures leads to the identification of improved blue fluorescent proteins. Biochemistry *46*, 5904-5910.

Albrecht, C., Boutrot, F., Segonzac, C., Schwessinger, B., Gimenez-Ibanez, S., Chinchilla, D., Rathjen, J.P., Vries, S.C.d., and Zipfel, C. (2012). Brassinosteroids inhibit pathogen-associated molecular pattern-triggered immune signaling independent of the receptor kinase BAK1. Proceedings of the National Academy of Sciences of the United States of America *109*, 303-308.

Amano, Y., Tsubouchi, H., Shinohara, H., Ogawa, M., and Matsubayashi, Y. (2007). Tyrosine-sulfated glycopeptide involved in cellular proliferation and expansion in Arabidopsis. Proceedings of the National Academy of Sciences of the United States of America *104*, 18333-18338.

Ambrose, E.J. (1961). The movements of fibrocytes. Experimental cell research *Suppl 8*, 54-73.

Arongaus, A.B., Chen, S., Pireyre, M., Glöckner, N., Galvão, V.C., Albert, A., Winkler, J.B., Fankhauser, C., Harter, K., and Ulm, R. (2018). Arabidopsis RUP2 represses UVR8-mediated flowering in noninductive photoperiods. Genes & development *32*, 1332-1343.

Aryal, B., Huynh, J., Hu, Z., Schneuwly, J., Di Donnato, M., Fukao, Y., Lehmann, S., Alejandro, S., Ludwig-Müller, J., and Glöckner, N., et al. (In preparation). Regulation of ABCG36/PEN3/PDR8 during Fusarium oxysporum infection involves the LRR receptor-like kinase, ALK1.

Axelrod, D. (1981). Cell-substrate contacts illuminated by total internal reflection fluorescence. The Journal of cell biology *89*, 141-145.

Axelrod, D. (2001). Total Internal Reflection Fluorescence Microscopy in Cell Biology. Traffic *2*, 764-774.

Bajar, B.T., Wang, E.S., Zhang, S., Lin, M.Z., and Chu, J. (2016). A Guide to Fluorescent Protein FRET Pairs. Sensors (Basel, Switzerland) *16*.

Baluska, F., Vitha, S., Barlow, P.W., and Volkmann, D. (1997). Rearrangements of F-actin arrays in growing cells of intact maize root apex tissues. A major developmental switch occurs in the postmitotic transition region. Eur J Cell Biol *72*, 113-121.

Baluska, F., Volkmann, D., and Barlow, P.W. (1996). Specialized zones of development in roots. View from the cellular level. Plant Physiology *112*, 3-4.

Baluška, F., Volkmann, D., and Barlow, P.W. (2001). A Polarity Crossroad in the TransitionGrowth Zone of Maize Root Apices. Cytoskeletal and DevelopmentalImplications. Journal of Plant Growth Regulation *20*, 170-181.

Barbez, E., Dünser, K., Gaidora, A., Lendl, T., and Busch, W. (2017). Auxin steers root cell expansion via apoplastic pH regulation in Arabidopsis thaliana. Proceedings of the National Academy of Sciences of the United States of America *114*, E4884-E4893.

Bednarek, P., Pislewska-Bednarek, M., Svatos, A., Schneider, B., Doubsky, J., Mansurova, M., Humphry, M., Consonni, C., Panstruga, R., and Sanchez-Vallet, A., et al. (2009). A glucosinolate metabolism pathway in living plant cells mediates broad-spectrum antifungal defense. Science (New York, N.Y.) *323*, 101-106.

Belkhadir, Y., Jaillais, Y., Epple, P., Balsemão-Pires, E., Dangl, J.L., and Chory, J. (2012). Brassinosteroids modulate the efficiency of plant immune responses to microbe-associated molecular patterns. Proceedings of the National Academy of Sciences of the United States of America *109*, 297-302.

Belkhadir, Y., Yang, L., Hetzel, J., Dangl, J.L., and Chory, J. (2014). The growth-defense pivot. Crisis management in plants mediated by LRR-RK surface receptors. Trends in biochemical sciences *39*, 447-456.

Betzig, E. (1995). Proposed method for molecular optical imaging. Opt. Lett. *20*, 237.

Betzig, E., Patterson, G.H., Sougrat, R., Lindwasser, O.W., Olenych, S., Bonifacino, J.S., Davidson, M.W., Lippincott-Schwartz, J., and Hess, H.F. (2006). Imaging intracellular fluorescent proteins at nanometer resolution. Science (New York, N.Y.) *313*, 1642-1645.

Bhosale, R., Giri, J., Pandey, B.K., Giehl, R.F.H., Hartmann, A., Traini, R., Truskina, J., Leftley, N., Hanlon, M., and Swarup, K., et al. (2018). A mechanistic framework for auxin dependent Arabidopsis root hair elongation to low external phosphate. Nature Communications *9*, 1409.

Bichet, A., Desnos, T., Turner, S., Grandjean, O., and Höfte, H. (2001). BOTERO1 is required for normal orientation of cortical microtubules and anisotropic cell expansion in Arabidopsis. The Plant journal : for cell and molecular biology *25*, 137-148.

Bienert, M.D., Siegmund, S.E.G., Drozak, A., Trombik, T., Bultreys, A., Baldwin, I.T., and Boutry, M. (2012). A pleiotropic drug resistance transporter in Nicotiana tabacum is involved in defense against the herbivore Manduca sexta. The Plant journal : for cell and molecular biology *72*, 745-757.

Bishop, G.J., and Koncz, C. (2002). Brassinosteroids and plant steroid hormone signaling. The Plant cell *14 Suppl*, S97-110.

Blakeslee, J.J., Peer, W.A., and Murphy, A.S. (2005). Auxin transport. Current Opinion in Plant Biology *8*, 494-500.

Bojar, D., Martinez, J., Santiago, J., Rybin, V., Bayliss, R., and Hothorn, M. (2014). Crystal structures of the phosphorylated BRI1 kinase domain and implications for brassinosteroid signal initiation. The Plant journal : for cell and molecular biology *78*, 31-43.

Bonner, J. (1934). The relation of hydrogen ions to the growth rate of the Avena coleoptile. Protoplasma *21*, 406-423.

Bowman, J.L., Smyth, D.R., and Meyerowitz, E.M. (2012). The ABC model of flower development. Then and now. Development (Cambridge, England) *139*, 4095-4098.

Brand, L.H., Kirchler, R., Hummel, S., Chaban, C., and Wanke, D. (2010). DPI-ELISA. A fast and versatile method to specify the binding of plant transcription factors to DNA in vitro. Plant methods *6*, 25.

Bücherl, C.A., van Esse, G.G., Kruis, A., Luchtenberg, J., Westphal, A.H., Aker, J., van Hoek, A., Albrecht, C., Borst, J.W., and Vries, S.C.d. (2013). Visualization of BRI1 and BAK1(SERK3) membrane receptor heterooligomers during brassinosteroid signaling. Plant Physiology *162*, 1911-1925.

Bunt, G., and Wouters, F.S. (2017). FRET from single to multiplexed signaling events. Biophysical reviews *9*, 119-129.

Burk, D.H., Liu, B., Zhong, R., Morrison, W.H., and Ye, Z.H. (2001). A katanin-like protein regulates normal cell wall biosynthesis and cell elongation. The Plant cell *13*, 807-827.

Caesar, K., Elgass, K., Chen, Z., Huppenberger, P., Witthöft, J., Schleifenbaum, F., Blatt, M.R., Oecking, C., and Harter, K. (2011). A fast brassinolide-regulated response pathway in the plasma membrane of Arabidopsis thaliana. The Plant journal : for cell and molecular biology *66*, 528-540.

Campbell, R.E., Tour, O., Palmer, A.E., Steinbach, P.A., Baird, G.S., Zacharias, D.A., and Tsien, R.Y. (2002). A monomeric red fluorescent protein. Proceedings of the National Academy of Sciences of the United States of America *99*, 7877-7882.

Campos, W.F., Dressano, K., Ceciliato, P.H.O., Guerrero-Abad, J.C., Silva, A.L., Fiori, C.S., Morato do Canto, A., Bergonci, T., Claus, L.A.N., and Silva-Filho, M.C., et al. (2018). Arabidopsis thaliana rapid alkalinization factor 1-mediated root growth inhibition is dependent on calmodulin-like protein 38. The Journal of biological chemistry *293*, 2159-2171.

Caño-Delgado, A., Yin, Y., Yu, C., Vafeados, D., Mora-García, S., Cheng, J.-C., Nam, K.H., Li, J., and Chory, J. (2004). BRL1 and BRL3 are novel brassinosteroid receptors that function in vascular differentiation in Arabidopsis. Development (Cambridge, England) *131*, 5341-5351.

Casimiro, I., Beeckman, T., Graham, N., Bhalerao, R., Zhang, H., Casero, P., Sandberg, G., and Bennett, M.J. (2003). Dissecting Arabidopsis lateral root development. Trends in plant science *8*, 165-171.

Cheng, X., and Smith, J.C. (2019). Biological Membrane Organization and Cellular Signaling. Chemical reviews *119*, 5849-5880.

Chinchilla, D., Shan, L., He, P., Vries, S. de, and Kemmerling, B. (2009). One for all - The receptor-associated kinase BAK1. Trends in plant science *14*, 535-541.

Clay, N.K., Adio, A.M., Denoux, C., Jander, G., and Ausubel, F.M. (2009). Glucosinolate metabolites required for an Arabidopsis innate immune response. Science (New York, N.Y.) *323*, 95-101.

Cloix, C., Kaiserli, E., Heilmann, M., Baxter, K.J., Brown, B.A., O'Hara, A., Smith, B.O., Christie, J.M., and Jenkins, G.I. (2012). C-terminal region of the UV-B photoreceptor UVR8 initiates signaling through interaction with the COP1 protein. Proceedings of the National Academy of Sciences of the United States of America *109*, 16366-16370.

Clouse, S.D., Langford, M., and McMorris, T.C. (1996). A Brassinosteroid-Insensitive Mutant in Arabidopsis thaliana Exhibits Multiple Defects in Growth and Development. Plant Physiology *111*, 671-678.

Corbesier, L., Vincent, C., Jang, S., Fornara, F., Fan, Q., Searle, I., Giakountis, A., Farrona, S., Gissot, L., and Turnbull, C., et al. (2007). FT protein movement contributes to long-distance signaling in floral induction of Arabidopsis. Science (New York, N.Y.) *316*, 1030-1033.

Cormack, B.P., Valdivia, R.H., and Falkow, S. (1996). FACS-optimized mutants of the green fluorescent protein (GFP). Gene *173*, 33-38.

Cosgrove, D.J. (2005). Growth of the plant cell wall. Nature Reviews Molecular Cell Biology *6*, 850-861.

Cosgrove, D.J. (2018). Diffuse Growth of Plant Cell Walls. Plant Physiology *176*, 16-27.

Costantini, L.M., Baloban, M., Markwardt, M.L., Rizzo, M., Guo, F., Verkhusha, V.V., and Snapp, E.L. (2015). A palette of fluorescent proteins optimized for diverse cellular environments. Nature Communications *6*, 7670 EP -.

Darwin, C.R. (1880). The power of movement in plants (London: John Murray).

Day, R.N., and Davidson, M.W. (2009). The fluorescent protein palette. Tools for cellular imaging. Chemical Society reviews *38*, 2887-2921.

De Meyts, P. (2008). The insulin receptor. A prototype for dimeric, allosteric membrane receptors? Trends in biochemical sciences *33*, 376-384.

Dertinger, T., Colyer, R., Vogel, R., Enderlein, J., and Weiss, S. (2010). Achieving increased resolution and more pixels with Superresolution Optical Fluctuation Imaging (SOFI). Optics express *18*, 18875-18885.

Di Rubbo, S., Irani, N.G., Kim, S.Y., Xu, Z.-Y., Gadeyne, A., Dejonghe, W., Vanhoutte, I., Persiau, G., Eeckhout, D., and Simon, S., et al. (2013). The clathrin adaptor complex AP-2 mediates endocytosis of brassinosteroid insensitive1 in Arabidopsis. The Plant cell *25*, 2986-2997.

Dickson, R.M., Cubitt, A.B., Tsien, R.Y., and Moerner, W.E. (1997). On/off blinking and switching behaviour of single molecules of green fluorescent protein. Nature *388*, 355-358.

Dinneny, J.R., and Yanofsky, M.F. (2004). Vascular Patterning. Xylem or Phloem? Current Biology *14*, R112-R114.

Dixit, R., and Cyr, R. (2003). Cell damage and reactive oxygen species production induced by fluorescence microscopy. Effect on mitosis and guidelines for non-invasive

fluorescence microscopy. The Plant journal : for cell and molecular biology *36*, 280-290.

Draeger, C., Ndinyanka Fabrice, T., Gineau, E., Mouille, G., Kuhn, B.M., Moller, I., Abdou, M.-T., Frey, B., Pauly, M., and Bacic, A., et al. (2015). Arabidopsis leucine-rich repeat extensin (LRX) proteins modify cell wall composition and influence plant growth. BMC plant biology *15*, 155.

Dünser, K., Gupta, S., Herger, A., Feraru, M.I., Ringli, C., and Kleine-Vehn, J. (2019). Extracellular matrix sensing by FERONIA and Leucine-Rich Repeat Extensins controls vacuolar expansion during cellular elongation in Arabidopsis thaliana. The EMBO journal *38*.

Ehsan, H., Ray, W.K., Phinney, B., Wang, X., Huber, S.C., and Clouse, S.D. (2005). Interaction of Arabidopsis BRASSINOSTEROID-INSENSITIVE 1 receptor kinase with a homolog of mammalian TGF-beta receptor interacting protein. The Plant journal : for cell and molecular biology *43*, 251-261.

Elgass, K., Caesar, K., Schleifenbaum, F., Stierhof, Y.-D., Meixner, A.J., and Harter, K. (2009). Novel application of fluorescence lifetime and fluorescence microscopy enables quantitative access to subcellular dynamics in plant cells. PloS one *4*, e5716.

Fábián, Á., Horváth, G., Vámosi, G., Vereb, G., and Szöllősi, J. (2013). TripleFRET measurements in flow cytometry. Cytometry. Part A : the journal of the International Society for Analytical Cytology *83*, 375-385.

Fàbregas, N., Li, N., Boeren, S., Nash, T.E., Goshe, M.B., Clouse, S.D., Vries, S. de, and Caño-Delgado, A.I. (2013). The brassinosteroid insensitive1-like3 signalosome complex regulates Arabidopsis root development. The Plant cell *25*, 3377-3388.

Fantini, J., and J. Barrantes, F. (2018). How membrane lipids control the 3D structure and function of receptors. AIMS Biophysics *5*, 22-35.

Fasano, J.M., Swanson, S.J., Blancaflor, E.B., Dowd, P.E., Kao, T.H., and Gilroy, S. (2001). Changes in root cap pH are required for the gravity response of the Arabidopsis root. The Plant cell *13*, 907-921.

Favory, J.-J., Stec, A., Gruber, H., Rizzini, L., Oravecz, A., Funk, M., Albert, A., Cloix, C., Jenkins, G.I., and Oakeley, E.J., et al. (2009). Interaction of COP1 and UVR8 regulates UV-B-induced photomorphogenesis and stress acclimation in Arabidopsis. The EMBO journal *28*, 591-601.

Förster, T. (1948). Zwischenmolekulare Energiewanderung und Fluoreszenz. Ann. Phys. *437*, 55-75.

Fried, S., Reicher, B., Pauker, M.H., Eliyahu, S., Matalon, O., Noy, E., Chill, J., and Barda-Saad, M. (2014). Triple-color FRET analysis reveals conformational changes in the WIP-WASp actin-regulating complex. Science signaling *7*, ra60.

Friedrichsen, D.M., Joazeiro, C.A.P., Li, J., Hunter, T., and Chory, J. (2000). Brassinosteroid-Insensitive-1 Is a Ubiquitously Expressed Leucine-Rich Repeat Receptor Serine/Threonine Kinase. Plant Physiology *123*, 1247-1256.

Gaedeke, N., Klein, M., Kolukisaoglu, U., Forestier, C., Müller, A., Ansorge, M., Becker, D., Mamnun, Y., Kuchler, K., and Schulz, B., et al. (2001). The Arabidopsis thaliana ABC transporter AtMRP5 controls root development and stomata movement. The EMBO journal *20*, 1875-1887.

Galperin, E., Verkhusha, V.V., and Sorkin, A. (2004). Three-chromophore FRET microscopy to analyze multiprotein interactions in living cells. Nature Methods *1*, 209 EP -.

Garnelo Gomez, B., Lozano-Duran, R., and Wolf, S. (2019). Phosphorylation-dependent routing of RLP44 towards brassinosteroid or phytosulfokine signalling. Supplemental Material.

Glöckner, N., Zur Oven-Krockhaus, S., Wackenhut, F., Burmeister, M., Wanke, F., Holzwart, E., Wolf, S., and Harter, K. (2019a). Three-fluorophore FRET-FLIM enables the study of trimeric protein interactions and complex formation with nanoscale resolution in living plant cells. In preparation for submission.

Glöckner, N., Zur Oven-Krockhaus, S., Wackenhut, F., Burmeister, M., Wanke, F., Holzwart, E., Wolf, S., and Harter, K. (2019b). Three-fluorophore FRET-FLIM enables the study of trimeric protein interactions and complex formation with nanoscale resolution in living plant cells. In preparation for submission.

González-García, M.-P., Vilarrasa-Blasi, J., Zhiponova, M., Divol, F., Mora-García, S., Russinova, E., and Caño-Delgado, A.I. (2011). Brassinosteroids control meristem size by promoting cell cycle progression in Arabidopsis roots. Development (Cambridge, England) *138*, 849-859.

Grefen, C., and Blatt, M.R. (2012). A 2in1 cloning system enables ratiometric bimolecular fluorescence complementation (rBiFC). BioTechniques *53*, 311-314.

Großeholz, R., Feldman-Salit, A., Wanke, F., Schulze, S., Glöckner, N., Kemmerling, B., Harter, K., and Kummer, U. (2019). Specifying the role of BAK1-interacting receptor-like kinase 3 in brassinosteroid signaling. Journal of integrative plant biology.

Gruber, H., Heijde, M., Heller, W., Albert, A., Seidlitz, H.K., and Ulm, R. (2010). Negative feedback regulation of UV-B-induced photomorphogenesis and stress acclimation in Arabidopsis. Proceedings of the National Academy of Sciences of the United States of America *107*, 20132-20137.

Gustafsson, M.G. (2000). Surpassing the lateral resolution limit by a factor of two using structured illumination microscopy. Journal of microscopy *198*, 82-87.

Hager, A., Menzel, H., and Krauss, A. (1971). Versuche und Hypothese zur Primärwirkung des Auxins beim Streckungswachstum. Planta *100*, 47-75.

Hamès, C., Ptchelkine, D., Grimm, C., Thevenon, E., Moyroud, E., Gérard, F., Martiel, J.-L., Benlloch, R., Parcy, F., and Müller, C.W. (2008). Structural basis for LEAFY floral switch function and similarity with helix-turn-helix proteins. The EMBO journal *27*, 2628-2637.

Hartmann, J., Fischer, C., Dietrich, P., and Sauter, M. (2014). Kinase activity and calmodulin binding are essential for growth signaling by the phytosulfokine receptor PSKR1. The Plant journal : for cell and molecular biology *78*, 192-202.

Haustein, E., Jahnz, M., and Schwille, P. (2003). Triple FRET. A tool for studying long-range molecular interactions. Chemphyschem : a European journal of chemical physics and physical chemistry *4*, 745-748.

He, L., Wu, X., Simone, J., Hewgill, D., and Lipsky, P.E. (2005). Determination of tumor necrosis factor receptor-associated factor trimerization in living cells by CFP-YFP-mRFP FRET detected by flow cytometry. Nucleic acids research *33*, e61.

Hecker, A., Wallmeroth, N., Peter, S., Blatt, M.R., Harter, K., and Grefen, C. (2015). Binary 2in1 Vectors Improve in Planta (Co)localization and Dynamic Protein Interaction Studies. Plant Physiology *168*, 776-787.

Hedde, P.N., and Nienhaus, G.U. (2014). Super-resolution localization microscopy with photoactivatable fluorescent marker proteins. Protoplasma *251*, 349-362.

Heijde, M., and Ulm, R. (2013). Reversion of the Arabidopsis UV-B photoreceptor UVR8 to the homodimeric ground state. Proceedings of the National Academy of Sciences of the United States of America *110*, 1113-1118.

Heim, R., and Tsien, R.Y. (1996). Engineering green fluorescent protein for improved brightness, longer wavelengths and fluorescence resonance energy transfer. Current biology : CB *6*, 178-182.

Hell, S.W., and Wichmann, J. (1994). Breaking the diffraction resolution limit by stimulated emission. Stimulated-emission-depletion fluorescence microscopy. Opt. Lett. *19*, 780-782.

Hess, S.T., Girirajan, T.P.K., and Mason, M.D. (2006). Ultra-high resolution imaging by fluorescence photoactivation localization microscopy. Biophysical journal *91*, 4258-4272.

Hink, M., Visser, A.J.W.G., Vysotski, E.S., and Lee, J. (2002). Critical Transfer Distance Determination Between FRET Pairs.

Hohng, S., Joo, C., and Ha, T. (2004). Single-molecule three-color FRET. Biophysical journal *87*, 1328-1337.

Holzwart, E., Glöckner, N., Höfte, H., Harter, K. and Wolf, S. (2019). A novel mutant allele uncouples brassinosteroid-dependent and independent functions of BRI1. https://www.biorxiv.org/content/10.1101/605923v1. 01.05.2019.

Holzwart, E., Huerta, A.I., Glöckner, N., Garnelo Gómez, B., Wanke, F., Augustin, S., Askani, J.C., Schürholz, A.-K., Harter, K., and Wolf, S. (2018). BRI1 controls vascular cell fate in the Arabidopsis root through RLP44 and phytosulfokine signaling. Proceedings of the National Academy of Sciences of the United States of America *115*, 11838-11843.

Hoppe, A.D., Scott, B.L., Welliver, T.P., Straight, S.W., and Swanson, J.A. (2013). N-way FRET microscopy of multiple protein-protein interactions in live cells. PloS one *8*, e64760.

Hosy, E., Martinière, A., Choquet, D., Maurel, C., and Luu, D.-T. (2015). Super-resolved and dynamic imaging of membrane proteins in plant cells reveal contrasting kinetic profiles and multiple confinement mechanisms. Molecular plant *8*, 339-342.

Hothorn, M., Belkhadir, Y., Dreux, M., Dabi, T., Noel, J.P., Wilson, I.A., and Chory, J. (2011). Structural basis of steroid hormone perception by the receptor kinase BRI1. Nature *474*, 467-471.

Hutten, S.J., Hamers, D.S., Aan den Toorn, M., van Esse, W., Nolles, A., Bücherl, C.A., Vries, S.C. de, Hohlbein, J., and Borst, J.W. (2017). Visualization of BRI1 and SERK3/BAK1 Nanoclusters in Arabidopsis Roots. PloS one *12*, e0169905.

Ibañes, M., Fàbregas, N., Chory, J., and Caño-Delgado, A.I. (2009). Brassinosteroid signaling and auxin transport are required to establish the periodic pattern of Arabidopsis shoot vascular bundles. Proceedings of the National Academy of Sciences of the United States of America *106*, 13630-13635.

Imkampe, J., Halter, T., Huang, S., Schulze, S., Mazzotta, S., Schmidt, N., Manstretta, R., Postel, S., Wierzba, M., and Yang, Y., et al. (2017). The Arabidopsis Leucine-Rich Repeat Receptor Kinase BIR3 Negatively Regulates BAK1 Receptor Complex Formation and Stabilizes BAK1. The Plant cell *29*, 2285-2303.

Irani, N.G., Di Rubbo, S., Mylle, E., van den Begin, J., Schneider-Pizoń, J., Hniliková, J., Šíša, M., Buyst, D., Vilarrasa-Blasi, J., and Szatmári, A.-M., et al. (2012). Fluorescent castasterone reveals BRI1 signaling from the plasma membrane. Nature chemical biology *8*, 583-589.

Ishikawa, H., and Evans, M.L. (1995). Specialized zones of development in roots. Plant Physiology *109*, 725-727.

Iyer-Pascuzzi, A.S., and Benfey, P.N. (2009). Transcriptional networks in root cell fate specification. Biochimica et biophysica acta *1789*, 315-325.

Jaeger, K.E., and Wigge, P.A. (2007). FT protein acts as a long-range signal in Arabidopsis. Current biology : CB *17*, 1050-1054.

Jaillais, Y., Belkhadir, Y., Balsemão-Pires, E., Dangl, J.L., and Chory, J. (2011a). Extracellular leucine-rich repeats as a platform for receptor/coreceptor complex formation. Proceedings of the National Academy of Sciences of the United States of America *108*, 8503-8507.

Jaillais, Y., Hothorn, M., Belkhadir, Y., Dabi, T., Nimchuk, Z.L., Meyerowitz, E.M., and Chory, J. (2011b). Tyrosine phosphorylation controls brassinosteroid receptor activation by triggering membrane release of its kinase inhibitor. Genes & development *25*, 232-237.

Jang, S., Marchal, V., Panigrahi, K.C.S., Wenkel, S., Soppe, W., Deng, X.-W., Valverde, F., and Coupland, G. (2008). Arabidopsis COP1 shapes the temporal pattern

of CO accumulation conferring a photoperiodic flowering response. The EMBO journal *27*, 1277-1288.

Jasiński, M., Stukkens, Y., Degand, H., Purnelle, B., Marchand-Brynaert, J., and Boutry, M. (2001). A plant plasma membrane ATP binding cassette-type transporter is involved in antifungal terpenoid secretion. The Plant cell *13*, 1095-1107.

Jean-Yves Tinevez. Simple tracker. https://de.mathworks.com/matlabcentral/fileexchange/34040-simple-tracker.

Jelenska, J., Davern, S.M., Standaert, R.F., Mirzadeh, S., and Greenberg, J.T. (2017). Flagellin peptide flg22 gains access to long-distance trafficking in Arabidopsis via its receptor, FLS2. Journal of experimental botany *68*, 1769-1783.

Jenkins, G.I. (2017). Photomorphogenic responses to ultraviolet-B light. Plant, cell & environment *40*, 2544-2557.

Johnson, A., and Vert, G. (2017). Single Event Resolution of Plant Plasma Membrane Protein Endocytosis by TIRF Microscopy. Frontiers in plant science *8*, 612.

Kang, Y.H., Breda, A., and Hardtke, C.S. (2017). Brassinosteroid signaling directs formative cell divisions and protophloem differentiation in Arabidopsis root meristems. Development (Cambridge, England) *144*, 272-280.

Kierszniowska, S., Seiwert, B., and Schulze, W.X. (2009). Definition of Arabidopsis sterol-rich membrane microdomains by differential treatment with methyl-beta-cyclodextrin and quantitative proteomics. Molecular & cellular proteomics : MCP *8*, 612-623.

Klar, T.A., Jakobs, S., Dyba, M., Egner, A., and Hell, S.W. (2000). Fluorescence microscopy with diffraction resolution barrier broken by stimulated emission. Proceedings of the National Academy of Sciences of the United States of America *97*, 8206-8210.

Kobae, Y., Sekino, T., Yoshioka, H., Nakagawa, T., Martinoia, E., and Maeshima, M. (2006). Loss of AtPDR8, a plasma membrane ABC transporter of Arabidopsis thaliana, causes hypersensitive cell death upon pathogen infection. Plant & cell physiology *47*, 309-318.

Kobayashi, Y., and Weigel, D. (2007). Move on up, it's time for change--mobile signals controlling photoperiod-dependent flowering. Genes & development *21*, 2371-2384.

Komis, G., Novák, D., Ovečka, M., Šamajová, O., and Šamaj, J. (2018). Advances in Imaging Plant Cell Dynamics. Plant Physiology *176*, 80-93.

Komori, R., Amano, Y., Ogawa-Ohnishi, M., and Matsubayashi, Y. (2009). Identification of tyrosylprotein sulfotransferase in Arabidopsis. Proceedings of the National Academy of Sciences of the United States of America *106*, 15067-15072.

Konopka, C.A., and Bednarek, S.Y. (2008). Variable-angle epifluorescence microscopy. A new way to look at protein dynamics in the plant cell cortex. The Plant journal : for cell and molecular biology *53*, 186-196.

Konrad, S.S.A., and Ott, T. (2015). Molecular principles of membrane microdomain targeting in plants. Trends in plant science *20*, 351-361.

Krattinger, S.G., Lagudah, E.S., Spielmeyer, W., Singh, R.P., Huerta-Espino, J., McFadden, H., Bossolini, E., Selter, L.L., and Keller, B. (2009). A putative ABC transporter confers durable resistance to multiple fungal pathogens in wheat. Science (New York, N.Y.) *323*, 1360-1363.

Kuo, H.-L., Ho, P.-C., Huang, S.-S., and Chang, N.-S. (2018). Chasing the signaling run by tri-molecular time-lapse FRET microscopy. Cell Death Discovery *4*, 45.

Kwezi, L., Ruzvidzo, O., Wheeler, J.I., Govender, K., Iacuone, S., Thompson, P.E., Gehring, C., and Irving, H.R. (2011). The phytosulfokine (PSK) receptor is capable of guanylate cyclase activity and enabling cyclic GMP-dependent signaling in plants. The Journal of biological chemistry *286*, 22580-22588.

Ladwig, F., Dahlke, R.I., Stührwohldt, N., Hartmann, J., Harter, K., and Sauter, M. (2015). Phytosulfokine Regulates Growth in Arabidopsis through a Response Module at the Plasma Membrane That Includes CYCLIC NUCLEOTIDE-GATED CHANNEL17, H+-ATPase, and BAK1. The Plant cell *27*, 1718-1729.

Laubinger, S., Fittinghoff, K., and Hoecker, U. (2004). The SPA quartet. A family of WD-repeat proteins with a central role in suppression of photomorphogenesis in arabidopsis. The Plant cell *16*, 2293-2306.

Lee, Y., Rubio, M.C., Alassimone, J., and Geldner, N. (2013). A mechanism for localized lignin deposition in the endodermis. Cell *153*, 402-412.

Li, J., and Chory, J. (1997). A Putative Leucine-Rich Repeat Receptor Kinase Involved in Brassinosteroid Signal Transduction. Cell *90*, 929-938.

Li, X., Wang, X., Yang, Y., Li, R., He, Q., Fang, X., Luu, D.-T., Maurel, C., and Lin, J. (2011). Single-molecule analysis of PIP2;1 dynamics and partitioning reveals multiple modes of Arabidopsis plasma membrane aquaporin regulation. The Plant cell *23*, 3780-3797.

Liang, X., Ding, P., Lian, K., Wang, J., Ma, M., Li, L., Li, L., Li, M., Zhang, X., and Chen, S., et al. (2016). Arabidopsis heterotrimeric G proteins regulate immunity by directly coupling to the FLS2 receptor. eLife *5*, e13568.

Lin, T., Scott, B.L., Hoppe, A.D., and Chakravarty, S. (2018). FRETting about the affinity of bimolecular protein-protein interactions. Protein science : a publication of the Protein Society *27*, 1850-1856.

Liu, L.-J., Zhang, Y.-C., Li, Q.-H., Sang, Y., Mao, J., Lian, H.-L., Wang, L., and Yang, H.-Q. (2008). COP1-mediated ubiquitination of CONSTANS is implicated in cryptochrome regulation of flowering in Arabidopsis. The Plant cell *20*, 292-306.

Lorbiecke, R., and Sauter, M. (2002). Comparative analysis of PSK peptide growth factor precursor homologs. Plant Science *163*, 321-332.

Lu, X., Dittgen, J., Piślewska-Bednarek, M., Molina, A., Schneider, B., Svatoš, A., Doubský, J., Schneeberger, K., Weigel, D., and Bednarek, P., et al. (2015). Mutant

Allele-Specific Uncoupling of PENETRATION3 Functions Reveals Engagement of the ATP-Binding Cassette Transporter in Distinct Tryptophan Metabolic Pathways. Plant Physiology *168*, 814-827.

Ludwig-Müller, J. (2007). Indole-3-butyric acid synthesis in ecotypes and mutants of Arabidopsis thaliana under different growth conditions. Journal of plant physiology *164*, 47-59.

Luschnig, C. (2002). Auxin transport. ABC proteins join the club. Trends in plant science *7*, 329-332.

Marowa, P., Ding, A., and Kong, Y. (2016). Expansins. Roles in plant growth and potential applications in crop improvement. Plant cell reports *35*, 949-965.

Martins, S., Dohmann, E.M.N., Cayrel, A., Johnson, A., Fischer, W., Pojer, F., Satiat-Jeunemaître, B., Jaillais, Y., Chory, J., and Geldner, N., et al. (2015). Internalization and vacuolar targeting of the brassinosteroid hormone receptor BRI1 are regulated by ubiquitination. Nature Communications *6*, 6151.

Masclaux-Daubresse, C., Daniel-Vedele, F., Dechorgnat, J., Chardon, F., Gaufichon, L., and Suzuki, A. (2010). Nitrogen uptake, assimilation and remobilization in plants. Challenges for sustainable and productive agriculture. Annals of botany *105*, 1141-1157.

Massagué, J. (1998). TGF-beta signal transduction. Annual Review of Biochemistry *67*, 753-791.

Mathieu, J. (2009). Regulation of flowering time in Arabidopsis thaliana (Tübingen).

Mathieu, J., Warthmann, N., Küttner, F., and Schmid, M. (2007). Export of FT protein from phloem companion cells is sufficient for floral induction in Arabidopsis. Current biology : CB *17*, 1055-1060.

Matsubayashi, Y., Morita, A., Matsunaga, E., Furuya, A., Hanai, N., and Sakagami, Y. (1999). Physiological relationships between auxin, cytokinin, and a peptide growth factor, phytosulfokine-α, in stimulation of asparagus cell proliferation. Planta *207*, 559-565.

Matsubayashi, Y., Ogawa, M., Morita, A., and Sakagami, Y. (2002). An LRR receptor kinase involved in perception of a peptide plant hormone, phytosulfokine. Science (New York, N.Y.) *296*, 1470-1472.

Matsubayashi, Y., and Sakagami, Y. (1996). Phytosulfokine, sulfated peptides that induce the proliferation of single mesophyll cells of Asparagus officinalis L. Proceedings of the National Academy of Sciences of the United States of America *93*, 7623-7627.

McCarthy, T.W., Der, J.P., Honaas, L.A., dePamphilis, C.W., and Anderson, C.T. (2014). Phylogenetic analysis of pectin-related gene families in Physcomitrella patens and nine other plant species yields evolutionary insights into cell walls. BMC plant biology *14*, 79.

McQueen-Mason, S., and Cosgrove, D.J. (1994). Disruption of hydrogen bonding between plant cell wall polymers by proteins that induce wall extension. Proceedings of the National Academy of Sciences of the United States of America *91*, 6574-6578.

Medintz, I. and Hildebrandt, N. (2014). FRET - Förster resonance energy transfer. From theory to applications (Weinheim: Wiley-VCH Verlag GmbH & Co. KGaA).

Moerner, and Kador (1989). Optical detection and spectroscopy of single molecules in a solid. Physical review letters *62*, 2535-2538.

Mohrholz, A., Sun, H., Gloeckner, N., Hummel, S., Kolukisaoglu, U., Schneeberger, K., and Harter, K. (2019). The striking flower-in-flower phenotype of Arabidopsis thaliana Nossen (No-0) is caused by a novel LEAFY allele. Supplemental Figures and Tables.

Mora-García, S., Vert, G., Yin, Y., Caño-Delgado, A., Cheong, H., and Chory, J. (2004). Nuclear protein phosphatases with Kelch-repeat domains modulate the response to brassinosteroids in Arabidopsis. Genes & development *18*, 448-460.

Nam, K.H., and Li, J. (2002). BRI1/BAK1, a Receptor Kinase Pair Mediating Brassinosteroid Signaling. Cell *110*, 203-212.

Naseer, S., Lee, Y., Lapierre, C., Franke, R., Nawrath, C., and Geldner, N. (2012). Casparian strip diffusion barrier in Arabidopsis is made of a lignin polymer without suberin. Proceedings of the National Academy of Sciences of the United States of America *109*, 10101-10106.

Noguchi, T., Fujioka, S., Choe, S., Takatsuto, S., Yoshida, S., Yuan, H., Feldmann, K.A., and Tax, F.E. (1999). Brassinosteroid-insensitive dwarf mutants of Arabidopsis accumulate brassinosteroids. Plant Physiology *121*, 743-752.

Noh, B., Murphy, A.S., and Spalding, E.P. (2001). Multidrug resistance-like genes of Arabidopsis required for auxin transport and auxin-mediated development. The Plant cell *13*, 2441-2454.

Noomnarm, U., and Clegg, R.M. (2009). Fluorescence lifetimes. Fundamentals and interpretations. Photosynthesis research *101*, 181-194.

Nyquist, H. (1928). Certain Topics in Telegraph Transmission Theory. Trans. Am. Inst. Electr. Eng. *47*, 617-644.

Oh, M.-H., Ray, W.K., Huber, S.C., Asara, J.M., Gage, D.A., and Clouse, S.D. (2000). Recombinant Brassinosteroid Insensitive 1 Receptor-Like Kinase Autophosphorylates on Serine and Threonine Residues and Phosphorylates a Conserved Peptide Motif in Vitro. Plant Physiology *124*, 751-766.

Ott, T. (2017). Membrane nanodomains and microdomains in plant-microbe interactions. Current Opinion in Plant Biology *40*, 82-88.

Pacifici, E., Di Mambro, R., Dello Ioio, R., Costantino, P., and Sabatini, S. (2018). Acidic cell elongation drives cell differentiation in the Arabidopsis root. The EMBO journal *37*.

Pauker, M.H., Hassan, N., Noy, E., Reicher, B., and Barda-Saad, M. (2012). Studying the dynamics of SLP-76, Nck, and Vav1 multimolecular complex formation in live human cells with triple-color FRET. Science signaling *5*, rs3.

Peng, Y., Chen, L., Li, S., Zhang, Y., Xu, R., Liu, Z., Liu, W., Kong, J., Huang, X., and Wang, Y., et al. (2018). BRI1 and BAK1 interact with G proteins and regulate sugar-responsive growth and development in Arabidopsis. Nature Communications *9*, 1522.

Petricka, J.J., Winter, C.M., and Benfey, P.N. (2012). Control of Arabidopsis root development. Annual review of plant biology *63*, 563-590.

Phyo, P., Gu, Y., and Hong, M. (2019). Impact of acidic pH on plant cell wall polysaccharide structure and dynamics. Insights into the mechanism of acid growth in plants from solid-state NMR. Cellulose *26*, 291-304.

Planas-Riverola, A., Gupta, A., Betegón-Putze, I., Bosch, N., Ibañes, M., and Caño-Delgado, A.I. (2019). Brassinosteroid signaling in plant development and adaptation to stress. Development (Cambridge, England) *146*.

Podolec, R., and Ulm, R. (2018). Photoreceptor-mediated regulation of the COP1/SPA E3 ubiquitin ligase. Current Opinion in Plant Biology *45*, 18-25.

Rizzini, L., Favory, J.-J., Cloix, C., Faggionato, D., O'Hara, A., Kaiserli, E., Baumeister, R., Schäfer, E., Nagy, F., and Jenkins, G.I., et al. (2011). Perception of UV-B by the Arabidopsis UVR8 protein. Science (New York, N.Y.) *332*, 103-106.

Rocchetti, A., Hawes, C., and Kriechbaumer, V. (2014). Fluorescent labelling of the actin cytoskeleton in plants using a cameloid antibody. Plant methods *10*, 12.

Russinova, E., Borst, J.-W., Kwaaitaal, M., Caño-Delgado, A., Yin, Y., Chory, J., and Vries, S.C. de (2004). Heterodimerization and endocytosis of Arabidopsis brassinosteroid receptors BRI1 and AtSERK3 (BAK1). The Plant cell *16*, 3216-3229.

Rust, M.J., Bates, M., and Zhuang, X. (2006). Sub-diffraction-limit imaging by stochastic optical reconstruction microscopy (STORM). Nature Methods *3*, 793-795.

Santiago, J., Henzler, C., and Hothorn, M. (2013). Molecular mechanism for plant steroid receptor activation by somatic embryogenesis co-receptor kinases. Science (New York, N.Y.) *341*, 889-892.

Scott, B.L., and Hoppe, A.D. (2015). Optimizing fluorescent protein trios for 3-Way FRET imaging of protein interactions in living cells. Scientific Reports *5*, 10270 EP -.

Sede, A.R., Borassi, C., Wengier, D.L., Mecchia, M.A., Estevez, J.M., and Muschietti, J.P. (2018). Arabidopsis pollen extensins LRX are required for cell wall integrity during pollen tube growth. FEBS letters *592*, 233-243.

Seidel, T., Seefeldt, B., Sauer, M., and Dietz, K.-J. (2010). In vivo analysis of the 2-Cys peroxiredoxin oligomeric state by two-step FRET. Journal of biotechnology *149*, 272-279.

Shaner, N.C., Lin, M.Z., McKeown, M.R., Steinbach, P.A., Hazelwood, K.L., Davidson, M.W., and Tsien, R.Y. (2008). Improving the photostability of bright monomeric orange and red fluorescent proteins. Nature Methods *5*, 545-551.

Shannon, C.E. (1949). Communication in the Presence of Noise. Proc. IRE *37*, 10-21.

Shimomura, O., Johnson, F.H., and Saiga, Y. (1962). Extraction, Purification and Properties of Aequorin, a Bioluminescent Protein from the Luminous Hydromedusan,Aequorea. J. Cell. Comp. Physiol. *59*, 223-239.

Shishkova, S., Rost, T.L., and Dubrovsky, J.G. (2008). Determinate root growth and meristem maintenance in angiosperms. Annals of botany *101*, 319-340.

Shyu, Y.J., Suarez, C.D., and Hu, C.-D. (2008). Visualization of ternary complexes in living cells by using a BiFC-based FRET assay. Nature Protocols *3*, 1693 EP -.

Siriwardana, N.S., and Lamb, R.S. (2012). A conserved domain in the N-terminus is important for LEAFY dimerization and function in Arabidopsis thaliana. The Plant journal : for cell and molecular biology *71*, 736-749.

Somssich, M., Ma, Q., Weidtkamp-Peters, S., Stahl, Y., Felekyan, S., Bleckmann, A., Seidel, C.A.M., and Simon, R. (2015). Real-time dynamics of peptide ligand-dependent receptor complex formation in planta. Science signaling *8*, ra76.

Song, Y.H., Shim, J.S., Kinmonth-Schultz, H.A., and Imaizumi, T. (2015). Photoperiodic flowering. Time measurement mechanisms in leaves. Annual review of plant biology *66*, 441-464.

Spaepen, S., and Vanderleyden, J. (2011). Auxin and plant-microbe interactions. Cold Spring Harbor perspectives in biology *3*.

Splivallo, R., Fischer, U., Göbel, C., Feussner, I., and Karlovsky, P. (2009). Truffles regulate plant root morphogenesis via the production of auxin and ethylene. Plant Physiology *150*, 2018-2029.

Staal, M., Cnodder, T. de, Simon, D., Vandenbussche, F., van der Straeten, D., Verbelen, J.-P., Elzenga, T., and Vissenberg, K. (2011). Apoplastic alkalinization is instrumental for the inhibition of cell elongation in the Arabidopsis root by the ethylene precursor 1-aminocyclopropane-1-carboxylic acid. Plant Physiology *155*, 2049-2055.

Stegmann, M., Monaghan, J., Smakowska-Luzan, E., Rovenich, H., Lehner, A., Holton, N., Belkhadir, Y., and Zipfel, C. (2017). The receptor kinase FER is a RALF-regulated scaffold controlling plant immune signaling. Science (New York, N.Y.) *355*, 287-289.

Stein, M., Dittgen, J., Sánchez-Rodríguez, C., Hou, B.-H., Molina, A., Schulze-Lefert, P., Lipka, V., and Somerville, S. (2006). Arabidopsis PEN3/PDR8, an ATP binding cassette transporter, contributes to nonhost resistance to inappropriate pathogens that enter by direct penetration. The Plant cell *18*, 731-746.

Stock, K., Sailer, R., Strauss, W.S.L., Lyttek, M., Steiner, R., and Schneckenburger, H. (2003). Variable-angle total internal reflection fluorescence microscopy (VA-TIRFM).

Realization and application of a compact illumination device. Journal of microscopy *211*, 19-29.

Strader, L.C., and Bartel, B. (2009). The Arabidopsis PLEIOTROPIC DRUG RESISTANCE8/ABCG36 ATP binding cassette transporter modulates sensitivity to the auxin precursor indole-3-butyric acid. The Plant cell *21*, 1992-2007.

Strader, L.C., and Bartel, B. (2011). Transport and metabolism of the endogenous auxin precursor indole-3-butyric acid. Molecular plant *4*, 477-486.

Stührwohldt, N., Dahlke, R.I., Steffens, B., Johnson, A., and Sauter, M. (2011). Phytosulfokine-α controls hypocotyl length and cell expansion in Arabidopsis thaliana through phytosulfokine receptor 1. PloS one *6*, e21054.

Suárez-López, P., Wheatley, K., Robson, F., Onouchi, H., Valverde, F., and Coupland, G. (2001). CONSTANS mediates between the circadian clock and the control of flowering in Arabidopsis. Nature *410*, 1116-1120.

Sun, W., Cao, Y., Jansen Labby, K., Bittel, P., Boller, T., and Bent, A.F. (2012). Probing the Arabidopsis flagellin receptor. FLS2-FLS2 association and the contributions of specific domains to signaling function. The Plant cell *24*, 1096-1113.

Sun, Y., Fan, X.-Y., Cao, D.-M., Tang, W., He, K., Zhu, J.-Y., He, J.-X., Bai, M.-Y., Zhu, S., and Oh, E., et al. (2010a). Integration of brassinosteroid signal transduction with the transcription network for plant growth regulation in Arabidopsis. Developmental cell *19*, 765-777.

Sun, Y., Han, Z., Tang, J., Hu, Z., Chai, C., Zhou, B., and Chai, J. (2013). Structure reveals that BAK1 as a co-receptor recognizes the BRI1-bound brassinolide. Cell Research *23*, 1326 EP -.

Sun, Y., Wallrabe, H., Booker, C.F., Day, R.N., and Periasamy, A. (2010b). Three-color spectral FRET microscopy localizes three interacting proteins in living cells. Biophysical journal *99*, 1274-1283.

Sussex, I.M., Godoy, J.A., Kerk, N.M., Laskowski, M.J., Nusbaum, H.C., Welsch, J.A., and Williams, M.E. (1995). Cellular and molecular events in a newly organizing lateral root meristem. Philosophical transactions of the Royal Society of London. Series B, Biological sciences *350*, 39-43.

Sziraki, I., Balazs, E., and Kiraly, Z. (1975). Increased levels of cytokinin and indoleacetic acid in peach leaves infected with Taphrina deformans. Physiological Plant Pathology *5*, 45-50.

Tang, D., Wang, G., and Zhou, J.-M. (2017). Receptor Kinases in Plant-Pathogen Interactions. More Than Pattern Recognition. The Plant cell *29*, 618-637.

Thompson, M.A., Lew, M.D., and Moerner, W.E. (2012). Extending microscopic resolution with single-molecule imaging and active control. Annual review of biophysics *41*, 321-342.

Tsien, R.Y. (1998). The green fluorescent protein. Annual Review of Biochemistry *67*, 509-544.

Turck, F., Fornara, F., and Coupland, G. (2008). Regulation and identity of florigen. FLOWERING LOCUS T moves center stage. Annual review of plant biology *59*, 573-594.

Turkowyd, B., Virant, D., and Endesfelder, U. (2016). From single molecules to life. Microscopy at the nanoscale. Analytical and bioanalytical chemistry *408*, 6885-6911.

van Esse, G.W., van Mourik, S., Stigter, H., Hove, C.A. ten, Molenaar, J., and Vries, S.C. de (2012). A mathematical model for BRASSINOSTEROID INSENSITIVE1-mediated signaling in root growth and hypocotyl elongation. Plant Physiology *160*, 523-532.

van Esse, G.W., Westphal, A.H., Surendran, R.P., Albrecht, C., van Veen, B., Borst, J.W., and Vries, S.C. de (2011). Quantification of the brassinosteroid insensitive1 receptor in planta. Plant Physiology *156*, 1691-1700.

van Zanten, T.S., and Mayor, S. (2015). Current approaches to studying membrane organization. F1000Research *4*.

Verbelen, J.-P., Cnodder, T. de, Le, J., Vissenberg, K., and Baluška, F. (2006). The Root Apex of Arabidopsis thaliana Consists of Four Distinct Zones of Growth Activities. Meristematic Zone, Transition Zone, Fast Elongation Zone and Growth Terminating Zone. Plant Signaling & Behavior *1*, 296-304.

Vermeer, J.E.M., Wangenheim, D. von, Barberon, M., Lee, Y., Stelzer, E.H.K., Maizel, A., and Geldner, N. (2014). A spatial accommodation by neighboring cells is required for organ initiation in Arabidopsis. Science (New York, N.Y.) *343*, 178-183.

Vert, G., and Chory, J. (2006). Downstream nuclear events in brassinosteroid signalling. Nature *441*, 96-100.

Voie, A.H., Burns, D.H., and Spelman, F.A. (1993). Orthogonal-plane fluorescence optical sectioning. Three-dimensional imaging of macroscopic biological specimens. Journal of microscopy *170*, 229-236.

Vos, D. de, Vissenberg, K., Broeckhove, J., and Beemster, G.T.S. (2014). Putting theory to the test. Which regulatory mechanisms can drive realistic growth of a root? PLoS computational biology *10*, e1003910.

Wallrabe, H., Cai, Y., Sun, Y., Periasamy, A., Luzes, R., Fang, X., Kan, H.-M., Cameron, L.-C., Schafer, D.A., and Bloom, G.S. (2013). IQGAP1 interactome analysis by in vitro reconstitution and live cell 3-color FRET microscopy. Cytoskeleton (Hoboken, N.J.) *70*, 819-836.

Wang, G., Ellendorff, U., Kemp, B., Mansfield, J.W., Forsyth, A., Mitchell, K., Bastas, K., Liu, C.-M., Woods-Tör, A., and Zipfel, C., et al. (2008a). A genome-wide functional investigation into the roles of receptor-like proteins in Arabidopsis. Plant Physiology *147*, 503-517.

Wang, J., Jiang, J., Wang, J., Chen, L., Fan, S.-L., Wu, J.-W., Wang, X., and Wang, Z.-X. (2014). Structural insights into the negative regulation of BRI1 signaling by BRI1-interacting protein BKI1. Cell Research *24*, 1328-1341.

Wang, L., Li, H., Lv, X., Chen, T., Li, R., Xue, Y., Jiang, J., Jin, B., Baluška, F., and Šamaj, J., et al. (2015). Spatiotemporal Dynamics of the BRI1 Receptor and its Regulation by Membrane Microdomains in Living Arabidopsis Cells. Molecular plant *8*, 1334-1349.

Wang, X., and Chory, J. (2006). Brassinosteroids regulate dissociation of BKI1, a negative regulator of BRI1 signaling, from the plasma membrane. Science (New York, N.Y.) *313*, 1118-1122.

Wang, X., Goshe, M.B., Soderblom, E.J., Phinney, B.S., Kuchar, J.A., Li, J., Asami, T., Yoshida, S., Huber, S.C., and Clouse, S.D. (2005a). Identification and functional analysis of in vivo phosphorylation sites of the Arabidopsis BRASSINOSTEROID-INSENSITIVE1 receptor kinase. The Plant cell *17*, 1685-1703.

Wang, X., Kota, U., He, K., Blackburn, K., Li, J., Goshe, M.B., Huber, S.C., and Clouse, S.D. (2008b). Sequential transphosphorylation of the BRI1/BAK1 receptor kinase complex impacts early events in brassinosteroid signaling. Developmental cell *15*, 220-235.

Wang, X., Li, X., Meisenhelder, J., Hunter, T., Yoshida, S., Asami, T., and Chory, J. (2005b). Autoregulation and homodimerization are involved in the activation of the plant steroid receptor BRI1. Developmental cell *8*, 855-865.

Wang, Y.V., Wade, M., Wong, E., Li, Y.-C., Rodewald, L.W., and Wahl, G.M. (2007). Quantitative analyses reveal the importance of regulated Hdmx degradation for p53 activation. Proceedings of the National Academy of Sciences of the United States of America *104*, 12365-12370.

Wang, Z.-Y., Seto, H., Fujioka, S., Yoshida, S., and Chory, J. (2001). BRI1 is a critical component of a plasma-membrane receptor for plant steroids. Nature *410*, 380-383.

Wangenheim, D. von, Hauschild, R., and Friml, J. (2017). Light Sheet Fluorescence Microscopy of Plant Roots Growing on the Surface of a Gel. Journal of visualized experiments : JoVE.

Ward, C.W., Lawrence, M.C., Streltsov, V.A., Adams, T.E., and McKern, N.M. (2007). The insulin and EGF receptor structures. New insights into ligand-induced receptor activation. Trends in biochemical sciences *32*, 129-137.

Weigel, D., Alvarez, J., Smyth, D.R., Yanofsky, M.F., and Meyerowitz, E.M. (1992). LEAFY controls floral meristem identity in Arabidopsis. Cell *69*, 843-859.

Weinberg, Z.Y., and Puthenveedu, M.A. (2019). Regulation of G protein-coupled receptor signaling by plasma membrane organization and endocytosis. Traffic (Copenhagen, Denmark) *20*, 121-129.

Wen, R., Wang, S., Xiang, D., Venglat, P., Shi, X., Zang, Y., Datla, R., Xiao, W., and Wang, H. (2014). UBC13, an E2 enzyme for Lys63-linked ubiquitination, functions in root development by affecting auxin signaling and Aux/IAA protein stability. The Plant journal : for cell and molecular biology *80*, 424-436.

Wigge, P.A., Kim, M.C., Jaeger, K.E., Busch, W., Schmid, M., Lohmann, J.U., and Weigel, D. (2005). Integration of spatial and temporal information during floral induction in Arabidopsis. Science (New York, N.Y.) *309*, 1056-1059.

Willats, W.G., McCartney, L., Mackie, W., and Knox, J.P. (2001). Pectin. Cell biology and prospects for functional analysis. Plant molecular biology *47*, 9-27.

Witthöft, J., Caesar, K., Elgass, K., Huppenberger, P., Kilian, J., Schleifenbaum, F., Oecking, C., and Harter, K. (2011). The activation of the Arabidopsis P-ATPase 1 by the brassinosteroid receptor BRI1 is independent of threonine 948 phosphorylation. Plant Signaling & Behavior *6*, 1063-1066.

Witthöft, J., Caesar, K., Elgass, K., Huppenberger, P., Kilian, J., Schleifenbaum, F., Oecking, C., and Harter, K. (2014). The activation of the Arabidopsis P-ATPase 1 by the brassinosteroid receptor BRI1 is independent of threonine 948 phosphorylation. Plant Signaling & Behavior *6*, 1063-1066.

Wolf, S., Mravec, J., Greiner, S., Mouille, G., and Höfte, H. (2012). Plant cell wall homeostasis is mediated by brassinosteroid feedback signaling. Current biology : CB *22*, 1732-1737.

Wolf, S., van der Does, D., Ladwig, F., Sticht, C., Kolbeck, A., Schürholz, A.-K., Augustin, S., Keinath, N., Rausch, T., and Greiner, S., et al. (2014). A receptor-like protein mediates the response to pectin modification by activating brassinosteroid signaling. Proceedings of the National Academy of Sciences of the United States of America *111*, 15261-15266.

Xin, X.-F., Nomura, K., Underwood, W., and He, S.Y. (2013). Induction and suppression of PEN3 focal accumulation during Pseudomonas syringae pv. tomato DC3000 infection of Arabidopsis. Molecular plant-microbe interactions : MPMI *26*, 861-867.

Xue, Y., Xing, J., Wan, Y., Lv, X., Fan, L., Zhang, Y., Song, K., Wang, L., Wang, X., and Deng, X., et al. (2018). Arabidopsis Blue Light Receptor Phototropin 1 Undergoes Blue Light-Induced Activation in Membrane Microdomains. Molecular plant *11*, 846-859.

Yang, H., Matsubayashi, Y., Hanai, H., and Sakagami, Y. (2000). Phytosulfokine-alpha, a peptide growth factor found in higher plants. Its structure, functions, precursor and receptors. Plant & cell physiology *41*, 825-830.

Yant, L., Methieu, J., and Schmid, M. (2009). Just say no. Floral repressors help Arabidopsis bide the time. Current Opinion in Plant Biology *12*, 580-586.

Yeagle, P. (2016). The membranes of cells. Chapter 9 - Cholesterol and Related Sterols: Roles in Membrane Structure and Function (London: Academic Press is an imprint of Elsevier).

Yin, R., Arongaus, A.B., Binkert, M., and Ulm, R. (2015). Two distinct domains of the UVR8 photoreceptor interact with COP1 to initiate UV-B signaling in Arabidopsis. The Plant cell *27*, 202-213.

Yin, Y., Vafeados, D., Tao, Y., Yoshida, S., Asami, T., and Chory, J. (2005). A new class of transcription factors mediates brassinosteroid-regulated gene expression in Arabidopsis. Cell *120*, 249-259.

Yokota, T. (1999). Brassinosteroids. In Biochemistry and Molecular Biology of Plant Hormones, P.J.J. Hooykaas, M.A. Hall and K.R. Libbenga, eds. (s.l.: Elsevier textbooks), pp. 277–293.

Yun, H.S., Bae, Y.H., Lee, Y.J., Chang, S.C., Kim, S.-K., Li, J., and Nam, K.H. (2009). Analysis of phosphorylation of the BRI1/BAK1 complex in arabidopsis reveals amino acid residues critical for receptor formation and activation of BR signaling. Molecules and Cells *27*, 183-190.

Zhang, X., Zhou, L., Qin, Y., Chen, Y., Liu, X., Wang, M., Mao, J., Zhang, J., He, Z., and Liu, L., et al. (2018). A Temperature-Sensitive Misfolded bri1-301 Receptor Requires Its Kinase Activity to Promote Growth. Plant Physiology *178*, 1704-1719.

Zhao, R., Li, N., Xu, J., Li, W., and Fang, X. (2018). Quantitative single-molecule study of TGF-β/Smad signaling. Acta biochimica et biophysica Sinica *50*, 51-59.

Zhu, J.-Y., Li, Y., Cao, D.-M., Yang, H., Oh, E., Bi, Y., Zhu, S., and Wang, Z.-Y. (2017). The F-box Protein KIB1 Mediates Brassinosteroid-Induced Inactivation and Degradation of GSK3-like Kinases in Arabidopsis. Molecular cell *66*, 648-657.e4.

5 List of publications

Brassinosteroid signalling
In preparation

1. **Glöckner et al. 2019:** Quantitative description and computational modelling of the BRI1 response module controlling cell elongation growth. *In preparation for submission.*

2. **Glöckner et al. 2019:** Single-particle tracking photoactivated localization microscopy analysis of BRASSINOSTEROID INSENSITIVE 1 receptor (BRI1) dynamics and BRI1-related microdomain functions in plants. *In preparation for submission.*

3. **Glöckner et al. 2019:** Three-fluorophore FRET-FLIM enables the study of trimeric protein interactions and complex formation with nanoscale resolution in living plant cells. *In preparation for submission.*

Submitted

4. **Holzwart et al. 2019:** A novel mutant allele uncouples brassinosteroid-dependent and independent functions of BRI1. *Preprint on bioRxiv 605923, doi: https://doi.org/10.1101/605923*

Accepted

5. **Holzwart et al. 2019:** BRI1 controls vascular cell fate in the *Arabidopsis* root through RLP44 and phytosulfokine signaling. *Proceedings of the National Academy of Sciences USA.*

6. **Großeholz et al. 2019:** Specifying the role of BAK1-interacting receptor-like kinase 3 in brassinosteroid signaling. *Journal of Integrative Plant Biology.*

Signalling integration of other pathways
In preparation

7. **Aryal et al. 2019:** Regulation of ABCG36/PEN3/PDR8 during *Fusarium oxysporum* infection involves the LRR receptor-like kinase, ALK1. *In preparation for submission.*

Submitted

8. **Mohrholz et al. 2019:** The striking flower-in-flower phenotype of *Arabidopsis thaliana* Nossen (No-0) is caused by a novel LEAFY allele. *Preprint on bioRxiv 535120; doi: https://doi.org/10.1101/535120*

Accepted

9. **Arongaus et al. 2018:** *Arabidopsis* RUP2 represses UVR8-mediated flowering in noninductive photoperiods. *Genes and Development.*

Other
Accepted

10. (**Bergmann et al. 2019:** Morphology of hindwing veins in the shield bug *Graphosoma italicum* (Heteroptera: Pentatomidae). *Arthropod Structure and Development.*) *-::not part of the thesis::-*

5.1 Scientific contribution

1. **Glöckner, N.*; Großeholz, R.*; Wanke, F.; Jaspert, N.; Shabala, L.; Shabala, S.; Kummer, U.; Harter, K.**
I designed, performed and evaluated the (wetlab) experiments, contributed to the research concept and wrote the manuscript. The computational modelling, the literature search for its relevant parameters, the computational predictions resulting from the model, the scaled sensitivities test and the figures resulting from modelling was done by Ruth Großeholz.

2. **Glöckner, N.*; zur Oven-Krockhaus, S.*; Meixner, A.J., Harter, K.**
I designed, performed and evaluated major parts of the research and wrote the manuscript. Specifically, I ensured the fluorescence signal of mEOS of the seedlings obtained from Hosy et al. and grew the test-seedlings of Hosy et al., I generated the BRI1-mEOS construct, transformed the tobacco plants, defined the concentrations of chemicals and the time points of observation. Also, I propagated and checked the brassinosteroid mutant and overexpression line and performed the physiological root growth measurements. The carrying out, evaluation and the figures of the super-resolved live-cell microscopy was done by Sven Zur Oven-Krockhaus.

3. **Glöckner, N., zur Oven-Krockhaus, S.; Wackenhut, F.; Burmeister, M.; Wanke, F.; Holzwart, E.; Wolf, S.; Harter, K.**
I have designed, performed and evaluated the research and wrote the manuscript. The code of the Matlab and Python scripts was provided by the co-authors. Eleonore Holzwart cloned the 2in1 constructs for RLP44-BRI1 and RLP44-FLS2.

4. **Holzwart, E.; Glöckner, N.; Höfte, H.; Harter, K.; Wolf, S.**
   The realization, evaluation and interpretation of the mating-based split ubiquitin assays in yeast between RECEPTOR LIKE PROTEIN 44 (RLP44) and the BRASSINOSTEROID INSENSITIVE 1 (BRI1) and its mutant forms was performed by me.

5. **Holzwart, E.; Huerta, A. I.; Glöckner, N.; Garnelo Gómez, B.; Wanke, F.; Augustin, S.; Askani, J. C.; Schürholz, A.-K.; Harter, K.; Wolf, S.**
   The realization, evaluation and interpretation of the interaction test between RLP44 and FLS2 by fluorescence lifetime imaging microscopy (FLIM) was performed by me. I was involved in scientific discussions on the mode of action of RLP44.

6. **Großeholz, R.; Feldman-Salit, A.; Wanke, F.; Schulze, S.; Glöckner, N.; Kemmerling, B,; Harter, K.; Kummer, U.**
   I performed the statistical evaluation of the FRET-FLIM data.

7. **Aryal, B.; Huynh, J.; Hu, Z.; Schneuwly, J.; Di Donato, M.; Fukao, Y.; Lehmann, S.; Alejandro, S.; Ludwig-Muller, J.; Glockner, N.; Hothorn, M.; Dengjel, J.; Harter, K.; Martinoia, E.; Metraux, J.-P.; Geisler, M.**
   The carrying out, evaluation and interpretation of the interaction tests between ATP-BINDING CASETTE TRANSPORTER G family member 36 (ABCG36) with AUXIN-INDUCED LRR KINASE 1 (ALK1) and the plasma membrane p-type proton pump isoform 2 (AHA2) by fluorescence lifetime imaging microscopy (FLIM) was performed by me.

8. **Mohrholz, A.; Sun, H.; Gloeckner, N.; Hummel, S.; Kolukisaoglu, Ü.; Schneeberger, K.; Harter, K.**
   I explained and set-up the parameters for the FLIM interaction tests of LEAFY (LFY) and the newly identified mutant leafy allele LFY^{FIF}. I explained the statistical analysed of the generated data.

9. **Arongaus, A. B.; Chen, S; Pireyre, M.; Glöckner, N.; Galvão, V. C.; Albert, A; Winkler, J. B.; Fankhauser, C; Harter, K; Ulm, R.**
   The carrying out, evaluation and interpretation of the interaction assays between REPRESSOR OF PHOTO-MORPHOGENESIS 1 and 2 (RUP1 and RUP2) with CONSTANS (CO) by fluorescence lifetime imaging microscopy (FLIM) was performed by me.

10. (**Bergmann, P.; Richter, S.; Glöckner, N.; Betz, O.**
    I adjusted the detection settings of the confocal laser scanning microscope and performed the imaging.) - not part of the thesis

∗ Authors contributed equally to this work.

A Attachment

A.1 Brassinosteroid signalling

A.1.1 Quantitative description and computational modelling of the BRI1 response module controlling cell elongation growth

In preparation

This article describes, how differential growth behaviour along the root axis of *Arabidopsis thaliana* in response to brassinosteroid signalling is established. Along the root axis of *A. thaliana*, the ratio between the amount of P-type proton pumps (AHAs) and the brassinosteroid receptors (BRI1) increases, whereas the ratio between BRI1 and the inhibitory BAK1-INTERACTING RECEPTOR-LIKE KINASE 3 (BIR3) stays constant. Both computational modelling and physiological experiments underline the importance of the proton pumps in combination with the hormone receptor for differential signalling outputs (e.g. apoplastic pH, elongation growth). Accounting for the varying protein levels, the model is able to describe the differential growth behaviour along the root axis. Thus, the changing ratio between BRI1 and AHAs likely determines the onset of elongation growth and consequently the location of the elongation zone.

Quantitative description and computational modelling of the BRI1 response module controlling cell elongation growth

Nina Glöckner[1a], Ruth Großeholz[1b], Friederike Wanke[a], Nina Jaspert[a], Lana Shabala[c], Sergej Shabala[c], Ursula Kummer [b] and Klaus Harter[a]

[1] R.G and N.G contributed equally to this work.
[a] Center for Plant Molecular Biology (ZMBP), Eberhard Karls University Tübingen, Germany
[b] Centre for Organismal Studies (COS), Ruprechts-Karl-University Heidelberg, Germany
[c] Stress Physiology Laboratory, University of Tasmania, Australia

Summary

The brassinosteroid plant hormone family (BR) is involved the fast control of cell elongation growth. The activation of the plasma membrane-resident brassinosteroid receptor BRASSINOSTEROID INSENSITIVE 1 (BRI1) and its cofactor BRI1-ASSOCIATED KINASE (BAK1) leads to the dissociation of the inhibitor BAK1-INTERACTING RECEPTOR-LIKE KINASE 3 (BIR3) and eventually to the activation of P-type ATPases (AHAs). This causes the acidification of the extracellular space, hyperpolarization of the PM and wall loosening, eventually leading to cell elongation. This signalling module is well described at constituent level; however, it is not yet understood, how these players act collectively in space and time to mediate differential cell elongation in response to BR in various plant tissues.

Here we show by quantitative *in vivo* approaches that the protein amount of AHA2 differs in the fast-growing elongation zone compared to that in the less/non-growing meristematic and root hair zone in *Arabidopsis thaliana* roots. While the protein ratio of BIR3 and BRI1 stays the same along the root axis, the ratio of AHAs and BRI1 is significant lower in the meristematic zone. Including the protein amounts in a computational model, we evaluated the regulation and dynamics of the fast BR response module *in silico* including membrane hyperpolarization and cell elongation. Both the model and experiments underline the importance of the proton pumps in combination with the hormone receptor. Accounting for the varying protein levels, the model is able to describe the differential growth behaviour along the root axis, including non-invasive proton flux measurements and apoplastic pH measurements. We, therefore, hypothesize that the ratio of AHA to BRI1 is the crucial parameter that controls the differential competence of cells to elongate in response to BR along the root axis.

Graphical abstract

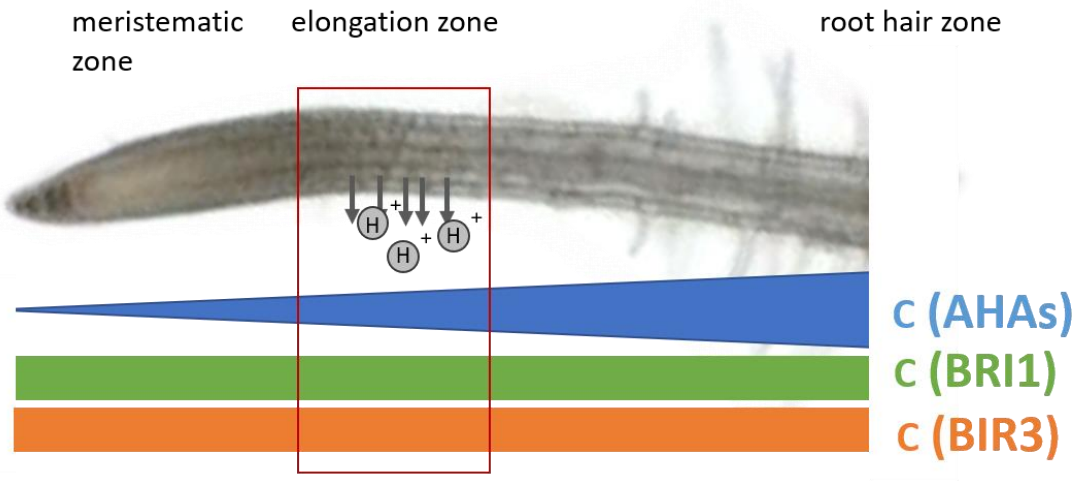

Along the root axis of the model plant *A. thaliana*, the ratio between the amount of P-type proton pumps (AHAs) and the brassinosteroid receptors (BRI1) increases, whereas the ratio between BRI1 and the inhibitory BAK1-interacting receptor-like kinase 3 (BIR3) stays constant. We hypothesize, that the changing ratio between BRI1 and AHAs determines the onset of elongation growth and consequently the location of the elongation zone.

Introduction

Plant cells are encased by rigid cell walls that protect them and provide stability. All growth-related developmental processes consequently involve the regulation or the modification of the cell wall and the intracellular turgor. An elegant example of this balance between cell wall rigidity and turgor is observed in the elongation zone of the root (EZ). It is defined as the region, where the newly produced cells of the meristematic zone (MZ) start to elongate and become twice as long as thick (Dünser et al., 2019). Master regulators on the precise position, where elongation growth starts, are determined by a differential auxin and cytokinin distribution along the root axis (Pacifici et al., 2018). Elongation growth is mediated by two mechanisms: Firstly, the stiffness/stability of the cell wall is decreased by acidification of the extracellular space (apoplast). It was shown, that the phytohormones auxin and brassinosteroid (BR) lead to the activation of the plasma membrane (PM)-resident P-type proton ATPases (AHAs). The active transport of protons into the extracellular space leads to the transient hyperpolarization of the PM. The acidic growth theory states, that this drop in the apoplastic pH followed by the activation of cell wall-resident expansins mediates polymer creep (McQueen-Mason and Cosgrove, 1994; Cosgrove, 2000), loosening of crosslinks between the components of the wall, followed by the swelling of the wall and eventually elongation growth (Rayle and Cleland, 1970; Cleland and Haughton, 1971; Hager et al., 1971). A recent study using nuclear magnetic resonance measurements found that indeed acidic medium led to weaker cellulose–pectin interactions (Phyo et al., 2019). At the same time, the protoplast presses against the wall as the intracellular turgor increases (Hager, 2003; Dünser et al., 2019).The direction of the cellulose microfibrils determines the direction of growth. During fast elongation growth, cells become four times their former size in only two hours (Verbelen et al., 2006), with a highest mean elongation rate of 0.7 µm min^{-1} observed for roots cells of 3-days old *Arabidopsis* seedlings (Fasano et al., 2001). With increasing distances from the root tip, the elongation rate decreases again, as cells reach their final size and differentiate. The differentiated root hair zone of the mature root is responsible for nutrient uptake, which is mediated by a variety of primary active and secondary active transporters (Blumwald, 1987; Shi, 2013).

Brassinosteroid (BR) signalling is mediated by the plasma membrane (PM)-resident leucin rich repeat receptor like kinases (LRR-RLK) BRASSINOSTEROID INSENSITIVE 1 (BRI1) and its co-receptor BRI1-ASSOCIATED KINASE 1 (BAK1). In the absence of the brassinosteroid hormone (BR), large populations of BRI1 and BAK1 are physically in close proximity and form heterodimers (Nam and Li, 2002; Wang et al., 2005b; Yun et al., 2009; Bücherl et al., 2013). The accidental activation of signalling from the BRI1 module is inhibited by several mechanisms: The C-terminus of the BRI1 receptor acts as an autoinhibitory domain of the kinase activity (Wang et al. 2005). Secondly, the C-terminus of the cytoplasmic inhibitor BRI1 KINASE INHIBITOR 1 (BKI1) interacts with the kinase domain of BRI1 (Wang and Chory, 2006), preventing trans-phosphorylation events between the receptor´s kinase domains (Wang et al., 2014). Only recently, the BAK1-INTERACTING RECEPTOR-LIKE KINASE 3 (BIR3), which is also a LRR-RK, was found to interact with both BRI1 and BAK1. It keeps the receptor and co-receptor in proximity, while inhibiting the trans-phosphorylation of the kinase domains (Imkampe et al., 2017; Großeholz et al., 2019). Lastly, the BOTRYTIS-INDUCED KINASE 1 (BIK1) contains a putative myristoylation motif and associates with both BRI1 and BAK1 (Veronese et al., 2006; Lin et al., 2013). It acts as a negative regulator in BR signalling and as a positive regulator in plant immunity (Lin et al., 2013). Binding of the BR hormone to the extracellular island domain of BRI1 creates a novel interface for the interaction with BAK1 (Wang et al., 2005a; Hothorn et al., 2011; Santiago et al., 2013; Sun et al., 2013). This in turn leads to the a release of the inhibitor BIR3 from BAK1 (Imkampe et al., 2017; Großeholz et al., 2019), the correct orientation of the cytoplasmic domains of BRI1 and BAK1 (Wang et al., 2014), the auto- and trans-phosphorylation of the two kinase domains, the phosphorylation of a tyrosine residue of BKI1 leading to its dissociation from the plasma membrane (PM) (Jaillais et al., 2011) and lastly the BAK1-independent phosphorylation of BKI1 by BRI1, followed by BIK1 dissociation (Lin et al., 2013). Eventually these events in the BRI1 module result in the activation or repression of BR-responsive genes, mediated by phosphorylation and dephosphorylation events of several downstream signalling proteins (Mora-García et al., 2004; Yin et al., 2005; Vert and Chory, 2006; Zhu et al., 2017) and in the activation of the PM-resident P-type proton pumps (AHAs) within 20 minutes (Caesar et al., 2011; Witthöft et al., 2011). This fast activation of the AHAs occurs in close vicinity with components of the BRI1 module, requires BRI1 kinase activity, includes their

phosphorylation and causes the hyperpolarization of the PM (Caesar et al., 2011; Witthöft et al., 2011; Miao et al., 2018; Minami et al., 2019) but is independent of transcriptional regulation, as the processes of signalling, transcription and translation takes longer than 20 minutes (Goda et al., 2008; Moore et al., 2018).

In summary, the constituents of the BR/BRI1 perception module and signalling pathway are well understood. However, it is less clear how the identical set of proteins leads to a differential regulation of plant growth in space and time. To address this question, we combined spatially resolved quantification of *in vivo* protein levels with computational modelling to elucidate, which parameters and factors within this multi-protein network are responsible for the precise regulation. With the repeated feed-back between model simulations from the computational model and experimental testing of those quantitative simulations *in vivo*, we found that (i) the proton pump to receptor ratio (AHAs/BRI1) suffices to explain how a specific elongation response to BR can be established precisely in the elongation zone of the root and (ii) that the absence of the inhibitor BIR3 has only minor effect on elongation growth.

Results

Computational modelling is a powerful tool for analysing a system of interest *in silico*. In particular, models consisting of ordinary differential equations (ODEs) contain detailed knowledge on the kinetic parameters of a system allowing for the analysis of the dynamics and regulation of the system. Here, we employed an ODE model to study the initiation and regulation of the fast BR response pathway. In this work, only the main results of the computational modelling are shown and all details for the model structure, parameter estimation and simulations can be found in the dissertation of Ruth Großeholz (Großeholz, 2018).

A computational model for the description of the brassinosteroid signalling module in the plasma membrane

We established an ODE-based computational model of the brassinosteroid signalling events in COPASI leading to proton extrusion and E_m hyperpolarization (Fig.1). The top rectangle represented the cell wall, the central one the PM with the proteins known to contribute to signalling as coloured boxes connected by transition rates (small numbers) and the bottom rectangle represented the cytoplasm. In the absence of BR, the receptor BRI1 (red) and the co-receptor BAK1 (blue) are inhibited by BIR3 (green). Upon binding of the brassinolide (BL, yellow circle), a potent BR, to BRI1 the inhibitor BIR3 is released from BAK1 and BRI1 (reaction number [3], [4]). Furthermore, BL binding to BRI1 [5] causes the (i) the activation of BIK1 (orange) [7], (ii) the dissociation of BKI1 (purple) from the PM into the cytoplasm [6] and the (iii) full interaction/hetero-dimerization of BRI1 and BAK1 [9] which leads to Ser/Thr auto- and trans-phosphorylation [10]. In addition, the C-terminal tail of the proton pump AHA (dark blue) is phosphorylated [11], which in turn leads to the up-regulation of its activity, proton extrusion into the apoplast extracellular space [1] and E_m hyperpolarization. This is counter-weighted by proton leakage back across the PM [2] and probably by cation import by a transporter (not incorporated yet). The deactivation reactions are shown as light grey lines [d1-d7].

With this model, we were able to describe the apoplast acidification and E_m hyperpolarization in response to BL application at cellular level. Unknown model parameters were fitted to data from Caesar et al. (2011) and allowed a precise

reproduction of the membrane potential over time after 10 nM, 50 nM and 100 nM BL hormone treatment with an exemplary model behavior for 10 nM BL shown (Fig. 1B). To reproduce the experimentally observed strain rates in the elongating cell model, the parameters of the growth function were adjusted to describe the data by Beemster & Baskin (1998), with a strain rate of about 30% h^{-1} for 6 days old seedling. The effective cell size after hormone application at time point zero can reproduce the training data and yielded an effective strain rate of about 32% h^{-1} (Fig. 1C).

Protein quantification reveals a steep gradient of AHA2 but not of BRI1 and BIR3 along the root axis

We next were interested of how specificity in the signalling events and differential response is achieved in the context of the entire root. If all components of the perception module and signalling pathway are present to the same abundance in each cell and there is no BR gradient along the root axis, then the signalling output should be identical (unless there is cross-talk from other pathways that modulate the sensitivity of the system). As the measurement of BR gradients at high spatial resolution is not yet possible, we tested the hypothesis, that the relative abundance of the different proteins in the BR/BRI1 perception and response module is the cause for the differential cellular response along the root axis.

To do so, we quantified the relative protein abundance of *pBIR3*-expressed BIR3-GFP in the *bir3-2* mutant (Imkampe et al., 2017) and *pAHA2*-expressed AHA2-GFP in the *aha2-4* mutant (Fuglsang et al., 2014) by applying biochemical and cell biological approaches. As an reference, we used the *pBRI1::BRI1-GFP* line generated by (Friedrichsen et al., 2000), in which the absolute number of BRI1-GFP receptor molecules per μm^2 of PM had been quantified before (van Esse et al., 2011; van Esse et al., 2012). As the GFP was identical for all used fusion proteins, a fluorescence intensity-based quantification was possible.

The GFP fluorescence intensity of roots of 5d old seedlings was quantified at identical regions of interest (ROI) in the meristem (red) near the quiescent centre (QC) and in the epidermis/cortex (brown) approx. 250 µm from the root tip (Fig. 2A). The amount of BIR3-GFP was 1.4 x the abundance of BRI1-GFP in both the meristem and the outer cell layers (epidermis/cortex). There was almost no AHA2-GFP fluorescence signal in the meristem (Fig. 2B, C); the relative amount of AHA2-GFP in the epidermis/cortex

about 250 µm from the tip was 0.3 x the abundance of BRI1-GFP. In order to assess, whether these amounts were representative for the entire root, we quantified the fusion proteins in total extracts and microsomal fractions of roots using a GFP antibody. Due to its high linear dynamic range, we used a IR-Dye-coupled secondary antibody for quantification (Wang et al., 2007). The amount of BIR3-GFP was approx. 1.5 x the abundance of BRI1-GFP, with variation in the values between 1.3 x and 2.3 x. (Supp. Mat. 1). The quantification of BIR3-GFP by Western blotting revealed similar results as with fluorescence quantification by confocal microscopy. The amount of AHA2-GFP was approx. 2.8 x the abundance of BRI1-GFP, with values between 2.5 x and 3.1 x (Supp. Mat. 1) and one western blot with 5 x (not shown). This result was in contrast to the much lower AHA2-GFP amount in the root tip as determined by fluorescence quantification. We, thus, analysed, whether AHA2-GFP accumulation was indeed increased in mature root tissues and quantified the fluorescence intensity of BRI1-GFP and AHA2-GFP in the root hair zone (RHZ), in the middle of the root (*brown*) and below the hypocotyl (blue). As shown in Fig. 3B, the AHA2-GFP amount was about 5x higher than the BRI1-GFP abundance in the RHZ. Below the hypocotyl, the relative amount of AHA2-GFP was 3 x to the abundance of BRI1-GFP and in the same order of magnitude as revealed by quantitative Western blotting.

The P-type ATPase family of *A. thaliana* consist of seven members. To get an additional estimation on the amount of proton pumps in the root, we checked the steady-state absolute transcript amount of all *AHA* members in the eFP browser (http://bar.utoronto.ca/efp/cgi-bin/efpWeb.cgi). *AHA1* and *AHA2* transcripts were more abundant in the root than the transcripts of the other pump members and their expression level is comparably strong (Table 1). In addition, the transcript data derived from the eFP browser (Table 1) and the *pAHA1*-expressed AHA1-GFP and *pAHA2*-expressed AHA2-GFP by Pacifici et al (2018) support our observation on protein level, that the expression of the proton pumps increases with the distance from the root tip. To improve our quantitative model, the values depicted in (Fig. 3C) were added. Here, the BRI1 receptor density is taken from van Esse et al. (2011), the AHA2:BRI1 ratio of 0.14 in the meristem results from the quantification of (Fig. 2A Meristem), of 0.28 in the epidermis and cortex from (Fig. 2A Epidermis/Cortex) and of 2.8 from the average of the Western Blotting (Supp. Mat. 1). For the values of BIR3 also result from Fig. 2A and Supp. Mat. 1 were used.

By combining the measured ratios with the number of BRI1 molecules per μm^2, we were able to estimate the molecule numbers (Supp. Mat. 2), which we added to our model and henceforth used the refined model.

Table 1. Steady-state absolute transcript levels (a.u.) in the root of the *Arabidopsis thaliana P-ATPase* (AHA) family members derived from the Arabidopsis eFP browser. From left to right: meristematic zone (MZ), the elongation zone (EZ), mature zone (MaZ). Asterisks (*) indicates expression only in procambium cells.

	MZ	EZ	MaZ
AHA1	939	1127	1691
AHA2	817	817	1635
AHA3	0*	0*	0*
AHA4	16*	16*	16*
AHA5	0-38*	0-38*	0-38*
AHA6	0*	0*	0*

Computational modelling predicts the AHA/BRI1 protein ratio being the major parameter for the activity of the BRI1 module in the plasma membrane

As shown above, the AHA(2):BRI1 ratio strongly changed along the root axis being low in the MZ and high in the EZ, whereas the BIR3:BRI1 ratio stayed constant. We therefore were interested, whether the model could provide insights, which parameters of the BRI1 response module might implement strong positive or negative effects. We thus used the computational model to calculate the influence of the model parameters and protein concentrations on the membrane potential. In this analysis, we calculated the scaled sensitivities, which represent the relative change of e.g. the membrane potential in response to a relative change in a parameter (Fig. 4, top). The output of such a test describes how strongly an increase of a single respective parameter

influences the parameter of interest, in our case the E_m. The scaled sensitivities were calculated for all 50 model parametrizations and each depicted as little, colour-coded block in a row (Fig. 4 left). Effective changes close to zero were marked as white or shades of white (Fig. 4). If an increase of a factor leads to increased proton efflux, it was marked in shades of blue (Fig. 4). If an increase of a parameter inhibits proton efflux, it was marked in red (Fig. 4), where the same shade of a colour represents a similar strength of the effect.

As depicted in Fig. 4, following parameters had consistently a strong positive effect on E_m: The activity of the proton pump k, the AHA1:AHA2 ratio, the BRI1 receptor density and especially the AHA2:BRI1 ratio (Fig. 4, blue). Concordantly, the factors that had a strong negative influence on the E_m were an increased proton leakage k back into the cell, an increasing inhibitory activity of the C-terminal tail of the AHAs, a higher value of the affinity for the BL binding to the receptor (BRI1) and higher amounts of BIR3 in comparison to BRI1 (Fig. 4, red). Interestingly, the interaction rate between BRI1 and BIR3 as well as BAK1 and BIR3 did not have a strong negative effect on the E_m (Fig. 4, reaction number 04 and 03, top). This indicates, that the ratio between the inhibitor and the receptor may be more important than mild changes in the affinity.

Brassinosteroid signalling actually leads to a spatially resolved acidification of the extracellular space along the root axis

Our observation that the AHA:BRI1 ratio changes significantly along the root axis, and the prediction of the ODE model that the AHA2:BRI1 ratio has a major impact on the apoplast acidification and linked E_m hyperpolarisation upon BL binding, prompted us to test, whether BL-triggered, spatially resolved proton extrusion and apoplast acidification can be in fact observed.

Therefore, we first performed proton-specific microelectrode ion flux estimation (MIFE; reference) measurements at the root elongation zone, approx. 400 µm from the tip (Fig. 5A), and the root hair zone (Fig. 5B) of 5-days old *Arabidopsis* seedlings. Net proton fluxes were normalized to the average ion flux determined for the period of 10 min before treatment. As a mock control, the seedlings were treated with DMSO with a concentration existing in the BL solution. After mock treatment, an increase in proton influx into the elongation zone of wild type seedlings (Col-0) was observed that stayed

constant for the following 20 min (Fig. 5A blue). Upon treatment of the wild type seedlings with 10 nM BL, the onset of a proton efflux of 10 nmol m^{-2} s^{-1} was detectable at the elongation zone that continued over the following 20 min (Fig. 5A red). However, the addition of 10 nM BL to *bri1-301* mutant seedlings, a variant of BRI1 with strongly reduced kinase activity (Zhang et al., 2018), did not induce a net proton efflux (Fig. 5A yellow).

Interestingly, the determination of the proton fluxes at the root hair zone did not reveal an increase in proton efflux in response to 1 nM BL treatment (Fig. 5B).

As a method complementary to MIFE, we measured the apoplastic pH by ratiometric confocal laser scanning microscopy after staining the roots with 8-hydroxypyrene-1,3,6-trisulfonicacid-trisodiumsalt (HPTS) (Barbez et al., 2017). The calibration curve for the ratiometric fluorescence intensity and the pH was linear between pH of 4.8 and 5.8 and the scattering error due to different tissue densities negligible (Supp. Mat. 3). The presence of both 0.1 nM and 1 nM BL for 1 h resulted in a decrease of the apolastic pH in the elongation zone roots compared to the elongation zone of mock-treated roots (Fig. 5C). Surprisingly, only addition of 0.1 nM BL led to a significant decrease in the ratiometric intensity in the elongation zone (Fig. 5C asterisk). Representative images of the ratiometric intensities in the root apoplast with set region of interest (data from figure 5C) is shown (Fig. 5D). The average pH of the mock-treated plants was 5.46 in the meristematic zone of the root tip and 5.35 in the elongation zone. The pH of the roots treated with 0.1 nM BL was 5.33 in the tip and 5.16 in the EZ. For the roots treated with 1 nM BL the pH was 5.41 in the tip and 5.27 in the EZ. Interestingly, the apoplastic pH in the in the tip and EZ in the roots treated with 0.1 nM BL was lower than for the roots treated with 1 nM BL (Fig. 5D).

In previous studies, proton gradient-linked E_m hyperpolarization was observed within 20 min after BL application (Caesar et al., 2011; Witthöft et al., 2014). Secondary regulatory effects may influence the apoplastic pH already after 1 h. It can be reasoned, that the response of the root cell to 1 nM BL is faster than the response to 0.1 nM BL and that the response to 1 nM BL is already fading out after 1 h treatment. In this case, it is possible that, with 0.1 nM BL, the pH will also increase at a later time point. We therefore performed a long-term measurement of the apoplastic pH after 0.1 nM BL treatment. Ratiometric images were acquired and evaluated after mock or BL (0.1 nM) treatment at the indicated time points (Fig. 5E). 10 min after onset of

treatment, there was no significant difference in the apoplastic pH between BL (0.1 nM) and mock treated roots (Fig. 5E). As shown before, the apoplastic pH in the EZ was significantly different from the control treatment after 1 h on 0.1 nM BL (Wilcoxon, $p < 0.05$) (Fig. 5E). 1h 40 min later, the apoplastic pH in the EZ of the BL-treated roots increased and was similar to the mock control. The ratio increased over the time-course of 2h40 independent of the treatment both in the meristem and the elongation zone, emphasizing that precise comparison in time necessary.

BRI1 regulates the basal activity of proton pumps

If the prediction of the computational model is correct, apoplast acidification and E_m hyperpolarization depend on the number (density) of functional BRI1 (Fig. 4). Therefore, we determined by MIFE and ratiometric HPTS measurements, whether BRI1 is important for the regulation of the apoplastic pH in the absence of exogenously applied BL. To this end, we again used 5-days-old seedlings of the wild type and the *bri1-301* mutant, with a strongly impaired kinase activity of BRI1 (Zhang et al. 2018). A strong gradient of proton fluxes from the root tip to the elongation zone with an onset of proton efflux approximately 450 µm from the root were observed for the wild type (Fig. 6A). In contrast, this gradient was almost diminished along the root axis of *bri1-301* seedlings (Fig. 6A). Comparable results were obtained by the HPTS measurements (Fig. 6B): The pH gradient between the meristematic zone of the tip (Tip) and the elongation zone (dEZ) was much less pronounced in roots of *bri1-301* mutant seedlings compared to those of the wild type (Fig. 6B).

These data indicate that the presence of kinase-active BRI1 is required for the establishment of the proton flux and pH gradient along the axis of the root.

Computational modelling of the ectopic overexpression of proton pumps predicts the competence for BL-induced elongation growth in cells of the meristematic zone

As shown in the previous sections, the predictions of the computational model on the significance of the AHA:BRI1 ratio and the BRI1 receptor density for apoplast acidification, pH-linked E_m hyperpolarization and elongation growth were experimentally supported by our MIFE and ratiometric HPTS measurements. In consequence, an increase in the AHA:BRI1 ratio should establish the competence for BL-induced apoplast acidification, E_m hyperpolarization and eventually elongation

growth in otherwise non-responsive cells. Therefore, we computationally modelled how the ectopic expression of AHAs in the cells of the meristematic zone would affect their elongation growth compared to meristematic cells that have wild type AHA:BRI1 ratios. To do so, we used a cell-based ODE model and performed *in silico* physiology by plotting the cell length over time. Compared to mock treatment (-BL; reflecting a BR biosynthetic mutant), the application of 10 nM BL did not lead to a significant elongation response of meristematic cells expressing the wild type AHA:BRI1 ratio and induces only a slight acidification of the apoplast (Fig. 7). However, the 10-fold over-expression of AHA2 (AHA-OE) in the presence of 10 nM BL induced apoplastic acidification and E_m hyperpolarization as well as the onset of elongation growth in the meristematic cells *in silico*: After four hours, the length was 40 µm for AHA-OE cells treated with 10 nM BL compared to 8 µm for wild type cells.

To corroborate the *in silico* results, we were able to access published data. Pacifici and colleagues (2018) had established a transgenic *Arabidopsis* line, which enables the dexamethasone (DEX) inducible overexpression of AHA2 in the root. As shown in figure 8A, the cells in the meristematic zone started to swell and elongate 20 h after DEX application. No such phenotype was observed for mock treated roots (Fig. 8A). Simultaneously, the division rate of the meristematic cells decreased after DEX treatment so that the overall length of the root tip became shorter (Fig. 8B). Interestingly, the length of the cells in the EZ does not significantly differ between DEX and mock treated roots, indicating that the BRI1 module (and other systems linked to it) functions at saturating level in the EZ with endogenous BR levels. In summary, this observation is in accordance with the prediction of our computational model in the sense that the relative AHA abundance in the cells along the root axis is the major rate limiting factor for the elongation growth competence of the different root tissues.

Discussion

Our approach to study cell elongation growth is unique, as the repeated interplay between the refinement of the model and the generation of new predictions from the computational model on physiological responses followed by testing of these hypothesis lead to a refined understanding on the brassinosteroid signalling module. We showed, that the amount of BRI1 and BIR3 stays the same in the meristematic zone and the elongation zone, whereas the amount of proton pumps (AHAs) increases along the root axis. Also other studies found, that the concentration of both AHA1 and AHA2, the most abundant proton pumps in roots, increases along the root axis (Pacifici et al., 2018). It could be expected, that with an increased AHA-expression level, also the cell elongation growth rises. In this case, a strong proton extrusion in the root hair zone would be expected upon BL treatment, as AHA-level was highest in the root hair zone. However, we did not find an increase in proton extrusion in the root hair zone upon 10nM BL treatment compared to control conditions. This suggests, that the amount of proton pumps is not the only factor for the signalling response. Also, in the RHZ, the proton pumps are the energy source for secondary active transport. Conceivably, a small BL-induced proton pump activation was not visible in the possibly steady-state active proton pumps.

We tested in the computational model, which factors have the strongest negative or positive influence on proton extrusion. The model clearly predicted, that the amount and activity of BRI1 and AHAs, and consequently the AHAs:BRI1 ratio was decisive for signalling output. In the root hair zone, the proton pump mediates the primary active transport that enables secondary active or passive transport of nutrients via antiporter and symporters. We propose, that in the root hair zone the amount of BRI1 relative to the AHAs is too small to activate a significant proportion of proton pumps. Any increase in proton efflux is probably masked by the constitutive activity of the AHAs in the root hair zone. Possibly, BL is also involved in this steady state activity, as epibrassinolide treatment of barley seedlings guarantees longer root hairs under saline conditions (Azhar et al., 2017). On the other hand, we propose, that the AHAs concentration relative to BRI1 in the meristematic zone is too low to induce significant proton efflux upon BL signalling. A mechanistic explanation on how the position of the elongation zone is determined in roots, could be, that it is always located where the AHAs:BRI1 ratio is in the dynamic range for efficient signalling output. To predict signalling

responses upon BL treatment, we thus propose the AHAs:BRI1 ratio as decisive elements in the long and complex signalling cascade.

This hypothesis was supported by two other observations: Firstly, we found that BRI1 was involved in the steady state proton efflux in the beginning of the elongation zone. The observed increase of proton efflux in the elongation zone in wild type plants is in accordance with previous observations (Staal et al., 2011; Xu et al., 2012). The reason for a relative proton influx in the meristem compared to elongation zone is, that the protons transported out of the elongation zone do not disappear, but cycle back into tissues with no or reduced efflux (Baluška and Mancuso, 2013). Consequently, the combination of proton extrusion in the elongation zone and proton influx at the tip cause this gradient in apoplastic pH between meristem and elongation zone. With a decreased functionality of the BRI1 kinase domain, the gradient in proton fluxes between the meristem and the elongation zone was decreased. It has been shown, that oscillations in proton and calcium fluxes precede thrusts in the elongation growth (Shabala and Newman, 1997). It will be interesting to test, if the inhibition of calcium fluxes modulates BL-induced growth and apoplastic acidification.

Secondly, upon a DEX-induced increase of AHA2 at the plasma membrane, the size of the meristematic zone decreased, as formerly non-elongating cells start to elongate. This observation matches the prediction from the computational model. It is noteworthy, that the model may overestimate the importance of BRI1, as it was the basis for the quantitative description of other parameters such as BIR3 and AHA2. It is unlikely, though, that our hypothesis is wrong, as physiological data support that indeed the ratio is important. In the future, this can be tested once more. If indeed the AHAs:BRI1 ratio is decisive (and not the AHAs abundance alone), then loss of BRI1 should counteract the AHA2-OE induced growth in the meristematic zone. It will be interesting to investigate the apoplastic pH upon DEX-treatment of *bri1-301* mutants transformed with *pUBQ::AHA2-GR* compared to the published pUBQ::AHA2-GR line. Alternatively, an additional shrinkage of the meristematic zone for DEX-treated seedlings transformed with both pBRI1::BRI1-GFP and pUBQ10::AHA2-GR could be tested. Also, BRI1 expression in the meristematic zone should lead to an increased cell elongation growth in the root tip. In the light of our findings, phenotypes that have been described as inhibition of the cell cycle progression (González-García et al.,

2011) may also be due secondary effects of the disrupted balance between cell elongation growth and cell divisions in favour of the prior one.

Interestingly, the computational model also found, that a decrease in inhibition by BIR3 would have a mild effect on proton extrusion and only a strong overexpression of BIR3 would significantly decrease proton efflux. Indeed, the *bir3-2* ko-mutant was shown to have weak growth-related phenotypes and only strong BIR3-OE plants showed strongly reduced growth (Imkampe et al., 2017). This remarkably shows, that by a continuous feed-back between modelling and testing of the predictions, new and correct predictions on signalling behaviour can be generated. This can lead to a better understand of the complex signalling pathways observed for many hormonal signalling pathways.

In summary we propose, that auxin and cytokinin are responsible for the patterning of the root on a larger scale (Di Mambro et al., 2018) that influences the basal state of the extracellular pH and with this, the basal competence to elongate. Interestingly, the extracellular domains of BRI1 and BAK1 were shown to interact only in acidic environment (Santiago 2013, Sun 2013, Hutten 2017, Hohmann 2018). This could provide a previously not mentioned cross-talk between auxin and BL signalling and an autoregulatory increase in interaction in the elongation zone. Brassinosteroid hormones provide an important additional layer for fine-tuned and fast responses on cell elongation growth. Regulation of elongation growth by the brassionosteroid signalling module could provide an additional or more fine-tuned layer of regulation than the modification of protein abundance of AHAs in the elongation zone (Haruta et al., 2018) alone. Several mechanisms on negative feed-back on cell elongation growth exists in the elongation zone, such as the peptide hormones rapid alkalinization factors (RALFs) by regulation of expansins (Park et al., 2010; Bergonci et al., 2014; Xu et al., 2014; Dressano et al., 2017; Campos et al., 2018), other cell wall integrity signalling cues (Feng et al., 2018; Dünser et al., 2019; Kesten et al., 2019), peptide hormones (Meng et al., 2012; Whitford et al., 2012; Matsubayashi, 2018), ethylene (Růzicka et al., 2007; Staal et al., 2011; Ma et al., 2014; Le Deunff et al., 2016; Lv et al., 2018), abscisic acid (Li et al., 2017; Ma et al., 2019; Takatsuka and Umeda, 2019), calcium signalling (Zhao et al., 2013; Shih et al., 2015; Campos et al., 2018; Vriese et al., 2019) and reactive oxygen species (Demidchik and Shabala, 2018; Lv et al., 2018) that could

provide fast cross-linking of the fibers of the extracellular matrix. As only recently a link between cell wall integrity sensing, phytosulfokine peptide hormones and brassinosteroid signalling has been established, it will be interesting to investigate their interplay on the regulation of the apoplastic pH in the elongation zone to better understand cell elongation growth (Wolf et al., 2014; Holzwart et al., 2018; Garnelo Gomez et al., 2019).

Material and methods

Plant material

Seeds were surface sterilized and placed on ½ MS (Murashige and Skoog) medium plates with 1% phytoagar and 1% succhrose followed by stratification at 4°C in the dark for two days. Then plants were grown upright in growth chambers under long day conditions (cycling 16 h light/ 8 h dark) at 19°C to 22°C for five days.

Quantification

Quantification of the GFP signal was performed by confocal laser scanning microscopy (CLSM) on a Leica SP8 microscope with HyD detectors. Detector was set to 400 and minimal laser power of 488nm laser line (1% Argon, 1% 488nm) with 6-fold line average for minimum bleaching. The low laser intensity also ensured intensities below the saturation limit. Same settings were used for all images of one microscopy session. Region of interest of the same size were quantified with Fiji with the integrated intensity feature. Only straight-lying roots of 5d old seedlings were quantified.

Quantification by Western blot was performed with α-GFP (mouse), 1:1000 from Roche and α-mouse-IR680RD (goat) 1:10000 from Licor or α-mouse-AP 1:6000 (goat) from Biorad. Overall protein amount was quantified and equal amounts were loaded. Loaded protein amount was double-checked by Coomassie staining of a reference gel. Gels were checked for complete transfer after wetblot. For precise quantification of the IR-Dye680LT fluorescence signal, background subtraction of the Col-0 lane at the same height for each specific band was performed with Image Studio Lite.

MIFE

For Microelectrode ion flux estimation (MIFE) measurements, seedlings were instead grown in continuous light conditions. Experiments were performed as described by (Fuglsang et al., 2007; Fuglsang et al., 2014; Wu et al., 2015). 5d old *A. thaliana* seedlings were equilibrated in bath medium (0.1 mm CaCl2, 0.5 mm KCl at pH 5.8) for 2h before the measurements. Only seedlings without proton oscillations were measured. At time point zero, 1 nM BL or an equivalent amount of DMSO was added. Bathing solution was mixed two times by carefully pipetting up and down after addition of treatment. The proximal position of the electrode (near the root) and the distal

position (far from the root) was swapped compared to a previous study with MIFE (Fuglsang et al., 2014). Consequently. for our measurements, a decrease in values represents proton efflux and an increase represents proton influx.

Apoplastic pH measurements with HPTS staining

HPTS measurements were performed as previously described (Barbez et al., 2017). The 100 mM stock solution of 8-hydroxypyrene-1,3,6-trisulfonicacid-trisodiumsalt (HPTS) (Sigma Aldrich, http://www.sigmaaldrich.com/catalog/substance/8hydroxypyrene136trisulfonicacidtrisodiumsalt52439635869611?lang=de&region=AT) was freshly dissolved in ddH_2O and added to warm ½ MS + 0.8% phytoagar medium to a final concentration of 1 mM before pouring the plates (½ MS+HPTS). 5 days old seedlings were pre-stained for 30-60 min on ½ MS+HPTS. For treatment, seedlings were carefully transferred to a thin piece of agar (½ MS+HPTS+treatment) so that the cotyledons were above the agar block and placed into large nunc-chambers (Ibidi^{TM}) with the roots facing the coverslip and the agar piece on top. Thus, physiological conditions were ensured over a long period of time. Brassinolide hormone (BL) had a final concentration of 1 nM with an effective dilution of DMSO (Thermo Scientific) of 1:10^9. Thus, for 0.1 nM BL the effective DMSO dilution was 1:10^{10}. For the measurement with both 0.1 nM and 1 nM DMSO with a 1:10^9 was used as mock-treatment. For the measurement with only 0.1 nM BL the 1:10^{10} DMSO dilution was used. Ratiometric imaging at the Leica SP8 confocal laser scanning microscope was performed with sequential scan with ex=405 nm and ex=458 nm on PMTs. Only for the calibration curve medium, a tip of MES (~0.01%) on 0.5 l ½ MS + 0.8% phytoagar was added to buffer the pH. Parameters of the automated script by Barbez and colleagues (2017) were adjusted to our settings (Supp. Material 4).

Computational modelling

The brassionsteroid signalling model consisting of ordinary differential equations was created using COPASI (Hoops et al., 2006) and comprises the known reactions of the fast BR response pathway. Generally, reaction rate laws were defined as mass action kinetics. An overview of the specific reactions and settings can be found in (Großeholz, 2018). The time course simulations were run deterministically using the LSODA

algorithm as implemented in COPASI. Parameter values were taken from literature wherever possible. The remaining, unknown parameters were estimated using the particle swarm algorithm (Eberhart & Kennedy, 1995) as implemented in COPASI. If the parameter range was completely unknown, an interval of 10^{-6} to 10^{6} was set during parameter estimation. To account for the uncertainty introduced by the unknown parameters, an ensemble of 50 models with equally good parameter values was created and all subsequent simulations were run for all models in the ensemble.

The scaled sensitivities of the model output (here: the membrane potential) with respects to all model parameters and global quantities were calculated as implemented in COPASI. Further details on the modelling can be found in the dissertation of Ruth Großeholz (Großeholz, 2018).

Statistics

For calculation of average, standard error (SE) and standard deviation (SD) Excel v1809 or SAS JMP 14 were used. Images were generated with Microsoft Excel v1809. For small sample numbers the 2-sample t-test was chosen (de Winter, J. C .F., 2013).

Figures

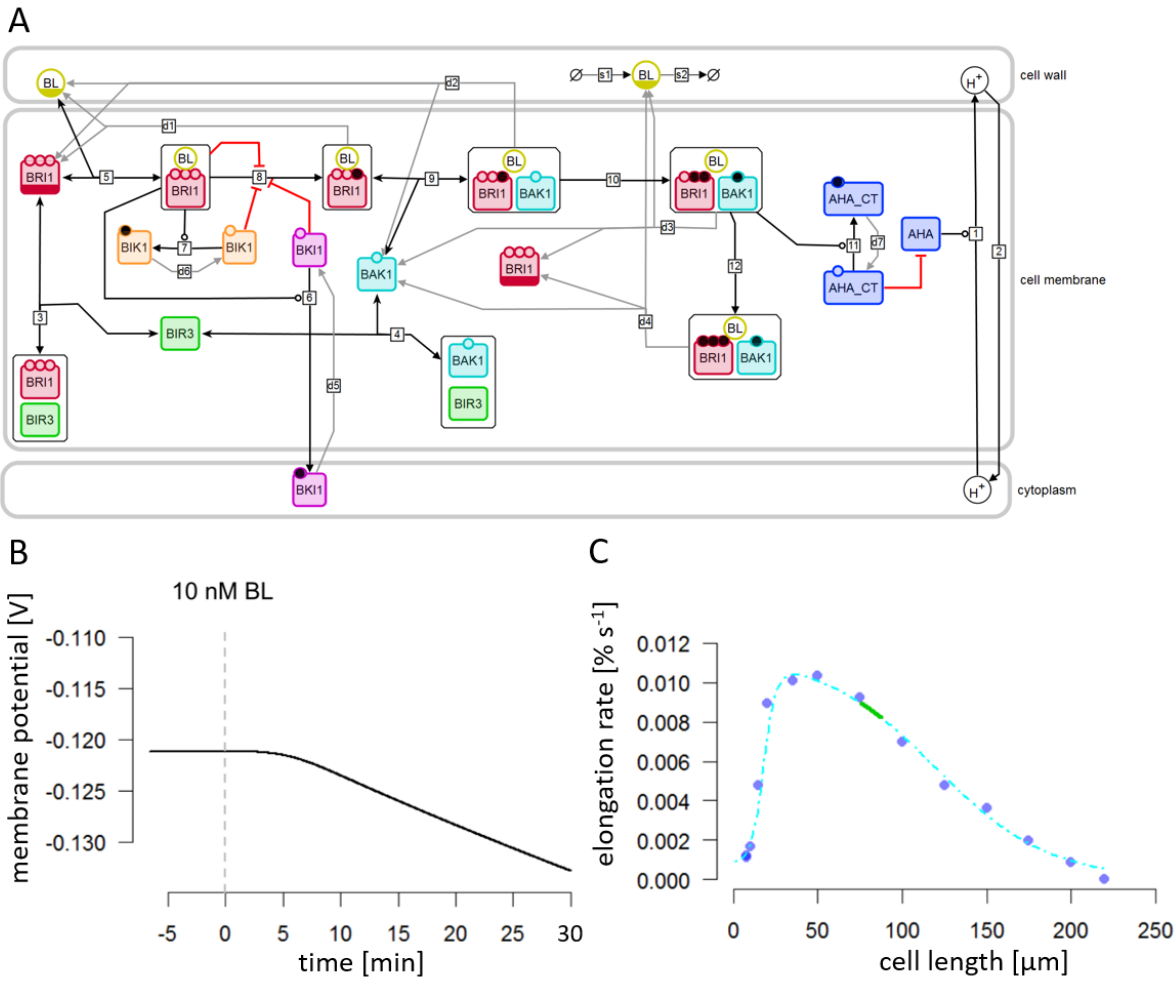

Figure 1. Quantitative computational ordinary differential equation (ODE) model in COPASI of the BRI1 response module at subcellular resolution, leading to proton extrusion, apoplast acification, E_m hyperpolarization and cell elongation growth.
(A) Model scheme adhering to the systems biology graphical notation (SBGN) (Le Novère et al., 2009). Representation of the cell wall (top grey rectangle), the plasma membrane (PM) with the signalling components as coloured boxes in it (middle grey rectangle) and the cytoplasm (bottom grey rectangle). The brassinosteroid hormone, in this case brassinolide (BL), is represented as yellow circle. In the absence of BL, the receptor BRI1 (red) and the co-receptor BAK1 (blue) are inhibited by BIR3 (green). BIK1 (pink) and BKI1 (orange) also inhibit the activation of BRI1. The proton extrusion mediated by AHA (dark blue) is activated by the BL-bound BRI1-BAK1 heterodimer. Phosphorylation is indicated as small black circle at the upper border of a protein. All reactions are indicated as numbers in boxes: transport of protons into the extracellular space by AHA [1], proton leakage across the PM [2], transient monomerization of BRI1 [3] and BAK1 [4], step-wise activation of BRI1 [5], phosphorylation of BKI [6], phosphorylation of BIK1 [7], phosphorylation of BKI1 [8], direct interaction/hetero-dimerization of BRI1 and BAK1 [9], full activation by further auto- and trans-phosphorylation events [10], phosphorylation of the c-terminal tail of AHA [11]. The reactions for the cessation of the signalling events is included as [d7-d1].

(B,C) Behaviour of the ODE model for the fast BR response including cell elongation.
(B) Simulated membrane hyperpolarization in response to 10 nM BL. Unknown model parameters were estimated based on the measurements by Caesar et al.
(C) The rate of the concurrent cell elongation (green) follows the experimentally determined growth rates (blue data points, cyan extrapolation) (Beemster & Baskin).

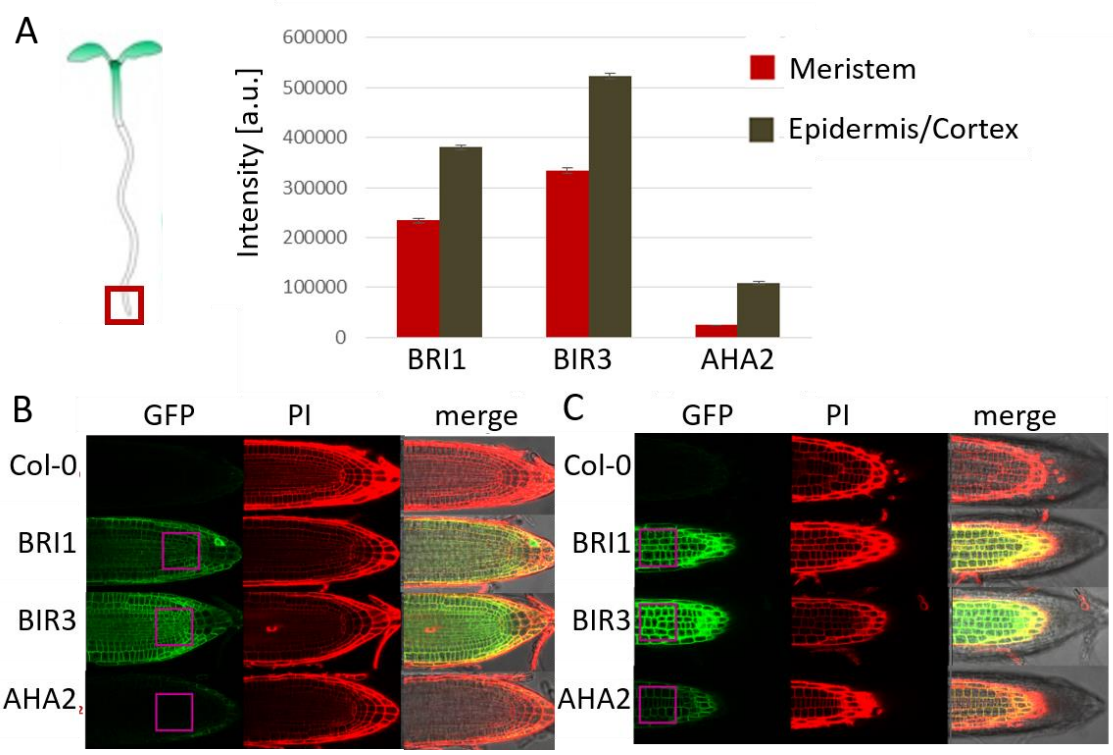

Figure 2. Quantification of the GFP fluorescence intensity in the meristematic zone revealed different abundance of AHA2-GFP, BRI1-GFP and BIR3-GFP in the root tip

(A) Quantified fluorescence intensity revealed from 50x50 µm squares in the root tip of 5-days-old *A. thaliana* seedlings containing either *pBRI1::BRI1-GFP* (BRI1; wild type background) (Friedrichsen et al., 2000), *pBIR3::BIR3-GFP* (BIR3; *bir3-2* background) (Imkampe et al., 2017), *pAHA2::AHA2-GFP* (AHA2; *aha2-4* background) (Fuglsang et al., 2014) in the meristem (*red*) and the epidermis/cortex (*brown*). Representative images for the meristem and the epidermis/cortex are shown in (B) and (C). Only straight-laying roots were used with $n \geq 39$ ROIs ± SE for each line in 6 repetitions.

(B) Representative images demonstrating the GFP quantification in the meristem. The GFP channel (GFP, *first column*), the propidium iodide cell wall staining (PI, *second column*), and a composite image including brightfield image (merge, *third column*) are shown. The designation of the transgenic *A. thaliana* lines is identical to that of (A). The background fluorescence of wild type roots (Col-0) is served as control. To always quantify the same ROI, the image was taken with the root tip at the central right side and the quiescent center (QC) visible. The ROI was placed with its central right side containing the QC.

(C) Representative images demonstrating the GFP quantification in the epidermis/cortex. The GFP channel (GFP, *first column*), the propidium iodide cell wall staining (PI, *second column*), and a composite image including brightfield image

(merge, *third column*) are shown. The designation of the transgenic *A. thaliana* lines is identical to that of (A) and (C). The background fluorescence of wild type roots (Col-0) served as control. After image acquisition of the meristem, the z-focus was shifted towards the cover slip, so that the cell layer below the epidermis (cortex) was visible. Rarely, parts of the endodermis were included. ROI was set with its left side approx. 250 µm from the root tip in the meristematic zone.

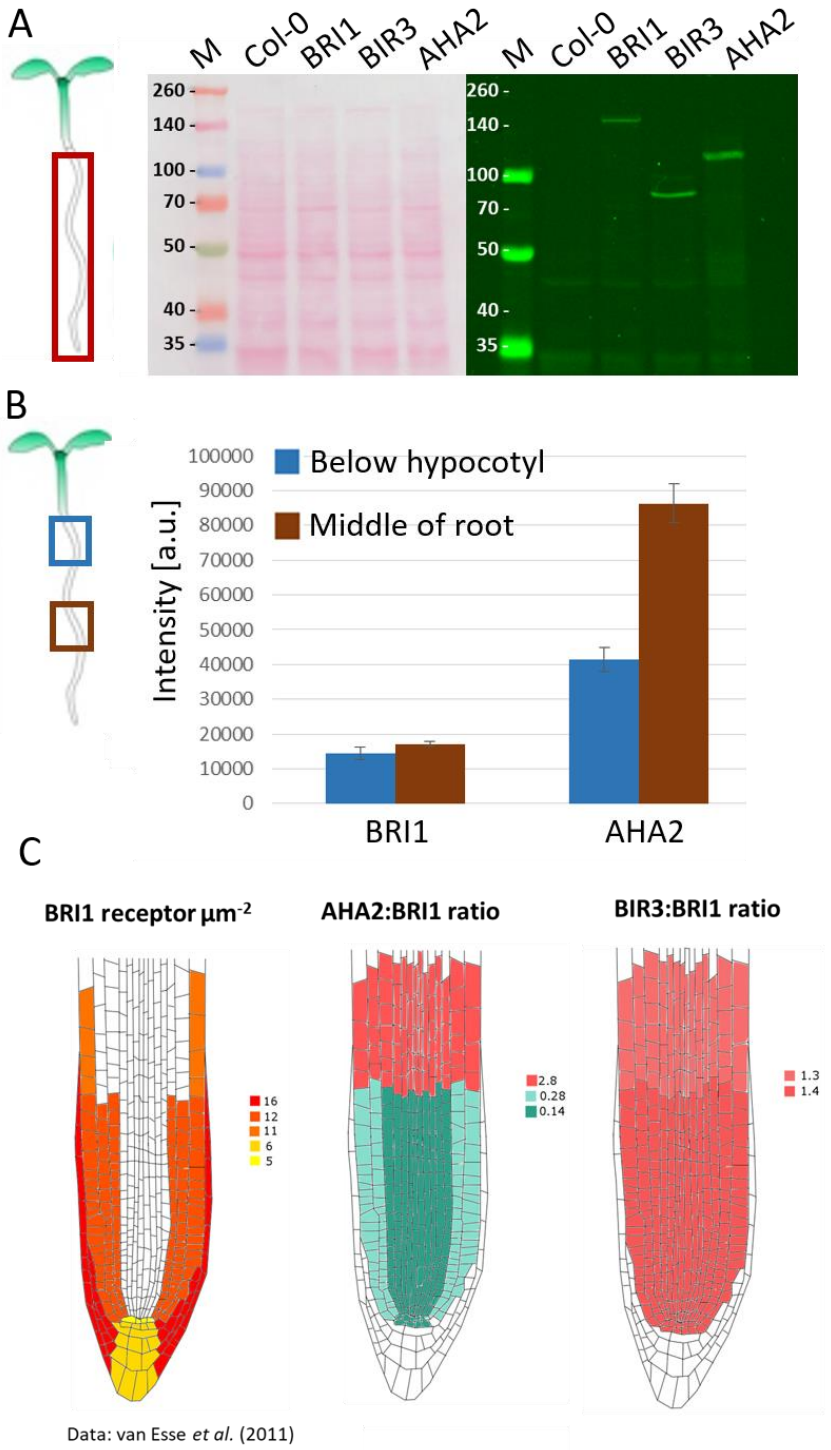

Figure 3. Quantification of the AHA2-GFP, BRI1-GFP and BIR3-GFP amounts by fluorescence intensity measurement and quantitative Western blots revealed a strong gradient of the AHA:BRI1 ratio along the root axis.

(A) Western blot of the indicated GFP fusion proteins. 40 µg of the microsomal fraction were loaded, which was extracted from roots of 5-days-old *A. thaliana* seedlings containing either *pBRI1::BRI1-GFP* (BRI1; wild type background) (Friedrichsen et al., 2000), *pBIR3::BIR3-GFP* (BIR3; *bir3-2* background) (Imkampe et al., 2017), *pAHA2::AHA2-GFP* (AHA2; *aha2-4* background) (Fuglsang et al., 2014). The

microsomal fraction of wild type roots (Col-0) served as a control. The blotted membrane was probed with an anti-GFP antibody from mouse followed by a IR-Dye680LT labelled secondary anti-mouse antibody. The apparent molecular weight of the GFP fusions is 160 kDa for BRI1, 95 kDa for BIR3 and 130 kDa for AHA2. The Ponceau staining of the blotted membrane (left) serves as loading control.
(B) Quantified fluorescence intensity *in vivo* in *A. thaliana* roots revealed from 50x50 µm squares in the root hair zone (brown) and below the hypocotyl (*blue*) of 5-days-old *A. thaliana* seedlings. The designation of the transgenic *A. thaliana* lines is identical to that of (A). Sample number was >7 ± SE.
(C) Graphical representation of the experimental data included in the quantitative computational model. The absolute BRI1-GFP abundance (*left*; number of receptors per μm^2 plasma membrane) were derived from the publication of (van Esse et al., 2012). The representation of the AHA2:BRI1 (*middle*) and BIR3:BRI1 ratio (right) is based on own measurements.

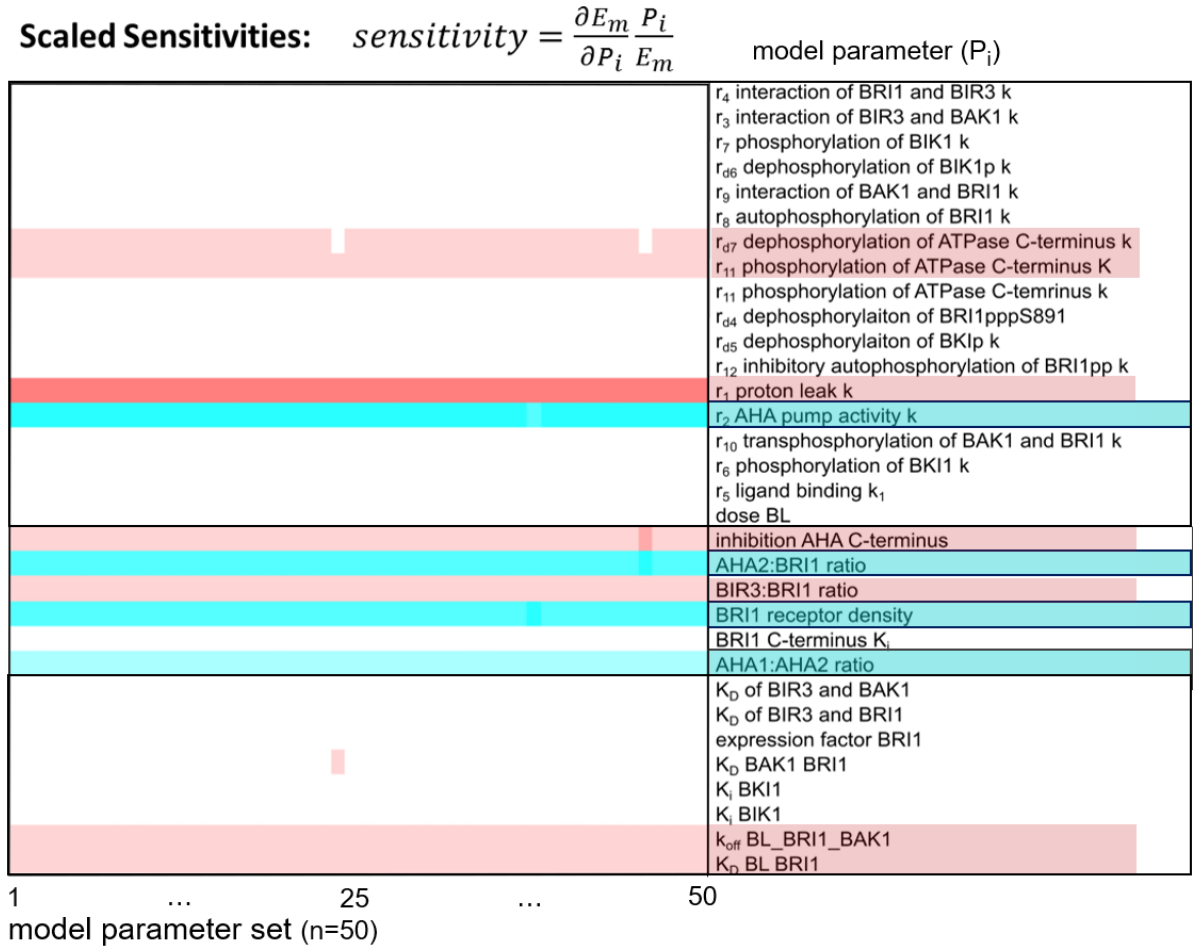

Figure 4. Prediction from the ODE model, which parameters (right column) have a positive (blue), negative (red) or no effect (white) on the membrane potential (E_m)

Scaled sensitivities of the E_m are determined by calculating the relative change of the membrane potential (δEm/Em) in response to the relative change of the model parameters (δPi/Pi), where δE_m is the change of the membrane potential and δPi the change in the parameter of interest. For each modified parameter (list on the right), a model ensemble consisting of 50 independent parameterizations (left, with count number indicated at bottom) and its relative impact on the proton efflux is colour-coded (white/blue/red). An increase in parameter Pi that increases proton efflux is indicated as blue rectangle, where different shades in colour indicates similar net effects. An increase in Pi that reduces proton efflux is colour-coded red and a neutral or no effect in white.

Numbers 1-12 indicate rate changes and d4-d7 the inactivation rates used in the model (compare Fig. 1A). The protein amounts and auto-inhibition (middle box) as well as the parameters that were involved in more than one reaction rate (lower box) are shown. In the lower box, Kd indicates the dissociation constants, Km the Michaelis constant, Ki the concentration of half-maximal inhibition and koff the dissociation rate of BL when BRI1-BAK1 are strongly interacting.

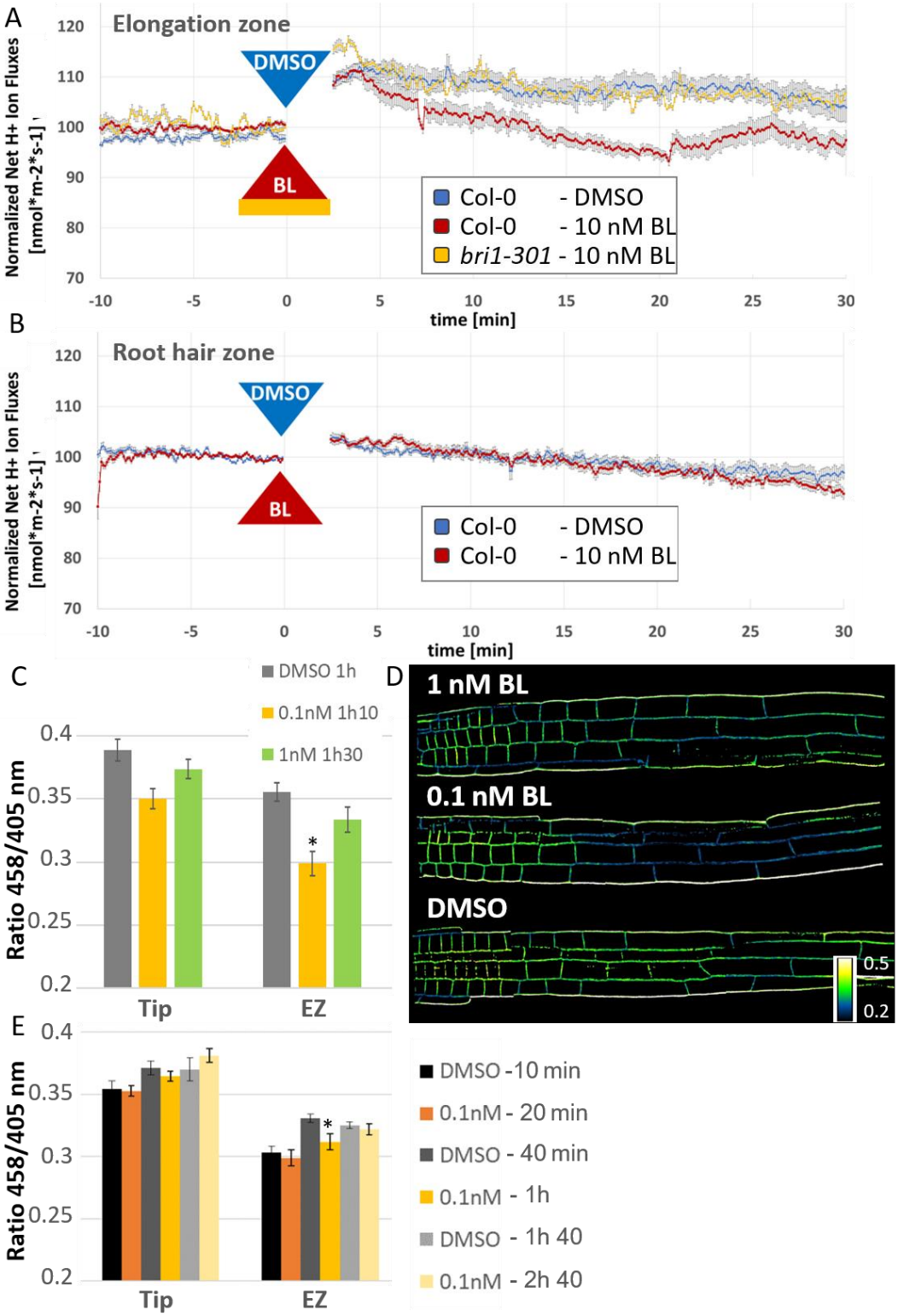

Figure 5. BL leads to acidification of the root surface in the elongation zone (A) but not in the root hair zone (B) and less in the meristematic zone (C, Tip).
(A) Microelectrode ion flux estimation (MIFE) measurements of the proton fluxes at the surface of the elongation zone approx. 400 µm from the root tip of 5-days-old *A. thaliana* wild type (Col-0) and *bri1-301* mutant seedlings. Proton fluxes were normalized to the average flux measured 10 min before treatment. Treatment at time point 0 was with either 10 nM BL or DMSO as a control. For the shorter roots of the

bri1-301 mutant seedlings, the distance from root tip was adjusted in a way that the tip of the electrode was placed next to the elongation zone. Only roots without H^+ oscillations before onset of treatment were chosen for measurements. Sample number (n) was ≥ 4 ± SE.
(B) MIFE measurements of the proton fluxes at the surface of the root hair zone. Conditions and treatments were as described in (A). Sample number (n) was ≥ 6 ± SE.
(C) Average apoplastic ratiometric intensity after 8-hydroxypyrene-1,3,6-trisulfonicacid-trisodiumsalt (HPTS) staining in the meristematic zone (Tip) and the elongation zone (EZ) for DMSO-treated control (*grey*), 0.1 nM BL (*yellow*) and 1.0 nM BL (*green*) treated roots of 5-days-old *A. thaliana* seedling. Treatment was done for either 1 h 10 min (0.1 nM BL) or 1 h 30 min (1.0 nM BL). Sample numbers (n) were ≥ 4 ± SE for the meristematic zone and ≥ 7 ± SE for the elongation zone.
(D) Representative example for the ratiometric HPTS measurement of the data shown in (C).
(E) Average apoplastic ratiometric HPTS intensity in the meristematic zone (Tip) and the elongation zone (EZ) for DMSO-treated control (*grey*) and 0.1 nM BL treated (yellow) roots of 5-days-old *A. thaliana* seedling over a time span of 2 h 40 min. Sample numbers (n) were ≥ 4 ± SE for the meristematic zone and ≥ 9 ± SE for the elongation zone. Statistically significant differences in the 2-sample t-test with $p<0.5\%$ are indicated by an asterisk.

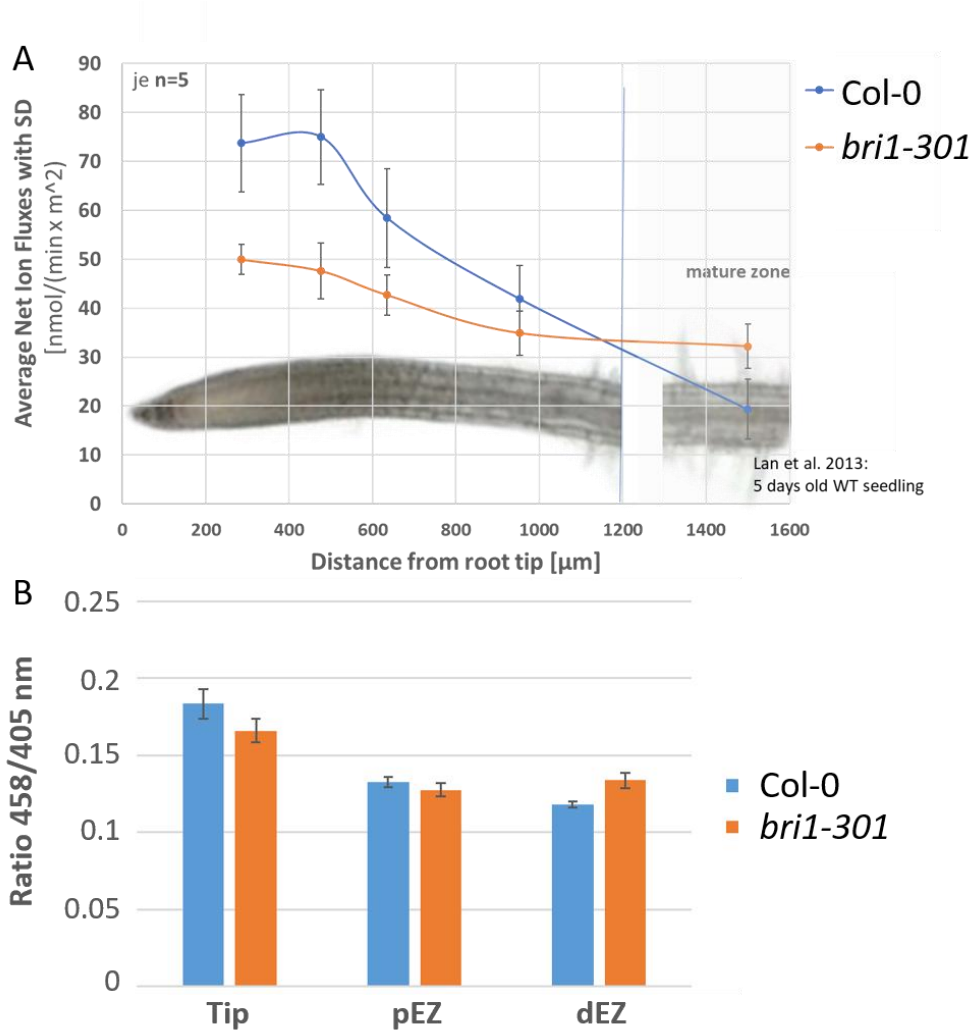

Figure 6. The establishment of the proton flux gradient along the root axis and apoplastic acidification in the elongation zone depends on functional BRI1.
(A) Microelectrode ion flux estimation (MIFE) measurements of the average proton fluxes along the root axis of 5-days-old wild type (Col-0) (blue) and *bri1-301* mutant *A. thaliana* seedlings (orange). The sample number was n = 5 ± SE each. The schematic root was adapted from Lan and colleagues (Lan et al., 2013).
(B) Average apoplastic ratiometric HPTS intensity in the meristematic zone (Tip), the proximal elongation zone (pEZ) and distal elongation zone (dEZ) for roots of 5-days-old wild type (blue) and *bri1-301* mutant (orange) *A. thaliana* seedlings. Treatment of the seedlings and calculation of the 458 nm/405 nm ratio was carried out described in figure 5. The sample numbers (n) were 4 ± SE for the meristematic zone, 4 ± SE for pEZ and 10 ± SE for dEZ.

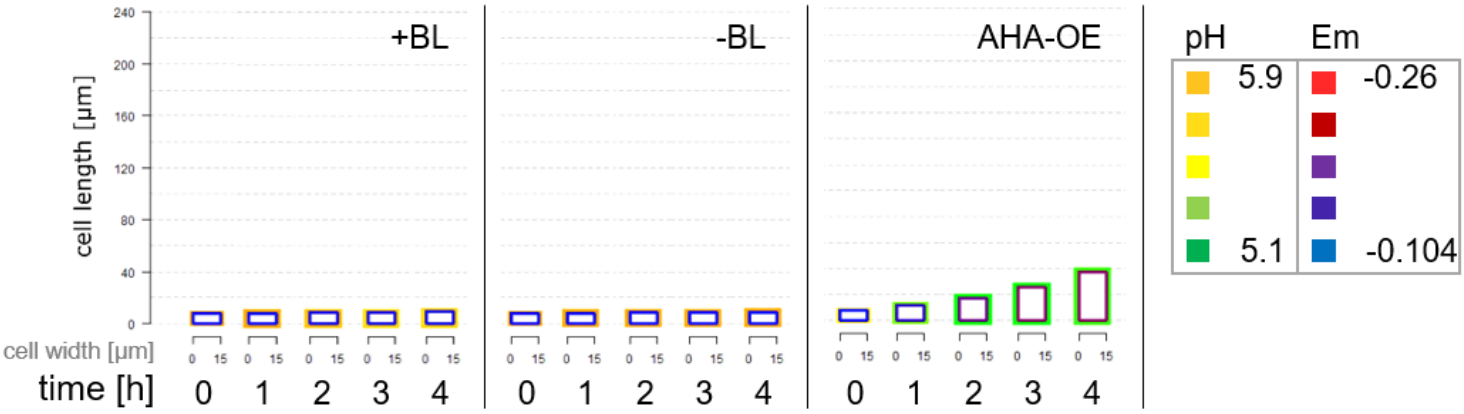

Figure 7. ODE modelling of apoplast acidification and E_m hyperpolarization leading to elongation growth of wt meristematic cells and for overexpression of AHA.

The cell physiological behaviour and elongation growth of meristematic cells with an initial cell length of 8 µm is simulated over the time course of 4 h in presence of 10 nM BL (left), without BL (middle) and for a 10-fold overexpression of AHA2 with 10nM BL (right). The apoplastic pH (pH; outer line) is represented as colour gradation between orange and green and the membrane potential (E_m; inner line) as colour gradation between red and blue.

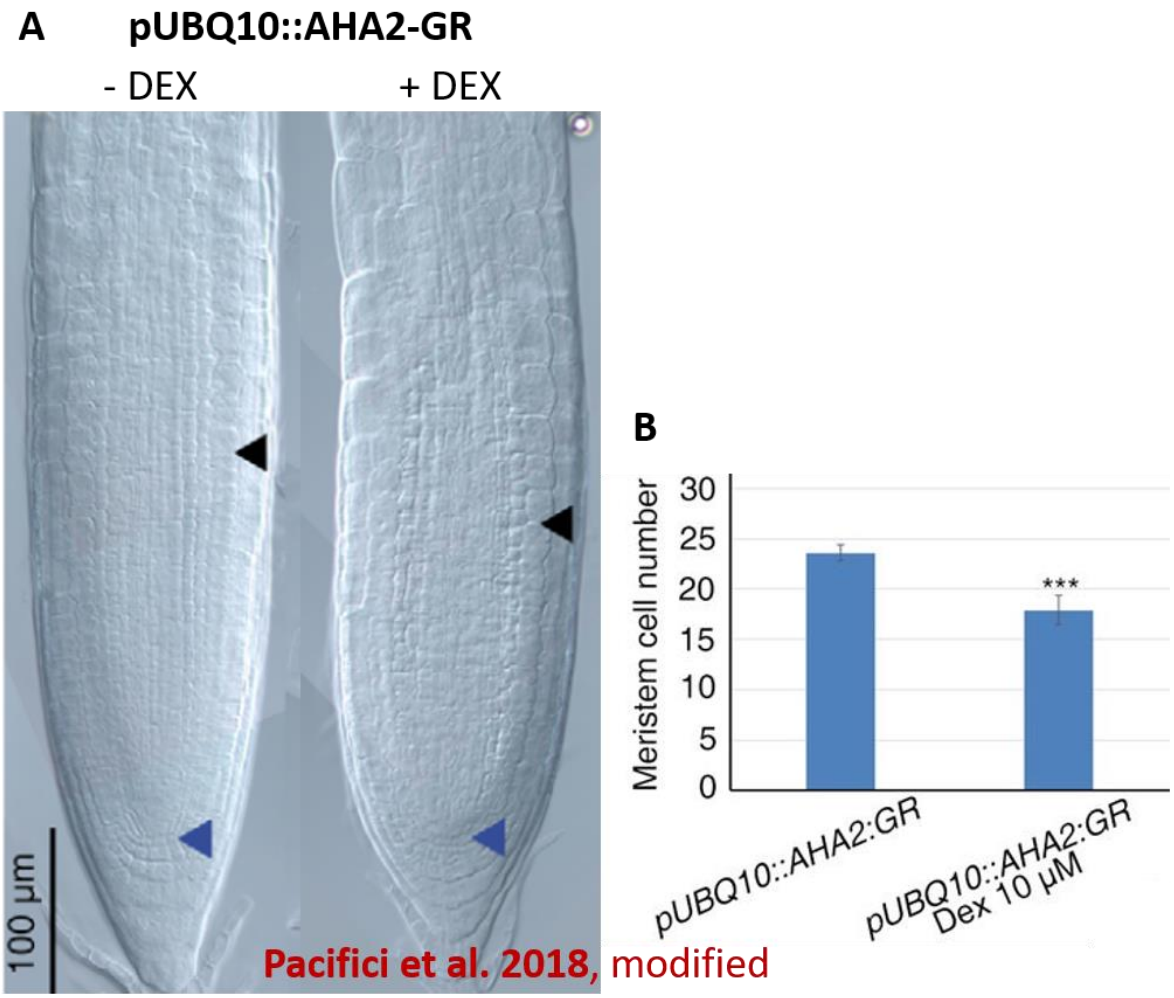

Figure 8. Dexamethasone (DEX)-induced increase of AHA2 protein level in the cells of the meristematic zone initiates elongation growth and reduces the cell division rate.

(A) DIC microscopy images of the root tip of 5-days-old *A. thaliana* seedlings containing the *pUBQ10::AHA2-GR* transgene. Seedlings were either left untreated (left) or were treated with 10 µM dexamethasone (+DEX) for 20 h (right). The meristematic zone lies between the quiescent centre (blue arrow) and the beginning of the elongation zone (black arrow). The figure was taken from Pacifici et al. (2018) and modified.

(B) Quantification of cell numbers in the meristematic zone of 5-days-old *A. thaliana* seedlings containing the *pUBQ10::AHA2-GR* transgene. The cell number was determined in either untreated tissue (left) or tissue that was treated for 20 h with 10 µM DEX. The sample size (n) was n=30, each; asterisks indicate significant differences with Students t-test. The figure was was taken from Pacifici et al. (2018) and modified.

Acknowledgements

The authors would like to thank Anne Mohrholz for critical reading of the manuscript. Research in our laboratories was supported by the German Research Foundation (DFG) with grants to KH (HA 2146/22-1) and to KH and UK (CRC 1101-D02) as well as the Heidelberg Graduate School for Mathematical and Computational Methods for the Sciences.

References

Azhar, N., Su, N., Shabala, L., and Shabala, S. (2017). Exogenously Applied 24-Epibrassinolide (EBL) Ameliorates Detrimental Effects of Salinity by Reducing K+ Efflux via Depolarization-Activated K+ Channels. Plant & cell physiology *58*, 802-810.

Baluška, F., and Mancuso, S. (2013). Root apex transition zone as oscillatory zone. Frontiers in plant science *4*, 354.

Barbez, E., Dünser, K., Gaidora, A., Lendl, T., and Busch, W. (2017). Auxin steers root cell expansion via apoplastic pH regulation in Arabidopsis thaliana. Proceedings of the National Academy of Sciences of the United States of America *114*, E4884-E4893.

Bergonci, T., Silva-Filho, M.C., and Moura, D.S. (2014). Antagonistic relationship between AtRALF1 and brassinosteroid regulates cell expansion-related genes. Plant Signaling & Behavior *9*, e976146.

Blumwald, E. (1987). Tonoplast vesicles as a tool in the study of ion transport at the plant vacuole. Physiol Plant *69*, 731-734.

Bücherl, C.A., van Esse, G.G., Kruis, A., Luchtenberg, J., Westphal, A.H., Aker, J., van Hoek, A., Albrecht, C., Borst, J.W., and Vries, S.C.d. (2013). Visualization of BRI1 and BAK1(SERK3) membrane receptor heterooligomers during brassinosteroid signaling. Plant Physiology *162*, 1911-1925.

Caesar, K., Elgass, K., Chen, Z., Huppenberger, P., Witthöft, J., Schleifenbaum, F., Blatt, M.R., Oecking, C., and Harter, K. (2011). A fast brassinolide-regulated response pathway in the plasma membrane of Arabidopsis thaliana. The Plant journal : for cell and molecular biology *66*, 528-540.

Campos, W.F., Dressano, K., Ceciliato, P.H.O., Guerrero-Abad, J.C., Silva, A.L., Fiori, C.S., Morato do Canto, A., Bergonci, T., Claus, L.A.N., and Silva-Filho, M.C., et al. (2018). Arabidopsis thaliana rapid alkalinization factor 1-mediated root growth inhibition is dependent on calmodulin-like protein 38. The Journal of biological chemistry *293*, 2159-2171.

Cleland, R., and Haughton, P.M. (1971). The effect of auxin on stress relaxation in isolated Avena coleoptiles. Plant Physiology *47*, 812-815.

Cosgrove, D.J. (2000). New genes and new biological roles for expansins. Current Opinion in Plant Biology *3*, 73-78.

de Winter, J. C .F. (2013). Using the Student's "t"-Test with Extremely Small Sample Sizes. Practical Assessment, Research & Evaluation *18*.

Demidchik, V., and Shabala, S. (2018). Mechanisms of cytosolic calcium elevation in plants. The role of ion channels, calcium extrusion systems and NADPH oxidase-mediated 'ROS-Ca2+ Hub'. Functional Plant Biol. *45*, 9.

Di Mambro, R., Sabatini, S., and Dello Ioio, R. (2018). Patterning the Axes. A Lesson from the Root. Plants (Basel, Switzerland) *8*.

Dressano, K., Ceciliato, P.H.O., Silva, A.L., Guerrero-Abad, J.C., Bergonci, T., Ortiz-Morea, F.A., Bürger, M., Silva-Filho, M.C., and Moura, D.S. (2017). BAK1 is involved in AtRALF1-induced inhibition of root cell expansion. PLoS genetics *13*, e1007053.

Dünser, K., Gupta, S., Herger, A., Feraru, M.I., Ringli, C., and Kleine-Vehn, J. (2019). Extracellular matrix sensing by FERONIA and Leucine-Rich Repeat Extensins controls vacuolar expansion during cellular elongation in Arabidopsis thaliana. The EMBO journal *38*.

Eberhart & Kennedy (1995). A new optimizer using particle swarm theory. MHS’95. Proceedings of the Sixth International Symposium on Micro Machine and Human Science. IEEE, pp 39–43.

Fasano, J.M., Swanson, S.J., Blancaflor, E.B., Dowd, P.E., Kao, T.H., and Gilroy, S. (2001). Changes in root cap pH are required for the gravity response of the Arabidopsis root. The Plant cell *13*, 907-921.

Feng, W., Kita, D., Peaucelle, A., Cartwright, H.N., Doan, V., Duan, Q., Liu, M.-C., Maman, J., Steinhorst, L., and Schmitz-Thom, I., et al. (2018). The FERONIA Receptor Kinase Maintains Cell-Wall Integrity during Salt Stress through Ca2+ Signaling. Current biology : CB *28*, 666-675.e5.

Friedrichsen, D.M., Joazeiro, C.A.P., Li, J., Hunter, T., and Chory, J. (2000). Brassinosteroid-Insensitive-1 Is a Ubiquitously Expressed Leucine-Rich Repeat Receptor Serine/Threonine Kinase. Plant Physiology *123*, 1247-1256.

Fuglsang, A.T., Guo, Y., Cuin, T.A., Qiu, Q., Song, C., Kristiansen, K.A., Bych, K., Schulz, A., Shabala, S., and Schumaker, K.S., et al. (2007). Arabidopsis protein kinase PKS5 inhibits the plasma membrane H+ -ATPase by preventing interaction with 14-3-3 protein. The Plant cell *19*, 1617-1634.

Fuglsang, A.T., Kristensen, A., Cuin, T.A., Schulze, W.X., Persson, J., Thuesen, K.H., Ytting, C.K., Oehlenschlæger, C.B., Mahmood, K., and Sondergaard, T.E., et al. (2014). Receptor kinase-mediated control of primary active proton pumping at the plasma membrane. The Plant journal : for cell and molecular biology *80*, 951-964.

Garnelo Gomez, B., Lozano-Duran, R., and Wolf, S. (2019). Phosphorylation-dependent routing of RLP44 towards brassinosteroid or phytosulfokine signalling. Supplemental Material.

Goda, H., Sasaki, E., Akiyama, K., Maruyama-Nakashita, A., Nakabayashi, K., Li, W., Ogawa, M., Yamauchi, Y., Preston, J., and Aoki, K., et al. (2008). The AtGenExpress hormone and chemical treatment data set. Experimental design, data evaluation, model data analysis and data access. The Plant Journal *55*, 526-542.

González-García, M.-P., Vilarrasa-Blasi, J., Zhiponova, M., Divol, F., Mora-García, S., Russinova, E., and Caño-Delgado, A.I. (2011). Brassinosteroids control meristem size by promoting cell cycle progression in Arabidopsis roots. Development (Cambridge, England) *138*, 849-859.

Großeholz, R. (2018). Computational Modeling of the Fast Brassinosteroid Response in the Plasma Membrane of Arabidopsis thaliana: From Molecules to Organ (University of Heidelberg).

Großeholz, R., Feldman-Salit, A., Wanke, F., Schulze, S., Glöckner, N., Kemmerling, B., Harter, K., and Kummer, U. (2019). Specifying the role of BAK1-interacting receptor-like kinase 3 in brassinosteroid signaling. Journal of integrative plant biology.

Hager, A. (2003). Role of the plasma membrane H+-ATPase in auxin-induced elongation growth. Historical and new aspects. Journal of plant research *116*, 483-505.

Hager, A., Menzel, H., and Krauss, A. (1971). Versuche und Hypothese zur Primärwirkung des Auxins beim Streckungswachstum. Planta *100*, 47-75.

Haruta, M., Tan, L.X., Bushey, D.B., Swanson, S.J., and Sussman, M.R. (2018). Environmental and Genetic Factors Regulating Localization of the Plant Plasma Membrane H+-ATPase. Plant Physiology *176*, 364-377.

Holzwart, E., Huerta, A.I., Glöckner, N., Garnelo Gómez, B., Wanke, F., Augustin, S., Askani, J.C., Schürholz, A.-K., Harter, K., and Wolf, S. (2018). BRI1 controls vascular cell fate in the Arabidopsis root through RLP44 and phytosulfokine signaling. Proceedings of the National Academy of Sciences of the United States of America *115*, 11838-11843.

Hoops, S., Sahle, S., Gauges, R., Lee, C., Pahle, J., Simus, N., Singhal, M., Xu, L., Mendes, P., and Kummer, U. (2006). COPASI--a COmplex PAthway SImulator. Bioinformatics (Oxford, England) *22*, 3067-3074.

Hothorn, M., Belkhadir, Y., Dreux, M., Dabi, T., Noel, J.P., Wilson, I.A., and Chory, J. (2011). Structural basis of steroid hormone perception by the receptor kinase BRI1. Nature *474*, 467-471.

Imkampe, J., Halter, T., Huang, S., Schulze, S., Mazzotta, S., Schmidt, N., Manstretta, R., Postel, S., Wierzba, M., and Yang, Y., et al. (2017). The Arabidopsis Leucine-Rich

Repeat Receptor Kinase BIR3 Negatively Regulates BAK1 Receptor Complex Formation and Stabilizes BAK1. The Plant cell *29*, 2285-2303.

Jaillais, Y., Hothorn, M., Belkhadir, Y., Dabi, T., Nimchuk, Z.L., Meyerowitz, E.M., and Chory, J. (2011). Tyrosine phosphorylation controls brassinosteroid receptor activation by triggering membrane release of its kinase inhibitor. Genes & development *25*, 232-237.

Kesten, C., Gámez-Arjona, F.M., Scholl, S., Menna, A., Dora, S., Huerta, A.I., Huang, H.-Y., Tintor, N., Kinoshita, T., and Rep, M., et al. (2019). Pathogen-induced pH changes regulate the growth-defense balance of plants.

Lan, P., Li, W., Lin, W.-D., Santi, S., and Schmidt, W. (2013). Mapping gene activity of Arabidopsis root hairs. Genome biology *14*, R67.

Le Deunff, E., Lecourt, J., and Malagoli, P. (2016). Fine-tuning of root elongation by ethylene. A tool to study dynamic structure-function relationships between root architecture and nitrate absorption. Annals of botany.

Le Novère, N., Hucka, M., Mi, H., Moodie, S., Schreiber, F., Sorokin, A., Demir, E., Wegner, K., Aladjem, M.I., and Wimalaratne, S.M., et al. (2009). The Systems Biology Graphical Notation. Nature Biotechnology *27*, 735.

Li, X., Chen, L., Forde, B.G., and Davies, W.J. (2017). The Biphasic Root Growth Response to Abscisic Acid in Arabidopsis Involves Interaction with Ethylene and Auxin Signalling Pathways. Frontiers in plant science *8*, 1493.

Lin, W., Lu, D., Gao, X., Jiang, S., Ma, X., Wang, Z., Mengiste, T., He, P., and Shan, L. (2013). Inverse modulation of plant immune and brassinosteroid signaling pathways by the receptor-like cytoplasmic kinase BIK1. Proceedings of the National Academy of Sciences of the United States of America *110*, 12114-12119.

Lv, B., Tian, H., Zhang, F., Liu, J., Lu, S., Bai, M., Li, C., and Ding, Z. (2018). Brassinosteroids regulate root growth by controlling reactive oxygen species homeostasis and dual effect on ethylene synthesis in Arabidopsis. PLoS genetics *14*, e1007144.

Ma, B., Yin, C.-C., He, S.-J., Lu, X., Zhang, W.-K., Lu, T.-G., Chen, S.-Y., and Zhang, J.-S. (2014). Ethylene-induced inhibition of root growth requires abscisic acid function in rice (Oryza sativa L.) seedlings. PLoS genetics *10*, e1004701.

Ma, X., Zhang, X., Yang, L., Tang, M., Wang, K., Wang, L., Bai, L., and Song, C. (2019). Hydrogen peroxide plays an important role in PERK4-mediated abscisic acid-regulated root growth in Arabidopsis. Functional Plant Biol. *46*, 165.

Matsubayashi, Y. (2018). Exploring peptide hormones in plants. Identification of four peptide hormone-receptor pairs and two post-translational modification enzymes. Proceedings of the Japan Academy. Series B, Physical and biological sciences *94*, 59-74.

McQueen-Mason, S., and Cosgrove, D.J. (1994). Disruption of hydrogen bonding between plant cell wall polymers by proteins that induce wall extension. Proceedings of the National Academy of Sciences of the United States of America *91*, 6574-6578.

Meng, L., Buchanan, B.B., Feldman, L.J., and Luan, S. (2012). CLE-like (CLEL) peptides control the pattern of root growth and lateral root development in Arabidopsis. Proceedings of the National Academy of Sciences of the United States of America *109*, 1760-1765.

Miao, R., Wang, M., Yuan, W., Ren, Y., Li, Y., Zhang, N., Zhang, J., Kronzucker, H.J., and Xu, W. (2018). Comparative Analysis of Arabidopsis Ecotypes Reveals a Role for Brassinosteroids in Root Hydrotropism. Plant Physiology *176*, 2720-2736.

Minami, A., Takahashi, K., Inoue, S.-i., Tada, Y., and Kinoshita, T. (2019). Brassinosteroid Induces Phosphorylation of the Plasma Membrane H+-ATPase during Hypocotyl Elongation in Arabidopsis thaliana. Plant & cell physiology *60*, 935-944.

Moore, S.J., MacDonald, J.T., Wienecke, S., Ishwarbhai, A., Tsipa, A., Aw, R., Kylilis, N., Bell, D.J., McClymont, D.W., and Jensen, K., et al. (2018). Rapid acquisition and model-based analysis of cell-free transcription-translation reactions from nonmodel bacteria. Proceedings of the National Academy of Sciences of the United States of America *115*, E4340-E4349.

Mora-García, S., Vert, G., Yin, Y., Caño-Delgado, A., Cheong, H., and Chory, J. (2004). Nuclear protein phosphatases with Kelch-repeat domains modulate the response to brassinosteroids in Arabidopsis. Genes & development *18*, 448-460.

Nam, K.H., and Li, J. (2002). BRI1/BAK1, a Receptor Kinase Pair Mediating Brassinosteroid Signaling. Cell *110*, 203-212.

Pacifici, E., Di Mambro, R., Dello Ioio, R., Costantino, P., and Sabatini, S. (2018). Acidic cell elongation drives cell differentiation in the Arabidopsis root. The EMBO journal *37*.

Park, C.H., Kim, T.-W., Son, S.-H., Hwang, J.-Y., Lee, S.C., Chang, S.C., Kim, S.-H., Kim, S.W., and Kim, S.-K. (2010). Brassinosteroids control AtEXPA5 gene expression in Arabidopsis thaliana. Phytochemistry *71*, 380-387.

Phyo, P., Gu, Y., and Hong, M. (2019). Impact of acidic pH on plant cell wall polysaccharide structure and dynamics. Insights into the mechanism of acid growth in plants from solid-state NMR. Cellulose *26*, 291-304.

Rayle, D.L., and Cleland, R. (1970). Enhancement of wall loosening and elongation by Acid solutions. Plant Physiology *46*, 250-253.

Růzicka, K., Ljung, K., Vanneste, S., Podhorská, R., Beeckman, T., Friml, J., and Benková, E. (2007). Ethylene regulates root growth through effects on auxin biosynthesis and transport-dependent auxin distribution. The Plant cell *19*, 2197-2212.

Santiago, J., Henzler, C., and Hothorn, M. (2013). Molecular mechanism for plant steroid receptor activation by somatic embryogenesis co-receptor kinases. Science (New York, N.Y.) *341*, 889-892.

Shabala, S.N., and Newman, I.A. (1997). Proton and calcium flux oscillations in the elongation region correlate with root nutation. Physiol Plant *100*, 917-926.

Shi, Y. (2013). Common folds and transport mechanisms of secondary active transporters. Annual review of biophysics *42*, 51-72.

Shih, H.-W., DePew, C.L., Miller, N.D., and Monshausen, G.B. (2015). The Cyclic Nucleotide-Gated Channel CNGC14 Regulates Root Gravitropism in Arabidopsis thaliana. Current biology : CB *25*, 3119-3125.

Staal, M., Cnodder, T. de, Simon, D., Vandenbussche, F., van der Straeten, D., Verbelen, J.-P., Elzenga, T., and Vissenberg, K. (2011). Apoplastic alkalinization is instrumental for the inhibition of cell elongation in the Arabidopsis root by the ethylene precursor 1-aminocyclopropane-1-carboxylic acid. Plant Physiology *155*, 2049-2055.

Sun, Y., Han, Z., Tang, J., Hu, Z., Chai, C., Zhou, B., and Chai, J. (2013). Structure reveals that BAK1 as a co-receptor recognizes the BRI1-bound brassinolide. Cell Research *23*, 1326 EP -.

Takatsuka, H., and Umeda, M. (2019). ABA inhibits root cell elongation through repressing the cytokinin signaling. Plant Signaling & Behavior *14*, e1578632.

van Esse, G.W., van Mourik, S., Stigter, H., Hove, C.A. ten, Molenaar, J., and Vries, S.C. de (2012). A mathematical model for BRASSINOSTEROID INSENSITIVE1-mediated signaling in root growth and hypocotyl elongation. Plant Physiology *160*, 523-532.

van Esse, G.W., Westphal, A.H., Surendran, R.P., Albrecht, C., van Veen, B., Borst, J.W., and Vries, S.C. de (2011). Quantification of the brassinosteroid insensitive1 receptor in planta. Plant Physiology *156*, 1691-1700.

Verbelen, J.-P., Cnodder, T. de, Le, J., Vissenberg, K., and Baluška, F. (2006). The Root Apex of Arabidopsis thaliana Consists of Four Distinct Zones of Growth Activities. Meristematic Zone, Transition Zone, Fast Elongation Zone and Growth Terminating Zone. Plant Signaling & Behavior *1*, 296-304.

Veronese, P., Nakagami, H., Bluhm, B., Abuqamar, S., Chen, X., Salmeron, J., Dietrich, R.A., Hirt, H., and Mengiste, T. (2006). The membrane-anchored BOTRYTIS-INDUCED KINASE1 plays distinct roles in Arabidopsis resistance to necrotrophic and biotrophic pathogens. The Plant cell *18*, 257-273.

Vert, G., and Chory, J. (2006). Downstream nuclear events in brassinosteroid signalling. Nature *441*, 96-100.

Vriese, K. de, Himschoot, E., Dünser, K., Nguyen, L., Drozdzecki, A., Costa, A., Nowack, M.K., Kleine-Vehn, J., Audenaert, D., and Beeckman, T., et al. (2019).

Identification of Novel Inhibitors of Auxin-Induced Ca2+ Signaling via a Plant-Based Chemical Screen. Plant Physiology *180*, 480-496.

Wang, J., Jiang, J., Wang, J., Chen, L., Fan, S.-L., Wu, J.-W., Wang, X., and Wang, Z.-X. (2014). Structural insights into the negative regulation of BRI1 signaling by BRI1-interacting protein BKI1. Cell Research *24*, 1328-1341.

Wang, X., and Chory, J. (2006). Brassinosteroids regulate dissociation of BKI1, a negative regulator of BRI1 signaling, from the plasma membrane. Science (New York, N.Y.) *313*, 1118-1122.

Wang, X., Goshe, M.B., Soderblom, E.J., Phinney, B.S., Kuchar, J.A., Li, J., Asami, T., Yoshida, S., Huber, S.C., and Clouse, S.D. (2005a). Identification and functional analysis of in vivo phosphorylation sites of the Arabidopsis BRASSINOSTEROID-INSENSITIVE1 receptor kinase. The Plant cell *17*, 1685-1703.

Wang, X., Li, X., Meisenhelder, J., Hunter, T., Yoshida, S., Asami, T., and Chory, J. (2005b). Autoregulation and homodimerization are involved in the activation of the plant steroid receptor BRI1. Developmental cell *8*, 855-865.

Wang, Y.V., Wade, M., Wong, E., Li, Y.-C., Rodewald, L.W., and Wahl, G.M. (2007). Quantitative analyses reveal the importance of regulated Hdmx degradation for p53 activation. Proceedings of the National Academy of Sciences of the United States of America *104*, 12365-12370.

Whitford, R., Fernandez, A., Tejos, R., Pérez, A.C., Kleine-Vehn, J., Vanneste, S., Drozdzecki, A., Leitner, J., Abas, L., and Aerts, M., et al. (2012). GOLVEN secretory peptides regulate auxin carrier turnover during plant gravitropic responses. Developmental cell *22*, 678-685.

Witthöft, J., Caesar, K., Elgass, K., Huppenberger, P., Kilian, J., Schleifenbaum, F., Oecking, C., and Harter, K. (2011). The activation of the Arabidopsis P-ATPase 1 by the brassinosteroid receptor BRI1 is independent of threonine 948 phosphorylation. Plant Signaling & Behavior *6*, 1063-1066.

Witthöft, J., Caesar, K., Elgass, K., Huppenberger, P., Kilian, J., Schleifenbaum, F., Oecking, C., and Harter, K. (2014). The activation of the Arabidopsis P-ATPase 1 by the brassinosteroid receptor BRI1 is independent of threonine 948 phosphorylation. Plant Signaling & Behavior *6*, 1063-1066.

Wolf, S., van der Does, D., Ladwig, F., Sticht, C., Kolbeck, A., Schürholz, A.-K., Augustin, S., Keinath, N., Rausch, T., and Greiner, S., et al. (2014). A receptor-like protein mediates the response to pectin modification by activating brassinosteroid signaling. Proceedings of the National Academy of Sciences of the United States of America *111*, 15261-15266.

Wu, H., Shabala, L., Zhou, M., and Shabala, S. (2015). MIFE Technique-based Screening for Mesophyll K+ Retention for Crop Breeding for Salinity Tolerance. BIO-PROTOCOL *5*.

Xu, P., Cai, X.-T., Wang, Y., Xing, L., Chen, Q., and Xiang, C.-B. (2014). HDG11 upregulates cell-wall-loosening protein genes to promote root elongation in Arabidopsis. Journal of experimental botany *65*, 4285-4295.

Xu, W., Jia, L., Baluška, F., Ding, G., Shi, W., Ye, N., and Zhang, J. (2012). PIN2 is required for the adaptation of Arabidopsis roots to alkaline stress by modulating proton secretion. Journal of experimental botany *63*, 6105-6114.

Yin, Y., Vafeados, D., Tao, Y., Yoshida, S., Asami, T., and Chory, J. (2005). A new class of transcription factors mediates brassinosteroid-regulated gene expression in Arabidopsis. Cell *120*, 249-259.

Yun, H.S., Bae, Y.H., Lee, Y.J., Chang, S.C., Kim, S.-K., Li, J., and Nam, K.H. (2009). Analysis of phosphorylation of the BRI1/BAK1 complex in arabidopsis reveals amino acid residues critical for receptor formation and activation of BR signaling. Molecules and Cells *27*, 183-190.

Zhang, X., Zhou, L., Qin, Y., Chen, Y., Liu, X., Wang, M., Mao, J., Zhang, J., He, Z., and Liu, L., et al. (2018). A Temperature-Sensitive Misfolded bri1-301 Receptor Requires Its Kinase Activity to Promote Growth. Plant Physiology *178*, 1704-1719.

Zhao, Y., Qi, Z., and Berkowitz, G.A. (2013). Teaching an old hormone new tricks. Cytosolic Ca2+ elevation involvement in plant brassinosteroid signal transduction cascades. Plant Physiology *163*, 555-565.

Zhu, J.-Y., Li, Y., Cao, D.-M., Yang, H., Oh, E., Bi, Y., Zhu, S., and Wang, Z.-Y. (2017). The F-box Protein KIB1 Mediates Brassinosteroid-Induced Inactivation and Degradation of GSK3-like Kinases in Arabidopsis. Molecular cell *66*, 648-657.e4.

Supplemental Material

Supp. Mat. 1: Quantification of Fig. 3A (microsomes) (A) and two Western Blots (B,C)

A

Sample	Intensity	Background on height	Net Intensity	Ratio rel. to BRI1	Normalized to Ponceau
BRI1	30800000	0	30800000	1	1
BIR3	59700000	1070000	58630000	1,904	2,379
AHA2	77300000	303000	76997000	2,500	3,125

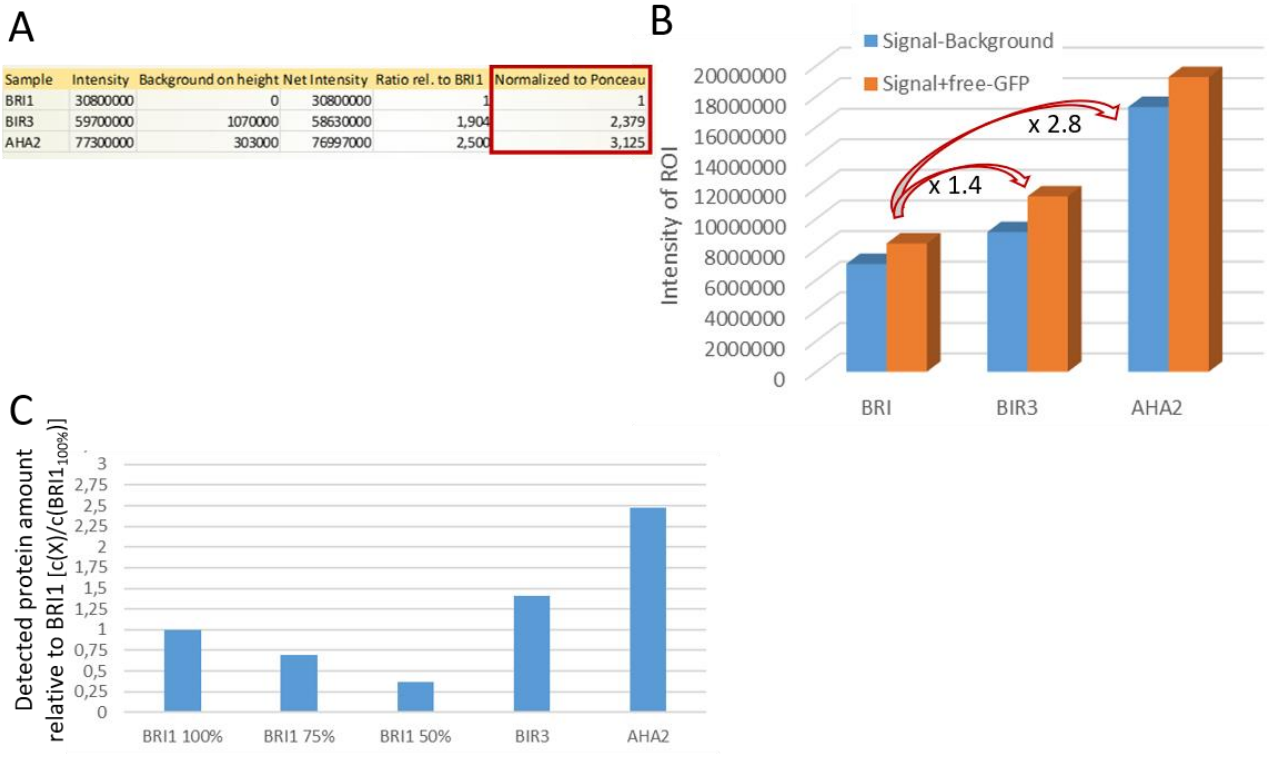

Supp. Fig. 1. Three replicates of Western blot quantification from roots with Image Studio Lite© (A-C)

(A) Raw values of the intensity of the protein band, the background at the same height, the net intensity (signal-background) and the ratio relative to BRI1 extracted from Western Blot of the microsomal preparation shown in Fig. 3A for BRI1-GFP, BIR3-GFP and AHA2-GFP with precise genotype indicated in Fig. 3A.

(B) Raw values of the intensity at the region of interest (signal-background, blue) and the signal of cleaved-off GFP included (signal+free GFP, orange) from Western Blot of root extract for BRI1-GFP, BIR3-GFP and AHA2-GFP with the precise genotype indicated in Fig. 3A. The ratio of the signal relative to the BRI1-GFP signal is indicated below arrows. Second biological replicate.

(C) Signal of GFP relative to 100% BRI1-GFP for BRI1-GFP, BIR3-GFP and AHA2-GFP for the in Fig. 3A indicated plant genotypes. As internal control for the western blot procedure, only three-quarters (75% BRI1) and half (50% BRI1) the amount of 100% BRI1-GFP was loaded. Western blotting procedure was in the linear dynamic range, as both controls show values close to expected ratio. Third biological replicate.

Supp. Mat. 2:

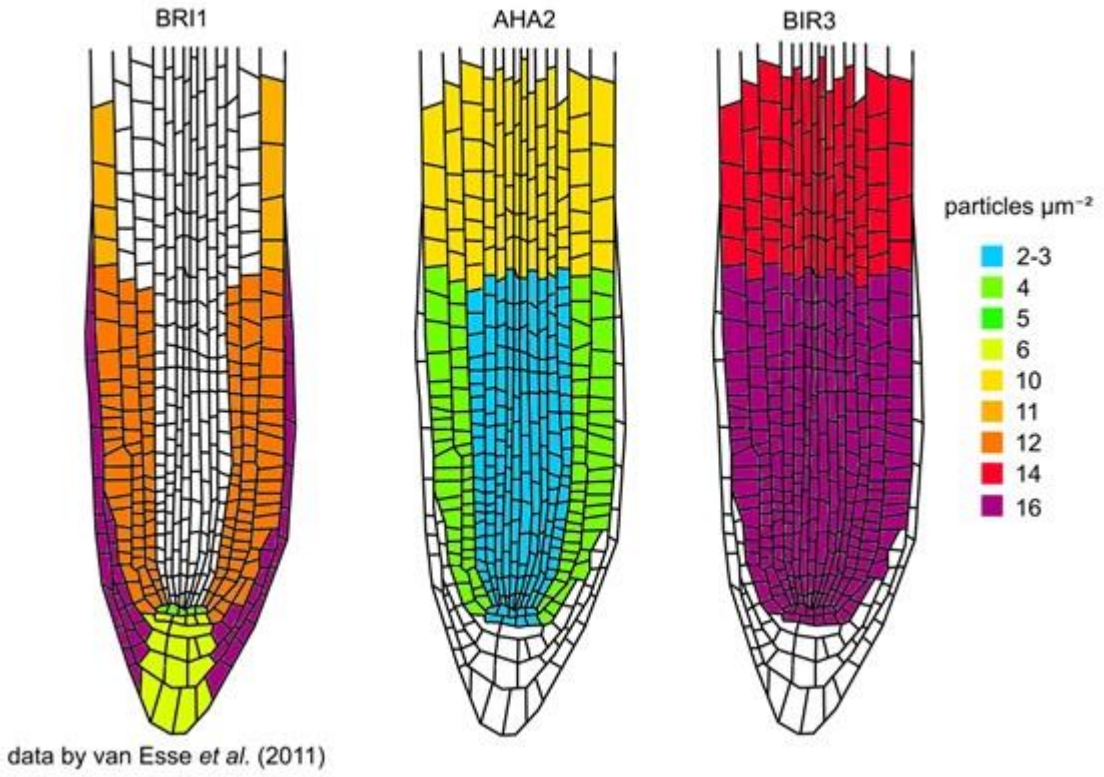

Supp. Fig. 2. Conversion to particles per µm² from the quantification of the AHA2-GFP, BRI1-GFP and BIR3-GFP amounts by fluorescence intensity measurement and quantitative Western blots revealed a strong gradient of the AHA:BRI1 ratio along the root axis.

Graphical representation of the number of particles used for the computational model. The absolute BRI1-GFP abundance (left; number of receptors per µm^2 plasma membrane) were derived from the publication of van Esse and colleagues (2011). By combining the measured ratios with the number of BRI1 molecules per µm^2, we were able to estimate the molecule numbers of AHA2 (middle) and BIR3 (right). More details in the precise calculations can be found in the dissertation of Ruth Großeholz (Großeholz, 2018).

Supp. Mat. 3: pH calibration curve and comparison of the effect on the ratio due to differences in tissue thickness for HPTS staining for apoplastic pH measurements

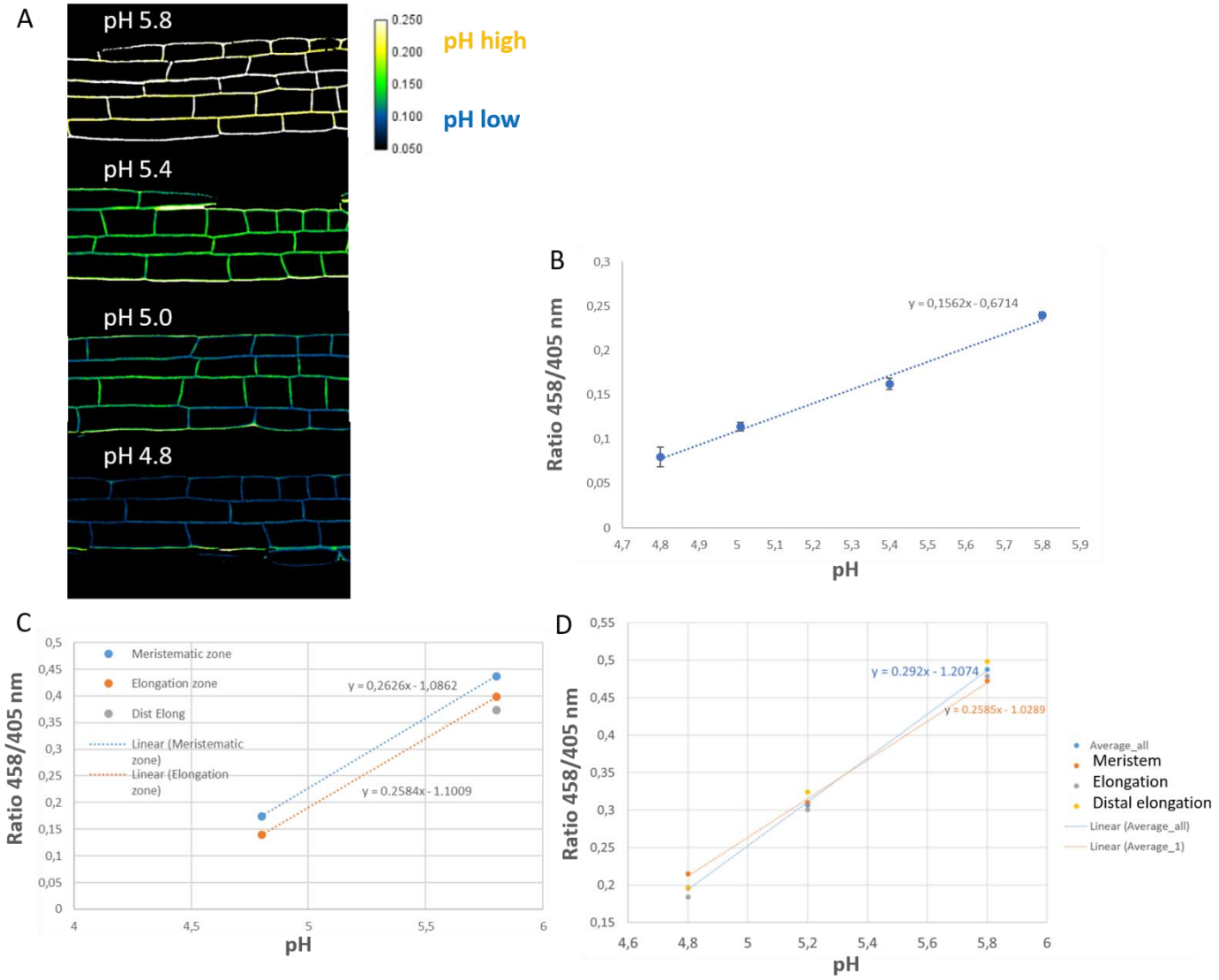

Supp. Fig. 3. pH calibration curve (A, B) and two biological repetitions of ratiometric measurements for the meristem and the elongation zone (B, C) after HPTS staining for apoplastic pH measurement on buffered plates (0.01% MES)
(A) Exemplary ratiometric images (458nm/405nm) on different buffered pH media between pH 4.8 and 5.8. Exemplary calibration curve.
(B) Ratio (458nm/405nm) in dependence of pH buffered medium. Quantitative analysis of the pH calibration curve of (A). Sample numbers were n ≥ 3.
(C) Ratio in dependence of pH buffered medium separately for the meristem (blue) and the elongation zone (orange). The slope of the linear regression is similar, but their heights are slightly different. Detection settings were optimized, and higher dynamic range was obtained than in (A, B).

(D) Ratio in dependence of pH buffered medium separately for the meristem (orange) and the elongation zone (blue) and the distal elongation zone (yellow). The slope and the absolute values are similar. Second biological replicate.

Supp. Mat. 4: Changes to the HPTS script by (Barbez et al., 2017) are indicated with an orange arrow.

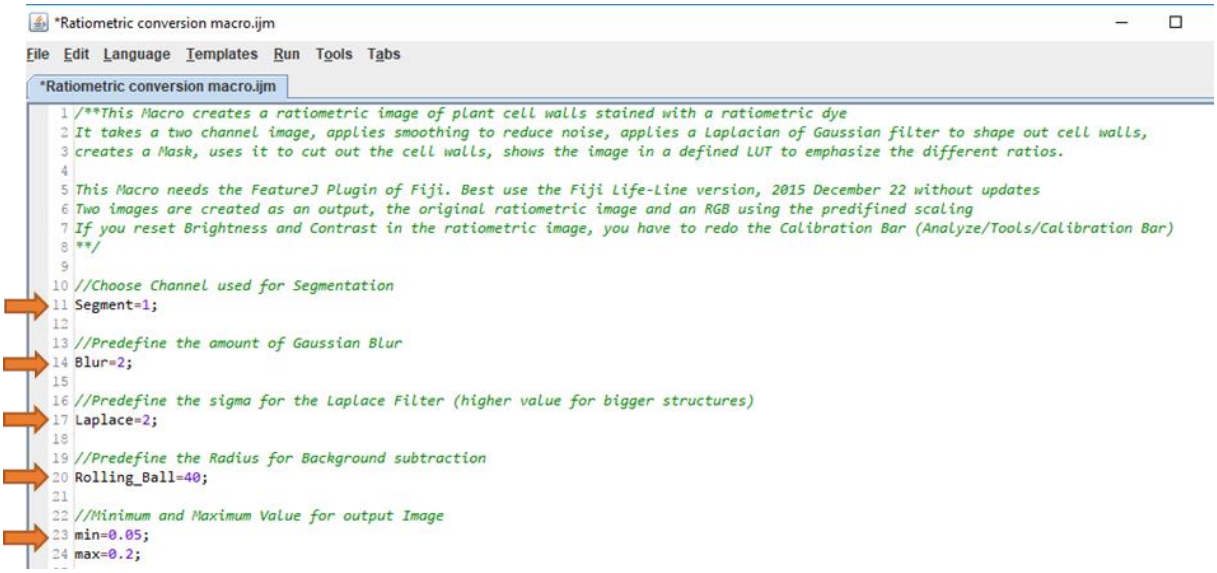

--::continued next page::--

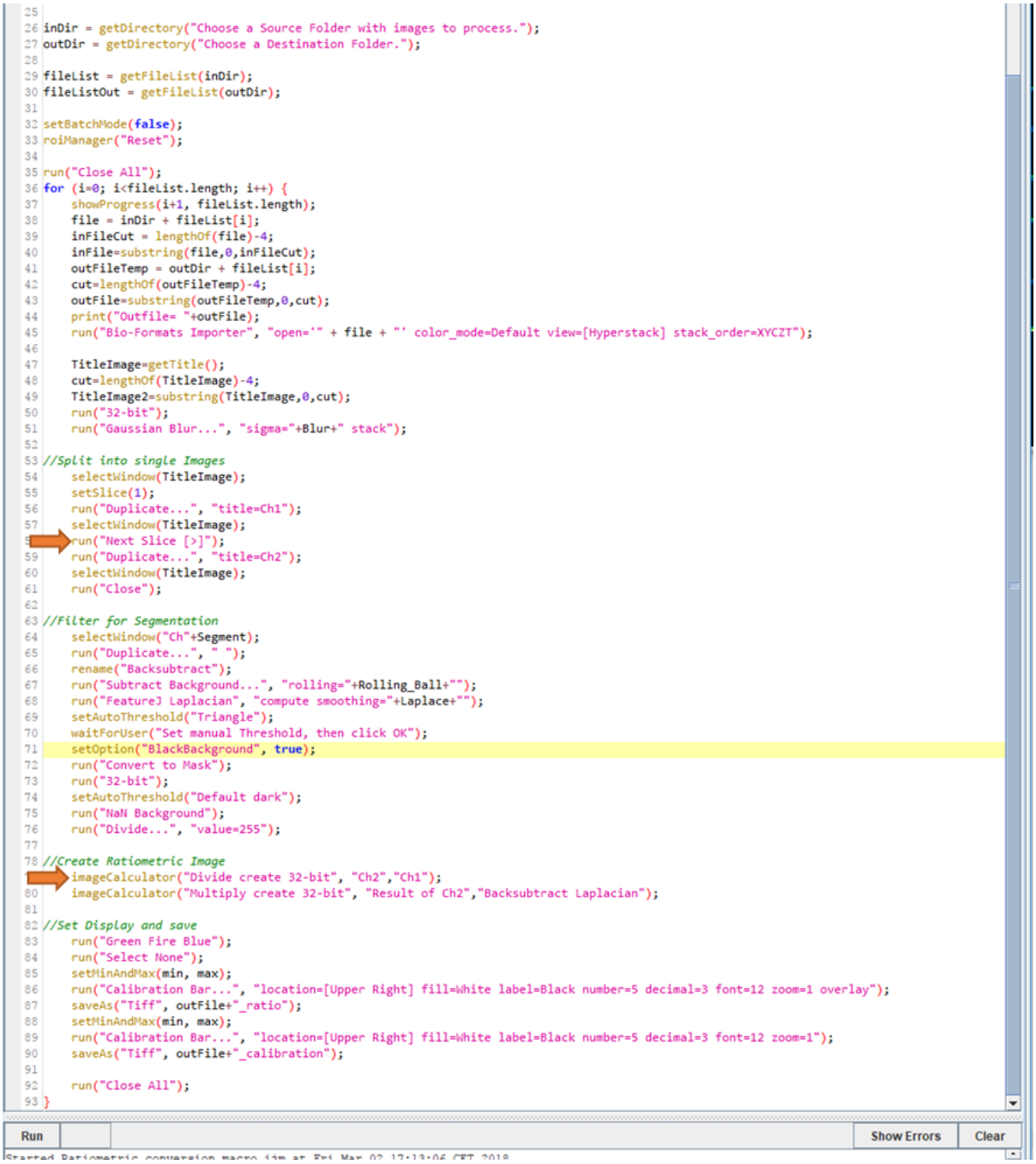

```
inDir = getDirectory("Choose a Source Folder with images to process.");
outDir = getDirectory("Choose a Destination Folder.");

fileList = getFileList(inDir);
fileListOut = getFileList(outDir);

setBatchMode(false);
roiManager("Reset");

run("Close All");
for (i=0; i<fileList.length; i++) {
    showProgress(i+1, fileList.length);
    file = inDir + fileList[i];
    inFileCut = lengthOf(file)-4;
    inFile=substring(file,0,inFileCut);
    outFileTemp = outDir + fileList[i];
    cut=lengthOf(outFileTemp)-4;
    outFile=substring(outFileTemp,0,cut);
    print("Outfile= "+outFile);
    run("Bio-Formats Importer", "open='" + file + "' color_mode=Default view=[Hyperstack] stack_order=XYCZT");

    TitleImage=getTitle();
    cut=lengthOf(TitleImage)-4;
    TitleImage2=substring(TitleImage,0,cut);
    run("32-bit");
    run("Gaussian Blur...", "sigma="+Blur+" stack");

//Split into single Images
    selectWindow(TitleImage);
    setSlice(1);
    run("Duplicate...", "title=Ch1");
    selectWindow(TitleImage);
    run("Next Slice [>]");
    run("Duplicate...", "title=Ch2");
    selectWindow(TitleImage);
    run("Close");

//Filter for Segmentation
    selectWindow("Ch"+Segment);
    run("Duplicate...", " ");
    rename("Backsubtract");
    run("Subtract Background...", "rolling="+Rolling_Ball+"");
    run("FeatureJ Laplacian", "compute smoothing="+Laplace+"");
    setAutoThreshold("Triangle");
    waitForUser("Set manual Threshold, then click OK");
    setOption("BlackBackground", true);
    run("Convert to Mask");
    run("32-bit");
    setAutoThreshold("Default dark");
    run("NaN Background");
    run("Divide...", "value=255");

//Create Ratiometric Image
    imageCalculator("Divide create 32-bit", "Ch2","Ch1");
    imageCalculator("Multiply create 32-bit", "Result of Ch2","Backsubtract Laplacian");

//Set Display and save
    run("Green Fire Blue");
    run("Select None");
    setMinAndMax(min, max);
    run("Calibration Bar...", "location=[Upper Right] fill=White label=Black number=5 decimal=3 font=12 zoom=1 overlay");
    saveAs("Tiff", outFile+"_ratio");
    setMinAndMax(min, max);
    run("Calibration Bar...", "location=[Upper Right] fill=White label=Black number=5 decimal=3 font=12 zoom=1");
    saveAs("Tiff", outFile+"_calibration");

    run("Close All");
}
```

Run | Show Errors | Clear

References

Barbez, E., Dünser, K., Gaidora, A., Lendl, T., and Busch, W. (2017). Auxin steers root cell expansion via apoplastic pH regulation in Arabidopsis thaliana. Proceedings of the National Academy of Sciences of the United States of America *114*, E4884-E4893.

Großeholz, R. (2018). Computational Modeling of the Fast Brassinosteroid Response in the Plasma Membrane of Arabidopsis thaliana: From Molecules to Organ (University of Heidelberg).

A.1.2 Dynamics of BRI1 and functional relevance of microdomains

Single-particle tracking photoactivated localization microscopy analysis of BRASSINOSTEROID INSENSITIVE 1 receptor (BRI1) dynamics and BRI1-related microdomain functions in plants

In preparation

This article describes single-particle tracking photoactivated localization microscopy analysis (sptPALM) of the BRASSINOSTEROID INSENSITIVE 1 receptor (BRI1) in the heterologous tobacco *N. benthamiana* system. In tobacco leaves, the majority of BRI1 receptors reveal subdiffusive behaviour, which is not altered by brassinosteroid hormone treatment, microdomain disruption by a sterol-extracting agent or actin depolimerization. Further tests will be performed in the model system *A. thaliana*. First measurements demonstrate, that the disruption of microdomains by a sterol-extracting agent attenuates brassinosteroid signalling. This suggests, that the subcompartimentation / structural organisation of signalling components in the plasma membrane are necessary for the effective signal transduction.

Single-particle tracking photoactivated localization microscopy analysis of BRASSINOSTEROID INSENSITIVE 1 receptor (BRI1) dynamics and BRI1-related microdomain functions in plants

Nina Glöckner[1*], Sven zur Oven-Krockhaus[1,2*], Alfred J. Meixner[2], Klaus Harter[1]

[1] Center for Plant Molecular Biology (ZMBP), University of Tübingen, Germany

[2] Institute for Physical and Theoretical Chemistry (IPTC), University of Tübingen, Germany

[*] N.G. and S.Z.O.-K. contributed equally to this work.

Summary

The plant hormone brassinosteroid (BR) is involved in the control of cell elongation growth. The activation of the plasma membrane-resident brassinosteroid receptor BRASSINOSTEROID INSENSITIVE 1 (BRI1) and its cofactor BRI1-ASSOCIATED KINASE (BAK1) leads to the activation of P-type ATPases (AHAs). This causes the acidification of the extracellular space, hyperpolarization of the PM, wall loosening and eventually cell elongation. This BRI1 is signalling module is very well described at constituent level; however, it is not yet understood, whether the partitioning of the complexes in the plasma membrane (microdomains) is relevant for the physiological output, namely cell elongation. By using single-particle tracking photoactivated localization microscopy (sptPALM), we found that the majority of BRI1 receptors show subdiffusive behaviour in *Nicotiana benthamiana* leaves. However, this heterologous system is probably not well suited for the detection of minor changes in receptor dynamics, as neither BR treatment, the disruption of microdomains with methyl-beta-cyclodextran (MβCD) and actin filament depolymerization significantly altered the BRI1 receptor dynamics. In contrast, the disturbance of microdomains by MβCD in *Arabidopsis thaliana* attenuates brassinosteroid signalling with respect to primary root growth and root waving indicating that the integrity of PM microdomains is crucial for BRI1 function.

Introduction

Plants as sessile organisms rely on the fast and efficient response to hormonal cues. The signalling cascade of the brassinosteroid (BR) hormone is one of the best understood in plants. Brassinosteroid signalling is involved in both growth and developmental processes. Specifically, it was shown to mediate elongation growth in the root elongation zone (Fridman and Savaldi-Goldstein, 2013; Tong et al., 2014; Lv et al., 2018; Glöckner et al., 2019). BR-related processes are mediated by the plasma membrane (PM) -resident receptor BRASSINOSTEROID INSENSITIVE 1 (BRI1) and its co-receptor BRI1-ASSOCIATED KINASE (BAK1). In the absence of the brassinosteroid hormone (BR), large populations of BRI1 and BAK1 are physically in close proximity (Nam and Li, 2002; Wang et al., 2005b; Yun et al., 2009; Bücherl et al., 2013). Several mechanisms inhibit the auto-activation of signalling of the BRI1-BAK1 heterodimer. Namely the cytoplasmic tail of the BRI1 receptor (Wang et al., 2005b), the inhibitor BRI1 KINASE INHIBITOR 1 (BKI1) (Wang and Chory, 2006), the BOTRYTIS-INDUCED KINASE 1 (BIK1) (Veronese et al., 2006; Lin et al., 2013) and the plasma-membrane resident BAK1-INTERACTING RECEPTOR-LIKE KINASE 3 (BIR3) (Imkampe et al., 2017; Großeholz et al., 2019). Binding of the BR hormone to the extracellular island domain of the receptor increases the affinity between BRI1 and BAK1 (Wang et al., 2005a; Hothorn et al., 2011; Santiago et al., 2013; Sun et al., 2013). This in turn changes the relative orientation of their cytoplasmic domains (Wang et al., 2014) and leads to auto- and trans-phosphorylation events of the two kinase domains. Finally, this activates a cytoplasmatic signalling cascade which regulate BR-related processes including gene expression (Mora-García et al., 2004; Yin et al., 2005; Vert and Chory, 2006; Zhu et al., 2017). Simultaneously, the PM-resident P-type proton pumps (AHAs) are phosphorylated and thus activated in response to BR hormone within a few minutes (Caesar et al., 2011; Witthöft et al., 2014). The acidification of the extracellular space enables cell elongation growth, as the activation of cell wall-resident expansins mediate polymer creep (McQueen-Mason and Cosgrove, 1994; Cosgrove, 2000) and cellulose–pectin interactions are weakened at low pH (Phyo et al., 2019). In summary, BR signalling is very well described at the constituent level. However, with the break-through in super-resolution light microscopy (Gahlmann and Moerner, 2013; Betzig, 2015; Hell et al., 2015) and the discovery of proteins specifically enriched in a detergent-resistant-fraction (Malinsky et al., 2013; Ott, 2017; Lu and Fairn, 2018) new

questions became addressable. Specifically, whether and how the receptors and their co-factors are restricted into micro- or nanodomains in the PM, what mechanisms restrict free diffusion (Konrad and Ott, 2015; Burkart and Stahl, 2017; Ott, 2017; Gronnier et al., 2018) and whether and to which extent the spatiotemporal arrangements and dynamics influences the signalling output. Recently, first measurements on the dynamics of the BRI1 receptor clusters were performed (Bücherl et al., 2013; Wang et al., 2015b; Hutten et al., 2017; McKenna et al., 2018). To this end, the combination of green fluorescent proteins (GFP) or red fluorophores (RFP) with variable-angle total internal reflection microscopy (VA-TIRFM) was used (Bücherl et al., 2017; McKenna et al., 2018; Xue et al., 2018) but the thick cell wall of plants impedes the usage of TIRF microscopy, which provides highest contrast enhancement in the z-axis (Li et al., 2013; Hutten et al., 2017).

However, single-particle tracking based on GFP or RFP is restricted by the density of proteins at the PM, since diffracted fluorescence emission prevents tracking of individual proteins (Hosy et al., 2015) separated by less than maximally half the emission wavelength (Abbe, 1873; Rayleigh, 1897). Typically, when using GFP, distances between two individual fluorescent particles cannot be resolved with VA-TIRF below 200 nm. Here, we report on the combination of VA-TIRF with photoactivated localization microscopy (PALM) to the dynamics of single-molecules over time. The use of photoactivatable or photoconvertible fluorophores, e.g. mEOS, increases the resolution considerably to ~20-80nm (Manley et al., 2008; Hosy et al., 2015). We tested whether BR hormone treatment, chemical disruption of microdomains and actin filaments affect BRI1-mEOS receptor dynamics in the heterologous *N. benthamiana* system. In addition, we investigated whether the chemical disruption of the organization of the plasma membrane affects the BR-signalling by monitoring the root growth and root waving response of *A. thaliana* seedlings.

Results

Super-resolved single-particle tracking (sptPALM) allows the analysis of protein dynamics in *Arabidopsis thaliana* roots

To test our new, custom-made VA-TIRF-PALM microscopy setup, we first performed measurements of published *A. thaliana* plant lines expressing PIP2;1-mEOS, an aquaporin, and LTI6a-mEOS under the control of the *PIP2;1* promoter (Hosy et al., 2015).

The extraction of single molecule tracks from movies of *A. thaliana* root epidermis cells showed that the movement of PIP2;1-mEOS was more restricted than that of LTI6a-mEOS (Fig. 1A). To quantify this observation, we determined the mean square displacement (MSD) for all recorded tracks of PIP2;1-mEOS and LTI6a-mEOS respectively. The MSD over lag times of 20 frames, which represents a lag time of 1 second, indicated that the small, single trans-membrane (TM) domain protein LTI6a-mEOS was much more mobile than the much larger PIP2;1-mEOS fusion protein with six TM domains (Fig. 1B). These observations were representative of previously found dynamics of the two PM-resident proteins (Hosy et al., 2015) and therefore validates the functionality of the custom-built VA-TIRF-PALM setup.

We tested whether different modes of movement for the small, TM-stub of LTI6a could be observed. Therefore, we classified the particles for $MSD = 4Dt_{lag}^{\alpha}$ as undergoing free diffusion for $0.9 > \alpha > 1.1$, as superdiffusive with $\alpha > 1.1$ and as subdiffusive with $\alpha < 0.9$ (Jean-Yves Tinivez). As shown in figure 1 C, the population of LTI6a-mEOS fusion protein did not behave uniformly, as there are subpopulations that exhibit superdiffusive behaviour, free diffusion or restricted diffusion (Fig. 1C). This suggests an inhomogeneous property of the PM influencing the mobility of even a very small PM-resident protein.

The majority of BRI1-mEOS receptor proteins showed subdiffusive behaviour in *N. benthamiana* cells

After having established the sptPALM setup successfully, we proceeded with the generation of pUBC::*BRI1-mEOS* constructs to be tested later in transgenic *A. thaliana* lines. To test the usability of BRI1-mEOS for sptPALM, we performed sptPALM measurements in epidermal leaf cells of the heterologous *N. benthamiana* system two days after transient transformation (Fig. 2A). The tracks of ten epidermis cells were classified, again, by the value of α in $MSD = 4Dt_{lag}^{\alpha}$ as described for LTI6a-mEOS.

The largest subpopulation, comprising ~ 70% of BRI1-mEOS molecules, showed a subdiffusive behaviour, the second largest, comprising ~20% of the receptors, free diffusion and the smallest, with ~10%, superdiffusive behaviour (Fig. 2B). These data indicate that the vast majority of BRI1-mEOS molecules are restricted in their free lateral movement in the PM of *N. benthamiana* cells.

The mobility of the BRI1-mEOS receptor protein is not significantly altered by hormone treatment, actin depolymerization or disturbance of the microdomains in *N. benthamiana*

The BRI1 receptor was reported to increase its interaction with BAK1 upon BR treatment, leading to hetero-oligomerization (Nam and Li, 2002; Wang et al., 2005b; Yun et al., 2009; Bücherl et al., 2013) that may lead to an altered dynamic in the PM. We therefore tested whether BRI1-mEOS shows changes in its mobility upon treatment of transiently transformed *N. benthamiana* cells with 1 nM brassinolide (BL), the most active form of the BRs, for 30 minutes. The actin cytoskeleton is located right below the PM and was proposed to separate the PM into smaller subcompartments (van Zanten and Mayor, 2015; Weinberg and Puthenveedu, 2019). We therefore assessed the diffusion coefficient of BRI1-mEOS in *N. benthamiana* leaf cells after 30 minutes of 25 µM latrunculin B (LatB) treatment. LatB inhibits actin polymerisation, and after 30 minutes treatment with 25 µM LatB, all but the largest actin filament bundles are dissolved in *N. benthamiana* leaf cells (Rocchetti et al., 2014). Lastly, we asked whether the disturbance of potential microdomains affects the dynamics of BRI1-mEOS in the PM by treatment of the cells with methyl-β-cyclodextran (MβCD) for 30 minutes. MβCD forms ring-like structures with an apolar core and is suggested to act as an acceptor compartment for sterol (Yeagle, 2016). The prolonged treatment thus disrupts the spatial organisation of the PM. After 30 minutes of treatment with 10 mM MβCD approx. 30% of the sterol content was depleted in A. thaliana roots (Li et al., 2011).

To compare the dynamics, movies of the BRI1-mEOS expressing *N. benthamiana* cells were recorded after treatment with 0.01% DMSO (mock-treatment for BL), 1 nM BL, 25 µM LatB, 10 mM mannitol (iso-osmolar mock treatment for MβCD) and 10 mM MβCD in three biological replicates. This time, a different type of data evaluation was planned, as almost all previous studies used a bimodal fit to separate the mobile subpopulation from the immobile subpopulation. If two subpopulations

exist, this method can determine their respective average diffusion coefficients. Additionally, the modal diffusion coefficient was calculated to extract the apparent diffusion coefficient.

Thus, the apparent diffusion coefficient D was calculated from the MSD using the first four points of each track and then plotted against the occurrence of the observation (Supp. Material 1). All tracks shorter than 5 data points and with fits below R^2 below 0.4 were excluded. From the distribution of the log-scaled diffusion coefficient D (log (D) distribution), no clear bimodal separation into a mobile and immobile fraction was visible for any treatment (Supp. Material 1). To extract the modal diffusion coefficient of the traces, a normal fit was applied to the log (D) distribution for each cell and the maximum of the fit calculated (Fig. 3A; data shown for 20-30 cells of one biological replicate; see Supp. Material 2 for the other two replicates). Thus, each point represents the most frequent diffusion coefficient of one cell (Fig. 3A). With a sufficiently high number of observations, no statistically significant differences in the diffusion coefficient were found for any treatment compared to the two mock treatments. The average diffusion coefficient of BRI1-mEOS was always about 0.002 $\mu m^2 s^{-1}$. Also, with a more refined mode of evaluation and after combining the data of the three biological replicates, no significant change in the diffusion coefficient was observed (Supp. Material 3).
In summary, the transient expression system in *N. benthamiana* appears not to be suitable for distinguishing potential subtle changes in the dynamics of the BRI1-mEOS receptor fusion in response to hormone treatment, depolymerization of actin filaments or microdomain disruption.

Disturbance of microdomains reduced brassinosteroid signalling strength

The measurements of the dynamics of the BRI1 receptor in the PM of *N. benthamiana* cells may not be representative for the dynamics in *A. thaliana* cells. Until now, no physiological evidence was provided, whether the disruption of sterol-dependent microdomains by MβCD indeed affects the physiological response to BR signalling. As a first glimpse, physiological measurements of the root length were performed. Therefore, 5-days-old seedlings of wild type Col-0, the *bri1-301* mutants with a reduced kinase activity (Zhang et al., 2018) and the mild BRI1-GFP overexpressor (*pBRI1::BRI1-GFP*) (Friedrichsen et al., 2000) were transferred to plates containing

0.1 mM MβCD plates supplemented with and without 1 nM BL and the initial root length was marked (Fig. 4A). After three days, the length of the primary root was measured. To account for differences in the initial size, the root length of each seedling was normalized to its size at the time point of the transfer (Fig. 4B). After three days of mock treatment, the average normalized root length of *bri1-301* and BRI1-GFP seedlings was not significantly altered compared to Col-0 seedlings. The treatment of the seedlings with 1 nM BL significantly reduced the root length of BRI1-GFP line compared to that of *bri1-301* and Col-0 seedlings. This observation is in accordance with previous findings (González-García et al., 2011). The treatment with 0.1 mM MβCD led to an increase in the root length for all three genotypes. Most interestingly, the presence of MβCD attenuated the inhibitory effect of 1 nM BL in the BRI1-GFP seedlings (Fig. 4A, B).

A second effect of enhanced BL signalling is the appearance of root waving (González-García et al., 2011). We quantified the root waving of wildtype, *bri1-301* and BRI1-GFP seedlings by comparing the distance between the initial position of the root and its position after three days with the length of the root contour length after this time (Fig. 4C). This way, for values close to one the root was growing straight. If the contour length is much larger than the end-to-end distance, agravitropic growth occurred. In accordance with previous findings, a statistically significant increase in root waving was observed for the BRI1-GFP seedlings on plates containing 1 nM BL compared to the control group of mock-treated BRI1-GFP seedlings with the Steel test (Fig. 4C black asterisk). This root-waving phenotype, however, was abolished for the combined treatment of the BRI1-GFP seedlings with 0.1 mM MβCD and 1 nM BL and no statistical difference to the control group was detected anymore. Also, for Col-0 in comparison to *bri1-301*, the root waving on 1 nm BL increased significantly (Fig. 4C grey asterisk). More repetitions will be performed in the future.

In summary, these results suggest that the disruption of microdomains with MβCD attenuates brassinosteroid signalling.

Discussion

We were able to establish VA-TIRF-sptPALM measurements on the custom-built microscope, as we could reproduce previously published results of the dynamics of the small, single transmembrane protein LTI6a and the large aquaporin PIP2;1 comprising six transmembrane domains fused to the photoconvertible mEOS. As expected, the movement of LTI6a-mEOS was highly dynamic, whereas the large PIP2;1-mEOS showed mostly subdiffusive behaviour. Here, not only the size of the protein may affect the movement properties, but also, as suggested by Hosy and colleagues (2015), the PM-underlying actin filaments and the cell wall. To test whether the BRI1 receptor might be restricted by similar mechanisms, we performed transient measurements of BRI1-mEOS dynamics in transiently transformed *N. benthamiana* epidermal leaf cells. We observed that, according to the classification of Jean-Yves Tinevez, approx. 70% of BRI1 receptors showed subdiffusive movement behaviour, 30% free diffusion or superdiffusive behaviour. The distribution of the apparent diffusion coefficient yielded a unimodal distribution, in which no clear-cut mobile fraction was visible. As the apparent diffusion coefficient of 0.002 $\mu m^2 s^{-1}$ was even lower than that of AtPIP2;1-EOS with 0.0047 $\mu m^2 s^{-1}$ (Hosy et al., 2015), BRI1-mEOS in *N. benthamiana* leaves can be characterized as immobile. The apparent diffusion coefficient of lipids in the plasma membrane is 0.03-0.6 $\mu m^2 s^{-1}$ (Dugas et al., 1989; Hosy et al., 2015). Our observation that the majority of BRI1 receptors showed subdiffusive behaviour, even in the absence of exogenously applied hormone, further supports the hypothesis that BRI1 is located in distinct micro-/nanodomains in the PM of plant cells (Wang et al., 2015a; Bücherl et al., 2017; Hutten et al., 2017).

Wang and colleagues (2015a) found by classical VA-TIRF microscopy that about 60% of BRI1-GFP particles were immobile and showed restricted diffusion with an average "motion range" of 0.5 µm. The remaining 40% showed long distance movement with an average "motion range" of 1 µm. However, the fitted bimodal distribution of Wang and colleagues (2015a) was essentially a unimodal distribution, indicating that their value for the diffusion coefficient of the mobile fraction may be artificial. It is questionable whether the fit of a bimodal distribution is a good method of evaluation, if the majority of single-particles shows restricted diffusion and no clear-cut second subfraction can be found. Forcing a bimodal fit may introduce artefacts instead of representing the *in vivo* situation.

According to Bücherl and colleges (2013) and Hutten and colleges (2017), there are two BRI1 nanoclusters per 1 μm^2 of PM with 6-22 BRI1-GFP receptor molecules per cluster in *A. thaliana*. Furthermore, a diameter of 172.6 ± 41.3 nm was proposed for one BRI1-GFP cluster in *A. thaliana* (McKenna et al., 2018). We determined the average diffusion coefficient of BRI1-mEOS in *N. benthamiana* epidermal leaf cells to 0.002 $\mu m\ s^{-1}$. This means that the average time of one BRI1 receptor molecule to move through an entire BRI1 cluster would require 3.7 s. The mammalian TRANSFORMING GROWTH FACTOR-BETA (TGF-β) receptor TβRI-EGFP was found to have a diffusion coefficient of 0.049 $\mu m^2\ s^{-1}$ (Zhao et al., 2018). Interestingly, only when coexpressing TβRII, a significant decrease to 0.015 $\mu m^2\ s^{-1}$ after TGF treatment was found (Zhao et al., 2018). Both BR and TGF signalling show hetero-oligomerization during signalling transduction (Bücherl et al. 2013; Massagué 1998; Eckardt 2005; Ehsan et al. 2005). Interestingly, the diffusion coefficient of BRI1-mEOS was in the same order of magnitude as an animal receptor with the same mode of signal transduction. Remarkably, our observation using VA-TIRF-PALM of single BRI1-mEOS molecules substantiates the results obtained by classical VA-TIRF of BRI1 clusters, that the majority of BRI1 receptors are immobile in the PM of plant cells.

The Picket-fence model postulates that plasma membrane-anchored proteins connected to the actin membrane skeleton meshwork act as rows of pickets (van Zanten and Mayor, 2015). Thus, the movement of lipids and proteins is confined temporarily by steric hindrance (van Zanten and Mayor, 2015). We tested whether actin depolymerization with latrunculin B significantly affects the movement properties of BRI1-mEOS receptor molecules in *N. benthamiana* epidermal leaf cells. However, this was not the case, suggesting that the actin cytoskeleton plays no role in the determination of the BRI1-mEOS single receptor dynamics in this heterologous cell type. The similar observation was made for the treatment of the *N. benthamiana* cells with the PM-disturbing compound MβCD, indicating that an alteration of the lipid composition properties in the PM does not interfere with BRI1-mEOS single receptor dynamics, at least not in this heterologous system. Previously, MβCD treatment did also not alter the mobility of LTI6a-mEOS and PIP2;1-mEOS in *Arabidopsis* epidermal root cells (Hosy et al., 2015).

As an increase in BRI1-BAK1 interaction upon BR treatment was reported throughout literature (Nam and Li, 2002; Wang et al., 2005b; Wang et al., 2005a; Yun et al., 2009;

Hothorn et al., 2011; Santiago et al., 2013; Sun et al., 2013; Hutten et al., 2017; Imkampe et al., 2017; Großeholz et al., 2019), we aimed to find out whether the free diffusive or superdiffusive subpopulation of BRI1-mEOS decreases upon BL treatment in *N. benthamiana*. However, that was also not the case. This finding would favour the hypothesis of Großeholz et al. (2019) that the BR concentration-triggered, dynamic and reversible interaction of the constituents of the BRI1 signalling module occurs in the one and the same BRI1 complex/cluster. In the absence of BR, the interaction between BAK1 and the inhibitory BIR3 is favoured over the interaction of BAK1 with BRI1; however, BRI1 associates with BAK1 at the same time, but *via* a different binding site. The BR binding to the island domain of BRI1 now thermodynamically favours the interaction between BRI1 and BAK1 causing the rotation of BIR3 away from BAK1 and the rotation of BAK1 towards the kinase domain of BRI1. This initiates the trans-phosphorylation events between the receptor/co-receptor pairs. In this scenario, none of the three proteins is required to leave the BRI1 complex/cluster in the presence of BR or to re-entry the complex/cluster in the absence of the hormone. Therefore, we would not expect changes in BRI1 receptor dynamics in response to alterations in BR levels.

Compared to the increase in the mobile fraction from 15% to 59% for PIP2;1-mEOS, as observed after plasmolysis by 300 and 400 mM sorbitol (Hosy et al., 2015), it becomes clear that the stabilizing effect of the cell wall is fundamental for the protein dynamics in the PM of plant cells. In comparison to that, all previously observed changes in dynamics caused, for instance, through the disturbance of the actin cytoskeleton or the lipid composition of the PM or in response to hormone treatment, had comparatively minor effects (Hosy et al., 2015). Interestingly, our control for the MβCD treatment, namely 10 mM mannitol, that induces a mild plasmolysis, caused a minor effect on the BRI1-mEOS receptor dynamics. Whether hyperosmotic stress and thus putative enhanced BRI1 receptor mobility in the PM also affects BRI1 function has to be elucidated in future.

Eventually, the heterologous *N. benthamiana* system may not be appropriate to study possibly minor changes in the dynamics of the BRI1 receptor. For a better understanding of the function of BRI1 receptor dynamics in BR signalling, sptPALM measurements in the native cellular context of *Arabidopsis* are required. While the generation of BRI1-mEOS expressing Arabidopsis lines are in progress, we performed

initial physiological experiments aiming on the effects of lipid microdomain disruption by MβCD on BR function.

Previous studies have found that BRI1 and BAK1 frequently form heterodimers and are located in close spatial proximity in preformed complexes/clusters (Nam and Li, 2002; Wang et al., 2005b; Yun et al., 2009; Bücherl et al., 2013). Such a close spatial arrangement and, consequently, a restricted mobility in the PM, would enable the fast, BR concentration-related and efficient signal transduction, leading to a quantitative physiological output. At a later time point, a close spatial arrangement would facilitate the collective endocytosis of the relevant signalling components. Several mechanisms how this could be achieved have been discussed (Konrad and Ott, 2015). So far, only few studies provided evidence that the spatial arrangement of signalling components in the PM affects the corresponding physiological output. We found that the disruption of the spatial organization of the PM by treatment with MβCD attenuated quantitatively the BR-triggered root growth and root waving, especially in an transgenic *Arabidopsis* line that mildly overexpresses BRI1-GFP (Friedrichsen et al., 2000). Neither the BL-regulated root elongation growth, nor root waving was detectable any longer when the hormone application was combined with MβCD treatment. It has been proposed, that MβCD entraps lipophilic molecules and acts as acceptor compartment for them (Kerns and Di, 2008; Stick and Williams, 2009). The precise function of MβCD is currently unknown, and experimental data have to be interpreted cautiously (Fantini and J. Barrantes, 2018). However, MβCD was shown to remove plant sterols (e.g. sitosterol, campesterol, cholesterol) and sterol-associated proteins from the membrane environment in a concentration-dependent manner (Kierszniowska et al., 2009). In the light of this observation, the reversion of the hypersensitive response of the BRI1-GFP overexpressor back to normal signalling strength in the presence of MβCD could be due to a reduced number of receptors in the PM. This could be tested by quantitative western blotting of the BRI1-GFP amount in MβCD treated seedlings.

MβCD also decreases the endocytosis rate of BRI1-GFP, which could be recovered by addition of campesterol or β-sitosterol (Wang et al., 2015a) pointing to the sterol extraction function of MβCD. Thus, after 30 minutes of MβCD treatment, the abundance of BRI1 receptors at the PM increased. Also, BR signalling was inhibited by MβCD, as BKI1-YFP dissociated less from the PM upon hormone treatment (Wang et al., 2015a), suggesting that the potential reduction BRI1 receptor amount by MβCD treatment is probably not the reason for the altered BR responses we observed.

Another possible mechanism of MβCD action could be that the organization of the BRI1 complex/cluster is disturbed and the constituent proteins are more evenly spread in the PM, thus reducing the efficiency of signalling. It was recently shown, that MβCD treatment depleted sterol, which in turn affected the confinement area and diffusion rate of the blue-light receptor phot1-GFP in *Arabidopsis*, which could be restored by addition of campesterol (Xue et al., 2018). Also here, MβCD treatment impaired phototropism to blue light (Xue et al., 2018). It will be, therefore, interesting to elucidate by sptPALM the membrane dynamics of BRI1-mEOS in epidermal root cells of transgenic *A. thaliana* lines in response to MβCD treatment and the consequences of such treatment also for BR-regulated, short-time cell physiological processes such as apoplast acidification (Barbez et al., 2017; Glöckner et al., 2019). In conclusion, even though the precise mechanism of MβCD action is currently not fully understood, our physiological results suggest that BR/BRI1 perception and signalling depend on the sterol content and proper lipid composition of the PM.

Material and methods

Plant material

Seeds were surface sterilized and placed on ½ MS (Murashige and Skoog) medium plates with 1% phytoagar and 1% sucrose followed by stratification at 4°C in the dark for two days. Then plants were grown upright in growth chambers under long day conditions (cycling 16 h light/ 8 h dark) at 19°C to 22°C for five days. The transformation of N. benthamiana leafs was performed as previously described (Ladwig et al., 2015).

Cloning

The BRI1 coding sequence was brought in pDONR201™ previously (Caesar et al., 2011) and brought into pUBC-EOS-Dest via LR cloning (Gateway™) according to the manufacturer protocol.

Single-particle tracking measurements

In essence, the measurements were performed as previously described (Hosy et al., 2015). The setup of the custom built microscope was described previously (Speth et al., 2018). The root epidermis of five-day-old seedlings was imaged at room temperature. The leaf epidermal cells of *N. benthamiana* were imaged two days after transformation. The root or small leaf cuts were mounted with a drop of water (or treatment) under coverslips. The movies were acquired on a custom-built super-resolution microscope with total internal reflection (TIRF) illumination. Fluorescence excitation of mEOS fusion proteins was performed with a 561 nm laser (50 mW, Vortran Stradus, Laser2000, Germany), which was first spectrally cleaned up by a band pass filter (BrightLine 561/14, Semrock, USA), then spatially cleaned up by a glass fiber (PM-S405-XP, Thorlabs, USA), before focusing the beam onto the back focal plane of a high-NA objective (Alpha Plan-Fluar 100x/1.49, Zeiss, Germany) with an off-axis lens focusing on the back focal plane to achieve (VA-) TIRF illumination. Photoconversion of mEOS was achieved with a 405 nm activation laser (NANO 250, Qioptiq, 608UK). A quad-line beam splitter (zt450/488/561/640rpc, Chroma, USA) between the TIRF lens and the objective was used to reflect the excitation and activation light onto the sample plane. The respective fluorescence emission was able to pass through to the detection path, where further emission colour filters (BrightLine 527/20, BrightLine 580/23, Semrock, USA) blocked residual excitation light. An

imaging lens projected the fluorescence emission to the water-cooled sCMOS camera (Hamamatsu Orca Flash4.0) with an acquisition time of 50 ms, 100 nm / pixel, 2000 frames per movie (100 s) in a 256 x 256 pixel area (25.6 x 25.6µm). Both lasers illuminated the sample simultaneously. The power of the 405 nm activation laser and the respective imaging lasers were adjusted to keep the number of the stochastically activated molecules constant and well separated during the acquisition. Laser intensities were tuned to ensure that the fluorescence of single molecules could be detected for multiple frames before being bleached. Localization of single molecule fluorescent spots was performed as described (Rossier et al., 2012; Nair et al., 2013). For single-particle tracking, the previously published localization algorithm was used (Li et al., 2018), taking into account the pixel-to-noise characteristics of sCMOS cameras. The track building algorithm was adapted from Jean-Yves Tinevez (https://de.mathworks.com/matlabcentral/fileexchange/34040-simple-tracker), using a maximal linking distance of 100 nm and maximum gap closing of four frames. Tracks that only lasted for five frames were excluded. For the apparent diffusion coefficient, a linear fit of the first four data points were used. All fits with R^2 below 0.4 were excluded. For the determination of the diffusion behaviour as suggested by Jean-Yves Tinevez, the first ten points of the MSD plot were used for the fit. For the combined evaluation of the three biological replicates, the parameters listed in SI table 1 (Supp. Mat. 2) were used.

The calculation of the time needed for a single particle with a diffusion coefficient of 0.002 $\mu m^2 s^{-1}$ to move a distance of 0.172 µm was performed with the formula of MSD in a two-dimensional space: $D = R^2 / (4 t)$ with D as the diffusion coefficient, R^2 as the mean squared distance and t as the time.

Quantification

Plates were scanned with a ruler next to them and root length was measured with Fiji. The script for automatic calculation of the distance between the first point (root length at timepoint of transfer) and the last point (final length of the root) is shown in Supp. Material 3.

Statistics

For calculation of average, standard error (SE) and standard deviation (SD) Excel v1809 or SAS JMP 14 were used. Images were generated with Microsoft Excel v1809. To test for homogeneity of variance Levene's test ($p < 0.05$) was employed and if not stated otherwise, statistical significance for non-parametic distributions was calculated by a two-tailed, all-pair Kruskal-Wallis test followed by a Steel-Dwass post hoc correction using SAS JMP version 14.0.0 (Ohmi et al., 2016).

Figures

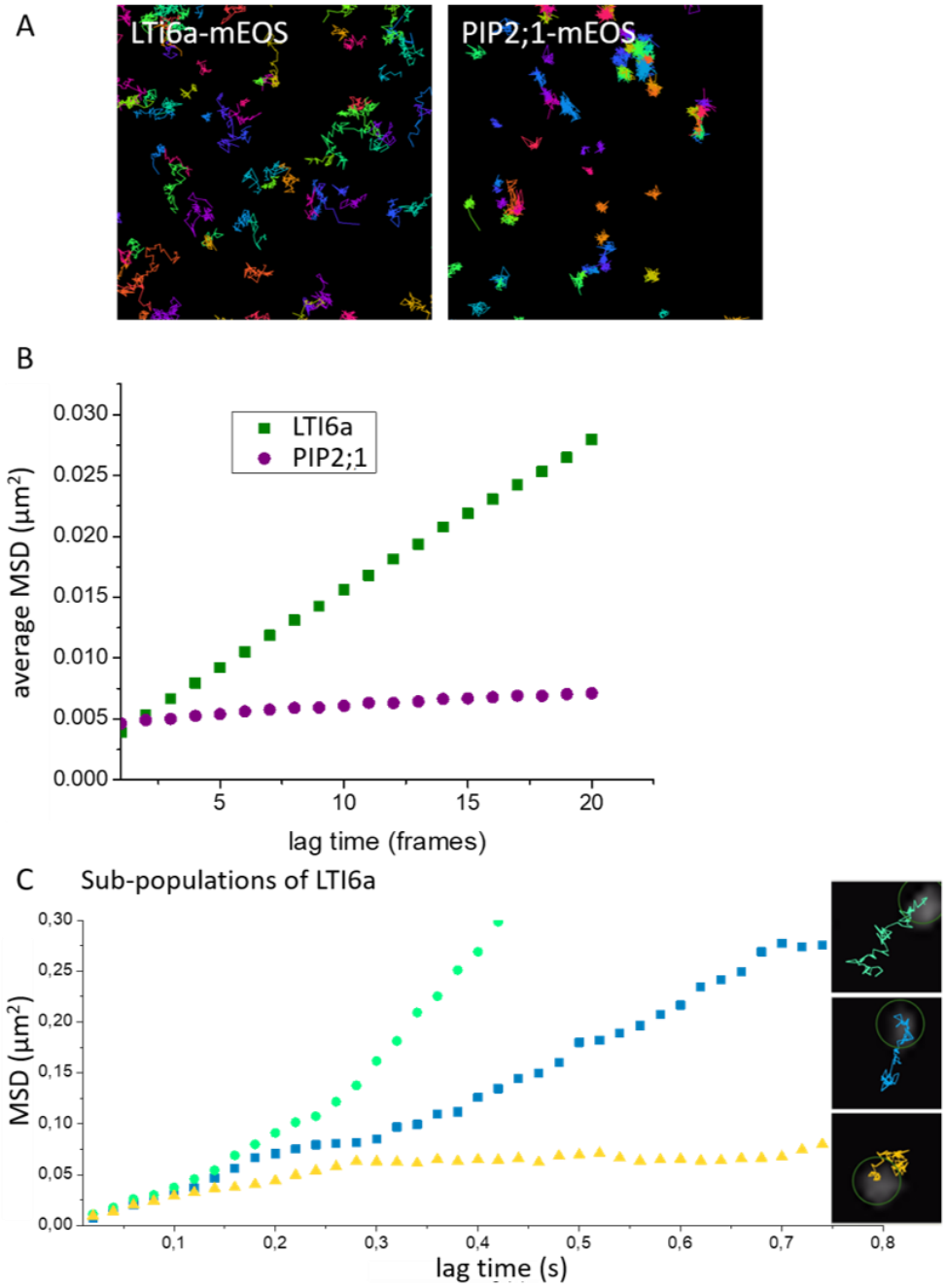

Figure 1. Mean square displacement of LTI6a-mEOS and PIP2;1-mEOS (an aquaporine) in the plasma membrane of epidermal root cells of *Arabidopsis thaliana* recorded by single particle tracking PALM (sptPALM).
(A) Representative images of single molecule trajectories in the plasma membrane of epidermal root cells of 5-days-old, light grown *A. thaliana* seedlings. The trajectories of every single LTI6a-mEOS protein (left) and PIP2;1-mEOS protein (right) are shown in a different colour. The expression of the mEOS fusion proteins is driven by the *PIP2;1* promoter.

(B) Average mean square displacement (MSD) of PIP2;1-mEOS and LTI6-mEOS in *A. thaliana* epidermal root cells over lag times of up to 20 frames, which is equivalent to a lag time of 1 s.
(C) Mean square displacement (MSD) of different single LTI6-mEOS molecules over lag times of up to 0.75 s in *A. thaliana* epidermal root cells, showing either subdiffusive behaviour ($\alpha < 0.9$; yellow), free diffusion ($0.9 < \alpha < 1.1$; blue) or superdiffusive behaviour ($\alpha > 1.1$; green). $MSD = 4D(t_{lag})^{\alpha}$ with D as the diffusion coefficient, t_{lag} as the lag times and α as parameter.

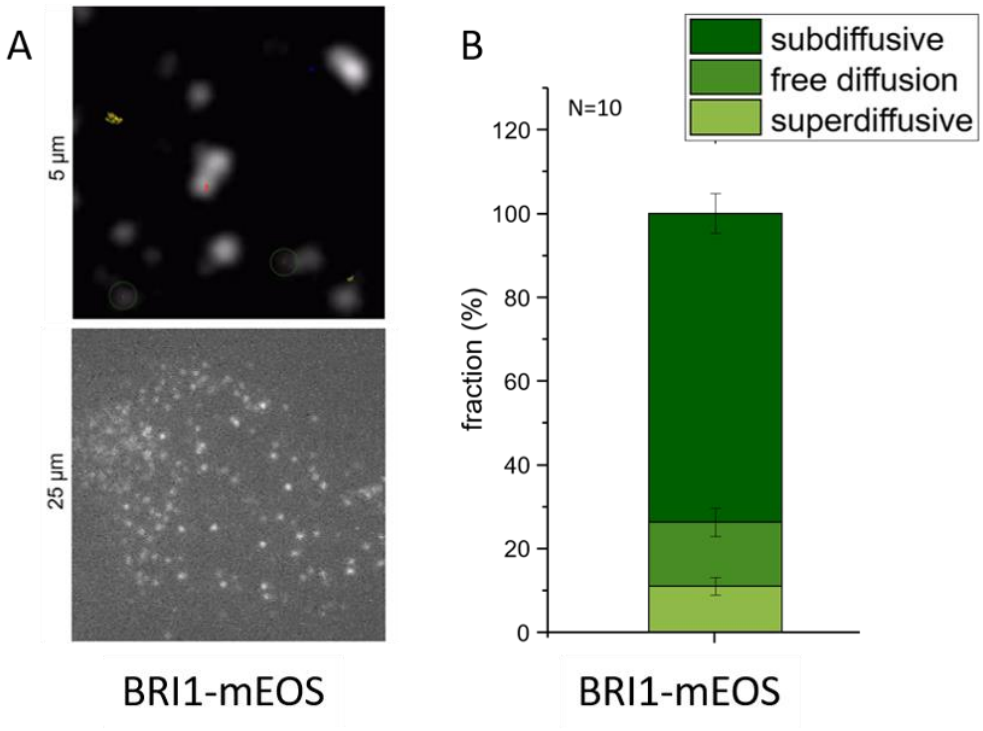

Figure 2. Determination of the mobility behaviour of BRI1-mEOS in epidermal leaf cells of *Nicotiana benthamiana* by single-particle tracking PALM (sptPALM). (A) Representative image of the obtained signal for BRI1-mEOS in the epidermis after transient transformation of *N. benthamiana* leaf cells with the *pUBC::BRI1-mEOS* construct *via Agrobacterium* infiltration, with accumulation of BRI1-mEOS for 2 days. Edge length is 25µm for the lower magnification (bottom) and 5µm for the high magnification (top). Contrast of top image was adjusted and a track (yellow) of a fluorophore is visible. Intensity and contrast of bottom image was not adjusted.
(B) Average proportion of the BRI1-mEOS subpopulations with different diffusion behaviour, which is classified by fitting the first 10 points of the obtained MSD plot for each molecule to MSD = $4D(t_{lag})^{\alpha}$ (Jean-Yves Tinevez). The subdiffusive subpopulation (dark green) is defined as $\alpha < 0.9$, the freely diffusive (green) as $0.9 < \alpha < 1.1$ and the superdiffusive (light green) as $\alpha > 1.1$. Sample size of epidermis cells (n): =10 ± SE.

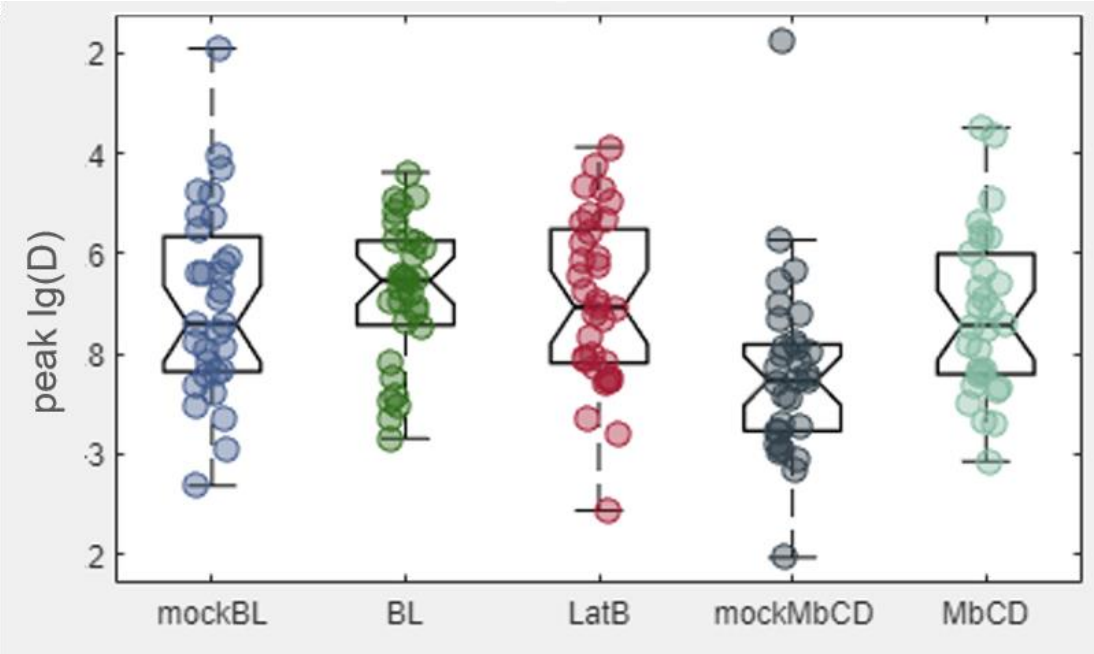

Figure 3. Diffusion coefficients of BRI1-mEOS in epidermal leaf cells of *Nicotiana benthamiana* in response to different treatments, as determined by single-particle tracking PALM (sptPALM).
Modal log-scaled diffusion coefficient D of BRI1-mEOS derived from ~30 cells (one biological replicate) after 20-30 minutes with mock-treatment 0.001% DMSO, 1 nM brassinolide hormone treatment, 0.25 µM latrunculin B (LatB), and 30-40 minutes after 10 mM mannitol as mock-treatment control for the plasmolysis possibly induced by the 10 mM methyl-β-cyclodextran (MβCD) treatment. A normal fit was applied to the log (D) distributions (as shown in Supp. Mat. 1) for each cell, meaning that each point represents the most frequent diffusion coefficient of one cell.

After transient transformation of *N. benthamiana* leaf cells with the *pUBC::BRI1-mEOS* construct *via Agrobacterium* infiltration, the accumulation of the BRI1-mEOS was allowed for 2 days. Boxplots indicate 25%, median and 75% quartils, allowing outliers which were not included in the statistical analysis. Boxplots of different treatments with overlapping inclinations are not statistically different from each other.

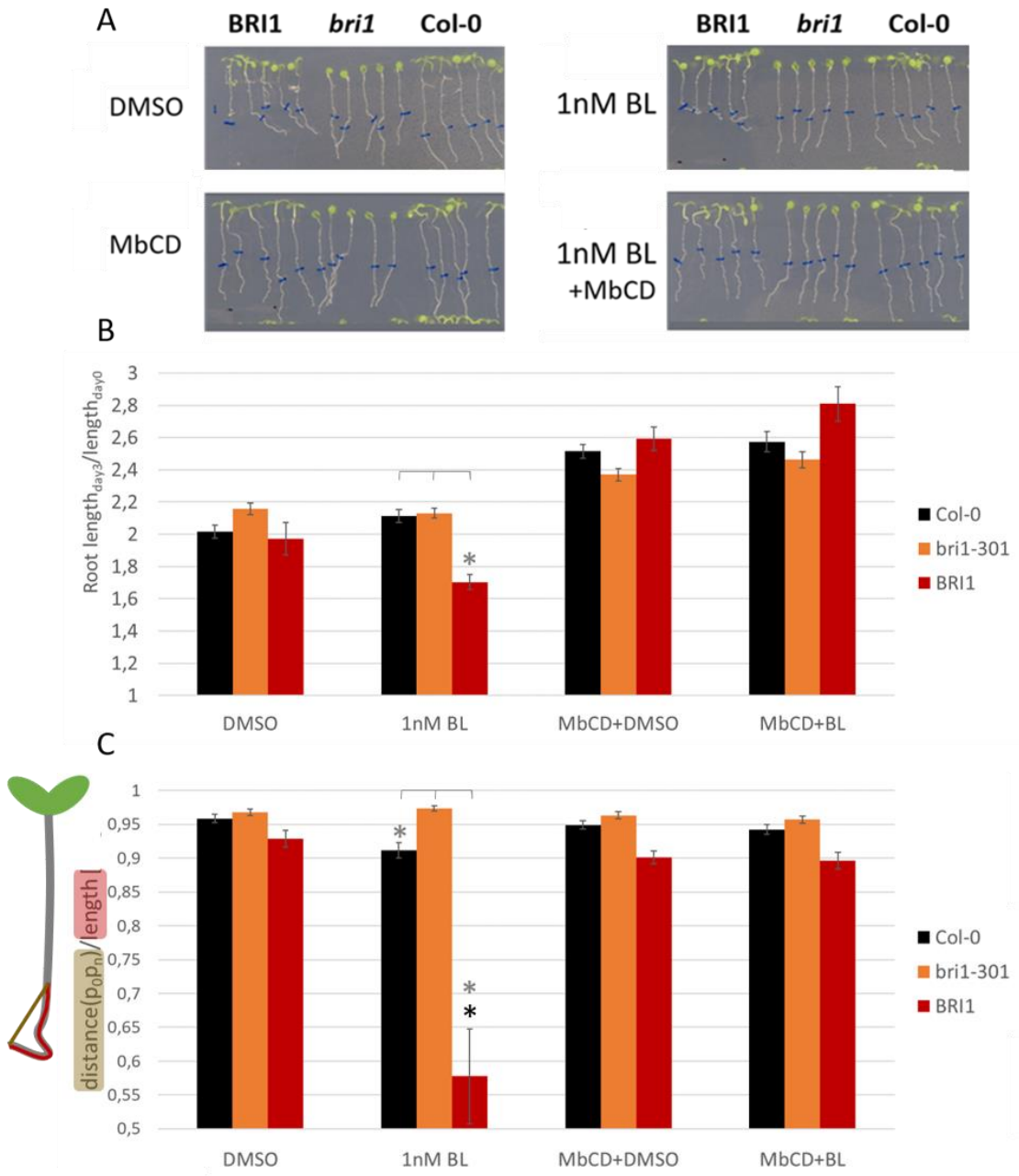

Figure 4. M**ethyl-β-cyclo-dextran (MβCD) treatment interferes with** t**he brassinosteroid regulation of the primary root growth and root waving in *Arabidopsis thaliana*.**

(A) Wild type (Col-0), *bri1-301* mutant and BRI1-GFP overexpressing (BRI1) seedlings were grown for 5 days on plates without any treatment. Seedlings were then transferred to control plates (DMSO for 1 nM BL) or plates containing either 1 nM BL (BL), 10 mM (MβCD+DMSO) or 1 nM BL+ 10 mM MβCD (MβCD+BL). Images were taken 3 days after the transfer and the blue lines indicates the root length immediately after the transfer.

(B) Relative increase in the root length of wild type Col-0, *bri1-301* mutant and BRI1-GFP overexpressing (BRI1) seedlings 3 days after transfer on plates containing the compounds as indicated in (A). Shown is the mean (n=10) ± SE.

(C) Straightness of the root of wild type Col-0, *bri1-301* mutant and BRI1-GFP overexpressing (BRI1) seedlings 3 days after transfer on plates containing the compounds as indicated in (A). The straightness of the root (cartoon at the left) was assessed, by dividing the distance between the initial and final position of the root tip (brown line) through the root length (red line). Shown is the mean (n=10) ± SE.

Statistical differences were tested with a two-tailed, all-pair Kruskal-Wallis test followed by a Steel-Dwass post hoc correction (grey asterisk). To statistically assess a possible rescue of the hormone-dependent root waving of BRI1-GFP, the Steel test with mock-treated BRI1-GFP as control group was performed (black asterisk). Sample numbers are low and have to be interpreted carefully.

Acknowledgements

The authors would like to thank Sabine Müller and Pantelis Livanos for kindly providing Lat B for a first test and Moritz Burmeister for advice with the automated script in FIJI for the calculation of the angle and distance between two points. The research was supported by the German Research Foundation (DFG) with grants to K.H. (HA 2146/22-1; CRC 1101-D02 & Z02).

References

Abbe, E. (1873). Beiträge zur Theorie des Mikroskops und der mikroskopischen Wahrnehmung. Archiv für mikroskopische Anatomie *9*, 413-418.

Barbez, E., Dünser, K., Gaidora, A., Lendl, T., and Busch, W. (2017). Auxin steers root cell expansion via apoplastic pH regulation in Arabidopsis thaliana. Proceedings of the National Academy of Sciences of the United States of America *114*, E4884-E4893.

Betzig, E. (2015). Single Molecules, Cells, and Super-Resolution Optics (Nobel Lecture). Angewandte Chemie (International ed. in English) *54*, 8034-8053.

Bücherl, C.A., Jarsch, I.K., Schudoma, C., Segonzac, C., Mbengue, M., Robatzek, S., MacLean, D., Ott, T., and Zipfel, C. (2017). Plant immune and growth receptors share common signalling components but localise to distinct plasma membrane nanodomains. eLife *6*.

Bücherl, C.A., van Esse, G.G., Kruis, A., Luchtenberg, J., Westphal, A.H., Aker, J., van Hoek, A., Albrecht, C., Borst, J.W., and Vries, S.C.d. (2013). Visualization of BRI1 and BAK1(SERK3) membrane receptor heterooligomers during brassinosteroid signaling. Plant Physiology *162*, 1911-1925.

Burkart, R.C., and Stahl, Y. (2017). Dynamic complexity. Plant receptor complexes at the plasma membrane. Current Opinion in Plant Biology *40*, 15-21.

Caesar, K., Elgass, K., Chen, Z., Huppenberger, P., Witthöft, J., Schleifenbaum, F., Blatt, M.R., Oecking, C., and Harter, K. (2011). A fast brassinolide-regulated response pathway in the plasma membrane of Arabidopsis thaliana. The Plant journal : for cell and molecular biology *66*, 528-540.

Cosgrove, D.J. (2000). New genes and new biological roles for expansins. Current Opinion in Plant Biology *3*, 73-78.

Dugas, C.M., Li, Q., Khan, I.A., and Nothnagel, E.A. (1989). Lateral diffusion in the plasma membrane of maize protoplasts with implications for cell culture. Planta *179*, 387-396.

Fantini, J., and J. Barrantes, F. (2018). How membrane lipids control the 3D structure and function of receptors. AIMS Biophysics *5*, 22-35.

Fridman, Y., and Savaldi-Goldstein, S. (2013). Brassinosteroids in growth control. How, when and where. Plant science : an international journal of experimental plant biology *209*, 24-31.

Friedrichsen, D.M., Joazeiro, C.A.P., Li, J., Hunter, T., and Chory, J. (2000). Brassinosteroid-Insensitive-1 Is a Ubiquitously Expressed Leucine-Rich Repeat Receptor Serine/Threonine Kinase. Plant Physiology *123*, 1247-1256.

Gahlmann, A., and Moerner, W.E. (2013). Exploring bacterial cell biology with single-molecule tracking and super-resolution imaging. Nature Reviews Microbiology *12*, 9 EP -.

Glöckner, N., Großeholz, R., Wanke, F., Jaspert, N., Shabala, L., Shabala, S., Kummer, U., and Harter, K. (2019). Quantitative description and computational modelling of the BRI1 response module controlling cell elongation growth. In preparation for submission.

González-García, M.-P., Vilarrasa-Blasi, J., Zhiponova, M., Divol, F., Mora-García, S., Russinova, E., and Caño-Delgado, A.I. (2011). Brassinosteroids control meristem size by promoting cell cycle progression in Arabidopsis roots. Development (Cambridge, England) *138*, 849-859.

Gronnier, J., Gerbeau-Pissot, P., Germain, V., Mongrand, S., and Simon-Plas, F. (2018). Divide and Rule. Plant Plasma Membrane Organization. Trends in plant science *23*, 899-917.

Großeholz, R., Feldman-Salit, A., Wanke, F., Schulze, S., Glöckner, N., Kemmerling, B., Harter, K., and Kummer, U. (2019). Specifying the role of BAK1-interacting receptor-like kinase 3 in brassinosteroid signaling. Journal of integrative plant biology.

Hell, S.W., Sahl, S.J., Bates, M., Zhuang, X., Heintzmann, R., Booth, M.J., Bewersdorf, J., Shtengel, G., Hess, H., and Tinnefeld, P., et al. (2015). The 2015 super-resolution microscopy roadmap. J. Phys. D: Appl. Phys. *48*, 443001.

Hosy, E., Martinière, A., Choquet, D., Maurel, C., and Luu, D.-T. (2015). Super-resolved and dynamic imaging of membrane proteins in plant cells reveal contrasting kinetic profiles and multiple confinement mechanisms. Molecular plant *8*, 339-342.

Hothorn, M., Belkhadir, Y., Dreux, M., Dabi, T., Noel, J.P., Wilson, I.A., and Chory, J. (2011). Structural basis of steroid hormone perception by the receptor kinase BRI1. Nature *474*, 467-471.

Hutten, S.J., Hamers, D.S., Aan den Toorn, M., van Esse, W., Nolles, A., Bücherl, C.A., Vries, S.C. de, Hohlbein, J., and Borst, J.W. (2017). Visualization of BRI1 and SERK3/BAK1 Nanoclusters in Arabidopsis Roots. PloS one *12*, e0169905.

Imkampe, J., Halter, T., Huang, S., Schulze, S., Mazzotta, S., Schmidt, N., Manstretta, R., Postel, S., Wierzba, M., and Yang, Y., et al. (2017). The Arabidopsis Leucine-Rich Repeat Receptor Kinase BIR3 Negatively Regulates BAK1 Receptor Complex Formation and Stabilizes BAK1. The Plant cell *29*, 2285-2303.

Kerns, E.H., and Di, L. (2008). Drug-like properties. Concepts, structure design and methods ; from ADME to toxicity optimization (Amsterdam, Boston: Academic Press).

Kierszniowska, S., Seiwert, B., and Schulze, W.X. (2009). Definition of Arabidopsis sterol-rich membrane microdomains by differential treatment with methyl-beta-cyclodextrin and quantitative proteomics. Molecular & cellular proteomics : MCP *8*, 612-623.

Konrad, S.S.A., and Ott, T. (2015). Molecular principles of membrane microdomain targeting in plants. Trends in plant science *20*, 351-361.

Ladwig, F., Dahlke, R.I., Stührwohldt, N., Hartmann, J., Harter, K., and Sauter, M. (2015). Phytosulfokine Regulates Growth in Arabidopsis through a Response Module at the Plasma Membrane That Includes CYCLIC NUCLEOTIDE-GATED CHANNEL17, H+-ATPase, and BAK1. The Plant cell *27*, 1718-1729.

Li, X., Luu, D.-T., Maurel, C., and Lin, J. (2013). Probing plasma membrane dynamics at the single-molecule level. Trends in plant science *18*, 617-624.

Li, X., Wang, X., Yang, Y., Li, R., He, Q., Fang, X., Luu, D.-T., Maurel, C., and Lin, J. (2011). Single-molecule analysis of PIP2;1 dynamics and partitioning reveals multiple modes of Arabidopsis plasma membrane aquaporin regulation. The Plant cell *23*, 3780-3797.

Li, Y., Mund, M., Hoess, P., Deschamps, J., Matti, U., Nijmeijer, B., Sabinina, V.J., Ellenberg, J., Schoen, I., and Ries, J. (2018). Real-time 3D single-molecule localization using experimental point spread functions. Nature Methods *15*, 367-369.

Lin, W., Lu, D., Gao, X., Jiang, S., Ma, X., Wang, Z., Mengiste, T., He, P., and Shan, L. (2013). Inverse modulation of plant immune and brassinosteroid signaling pathways by the receptor-like cytoplasmic kinase BIK1. Proceedings of the National Academy of Sciences of the United States of America *110*, 12114-12119.

Lu, S.M., and Fairn, G.D. (2018). Mesoscale organization of domains in the plasma membrane - beyond the lipid raft. Critical reviews in biochemistry and molecular biology *53*, 192-207.

Lv, B., Tian, H., Zhang, F., Liu, J., Lu, S., Bai, M., Li, C., and Ding, Z. (2018). Brassinosteroids regulate root growth by controlling reactive oxygen species homeostasis and dual effect on ethylene synthesis in Arabidopsis. PLoS genetics *14*, e1007144.

Malinsky, J., Opekarová, M., Grossmann, G., and Tanner, W. (2013). Membrane microdomains, rafts, and detergent-resistant membranes in plants and fungi. Annual review of plant biology *64*, 501-529.

Manley, S., Gillette, J.M., Patterson, G.H., Shroff, H., Hess, H.F., Betzig, E., and Lippincott-Schwartz, J. (2008). High-density mapping of single-molecule trajectories with photoactivated localization microscopy. Nature Methods *5*, 155 EP -.

McKenna, J.F., Rolfe, D., Webb, S.E.D., Tolmie, A.F., Botchway, S.W., Martin-Fernandez, M., Hawes, C., and Runions, J. (2018). The cell wall regulates dynamics and size of plasma-membrane nanodomains in Arabidopsis.

McQueen-Mason, S., and Cosgrove, D.J. (1994). Disruption of hydrogen bonding between plant cell wall polymers by proteins that induce wall extension. Proceedings of the National Academy of Sciences of the United States of America *91*, 6574-6578.

Mora-García, S., Vert, G., Yin, Y., Caño-Delgado, A., Cheong, H., and Chory, J. (2004). Nuclear protein phosphatases with Kelch-repeat domains modulate the response to brassinosteroids in Arabidopsis. Genes & development *18*, 448-460.

Nair, D., Hosy, E., Petersen, J.D., Constals, A., Giannone, G., Choquet, D., and Sibarita, J.-B. (2013). Super-resolution imaging reveals that AMPA receptors inside synapses are dynamically organized in nanodomains regulated by PSD95. The Journal of neuroscience : the official journal of the Society for Neuroscience *33*, 13204-13224.

Nam, K.H., and Li, J. (2002). BRI1/BAK1, a Receptor Kinase Pair Mediating Brassinosteroid Signaling. Cell *110*, 203-212.

Ott, T. (2017). Membrane nanodomains and microdomains in plant-microbe interactions. Current Opinion in Plant Biology *40*, 82-88.

Phyo, P., Gu, Y., and Hong, M. (2019). Impact of acidic pH on plant cell wall polysaccharide structure and dynamics. Insights into the mechanism of acid growth in plants from solid-state NMR. Cellulose *26*, 291-304.

Rayleigh (1897). XXXI. Investigations in optics, with special reference to the spectroscope. The London, Edinburgh, and Dublin Philosophical Magazine and Journal of Science *8*, 261-274.

Rocchetti, A., Hawes, C., and Kriechbaumer, V. (2014). Fluorescent labelling of the actin cytoskeleton in plants using a cameloid antibody. Plant methods *10*, 12.

Rossier, O., Octeau, V., Sibarita, J.-B., Leduc, C., Tessier, B., Nair, D., Gatterdam, V., Destaing, O., Albigès-Rizo, C., and Tampé, R., et al. (2012). Integrins β1 and β3 exhibit distinct dynamic nanoscale organizations inside focal adhesions. Nature Cell Biology *14*, 1057-1067.

Santiago, J., Henzler, C., and Hothorn, M. (2013). Molecular mechanism for plant steroid receptor activation by somatic embryogenesis co-receptor kinases. Science (New York, N.Y.) *341*, 889-892.

Speth, C., Szabo, E.X., Martinho, C., Collani, S., Zur Oven-Krockhaus, S., Richter, S., Droste-Borel, I., Macek, B., Stierhof, Y.-D., and Schmid, M., et al. (2018). Arabidopsis RNA processing factor SERRATE regulates the transcription of intronless genes. eLife *7*.

Stick, R.V. and Williams, S.J. (2009). Carbohydrates: The Essential Molecules of Life (Second Edition). Chapter 9 - Disaccharides, Oligosaccharides and Polysaccharides (Oxford: Elsevier).

Sun, Y., Han, Z., Tang, J., Hu, Z., Chai, C., Zhou, B., and Chai, J. (2013). Structure reveals that BAK1 as a co-receptor recognizes the BRI1-bound brassinolide. Cell Research *23*, 1326 EP -.

Tong, H., Xiao, Y., Liu, D., Gao, S., Liu, L., Yin, Y., Jin, Y., Qian, Q., and Chu, C. (2014). Brassinosteroid regulates cell elongation by modulating gibberellin metabolism in rice. The Plant cell *26*, 4376-4393.

van Zanten, T.S., and Mayor, S. (2015). Current approaches to studying membrane organization. F1000Research *4*.

Veronese, P., Nakagami, H., Bluhm, B., Abuqamar, S., Chen, X., Salmeron, J., Dietrich, R.A., Hirt, H., and Mengiste, T. (2006). The membrane-anchored BOTRYTIS-INDUCED KINASE1 plays distinct roles in Arabidopsis resistance to necrotrophic and biotrophic pathogens. The Plant cell *18*, 257-273.

Vert, G., and Chory, J. (2006). Downstream nuclear events in brassinosteroid signalling. Nature *441*, 96-100.

Wang, J., Jiang, J., Wang, J., Chen, L., Fan, S.-L., Wu, J.-W., Wang, X., and Wang, Z.-X. (2014). Structural insights into the negative regulation of BRI1 signaling by BRI1-interacting protein BKI1. Cell Research *24*, 1328-1341.

Wang, L., Li, H., Lv, X., Chen, T., Li, R., Xue, Y., Jiang, J., Jin, B., Baluška, F., and Šamaj, J., et al. (2015a). Spatiotemporal Dynamics of the BRI1 Receptor and its Regulation by Membrane Microdomains in Living Arabidopsis Cells. Molecular plant *8*, 1334-1349.

Wang, X., and Chory, J. (2006). Brassinosteroids regulate dissociation of BKI1, a negative regulator of BRI1 signaling, from the plasma membrane. Science (New York, N.Y.) *313*, 1118-1122.

Wang, X., Goshe, M.B., Soderblom, E.J., Phinney, B.S., Kuchar, J.A., Li, J., Asami, T., Yoshida, S., Huber, S.C., and Clouse, S.D. (2005a). Identification and functional analysis of in vivo phosphorylation sites of the Arabidopsis BRASSINOSTEROID-INSENSITIVE1 receptor kinase. The Plant cell *17*, 1685-1703.

Wang, X., Li, X., Deng, X., Luu, D.-T., Maurel, C., and Lin, J. (2015b). Single-molecule fluorescence imaging to quantify membrane protein dynamics and oligomerization in living plant cells. Nature Protocols *10*, 2054-2063.

Wang, X., Li, X., Meisenhelder, J., Hunter, T., Yoshida, S., Asami, T., and Chory, J. (2005b). Autoregulation and homodimerization are involved in the activation of the plant steroid receptor BRI1. Developmental cell *8*, 855-865.

Weinberg, Z.Y., and Puthenveedu, M.A. (2019). Regulation of G protein-coupled receptor signaling by plasma membrane organization and endocytosis. Traffic (Copenhagen, Denmark) *20*, 121-129.

Witthöft, J., Caesar, K., Elgass, K., Huppenberger, P., Kilian, J., Schleifenbaum, F., Oecking, C., and Harter, K. (2014). The activation of the Arabidopsis P-ATPase 1 by the brassinosteroid receptor BRI1 is independent of threonine 948 phosphorylation. Plant Signaling & Behavior *6*, 1063-1066.

Xue, Y., Xing, J., Wan, Y., Lv, X., Fan, L., Zhang, Y., Song, K., Wang, L., Wang, X., and Deng, X., et al. (2018). Arabidopsis Blue Light Receptor Phototropin 1 Undergoes Blue Light-Induced Activation in Membrane Microdomains. Molecular plant *11*, 846-859.

Yeagle, P. (2016). The membranes of cells. Chapter 9 - Cholesterol and Related Sterols: Roles in Membrane Structure and Function (London: Academic Press is an imprint of Elsevier).

Yin, Y., Vafeados, D., Tao, Y., Yoshida, S., Asami, T., and Chory, J. (2005). A new class of transcription factors mediates brassinosteroid-regulated gene expression in Arabidopsis. Cell *120*, 249-259.

Yun, H.S., Bae, Y.H., Lee, Y.J., Chang, S.C., Kim, S.-K., Li, J., and Nam, K.H. (2009). Analysis of phosphorylation of the BRI1/BAK1 complex in arabidopsis reveals amino acid residues critical for receptor formation and activation of BR signaling. Molecules and Cells *27*, 183-190.

Zhang, X., Zhou, L., Qin, Y., Chen, Y., Liu, X., Wang, M., Mao, J., Zhang, J., He, Z., and Liu, L., et al. (2018). A Temperature-Sensitive Misfolded bri1-301 Receptor Requires Its Kinase Activity to Promote Growth. Plant Physiology *178*, 1704-1719.

Zhao, R., Li, N., Xu, J., Li, W., and Fang, X. (2018). Quantitative single-molecule study of TGF-β/Smad signaling. Acta biochimica et biophysica Sinica *50*, 51-59.

Zhu, J.-Y., Li, Y., Cao, D.-M., Yang, H., Oh, E., Bi, Y., Zhu, S., and Wang, Z.-Y. (2017). The F-box Protein KIB1 Mediates Brassinosteroid-Induced Inactivation and Degradation of GSK3-like Kinases in Arabidopsis. Molecular cell *66*, 648-657.e4.

Supplemental Material

Supp. Mat. 1: Occurrence of log-scaled diffusion coefficients

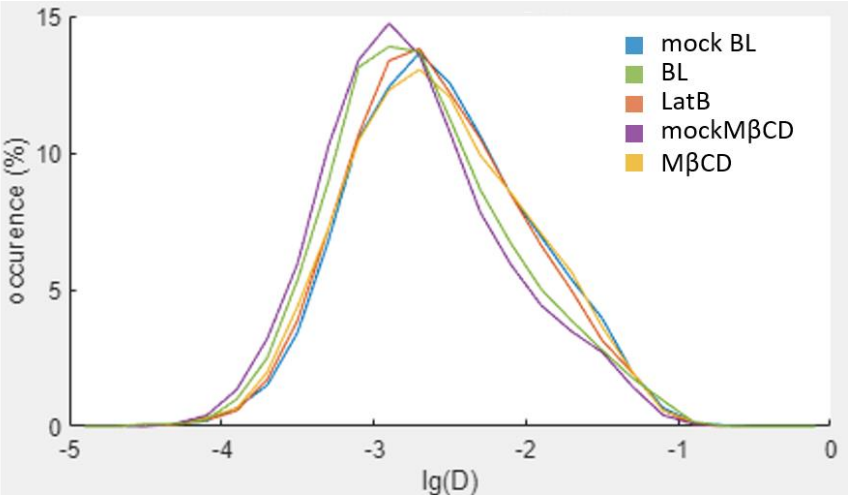

Supp. Fig. 1. Diffusion coefficients of BRI1-mEOS in epidermal leaf cells of *Nicotiana benthamiana* in reaction to different treatments, as determined single-particle tracking PALM (sptPALM).
Representative occurence of the log-scaled distribution of the diffusion coefficients of BRI1-mEOS after about 30 minutes mock treatment (0.01% DMSO; mockBL), treatment with 1 nM brassinolide treatment (BL), 25 µM latrunculin B (LatB), or mock treatment for methyl-β-cyclodextran (10 mM mannitol; mockMβCD) or treatment with 10 mM methyl-β-cyclodextran (MβCD). Data for one biological replicate are shown.

Supp. Mat. 2: Data of the two other biological replicates

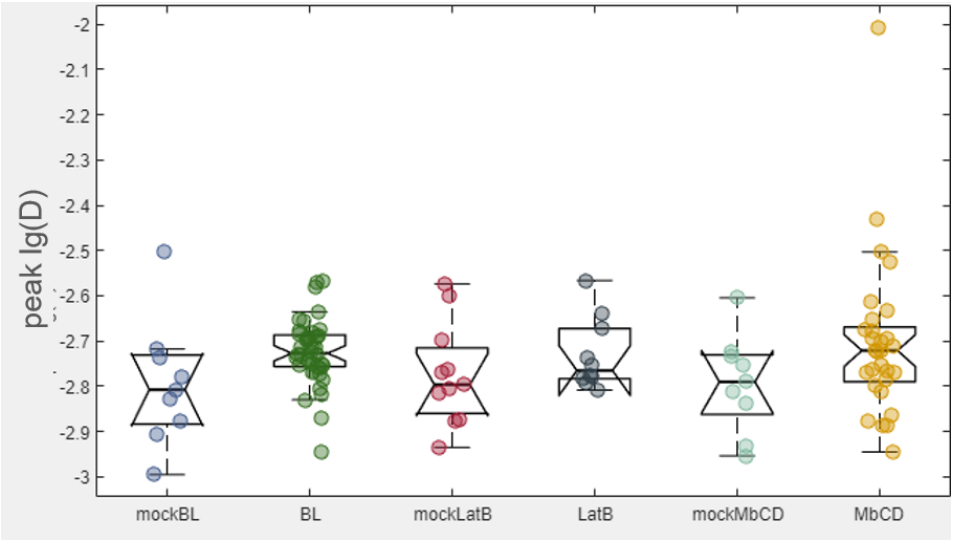

Supp. Fig. 2: Diffusion coefficient of BRI1-mEOS in VA-TIRM-PALM measurements in *N. benthamiana*

Modal log-scaled diffusion coefficient D of one biological replicate of BRI1-mEOS after 20-30 minutes with mock-treatment 0.001% DMSO, 1 nM brassinolide hormone treatment, mock-treatment for LatB with 0.01% DMSO, 0.25 µM latrunculin B (LatB), and 30-40 minutes after 10 mM mannitol as mock-treatment control for the plasmolysis possibly induced by the 10 mM methyl-β-cyclodextran (MβCD) treatment. A normal fit was applied to the log D distributions for each cell, meaning that each point represents the most abundantly observed diffusion coefficient of one cell. Measurement number was n = 30.

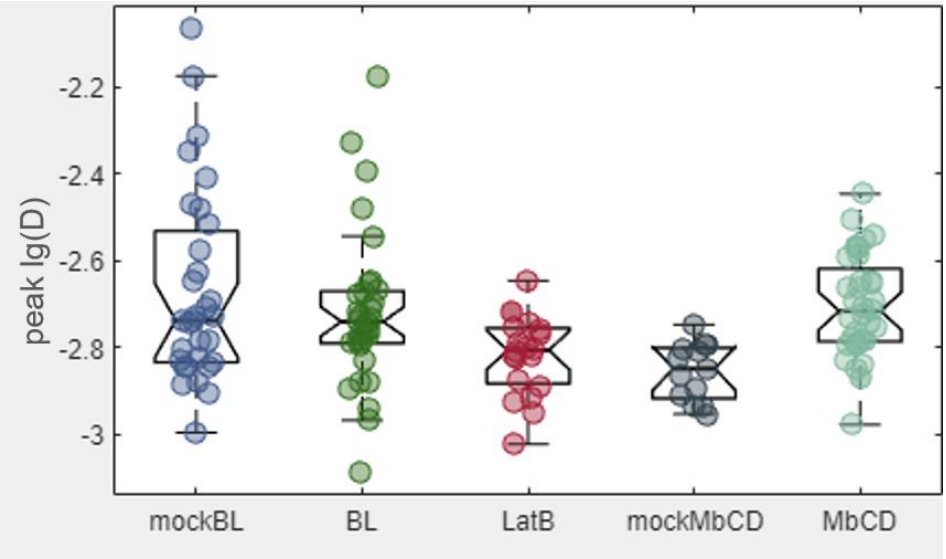

Supp. Fig. 3: Diffusion coefficient of BRI1-mEOS in VA-TIRM-sptPALM measurements in *N. benthamiana*

Modal log-scaled diffusion coefficient D of one biological replicate of BRI1-mEOS Treatment was performed as described earlier (Supp. Fig 2 or Fig.3). A normal fit was applied to the log D distributions for each cell, meaning that each point represents the most abundantly observed diffusion coefficient of one cell. Measurement number was n = 30.

Supp. Mat. 3: Combination of the three biological replicates

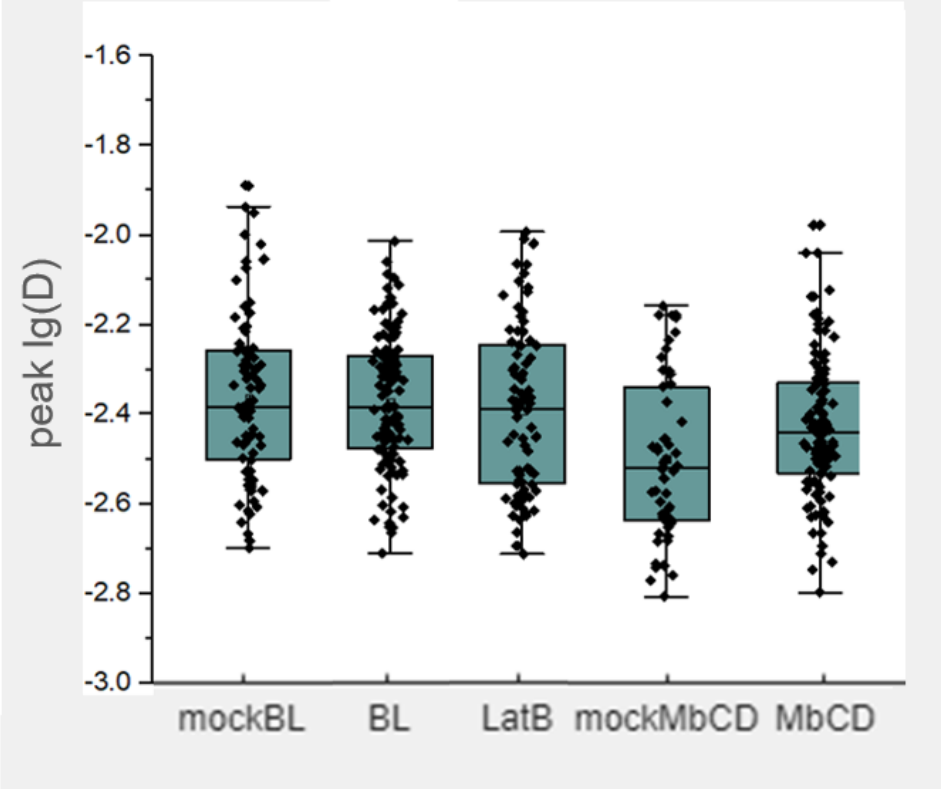

Supp. Fig. 4: Diffusion coefficient of BRI1-mEOS in VA-TIRM-PALM measurements in *N. benthamiana*

Modal log-scaled diffusion coefficient D of the three biological replicates of BRI1-mEOS. Treatment was performed as described earlier (Supp. Fig 2 or Fig.3) A normal fit was applied to the log D distributions for each cell, meaning that each point represents the most abundantly observed diffusion coefficient of one cell. The parameters listed in SI Table 1 was used for this graph.

SI Table 1: Parameters, that were used for the repeated evaluation of the three biological replicates

Fitting parameter:	Localization histogram filters:
localization algorithm: fit3Dcspline (Ries Group, Heidelberg), with sCMOS correction conversion (e-/ADU): 0.45 offset (ADU): from sCMOS correction map, usually ~100 pixel size (nm): 100 filter size (px): 1.2 cut-off (photons): 3 ROI size (px): 9	PSF size (nm): 60 < PSF size < 240 photons: 50 < photons < 800 CRLB localization precision: CRLB < 35
Track building parameters:	track fitting parameters:
acquisition time (s): 0.05 max. linking distance (nm): 200 max. gap closing (frames): 4	min. track length (data points): 5 min. adj. R^2 (indiv. MSD fits): 0.4 data points for linear fits: 4

Supp. Mat. 4: Macro in Fiji (Image J) for automated measurement of the distance between the initial point and the last point with any number of points between them

```
// This macro measures the angle and length of a line selection.
// Save this file to the plugins folder and restart
// ImageJ to create a "Measure Angle And Length" command.
// Use the Plugins>Shortcuts>Create Shortcut command
// to create a keyboard shortcut.
//
// Or define a shortcut key and add this macro to the
// StartupMacros file. For example, to use the "1" key
// as the shortcut, change the first line from
//     macro "Measure Segmented Line" {
// to
//    macro "Measure Segmented Line [1]" {

macro "Measure Segmented Line"{
  if (selectionType!=6)
     exit("Segmented line selection required");
  getSelectionCoordinates(x, y);
  N = x.length-1;
```

```
  getPixelSize(unit, width, height, depth);
  x0=x[0]*width; y0=y[0]*height; xN=x[N]*width; yN=y[N]*height;
  length = 0;
  for (i = 0; i < N; i++) {
        segment = sqrt((x[i+1]-x[i])*(x[i+1]-x[i])*width*width+(y[i+1]-y[i])*(y[i+1]-
y[i])*height*height);
        length = length + segment;
  }
  angle = getAngle(x0, y0, xN, yN);
  distance = sqrt((xN-x0)*(xN-x0)+(yN-y0)*(yN-y0));
  row = nResults();
  setResult("Length", row, length);
  setResult("End-to-End Distance", row, distance);
  setResult("Unit", row, unit);
  setResult("End-to-End Angle", row, angle);
  updateResults();
}

// Returns the angle in degrees between the specified line and the horizontal axis.
function getAngle(x1, y1, x2, y2) {
  q1=0; q2orq3=2; q4=3; //quadrant
  dx = x2-x1;
  dy = y1-y2;
  if (dx!=0)
     angle = atan(dy/dx);
  else {
     if (dy>=0)
        angle = PI/2;
     else
        angle = -PI/2;
  }
  angle = (180/PI)*angle;
  if (dx>=0 && dy>=0)
      quadrant = q1;
  else if (dx<0)
     quadrant = q2orq3;
  else
     quadrant = q4;
  if (quadrant==q2orq3)
     angle = angle+180.0;
  else if (quadrant==q4)
     angle = angle+360.0;
  return angle;
}
```

A.1.3 Three-fluorophore FRET-FLIM for trimeric protein interactions

Three-fluorophore FRET-FLIM enables the study of trimeric protein interactions and complex formation with nanoscale resolution in living plant cells

Submitted

This article describes the establishment of three-fluorophore FRET-FLIM, an *in vivo* spectroscopic method, to test trimeric protein interaction. Förster resonance energy transfer (FRET) describes the energy transfer of a donor fluorophore (D) to an acceptor fluorophore (A1) if they are in close proximity, typically below 10 nm. Three fluorophore FRET-FLIM combines two FRET pairs in such a fashion, that the acceptor (A1) of the first pair, is at the same time donor to a second acceptor (A2). Thus, energy of D can either sequentially move from D via A1 to A2 and directly between D-A1, D-A2 and A1-A2. It demonstrates, that FRET is observeable specifically for interacting proteins, but not for identically localizing, structurally similar but non-interacting proteins in two ways: By acquisition of spectra (intensity-based FRET) and measurement of the donor fluorescence lifetime (FLIM). Three-fluorophore FRET-FLIM measurements demonstrate the trimeric complex formation of RLP44, BRI1 and BAK1 and circumvents the extensive correction procedure, that is necessary for intensity-based FRET.

Three-fluorophore FRET-FLIM enables the study of trimeric protein interactions and complex formation with nanoscale resolution in living plant cells

Nina Glöckner[a], Sven zur Oven-Krockhaus[a], Frank Wackenhut[b], Moritz Burmeister, Friederike Wanke[a], Eleonore Holzwart[c], Sebastian Wolf[c] and Klaus Harter[a]

[a] Center for Plant Molecular Biology (ZMBP), Eberhard Karls University Tübingen, Germany
[b] Institut for physical and theoretical chemistry, Eberhard Karls University Tübingen, Germany
[c] Centre for Organismal Studies (COS), Ruprecht-Karls-Universität Heidelberg, Germany

Summary

Integration of signalling on the cellular level is essential for the survival of organisms. Protein-protein interaction studies provide valuable insights in these signalling events. One of the best understood signalling pathways in plants is the brassinosteroid (BR) hormone signalling pathway, which is mediated by the receptor BRASSINOSTEROID INSENSITIVE 1 (BRI1) with its co-receptor BRI1-ASSOCIATED KINASE (BAK1). Both BRI1 and BAK1 have been shown to interact with RECEPTOR LIKE PROTEIN 44 (RLP44), which was implicated in cell wall integrity sensing by modulation of BL signalling. Here we provide evidence by quantitative *in vivo* three-fluorophore FRET-FLIM measurements, that RLP44, BRI1 and BAK1 form a trimeric complex in the plasma membrane of *N.* benthamiana leaf cells in the absence of exogenous BL, with an estimated distance between them below 15 nm. The immune receptor FLAGELLIN SENSING 2 (FLS2), which is also a receptor-like kinase like BRI1, is not integrated in a similar complex with RLP44 and BAK1. Our study supports, that BRI1 and FLS2 are localized in distinct nanodomains in the PM. Furthermore, RLP44 appears to be specific for BRI1 containing microdomains, as FRET was never observed with FLS2. As the fluorescence lifetime of the donor is monitored, our method circumvents the extensive calculations necessitated by intensity-based FRET interaction assays and thus provides a feasible base for studying the sub-compartmentalization in the plasma membrane of living plant cells with a nanoscale resolution.

Graphical abstract

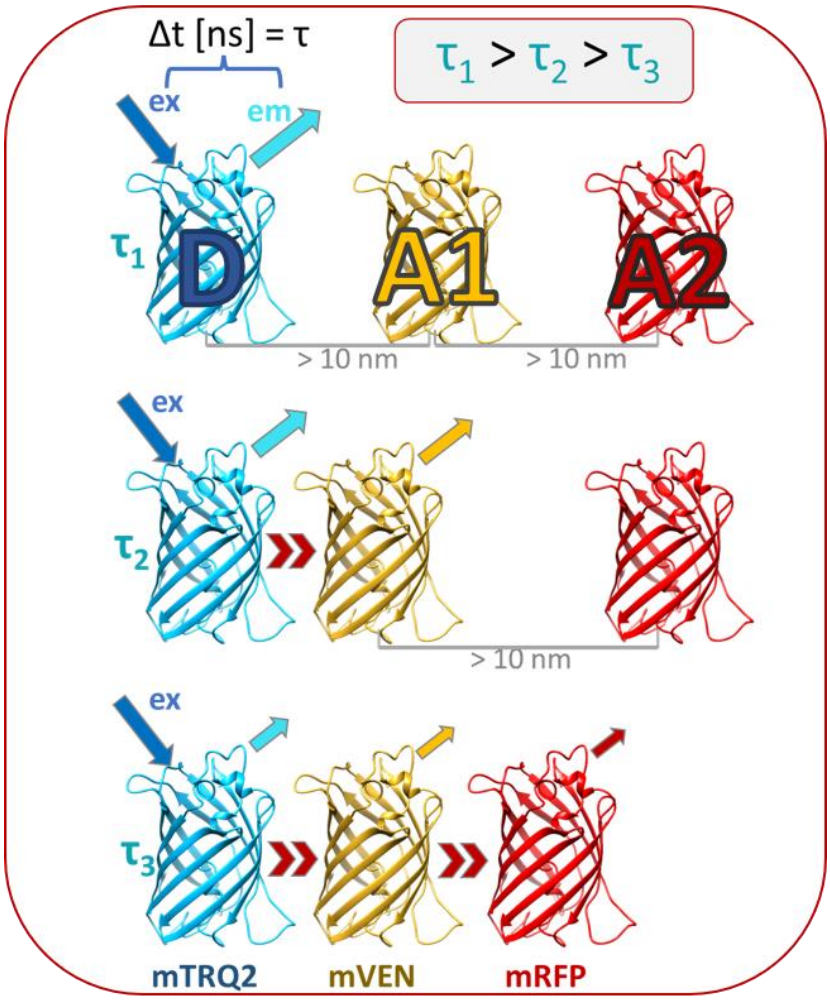

Principle of three fluorophore FRET-FLIM

Förster resonance energy transfer (FRET) describes the energy transfer of a donor fluorophore (D) to an acceptor fluorophore (A1) if they are in close proximity, typically below 10 nm. Three fluorophore FRET-FLIM combines two FRET pairs in such a fashion, that the acceptor (A1) of the first pair, is at the same time donor to a second acceptor (A2). Thus, energy of D can either sequentially move from D via A1 to A2 and directly between D-A1 and D-A2. Previous studies have quantified the fluorescence intensities to monitor the distances between the three fluorophores. Here we establish the use of fluorescence lifetime imaging microscopy (FLIM), which measures the donor fluorescence lifetime (τ) to assess complex formation of three proteins of interest in the plasma membrane. Specifically, if both A1 and A2 drain energy from D, (or sequentially from D via A1 to A2), then the fluorescence lifetime decreases.

Introduction

Biological background

Integration of different signalling cues on the cellular level is essential for the survival of any living organism, as only a fine-tuned response incorporating all available information will mediate an optimal cellular response. For example, upon infection with pathogens or mechanical damaging of the cell wall, the cellular growth response must be attenuated while the resources are e.g. redistributed to immune responses or the integrity of the cell wall. With the advent of superresolution techniques (Betzig, 1995; Klar et al., 2000; Betzig et al., 2006), the discovery of proteins specifically enriched in a detergent-resistant-fraction (Ott 2017; Malinsky et al. 2013; Lu and Fairn 2018), and the specific distribution of phosphoinositides (Mamode Cassim et al. 2019), the discussions on the spatial distribution of receptors and their co-receptors in the plasma membrane have grown (Ott 2017; Konrad and Ott 2015; Burkart and Stahl 2017; Gronnier et al. 2018). This motivated new questions, for example to which extent the receptors/co-receptors undergo diffusion and to which extent they are restricted into signalling complexes. One of the best understood pathways in plants is the brassinosteroid (BR) hormone signal transduction. It is mediated by the plasma membrane (PM) -resident leucin rich repeat receptor like kinases (LRR-RLK) BRASSINOSTEROID INSENSITIVE 1 (BRI1) and a co-receptor BRI1-ASSOCIATED KINASE (BAK1) which is also called SOMATIC EMBRYOGENESIS RECEPTOR-LIKE KINASE 3 (SERK3) (Clouse et al., 1996; Li and Chory, 1997; Friedrichsen et al., 2000; Nam and Li, 2002). BRI1 can frequently form homodimers (Wang et al., 2005b), whereas BAK1 does only rarely or does not form homodimers (Russinova et al., 2004; Bojar et al., 2014). Large populations of BRI1 and BAK1 form heterodimers in *Arabidopsis* independently of BR (Nam and Li, 2002; Wang et al., 2005b; Yun et al., 2009; Bücherl et al., 2013). Addition of the BR biosynthesis inhibitor brassinazole mildly influenced BRI1-BAK1 heterodimer detection in Co-IP (Wang et al., 2005a) and more pronouncedly reduced the phosphorylation state of BRI1 (Wang et al., 2005a). It also did not affect hetero-oligomerisation of BRI1 and SERK3 in the nanoclusters observed by SSO-FLIM (Hutten et al., 2017). In the absence of BR, the activation by trans-phosphorylation events between the cytoplasmic kinase domains is inhibited by the cytoplasmic BKI1 protein and a LRR-RK named BIR3 (Wang and Chory, 2006; Wang et al., 2014; Imkampe et al., 2017). BIR3 seems to keep BAK1 and the receptor in close proximity,

and, at the same time, acts as an inhibitor on signalling in the absence of the hormone (Imkampe et al., 2017; Großeholz et al., 2019). Binding of BR to the extracellular island domain of the receptor (Wang et al., 2001) acts as molecular glue between BRI1 and BAK1 and enhances interaction (Wang et al., 2005a; Hothorn et al., 2011; Santiago et al., 2013; Sun et al., 2013a). This leads to the auto- and trans-phosphorylation of the Ser/Thr-kinase domains, the dissociation of BKI1 from the PM (Friedrichsen et al., 2000; Oh et al., 2000; Wang et al., 2005a; Wang et al., 2008; Jaillais et al., 2011) and the partial release of BIR3 (Imkampe et al., 2017). In consequence, increased interaction, colocalization and hetero-oligomerization was observed (Wang et al., 2005a; Bücherl et al., 2013). These events at the PM then lead to (i) the activation or repression of BR-responsive genes by a signalling cascade mediated via several cytoplasmic proteins (Mora-García et al., 2004; Yin et al., 2005; Vert and Chory, 2006; Zhu et al., 2017) and (ii) the fast activation of PM-resident P-type proton pumps (AHAs) within 20 minutes (Caesar et al., 2011; Witthöft et al., 2014). The amount of BRI1 and BAK1 at the PM has been shown to correlate with signalling output. For example, the endocytosis of BRI1 is mainly required for BR signal attenuation (Russinova et al., 2004; Irani et al., 2012; Di Rubbo et al., 2013; Wen et al., 2014; Martins et al., 2015; Liang et al., 2016; Peng et al., 2018). Also, glucose modulates the PM-localizations of BRI1 and BAK1 in a concentration-dependent manner (Peng et al., 2018). Currently, it is not understood, how the endocytosis of components of a signalling module affects the distribution and dynamics of proteins in the PM. Proteins associate to homo- or heterodimers with a certain affinity and their dissociation rate is described by the dissociation constant (Kd). The determination of Kd is a highly desirable in protein biochemistry for the understanding of signalling events (Lin et al., 2018). It is defined as the state, when half of the overall acceptor sites are occupied at equilibrium (Kuemmerle H., 1991; Vuignier et al., 2010). With a higher Kd, the equilibrium for A + B ⇔ AB will shift to the left (Lin et al., 2018). With the same Kd and a decrease in relative concentration of A (compared to B), again, the dissociation rate is increased.

Also for the plant recognition of the bacteria-derived pathogen-associated molecular pattern (PAMP) flagellin, the importance of homo- and heterodimer formation is under discussion: The LRR receptor kinase FLAGELLIN SENSING 2 (FLS2) was reported to be in a preformed complex with the receptor kinase BAK1 (Sun et al., 2013b; Tang et al., 2017). Also, the formation of FLS2-FLS2 homodimers was reported (Sun et al., 2012).

However, a later study with multiparameter fluorescence imaging spectroscopy (MFIS) reports FLS2 to predominantly be monomeric and to form FLS2-BAK1 heterodimers only upon flg22 sensing (Somssich et al., 2015). Interestingly, BIR3 also interacts with FLS2 and EFR (Imkampe et al., 2017), renewing the question on their mode of regulation.

The RECEPTOR-LIKE PROTEIN 44 (RLP44) was previously described to play a role in cell wall integrity sensing via modulation of brassinosteroid-mediated responses (Wolf et al., 2014). It directly interacts with both BRI1 and BAK1 (Wolf et al., 2014; Holzwart et al., 2018) (Holzwart et al., 2019). A recent study also showed that RLP44 plays a role in Protoxylem development, which involves the phytosulfokine receptor PSKR1 (Holzwart et al., 2018). The phospho-state of the short, C-terminal tail of RLP44 determines, whether it is located at the PM or internalized into intracellular compartments (Garnelo Gomez et al., 2019). Its C-terminal phospho-site is also important for the interaction with BRI1, but not with the phytosulfokine receptor PSKR1 (Garnelo Gomez et al., 2019). This suggests, that RLP44 directly modulates BR-signalling upon input from cell wall integrity signalling cues. This would make sense mechanistically, as damage to a cell wall that grows too fast or long could directly attenuate growth. If RLP44, BRI1 and BAK1 are in a preformed complex *in vivo*, this would enable the (i) fast integration of signalling cues and (ii) the efficient internalization after signalling or upon cell wall damage signalling.

Experimental background

To test this hypothesis, we developed the three-fluorophore Förster resonance energy transfer (FRET) by fluorescence lifetime imaging microscopy (FLIM) (Three-fluorophore FRET-FLIM) in *N. benthamiana* leaves. FRET describes the energy transfer (without emission of a photon) from a donor-fluorophore (D) to an acceptor fluorophore (A) (Förster, 1948). FRET is only possible at small distances (typically below 10 nm), and strongly depends on the relative orientation of the dipole moments of A and D. If A drains energy from D, then the fluorescence intensity of D decreases. The acceptor can then emit photons itself, noticeable as an increased fluorescence intensity at a higher wavelength compared with the donor. This effect is measured in intensity-based FRET assays. FRET also influences the fluorophore's excited state life time (FLT), i.e. the time the fluorophore stays in the excited state undergoing

vibrational relaxation/internal conversion before emitting a photon. The alternative relaxation path from D to A provided by FRET consequently decreases the radiative decay rate of the donor, quantifiable as an apparently reduced FLT, which is the basis for FRET-FLIM experiments (Noomnarm and Clegg, 2009). The FLT is independent of the local concentration, the local excitation intensity and provides good time resolution (Lakowicz et al., 1992; Hum et al., 2012). However, it is sensitive to changes in chemical parameters that can quench D, like pH, polarity, temperature or the refractive index of the medium (Caesar et al., 2011; Ishikawa-Ankerhold et al., 2012; Hochreiter et al., 2015). Currently, correctly performed FLIM is considered the most accurate way to determine FRET, as it allows the examination of the physical nanoenvironment of the protein with very high accuracy and avoids typically error-prone intensity measurements (Hochreiter et al., 2015). Three-fluorophore FRET-FLIM investigates the energy transfer between fluorophores that will be referred to as D, A1 and A2 for the rest of this study. This order reflects their spectral characteristics, with D as the most blue-shifted fluorophore, A2 as the most red-shifted fluorophore and A1 as the intermediate between these spectral positions. Therefore, the following FRET paths are possible: (i) D to A1, (ii) D to A2 and (iii) A1 to A2.

The FRET efficiency (E_{FRET}) between a donor (D) and an acceptor fluorophore (A) is given by:

$$\mathrm{E_{FRET}} = \frac{1}{1+(\mathrm{R_{DA}}/\mathrm{R_0})^6} \ , \qquad (1)$$

with E_{FRET} as the FRET efficiency, R_{DA} the distance between the donor and acceptor fluorophore and R_0 the Förster distance. R_0 is defined as the distance between D and A, with 50% energy transfer efficiency. It can be calculated by:

$$R_0 = 0.2108\ [\kappa^2\ \phi_0\ n^{-4}\ \mathrm{J}\ ]^{1/6}\ . \qquad (2)$$

Here, κ^2 represents the dipole orientation factor between D and A (usually assumed to be 2/3 for freely rotating fluorophores); $\phi 0$ the quantum yield of D; n the refractive index of the medium (1.4 for buffer salts dissolved in water) and J the spectral overlap integrand (in $M^{-1}\ cm^{-1}\ nm^4$) between D fluorescence and A absorbance, given by:

$$\mathrm{J} = \int_0^\infty \mathrm{F}_D(\lambda)\ \varepsilon_\mathrm{A}(\lambda)\ \lambda^4\ \mathrm{d}\lambda \ , \qquad (3)$$

where $F_D(\lambda)$ represents the emission spectrum of D, which was normalized so that the sum of the integral equals one, at wavelength λ; $\varepsilon(\lambda)$ the absorption spectrum of A, scaled to the molar attenuation coefficient (extinction coefficient) of A (in $M^{-1}cm^{-1}$) (Wu and Brand, 1994; Hink et al., 2002; Lakowicz, 2006).

As evident in equation (2), the dipole orientation factor κ2 has a strong influence on the calculated R0 and thus the FRET efficiency:

$$\kappa^2 = cos^2\,\omega\,(1 + 3cos^2\theta)\,. \qquad (4)$$

Where ω is the angle between the electric field vector of D at the location of A and the absorption dipole orientation of A. θ is the angle between the emission dipole orientation of D and the separation vector of D-A (Lakowicz, 2006; Vogel et al., 2014).

For the standard assumption of $\kappa^2 = 2/3$ to be true, the rotational diffusion of a fluorophore has to be faster than the FLT of D (Hink et al., 2002; Müller et al., 2013). However, this may not be true for genetically-encoded fluorescent proteins used in FRET studies for several reasons: (i) the fluorophore barrel is large and has a rotation correlation time of about 20–30 ns whereas the FLT is in a range of 1–4 ns (Vogel et al., 2012); (ii) fluorophores are attached to the proteins of interest with a flexible linker (George and Heringa, 2002; Chen et al., 2013, 2013; van Rosmalen et al., 2017). In previous studies, a linker length of 15 amino acids was assumed to allow free rotation of the fluorophore, even though this may not be fully true (Szöllosi et al., 2006; Chen et al., 2013; Shrestha et al., 2015; van Rosmalen et al., 2017; Ujlaky-Nagy et al., 2018). But as no better options are available, the standard assumption is used. This introduces an error due to different fluorophore orientations. Hink et al. (2002) proposed to use $\kappa^2 = 0.476$, which is the value of the orientation factor for a rigid, randomized ensemble of D-A pairs (Steinberg, 1971). This effectively reduces the calculated Förster. It does not eliminate the possibility of specifically existent deviations due to fixed protein arrangements e.g. preventing FRET or other spatial arrangements. It is important to keep in mind, that the FRET efficiency does not correspond to fixed real distances (Müller et al., 2013): The presence of FRET always means that they are in close proximity, but how close exactly can rarely be precisely determined, especially in live-cell imaging. The distance R that is accessible through FRET-measurements is in average between $0.5\,R_0 \leq R \leq 1.5\,R_0$ (Gadella, 2009; Müller et al., 2013). Most FRET pairs have Förster distances between 4 and 7 ns (Bajar et

al., 2016; Mastop et al., 2017). As a rule of thumb, FRET is restricted to distances below 10 nm. The absence of FRET does not necessarily mean that the proteins of interest are not interacting, e.g. due to unfavourable fluorophore attachment positions. Three-fluorophore FRET-FLIM, in turn, has the same limitations.

Most three-fluorophore FRET approaches use a combination of fluorescent proteins that emit in the blue, yellow and red spectral region (Galperin et al., 2004; He et al., 2005; Seidel et al., 2010, 2010; Sun et al., 2010; Pauker et al., 2012; Fábián et al., 2013; Hoppe et al., 2013; Krause et al., 2013; Wallrabe et al., 2013; Woehler, 2013; Fried et al., 2014; Scott and Hoppe, 2015; Kastantin et al., 2017) or organic dyes as Cy-, Atto- or Alexa- chromophores (Hohng et al., 2004; Lee et al., 2010; Kastantin et al., 2017). Rarely, the intermediate fluorophore was chosen to emit in the green spectral region (Hur et al., 2016; Kuo et al., 2018). One report demonstrated the close proximity of three proteins of interest by labelling one protein with a blue-emitting fluorophore, and the other two with the same yellow-emitting fluorophore (Yu et al., 2013).

In order to establish our three-fluorophore FRET-FLIM for the first time in plants, we asked, which fluorophores can be used *in planta* and how the dynamic range between D and A2 changes with the presence of A1 between them. We then assessed, how different spatial arrangements influence the FRET efficiency and what other factors may influence our dynamic range. We then decided to first establish three-fluorophore FRET by following the example of an early, intensity-based FRET measurement by acquisition of spectra with continuous excitation of D (Haustein et al., 2003) for the three proteins RLP44, BRI1 and BAK1 respectively fused to D, A1 and A2. We showed, that a different sequence of labelling did not inhibit energy transfer to A2. Lastly, we demonstrate, that RLP44-D, BRI1-A1 and BAK1-A2 are in proximity in three-fluorophore FRET-FLIM and assess, whether changes in donor-acceptor stoichiometry may have affected the FLT.

Results

When investigating protein-protein interactions by FRET-FLIM, the physicochemical properties of the fluorophores substantially influence the quality of data. To ensure similar expression levels of at least two fusion proteins, we chose the previously published 2in1 vector system that was developed for FRET-FLIM studies (Grefen and Blatt, 2012; Hecker et al., 2015; Lin et al., 2018). Thus, the D fluorophore was mTRQ2, the A1 fluorophore was mVEN and the A2 fluorophore was mRFP. The vector for the expression of the A2-fusion proteins, was pB7RWG2-Dest by (Karimi et al., 2002), as it also contained the 35S promoter and was successfully applied in previous FRET-FLIM approaches (Boutant et al., 2010; Schoberer et al., 2013; Ladwig et al., 2015; Holzwart et al., 2018; Mohrholz et al., 2019). To facilitate the nomenclature, whenever protein X was labelled with D, protein Y was labelled with A1 and protein Z with A2, then only the sequence of the proteins will be written without mentioning the fluorophores: X-Y-Z. If for example instead Y was labelled with D and X with A1, then the writing would change to Y-X-Z.

Physicochemical properties of the fluorophores mTRQ2, mVEN and mRFP

Using mTRQ2 as D provided numerous advantages: a long, mono-exponential lifetime, relative fast maturation, low pH-sensitivity, high photostability, and the highest quantum yield of a monomeric fluorescent protein (Goedhart et al., 2012). The spectral overlap between D emission and A1 absorbance was high, yielding the largest Förster distance R_0 for comparable CFP-YFP fluorophores (Müller et al., 2013; Hecker et al., 2015; Martin et al., 2018). For values on quantum yield, extinction coefficient, molecular brightness, maturation time, photostability, pH stability and portion of monomeric state see (Supp. Mat. 1). The maturation time is an important factor for FRET efficiency (Miyawaki and Tsien, 2000; Nagai et al., 2002). In our three-fluorophore system, both A1 and A2 had faster maturation rates than D, ensuring favourable FRET conditions with a surplus of acceptors. All fluorophores were monomeric, minimizing false-positive FRET originating from aggregation.

Characterization of FRET properties

To determine the operational FRET range for the chosen fluorophores, we next calculated the corresponding Förster distances (R_0) **(1)**. For the more complex flow of energy in a three-fluorophore setting, an adjusted R_0 value was calculated for the D-A2 pair, taking into account the effect of the intermediate fluorophore A1 and different spatial arrangements **(2)**. As the planar fluorophore distribution in the PM and the donor-to-acceptor ratio influences FRET (Bunt and Wouters, 2017), we lastly assessed how these effects may influence R_0 **(3)**.

(1) To characterize the FRET properties of the chosen fluorophores, we plotted their absorption and emission spectra (Fig. 1A). The emission of D had spectral overlap with the absorption of both A1 and A2 (Fig. 1A, *light* and *dark grey areas*, respectively), while the emission of A1 significantly overlapped with the absorption of A2 (Fig. 1A, *brown area*). Therefore, energy transfer was possible between D-A1, A1-A2 and D-A2. We calculated the R_0 with $n = 1.4$ and $k^2 = 2/3$ as described by (Hink et al., 2002). With the known R_0, the FRET-efficiency (E_{FRET}) in dependence of the distance (R) for each donor-acceptor pair was plotted (Fig. 1B). Calculation of R_0 for the D-A1 (*blue*), A1-A2 (*orange*) and D-A2 (*red*) pairs yielded values of 5.7 nm, 5.1 nm and 4.6 nm (Fig. 1B, *grey lines* and Table 1). Therefore, highest E_{FRET} was obtained between D and A1, and lowest between D and A2 (Fig. 1B). Furthermore, in contrast to the fluorescent dye-based study of (Haustein et al. 2003), FRET events were not limited to sequential energy transfer from D via A1 to A2 (Fig. 1C *top*). With our genetically encoded fluorophores, both sequential (D-A1-A2) and direct FRET (D-A2) was possible (Fig. 1C *bottom*). A similar study in animal COS-1 cells, using CFP, YFP and mRFP calculated a proportion of 45% direct FRET from CFP to mRFP and the remaining 55% as the result of the sequential FRET, showing for the first time that both FRET modes occurred simultaneously (Galperin et al., 2004).

(2) For large distances between D and A2, however, no direct FRET is possible. At large distances, the introduction of an intermediate acceptor A1 should increase the dynamic range between them. To estimate this long-range effect, we calculated how the presence of our intermediate acceptor changed the effective R_0 between D and A2 according to (Haustein et al., 2003). The Förster distance R_0 is not defined for three-way interactions. But by calculating an adjusted R_0, this was taken as an

estimate on the effective dynamic range. For our D-A2 pair, this resulted in an increase from 4.6 nm to 9.2 nm (Fig. 1D *red* vs. *black* and Table 1), which was in accordance with values previously reported (Haustein et al., 2003). They used a DNA-helix to fix the distances between fluorophores to calculate the FRET increase for A1 between D and A2. This setting, however, seemed artificial for our dynamic *in vivo* system. Therefore, the average E_{FRET} for all possible positions of A1 between the D and A2 fluorophore with a step size of Δ 1 nm was calculated for each distance between D-A2 (Supp. Material 2). This more realistic representation of a system with possibly changing distances resulted in an increase to $R_0 = 6.8$ nm for D-A2 (Fig. 1D *grey* and Table 1). Hence, long-range interactions can be studied with three-fluorophore FRET.

(3) The third factor, influencing the likelihood of FRET is the dipole orientation κ^2. For membrane-localized proteins, the distribution of k^2 is drastically changed (Bunt and Wouters, 2017). Also, the faster maturation time of both A1 and A2 than D causes a surplus of acceptors which increases the likelihood of FRET (‘Antenna effect’) (Bunt and Wouters, 2017). We were interested to what extent the planar distribution and a favourable donor-to-acceptor ratio can influence the average FRET efficiency. As a measure for this, we again calculated an adjusted R_0. Bunt and Wouters (2017) proposed a correction for E_{FRET} in planar systems for different ratios between donor and acceptor fluorophores: We calculated an adjusted R_0 for the highest provided donor-to-acceptor ratio, which was a ratio of 1:5 and values were listed in Table 1. For our three-fluorophore system with a variable position of A1, this additional correction yielded an adjusted R_0 of 11.7 nm for D-A2 (Table 1). A projection of the FRET efficiency with variable position of A1 to a stoichiometry of 1:5 showed, that 10% FRET would occur at distances below 15 nm (SI Fig. 1).

In summary, depending on the donor-to-acceptor ratios, long-range energy transfer between D and A2 may occur already below 15 nm.

Table 1: Förster distances (R_0) in nm for the FRET-pairs D-A1, A1-A2 and D-A2 (bold) and adjusted R_0, with mTRQ2 as (D), mVEN as (A1) and mRFP (A2). Fluorophore in italic brackets *(A1)* assumes presence of A1 between D and A2. For a stochiometry of 1:5 of plasma membrane-resident proteins, a factor of 1.725 was used to calculate the adjusted R_0 (Bunt and Wouters, 2017).

	D » A1	A1 » A2	D » A2	D » *(A1)* » A2 *middle*	D » *(A1)* » A2* *variable*
R_0 [nm]	**5.67**	**5.14**	**4.63**	9.2	6.8
R_0 [nm] 1:5, planar	9.7	8.9	8.0	15.9	11.7

To assess, how a dynamic range of 15 nm relates to the sizes of our proteins, we combined the cytoplasmic domains of RLP44, BRI1 and BAK1 with the respectively attached fluorophores and the adjusted R_0 between D-A2 in scale in a graph (Fig. 1E). The size of each intracellular domain ($Protein_{Cyto}$) was calculated from the distance of Δ 5.4 Å from one turn to the next in the secondary protein structure of helical alpha-barrels. The structures of the fluorophore-barrels, $BRI1_{Cyto}$ and $BAK1_{Cyto}$ were resolved previously (Rekas et al., 2002; Yan et al., 2012; Bojar et al., 2014) and a solvent-accessible surface representation was chosen. The orientations of the two kinase domains of BRI1 (*yellow*) and BAK1 (*brown*) were depicted according to the highest probability in molecular docking analyses (Großeholz et al., 2019). The structure of $RLP44_{Cyto}$ (*blue*) and the Gateway®-linkers (*grey*) was not resolved and thus predicted with PEP-FOLD3. For clarity, all structure-predicted proteins were depicted as Cartoon. On average, the stoichiometry-adjusted R_0 for plasma membrane-resident proteins were 8-9 nm (Table 1) and can thus span the distance of two kinase domains, which possess diameters of ~4.5 nm. The adjusted R_0 for our three-fluorophore FRET-FLIM of 15 nm reached from RLP44 well beyond the linear arrangement of BRI1 and BAK1 (Fig. 1E).

In summary, direct FRET is possible for each donor-acceptor pair. For our three-fluorophore FRET, the calculated 15 nm may well reach beyond one assumed signalling module of RLP44, BRI1 and BAK1. Depending on the density and the

arrangement of the components in the PM, three-fluorophore FRET may occur even between different signalling modules.

Determination of background in spectra with simulations

In the last years, many studies have assessed three-fluorophore FRET with intensity-based methods in animal cells (Galperin et al., 2004; Hohng et al., 2004; He et al., 2005; Lee et al., 2007; Shyu et al., 2008; Seidel et al., 2010; Pauker et al., 2012; Hoppe et al., 2013; Wallrabe et al., 2013; Woehler, 2013; Fried et al., 2014; Scott and Hoppe, 2015; Hur et al., 2016; Cotnoir-White et al., 2018), specifically by acquisition of spectra (Haustein et al., 2003; Galperin et al., 2004; He et al., 2005; Sun et al., 2010; Hoppe et al., 2013; Woehler, 2013). Therefore, we decided to first assess the ternary complex formation for our proteins with such an established method.

To assess the influence of FRET compared to different expression levels on the detectable emission spectra, calculations with Matlab™ were performed (Fig. 2) (see Supp. Material 3A), assuming equidistant fluorophores. For a 1:1:1 ratio of fluorophores with distances > 10 nm (no FRET) and an excitation wavelength of 458 nm, a peak at 520 nm due to cross excitation appears (Fig. 2A *top*). With distances below 10 nm, FRET can occur and the energy transfer from D to A1 and A2 was visible in the spectra, as the D peak decreased and the A1 and A2 peaks increased (Fig. 2A).

In the absence of FRET, the bleed-through and cross excitation strongly depended on the donor-to-acceptor ratio of the fluorophores (Fig. 2B). For changes in the Matlab™ script, see (Supp. Material 3B). Importantly, bleed-through and cross excitation had a larger influence on the mVEN signal than effects due to FRET: A donor-to-acceptor ratio of 1:3 resulted in a similar peak intensity at 520 nm in the spectra as a Förster distance of 6 nm (Fig. 2A,B).

This means, that for intensity-based FRET measurements, careful calibrations of the fluorescence intensity for each fluorophore-tagged protein are essential (Galperin et al., 2004; Hohng et al., 2004; He et al., 2005; Lee et al., 2007; Shyu et al., 2008; Seidel et al., 2010; Pauker et al., 2012; Hoppe et al., 2013; Wallrabe et al., 2013; Woehler, 2013; Fried et al., 2014; Scott and Hoppe, 2015; Hur et al., 2016; Cotnoir-White et al., 2018). It is a draw-back of good FRET properties, that both the spectral bleed through

and cross-excitation are high and corrections for these factors have to be performed. Therefore, we determined the bleed through and cross-excitation in the absorption and emission spectra and quantified them in confocal images (see Supp. Material 4). All following experiments were performed with identical excitation and emission settings.

Determination of background in the acquired spectra due to cross-excitation and bleed-through

It was shown previously, that BRI1–BAK1, RLP44–BRI1 and RLP44–BAK1 form heterodimers (Wolf et al., 2014; Holzwart et al., 2018). As control, FLS2 was used as it is a plasma membrane-localized LRR-RLK like BRI1, but that did not interact with RLP44 or BRI1 previously (Bücherl et al., 2017; Garnelo Gomez et al., 2019). The spectra were acquired in transiently transformed *N. benthamiana* leaves. All fusion-proteins were expressed at the plasma membrane after two days (see SI Fig. 2).

The excitation wavelength for all shown spectra was at 458 nm. As spectral bleed through and cross-excitation were important factors, in a first step the background in the spectra due to cross-excitation was determined (Fig 3A). Expression of RLP44-D resulted in a peak at 480 nm in the spectrum (Fig. 3A *blue*). The expression of FLS1-A1 yielded a peak at 520 nm due to cross-excitation (*yellow arrow*) and BAK1-A2 did not lead to a visible peak (Fig. 3A *red*).

As the expression level is an important factor for intensity-based FRET, the fluorescence intensity was taken as an estimation of the expression level. Thus, the respective average raw intensity (as arbitrary unit) at the plasma membrane (PM) was quantified for each channel. In a second step, the background due to cross-excitation and bleed through was determined. Thus, the fluorescence intensities for simultaneous excitation with 458 nm, 514 nm and 651 nm is shown (Fig. 1B). It will always be discussed in a separate section.

The quantification of the fluorescence intensity of RLP44-D showed, that the average raw intensity of 120 at the PM (Fig. 3B *blue*) also caused a peak-intensity of 120 in the spectrum (Fig. 3A). A relative high expression levels of FLS2-A1 with an average raw intensity of 200 (Fig. 3B *yellow*) caused a much smaller background-signal of 8 arbitrary units in the spectrum (Fig. 3A *yellow*). The expression of BAK1-A2 with an average raw intensity of 110 (Fig. 3B *red*) did not cause a distinct peak in the spectrum (Fig. 3A *red*). Different expression level lead to the same shape of spectra, only with variation in the peak-value (see SI Fig. 3).

Protein-protein interaction study by spectra acquisition

(1) FRET from D to A1

First, we assessed FRET from D to A1. Since the spectra simulations showed, that the expression levels have a larger influence on the shape of the spectra than FRET, a correction for the expression levels were performed. We compared the spectra of interacting RLP44–BRI1 samples with that of non-interacting RLP44–FLS2 samples with the same donor-to-acceptor ratio. To this end, each recorded spectrum at the plasma membrane of cells was interpolated (see Supp. Material 5) and subjected to spectral unmixing in Matlab^{TM} to calculate the proportion of D, A1 and A2 in it (see Supp. Material 6). Then, the spectral unmixing information was combined with the respective estimates on the expression level. For all consecutive quantifications of the fluorescence intensities, each channel was imaged with sequential excitation right before acquisition of the spectra (excitation with only 458 nm, then only 514 nm, lastly only 561 nm).

The average of the spectra with the same expression levels of interacting RLP44–BRI1 vs. non-interacting RLP44–FLS2 samples was calculated (Fig. 3C). In the spectra with the same donor-to-acceptor ratio, the average peak value at 520 nm (*arrow*) was higher for the interacting proteins (RLP44–BRI1, Fig. 3C *blue*) than for non-interacting proteins (RLP44–FLS2, Fig. 3C *grey*).
The combination of spectral unmixing and identical donor-to-acceptor ratios revealed, that the A1 proportion in the spectra of interacting samples differed significantly ($p<0.05$) from non-interacting samples (Fig. 3D *stars*). This was true for both donor-to-acceptor ratios of approximately 1:10 (Fig. 3D *left two samples with ratio: 0.12*) and

of 1:4 (Fig. 1D *right two samples with ratio: 0.26*). In summary, FRET from RLP44-D to BRI1-A1 was demonstrated with the acquisition of spectra. But only, after careful comparison to non-FRET signal.

(2) FRET from D to A2

We then tested, whether the energy transfer from D to A2 was visible in the spectra. For co-expression of RLP44-D with FLS2-A2 (RLP44– –FLS2), no significant elevation at 610 nm was detected (*black*) compared to the absence of a red fluorophore (*blue*) (Fig. 3E). Co-expression of interacting BAK1-A2 (*brown*) or BRI1-A2 (*red*) lead to significant elevations of the intensity at 610 nm compared to control samples (Fig. 3E *arrow*).

The ratio in the fluorescence intensity between D and A2 was 1:1 for RLP44– –FLS2 (Fig. 3D *black)*. However, the fluorescence intensity ratio revealed, that RLP44– –BRI1 (*red*) and RLP44– –BAK1 (brown) had higher expression levels of the A2 fusion, with respective ratios of 1:2 (Fig 3F *brown*) and 1:5 (Fig. 3F *red*). The difference in expression level may have had an influence on the detectable A2 signal.

The energy from mTRQ2 was transmitted via mVEN to mRFP

If RLP44, BRI1 and BAK1 form a complex, then the average distance between RLP44–BAK1 may differ from that of RLP44–BRI1–BAK1. For example, BRI1 may be located between RLP44 and BAK1, increasing the distance between them. It might also decrease the total number of RLP44–BAK1 interactions as new pairs (RLP44–BRI1 or BAK1-BRI1) are formed (Galperin et al., 2004). To test for this possibility, we labelled BRI1 with the non-fluorescent HA-tag ($BRI1^{HA}$) (SI Fig. 4). Again, for the intensity-based FRET measurements, effects due to different donor-to-acceptor ratios have to be excluded and thus the expression levels by quantification of the fluorescence intensity are discussed in a separate section.

Non-fluorescent BRI1 disrupted the FRET from RLP44-D to BAK1-A2

Co-expression of HA-tagged BRI1 did not change the shape of the RLP44-D spectrum (compare Fig. 4A *blue* and Fig. 3A *blue*). As before, co-expression of BAK1-A2 yielded a small intensity elevation around 610 nm (Fig. 4A *red*). This elevation was not present anymore when $BRI1^{HA}$ was co-expressed (Fig. 4A *black*), In contrast to this, the co-

expression of the non-interacting RLP44–FLS2–BRI1 did not lead to a disappearance of the intensity peak at 610 nm (SI Fig. 5 *black*). Thus, the addition of HA-tagged BRI1 increased the average distance between RLP44 and BAK1 or lead to conformational changes, that influences the relative dipole orientation (Galperin et al., 2004; Bunt and Wouters, 2017) or lead to changes in expression level.

However, the expression of different protein combinations did not change the donor-to-acceptor ratio: The ratio between RLP44 and BAK1 was 1:1.1 for RLP44––BAK1 (*bright red*), 1:1.2 for RLP44–(BRI1^{HA})–BAK1 (*black*) (Fig. 4B). This means, that indeed the distance or the dipole orientation between RLP44 and BAK1 changed upon BRI1^{HA} co-expression.

Using instead BRI1-A1, restored the FRET from RLP44-D to BAK1-A2

For comparison, the spectra of RLP44––BAK1 and RLP44–(BRI1^{HA})–BAK1 from Fig. 4A were included. When using the fluorophore-tagged BRI1-A1 instead, the peak in intensity at 610 nm was restored (Fig. 5A *dark red*). We showed earlier, that the presence of an intermediate fluorophore increases the Förster distance between D and A2 (Fig. 1D). This increase in in the dynamic FRET range between D-A2 with an intermediate acceptor likely restored the A2 peak (Haustein et al., 2003; Galperin et al., 2004), assuming the donor-to-acceptor ratio stayed the same.
At the same time, an energy transfer from A1 to A2 was visible for the interacting samples: the peak at 520 nm (*yellow arrow*) strongly decreased for RLP44–BRI1–BAK1 (*dark red*) in comparison to RLP44–BRI1 (*yellow*) expression (Fig. 4C). An influence of cross-excitation of A1 and subsequent FRET directly from A2 could not be fully excluded. But as no energy transfer from A1 to A2 was observed for RLP44–FLS2–FLS2 with high A2 fluorescence intensity levels (ratio of ~1:10 for D:A1) this effect was likely of minor importance, (see SI Fig. 5 *brown*). In summary, the intensity peak at 610 nm that was disrupted by BRI1^{HA} was restored by BRI1-A1 and the intensity peak at 520 nm was reduced, if BAK1-A2 was present. This energy transfer from D to A1 (*yellow arrow*) to A2 (*red arrow*) fits the expectations of three-fluorophore FRET-FLIM, unless it was due to changes in the expression level.

Also here, the expression of different protein combinations did not change the donor-to-acceptor ratios: For RLP44–BRI1–BAK1, the RLP44:BAK1 ratio was 1:1.2 (Fig. 4D

dark red). The ratio between RLP44 and BRI1 stayed constant with ratios of 1:2 for RLP44–BRI1 (*yellow*) and 1:1.4 for RLP44–BRI1–BAK (Fig. 4B *red*). This supported the interpretation, that the energy from A1 was transferred to A2 specifically for interacting proteins.

In summary, the unaltered ratios suggest, that the addition of BRI^{HA} increased the average distance or changed the dipole orientation between RLP44 and BAK1, thus disrupting the energy transfer from D to A2 (Galperin et al., 2004). Addition of BRI1-A1 as interacting intermediate, restored the energy transfer from RLP44-D to BAK1-A2, meaning that RLP44, BRI1 and BAK1 were in close spatial proximity, enabling FRET between them.

Determination of complex formation by spectra acquisition

We next asked, whether the energy transfer from D via A1 to A2 was also possible, if the fluorophores were swapped. We therefore tagged BAK1 with A1 and BRI1 with A2 (RLP44–BAK1–BRI1). As controls, the spectra of RLP44— (*blue*), RLP44–BRI1–FLS2 (*red*) and RLP44-BAK1–FLS2 (*brown*) were measured (Fig. 5A). For both combinations with FLS2-A2, a large peak in intensity at 520 nm (orange arrow) and no peak at 610 nm (red arrow) was detectable, indicating that energy from D was exclusively transferred to A1, but not to A2. The 520 nm intensity peak includes signal due to cross-excitation.

The D:A1 ratios were 1:3 for RLP44-BRI1-FLS2 and 1:4 for RLP44-BAK1-FLS2 (Fig. 5B). This increase in A1 for RLP44-BAK1-FLS2 compared to RLP44-BRI1-FLS2 did not increase the peak value in the spectrum at 520 nm. The D:A2 ratio was 1:3 for RLP44–BRI1–FLS2 and 1:4 for RLP44–BAK1–FLS2. Thus, the absence of a peak at 610 nm was not due to weak expression, as an energy transfer to A2 was previously detected already for a ratio of 1:1 (e.g. Fig. 4C with RLP44–BRI1–BAK1, *dark red*).

For interacting proteins, namely RLP44–BRI1-BAK1 (*red*) and RLP44–BAK1–BRI1 (*brown*) (Fig. 5C) two effects were visible: the peak value at 520 nm decreased (*yellow arrow*) and a peak at 610 nm appeared (*red arrow*) (Fig. 5C) compared to the

FLS2-A2 samples (Fig. 5A). This suggests, that the energy from A1 was specifically transferred to A2, provided that the protein ratios were unaltered. The peak at 520 nm was higher for RLP44–BAK1–BRI1 (brown) than for RLP44–BRI1-BAK1 (*red*) (Fig. 5C).

The D:A1 ratio was 1:2 for RLP44–BRI1–BAK1 and 1:3 for RLP44–BAK1–BRI1 (Fig. 5D). This increase in A1 expression for RLP44–BRI1–BAK1 may be responsible for the observed higher peak at 520 nm. The D:A1 ratio of the interacting protein sequences was slightly lower (Fig. 4D) than that for the combinations with FLS-A2 (Fig. 4B). Consequently, a part of the decrease at 520 nm can be due to decreased expression. But as the D:A1 ratio in RLP44–BAK1–BRI1 was the same as in RLP44-BRI1-FLS2, similar characteristics was expected, when there is no FRET. This was clearly not the case, indicating FRET between BAK1-A1 and BRI1-A2.
The D:A2 ratio was 1:2 for RLP44–BRI1–BAK1 and 1:3 for RLP44–BAK1–BRI1. Higher A2 expression for RLP44–BAK1–BRI1 did not lead to a higher peak intensity at 610 nm. Also, higher expression levels of FLS2-A2 (with D:A2 ratios of 1:3 and 1:4) did previously not lead to a detectible peak at 610 nm (Fig. 5A), indicating that

In summary, FRET from D via A1 to A2 was shown specifically for RLP44–BRI1–BAK1 and RLP44–BAK1–BRI1. As we could establish three-fluorophore FRET, we now tested, whether the complex formation could also be shown with fluorescence lifetime imaging (FLIM), which can be carried out more accurately.

RLP44, BRI1 and BAK1 form a multiprotein complex *in vivo*

When studying three-way interactions with intensity-based methods, the ratio between donor and acceptor molecules is of major importance, as spectral bleed-through and cross excitation mask FRET. In contrast, when monitoring the fluorescence lifetime FLT of D (τ) with FLIM, no such careful calibrations are necessary and hence circumvents the extensive correction analysis. We therefore tested, whether complex formation of RLP44, BRI1 and BAK1 could be shown by monitoring the FLT of the D fluorophore (Fig 5).

The average FLT of RLP44-D was 4 ns (Fig 5A), which was in accordance with previously published studies (Goedhart et al., 2012; Hecker et al., 2015). Co-

expression of BRI1 coupled to either A1 or A2 caused a significant decrease in τ, meaning that FRET was possible from D to both A1 and A2. As the Förster distance of the D-A1 fluorophore pair was larger than that of D-A2, this could account for the slightly lower τ for RLP44–BRI1 compared to RLP44– –BRI1.

Co-expression of FLS2 with RLP44-D did not cause a significant decrease in τ, irrespective of the acceptor fluorophore (Fig 5A,B). The expression of FLS2-A2 with the RLP44–BRI1 pair did not further change the τ significantly. In contrast, the expression of BAK1-A2 with the RLP44–BRI1 pair lead to a significant decrease in τ compared to both RLP44–BRI1 and RLP44–BRI1–FLS2. If only RLP44-BRI1 heterodimers and RLP44-BAK1 heterodimers were present, then the fluorescence lifetime would be expected to be the average between them. But as the τ further decreased, both BRI1 and BAK1 must have drained energy from RLP44-D at the same time. This clearly indicates, that RLP44, BRI1 and BAK1 formed a trimeric complex *in vivo*.

In summary, in comparison to the intensity-based FRET, we could fast and conveniently show the specific complex formation of RLP44, BRI1 and BAK1 with three-fluorophore FRET-FLIM.

Only FLS2-mRFP was less abundant compared to BAK1-mRFP when co-expressed with RLP44 and BRI1

It was shown previously, that FRET-FLIM is independent of the donor concentration (Becker, 2012). However, the relative amount of acceptor in comparison to the donor (the donor-to-acceptor ratio) may influence the measured FLT (Sun et al., 2010; Bunt and Wouters, 2017). Therefore, we tested, whether different fluorescent protein ratios were an additional factor, that influenced the measured lifetimes of Fig. 6A.

We thus quantified, whether the ratios in fluorescence intensity for each FRET-pair changed for different co-expression in *N. benthamiana* leaves (see Supplemental Material 7, SI Fig. 6B). Only the donor-to-acceptor ratio D:A2 between RLP44–BRI1–FLS2 and RLP44–BRI1–BAK1 was changed significantly, meaning that FLS2-A2 was significantly less abundant than BAK1-A2 when co-expressed with RLP44-BRI1 (SI Fig. 6B). Indeed, the fluorescence lifetime was slightly higher for RLP44–BRI1–FLS2 compared to RLP44–BRI1.

However, as only one donor-to-acceptor ratio was changed significantly, differences in expression strength were not a major factor that influenced the fluorescence lifetimes. Only if the donor-to-acceptor ratio would be changed at the same time, the additional decrease in FLT for RLP44–BRI1–BAK1 compared to RLP44–BRI1 and RLP44– –BAK1 could be explained with only heterodimers. But as ratios were not significantly changed, trimeric interaction must have been present. Furthermore, our data indicate, that if the fusion proteins are expressed from one plasmid, no further measurement of the donor-to-acceptor ratios are necessary and thus simplify the work flow. In summary, we could establish an interaction test for three proteins *in vivo*.

Discussion

Many studies in the animal field have independently established a set of fluorophores for studying the complex formation of three proteins within the cellular context (localization) and in time (Scott and Hoppe, 2015). Here we provide three-fluorophore-FRET and FLIM measurements with the best and widely tested donor fluorophore mTRQ2, mVenus as intermediate and mRFP as second acceptor in plant cells, namely the epidermal leaf cells of *N. benthamiana*. Lin et al 2018 found, that with the expression of a donor-acceptor pair from one vector, a linear relationship between FRET efficiency and Kd existed, and that different orientation factors had only a minor influence compared to 10-fold differences in affinity. Importantly they concluded, that if [A] and [B] are at the same concentration, the equilibrium, A + B ⇔ AB, will be driven toward an increase in [AB] when the affinity increases. This means, that as long as A and B have the same concentration, the actual molarity of both (nM, µM, …) is of minor importance. This is only true until a certain concentration, at which a correction factor f has to be included, as additional density-dependent nonspecific aggregation effects happen (Oravcova´ et al., 1996; Mallik et al., 2008; Vuignier et al., 2010). Relative fluorescent quantifications are thus a means to compare two samples with each other, as both the correction factor and the molarity are in the same order of magnitude. Interaction studies in *N benthamiana* leaves may provide an important first glimpse on native cellular dynamics.

A comparative study on viable fluorophores has found that mTRQ2, YPet and mCherry is the most promising combination for three-fluorophore FRET (Scott and Hoppe, 2015). Even though mVenus is less bright than e.g. YPet, it importantly is a monomer (Bajar et al., 2016). We reasoned, that a reduced Förster distance is of less concern than the tendency to form homo-oligomer aggregates at high concentrations or when confined, which is the case for plasma membrane-resident proteins (Miyawaki, 2011; Bajar et al., 2016). Surprisingly, high brightness fluorophores like Ruby2 or TagRFPs were outperformed by mCherry, that overcompensates its low brightness with its fast maturation rate (Hoppe et al., 2013).Even though mRFP is a very old fluorophore, the maturation time is very short, which makes it an appropriate A2 fluorophore. Future studies may consider using mCherry instead of mRFP. Especially, since mCherry has been shown to only weakly oligomerize even under harsh oxidizing environments such as in the lumen of the ER and Golgi stacks (Costantini et al., 2015). The usage of a

blue, yellow and red fluorophore was the most abundant application for triple-FRET studies, as it provides a good compromise between large Förster distances due to high spectral overlap, and enough differences in excitation and emission spectra to detect each one separately. Until now, no study circumvented the direct FRET between D-A2 for genetically encoded fluorophores (He et al., 2005; Sun et al., 2010; Pauker et al., 2012; Hoppe et al., 2013; Wallrabe et al., 2013; Kuo et al., 2018). Possibly, because corrections for cross-talk would be still necessary and because it provides an additional layer of information on how the two fluorophores are located relative to each other. The use of dyes would have provided even better detection boundaries with excellent physicochemical properties. For plant cells, however, this may prove very challenging, as the cell wall likely interferes with *in vivo* labelling. Already in animal cells, which are rendered permeable as a matter of routine, different labelling efficiencies have shown to be problematic for three-fluorophore-FRET as the correction for directly excited acceptor fluorescence becomes difficult (Fazekas et al., 2008; Becker, 2012; Fábián et al., 2013).

Yet only one study has tried to estimate, what distances between the fluorophores represent the dynamic range of their set. We think, that a realistic estimation of the variability/boundaries of a system (due to secondary factors) is important for the interpretation of data. For example, the general rule of thumb for FRET to happen, stating “below 10 nm” may be unprecise or incorrect. In this study, we have calculated adapted Förster distances to take several factors into account: first, the spatial arrangement of the fluorophores, which influences the amount of energy moving to the A2. If the intermediate fluorophore A1 is located between D and A2, the energy moving to A1 can be transferred to A2, thus increasing the range. Our calculation on long-distance FRET with an intermediate A1 did not account for the additionally present direct FRET between D-A2. Direct D-A2 FRET reduces the energy that can move along D-A1-A2, as two acceptors drain energy from D. We assumed, that the distance between D and A2 was too large for direct FRET, as we were interested in the FRET efficiency at larger distances. Consequently, our calculations on the D-A2 FRET efficiency are underestimations for small D-A2 distances: at small distances, energy can move directly between D-A2 and use the relay system D-A1-A2, giving more freedom on spatial arrangements. When assuming D is located in the middle, the likelihood of energy moving via A1 to A2 decreases, as the distance between A1 and

A2 increases. These spatial arrangements may be considered with intensity-based FRET measurements. For FLIM-based FRET measurements, the differences between spatial conformations may not be visible, as no information is available on where the energy is transferred to. In general, such interpretations are extremely difficult, as the average of many arrangements is taken and the unpredictable influence of the dipole orientation. In exchange, FLIM-based measurements have the advantage of a higher sensitivity, as the signal-to-noise ratio in intensity-based FRET measurements is worse after unmixing and sensitized emission calculations. Secondly, the planar distribution of plasma membrane-resident proteins increases the likelihood of FRET to happen, as the standard assumption of $\kappa^2 = 2/3$ is modified. Lastly, the ratio in donor-to-acceptor fluorophore ratios may influence FRET, making energy transfer more likely with a surplus of acceptors. Another study estimated the influence to be even more severe, so that with multiple acceptors (n) proximal to a single donor fluorophore, the operational R_0 becomes n-times R_0 (Jares-Erijman and Jovin, 2003; Müller et al., 2013). All these factors mask the possibly linear relationship between FRET and the dissociation constant. Therefore, no conclusions on affinity can be drawn, only limited information on the distance between the three fluorophores.

If the time-scale of an interaction is important, three-fluorophore FRET or three-fluorophore FRET-FLIM is preferable to the combination of BIFC with FRET as successfully employed by (Shyu et al., 2008; Kwaaitaal et al., 2010) or the split of mVenus into three parts as performed by (Chen et al., 2018), as the protein-protein interaction is locked upon complementation of the fluorophore (Cabantous et al., 2005; Magliery et al., 2005). By monitoring the FLT of the donor, conclusions on the amount of donors in donor-acceptor complexes and the amount of free donors are possible (Mustafa et al., 2013). However, it is not possible to monitor where the excitation energy is transferred to, or how many acceptors are involved in FRET. Without a doubt, monitoring interactions by intensity-based FRET provides more information on energy flow, but has a higher level of uncertainty, as protein expression levels, spectral bleed-through and cross-excitation with non-interacting, but identical localizing proteins have to be considered.

In summary, for our fluorophores mTRQ2, mVEN and mRFP, the adjusted Förster distance can span up to ~12 nm, with 10% FRET occurring below distances of 15 nm. When imagining how receptors with their signalling components are dispersed in the

plasma membrane, not only monomers, dimers and trimers have to be considered. Also, intermediate forms are possible, where the A1 of another signalling complex can function as acceptor, relaying the energy to an even further located A2 of a completely different signalling complex (Fig. 7A). Consequently, triple-FRET in plasma membrane applications can possibly span to other, not that far distanced signalling components.

In this study, we provided evidence that RLP44 is located in close proximity to both the brassinosteroid-sensing receptor BRI1 and its co-factor BAK1 (below 15 nm) by applying both FRET and FRET-FLIM measurements. Furthermore, we observed an additional decrease in the FLT upon addition of BAK1-A2 to the RLP44-D / BRI1-A1 pair. Also, in FRET measurements the energy transfer from D via A1 to A2 was detectable specifically for RLP44–BRI1–BAK1 and RLP44–BAK1–BRI1. This is only possible, if either trimers (Fig. 7B) or intermediate spatial arrangements (Fig. 7A) are present. If only heterodimers are formed, then the measured FLT of RLP44–BRI–BAK1 would be the average of RLP44–BRI1 and RLP44– –BAK1. (Or the FLT would increase, as D-A1 and D-A2 pairs would be split, as new pairs A1-A2 are formed.) Only with a changed donor-to-acceptor ratio, the additional decrease in FLT could be explained with only heterodimers. But as ratios were not significantly changed, intermediate forms and/or trimeric arrangements must have been present. The restoration of the A2 peak and the energy transfer from A1 to A2 visible in the spectra of RLP44–BRI1–BAK1 compared to RLP44–BRI1–FLS2 is an additional evidence for close complex formation.

Interestingly, the BAK1 co-receptors that interact with RLP44 seem to be in a different membrane compartment than FLS2, as no energy transfer to FLS2 was detected. Consequently, FLS2 must have been distanced more than 15 nm from the RLP44-BAK1 and RLP44-BRI1 heterodimers. This in turn means, that the BAK1 co-receptors that interact with FLS2 may be specific to FLS2 complexes. Otherwise, intermediate BAK1-A1 could have bridged the distance between BRI1 and FLS2. However, for FLS2 and BAK1 were shown to only associate upon flg2 treatment (Somssich et al., 2015). The observation, that some residues of the BAK1 kinase domain are specifically phosphorylated by brassinosteroid signalling and other residues are regulated by immune signalling (Perraki et al., 2018) supports this hypothesis.

Throughout the study, the expression level of FLS2-A2 was much lower than for the other A2-fusion proteins. An influence on expression level due to differences in size was unlikely, as FLS2 with 1173 amino acids was as large as BRI1 with 1196 AA. Possibly, the overexpression of growth-/development-mediating proteins decreases the level of FLS2 in the PM. In theory, the lower expression of FLS2 could mask a possible interaction between RLP44 and FLS2 in intensity-based FRET measurements. However, no interaction between them was observed in the more sensitive FRET-FLIM measurements and previously, no interaction was found in BiFC (Garnelo Gomez et al., 2019).

Our observation that BRI1 and FLS2 are located in distinct sub-compartments in the PM is in accordance with previous evidence by variable angle epifluorescence microscopy (VAEM) using BRI1-eGFP and FLS2-RFP (Bücherl et al., 2017).

Material and methods

Plasmid construction

The cDNA sequence of the gene of interest *wo stop* was brought into pDONR221-P3P2 (donor) or pDONR221-P1P4 (first acceptor) or pENTR™/D-TOPO® (second acceptor) as described by guidelines in the Gateway manual (Life Technologies) with primers listed in Supp. material 8. The coding sequence of BRI1 and BAK1 was brought in the pENTR-D-TOPO previously (Caesar et al., 2011; Witthöft et al., 2014). For the generation of BRI1-HA, primer previously published were used (Wolf et al., 2014) to bring CDS of BRI1 in pDONR207 and an LR with pGWB14 was performed. The LR into pB7RWG2 (RFP) (Karimi et al., 2002) and the 2in1 FRET vector pFRETtv-2in1-CC (Hecker et al., 2015) was performed as described previously (Grefen and Blatt, 2012; Hecker et al., 2015).

Localization and FRET-FLIM studies

Transformation of *N. benthamiana* was performed as described by (Hecker et al., 2015; Ladwig et al., 2015), omitting the washing step with sterile water. For transformations with multiple constructs, an OD_{600} of 0.1 was set and mixed 1:1:1 with silencing inhibitor p19. Plants were watered and left to ambient conditions (24°C) with lid on top and imaged two days past transformation at the SP8 confocal laser scanning microscope (CLSM) (Leica Microsystems GMBH) with LAS AF and SymPhoTime software using a 63x/1.20 water immersion objective (Ladwig et al., 2015; Mohrholz et al., 2019). Data were derived from measurements of the lower epidermis, avoiding guard cells and stomata, with at least two biological replicates, comprising in average 20 data points and 11 data points for mTRQ2 – mRFP controls. Localization and quantification were performed with a minimum 3-fold line average for mTRQ2, mVEN and mRFP with Argon laser set to 2 % and excitations of 458 nm 40 %, 514 nm 20 % and 594 nm 30 % and emission detection with 465-505 nm 400 % on HyD, 525-565 nm 400 % on SMD HyD and 605-650 nm 300 % on SMD HyD, respectively. For the FLIM study, excitation of fluorophores was simultaneous due to the inability in Leica software to use sequential excitation while in FLIM-mode.

FLIM measurements were performed with a 440 nm puled laser (LDH-P-C-470) with 40 MHz repetition rate and a reduced speed yielding, with an image resolution of

256x256, a pixel dwell time of ~20 µs. Max count rate was set to ~2000 cps. Measurements were stopped, when the brightest pixel had a photon count of 500. Only measurements with an even intensity distribution at the PM were included. The corresponding emission was detected with a Leica HyD SMD detector from 455 nm to 505 nm by time-correlated single-photon counting using a Picoharp 300 module (PicoQuant, Berlin). The calculation of FLTs was performed by iterative reconvolution, i.e. the instrument response function was convolved with exponential test functions to minimize the error with regard to the original TCSPC histograms in an iterative process. While the donor-only samples were fitted with monoexponential decay functions, the energy transfer to fluorophores in the other samples resulted in additional decay rates. These histograms necessitated biexponential fitting functions, from which the fluorescent lifetime was derived by intensity weighted averaging. For the fastFLIM measurements, the max. count rate was increased.

Acquisition of λ-stacks (spectra)

Expression of relevant fluorophores were checked via fluorescence level prior λ-stack acquisition. For λ-stacks, both sequential excitation and simultaneous excitation was used as mentioned in results and an average of at least 6 ROI of the PM with different expression levels of at least 2 biological replicates. At the Leica SP8 excitation at 458 nm 80 % was used with SMD HyD ~250 %, measuring 460-625 nm with Δ7.5 nm with 256x256 resolution, a pixel dwell time of ~20 µs and three-fold line accumulation. At Zeiss LSM880 excitation at 485 nm with 30%, NF458, 800 V of airy-scan detectors were used, measuring 460-650 nm or 560-650 nm with Δ4.5 nm, resolution of 256x256, speed 2, digital gain set to 2, pinhole set to 14.25 airy units and a three-fold line accumulation. If over-all expression was very high, then for all samples measured that day line average was taken instead.

Protein structures and sizes

The intracellular domain of BRI1 and BAK1 as well as the fluorophore barrel (GFP/KKK. A redesigned GFP with improved solubility) was exported from Protein Data Base (PDB). As viewer JSmol (JavaScript) with solvent accessible depiction was chosen and color of proteins were changed. The secondary structure of linkers and the intracellular RLP44 domain was predicted with PEP-FOLD 3.5, de-novo prediction,

with standard settings and always model no1 (of 10) was used. Aminoacid sequences were HPTFLYKVGQLLGTS for the donor-linker, NPAFLYKVVSRLGTS for the acceptor-linker, KGGRADPAFLYKVVIS for the second acceptor linker and CLWLRITEKKIVEEEGKISQSMPDY for RLP44$_{Cyto}$. The size of intracellular domains was calculated from the known distance of the alpha-barrel secondary structure, which is Δ5.4 Å from turn-to-turn and 4 Å inner diameter.

Scripts

Calculation of Förster distance and FRET-efficiency was performed with excel sheet provided by Mark Hink (2003), which was adapted by Nina Visser (2011) and values in Supp. Material Table 1. Calculation of FRET-efficiency for variable position of mVEN was performed with python script in Supp. Material 2 and executed online in “Coding Ground – Execute Python online” (Python v2.7.13).

Simulation of spectra with mTRQ2, mVEN and mRFP were performed in MatLabR2017b or MatLabR2018b with the script in Supp. Material 4A. For simulation of cross-talk with different fluorophore ratios, changes in Supp. Material 4B were applied. Spectra were interpolated from data points with Supp. Material 5 and then subjected to spectral unmixing with the Matlab script in Supp. Material 6.

Statistics

Images were generated with Microsoft Excel v1809, SAS JMP 14 or MatLabR2017b and MatLabR2018b, also using those programs for calculation of average, standard error (SE) and standard deviation (SD). To test for homogeneity of variance Levene’s test ($p < 0.05$) was employed and statistical significance for non-parametic distributions was calculated by a two-tailed, all-pair Kruskal-Wallis test followed by a Steel-Dwass *post hoc* correction using SAS JMP version 14.0.0 (Ohmi *et al.*, 2016). For small sample numbers in Fig. 3d the 2-sample t-test was chosen (de Winter, J. C .F., 2013).

Figure Legends

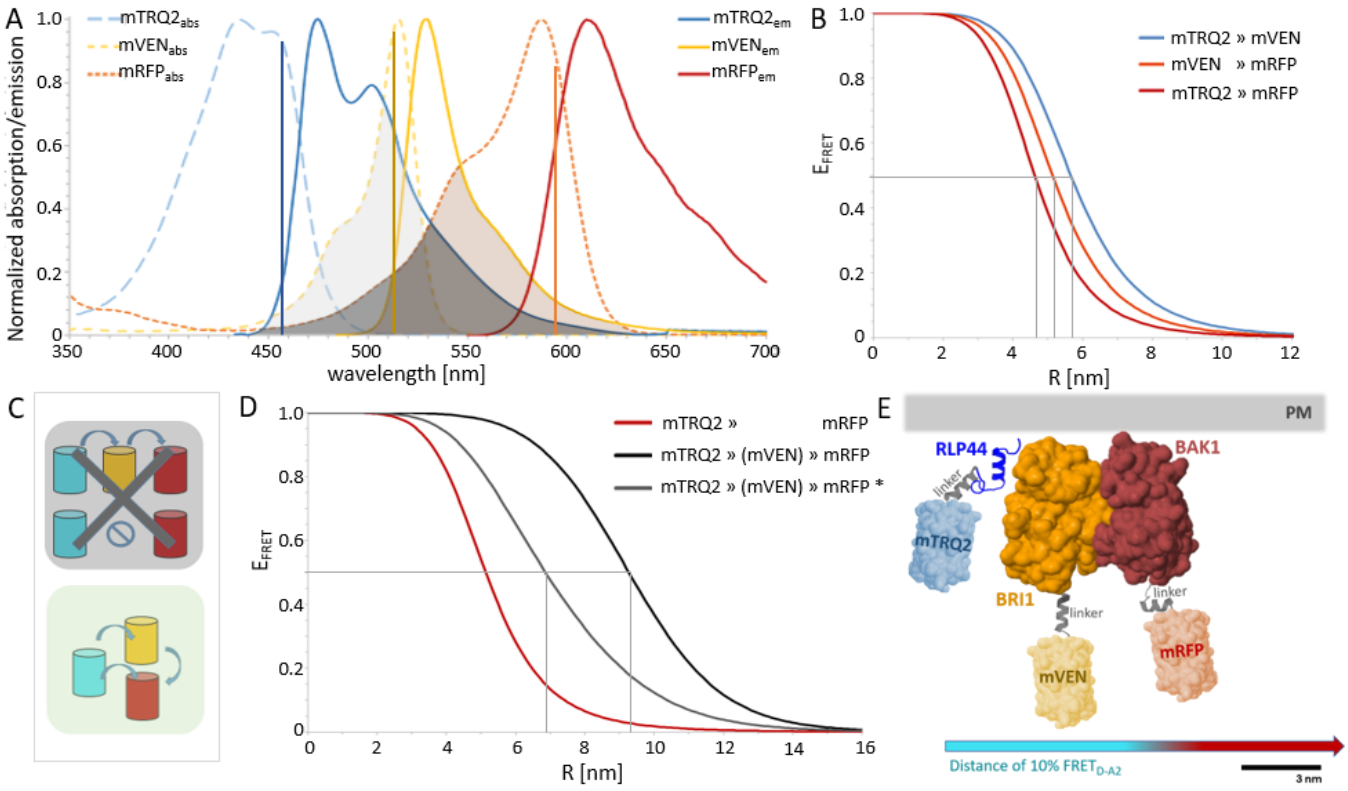

Figure 1. FRET properties of the used fluorophores and dimensions of the fusion proteins

(A) Normalized absorption (*dotted lines*) and emission (*solid lines*) of mTRQ2 (*blue*), mVEN (*yellow*) and mRFP (*red*). mTRQ2 is donor to both mVEN and mRFP and mVEN is donor to mRFP: the spectral overlap between mTRQ2 emission and mVEN absorption (*light grey area*), between $mTRQ2_{em}$ and $mRFP_{abs}$ (*dark grey area*) and between mVEN emission and mRFP absorption (*brown area*) is depicted. The laser lines for imaging of mTRQ2 (blue), mVEN (yellow) and mRFP (orange) are marked as vertical lines at respective positions.

(B) Calculation of the relationship between the FRET-efficiency (E_{FRET}) and the distance R between donor and acceptor fluorophores for mTRQ2-mVEN (*blue*), mVEN-mRFP (*orange*) and mTRQ2-mRFP (*red*). The Förster distance ($E_{FRET} = 0.5$) for each pair is marked with grey lines and their precise R_0 values are listed in table 1.

(C) Scheme of the possible pathway of Förster energy transfer for our set of proteins. Not only sequential FRET from mTRQ2 via mVEN to mRFP is possible (*grey*), but both sequential FRET via mVEN and direct FRET from mTRQ2 to mRFP is possible (*green*).

(D) Calculation of the relationship between the FRET-efficiency (E_{FRET}) and the distance R between donor and acceptor fluorophores for mTRQ2 and mRFP with and without and intermediate acceptor fluorophore. The Förster distance (R_0) for mTRQ2-mRFP (*red*) is shown. Calculation of an adjusted R_0 between mTRQ2 and mRFP, if

mVEN is in the middle (*black*) as calculated by (Haustein et al., 2003). For an in vivo system, the intermediate fluorophore is unlikely to be precisely in the middle between donor and second acceptor. Calculation of the average FRET-efficiency of each possible distance of mVEN between mTRQ2 and mRFP with Δ 1 nm step size (*grey*). (E) Composite image of the cytoplasmic domains of RLP44 (*blue*), BRI1 (*orange*) and BAK1 (*brown*) fused with 15 amino acid-long Gateway®-linker to mTRQ2 (*light blue*), mVEN (light *yellow*) and mRFP (light red). Proteins with known structure were depicted as solvent-accessible surface models ($BRI1_{Cyto}$, $BAK1_{Cyto}$, Fluorophore-barrel: GFP (1EMA) in RCSB). Structures of $RLP44_{Cyto}$ and the three Gateway®-linker (*grey*) were predicted with PEP-FOLD3 and depicted as cartoons. The plasma membrane was located above. The distance, at which 10% FRET between mTRQ2 and mRFP occurs for a stochiometry of 1:5 in the plasma membrane is shown below (blue-to-red arrow).

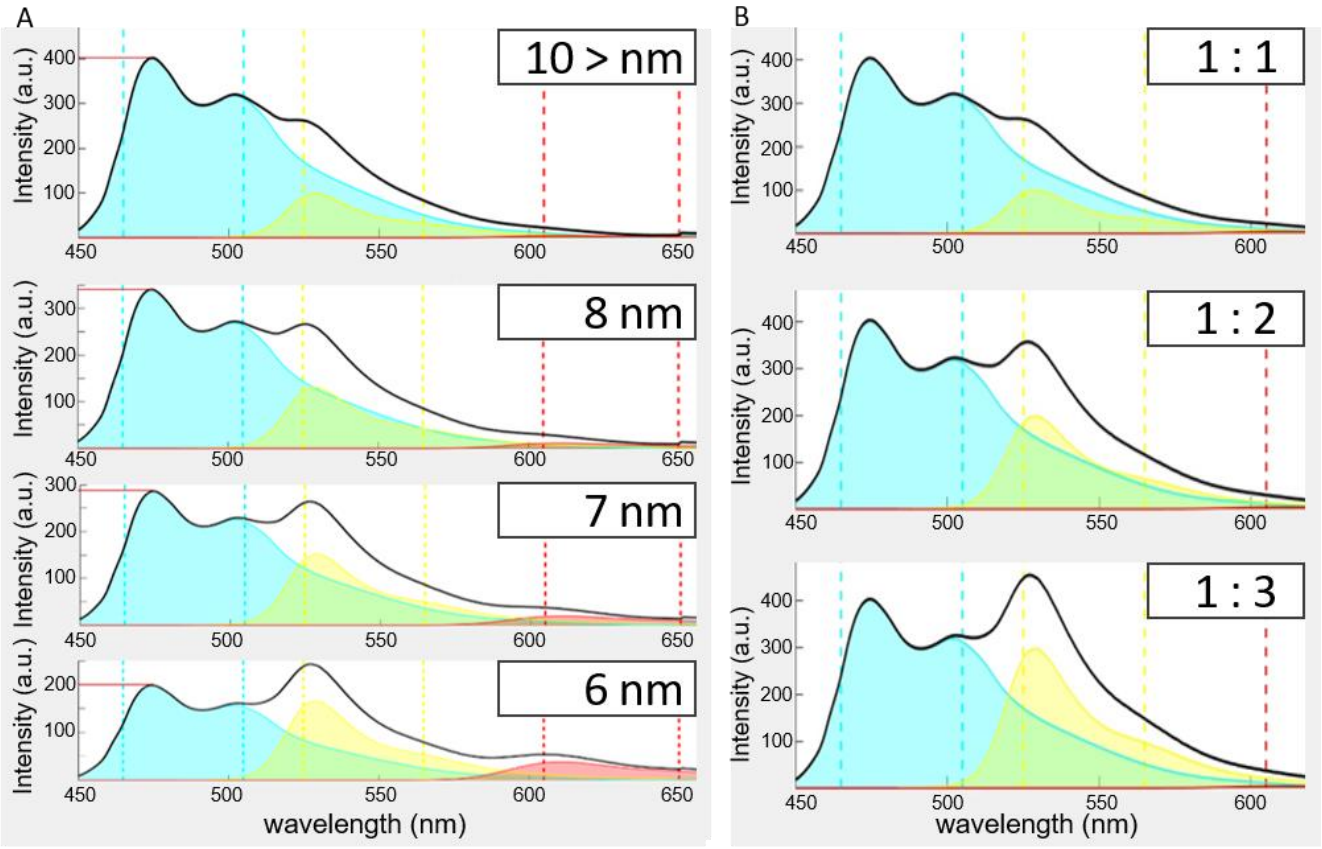

Figure 2. Simulation of spectra for excitation at 458 nm with MatLab™
(A) Simulation of the spectra that result from excitation with 458 nm for equidistant changes between mTRQ2, mVEN and mRFP and equal stochiometry (1:1:1). The emission of mTRQ (*blue area*), mVEN (*yellow area*) and mRFP (*red area*) and the overall spectrum when combining them (black line) is shown. With distances larger than 10 nm (*top*), cross-excitation of mVEN is visible in the spectrum (*yellow arrow*). With decreasing distances between the fluorophores of 8 nm (*upper middle*), 7 nm (*lower middle*) and 6 nm (bottom) and FRET occurs, the intensity of mTRQ2 decreases (*red line*) and the intensity peak of mVEN at ~520 nm and of mRFP at ~610 nm (red arrow) get higher.
(B) Simulation of the spectra that result from excitation with 458 nm for different ratios of mTRQ2 to mVEN without FRET occurring. The emission of mTRQ (*blue area*), mVEN (*yellow area*) and mRFP (*red area*) and the overall spectrum when combining them (black line) is shown. With distances larger than 10 nm (no FRET) and increasing amount of mVEN resulting in D:A1 fluorophore ratios of 1:1 (*top*), 1:2 (*middle*) and 1:3 (*bottom*), the intensity peak at ~520 nm of mVEN increases (yellow arrow). Without information on the expression levels, the shape of a spectrum with a 1:3 ratio resembles the shape of donor-acceptor pairs undergoing FRET with distances of 6 nm.

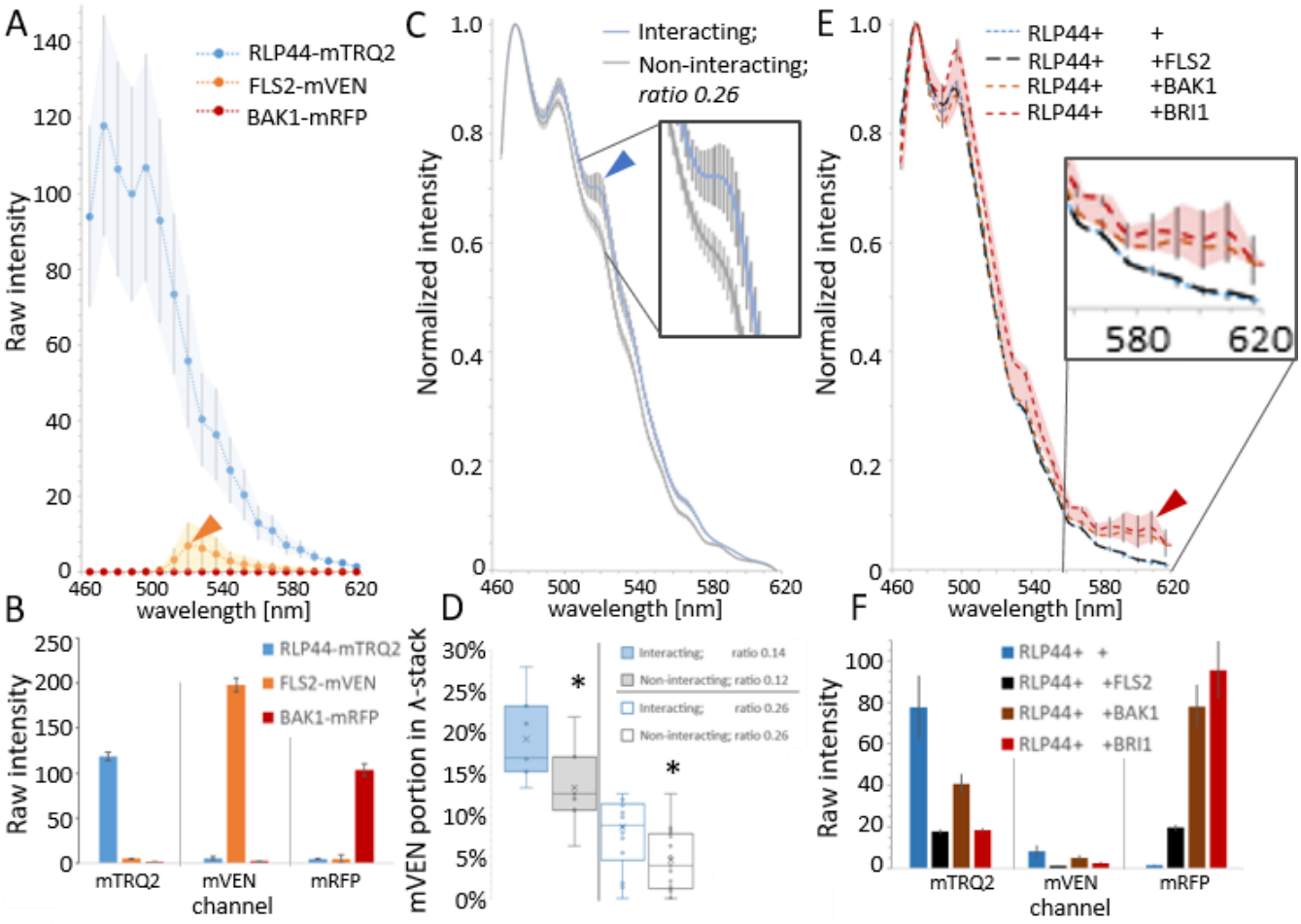

Figure 3. Measured spectra for excitation at 458 nm (top) and quantification of fluorescence intensities (bottom) in *N. benthamiana* leaf cells

(A) The average raw intensity ± SD in dependence of the wavelength for excitation at 458 nm is shown for RLP44-mTRQ2 (*blue*), FLS2-mVEN (*yellow*) and BAK1-mRFP (*red*). Measurement of spectra for the transformation of single fusion proteins in *N. benthamiana.*

(B) Average raw intensity ± SE in the mTRQ2 channel (*left*), mVEN channel (*middle*) and mRFP channel (*right*) of 8bit images after correction for spectral bleed through for RLP44-mTRQ2 (*blue*), FLS2-mVEN (*yellow*) and BAK1-mRFP (*red*). Quantification of the fluorescence intensities of the spectra shown in (A).

(C) The average normalized intensity ± SE in dependence of the wavelength is shown for co-expression of RLP44-mTRQ2 with BRI1-mVEN (*interacting, blue*) and for the co-expression of RLP44-mTRQ2 with FLS2-mVEN (*non-interacting, grey*) is shown. For both spectra, the average donor-to-acceptor ratio is ~1:4 (0.26). The peak in intensity around 520 nm of the mVEN signal is indicated (*arrow*). A magnification of the wavelengths that are relevant for mVEN detection is shown.

(D) Proportion of mVEN signal in the recorded spectra with the same donor-to-acceptor ratio for excitation at 458 nm. Ratios of 0.26 (filled boxes, left) and ratios of ~ 0.12 (empty boxes, right) of interacting (RLP44–BRI1, *blue*) and non-interacting

samples (RLP44–FLS2, *grey*) are shown. The ratio of 0.26 comprises n=7 measurements and the 0.12 ratio n=12 measurements. Significant changes in a two-sided 2-sample t-test with $p<0.05$ is indicated by an asterisk.
(E) The average normalized intensity ± SE in dependence of the wavelength is shown for the expression of RLP44-mTRQ2 (*blue*), RLP44-mTRQ with FLS2-mRFP (*black*), RLP44-mTRQ with BAK1-mRFP (*brown*) and for RLP44-mTRQ with BRI1-mRFP (*red*). Förster resonance energy transfer from mTRQ2 to mRFP for interacting proteins (*brown, red*) in comparison to non-interacting proteins (*black*) is indicated (arrow). A magnification of the wavelengths that are relevant for mRFP detection is shown.
(F) Average raw intensity ± SE in the mTRQ2 channel (*left*), mVEN channel (*middle*) and mRFP channel (*right*) of 8bit images for of RLP44-mTRQ2 (*blue*), RLP44-mTRQ with FLS2-mRFP (*black*), RLP44-mTRQ with BAK1-mRFP (*brown*) and for RLP44-mTRQ with BRI1-mRFP (*red*). Quantification of the fluorescence intensities of the spectra shown in (E).

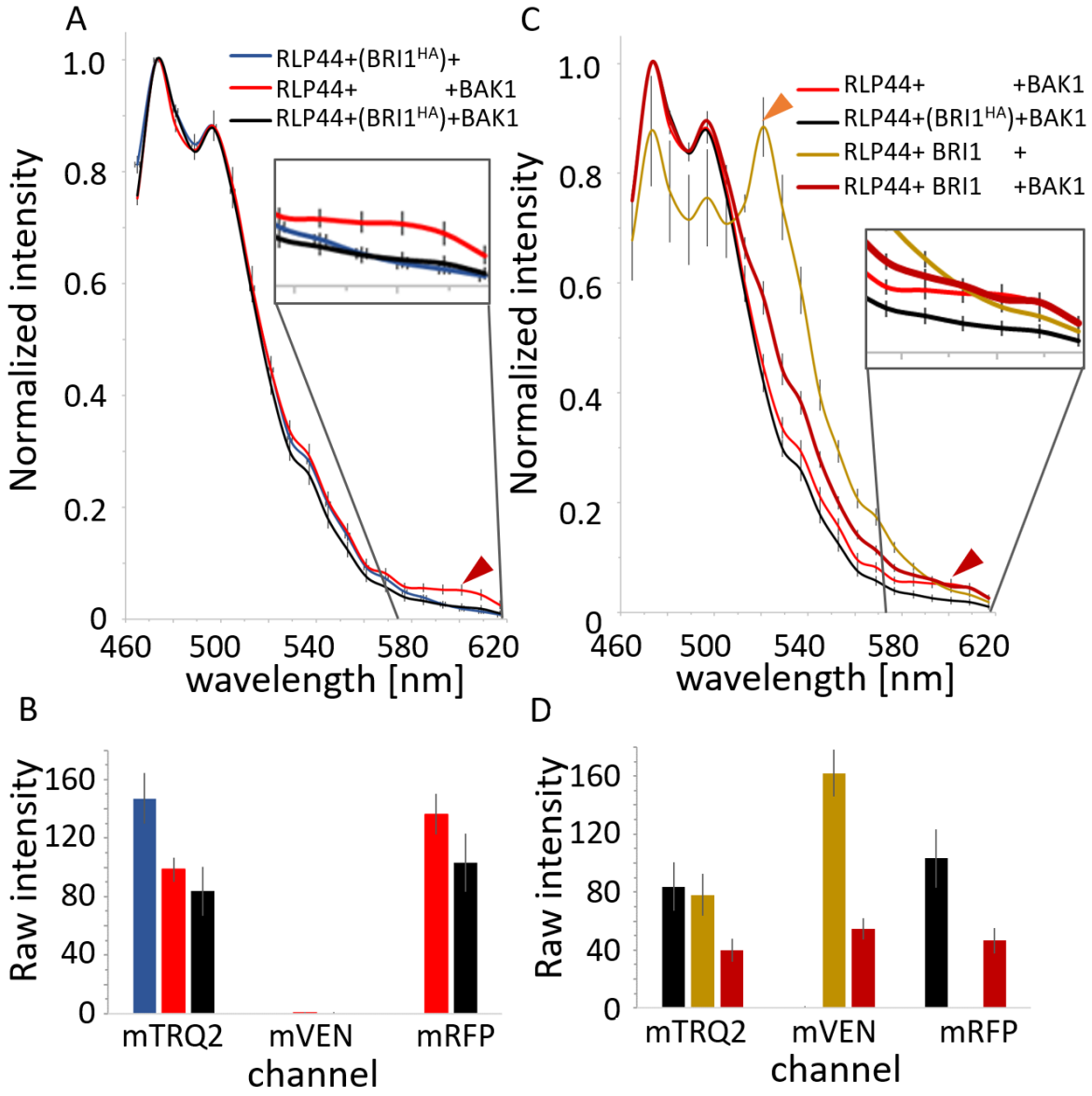

Figure 4. Measured spectra for excitation at 458 nm and quantification of fluorescence intensities in *N. benthamiana* leaf cells

(A) The average normalized intensity ± SE in dependence of the wavelength is shown for the expression of RLP44-mTRQ2 with the non-fluorescent BRI1-HA (BRI^{HA}) (*blue*), RLP44-mTRQ with BAK1-mRFP (red) and RLP44 with $BRI1^{HA}$ and BAK1-mRFP (*black*). A magnification of the wavelengths that are relevant for mRFP detection is shown.

(B) Average raw intensity ± SE in the mTRQ2 channel (*left*), mVEN channel (*middle*) and mRFP channel (*right*) of 8bit images for RLP44-mTRQ2 with BRI1-HA (BRI^{HA}) (*blue*), RLP44-mTRQ2 with BAK1-mRFP (red) and RLP44-mTRQ2 with $BRI1^{HA}$ and BAK1-mRFP (*black*). Quantification of the fluorescence intensities of the spectra shown in (A). Each channel was excited sequentially.

(C) The average normalized intensity ± SE in dependence of the wavelength is shown for the expression of RLP44-mTRQ with BAK1-mRFP (red[1]), RLP44-mTRQ2 with BRI1^{HA} and BAK1-mRFP (*black*[1]), RLP44-mTRQ2 with BRI1-mVEN (*yellow*) and of RLP44-mTRQ2 with BRI1-mVEN and BAK1-mRFP (*dark red*). A magnification of the wavelengths that are relevant for mRFP detection is shown. [note[1]: same curves as in A].
(D) Average raw intensity ± SE in the mTRQ2 channel (*left*), mVEN channel (*middle*) and mRFP channel (*right*) of 8bit images for RLP44-mTRQ2 with BRI1^{HA} and BAK1-mRFP (*black*[1]), RLP44-mTRQ2 with BRI1-mVEN (*yellow*) and of RLP44-mTRQ2 with BRI1-mVEN and BAK1-mRFP (*dark red*). Quantification of the fluorescence intensities of the spectra shown in (C). Each channel was excited sequentially.

Figure 5. Measured spectra for excitation at 458 nm and quantification of

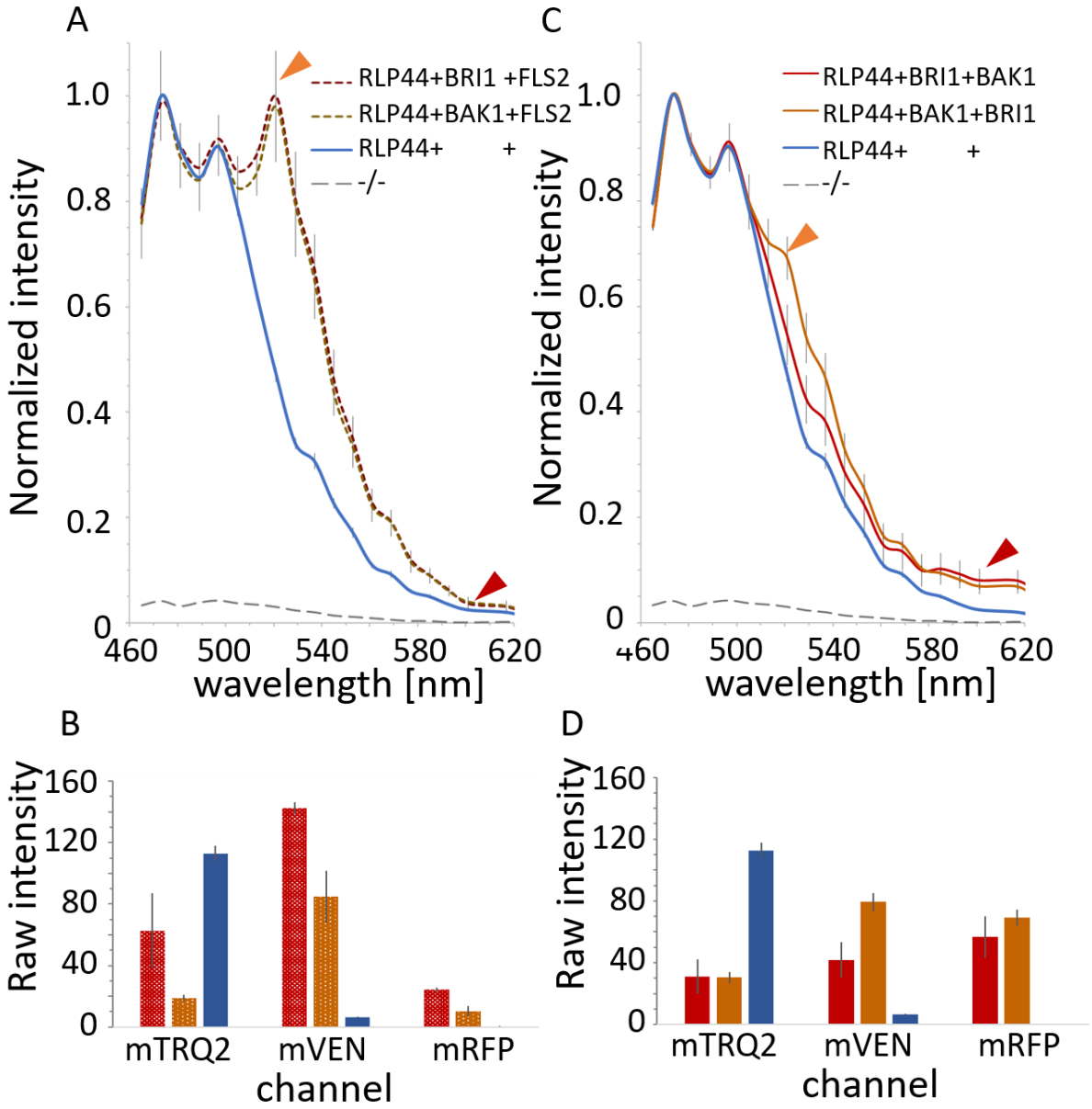

fluorescence intensities in *N. benthamiana* leaf cells

(A) The average normalized intensity ± SE in dependence of the wavelength is shown for the expression of RLP44-mTRQ2 (*blue*), RLP44-mTRQ2 with BRI1-mVEN and FLS-mRFP (*red*) and RLP44-mTRQ2 with BAK1-mVEN and FLS2-mRFP (*brown*). The peak in the spectrum of mVEN (*yellow arrow*) and of mRFP (*red arrow*) is marked. (B) Average raw intensity ± SE after correction for bleed-through and cross excitation in the mTRQ2 channel (*left*), mVEN channel (*middle*) and mRFP channel (*right*) of 8bit images for RLP44-mTRQ2 (*blue*), RLP44-mTRQ2 with BRI1-mVEN and FLS-mRFP (*red*) and RLP44-mTRQ2 with BAK1-mVEN and FLS2-mRFP (*brown*). Quantification of the fluorescence intensities of the spectra shown in (A).

(C) The average normalized intensity ± SE after correction for bleed-through and cross excitation in dependence of the wavelength is shown for the expression of RLP44-mTRQ (*blue*[1]), RLP44-mTRQ2 with BRI1-mVEN and BAK1-mRFP (*red*) and RLP44-mTRQ2 with BAK1-mVEN and BRI1-mRFP (*brown*). The peak in the spectrum of mVEN (*yellow arrow*) and of mRFP (*red arrow*) is marked. [note[1]: same curve as in A]. (D) Average raw intensity ± SE in the mTRQ2 channel (*left*), mVEN channel (*middle*) and mRFP channel (*right*) of 8bit images for RLP44-mTRQ (*blue*[1]), RLP44-mTRQ2 with BRI1-mVEN and BAK1-mRFP (*red*) and RLP44-mTRQ2 with BAK1-mVEN and BRI1-mRFP (*brown*). Quantification of the fluorescence intensities of the spectra shown in (B).

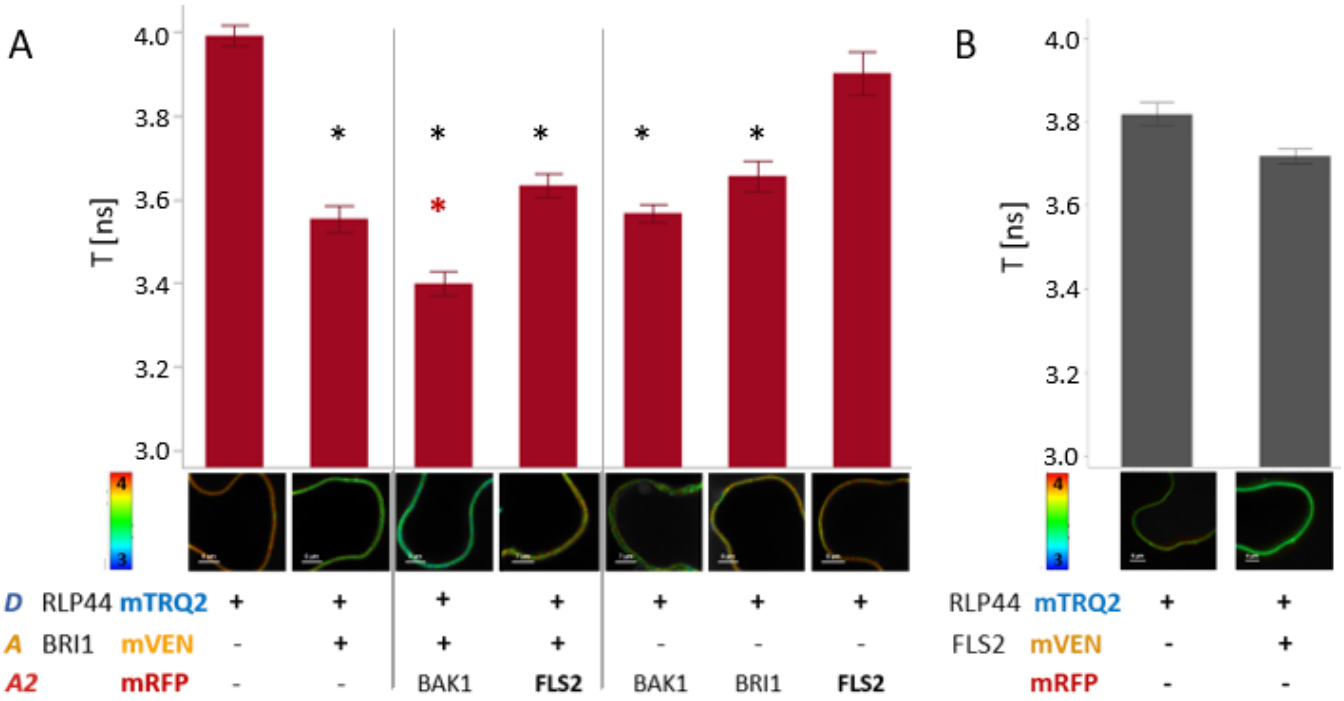

Figure 6. Fluorescence lifetime imaging in *N. benthamiana* leaf cells

(A) Fluorescence lifetime τ ± SE of RLP44-mTRQ2 measured with FLIM. A pulsed excitation at 440 nm is used. Expression of RLP44-mTRQ2 alone, or in combination with BRI1-mVEN as first acceptor and BAK1-mRFP or FLS2-mRFP as second acceptor. An exemplary part of the PM with color-coded τ is displayed below. Asterisks indicate statistically significant differences from RLP44-mTRQ2 and from the co-expression of RLP44-mTRQ2 with FLS2-mRFP ($p<0.001$, *black stars*) and from RLP44+BRI1+FLS2 and RLP44-BRI1 ($p=0.005$, *red star*) in an ANOVA followed by Tukey-Kramer HSD post-hoc test.

(B) Fluorescence lifetime τ ± SE of RLP44-mTRQ2 measured with Fast-FLIM. A pulsed excitation at 440 nm is used. Expression of RLP44-mTRQ2 alone, or in combination with FLS2-mVEN. An exemplary part of the PM with color-coded τ is displayed below. Statistical significance was tested with ANOVA followed by Tukey-Kramer HSD post-hoc test.

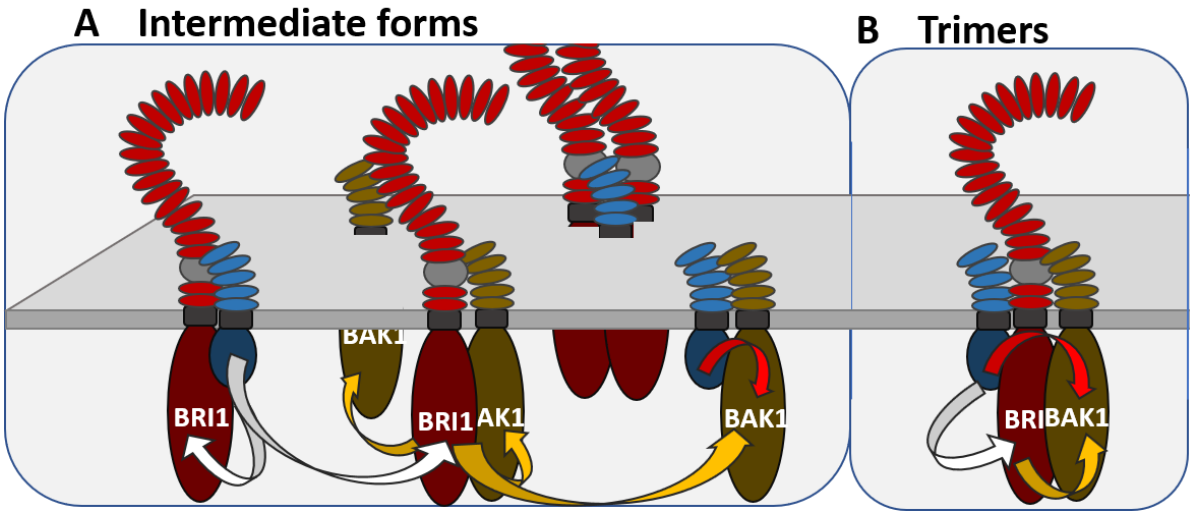

Figure 7. Three-fluorophore FRET-FLIM is possible for intermediate distances and for trimeric interaction

Scheme of a possible spatial distribution of RLP44 (*blue*), BRI1 (*red*) and BAK1 (brown) in the plasma membrane. For simplicity, the labelling fluorophore was not depicted. In this example, RLP44-D, BRI1-A1 and BAK1-A2 fusions are present. FRET between D and A1 (*white arrow*), between A1 and A2 (*yellow arrow*) and between D and A2 (*red arrow*) are shown. Proteins and distances are not in scale. (A) Three-fluorophore FRET is possible between different signalling complexes. If one complex is located close to another distinct signalling complex, FRET is possible. In theory, a different complex containing the appropriately labelled fluorophore can function as relay to a further distanced complex. (B) FRET is possible between a complex without any relay.

Acknowledgements

The authors would like to thank Florian Fässler for critical reading of the manuscript. Research in our laboratories was supported by the German Research Foundation (DFG) with grants to SW (WO 1660/6-1, WO 1660/2) and to KH (HA 2146/22-1; CRC 1101-D02).

References

Bajar, B.T., Wang, E.S., Zhang, S., Lin, M.Z., and Chu, J. (2016). A Guide to Fluorescent Protein FRET Pairs. Sensors (Basel, Switzerland) *16*.

Becker, W. (2012). Fluorescence lifetime imaging--techniques and applications. Journal of microscopy *247*, 119-136.

Betzig, E. (1995). Proposed method for molecular optical imaging. Opt. Lett. *20*, 237.

Betzig, E., Patterson, G.H., Sougrat, R., Lindwasser, O.W., Olenych, S., Bonifacino, J.S., Davidson, M.W., Lippincott-Schwartz, J., and Hess, H.F. (2006). Imaging intracellular fluorescent proteins at nanometer resolution. Science (New York, N.Y.) *313*, 1642-1645.

Bojar, D., Martinez, J., Santiago, J., Rybin, V., Bayliss, R., and Hothorn, M. (2014). Crystal structures of the phosphorylated BRI1 kinase domain and implications for brassinosteroid signal initiation. The Plant journal : for cell and molecular biology *78*, 31-43.

Boutant, E., Didier, P., Niehl, A., Mély, Y., Ritzenthaler, C., and Heinlein, M. (2010). Fluorescent protein recruitment assay for demonstration and analysis of in vivo protein interactions in plant cells and its application to Tobacco mosaic virus movement protein. The Plant journal : for cell and molecular biology *62*, 171-177.

Bücherl, C.A., Jarsch, I.K., Schudoma, C., Segonzac, C., Mbengue, M., Robatzek, S., MacLean, D., Ott, T., and Zipfel, C. (2017). Plant immune and growth receptors share common signalling components but localise to distinct plasma membrane nanodomains. eLife *6*.

Bücherl, C.A., van Esse, G.G., Kruis, A., Luchtenberg, J., Westphal, A.H., Aker, J., van Hoek, A., Albrecht, C., Borst, J.W., and Vries, S.C.d. (2013). Visualization of BRI1 and BAK1(SERK3) membrane receptor heterooligomers during brassinosteroid signaling. Plant Physiology *162*, 1911-1925.

Bunt, G., and Wouters, F.S. (2017). FRET from single to multiplexed signaling events. Biophysical reviews *9*, 119-129.

Cabantous, S., Terwilliger, T.C., and Waldo, G.S. (2005). Protein tagging and detection with engineered self-assembling fragments of green fluorescent protein. Nature Biotechnology *23*, 102-107.

Caesar, K., Elgass, K., Chen, Z., Huppenberger, P., Witthöft, J., Schleifenbaum, F., Blatt, M.R., Oecking, C., and Harter, K. (2011). A fast brassinolide-regulated response pathway in the plasma membrane of Arabidopsis thaliana. The Plant journal : for cell and molecular biology *66*, 528-540.

Chen, M., Li, W., Zhang, Z.-P., Pan, J., Sun, Y., Zhang, X., Zhang, X.-E., and Cui, Z. (2018). Three-Fragment Fluorescence Complementation for Imaging of Ternary Complexes under Physiological Conditions. Analytical chemistry *90*, 13299-13305.

Chen, X., Zaro, J.L., and Shen, W.-C. (2013). Fusion protein linkers. Property, design and functionality. Advanced drug delivery reviews *65*, 1357-1369.

Clouse, S.D., Langford, M., and McMorris, T.C. (1996). A Brassinosteroid-Insensitive Mutant in Arabidopsis thaliana Exhibits Multiple Defects in Growth and Development. Plant Physiology *111*, 671-678.

Costantini, L.M., Baloban, M., Markwardt, M.L., Rizzo, M., Guo, F., Verkhusha, V.V., and Snapp, E.L. (2015). A palette of fluorescent proteins optimized for diverse cellular environments. Nature Communications *6*, 7670 EP -.

Cotnoir-White, D., El Ezzy, M., Boulay, P.-L., Rozendaal, M., Bouvier, M., Gagnon, E., and Mader, S. (2018). Monitoring ligand-dependent assembly of receptor ternary complexes in live cells by BRETFect. Proceedings of the National Academy of Sciences of the United States of America *115*, E2653-E2662.

de Winter, J. C .F. (2013). Using the Student's "t"-Test with Extremely Small Sample Sizes. Practical Assessment, Research & Evaluation *18*.

Di Rubbo, S., Irani, N.G., Kim, S.Y., Xu, Z.-Y., Gadeyne, A., Dejonghe, W., Vanhoutte, I., Persiau, G., Eeckhout, D., and Simon, S., et al. (2013). The clathrin adaptor complex AP-2 mediates endocytosis of brassinosteroid insensitive1 in Arabidopsis. The Plant cell *25*, 2986-2997.

Fábián, Á., Horváth, G., Vámosi, G., Vereb, G., and Szöllősi, J. (2013). TripleFRET measurements in flow cytometry. Cytometry. Part A : the journal of the International Society for Analytical Cytology *83*, 375-385.

Fazekas, Z., Petrás, M., Fábián, A., Pályi-Krekk, Z., Nagy, P., Damjanovich, S., Vereb, G., and Szöllosi, J. (2008). Two-sided fluorescence resonance energy transfer for assessing molecular interactions of up to three distinct species in confocal microscopy. Cytometry. Part A : the journal of the International Society for Analytical Cytology *73*, 209-219.

Förster, T. (1948). Zwischenmolekulare Energiewanderung und Fluoreszenz. Ann. Phys. *437*, 55-75.

Fried, S., Reicher, B., Pauker, M.H., Eliyahu, S., Matalon, O., Noy, E., Chill, J., and Barda-Saad, M. (2014). Triple-color FRET analysis reveals conformational changes in the WIP-WASp actin-regulating complex. Science signaling *7*, ra60.

Friedrichsen, D.M., Joazeiro, C.A.P., Li, J., Hunter, T., and Chory, J. (2000). Brassinosteroid-Insensitive-1 Is a Ubiquitously Expressed Leucine-Rich Repeat Receptor Serine/Threonine Kinase. Plant Physiology *123*, 1247-1256.

Gadella, T.W.J. (2009). FRET and FLIM techniques (Amsterdam, London: Elsevier).

Galperin, E., Verkhusha, V.V., and Sorkin, A. (2004). Three-chromophore FRET microscopy to analyze multiprotein interactions in living cells. Nature Methods *1*, 209 EP -.

Garnelo Gomez, B., Lozano-Duran, R., and Wolf, S. (2019). Phosphorylation-dependent routing of RLP44 towards brassinosteroid or phytosulfokine signalling. Supplemental Material.

George, R.A., and Heringa, J. (2002). An analysis of protein domain linkers. Their classification and role in protein folding. Protein engineering *15*, 871-879.

Goedhart, J., Stetten, D.v., Noirclerc-Savoye, M., Lelimousin, M., Joosen, L., Hink, M.A., van Weeren, L., Jr, T.W.J.G., and Royant, A. (2012). Structure-guided evolution of cyan fluorescent proteins towards a quantum yield of 93%. Nature Communications *3*, 751.

Grefen, C., and Blatt, M.R. (2012). A 2in1 cloning system enables ratiometric bimolecular fluorescence complementation (rBiFC). BioTechniques *53*, 311-314.

Großeholz, R., Feldman-Salit, A., Wanke, F., Schulze, S., Glöckner, N., Kemmerling, B., Harter, K., and Kummer, U. (2019). Specifying the role of BAK1-interacting receptor-like kinase 3 in brassinosteroid signaling. Journal of integrative plant biology.

Haustein, E., Jahnz, M., and Schwille, P. (2003). Triple FRET. A tool for studying long-range molecular interactions. Chemphyschem : a European journal of chemical physics and physical chemistry *4*, 745-748.

He, L., Wu, X., Simone, J., Hewgill, D., and Lipsky, P.E. (2005). Determination of tumor necrosis factor receptor-associated factor trimerization in living cells by CFP-YFP-mRFP FRET detected by flow cytometry. Nucleic acids research *33*, e61.

Hecker, A., Wallmeroth, N., Peter, S., Blatt, M.R., Harter, K., and Grefen, C. (2015). Binary 2in1 Vectors Improve in Planta (Co)localization and Dynamic Protein Interaction Studies. Plant Physiology *168*, 776-787.

Hink, M., Visser, A.J.W.G., Vysotski, E.S., and Lee, J. (2002). Critical Transfer Distance Determination Between FRET Pairs.

Hochreiter, B., Garcia, A.P., and Schmid, J.A. (2015). Fluorescent proteins as genetically encoded FRET biosensors in life sciences. Sensors (Basel, Switzerland) *15*, 26281-26314.

Hohng, S., Joo, C., and Ha, T. (2004). Single-molecule three-color FRET. Biophysical journal *87*, 1328-1337.

Holzwart, E., Glöckner, N., Höfte, H., Harter, K. and Wolf, S. (2019). A novel mutant allele uncouples brassinosteroid-dependent and independent functions of BRI1. https://www.biorxiv.org/content/10.1101/605923v1. 01.05.2019.

Holzwart, E., Huerta, A.I., Glöckner, N., Garnelo Gómez, B., Wanke, F., Augustin, S., Askani, J.C., Schürholz, A.-K., Harter, K., and Wolf, S. (2018). BRI1 controls vascular cell fate in the Arabidopsis root through RLP44 and phytosulfokine signaling. Proceedings of the National Academy of Sciences of the United States of America *115*, 11838-11843.

Hoppe, A.D., Scott, B.L., Welliver, T.P., Straight, S.W., and Swanson, J.A. (2013). N-way FRET microscopy of multiple protein-protein interactions in live cells. PloS one *8*, e64760.

Hothorn, M., Belkhadir, Y., Dreux, M., Dabi, T., Noel, J.P., Wilson, I.A., and Chory, J. (2011). Structural basis of steroid hormone perception by the receptor kinase BRI1. Nature *474*, 467-471.

Hum, J.M., Siegel, A.P., Pavalko, F.M., and Day, R.N. (2012). Monitoring biosensor activity in living cells with fluorescence lifetime imaging microscopy. International journal of molecular sciences *13*, 14385-14400.

Hur, K.-H., Chen, Y., and Mueller, J.D. (2016). Characterization of Ternary Protein Systems In Vivo with Tricolor Heterospecies Partition Analysis. Biophysical journal *110*, 1158-1167.

Hutten, S.J., Hamers, D.S., Aan den Toorn, M., van Esse, W., Nolles, A., Bücherl, C.A., Vries, S.C. de, Hohlbein, J., and Borst, J.W. (2017). Visualization of BRI1 and SERK3/BAK1 Nanoclusters in Arabidopsis Roots. PloS one *12*, e0169905.

Imkampe, J., Halter, T., Huang, S., Schulze, S., Mazzotta, S., Schmidt, N., Manstretta, R., Postel, S., Wierzba, M., and Yang, Y., et al. (2017). The Arabidopsis Leucine-Rich Repeat Receptor Kinase BIR3 Negatively Regulates BAK1 Receptor Complex Formation and Stabilizes BAK1. The Plant cell *29*, 2285-2303.

Irani, N.G., Di Rubbo, S., Mylle, E., van den Begin, J., Schneider-Pizoń, J., Hniliková, J., Šíša, M., Buyst, D., Vilarrasa-Blasi, J., and Szatmári, A.-M., et al. (2012). Fluorescent castasterone reveals BRI1 signaling from the plasma membrane. Nature chemical biology *8*, 583-589.

Ishikawa-Ankerhold, H.C., Ankerhold, R., and Drummen, G.P.C. (2012). Advanced fluorescence microscopy techniques--FRAP, FLIP, FLAP, FRET and FLIM. Molecules (Basel, Switzerland) *17*, 4047-4132.

Jaillais, Y., Hothorn, M., Belkhadir, Y., Dabi, T., Nimchuk, Z.L., Meyerowitz, E.M., and Chory, J. (2011). Tyrosine phosphorylation controls brassinosteroid receptor

activation by triggering membrane release of its kinase inhibitor. Genes & development *25*, 232-237.

Jares-Erijman, E.A., and Jovin, T.M. (2003). FRET imaging. Nature Biotechnology *21*, 1387-1395.

Karimi, M., Inzé, D., and Depicker, A. (2002). GATEWAY vectors for Agrobacterium-mediated plant transformation. Trends in plant science *7*, 193-195.

Kastantin, M., Faulón Marruecos, D., Grover, N., Yu McLoughlin, S., Schwartz, D.K., and Kaar, J.L. (2017). Connecting Protein Conformation and Dynamics with Ligand-Receptor Binding Using Three-Color Förster Resonance Energy Transfer Tracking. Journal of the American Chemical Society *139*, 9937-9948.

Klar, T.A., Jakobs, S., Dyba, M., Egner, A., and Hell, S.W. (2000). Fluorescence microscopy with diffraction resolution barrier broken by stimulated emission. Proceedings of the National Academy of Sciences of the United States of America *97*, 8206-8210.

Krause, C.D., Izotova, L.S., and Pestka, S. (2013). Analytical use of multi-protein Fluorescence Resonance Energy Transfer to demonstrate membrane-facilitated interactions within cytokine receptor complexes. Cytokine *64*, 298-309.

Kuemmerle H., S.T. (1991). Human pharmacology. The basis of clinical pharmacology. Methods in drug protein binding analysis pp 235–282 (Amsterdam u.a.: Elsevier).

Kuo, H.-L., Ho, P.-C., Huang, S.-S., and Chang, N.-S. (2018). Chasing the signaling run by tri-molecular time-lapse FRET microscopy. Cell Death Discovery *4*, 45.

Kwaaitaal, M., Keinath, N.F., Pajonk, S., Biskup, C., and Panstruga, R. (2010). Combined bimolecular fluorescence complementation and Forster resonance energy transfer reveals ternary SNARE complex formation in living plant cells. Plant Physiology *152*, 1135-1147.

Ladwig, F., Dahlke, R.I., Stührwohldt, N., Hartmann, J., Harter, K., and Sauter, M. (2015). Phytosulfokine Regulates Growth in Arabidopsis through a Response Module at the Plasma Membrane That Includes CYCLIC NUCLEOTIDE-GATED CHANNEL17, H+-ATPase, and BAK1. The Plant cell *27*, 1718-1729.

Lakowicz, J.R. (2006). Principles of Fluorescence Spectroscopy.

Lakowicz, J.R., Szmacinski, H., Nowaczyk, K., Berndt, K.W., and Johnson, M. (1992). Fluorescence lifetime imaging. Analytical Biochemistry *202*, 316-330.

Lee, N.K., Kapanidis, A.N., Koh, H.R., Korlann, Y., Ho, S.O., Kim, Y., Gassman, N., Kim, S.K., and Weiss, S. (2007). Three-color alternating-laser excitation of single molecules. Monitoring multiple interactions and distances. Biophysical journal *92*, 303-312.

Lee, S., Lee, J., and Hohng, S. (2010). Single-molecule three-color FRET with both negligible spectral overlap and long observation time. PloS one *5*, e12270.

Li, J., and Chory, J. (1997). A Putative Leucine-Rich Repeat Receptor Kinase Involved in Brassinosteroid Signal Transduction. Cell *90*, 929-938.

Liang, X., Ding, P., Lian, K., Wang, J., Ma, M., Li, L., Li, L., Li, M., Zhang, X., and Chen, S., et al. (2016). Arabidopsis heterotrimeric G proteins regulate immunity by directly coupling to the FLS2 receptor. eLife *5*, e13568.

Lin, T., Scott, B.L., Hoppe, A.D., and Chakravarty, S. (2018). FRETting about the affinity of bimolecular protein-protein interactions. Protein science : a publication of the Protein Society *27*, 1850-1856.

Magliery, T.J., Wilson, C.G.M., Pan, W., Mishler, D., Ghosh, I., Hamilton, A.D., and Regan, L. (2005). Detecting protein-protein interactions with a green fluorescent protein fragment reassembly trap. Scope and mechanism. Journal of the American Chemical Society *127*, 146-157.

Mallik, R., Yoo, M.J., Chen, S., and Hage, D.S. (2008). Studies of verapamil binding to human serum albumin by high-performance affinity chromatography. Journal of chromatography. B, Analytical technologies in the biomedical and life sciences *876*, 69-75.

Martin, K.J., McGhee, E.J., Schwarz, J.P., Drysdale, M., Brachmann, S.M., Stucke, V., Sansom, O.J., and Anderson, K.I. (2018). Accepting from the best donor; analysis of long-lifetime donor fluorescent protein pairings to optimise dynamic FLIM-based FRET experiments. PloS one *13*, e0183585.

Martins, S., Dohmann, E.M.N., Cayrel, A., Johnson, A., Fischer, W., Pojer, F., Satiat-Jeunemaître, B., Jaillais, Y., Chory, J., and Geldner, N., et al. (2015). Internalization and vacuolar targeting of the brassinosteroid hormone receptor BRI1 are regulated by ubiquitination. Nature Communications *6*, 6151.

Mastop, M., Bindels, D.S., Shaner, N.C., Postma, M., Gadella, T.W.J., and Goedhart, J. (2017). Characterization of a spectrally diverse set of fluorescent proteins as FRET acceptors for mTurquoise2. Scientific Reports *7*, 11999.

Miyawaki, A. (2011). Development of probes for cellular functions using fluorescent proteins and fluorescence resonance energy transfer. Annual Review of Biochemistry *80*, 357-373.

Miyawaki, A., and Tsien, R.Y. (2000). Monitoring protein conformations and interactions by fluorescence resonance energy transfer between mutants of green fluorescent protein. In Cell biology and physiology, J. Thorner, ed. (San Diego, Calif.: Acad. Press), pp. 472–500.

Mohrholz, A., Sun, H., Gloeckner, N., Hummel, S., Kolukisaoglu, U., Schneeberger, K., and Harter, K. (2019). The striking flower-in-flower phenotype of Arabidopsis thaliana Nossen (No-0) is caused by a novel LEAFY allele. Supplemental Figures and Tables.

Mora-García, S., Vert, G., Yin, Y., Caño-Delgado, A., Cheong, H., and Chory, J. (2004). Nuclear protein phosphatases with Kelch-repeat domains modulate the response to brassinosteroids in Arabidopsis. Genes & development *18*, 448-460.

Müller, S.M., Galliardt, H., Schneider, J., Barisas, B.G., and Seidel, T. (2013). Quantification of Förster resonance energy transfer by monitoring sensitized emission in living plant cells. Frontiers in plant science *4*, 413.

Mustafa, S., Hannagan, J., Rigby, P., Pfleger, K., and Corry, B. (2013). Quantitative Förster resonance energy transfer efficiency measurements using simultaneous spectral unmixing of excitation and emission spectra. Journal of biomedical optics *18*, 26024.

Nagai, T., Ibata, K., Park, E.S., Kubota, M., Mikoshiba, K., and Miyawaki, A. (2002). A variant of yellow fluorescent protein with fast and efficient maturation for cell-biological applications. Nature Biotechnology *20*, 87-90.

Nam, K.H., and Li, J. (2002). BRI1/BAK1, a Receptor Kinase Pair Mediating Brassinosteroid Signaling. Cell *110*, 203-212.

Noomnarm, U., and Clegg, R.M. (2009). Fluorescence lifetimes. Fundamentals and interpretations. Photosynthesis research *101*, 181-194.

Oh, M.-H., Ray, W.K., Huber, S.C., Asara, J.M., Gage, D.A., and Clouse, S.D. (2000). Recombinant Brassinosteroid Insensitive 1 Receptor-Like Kinase Autophosphorylates on Serine and Threonine Residues and Phosphorylates a Conserved Peptide Motif in Vitro. Plant Physiology *124*, 751-766.

Oravcova´, J., Bo¨hs, B., and Lindner, W. (1996). Drug-protein binding studies new trends in analytical and experimental methodology. Journal of Chromatography B: Biomedical Sciences and Applications *677*, 1-28.

Pauker, M.H., Hassan, N., Noy, E., Reicher, B., and Barda-Saad, M. (2012). Studying the dynamics of SLP-76, Nck, and Vav1 multimolecular complex formation in live human cells with triple-color FRET. Science signaling *5*, rs3.

Peng, Y., Chen, L., Li, S., Zhang, Y., Xu, R., Liu, Z., Liu, W., Kong, J., Huang, X., and Wang, Y., et al. (2018). BRI1 and BAK1 interact with G proteins and regulate sugar-responsive growth and development in Arabidopsis. Nature Communications *9*, 1522.

Perraki, A., DeFalco, T.A., Derbyshire, P., Avila, J., Séré, D., Sklenar, J., Qi, X., Stransfeld, L., Schwessinger, B., and Kadota, Y., et al. (2018). Phosphocode-dependent functional dichotomy of a common co-receptor in plant signalling. Nature *561*, 248-252.

Rekas, A., Alattia, J.-R., Nagai, T., Miyawaki, A., and Ikura, M. (2002). Crystal structure of venus, a yellow fluorescent protein with improved maturation and reduced environmental sensitivity. J. Biol. Chem. *277*, 50573-50578.

Russinova, E., Borst, J.-W., Kwaaitaal, M., Caño-Delgado, A., Yin, Y., Chory, J., and Vries, S.C. de (2004). Heterodimerization and endocytosis of Arabidopsis brassinosteroid receptors BRI1 and AtSERK3 (BAK1). The Plant cell *16*, 3216-3229.

Santiago, J., Henzler, C., and Hothorn, M. (2013). Molecular mechanism for plant steroid receptor activation by somatic embryogenesis co-receptor kinases. Science (New York, N.Y.) *341*, 889-892.

Schoberer, J., Liebminger, E., Botchway, S.W., Strasser, R., and Hawes, C. (2013). Time-resolved fluorescence imaging reveals differential interactions of N-glycan processing enzymes across the Golgi stack in planta. Plant Physiology *161*, 1737-1754.

Scott, B.L., and Hoppe, A.D. (2015). Optimizing fluorescent protein trios for 3-Way FRET imaging of protein interactions in living cells. Scientific Reports *5*, 10270 EP -.

Seidel, T., Seefeldt, B., Sauer, M., and Dietz, K.-J. (2010). In vivo analysis of the 2-Cys peroxiredoxin oligomeric state by two-step FRET. Journal of biotechnology *149*, 272-279.

Shrestha, D., Jenei, A., Nagy, P., Vereb, G., and Szöllősi, J. (2015). Understanding FRET as a research tool for cellular studies. International journal of molecular sciences *16*, 6718-6756.

Shyu, Y.J., Suarez, C.D., and Hu, C.-D. (2008). Visualization of ternary complexes in living cells by using a BiFC-based FRET assay. Nature Protocols *3*, 1693 EP -.

Somssich, M., Ma, Q., Weidtkamp-Peters, S., Stahl, Y., Felekyan, S., Bleckmann, A., Seidel, C.A.M., and Simon, R. (2015). Real-time dynamics of peptide ligand-dependent receptor complex formation in planta. Science signaling *8*, ra76.

Steinberg, I.Z. (1971). Long-range nonradiative transfer of electronic excitation energy in proteins and polypeptides. Annual Review of Biochemistry *40*, 83-114.

Sun, W., Cao, Y., Jansen Labby, K., Bittel, P., Boller, T., and Bent, A.F. (2012). Probing the Arabidopsis flagellin receptor. FLS2-FLS2 association and the contributions of specific domains to signaling function. The Plant cell *24*, 1096-1113.

Sun, Y., Han, Z., Tang, J., Hu, Z., Chai, C., Zhou, B., and Chai, J. (2013a). Structure reveals that BAK1 as a co-receptor recognizes the BRI1-bound brassinolide. Cell Research *23*, 1326 EP -.

Sun, Y., Li, L., Macho, A.P., Han, Z., Hu, Z., Zipfel, C., Zhou, J.-M., and Chai, J. (2013b). Structural basis for flg22-induced activation of the Arabidopsis FLS2-BAK1 immune complex. Science (New York, N.Y.) *342*, 624-628.

Sun, Y., Wallrabe, H., Booker, C.F., Day, R.N., and Periasamy, A. (2010). Three-color spectral FRET microscopy localizes three interacting proteins in living cells. Biophysical journal *99*, 1274-1283.

Szöllosi, J., Damjanovich, S., Nagy, P., Vereb, G., and Mátyus, L. (2006). Principles of resonance energy transfer. Current protocols in cytometry *Chapter 1*, Unit1.12.

Tang, D., Wang, G., and Zhou, J.-M. (2017). Receptor Kinases in Plant-Pathogen Interactions. More Than Pattern Recognition. The Plant cell *29*, 618-637.

Ujlaky-Nagy, L., Nagy, P., Szöllősi, J., and Vereb, G. (2018). Flow Cytometric FRET Analysis of Protein Interactions. Methods in molecular biology (Clifton, N.J.) *1678*, 393-419.

van Rosmalen, M., Krom, M., and Merkx, M. (2017). Tuning the Flexibility of Glycine-Serine Linkers To Allow Rational Design of Multidomain Proteins. Biochemistry *56*, 6565-6574.

Vert, G., and Chory, J. (2006). Downstream nuclear events in brassinosteroid signalling. Nature *441*, 96-100.

Vogel, S.S., van der Meer, B.W., and Blank, P.S. (2014). Estimating the distance separating fluorescent protein FRET pairs. Methods (San Diego, Calif.) *66*, 131-138.

Vuignier, K., Schappler, J., Veuthey, J.-L., Carrupt, P.-A., and Martel, S. (2010). Drug-protein binding. A critical review of analytical tools. Analytical and bioanalytical chemistry *398*, 53-66.

Wallrabe, H., Cai, Y., Sun, Y., Periasamy, A., Luzes, R., Fang, X., Kan, H.-M., Cameron, L.-C., Schafer, D.A., and Bloom, G.S. (2013). IQGAP1 interactome analysis by in vitro reconstitution and live cell 3-color FRET microscopy. Cytoskeleton (Hoboken, N.J.) *70*, 819-836.

Wang, J., Jiang, J., Wang, J., Chen, L., Fan, S.-L., Wu, J.-W., Wang, X., and Wang, Z.-X. (2014). Structural insights into the negative regulation of BRI1 signaling by BRI1-interacting protein BKI1. Cell Research *24*, 1328-1341.

Wang, X., and Chory, J. (2006). Brassinosteroids regulate dissociation of BKI1, a negative regulator of BRI1 signaling, from the plasma membrane. Science (New York, N.Y.) *313*, 1118-1122.

Wang, X., Goshe, M.B., Soderblom, E.J., Phinney, B.S., Kuchar, J.A., Li, J., Asami, T., Yoshida, S., Huber, S.C., and Clouse, S.D. (2005a). Identification and functional analysis of in vivo phosphorylation sites of the Arabidopsis BRASSINOSTEROID-INSENSITIVE1 receptor kinase. The Plant cell *17*, 1685-1703.

Wang, X., Kota, U., He, K., Blackburn, K., Li, J., Goshe, M.B., Huber, S.C., and Clouse, S.D. (2008). Sequential transphosphorylation of the BRI1/BAK1 receptor kinase complex impacts early events in brassinosteroid signaling. Developmental cell *15*, 220-235.

Wang, X., Li, X., Meisenhelder, J., Hunter, T., Yoshida, S., Asami, T., and Chory, J. (2005b). Autoregulation and homodimerization are involved in the activation of the plant steroid receptor BRI1. Developmental cell *8*, 855-865.

Wang, Z.-Y., Seto, H., Fujioka, S., Yoshida, S., and Chory, J. (2001). BRI1 is a critical component of a plasma-membrane receptor for plant steroids. Nature *410*, 380-383.

Wen, R., Wang, S., Xiang, D., Venglat, P., Shi, X., Zang, Y., Datla, R., Xiao, W., and Wang, H. (2014). UBC13, an E2 enzyme for Lys63-linked ubiquitination, functions in root development by affecting auxin signaling and Aux/IAA protein stability. The Plant journal : for cell and molecular biology *80*, 424-436.

Witthöft, J., Caesar, K., Elgass, K., Huppenberger, P., Kilian, J., Schleifenbaum, F., Oecking, C., and Harter, K. (2014). The activation of the Arabidopsis P-ATPase 1 by the brassinosteroid receptor BRI1 is independent of threonine 948 phosphorylation. Plant Signaling & Behavior *6*, 1063-1066.

Woehler, A. (2013). Simultaneous quantitative live cell imaging of multiple FRET-based biosensors. PloS one *8*, e61096.

Wolf, S., van der Does, D., Ladwig, F., Sticht, C., Kolbeck, A., Schürholz, A.-K., Augustin, S., Keinath, N., Rausch, T., and Greiner, S., et al. (2014). A receptor-like protein mediates the response to pectin modification by activating brassinosteroid signaling. Proceedings of the National Academy of Sciences of the United States of America *111*, 15261-15266.

Wu, P.G., and Brand, L. (1994). Resonance Energy Transfer. Methods and Applications. Analytical Biochemistry *218*, 1-13.

Yan, L., Ma, Y., Liu, D., Wei, X., Sun, Y., Chen, X., Zhao, H., Zhou, J., Wang, Z., and Shui, W., et al. (2012). Structural basis for the impact of phosphorylation on the activation of plant receptor-like kinase BAK1. Cell Research *22*, 1304-1308.

Yin, Y., Vafeados, D., Tao, Y., Yoshida, S., Asami, T., and Chory, J. (2005). A new class of transcription factors mediates brassinosteroid-regulated gene expression in Arabidopsis. Cell *120*, 249-259.

Yu, H., Zhang, J., Li, H., and Chen, T. (2013). Ma-PbFRET. Multiple acceptors FRET measurement based on partial acceptor photobleaching. Microscopy and microanalysis : the official journal of Microscopy Society of America, Microbeam Analysis Society, Microscopical Society of Canada *19*, 171-179.

Yun, H.S., Bae, Y.H., Lee, Y.J., Chang, S.C., Kim, S.-K., Li, J., and Nam, K.H. (2009). Analysis of phosphorylation of the BRI1/BAK1 complex in arabidopsis reveals amino acid residues critical for receptor formation and activation of BR signaling. Molecules and Cells *27*, 183-190.

Zhu, J.-Y., Li, Y., Cao, D.-M., Yang, H., Oh, E., Bi, Y., Zhu, S., and Wang, Z.-Y. (2017). The F-box Protein KIB1 Mediates Brassinosteroid-Induced Inactivation and Degradation of GSK3-like Kinases in Arabidopsis. Molecular cell *66*, 648-657.e4.

Supplemental figures

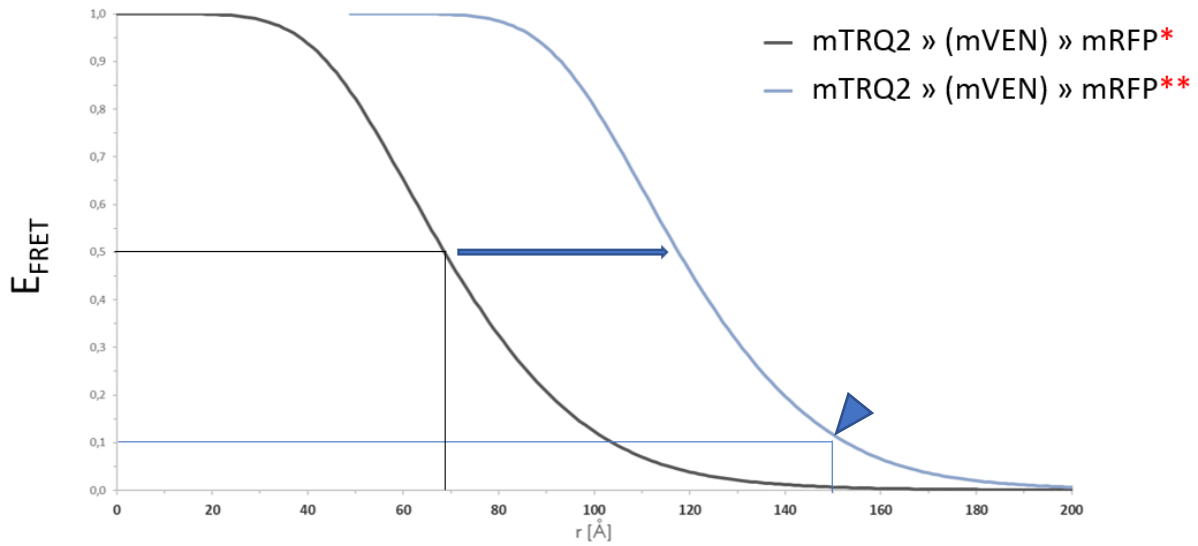

SI Figure 1. Projection of the adjusted R_0 (*) if additionally, a stochiometry of 1:5 in the plasma membrane is considered (**)

Calculation of the relationship between the FRET-efficiency (E_{FRET}) and the distance R between donor and acceptor fluorophores for mTRQ2 and mRFP. The adjusted R_0 for mTRQ2 and mRFP, if mVEN is in the middle with variable position (*black*) and a projection, if the adjusted R_0 equals the 1:5 stochiometry and plasma membrane adjusted R_0 of ~12 nm (*blue*). At a distance below ~15 nm between mTRQ2 and mRFP approx. 10% FRET occurs for a 1:5 stochiometry for plasma membrane-resident proteins.

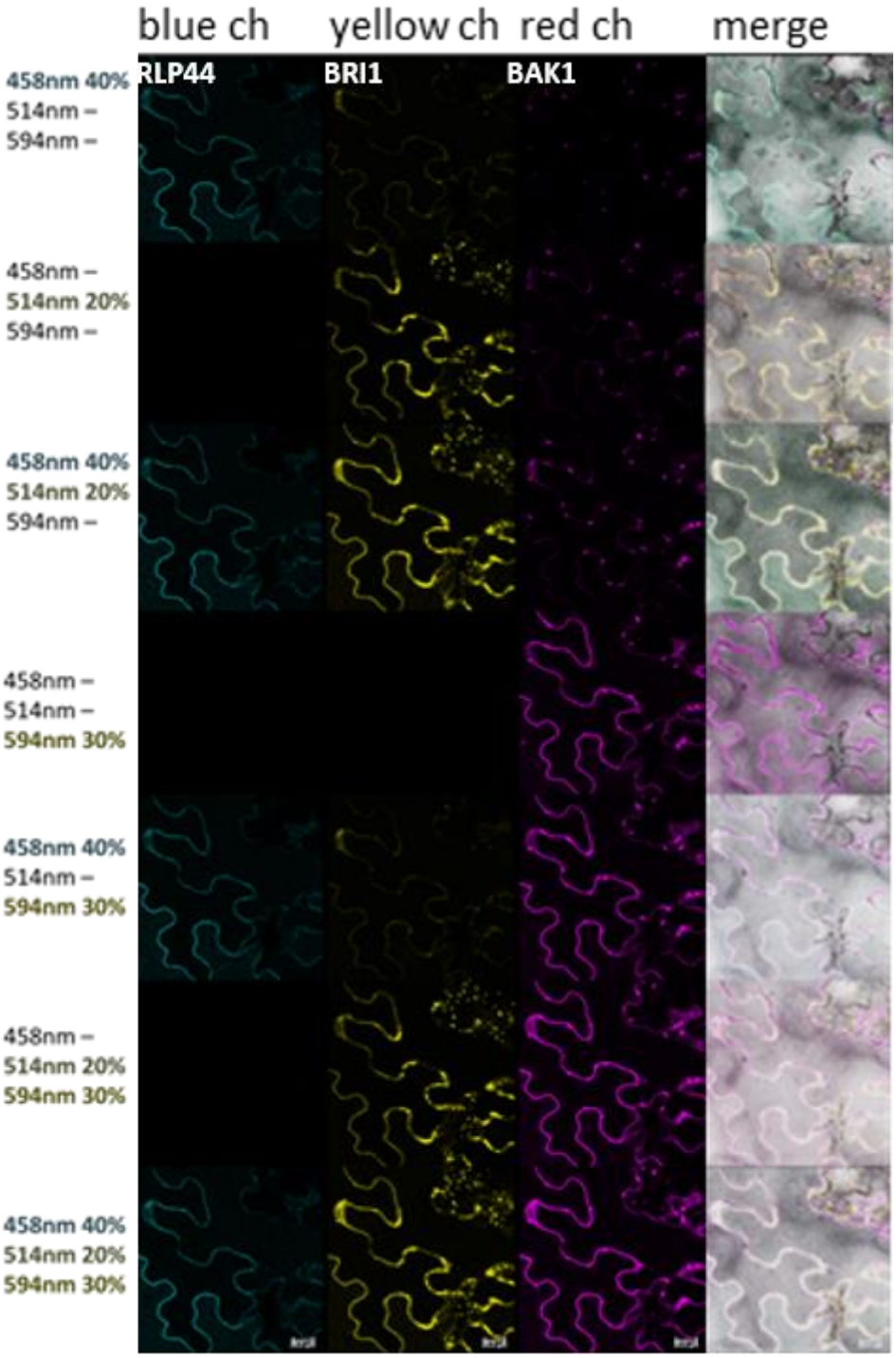

SI Figure 2. Representative image the signal in N. benthamiana two days after transformation with RLP44-mTRQ2, BRI1-mVEN and BAK1-mRFP

Representative images of the fluorescence intensity in the mTRQ2 channel, the mVEN channel and the mRFP channel and a merge with a bright field image with the used setting and different combinations of switched-on excitation laser lines. Blue channel for detection of RLP44-mTRQ was 465-505 nm, yellow channel for detection of BRI1-mVEN was 525-565 nm and red channel for detection of mRFP was 605-650 nm. Merge additionally contains bright-field. Scale bar represents 20µm.Before the acquisition of spectra or the fluorescence intensity, the expression of each fusion-

construct was tested with sequential excitation, meaning that one laser line was switched on at a time.

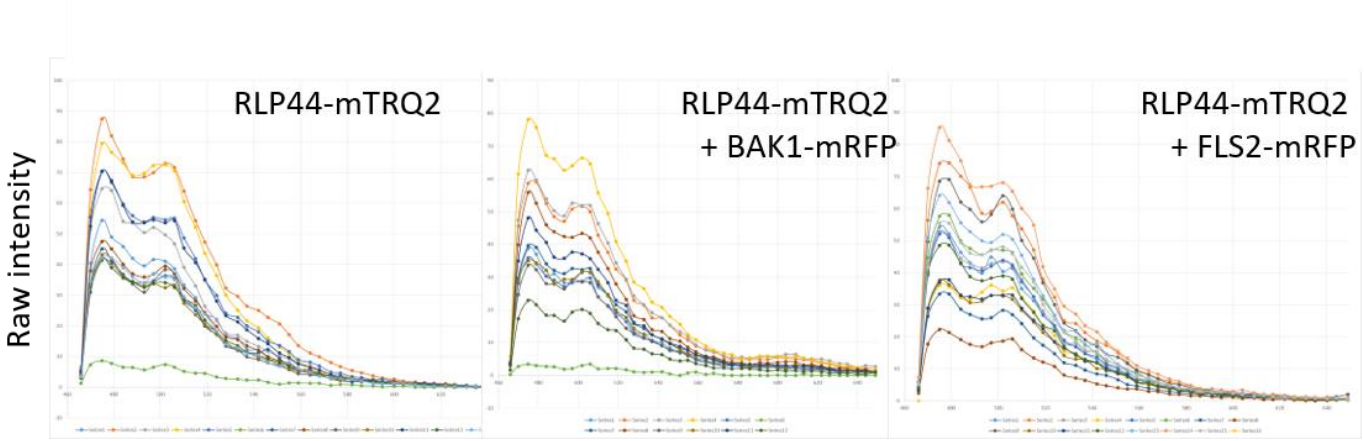

SI Figure 3. Raw intensity in dependence of the wavelength for different regions of interest with changing expression strengths

The raw intensity for different regions of interest in the plasma membrane with different expression strength in dependence of the wavelength for excitation at 458 nm is shown for RLP44-mTRQ2 (left), RLP44-mTRQ2 with FLS2-mRFP (middle) and RLP44-mTRQ2 with FLS2-mRFP (right).

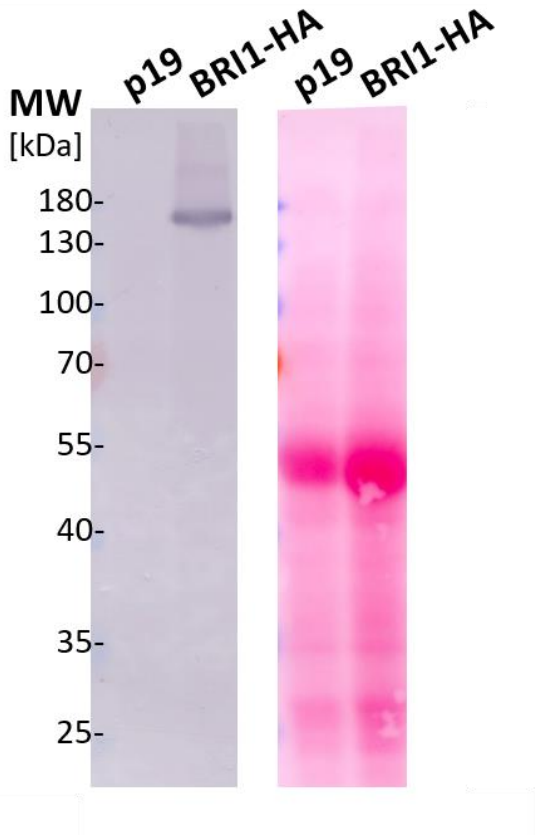

SI Figure 4. Western blot of BRI1^{HA}

Western blot (left) and proteins on the membrane, stained with Ponceau S after transfer (right) of a *N. benthamiana* leaf two days after transformation with the silencing inhibitor p19 or with p19 and BRI1^{HA}. The sizes of the protein ladder are indicated. Primary antibody was α-HA (rat), Roche, 1:1000 and secondary antibody was α-rat-AP (goat), Sigma, 1:7000.

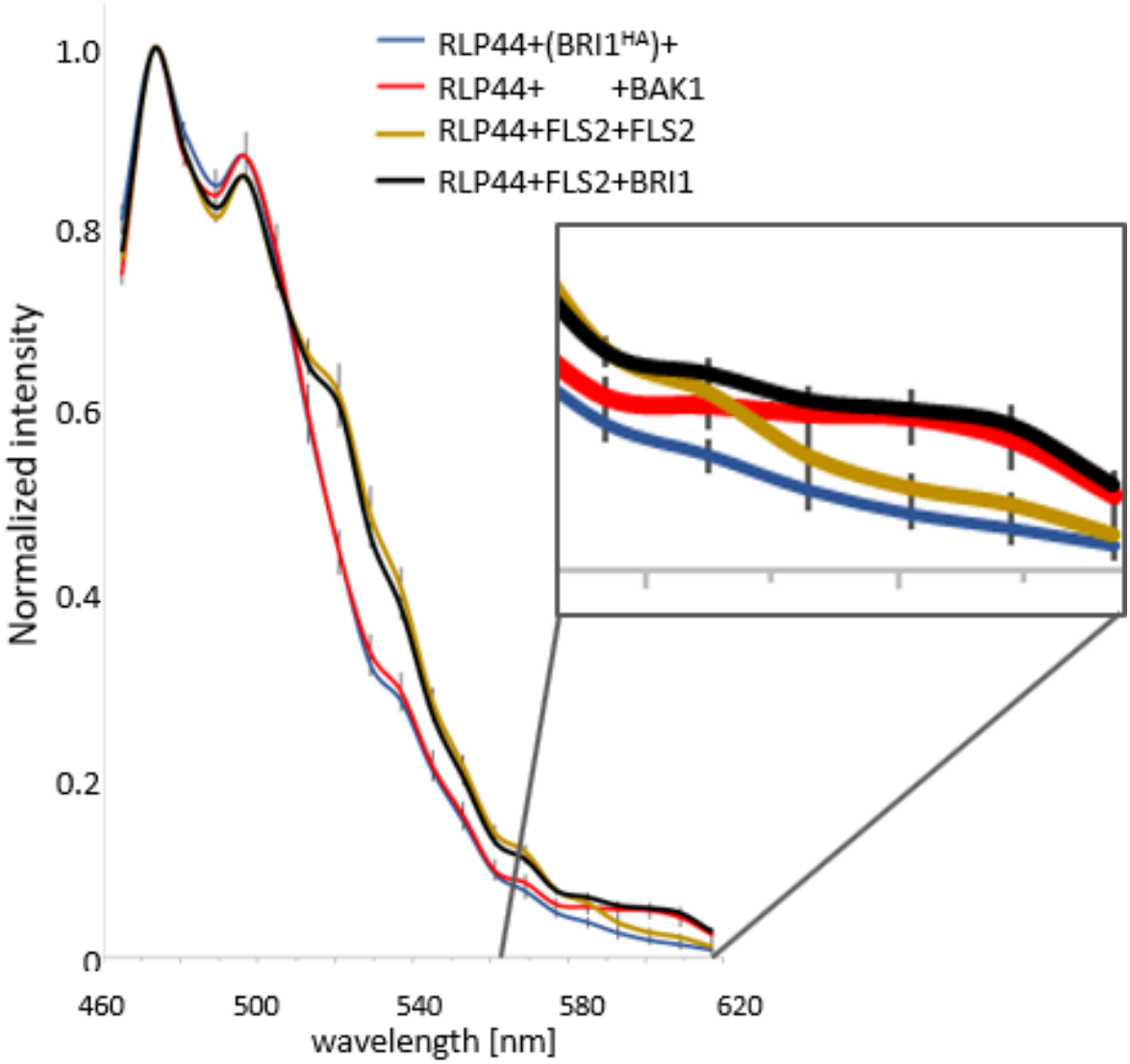

SI Figure 5. Measured spectra for excitation at 458 nm

The average normalized intensity ± SE in dependence of the wavelength is shown for the expression of RLP44-mTRQ2 with the non-fluorescent BRI1-HA (BRI^{HA}) (*blue*), RLP44-mTRQ with BAK1-mRFP (*red*), RLP44 with FLS2-mVEN and FLS2-mRFP (*brown*) and RLP44 with FLS2-mVEN and BRI1-mRFP (*brown*). A magnification of the wavelengths that are relevant for mRFP detection is shown.

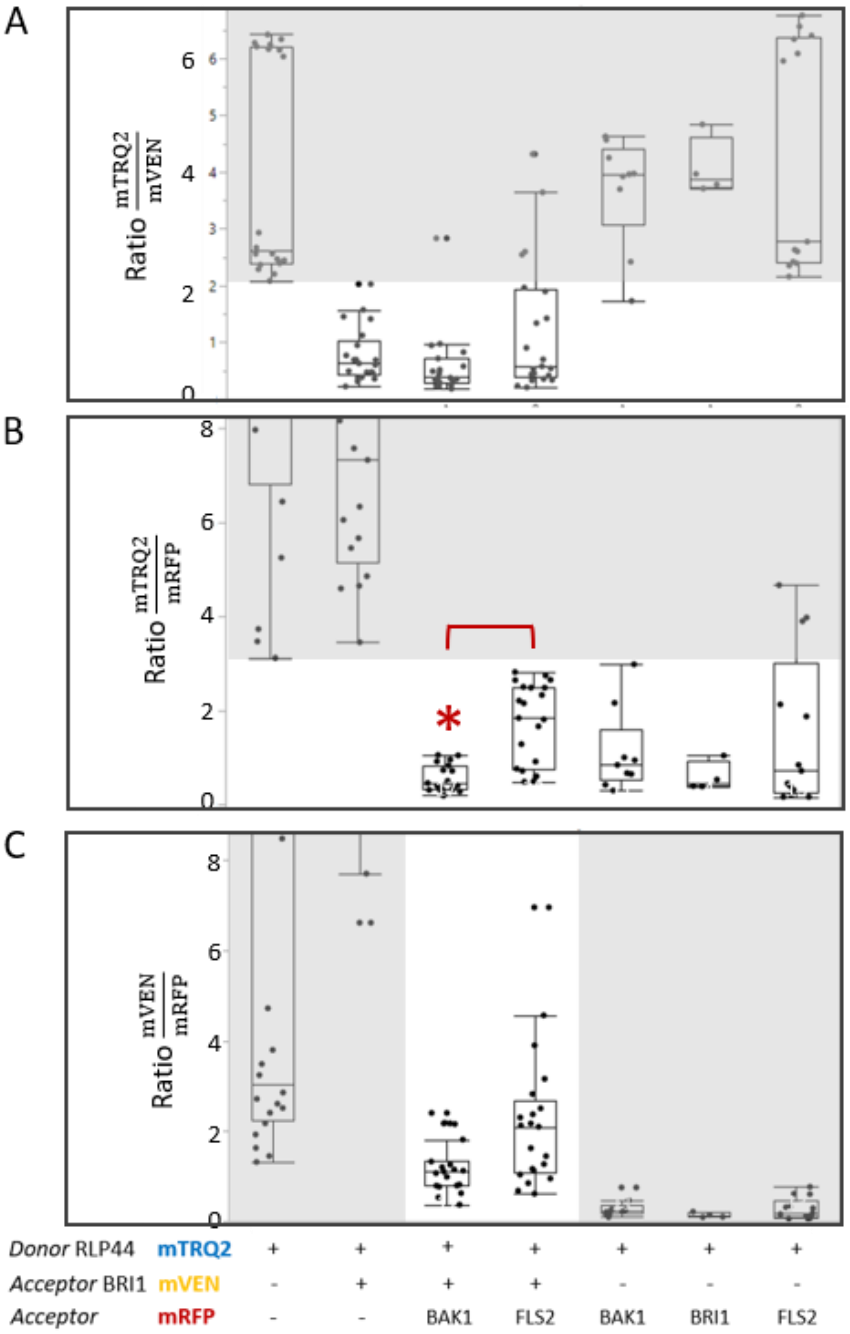

SI Figure 6. The overall donor to acceptor ratios did not change significantly
(A-C) Ratios of fluorescence intensity for donor-acceptor pairs. Data points were left-right scattered (*black dots*) and combined with boxplot information, permitting outliers. RLP44 was always fused to mTRQ2, BRI1 always to mVEN and as second acceptor, either BAK1 or FLS2 fused to mRFP was expressed. The ratios for mTRQ2-mVEN (A), mTRQ2-mRFP (B) and mVEN-mRFP (C) were tested for significant differences with a two-tailed, all-pair Kruskal-Wallis test followed by a Steel-Dwass post hoc correction. Background-level ratios (ratio that is present only because of bt and ce in respective samples) were marked in grey. Asterisk marks the only significant change ($p<0.05$) in donor-to-acceptor ratio, which was the mTRQ2:mRFP ratio between RLP44–BRI1–BAK1 and RLP44–BRI1–FLS2.

Supplemental material

Supp. Material 1

Physicochemical properties of fluorophores

SI Table 1: Parameters of fluorophores in this study: quantum yield (QY), extinction coefficient (ExCoeff), molecular brightness (MolBright), maturation time as half-maximal intensity (I_{max} 2^{-1}) and as half-time at 37°C in *E. coli* (t_{50}), photostability (PhotStab) as time until half-maximal intensity decrease when excited with 80uW, pH stability (pK_a) and proportion of monomeric state (MS). For comparison: EGFP has a brightness of 33.60 10^{-3} M^{-1} cm^{-1} and a Photostability of 159.6 s until a 50% decrease with 80uW is reached. pKa of EGFP lies at 6.0.

	QY	ExCoeff [M^{-1} cm^{-1}]	MolBright [10^{-3} M^{-1} cm^{-1}]	Maturation I_{max} 2^{-1} / t_{50}	PhotStab $t_{50(80uW)}$ [s]	pH stability pKa	MS [%]
mTRQ2	0.93	30	27.9	5.5 h / 33.5 min	71.7	3.1	93.8
	(Goedhart et al., 2012; Scott and Hoppe, 2015; Cranfill et al., 2016; Balleza et al., 2018)						
mVEN	0.64	105	67.2	/ 4.1 min	26.4	6.0	83.9
	(Kremers et al., 2006; Cranfill et al., 2016; Balleza et al., 2018)						
mRFP	0.25	44	12.5	1 h / 24 min	26.3	4.5	95.8
	(Campbell et al., 2002; Cranfill et al., 2016; Balleza et al., 2018)						

Supp. Material 2

Python script for calculation of FRET-efficiency with variable distances of middle fluorophore:

In a system of three fluorophores, which are donor (1), acceptor (2) and second acceptor (3) (Haustein et al. 2003) reported, that the overall FRET efficiency (E) from 1 to 3 (via 2) can be estimated by E_13= E_12 * E_23 with r_13 the distance between 1 and 3. We now keep the distance between 1 and 3 constant, and move 2 stepwise from 1 to 3: for example

Zero	1_____3	distance13: r_13=5	distance12: 0	distance23: 5
First step:	12____3	distance13: r_13=5	distance12: 1	distance23: 4
Second step:	1_2___3	distance13: r_13=5	distance12: 2	distance23: 3
Third step:	1__2__3	distance13: r_13=5	distance12: 3	distance23: 2
Fourth step:	1____23	distance13: r_13=5	distance12: 4	distance23: 1
Nth step:	1_____3	distance13: r_13=5	distance12: 5	distance23: 0

For each step we calculate E and list each value in an intermediate list (E_int). Then the average of the E_int is calculated and listed as the nth entry in the list E_13. Then, empty E_int before new round. This is repeated for each next larger r_13

For example several steps later, at r = 11 Å for

First step:	12_____3	r_13:11	r_12: 1	r_23: 10
Second step:	1_2_____3	r_13:11	r_12: 2	r_23: 9
(…)				
Nth step:	1_____3	r_13:11	r_12: 11	r_23: 0

And list each value in an intermediate list (E_int). Then average of the E_int list is calculated and listed in E_13 at the respective position in the list. Empty E_int of content -> New round until value before stop.
! Note, that distance r_13 is r_12+r_23
! → Thus r_23 = r - r_12

```
# Constants in Angstroem
# np.arange(start, stop, step) creates an array of values
import numpy as np
dist_step = 1
distance = np.arange(0.0, 218.0 + dist_step, dist_step)
foerster_radius_12 = 56.7
foerster_radius_23 = 51.4

# For any Donor (D) Acceptor (A) pair FRET efficiency is calculated with distance_DA and respective foerster_radius as input:
def calc_E_DA(distance_DA, foerster_radius):
    E_DA = 1/(1+(distance_DA/foerster_radius)**6)
    return E_DA

# Create empty vectors
E_13 = []
E_int = []

# Calculate stepweise for each distance r_13 the FRET efficiency E
for r in distance:
# if r_13=0 then the FRET efficiency will be one
    if      r == 0:
            E_int = 1
# Calculate E for all positions of 2 between 1 and 3 in an intermediate list (E_zw)
# Adaption because r_13=r_12+r_23
    else:
        for r_12 in np.arange(0, r+dist_step, dist_step):
            r_23 = r - r_12
            E_int.append(calc_E_DA (r_12, foerster_radius_12)* calc_E_DA (r_23,
foerster_radius_23))
# average efficiency for all positions of 2 and save to E_13
    E_13.append(np.mean(E_int))
# empty the intermediate list before next turn
    E_int = []

print(E_13)                    #y-axis
#print(distance)               #x-axis
```

numpy package version 1.12.1

Supp. Material 3A

Matlab script for λ-stack simulation

```
Function
tripleFRET_sim(CFPabs,CFPem,YFPabs,YFPem,RFPabs,RFPem,raw_image,QE_det)

% calculation of intensities and FRET based on publication:
% Sun et al., "Three-Color Spectral FRET Microscopy Localizes Three
% Interacting Proteins in Living Cells", Biophysical Journal 99(4)
% 1274?1283.
%
% CFP also denoted as F1 or 1 in indices, YFP as F2 or 2, RFP as F3 or 3.
%
% comparably "simple" simulation that includes photophysical properties
% like quantum yield, extinction coefficients, cross-excitation and
% spectral bleedthrough, but all steady-state.
%
% not yet considered:
%   * different complex stoichiometries
%   * alterations in the the FPs' photophysical properties when bound to a
%       target protein or being in otherwise different nano-environments
%   * binding affinities (Kd) of the proteins
%   * dark/bleached/misfolded fluorophores
%
% 2018-12-09 Zok

% refractive index
n = 1.33;

% orientation factor for FRET
kappa = 2/3;

% FRET pair distances (nm), e.g. r13 is the distance between F1 and F3
r12=100;
r13=100;
r23=6;

% relative protein concentrations. This will influence the results if the
% proteins are present in in different amounts. For example, assuming that
% the complex stoichiometry is 1:1:1 but the proteins are present at a
% 1:2:1 ratio, then the additional amount of F2 will be outside of the
% complex, but will still result in fluorescence emission originating from
% direct excitation and cross-excitation
% not done yet, do not change! ++++++++++++++++++++
c1=1;
c2=1;
c3=1;

% quantum yields
QY1=0.93;
QY2=0.57;
QY3=0.25;

% extinction coefficients (M-1*cm-1)
EC1=30000;
EC2=92200;
EC3=44000;

% excitation laser wavelengths (nm)
laser1=458;
```

```
laser2=514;
laser3=651;

% relative laser intensities
laserint1=1;
laserint2=0;
laserint3=0;

% absorption factors for all relevant wavelengths
% e.g. A12: absorption factor of fluorophore 2 at excitation wavelength 1
% missing combinations are assumed to be not absorbing
% (e.g. CFP does not absorb at the excitation wavelength for RFP)
A11=EC1*CFPabs(CFPabs(:,1)==laser1, 2);
A12=EC2*YFPabs(YFPabs(:,1)==laser1, 2);
A13=EC3*RFPabs(RFPabs(:,1)==laser1, 2);
A22=EC2*YFPabs(YFPabs(:,1)==laser2, 2);
A23=EC3*RFPabs(RFPabs(:,1)==laser2, 2);
A33=EC3*RFPabs(RFPabs(:,1)==laser3, 2);

% emission filter boundaries (nm)
BP1=[465 505];
BP2=[525 565];
BP3=[605 650];

% x-axis wavelength plot range
x_plotrange=[450 700];

% area normalization of emission spectra
CFPem_norm=CFPem;
CFPem_norm(:,2)=CFPem(:,2)/trapz(CFPem(:,1),CFPem(:,2));
YFPem_norm=YFPem;
YFPem_norm(:,2)=YFPem(:,2)/trapz(YFPem(:,1),YFPem(:,2));
RFPem_norm=RFPem;
RFPem_norm(:,2)=RFPem(:,2)/trapz(RFPem(:,1),RFPem(:,2));

% get R0's for all possible FRET pairs
R0_12 = calculateR0(CFPem,YFPabs,n,kappa,QY1,EC2);
R0_13 = calculateR0(CFPem,RFPabs,n,kappa,QY1,EC3);
R0_23 = calculateR0(YFPem,RFPabs,n,kappa,QY2,EC3);

% calculate FRET efficiencies
E12 = (R0_12*r13)^6/((R0_12*r13)^6 + (R0_13*r12)^6 + (r12*r13)^6);
E13 = (R0_13*r12)^6/((R0_13*r12)^6 + (R0_12*r13)^6 + (r12*r13)^6);
E23 = R0_23^6/(R0_23^6 + r23^6);

% calculations for fluorophores in the complex
% ---------------------------------------------
% emission factors for F1
% -----------------------
% when excited by laser1 (->I11)

% QY1*laserint1*A11 -> fluorescence following direct excitation
% *(1-E12-E13) -> fluorescence fraction lost due to FRET from 1->2 and 2->3
I11=QY1*laserint1*A11*(1-E12-E13);

% emission factors for F2
% -----------------------
% when excited by laser1 (->I12)

% QY2*laserint1*A11*E12 -> fluorescence of F2 due to FRET from 1->2
```

```
% *(1-E23) -> fluorescence fraction lost due to FRET 2->3
% + QY2*laserint1*A12 -> fluorescence of F2 due to cross-excitation
% *(1-E23) -> fluorescence fraction lost due to FRET 2->3 (from cross-exc.)
I12=QY2*laserint1*A11*E12*(1-E23)+QY2*laserint1*A12*(1-E23);

% when excited by laser2 (->I22)
% QY2*laserint2*A22 -> fluorescence following direct excitation
% *(1-E23) -> lost fraction due to FRET from 2->3
I22=QY2*laserint2*A22*(1-E23);

% emission factors for F3
% ----------------------
% when excited by laser1 (->I13)

% QY3*laserint1*A11*E13 -> fluorescence of F3 due to FRET from 1->3
% +QY3*laserint1*A11*E12*E23 -> FRET from 1->2->3
% +QY3*laserint1*A12*E23 -> FRET from 2->3 (via cross-excited F2)
% +QY3*laserint1*A13 -> cross-excitation
I13=QY3*laserint1*A11*E13+QY3*laserint1*A11*E12*E23+QY3*laserint1*A12*E23+Q
Y3*laserint1*A13;

% when excited by laser2 (->I23)

% QY3*laserint2*A22*E23 -> fluorescence of F3 due to FRET from 2->3
% +QY3*laserint2*A23 -> fluorescence of F3 due to cross-excitation
I23=QY3*laserint2*A22*E23+QY3*laserint2*A23;

% when excited by laser3 (->I33), -> direct excitation of F3
I33=QY3*laserint3*A33;


% calculations for free fluorophores (++++++++++++doesn't work!!!++++++++++)
% will be changes in a future version
% these could also be included in the calculations for fluorophores in the
% complex as fractional amounts (unbound/bound ratios). However, for better
% readability, the emission of free fluorophores will be calculated
% separately.
%-------------------------------------------

% normalize the ratios to the smallest protein concentration. Subtract 1,
% then c contains the free fluorophore fractions
c=[c1 c2 c3]/min([c1 c2 c3])-1;

% emission factors for free F1
% laser1
I11free = QY1*laserint1*A11*c(1);
% emission factors for free F2
% laser1 (cross-exc.)
I12free = QY2*laserint1*A12*c(2);
% laser2 (direct exc.)
I22free = QY2*laserint2*A22*c(2);
% emission factors for free F3
% laser1 (cross-exc.)
I13free = QY3*laserint1*A13*c(3);
% laser2 (cross-exc.)
I23free = QY3*laserint2*A23*c(3);
% laser3 (direct exc.)
I33free = QY3*laserint3*A33*c(3);
```

```
% spectra addition
% ----------------
% find smallest/largest wavelength
minwave=min(vertcat(CFPem(:,1),YFPem(:,1),RFPem(:,1)));
maxwave=max(vertcat(CFPem(:,1),YFPem(:,1),RFPem(:,1)));

% wavelength scale for all spectra
sumspec=(minwave:1:maxwave)';
sumspec(:,2:5)=0;

% find wavelength indices for CFP and position into sumspec
CFP_waveindstart=find(CFPem(1,1)==sumspec(:,1));
CFP_waveindend=find(CFPem(end,1)==sumspec(:,1));
sumspec(CFP_waveindstart:CFP_waveindend,2)=CFPem_norm(:,2);

% find wavelength indices for YFP and position into sumspec
YFP_waveindstart=find(YFPem(1,1)==sumspec(:,1));
YFP_waveindend=find(YFPem(end,1)==sumspec(:,1));
sumspec(YFP_waveindstart:YFP_waveindend,3)=YFPem_norm(:,2);

% find wavelength indices for RFP and position into sumspec
RFP_waveindstart=find(RFPem(1,1)==sumspec(:,1));
RFP_waveindend=find(RFPem(end,1)==sumspec(:,1));
sumspec(RFP_waveindstart:RFP_waveindend,4)=RFPem_norm(:,2);

% duplicate for each laser excitation wavelength
[sumspec1, sumspec2, sumspec3] = deal(sumspec);

% multiply each column with corresponding emission factor and
% sum up in 5th column
sumspec1(:,2:4)=sumspec1(:,2:4).*[I11+I11free I12+I12free I13+I13free];
sumspec1(:,5)=sum(sumspec1(:,2:4),2);

sumspec2(:,2:4)=sumspec2(:,2:4).*[0 I22+I22free I23+I23free];
sumspec2(:,5)=sum(sumspec2(:,2:4),2);

sumspec3(:,2:4)=sumspec3(:,2:4).*[0 0 I33+I33free];
sumspec3(:,5)=sum(sumspec3(:,2:4),2);

% add everything up, restore wavelength scale
sumspec_all=sumspec1+sumspec2+sumspec3;
sumspec_all(:,1)=sumspec(:,1);

% correct for detector sensitivity
% first interpolate QE_det to wavelength scale
QE_det_vector=interp1(QE_det(:,1),QE_det(:,2),sumspec(:,1));
sumspec_all(:,2:4)=sumspec_all(:,2:4).*QE_det_vector;

% find emission intensity per BP (channel)
CFP_BPstartind=find(sumspec(:,1)==BP1(1));
CFP_BPendind=find(sumspec(:,1)==BP1(2));
CFP_channelint=trapz(sumspec(CFP_BPstartind:CFP_BPendind,1),sumspec_all(CFP
_BPstartind:CFP_BPendind,5));

YFP_BPstartind=find(sumspec(:,1)==BP2(1));
YFP_BPendind=find(sumspec(:,1)==BP2(2));
YFP_channelint=trapz(sumspec(YFP_BPstartind:YFP_BPendind,1),sumspec_all(YFP
_BPstartind:YFP_BPendind,5));
```

```
RFP_BPstartind=find(sumspec(:,1)==BP3(1));
RFP_BPendind=find(sumspec(:,1)==BP3(2));
RFP_channelint=trapz(sumspec(RFP_BPstartind:RFP_BPendind,1),sumspec_all(RFP
_BPstartind:RFP_BPendind,5));

% normalize intensity factors
int_factors=[CFP_channelint, YFP_channelint,
RFP_channelint]/max([CFP_channelint, YFP_channelint, RFP_channelint]);

raw_image=rescale(raw_image);
rgb=zeros(200,200,3);

close all;
fig=figure;
fig.Units='normalized';
fig.OuterPosition=[0.5 0.5 0.5 0.5];
fig.MenuBar='none';
fig.ToolBar='none';
fig.NumberTitle='off';
fig.Name='tripleFRET simulation';

subplot(2,3,1);
image_CFP=rgb;
image_CFP(:,:,2)=raw_image;
image_CFP(:,:,3)=raw_image;
image(image_CFP*int_factors(1));
axis image;
axis off;
title('CFP channel')

subplot(2,3,2);
image_YFP=rgb;
image_YFP(:,:,1)=raw_image;
image_YFP(:,:,2)=raw_image;
image(image_YFP*int_factors(2));
axis image;
axis off;
title('YFP channel')

subplot(2,3,3);
image_RFP=rgb;
image_RFP(:,:,1)=raw_image;
image(image_RFP*int_factors(3));
axis image;
axis off;
title('RFP channel')


subplot(2,3,[4,5,6])
EdgeColor_list = {'c', 'y', 'r', 'k'};
FaceColor_list = {'c', 'y', 'r', 'none'};
LineWidth_list = [1 1 1 2];

hold on
% areas for emission spectra
for i = 1:4
    area(sumspec_all(:,1),sumspec_all(:,i+1),...
        'EdgeColor','none',...
        'FaceColor',FaceColor_list{i},...
        'FaceAlpha',0.3)
```

```
end

% plot positions of emission filters
ylimits = ylim;
BPs=horzcat(BP1,BP2,BP3);

BPcolors={'c--','c--','y--','y--','r--','r--'};
for i = 1:6
   plot([BPs(i) BPs(i)],ylimits,BPcolors{i},'LineWidth',2);
end

% plot lines for emission spectra
for i = 1:4
    plot(sumspec_all(:,1),sumspec_all(:,i+1),...
        'Color',EdgeColor_list{i},...
        'LineWidth',LineWidth_list(i));
end

xlabel('wavelength (nm)')
ylabel('intensity (a.u.)')
xlim(x_plotrange)
hold off

end

function R0 = calculateR0(don_spec,acc_spec,n,kappa,QY,epsilon)

            % get axis limits from both spectra
            lims=[min(don_spec(:,1)) max(don_spec(:,1)) min(acc_spec(:,1))
max(acc_spec(:,1))];
            % create new x_axis for merged spectra
            new_spec=(min(lims):max(lims))';
            % find positions for donor and put it into the second column
            pos_don_start=find(new_spec==lims(1));
            pos_don_end=find(new_spec==lims(2));
            new_spec(pos_don_start:pos_don_end,2)=don_spec(:,2);
            % find position for acceptor and put it into the third column
            pos_acc_start=find(new_spec==lims(3));
            pos_acc_end=find(new_spec==lims(4));
            new_spec(pos_acc_start:pos_acc_end,3)=acc_spec(:,2);

            % calculate cumulative normalization factor
            F=sum(new_spec(:,2));

            % calculate spectral overlap integrand
            J=(new_spec(:,1).^4).*epsilon.*new_spec(:,2).*new_spec(:,3)./F;

            % sum up for integral
            J=sum(J);

            % calculate R0
            R0 = 0.02108*((kappa*(n^-4)*QY*J)^(1/6));

        End

%command:
tripleFRET_sim_NG(TRQabs,TRQem,VENabs,VENem,RFPabs,RFPem,raw_image,QEdetuse
)
```

Supp. Material 3B

Change in Matlab script (3.) to account for different fluorophore ratios:

```
% relative ratio of fluorophores to each other
% e.g. 1:2:1  or 1:5:1
% Attention: simple multiplication of absorption - nowhere else implemented
k1=1;
k2=5;
k3=1;

% absorption factors for all relevant wavelengths
% e.g. A12: absorption factor of fluorophore 2 at excitation wavelength 1
% missing combinations are assumed to be not absorbing
% (e.g. CFP does not absorb at the excitation wavelength for RFP)
A11=k1*EC1*CFPabs(CFPabs(:,1)==laser1, 2);
A12=k2*EC2*YFPabs(YFPabs(:,1)==laser1, 2);
A13=k3*EC3*RFPabs(RFPabs(:,1)==laser1, 2);
A22=k2*EC2*YFPabs(YFPabs(:,1)==laser2, 2);
A23=k3*EC3*RFPabs(RFPabs(:,1)==laser2, 2);
A33=k3*EC3*RFPabs(RFPabs(:,1)==laser3, 2);
```

Supp. Material 4

Cross-talk during imaging

Cross-talk in the form of spectral bleed through (bt) and cross-excitation (ce) was present for our fluorophores. To account for this, the bt and ce was assessed from normalized absorption and emission spectra and quantified by imaging single-fluorophore expressing *N. benthamiana* plants.

Excitation at 458 nm lead to a relative absorption of 91% for mTRQ2 and a cross-excitation of 8% for mVEN and 3% for mRFP (Fig. 1A purple, vertical line). Excitation at 514 nm for mVEN yielded a relative absorption of 99% and a cross-excitation of mRFP of 20% (Fig. 1A green line). mRFP was excited with 561 nm with a relative absorption of 61% (Fig. 1A orange line). Spectral bleed-through was present from mTRQ2 to mVEN and from mVEN to mRFP: When detecting mVEN with a bandwidth from 525 to 565 nm, 35% of the signal originates from mTRQ2 (SI Fig. 2, SI Table 2) [For SI Table 2, see next page]]. Detection of mRFP between 605 and 650 nm included 6% of mVEN emission (SI Fig. 2, SI Table 2). When quantifying the FI, also the molecular brightness of a fluorophore, detection settings such as detector gain and laser strength are influencing the amount of bleed-through and cross-talk. Thus, we calculated the coefficients from imaging single-labelled samples with sequential excitation (SI Table 2). Measured bt and ce from mTRQ2 to the yellow and red channel

was higher than calculated, as higher laser settings were used to excite mTRQ2. Measured ce from mVEN to the red channel was in the same order of magnitude as calculated. As the molecular brightness of mVEN is relatively high (SI Table 1), the bt to the red channel was higher than calculated (SI Table 2), even with reduced laser power for 514 nm compared to the 458 nm and 561 nm laser lines (see Material and methods).

SI Table 2 Coeffiecients for spectral bleed-through (bt) and cross-excitation (ce) with standard error (SE) for relevant laser lines was both measured in images when only relevant fluorophore was expressed (D:A_1:A_2) and additionally calculated based on normalized spectra.

	bleed-through (bt)			cross-excitation (ce)		
	1 » 2	1 » 3	2 » 3	1 » 2	1 » 3	2 » 3
Average $\frac{false}{true}$ signal	0.41	0.04	0.14	0.11	0.03	0.16
SE	0.01	0.001	0.02	0.01	0.01	0.01
Ratio D:A1:A2	1:0:0	1:0:0	0:1:0	0:1:0	0:0:1	0:0:1
Excitation laser [nm]	458	458	514	458	458	514
Calculated $\frac{false}{true}$ signal	0.35	0.01	0.06	0.08	0.03	0.2

Supp. Material 5

Matlabscript for interpolation:

```
function spectrum = interpol_spec(input,steps,normalization)
% INTERPOL_SPEC interpolates spectra
%   input: matrix of two columns - wavelength, intensity data
%   steps: desired distance of wavelength values
%   normalization: 1 for normalization (default), 0 otherwise

x=input(:,1);
y=input(:,2);

if normalization==0
    normy=y;
else
    normy=mat2gray(y);
end

rnd_minx=round(x(1));
rnd_maxx=round(x(end));

xq=rnd_minx:steps:rnd_maxx;
yq=interp1(x,normy,xq','spline');

spectrum=[xq' yq];

end

% command: spectrum = interpol_spec(filename,1,1)
```

Supp. Material 6

Matlabscript for spectral unmixing

```
function [ ratios ] = unmix_tripleFRET(spec,CFP,YFP,RFP)
% unmix_tripleFRET linear combination of original fluorescence data
%   Being provided with the original spectra of CFP, YFP, RFP (first column
%   wavelength, second column emission intensity), this program tries to
%   find a linear combination of these three spectra to calculate the
%   relative ratios of the components in a measured spectrum (spec).
%   The component spectra CFP,YFP,RFP will be interpolated and area
%   normalized.
%   results vector:
%   ratios(peak intensities), ratios(areas), area(rawdata),
area(fitspectrum)
%

% Get wavelengths of the component spectra & look for maxima
% ---------------------------------------------------------------------
wave_spec=spec(:,1);
int_spec=spec(:,2);
wave1=CFP(:,1);
wave2=YFP(:,1);
wave3=RFP(:,1);
comp1=CFP(:,2);
comp2=YFP(:,2);
comp3=RFP(:,2);

% component maxima
[~,I(1)]=max(comp1);
[~,I(2)]=max(comp2);
[~,I(3)]=max(comp3);

% get the wavelengths
comp1_maxwave=wave1(I(1));
comp2_maxwave=wave2(I(2));
comp3_maxwave=wave3(I(3));

% wavelength window in which to search for the exact maximum
width=20;

% get row indices when the windows start and end.
[~,comp1_start]=min(abs(wave_spec-round(comp1_maxwave-0.5*width)));
[~,comp1_end]=min(abs(wave_spec-round(comp1_maxwave+0.5*width)));
[~,comp2_start]=min(abs(wave_spec-round(comp2_maxwave-0.5*width)));
[~,comp2_end]=min(abs(wave_spec-round(comp2_maxwave+0.5*width)));
[~,comp3_start]=min(abs(wave_spec-round(comp3_maxwave-0.5*width)));
[~,comp3_end]=min(abs(wave_spec-round(comp3_maxwave+0.5*width)));

% shift and interpolation of the component spectra
%---------------------------------------------------------

% search for the maxima (row indices) in measured spectrum after some
% smoothing.
checkmax = sgolayfilt(int_spec,7,33);
[~,J1]=max(checkmax(comp1_start:comp1_end));
[~,J2]=max(checkmax(comp2_start:comp2_end));
[~,J3]=max(checkmax(comp3_start:comp3_end));

% translate to wavelengths
spec_maxwave1=wave_spec(J1+comp1_start);
```

```
spec_maxwave2=wave_spec(J2+comp2_start);
spec_maxwave3=wave_spec(J3+comp3_start);

% this results in the shift of the components (in nm)
shift1=spec_maxwave1-comp1_maxwave;
shift2=spec_maxwave2-comp2_maxwave;
shift3=spec_maxwave3-comp3_maxwave;

% Interpolation of the components to the same wavelength scale as the
% measured data, also shift them. Replace NaN with 0.
shifted_comps(:,1)=interp1(wave1,comp1,wave_spec-shift1);
shifted_comps(:,2)=interp1(wave2,comp2,wave_spec-shift2);
shifted_comps(:,3)=interp1(wave3,comp3,wave_spec-shift3);
shifted_comps(isnan(shifted_comps))=0;

% area normalization of the component spectra
A(1)=trapz(wave_spec,shifted_comps(:,1));
A(2)=trapz(wave_spec,shifted_comps(:,2));
A(3)=trapz(wave_spec,shifted_comps(:,3));
shifted_comps(:,1)=shifted_comps(:,1)/A(1);
shifted_comps(:,2)=shifted_comps(:,2)/A(2);
shifted_comps(:,3)=shifted_comps(:,3)/A(3);

% weight and background
%-----------------------------------------------------------------

% create weight vectors (regions with less fluorescence - i.e. worse s/n -
% are considered less in the fit).
% To reduce outliers, the spectra will be smoothed significantly for this.
smoothspec=sgolayfilt(int_spec,7,151);
weight=zeros(size(int_spec));

for i = 1:size(int_spec,2)
weight(:,i) = mat2gray(smoothspec(:,i));
end

% the background (vector of constants) can be included as an additional
% component, this sometimes leads to better fits. If it is only a minor
% contribution or was subtracted before, replace "ones" with "zeros". The
% matrix will be "rank deficient" (but this does not change the results).
% The warning will be suppressed anyway.

comps_final=[zeros(size(wave_spec)) shifted_comps];
%comps_final=[ones(size(wave_spec)) shifted_comps];
warning('off','MATLAB:rankDeficientMatrix');

% Calculation of the components' contribution to the spectrum (unmixing)
%-----------------------------------------------------------------

% Pre-allocation of the results vector
ratios = zeros(size(int_spec,2),8);

% erste Spalte laufende Nummer
ratios(:,1)=(1:(size(int_spec,2)))';

for i=1:size(int_spec,2)
    % weight is multiplied with each column. Without it, the formula would
    % just be C=comps_final\spec
```

```
    %c=([weight(:,i) weight(:,i) weight(:,i) weight(:,i)] .*
comps_final)\(int_spec(:,i) .* weight(:,i));
    c=lsqnonneg([weight(:,i) weight(:,i) weight(:,i) weight(:,i)] .*
comps_final,int_spec(:,i) .* weight(:,i));

    % to refine the results, the fit spectrum is defined as a new
    % weight factor
    weight(:,i)=mat2gray(comps_final*c);

    % re-calculation
    % c=([weight(:,i) weight(:,i) weight(:,i) weight(:,i)] .*
comps_final)\(int_spec(:,i) .* weight(:,i));
     c=lsqnonneg([weight(:,i) weight(:,i) weight(:,i) weight(:,i)] .*
comps_final,int_spec(:,i) .* weight(:,i));

% CFP/YFP/RFP ratios and intensities
% ------------------------------------------------------------

    % via max intensities of the measured spectra
    Imax1=max(spec(comp1_start:comp1_end,i+1));
    Imax2=max(spec(comp2_start:comp2_end,i+1));
    Imax3=max(spec(comp3_start:comp3_end,i+1));
    ratio_int=[Imax1 Imax2 Imax3]/(Imax1+Imax2+Imax3);

    % overall intensity of the measured spectrum
    int_total1 = trapz(wave_spec,spec(:,i+1));

    % via unmixing
    ratio_comp=[c(2) c(3) c(4)]/(c(2)+c(3)+c(4));

    % overall intensity of the fit spectrum
    int_total2 = trapz(wave_spec,[ones(size(wave_spec)) shifted_comps]*c);

% results vector
% ------------------------------------------------------------
    ratios(i,:) = [ratio_int ratio_comp int_total1 int_total2];
end

% if input was only one measured spectrum, then show plot
if size(ratios,1)==1
    plot(spec(:,1),spec(:,2));
    hold on; plot(spec(:,1),[ones(size(wave_spec)) shifted_comps]*c);
    plot(spec(:,1),comps_final(:,2:4).*c(2:4)');
end

warning('on','MATLAB:rankDeficientMatrix');

end

% command: [ ratios ] =
unmix_tripleFRET(Interpolatedspectra,TRQem,VENem,mRFP1em)
```

Supp. Material 7

Expression ratios of fluorescence lifetime measurements

As the fluorescence intensities were quantified with the simultaneous excitation of all fluorophores, the background levels due to cross-excitation (ce) and bleed through (bt) of control samples were coloured in grey (SI Fig. 6A-C). For example, when comparing the ratio between mTRQ2 and mVEN (SI Fig. 6A), all samples not expressing mVEN were control samples (RLP44–, RLP44––BAK1, RLP44––BRI1, RLP44––FLS2). The fluorescence intensity was taken as estimation on expression level.

The ratio between RLP44 and BRI1 was not altered significantly between co-expression of RLP44–BRI1, RLP44–BRI1–BAK1 and RLP44–BRI1–FLS2 (SI Fig. 6A). There was a tendency of reduced BRI1 expression when FLS2 was co-expressed (SI Fig. 6A), even reaching into levels in which BRI1 was not expressed (SI Fig. 6A *grey shade*). Only the ratio of RLP44 to BAK1 (in RLP44–BRI1–BAK1) was significantly lower compared to that of RLP44 to FLS44 (in RLP44–BRI1–FLS2) (SI Fig. 6B *red star*). Or in other words, only FLS2 was significantly less abundant in triple-coexpressions than BAK1 ($p<0.01$) (SI Fig. 6B). The ratio between BRI1 and BAK1 (in RLP44–BRI1–BAK1) was not significantly different to that of BRI1 and FLS2 (in RLP44–BRI1–FLS2) (SI Fig. 6C). There was a tendency, though, of reduced FLS2 expression level SI Fig. 6C).

Supp. Material 8

Primer list

GOI – vector	Forward primer 5‘ » 3‘	Reverse primer 5‘ » 3‘
RLP44 - pDONR221-P3P2	GGGGACAACTTTGTATAATAAAGTTGtaATGACAAGGAGTCACCGGTTAC	GGGGACCACTTTGTACAAGAAAGCTGGGTtGTAATCAGGCATAGATTGAC
BRI1 - pDONR221-P1P4	GGGGACAAGTTTGTACAAAAAAGCAGGCTtaATGAAGACTTTTTCAAGCTTCTT	GGGGACAACTTTGTATAGAAAAGTTGGGTGTAATTTTCCTTCAGGAACTTCTT
FLS2 - pDONR221-P1P4	GGGGACAAGTTTGTACAAAAAAGCAGGCTtaATGAAGTTACTCTCAAAGAC	GGGGACAACTTTGTATAGAAAAGTTGGGTGAACTTCTCGATCCTCGTTACG
FLS2 - pDONR207	GGGGACAAGTTTGTACAAAAAAGCAGGCTtaATGAAGTTACT	GGGGACCACTTTGTACAAGAAAGCTGGGTgAACTTCTCGATCCT

References

Balleza, E., Kim, J.M., and Cluzel, P. (2018). Systematic characterization of maturation time of fluorescent proteins in living cells. Nature Methods *15*, 47-51.

Campbell, R.E., Tour, O., Palmer, A.E., Steinbach, P.A., Baird, G.S., Zacharias, D.A., and Tsien, R.Y. (2002). A monomeric red fluorescent protein. Proceedings of the National Academy of Sciences of the United States of America *99*, 7877-7882.

Cranfill, P.J., Sell, B.R., Baird, M.A., Allen, J.R., Lavagnino, Z., Gruiter, H.M. de, Kremers, G.-J., Davidson, M.W., Ustione, A., and Piston, D.W. (2016). Quantitative assessment of fluorescent proteins. Nature Methods *13*, 557-562.

Goedhart, J., Stetten, D.v., Noirclerc-Savoye, M., Lelimousin, M., Joosen, L., Hink, M.A., van Weeren, L., Jr, T.W.J.G., and Royant, A. (2012). Structure-guided evolution of cyan fluorescent proteins towards a quantum yield of 93%. Nature Communications *3*, 751.

Kremers, G.-J., Goedhart, J., van Munster, E.B., and Gadella, T.W.J., JR (2006). Cyan and yellow super fluorescent proteins with improved brightness, protein folding, and FRET Forster radius. Biochemistry *45*, 6570-6580.

Scott, B.L., and Hoppe, A.D. (2015). Optimizing fluorescent protein trios for 3-Way FRET imaging of protein interactions in living cells. Scientific Reports *5*, 10270 EP -.

A.1.4 Novel BRI1^{cnu4} reveals BR-dependent and independent functions

A novel mutant allele uncouples brassinosteroid-dependent and independent functions of BRI1

Submitted

This article describes a novel mutation in the brassinosteroid (BR) receptor BRI1. It was found in a screen for mutants that do not perceive information of cell wall damage and was thus named *comfortably numb 4* (*bri1^{cnu4}*). The cnu4 mutation changes glycin to serine in the first leucin rich repeat in the extracellular domain of BRI1. The *bri1^{cnu4}* mutant is mildly impaired in canonical brassinosteroid signalling and shows a defect in the vasculature development. The BRI1^{cnu4} protein shows increased interaction with RLP44. The increase in interaction does not affect canonical brassinosteroid signalling, but keeps RLP44 from performing its function during vasculature development. This can mechanistically explain the semi-domint ectopic xylem in the position of the procambium and the recessive reduction in BR signalling strength.

Short Title: Dissecting non-canonical functions of BRI1

Author for contact: Sebastian Wolf

A novel mutant allele uncouples brassinosteroid-dependent and independent functions of BRI1

Eleonore Holzwart[1], Nina Glöckner[2], Herman Höfte[3], Klaus Harter[2], and Sebastian Wolf[1]

Footnotes

Author Affiliations

[1]Department of Cell Biology, Centre for Organismal Studies Heidelberg, Heidelberg University, Im Neuenheimer Feld 230, 69120 Heidelberg, Germany

[2]Plant Physiology, Center for Plant Molecular Biology, Universität Tübingen, Auf der Morgenstelle 32, 72076 Tübingen, Germany

[3]Institut Jean-Pierre Bourgin, INRA, AgroParisTech, CNRS, Université Paris-Saclay, 78000 Versailles, France

Author contribution:

E.H. and N.G. performed experiments. E.H., N.G., and S.W. analysed data. H.H., K.H. and S.W. conceived and supervised research. S.W. agrees to serve as the author responsible for contact and ensures communication.

One sentence summary:

A novel mutant allows to dissect brassinosteroid signalling related and non-canonical functions of the receptor-like kinase BRI1.

Abstract

Plants depend on an array of cell surface receptors to integrate extracellular signals with developmental programs. One of the best-studied receptors is BRASSINOSTEROID INSENSITIVE 1 (BRI1), which upon binding of its hormone ligands forms a complex with shape-complimentary co-receptors and initiates a signal transduction cascade leading to a wide range of responses. BR biosynthetic and receptor mutants have similar growth defects on the macroscopic level, which had initially led to the assumption of a largely linear signalling pathway. However, recent evidence suggests that BR signalling is interconnected with a number of other pathways through a variety of different mechanisms. We recently described that feedback information from the cell wall is integrated at the level of the receptor complex through interaction with RLP44. Moreover, BRI1 is required for a second function of RLP44, the control of procambial cell fate. Here, we report on a *BRI1* mutant, *bri1*^{cnu4}, which differentially affects canonical BR signalling and RLP44 function in the vasculature. While BR signalling is only mildly impaired, *bri1*^{cnu4} mutants show ectopic xylem in the position of procambium. Mechanistically, this is explained by an increased association of RLP44 and the mutated BRI1 protein, which prevents the former from acting in vascular cell fate maintenance. Consistent with this, the mild BR response phenotype of *bri1*^{cnu4} is a recessive trait, whereas the RLP44-mediated xylem phenotype is semi-dominant. Our results highlight the complexity of plant plasma membrane receptor function and provide a tool to dissect BR signalling-related roles of BRI1 from its non-canonical functions.

Introduction

Plant cells perceive a multitude of extracellular signals through a battery of plasma membrane-bound receptors that are crucial for the integration of environmental and developmental signals. The response to the growth-regulatory brassinosteroid (BR) phytohormones is mediated by one of the best-characterized plant signalling pathways (Singh and Savaldi-Goldstein, 2015) initiated by a receptor complex containing the leucine-rich repeat receptor-like kinase BRASSINOSTEROID INSENSITIVE 1 (BRI1) (Li and Chory, 1997) and its co-receptors of the SOMATIC EMBRYOGENESIS RECEPTOR-LIKE KINASE (SERK) family (Ma *et al.*, 2016, Hohmann *et al.*, 2017). Binding of the brassinosteroid ligand mediates hetero-dimerization of BRI1 and SERK family members such as BRI1-ASSOCIATED RECEPTOR KINASE 1 (BAK1) (Li *et al.*, 2002, Nam and Li, 2002), which in turn triggers extensive auto- and trans-phosphorylation of the intracellular BAK1 and BRI1 kinase domains (Hohmann *et al.*, 2017). The activated kinases recruit and activate downstream BR signalling components, which eventually leads to vast changes in gene expression mediated by BR signalling-regulated transcription factors such as BRASSINAZOLE-RESISTANT 1 (BZR1) (Wang *et al.*, 2002) and BRI1-EMS-SUPPRESSOR 1 (BES1) (Yin *et al.*, 2002). Among the transcriptional targets of these transcription factors, cell wall related genes are strongly overrepresented, consistent with a growth-regulatory function of BR signalling (Sun *et al.*, 2010, Yu *et al.*, 2011, Chaiwanon and Wang, 2015). Recently, we reported that the state of the cell wall is connected to BR signalling through a feedback mechanism mediated by the RECEPTOR-LIKE PROTEIN 44 (RLP44). Plants in which the activity of the important cell wall modifying enzyme PECTIN METHYLESTERASE (PME) is impaired through ectopic expression of a PME inhibitor protein (PMEIox), BR signalling is activated in a compensatory response that includes transcriptional upregulation of PMEs to prevent cell (wall) rupture (Wolf *et al.*, 2012). RLP44 is sufficient to activate BR signalling, likely by acting as a scaffold to promote association of BRI1 and BAK1 (Wolf *et al.*, 2014), and this interaction is not affected by increasing BR levels. Thus, information from the cell wall is integrated with BR signalling activity at the level of the plasma membrane. Furthermore, RLP44 is under transcriptional control of BRI1 and is able to promote activity of a second LRR-RLK complex, containing the receptor for the phytosulfokine (PSK) peptide, PSK RECEPTOR 1 (PSKR1), through the same scaffolding mechanism as observed for the activation of BR signalling (Holzwart *et al.*, 2018). As a result, both BRI1 and RLP44 are required for full functionality of PSK signalling in the vasculature, demonstrated by the observation that *bri1* null mutants, *rlp44* mutants, and PSK-related mutants share the same vascular phenotype in the primary Arabidopsis root: ectopic xylem cells in the position of the procambium (Holzwart *et al.*, 2018). Interestingly, hypomorphic mutants of BRI1 with intermediate growth phenotypes and BR biosynthetic mutants with strong growth phenotypes

show wild type-like xylem, suggesting that BRI1's role in BR signalling is independent from its role in procambial maintenance. Here, we further dissect BRI1 function through the characterization of a novel *bri1* allele, which is only marginally affected in canonical BR signalling, but strongly affected in RLP44-mediated control of procambial cell fate. These observations demonstrate that the function of BRI1 in BR signalling can be uncoupled from its emerging additional functions.

Results

Two novel suppressor mutants of PMEIox

We have previously described that plants overexpressing a pectin methylesterase inhibitor protein (PMEIox) show a pleiotropic growth phenotype caused by cell wall feedback signalling. We have used these plants to perform a genetic screen which identified the *comfortably numb (cnu) 1* and *cnu2* suppressor mutants affected in the BR receptor BRI1 (Wolf *et al.*, 2012) and RLP44 (Wolf *et al.*, 2014), respectively. Reduced pectin methylesterase activity in PMEIox leads to a compensatory upregulation of BR signalling, which restores cell wall integrity but causes directional growth phenotypes as a secondary effect (Wolf *et al.*, 2012). RLP44 is required and sufficient for enhancing BR signalling in response to cell wall modification (Wolf *et al.*, 2014), presumably by promoting the interaction between BRI1 and its co-receptor BAK1 (Holzwart *et al.*, 2018). From the *cnu* suppressor screen we identified two new extragenic suppressor mutants, which we called *cnu3* and *cnu4* (Fig. 1A). Similar to *cnu1* and *cnu2*, both *cnu3* and *cnu4* strongly suppressed the macroscopic PMEIox growth phenotype in seedlings, with the exception of a residual root waving phenotype in *cnu3*, as indicated by measurement of the vertical growth index (Grabov *et al.*, 2005) (vertical distance between hypocotyl junction and root tip divided by root length) (Fig 1A). As adult plants, *cnu3* and *cnu4* appeared similar to wild type plants, in contrast to their parental line PMEIox (Fig. 1B). Moreover, *cnu3* and *cnu4* showed suppression of the malformed and short silique phenotype of PMEIox (Fig. 1C). Quantitative real time PCR analysis revealed that transcript levels of the BR signalling marker gene *DWF4* in *cnu3* and *cnu4* is intermediate between Col-0 and PMEIox, suggesting partial suppression of PMEIox-mediated activation of BR signalling (Fig 1D). Consistent with this notion, and similar to the *cnu1* (mutated in *BRI1*) and *cnu2* (mutated in *RLP44*) suppressor mutants, *cnu3* and *cnu4* were more resistant than Col-0 to the depletion of endogenous BR by propiconazole (PPZ) (Hartwig *et al.*, 2012), but showed a relatively normal response to exogenous application of epi-brassinolide (BL), in contrast to the largely insensitive *cnu1* mutant (Fig. 1E).

The *cnu3* and *cnu4* suppressor mutants carry two novel hypomorphic alleles of *bri1*

To gain insight into the relationship of *cnu3*, *cnu4,* and the previously described *rlp44* mutant *cnu2*, we performed allelism tests by crossing the different suppressor mutants with each other. F1 plants resulting from a cross between *cnu3* and *cnu4* showed suppression of PMEIox growth defects (Supplemental Fig. S1), whereas F1 plants generated by crossing with *cnu2* showed the PMEIox phenotype (Supplemental Fig. S1). This suggests that *cnu3* and *cnu4* are mutated in the same gene, which is, however, different from *RLP44*. As we had previously identified a PMEIox suppressor mutation in the BR receptor, we sequenced *BRI1* in the novel mutants. We revealed a mutation in *cnu3* leading to exchange of arginine 769, located in the extracellular membrane-proximal region, to tryptophan (R769W). In *cnu4*, we detected a SNP leading to the exchange of glycine 746, located in the last LRR repeat of the extracellular domain, to serine (G746S) (Fig. 2A). To test whether these variants were causative for the PMEIox suppressor phenotype, we complemented *cnu3* and *cnu4* by expressing GFP-tagged BRI1 under the control of its native 5' regulatory sequences. Transgenic BRI1-GFP expression resulted in restoration of the PMEIox phenotype or even a dwarf phenotype (Supplemental Fig. S2A), presumably because expression of BRI1 in these hypomorphic mutants in the presence of PMEIox-induced cell wall alterations can lead to excessive BRI1 activity detrimental to growth. Consistent with this assumption, our complementation lines were infertile and reminiscent of plants derived from a cross between PMEIox and BRI1 overexpressing plants (Friedrichsen *et al.*, 2000), which also showed extreme dwarfism and were unable to reproduce (Wolf *et al.*, 2012). To characterize the effect of the mutations in the absence of PMEIox-induced cell wall alterations, we crossed *cnu3* and *cnu4* to the Col-0 wild type, and genotyped the F2 population to identify individuals that contained the homozygous *bri1* mutations but had lost the PMEIox transgene. We called those mutants derived from *cnu3* and *cnu4* $bri1^{cnu3}$ and $bri1^{cnu4}$, respectively. In sharp contrast to our previously identified PMEIox-suppressing mutant $bri1^{cnu1}$ (Wolf *et al.*, 2012), both mutants showed relatively normal growth and were not strongly deviating from the wild type with respect to classical BR signalling hallmarks such as fertility, leaf shape, leaf colour, silique length, and marker gene expression (Fig. 2B-D). To assess the capacity of the *bri1* mutants to respond to altered BR levels, we grew seedlings on plates under BR-depleting conditions and externally applied varying concentration of BL. Depletion of BRs by PPZ reduced root length of 5-days-old seedlings to approximately 5 mm in all genotypes. Co-treatment with 0.5 nM BL completely restored Col-0 root length, whereas 1 nM of BL was required to achieve maximal root length in $bri1^{cnu3}$ and $bri1^{cnu4}$ (Fig. 2E). Further increase of BL led to growth depression in WT, and, to slightly lesser degree, in the $bri1^{cnu3}$ and $bri1^{cnu4}$ mutants. Thus, in accordance with the subtle growth phenotype, $bri1^{cnu3}$ and $bri1^{cnu4}$ were only mildly affected in their response to

altered levels of BRs. In contrast, *bri1*^{cnu1} was much less responsive to exogenous BR and did not reach growth depression with the concentrations tested here (up to 10 nM) (Fig. 2E), as reported for other *bri1* hypomorphic alleles of similar strength (Sun *et al.*, 2017). Consistent with the mild growth phenotype, transformation with constructs encoding the two *BRI1* mutant versions alone or a combination of both mutations rescued hypomorphic *bri1-301* and *bri1-null* mutants (Fig 3A, B). The subcellular localization of *pBRI1*-expressed BRI1cnu4-GFP was indistinguishable from *pBRI1*-expressed BRI1-GFP (Fig 3C). Taken together, *bri1*^{cnu3} and *bri1*^{cnu4} are two weak BRI1 mutants with a mild growth phenotype.

We have previously reported that *bri1* null but not *bri1* hypomorphic mutants show ectopic xylem cells in place of procambium in the *Arabidopsis* primary root. BRI1 controls vascular cell fate through a non-canonical, BR signalling-independent pathway acting through RLP44 and PSK signalling (Holzwart *et al.*, 2018). We therefore tested the xylem phenotype in *bri1*^{cnu4}, expecting it would behave like other *bri1* hypomoprphic mutants such as *bri1*^{cnu1}, *bri1-301*, and *bri1-5* (Noguchi *et al.*, 1999, Xu *et al.*, 2008, Wolf *et al.*, 2012, Holzwart *et al.*, 2018). In contrast, *bri1*^{cnu4} showed a strong increase in xylem cell number, comparable with *rlp44* mutants and slightly less pronounced than in *bri1*-null mutants (Fig. 4A) (Holzwart *et al.*, 2018). This clearly distinguishes *bri1*^{cnu4} from other BR-related mutants and suggests that the mutation in the BRI1cnu4 protein has a negative effect on RLP44 function. We reasoned that this could provide valuable insight into the mechanism of xylem cell fate determination by BRI1 and RLP44, concentrating on *bri1*^{cnu4} for the remainder of the study. We tested genetic interaction between *bri1*^{cnu4} and *rlp44*^{cnu2} by generating the double mutant and assessing its xylem phenotype. Simultaneous mutation of *rlp44* did not further enhance the *bri1*^{cnu4} mutant phenotype, suggesting that *bri1*^{cnu4} and *rlp44*^{cnu2} are affected in the same pathway with respect to xylem cell fate (Fig. 4A) Likewise, the subtle growth phenotype of *rlp44*^{cnu2} and *bri1*^{cnu4} was not aggravated in the double mutant (Fig. 4B).

The *bri1*^{cnu4} mutant uncouples BRI1 roles in BR signalling and RLP-mediated control of cell fate

To further test our hypothesis that BRI1cnu4 negatively affects the function of RLP44 we assessed whether the mutation had a dominant effect. We analysed F1 hybrid seedlings derived from a cross of *bri1*^{cnu4} and Col-0, and revealed that the subtle BR insensitivity observed in *bri1*^{cnu4} root growth is a recessive trait (Fig. 5A). In line with this, the morphological phenotype of the F1 hybrids appeared closer to the wild type than to that of plants homozygous for the *bri1*^{cnu4} mutation (Fig. 5B). In addition, plants heterozygous for the *bri1*^{cnu4} mutation were not able to suppress PMEIox-mediated activation of BR signalling (Fig. 5C), indicating that *bri1*^{cnu4} rescues PMEIox in the *cnu4* mutant through reduced BR signalling strength. Intriguingly, despite the recessive nature of its BR signalling defect, the xylem phenotype of

bri1^{cnu4} was clearly dominant in the F1 seedlings, supporting the idea that the mutation might directly or indirectly impair RLP44 function (Fig. 5D). Consistent with this hypothesis, expression of the *BRI1cnu4* transgene in the *bri1-301* hypomorphic mutant recapitulated the *bri1*^{cnu4} phenotype, whereas expression of wild type *BRI1* did not (Fig. 5E). Interestingly, RLP44-mediated activation of BR signalling was not blocked in *bri1*^{cnu4}, as the phenotype of plants overexpressing *RLP44* in the *bri1*^{cnu4} background was intermediate between the overexpressing line and the mutant (Fig. 5F). This is in contrast to what was observed with overexpression of RLP44 in *bri1-null* (Holzwart *et al.*, 2018) and *bri1*^{cnu1}, which harbours a mutation in the kinase domain (Wolf et al., 2014). Moreover, increasing the amount of RLP44 through transgenic expression under control of its own promoter rescued the mild BR response phenotype of *bri1*^{cnu4} (Supplemental Fig. S3), and partially rescued xylem cell number (Fig. 5G).

To understand the mechanism by which BRI1cnu4 negatively affects RLP44 function, we analysed protein-protein interaction. To this end, we compared the association of RLP44 with BRI1 and BRI1cnu4 by immunoprecipitating *RLP44-RFP* in the Col-0 and *bri1*^{cnu4} background, respectively. Interestingly, BRI1cnu4 showed increased abundance in RLP44-containing complexes (Fig. 6A). Furthermore, split-ubiquitin assays in yeast supported stronger direct interaction between BRI1cnu4 and RLP44 as well as between BRI1cnu4 and BAK1 compared to wild type BRI1 (Fig. 6B). Thus, we assume that BRI1cnu4 exerts its effect on the maintenance of xylem cell fate by RLP44 sequestration thereby preventing RLP44 from acting in PSK signalling (Fig 6C).

Discussion

We have previously shown that BRI1 have functions that are independent of classical BR signalling outputs mediated by the canonical BR signalling pathway (Holzwart et al., 2018). Here, we demonstrate that BRI1 mutants, depending on the nature of the allele, differentially affect these functions and can thus serve as a tool to uncouple canonical BR signalling-mediated from non-canonical effects. We isolated a novel *bri1* allele, *bri1*^{cnu4}, and compared its impact on classical BR read-outs and the role of BRI1 in the maintenance of procambial cell fate, which depends on RLP44-mediated activation of PSK signalling (Holzwart *et al.*, 2018). These analyses revealed that BR signalling dependent BRI1 functions are only mildly affected in *bri1*^{cnu4}, whereas we observed a strong negative effect on RLP44 function in the regulation of vascular cell fate. Interestingly, the same mutation we report here as *bri1*^{cnu4}, G746A (G2236A on nucleic acid level) has been recently described as *bri1-711* in a tilling approach to obtain new *bri1* mutants (Sun *et al.*, 2017). Consistent with our results, *bri1-711*

showed subtle growth defects and mild insensitivity to exogenous application of BL. In addition, the accumulation of non-phosphorylated BES1 as a readout of BR signalling was similar to that of the Col-0 WT in response to BL (Sun *et al.*, 2017). In contrast to our results obtained with *bri1*^{cnu4}, other *bri1* hypomorphic mutants such as *bri1-301* and *bri1-5* have negligible effects on xylem cell fate in the root, despite their pronounced effect on BR signalling (Holzwart *et al.*, 2018). A possible explanation for the divergent effect of *bri1*^{cnu4} is provided by the observation that the BRI1cnu4 protein interacts more strongly with RLP44 than with wild type BRI1, and that additional RLP44 alleviates the *bri1*^{cnu4} xylem phenotype. From these observations we propose that BRI1cnu4 may sequester RLP44, which consequentially has a negative effect on PSK signalling. It has to be noted that in yeast mating-based split-ubiquitin system, BRI1cnu4 also shows increased interaction with its co-receptor BAK1, corroborating the complexity of receptor associations in the plasma membrane and the challenges associated with deciphering the multi-lateral interactions observed with many members of the LRR-RLK family (Stegmann *et al.*, 2017, Smakowska-Luzan *et al.*, 2018).

As revealed by the RLP44 interaction pattern, signalling integration and ramification is realised at the level of the receptor complex in the plasma membrane. Additional examples are the interaction of the BRI1-BAK1 complex with G-proteins to mediate sugar-responsive growth (Peng *et al.*, 2018), with the proton pumps of the P-ATPase type to regulate plasma membrane hyperpolarisation and wall swelling that precede cell elongation growth (Caesar *et al.*, 2011) and with the BAK1-interacting receptor-like kinase 3 (BIR3) that represses the activity of the complex in the absence of BR (Großeholz *et al.*, Imkampe *et al.*, 2017, Hohmann *et al.*, 2018)(Imkampe et al., 2017; Hohmann et al., 2018; Großeholz et al., 2019). In addition, BRI1 phosphorylates a homolog of the mammalian TGF-β receptor interacting protein/eIF3 eukaryotic translation initiation factor subunit TRIP-1 (Ehsan *et al.*, 2005). While the function of the latter protein is not completely clear at this stage, it seems at least conceivable that it bypasses the canonical BR signalling pathway, even if the morphological defects observed in plants expressing *TRIP-1* antisense RNA are reminiscent of BR-deficiency phenotypes (Jiang and Clouse, 2001).

The challenges emerging from the recent discoveries on the example of BRI1 is to understand of how distinct responses to extrinsic cues can be generated by the multifaceted network of a receptor in the plasma membrane. Thus, more sophisticated *in vivo* cell biological approaches in combination with genetic and biochemical tools are required to dissect and understand the function of this important signalling integrator, BRI1.

Material and Methods

Plant Material and growth conditions

All mutants and transgenic lines used in this study are in the Col-0 background. The *bri1*^{cnu1}, *rlp44*^{cnu2}, *bri1-null*, and *bri1-301* mutants have been described before (Xu *et al.*, 2008, Wolf *et al.*, 2012, Wolf *et al.*, 2014). The 35S:RLP44-RFP and pRLP44:RLP44-GFP (Wolf *et al.*, 2014, Holzwart *et al.*, 2018) described previously were used for crossing. All plants were grown in half-strength Murashige and Skoog (MS) medium supplemented with 1 % sucrose and 0.9 % plant agar. PPZ and 24-epi-brassinolide were added to the sterilized medium where appropriate.

Plasmid generation

For mating-based split-ubiquitin assay (mbSUS) (Grefen et al., 2009), the coding sequence of RLP44, BAK1 and BRI1 in pDONR207 (Wolf et al., 2014) and were cloned into pMetYC-Dest. For generating the BRI1cnu3 Nub construct, primers BRI1_attB1_L + BRI1_attB2_R were used with gDNA of *bri1*^{cnu3} plants to create the full-length BRI1cnu3 cDNA in pDONR207. For generating the BRI1cnu4 Nub construct, primers BRI1_attB1_L + BRI1_attB2_R were used with gDNA of *bri1*^{cnu4} plants to create the full-length BRI1cnu4 cDNA in pDONR207.All other constructs used in this study were generated with GreenGate cloning as previously described (Lampropoulos et al., 2013). For generating BRI1cnu3,4 Nub construct, primers BRI1_attB1_L + BRI1_attB2_R wree used with the C-Module of BRI1cnu3,4 as a template to create the full-length BRI1cnu3,4 cDNA in pDONR207. The pDONR207 entry modules were recombined with pXNUbA22-Dest. For details regarding primers and constructs please see Supplemental Tables S1 and S2. For BRI1 (at4g39400) CDS GreenGate Cloning, three internal BsaI/Eco31I recognition sites were silently mutagenized via the generation of 4 PCR fragments with the primers BRI1_GGC_1F, BRI1_GGC_1R, BRI1_GGC_2F BRI1_GGC_2R, BRI1_GGC_3F, BRI1_GGC_3R, BRI1_GGC_4F and BRI1_GGC_4R as previously described (Holzwart et al., 2018). For generating the BRI1cnu4 module the second fragment was amplified with BRI1_GGC_2F BRI1_GGC_2R using gDNA of *bri1*^{cnu4} plants as template. For generating the BRI1cnu3 module the second fragment was amplified with BRI1_GGC_3F BRI1_GGC_3R with gDNA of *bri1*^{cnu3} plants. For the combined BRI1-cnu3,4 construtct, fragments 1 and 4 from BRI1 WT were combined with the second fragment of BRI1cnu4 and the third fragment of BRI1cnu3. PCR products of all combinations were gel purified, digested with Eco31I, subsequently ligated and processed according to the GreenGate protocol (Lampropoulos et al., 2013).

Genotyping

Genotyping of *bri1*^{cnu1}, *rlp44*^{cnu2}, *bri1-301*, and *bri1-null* was described previously (Wolf et al., 2012, Wolf et al., 2014, Holzwart et al., 2018). For genotyping of the two new *bri1* alleles, we generated CAPS marker using primers bri1cnu3_CAPS_F, bri1cnu3_CAPS_R and restriction enzyme *Cfr*42I (*bri1*^{cnu3}) or primers bri1cnu4_CAPS_F, bri1cnu4_CAPS_R with restriction enzyme *Bse*LI (*bri1*^{cnu4}).

Mating-based split ubiquitin assays

Yeast-based mbSUS assays were performed as described (Grefen *et al.*, 2009, Wolf *et al.*, 2014).

Co-Immunoprecipitation

Material from transgenic plants expressing 35S:RLP44-RFP was frozen in liwuid nitrogen and ground to a fine powder using mortar and pestle. Extraction buffer (100 mM Tris-HCl (pH 8.0), 150 mM NaCl, 10% (v/v) Glycerol, 5 mM EDTA (Sigma-Aldrich), 2% (v/v) Igepal CA-630 (Sigma-Aldrich), 5 mM DTT (Sigma-Aldrich, added immediately prior to use), 1% (v/v) Protease Inhibitor Cocktail (Bimake, added immediately prior to use) was added to the frozen powder (2 ml per g fresh weight) and the homogenate was centrifuged at 12 000 x g and 4 °C after thawing. The supernatant was incubated with 15 µl of RFP-trap slurry (Chromotek) for 2 hours at 4°C on a rotary shaker. The beads were subsequently washed with extraction buffer 4 times and then boiled in 60 µl 2x SDS-PAGE sample buffer at 95 °C for 5 min. SDS-PAGE, Western Blotting and Immunological detection of RLP44-GFP and BRI1 was performed as described (Holzwart *et al.*, 2018).

Confocal microscopy

GFP, FM4-64, and basic fuchsin fluorescence was analysed on a Leica SP5 microscope system equipped with a 63x water immersion objective using laser lines of 488 nm (GFP), 514 nm (basic fuchsin), and 543 nm (FM4-64). Fluorescence was recorded between 490 and 525 nm for GFP, between 530 and 600 nm for basic fuchsin, and between 600 nm and 720 nm for FM4-64. Images were analysed with Fiji.

Xylem imaging

Basic fuchsin staining of seedling roots was performed as described (Holzwart *et al.*, 2018).

Quantitative Real-Time PCR

Total RNA was extracted from 100 mg of tissue harvested form 5 day old seedlings using the GeneMATRIX Universal RNA Purification Kit (EURx/Roboklon). AMV Reverse Transcriptase Native according the manufacturer's protocol (Roboklon E1372) with RiboLock RNase

Inhibitor (Thermo Fisher Scientific EO0381) was used for generating cDNA. PCR reactions were performed in a Rotor Gene Q 2plex cycler (Qiagen) using 1:40 diluted cDNA template, JumpStart Taq DNA polymerase (Sigma-Aldrich) and SYBR-GreenI (Sigma-Aldrich). Expression of DWF4 was normalized against at5g46630 (see Supplemetary Table S1 for oligonucleotide sequences).

Acknowledgements

The authors would like to thank Michael Hothorn for antiserum against BRI1 and Karin Schumacher for antiserum against RFP. Research in our laboratories was supported by the German Research Foundation (DFG) with grants WO 1660/6-1 (to S.W.), HA2146/22-1 (to K.H.), and CRC 1101-D02 (to K.H.). S.W. acknowledges funding by the DFG through the Emmy Noether Programme grant WO 1660/2. H.H. was financed in part by ANR grant "Pectosign". The authors benefited from the IJPB Plant Observatory facilities. The IJPB benefits from the support of the LabEx Saclay Plant Sciences-SPS (ANR-10-LABX-0040-SPS).

Figure Legends

Figure 1. Identification of the PMEIox suppressor mutants *cnu3* and *cnu4*. **A**, seedling morphology and root vertical growth index (Grabov *et al.*, 2005) of Col-0, PMEIox, the previously published PMEIox suppressor mutants *cnu1* (Wolf *et al.*, 2012) and *cnu2* (Wolf *et al.*, 2014), and the two novel suppressor mutants, *cnu3* and *cnu4*. Letters indicate statistically significant difference according to one-way ANOVA with $p < 0.05$ ($n = 13$). **B**, Adult *cnu3* and *cnu4* mutants resemble wild type plants, in contrast to the PMEIox parental line. **C**, Silique length of Col-0, PMEIox, and the four PMEIox suppressor mutants *cnu1* to *cnu4*. Box plots in (A) indicate interquartile range (box), median (bar) and 1.5x IQR (whiskers), outliers are indicated with a cross, n = 24-36. **D**, qRT-PCR analysis of the BR biosynthetic gene *DWF4* in wild type (Col-0), PMEIox and the *cnu1* to *cnu4* the suppressor mutants. Bars depict average ± S.D., n = 3. E, Root length response of Col-0, PMEIox and the *cnu1* to *cnu4* suppressor mutants to BR depletion by PPZ and exogenous application of BL. Bars depict average ± S.D., n = 19-53.

Figure 2. The *cnu3* and *cnu4* mutants are two novel alleles of *BRI1*. **A**, Schematic view of BRI1 with indicated position and amino acid substitution of the mutations in $bri1^{cnu1}$, $bri1^{cnu3}$ (derived from *cnu3*, but in the absence of the PMEIox transgene), and $bri1^{cnu4}$ (derived from *cnu4*, but in the absence of the PMEIox transgene). **B**, Comparison of adult plant phenotype

of Col-0, *bri1*^{cnu1}, *rlp44*^{cnu2}, *bri1*^{cnu3}, and *bri1*^{cnu4}. **C**, Silique length of Col-0, and the mutants derived from the *cnu1* to *cnu4* suppressor mutants. Box plots indicate interquartile range (box), median (bar) and 1.5x IQR (whiskers), n = 25-36. **D**, qRT-PCR analysis of the BR biosynthetic gene *DWF4* in wild type (Col-0), *bri1*^{cnu1}, *rlp44*^{cnu2}, *bri1*^{cnu3}, and *bri1*^{cnu4}. Bars depict average ± S.D., n = 3. **E**, Root length response of wild type (Col-0), *bri1*^{cnu1}, *bri1*^{cnu3} and *bri1*^{cnu4} to BR depletion by PPZ and exogenous application of BL. Bars depict average ± S.D., n = 34-70.

Figure 3. BRI1cnu4 and BRI1cnu3 proteins are functional. **A**, Mutant BRI1 constructs complement the hypomorphic *bri1-301* mutant. **B**, Constructs encoding mutated BRI1 versions complement the *bri-null* mutant. **C**, GFP fluorescence in root meristems of *bri1 null* mutants complemented with GFP fusion proteins from either the construct pBRI1:BRI1-GFP or pBRI1:BRI1cnu4-GFP, shows no apparent difference in subcellular localization. FM4-64 was used as an endocytic membrane tracer dye. Scale bars = 10 µm.

Figure 4. The mutation in *bri1*^{cnu4} negatively affects RLP44 function. **A**, Frequency of roots with the indicated number of metaxylem cells in Col-0, *rlp44*^{cnu2}, *bri1*^{cnu4}, and the *rlp44*^{cnu2} *bri1*^{cnu4} double mutant. **B**, Morphological phenotype of Col-0, *rlp44*^{cnu2}, *bri1*^{cnu4}, and the *rlp44*^{cnu2} *bri1*^{cnu4} double mutant.

Figure 5. The *bri1*^{cnu4} mutant interferes with RLP44 function. **A**, Root length of 5-d-old F1 hybrid seedlings of a cross between *bri1*^{cnu4} and Col-0 after PPZ treatment and exogenous supply of BL. Bars indicate mean root length of 5-d-old seedlings ± SD (n = 22-49). Asterisks indicate significance with *p < 0.05, **p < 0.01, and ***p < 0.001 as determined by Tukey's test after two-way ANOVA. Note that significance is only indicated for comparisons within each treatment. **B**, Morphological phenotype of Col-0, *bri1*^{cnu4}, and F1 hybrid plants resulting from crossing the two genotypes. **C**, Suppression of PMEI5 overexpression phenotype (PMEIox) by the *bri1*^{cnu4} allele (*cnu4*) is a recessive trait, as indicated by the PMEIox-like phenotype of F1 plants from a cross between *cnu4* and Col-0. **D**, Ectopic xylem phenotype in *bri1*^{cnu4} and F1 plants from a cross between *bri1*^{cnu4} and Col-0. **E**, Expression of BRI1cnu4, but not of wildtype BRI1 in the *bri1-301* mutant results in supernumerary xylem cells. **F**, RLP44 overexpression can partially rescue the morphological phenotype of *bri1*^{cnu4}. **G**, Increased expression of RLP44 can alleviate the *bri1*^{cnu4} phenotype. Asterisks indicate statistically significant difference from Col-0 based on Dunn's post-hoc test with Benjamini-Hochberg correction after Kruskal-Wallis modified U-test (*p < 0.05).

Figure 6. The BRI1cnu4 protein shows increased interaction with RLP44 and BAK1. **A**, Co-immunoprecipitation of BRI1-GFP by RLP44-RFP from crude extracts of wild type (Col-0) and *bri1*^{cnu4} mutant plants. **B**, Mating-based split ubiquitin assays in yeast displaying the interaction of BRI1, BRI1cnu3, BRI1cnu4 and BAK1 with RLP44. **C**, Model of RLP44 interactions with

BRI1 and PSKR1 in the wild type and the *bri1*^{cnu4} mutant. The mutation at the base of BRI1´s extracellular domain sequesters RLP44 and prevents it from promoting PSK/PSKR1 signalling.

Supplemental Figure 1. *cnu3* and *cnu4* are allelic mutants. PMEIox silique morphology (upper panel) and plant stature (lower panel) remain suppressed in F1 plants of a cross between *cnu3* and *cnu4*, whereas F1 plants of a cross between *cnu2* (carrying a mutation in RLP44) and *cnu4* show PMEIox phenotype.

Supplemental Figure 2. Mutant BRI1 constructs complement the *cnu3* and *cnu4* mutant**s**.

Supplemental Figure 3. RLP44 promotes BR response in the *bri1*^{cnu4} mutant. Response of Col-0, pRLP44:RLP44-GFP, *bri1*^{cnu4}, and pRLP44:RLP44-GFP (*bri1*^{cnu4}) to depletion (PPZ) and exogenous supply of brassinosteroids. Bars indicate average relative root length ± S.D. (n =17 - 35).

Supplemental Table S1. Oligonucleotides used in this study

Supplemental Table S2. GreenGate Cloning modules and destination constructs

References

Caesar, K., Elgass, K., Chen, Z., Huppenberger, P., Witthoft, J., Schleifenbaum, F., Blatt, M.R., Oecking, C. and Harter, K. (2011) A fast brassinolide-regulated response pathway in the plasma membrane of Arabidopsis thaliana. *Plant J*, **66**, 528-540.

Chaiwanon, J. and Wang, Z.Y. (2015) Spatiotemporal brassinosteroid signaling and antagonism with auxin pattern stem cell dynamics in Arabidopsis roots. *Curr Biol*, **25**, 1031-1042.

Ehsan, H., Ray, W.K., Phinney, B., Wang, X., Huber, S.C. and Clouse, S.D. (2005) Interaction of Arabidopsis BRASSINOSTEROID-INSENSITIVE 1 receptor kinase with a homolog of mammalian TGF-beta receptor interacting protein. *Plant J*, **43**, 251-261.

Friedrichsen, D.M., Joazeiro, C.A., Li, J., Hunter, T. and Chory, J. (2000) Brassinosteroid-insensitive-1 is a ubiquitously expressed leucine-rich repeat receptor serine/threonine kinase. *Plant Physiol*, **123**, 1247-1256.

Grabov, A., Ashley, M.K., Rigas, S., Hatzopoulos, P., Dolan, L. and Vicente-Agullo, F. (2005) Morphometric analysis of root shape. *New Phytol*, **165**, 641-651.

Grefen, C., Obrdlik, P. and Harter, K. (2009) The determination of protein-protein interactions by the mating-based split-ubiquitin system (mbSUS). *Methods Mol Biol*, **479**, 217-233.

Großeholz, R., Feldman-Salit, A., Wanke, F., Schulze, S., Glöckner, N., Kemmerling, B., Harter, K. and Kummer, U. Specifying the role of BAK1-interacting receptor-like kinase 3 in brassinosteroid signaling. *Journal of integrative plant biology*, **0**.

Hartwig, T., Corvalan, C., Best, N.B., Budka, J.S., Zhu, J.Y., Choe, S. and Schulz, B. (2012) Propiconazole is a specific and accessible brassinosteroid (BR) biosynthesis inhibitor for Arabidopsis and maize. *PLoS One*, **7**, e36625.

Hohmann, U., Lau, K. and Hothorn, M. (2017) The Structural Basis of Ligand Perception and Signal Activation by Receptor Kinases. *Annu Rev Plant Biol*, **68**, 109-137.

Hohmann, U., Nicolet, J., Moretti, A., Hothorn, L.A. and Hothorn, M. (2018) The SERK3 elongated allele defines a role for BIR ectodomains in brassinosteroid signalling. *Nat Plants*, **4**, 345-351.

Holzwart, E., Huerta, A.I., Glockner, N., Garnelo Gomez, B., Wanke, F., Augustin, S., Askani, J.C., Schurholz, A.K., Harter, K. and Wolf, S. (2018) BRI1 controls vascular cell fate in the Arabidopsis root through RLP44 and phytosulfokine signaling. *Proc Natl Acad Sci U S A*, **115**, 11838-11843.

Imkampe, J., Halter, T., Huang, S., Schulze, S., Mazzotta, S., Schmidt, N., Manstretta, R., Postel, S., Wierzba, M., Yang, Y., van Dongen, W., Stahl, M., Zipfel, C., Goshe, M.B., Clouse, S., de Vries, S.C., Tax, F., Wang, X. and Kemmerling, B. (2017) The Arabidopsis Leucine-Rich Repeat Receptor Kinase BIR3 Negatively Regulates BAK1 Receptor Complex Formation and Stabilizes BAK1. *Plant Cell*, **29**, 2285-2303.

Jiang, J. and Clouse, S.D. (2001) Expression of a plant gene with sequence similarity to animal TGF-beta receptor interacting protein is regulated by brassinosteroids and required for normal plant development. *Plant J*, **26**, 35-45.

Lampropoulos, A., Sutikovic, Z., Wenzl, C., Maegele, I., Lohmann, J.U. and Forner, J. (2013) GreenGate---a novel, versatile, and efficient cloning system for plant transgenesis. *PLoS One*, **8**, e83043.

Li, J. and Chory, J. (1997) A putative leucine-rich repeat receptor kinase involved in brassinosteroid signal transduction. *Cell*, **90**, 929-938.

Li, J., Wen, J., Lease, K.A., Doke, J.T., Tax, F.E. and Walker, J.C. (2002) BAK1, an Arabidopsis LRR receptor-like protein kinase, interacts with BRI1 and modulates brassinosteroid signaling. *Cell*, **110**, 213-222.

Ma, X., Xu, G., He, P. and Shan, L. (2016) SERKing Coreceptors for Receptors. *Trends Plant Sci*.

Nam, K.H. and Li, J. (2002) BRI1/BAK1, a receptor kinase pair mediating brassinosteroid signaling. *Cell*, **110**, 203-212.

Noguchi, T., Fujioka, S., Choe, S., Takatsuto, S., Yoshida, S., Yuan, H., Feldmann, K.A. and Tax, F.E. (1999) Brassinosteroid-insensitive dwarf mutants of Arabidopsis accumulate brassinosteroids. *Plant Physiol*, **121**, 743-752.

Peng, Y., Chen, L., Li, S., Zhang, Y., Xu, R., Liu, Z., Liu, W., Kong, J., Huang, X., Wang, Y., Cheng, B., Zheng, L. and Li, Y. (2018) BRI1 and BAK1 interact with G proteins and regulate sugar-responsive growth and development in Arabidopsis. *Nature communications*, **9**, 1522.

Singh, A.P. and Savaldi-Goldstein, S. (2015) Growth control: brassinosteroid activity gets context. *J Exp Bot*, **66**, 1123-1132.

Smakowska-Luzan, E., Mott, G.A., Parys, K., Stegmann, M., Howton, T.C., Layeghifard, M., Neuhold, J., Lehner, A., Kong, J., Grunwald, K., Weinberger, N., Satbhai, S.B., Mayer, D., Busch, W., Madalinski, M., Stolt-Bergner, P., Provart, N.J., Mukhtar, M.S., Zipfel, C., Desveaux, D., Guttman, D.S. and Belkhadir, Y. (2018) An extracellular network of Arabidopsis leucine-rich repeat receptor kinases. *Nature*, **553**, 342-346.

Stegmann, M., Monaghan, J., Smakowska-Luzan, E., Rovenich, H., Lehner, A., Holton, N., Belkhadir, Y. and Zipfel, C. (2017) The receptor kinase FER is a RALF-regulated scaffold controlling plant immune signaling. *Science*, **355**, 287-289.

Sun, C., Yan, K., Han, J.T., Tao, L., Lv, M.H., Shi, T., He, Y.X., Wierzba, M., Tax, F.E. and Li, J. (2017) Scanning for New BRI1 Mutations via TILLING Analysis. *Plant Physiol*, **174**, 1881-1896.

Sun, Y., Fan, X.Y., Cao, D.M., Tang, W., He, K., Zhu, J.Y., He, J.X., Bai, M.Y., Zhu, S., Oh, E., Patil, S., Kim, T.W., Ji, H., Wong, W.H., Rhee, S.Y. and Wang, Z.Y. (2010) Integration of brassinosteroid signal transduction with the transcription network for plant growth regulation in Arabidopsis. *Dev Cell*, **19**, 765-777.

Wang, Z.Y., Nakano, T., Gendron, J., He, J., Chen, M., Vafeados, D., Yang, Y., Fujioka, S., Yoshida, S., Asami, T. and Chory, J. (2002) Nuclear-localized BZR1 mediates brassinosteroid-induced growth and feedback suppression of brassinosteroid biosynthesis. *Dev Cell*, **2**, 505-513.

Wolf, S., Mravec, J., Greiner, S., Mouille, G. and Hofte, H. (2012) Plant cell wall homeostasis is mediated by brassinosteroid feedback signaling. *Curr Biol*, **22**, 1732-1737.

Wolf, S., van der Does, D., Ladwig, F., Sticht, C., Kolbeck, A., Schurholz, A.K., Augustin, S., Keinath, N., Rausch, T., Greiner, S., Schumacher, K., Harter, K., Zipfel, C. and Hofte, H. (2014) A receptor-like protein mediates the response to

pectin modification by activating brassinosteroid signaling. *Proc Natl Acad Sci U S A*, **111**, 15261-15266.

Xu, W., Huang, J., Li, B., Li, J. and Wang, Y. (2008) Is kinase activity essential for biological functions of BRI1? *Cell research*, **18**, 472-478.

Yin, Y., Wang, Z.Y., Mora-Garcia, S., Li, J., Yoshida, S., Asami, T. and Chory, J. (2002) BES1 accumulates in the nucleus in response to brassinosteroids to regulate gene expression and promote stem elongation. *Cell*, **109**, 181-191.

Yu, X., Li, L., Zola, J., Aluru, M., Ye, H., Foudree, A., Guo, H., Anderson, S., Aluru, S., Liu, P., Rodermel, S. and Yin, Y. (2011) A brassinosteroid transcriptional network revealed by genome-wide identification of BESI target genes in Arabidopsis thaliana. *Plant J*, **65**, 634-646.

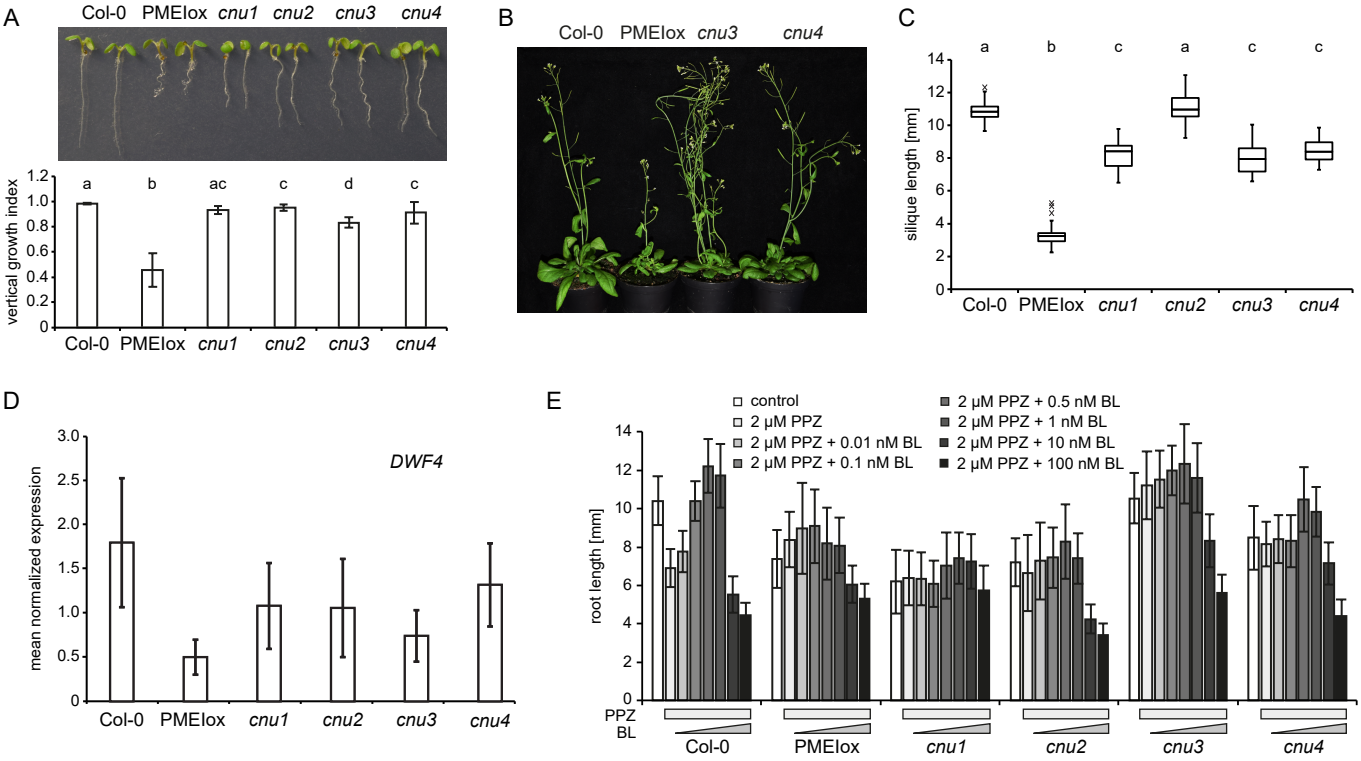

Figure 1. Identification of the PMEIox suppressor mutants *cnu3* and *cnu4*. **A**, seedling morphology and root vertical growth index (Grabov *et al.*, 2005) of Col-0, PMEIox, the previously published PMEIox suppressor mutants *cnu1* (Wolf *et al.*, 2012) and *cnu2* (Wolf *et al.*, 2014), and the two novel suppressor mutants, *cnu3* and *cnu4*. Letters indicate statistically significant difference according to one-way ANOVA with $p < 0.05$ (n = 13). **B**, Adult *cnu3* and *cnu4* mutants resemble wild type plants, in contrast to the PMEIox parental line. **C**, Silique length of Col-0, PMEIox, and the four PMEIox suppressor mutants *cnu1* to *cnu4*. Box plots in (A) indicate interquartile range (box), median (bar) and 1.5x IQR (whiskers), outliers are indicated with a cross, n = 24-36. **D**, qRT-PCR analysis of the BR biosynthetic gene *DWF4* in wild type (Col-0), PMEIox and the *cnu1* to *cnu4* the suppressor mutants. Bars depict average ± S.D., n = 3. E, Root length response of Col-0, PMEIox and the *cnu1* to *cnu4* suppressor mutants to BR depletion by PPZ and exogenous application of BL. Bars depict average ± S.D., n = 19-53.

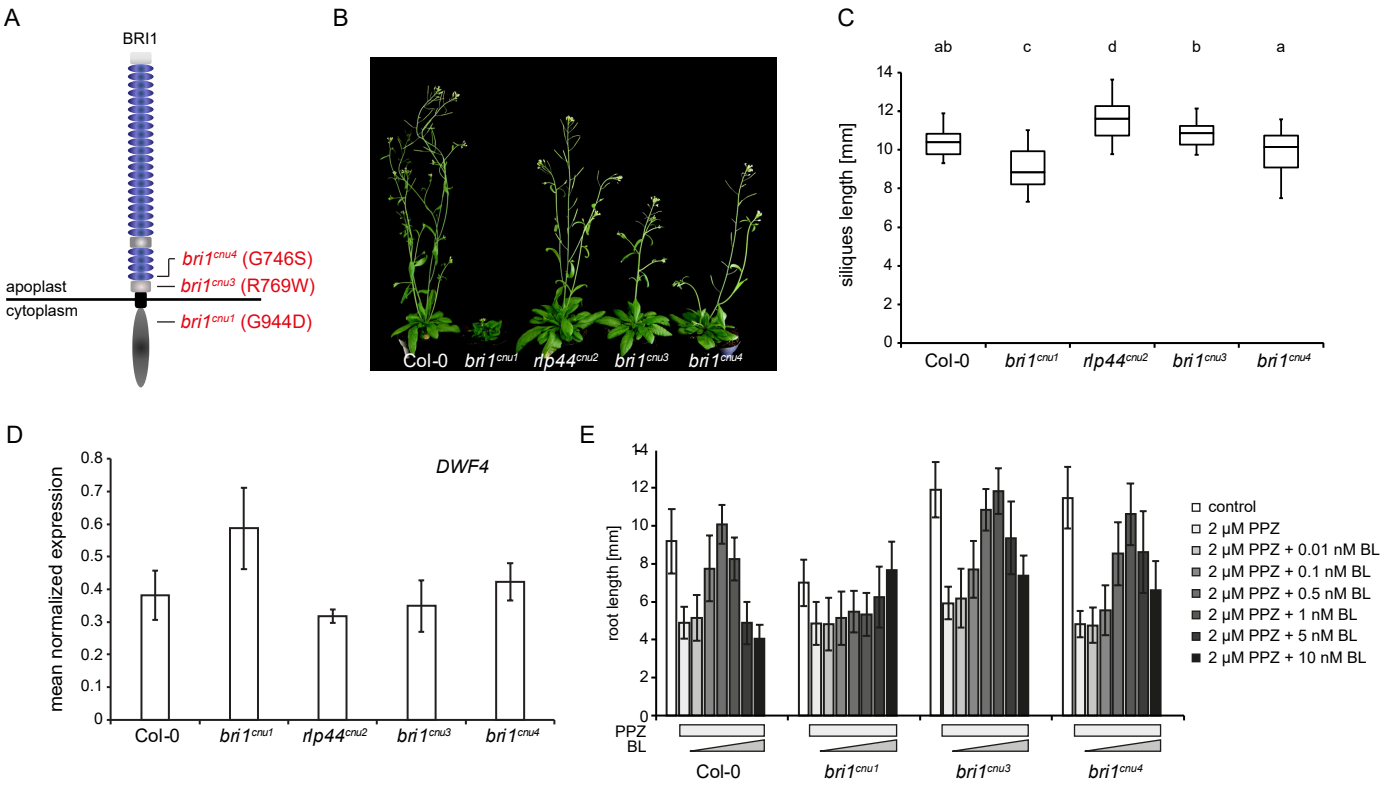

Figure 2. The *cnu3* and *cnu4* mutants are two novel alleles of *BRI1*. **A**, Schematic view of BRI1 with indicated position and amino acid substitution of the mutations in *bri1*^{cnu1}, *bri1*^{cnu3} (derived from *cnu3*, but in the absence of the PMEIox transgene), and *bri1*^{cnu4} (derived from *cnu4*, but in the absence of the PMEIox transgene). **B**, Comparison of adult plant phenotype of Col-0, *bri1*^{cnu1}, *rlp44*^{cnu2}, *bri1*^{cnu3}, and *bri1*^{cnu4}. **C**, Silique length of Col-0, and the mutants derived from the *cnu1* to *cnu4* suppressor mutants. Box plots indicate interquartile range (box), median (bar) and 1.5x IQR (whiskers), n = 25-36. **D**, qRT-PCR analysis of the BR biosynthetic gene *DWF4* in wild type (Col-0), *bri1*^{cnu1}, *rlp44*^{cnu2}, *bri1*^{cnu3}, and *bri1*^{cnu4}. Bars depict average ± S.D., n = 3. **E**, Root length response of wild type (Col-0), *bri1*^{cnu1}, *bri1*^{cnu3} and *bri1*^{cnu4} to BR depletion by PPZ and exogenous application of BL. Bars depict average ± S.D., n = 34-70.

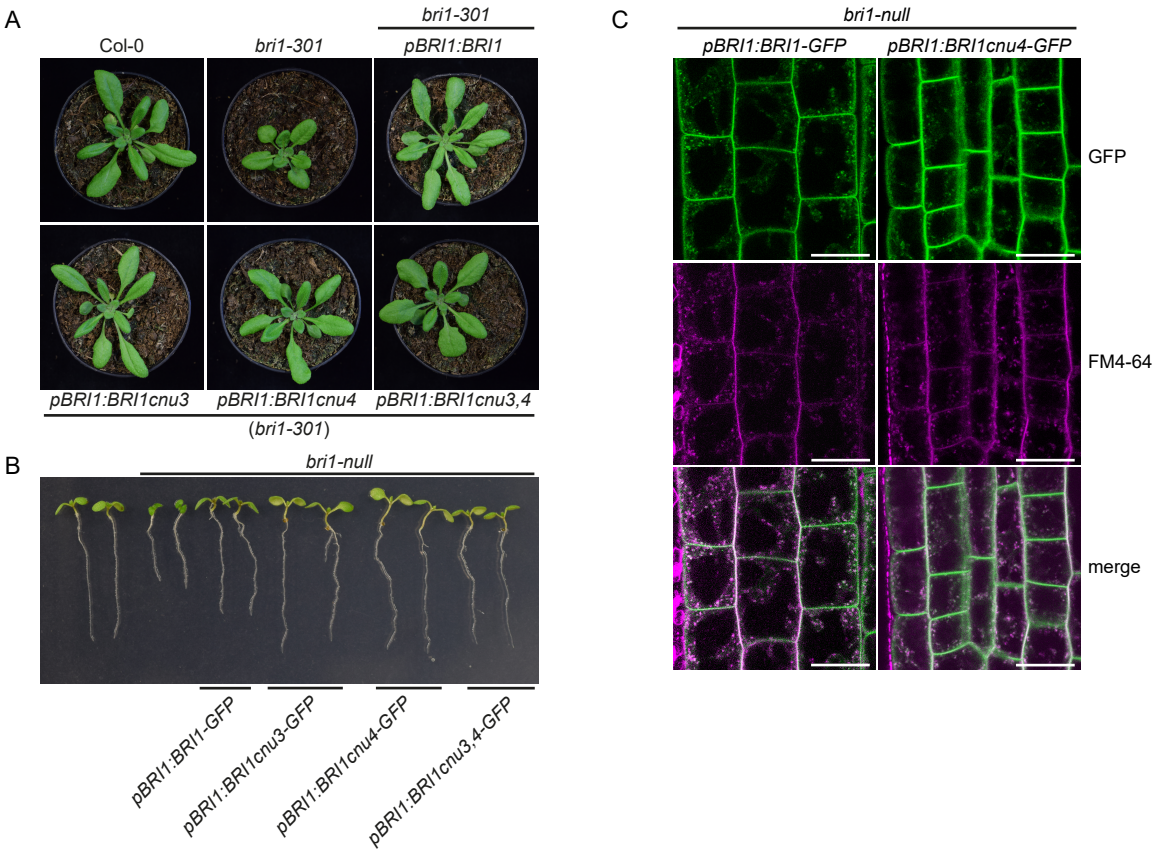

Figure 3. BRI1cnu4 and BRI1cnu3 proteins are functional. **A**, Mutant BRI1 constructs complement the hypomorphic *bri1-301* mutant. **B**, Constructs encoding mutated BRI1 versions complement the *bri-null* mutant. **C**, GFP fluorescence in root meristems of *bri1 null* mutants complemented with GFP fusion proteins from either the construct pBRI1:BRI1-GFP or pBRI1:BRI1cnu4-GFP, shows no apparent difference in subcellular localization. FM4-64 was used as an endocytic membrane tracer dye. Scale bars = 10 μm.

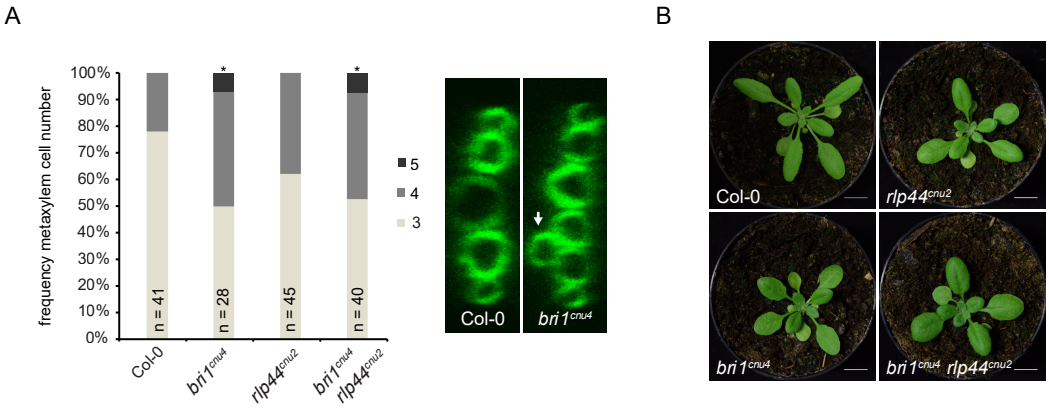

Figure 4. The mutation in *bri1*^{cnu4} negatively affects RLP44 function. **A**, Frequency of roots with the indicated number of metaxylem cells in Col-0, *rlp44*^{cnu2}, *bri1*^{cnu4}, and the *rlp44*^{cnu2} *bri1*^{cnu4} double mutant. **B**, Morphological phenotype of Col-0, *rlp44*^{cnu2}, *bri1*^{cnu4}, and the *rlp44*^{cnu2} *bri1*^{cnu4} double mutant.

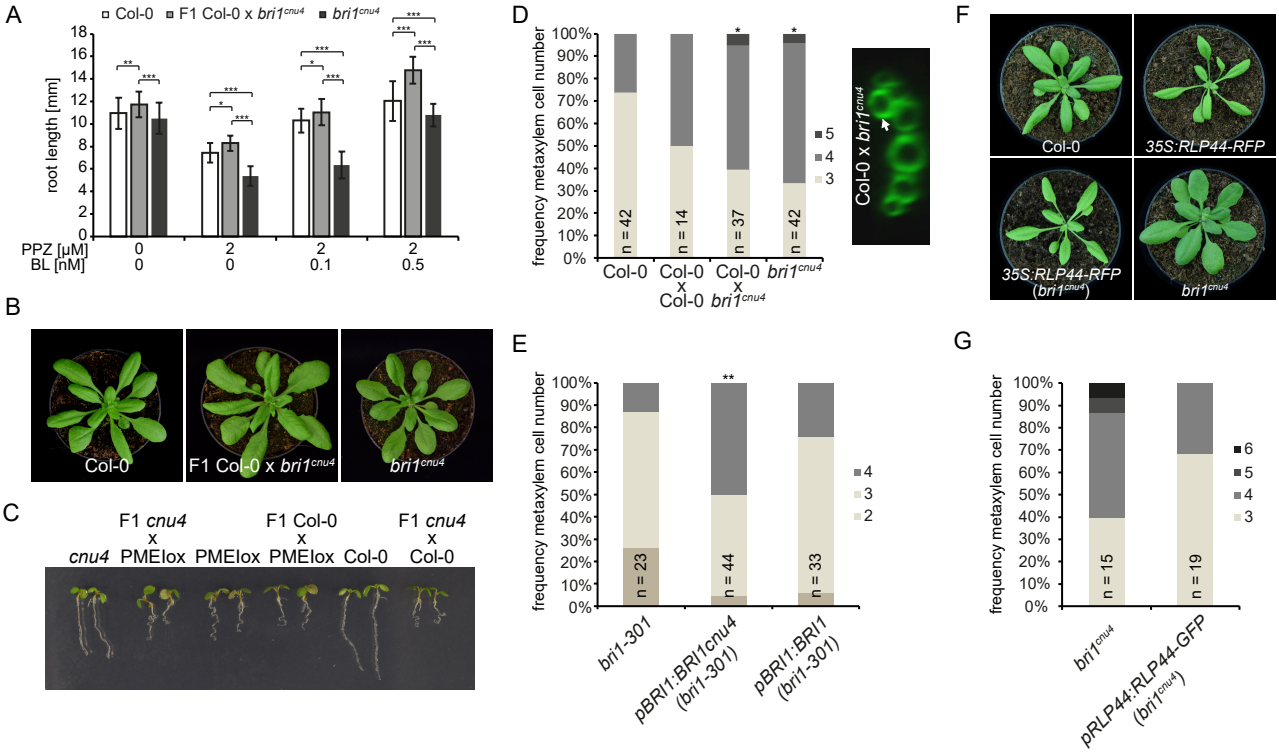

Figure 5. The *bri1*^{cnu4} mutant interferes with RLP44 function. **A**, Root length of 5-d-old F1 hybrid seedlings of a cross between *bri1*^{cnu4} and Col-0 after PPZ treatment and exogenous supply of BL. Bars indicate mean root length of 5-d-old seedlings ± SD (n = 22-49). Asterisks indicate significance with *p < 0.05, **p < 0.01, and ***p < 0.001 as determined by Tukey's test after two-way ANOVA. Note that significance is only indicated for comparisons within each treatment. **B**, Morphological phenotype of Col-0, *bri1*^{cnu4}, and F1 hybrid plants resulting from crossing the two genotypes. **C**, Suppression of PMEI5 overexpression phenotype (PMEIox) by the *bri1*^{cnu4} allele (*cnu4*) is a recessive trait, as indicated by the PMEIox-like phenotype of F1 plants from a cross between *cnu4* and Col-0. **D**, Ectopic xylem phenotype in *bri1*^{cnu4} and F1 plants from a cross between *bri1*^{cnu4} and Col-0. **E**, Expression of BRI1cnu4, but not of wildtype BRI1 in the *bri1-301* mutant results in supernumerary xylem cells. **F**, RLP44 overexpression can partially rescue the morphological phenotype of *bri1*^{cnu4}. **G**, Increased expression of RLP44 can alleviate the *bri1*^{cnu4} phenotype. Asterisks indicate statistically significant difference from Col-0 based on Dunn's post-hoc test with Benjamini-Hochberg correction after Kruskal-Wallis modified U-test (*p < 0.05).

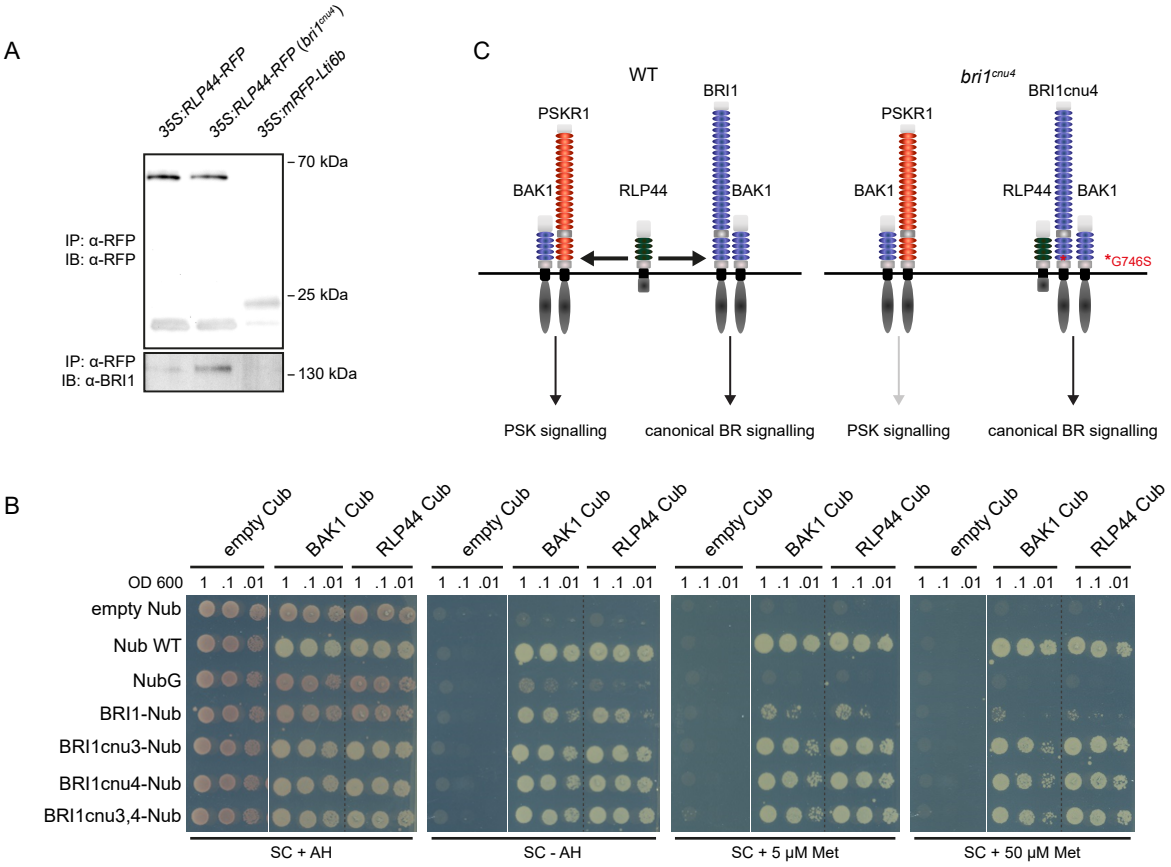

Figure 6. The BRI1cnu4 protein shows increased interaction with RLP44 and BAK1. **A**, Co-immunoprecipitation of BRI1-GFP by RLP44-RFP from crude extracts of wild type (Col-0) and *bri1*^{cnu4} mutant plants. **B**, Mating-based split ubiquitin assays in yeast displaying the interaction of BRI1, BRI1cnu3, BRI1cnu4 and BAK1 with RLP44. **C**, Model of RLP44 interactions with BRI1 and PSKR1 in the wild type and the *bri1*^{cnu4} mutant. The mutation at the base of BRI1´s extracellular domain sequesters RLP44 and prevents it from promoting PSK/PSKR1 signalling.

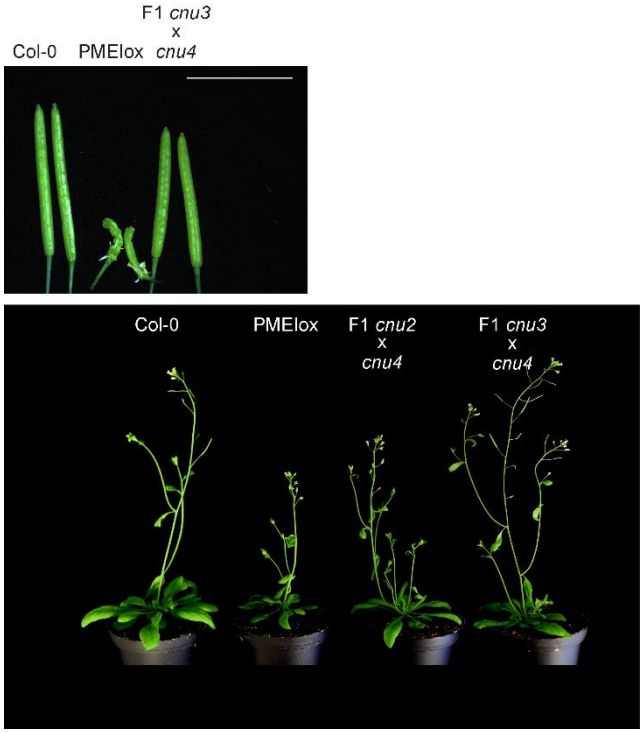

Supplemental Figure 1. *cnu3* and *cnu4* are allelic mutants. PMEIox silique morphology (upper panel) and plant stature (lower panel) remain suppressed in F1 plants of a cross between *cnu3* and *cnu4*, whereas F1 plants of a cross between *cnu2* (carrying a mutation in RLP44) and *cnu4* show PMEIox phenotype.

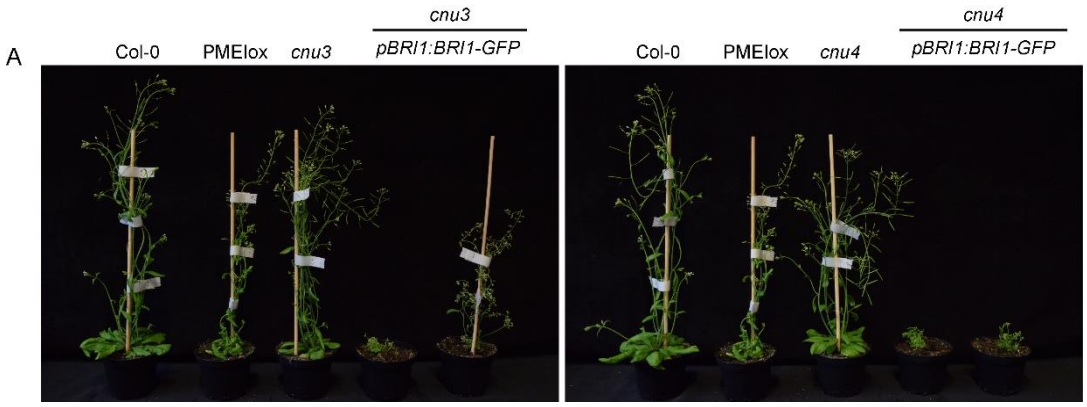

Supplemental Figure 2. Mutant BRI1 constructs complement the *cnu3* and *cnu4* mutants.

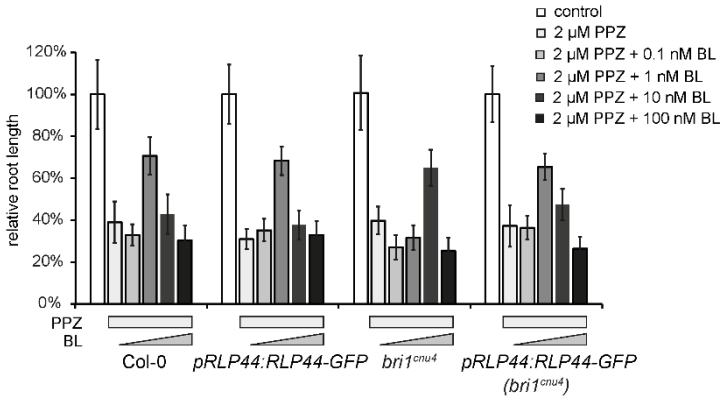

Supplemental Figure 3. RLP44 promotes BR response in the *bri1^{cnu4}* mutant. Response of Col-0, pRLP44:RLP44-GFP, *bri1^{cnu4}*, and pRLP44:RLP44-GFP (*bri1^{cnu4}*) to depletion (PPZ) and exogenous supply of brassinosteroids. Bars indicate average relative root length ± S.D. (17 < n < 35).

Supplemental Table S1. Oligonucleotides used in this study

oligonucleotide	sequence 5'-3'	remark
bri1cnu3_CAPS_F	TCGATTCCTGATGAGGTAGGTG	Cfr42I
bri1cnu3_CAPS_R	AAGATCCGCAAACGTGAGCTTC	Cfr42I
bri1cnu4_CAPS_F	TCAGGAGCTCATGTATGTCA	BseL1
bri1cnu4_CAPS_R	TCCAATTGGTGTTGTTAGCAG	BseL1
BRI1_attB1_L	GGGGACAAGTTTGTACAAAAAAGCAGGCTATGAAGACTTTTTCAAGCTTCTT	
BRI1_attB2_R	GGGGACCACTTTGTACAAGAAAGCTGGGTtTAATTTTCCTTCAGGAACTTCTT	
BRI1_GGC_1F	AACAGGTCTCAGGCTCATGAAGACTTTTTCAAGCTTCT	
BRI1_GGC_1R	AACAGGTCTCaATCACACGCGCCGGAGAGAAAGTCAG	
BRI1_GGC_2F	aacaGGTCTCaTGATACACTCACTGGaCTCGATCTCTCTGGA	
BRI1_GGC_2R	aacaGGTCTCaGAGtCCAGGATTGTTCAAGAA	
BRI1_GGC_3F	aacaGGTCTCaACTCTGTGGTTATCCTCTT	
BRI1_GGC_3R	aacaggTCTCaGGCCTCCTTCCATGAGATCT	
BRI1_GGC_4F	aacaGGTCTCaGgCCAGCGTCCCTTGCTGGT	
BRI1_GGC_4R	AACAGGTCTCACTGATAATTTTCCTTCAGGAACTTC	
at5G46630_cod_F	TCGATTGCTTGGTTTGGAAGAT	
at5G46630_cod_R	GCACTTAGCGTGGACTCTGTTTGC	
DWF4_F	caacagcaaaacaacggagcg	
DWF4_R	Tctgaaccagcacatagccttg	

Supplemental Table S2. GreenGate Cloning modules and destination constructs

pSW388	**pBRI1:BRI1**	
pSW379	BRI1(AT4G39400) promoter	Holzwart et al., 2018
GGB003	B-Dummy	Lampropoulos et al., 2013
pSW380	BRI1(AT4G39400) CDS	Holzwart et al., 2018
pGGD002	D-Dummy	Lampropoulos et al., 2013
pGGE009	UBQ10 terminator	Lampropoulos et al., 2013
pGGF001	pMAS::BastaR::tMAS	Lampropoulos et al., 2013
pGGZ0001	destination vector	Lampropoulos et al., 2013

pSW389	**pBRI1:BRI1cnu3**	
pSW379	BRI1(AT4G39400) promoter	Holzwart et al., 2018
pGGB003	B-Dummy	Lampropoulos et al., 2013
pSW391	BRI1cnu3	This study
pGGD002	D-Dummy	Lampropoulos et al., 2013
pGGE009	UBQ10 terminator	Lampropoulos et al., 2013
pGGF001	pMAS::BastaR::tMAS	Lampropoulos et al., 2013
pGGZ001	destination vector	Lampropoulos et al., 2013

pSW390	**pBRI1:BRI1cnu4**	
pSW379	BRI1(AT4G39400) promoter	Holzwart et al., 2018
pGGB003	B-Dummy	Lampropoulos et al., 2013
pSW381	BRI1cnu4 CDS	This study
pGGD002	D-Dummy	Lampropoulos et al., 2013
pGGE009	UBQ10 terminator	Lampropoulos et al., 2013
pGGF001	pMAS::BastaR::tMAS	Lampropoulos et al., 2013
pGGZ001	destination vector	Lampropoulos et al., 2013

pSW427	**pBRI1:BRI1cnu3,4**	
pSW379	BRI1(AT4G39400) promoter	Holzwart et al., 2018
pGGB003	B-Dummy	Lampropoulos et al., 2013
pSW419	BRI1cnu3,4	This study
pGGD002	D-Dummy	Lampropoulos et al., 2013
pGGE009	UBQ10 terminator	Lampropoulos et al., 2013
pGGF001	pMAS::BastaR::tMAS	Lampropoulos et al., 2013
pGGZ001	destination vector	Lampropoulos et al., 2013

pSW421	**pBRI1:BRI1cnu3-GFP**	
pSW379	BRI1(AT4G39400) promoter	Holzwart et al., 2018
pGGB003	B-Dummy	Lampropoulos et al., 2013
pSW391	BRI1cnu3	This study
pGGD001	GFP	Lampropoulos et al., 2013
pGGE009	UBQ10 terminator	Lampropoulos et al., 2013
pGGF001	pMAS::BastaR::tMAS	Lampropoulos et al., 2013
pGGZ001	destination vector	Lampropoulos et al., 2013

pSW422	**pBRI1:BRI1cnu4-GFP**	
pSW379	BRI1(AT4G39400) promoter	Holzwart et al., 2018
pGGB003	B-Dummy	Lampropoulos et al., 2013
pSW381	BRI1cnu4	This study
pGGD001	GFP	Lampropoulos et al., 2013
pGGE009	UBQ10 terminator	Lampropoulos et al., 2013
pGGF001	pMAS::BastaR::tMAS	Lampropoulos et al., 2013

pGGZ001	destination vector	Lampropoulos et al., 2013
pSW423	**pBRI1:BRI1cnu3,4-GFP**	
pSW379	BRI1(AT4G39400) promoter	Holzwart et al., 2018
pGGB003	B-Dummy	Lampropoulos et al., 2013
pSW419	BRI1cnu3,4	This study
pGGD001	GFP	Lampropoulos et al., 2013
pGGE009	UBQ10 terminator	Lampropoulos et al., 2013
pGGF001	pMAS::BastaR::tMAS	Lampropoulos et al., 2013
pGGZ001	destination vector	Lampropoulos et al., 2013

A.1.5 The role of BIR3 for BRI1-BAK1 interaction

Specifying the role of BAK1-interacting receptor-like kinase 3 in brassinosteroid signaling

Accepted

This article describes the use of computational modelling to simulate the biophysical and energetic requirements for the interaction of the cytoplasmic domains of three membrane-resident proteins involved in brassinosteroid signalling. The inhibitor of brassinosteroid signalling BAK1 INTERACTING RECEPTOR-LIKE KINASE 3 (BIR3) interacts with both the brassinosteroid receptor BRASSINOSTEROID INSENSITIVE 1 (BRI1) and its co-factor BRI1-INTERACTING KINASE 1 (BAK1). Both the modelling and interaction study approaches show, that BIR3-BAK1 interaction is favoured in the abscence of ligand. An additional binding site between BRI1 and BAK1 enables the binding even when BIR3-BAK1 heterodimers are formed. Consequently, the BRI1 receptor the BRI1 receptor competes with the inhibitor BIR3 for the catalytic site of BAK1. The model suggests, that a small difference in orientation of the two kinase domains of BRI1 and BAK1 is enough for activation of signalling.

JIPB Journal of Integrative Plant Biology

Specifying the role of BAK1-interacting receptor-like kinase 3 in brassinosteroid signaling

Ruth Großeholz[1], Anna Feldman-Salit[1], Friederike Wanke[2], Sarina Schulze[2], Nina Glöckner[2], Birgit Kemmerling[2], Klaus Harter[2] and Ursula Kummer[1]*

1. Centre for Organismal Studies/ BioQuant, Heidelberg University, 69120 Heidelberg, Germany
2. Center for Plant Molecular Biology (ZMBP), University Tübingen, 72076 Tübingen, Germany
*Correspondence: Ursula Kummer (ursula.kummer@bioquant.uni-heidelberg.de)
doi: 10.1111/jipb.12803

Research Article

Abstract Brassinosteroids (BR) are involved in the control of several developmental processes ranging from root elongation to senescence and adaptation to environmental cues. Thus, BR perception and signaling have to be precisely regulated. One regulator is BRI1-associated kinase 1 (BAK1)-interacting receptor-like kinase 3 (BIR3). In the absence of BR, BIR3 forms complexes with BR insensitive 1 (BRI1) and BAK1. However, the biophysical and energetic requirements for complex formation in the absence of the ligand have yet to be determined. Using computational modeling, we simulated the potential complexes between the cytoplasmic domains of BAK1, BRI1 and BIR3. Our calculations and experimental data confirm the interaction of BIR3 with BAK1 and BRI1, with the BAK1 BIR3 interaction clearly favored. Furthermore, we demonstrate that BIR3 and BRI1 share the same interaction site with BAK1. This suggests a competition between BIR3 and BRI1 for binding to BAK1, which results in preferential binding of BIR3 to BAK1 in the absence of the ligand thereby preventing the active participation of BAK1 in BR signaling. Our model also suggests that BAK1 and BRI1 can interact even while BAK1 is in complex with BIR3 at an additional binding site of BAK1 that does not allow active BR signaling.

Edited by: Miguel A. Piñeros, USDA-ARS, Cornell University, USA **Received** Jul. 5, 2018; **Accepted** Feb. 27, 2019; **Online on** Mar. 26, 2019

INTRODUCTION

Brassinosteroids (BR) are plant steroid hormones playing a crucial role in plant growth, development and regulation of responses to environmental cues (Nakaya et al. 2002). BRs are detected on the plant cell surface by the receptor kinase BR insensitive 1 (BRI1) (Clouse et al. 1996). Subsequently, BRI1-associated receptor kinase (BAK1) is recruited to BRI1 (Li et al. 2002; Nam and Li 2002) and transphosphorylation between BRI1 and BAK1 occurs which results in the fully active BRI1-BAK1 complex and the initiation of downstream signaling (Wang et al. 2008; Belkhadir and Jaillais 2015). This results in alterations in gene expression patterns (Müssig et al. 2002), but the active BRI1-BAK1 complex also initiates a fast response pathway located in the plasma membrane that leads to membrane hyperpolarization, apoplastic acidification and cell wall swelling (Caesar et al. 2011; Witthöft and Harter 2011; Witthöft et al. 2011).

Cell biology and *in vivo* protein-protein interaction studies showed that in the absence of BR and in BR-depleted cells, BRI1 and BAK1 interact with each other and establish preformed hetero-oligomers in nanoclusters located in the plasma membrane (Bücherl et al. 2013; Hutten et al. 2017). Remarkably, experiments indicate that the spatial distance between the BRI1 and BAK1 molecules and the hetero-oligomerization status of BRI1 and BAK1 in the nanoclusters do not dramatically change upon BR application (Caesar et al. 2011; Hutten et al. 2017). The switch from the preformed inactive to the active BRI1-BAK1 hetero-oligomer is thought to be initiated by the binding of the BAK1's extracellular leucine-repeat-rich (LRR) domain to the BR-bound extracellular LRR domain of BRI1 (Santiago et al. 2013; Sun et al. 2013; Hohmann et al. 2017). This initiates

transphosphorylation between BRI1 and BAK1 intracellular domains, the release of inhibitory control mechanisms and further downstream signaling events (Wang et al. 2008; Belkhadir and Jaillais 2015).

Several inhibitory mechanisms acting on the level of BRI1 were described and characterized experimentally in recent years: the inhibition of BRI1 activity by its C-terminus (Wang et al. 2005), by the BRI1 kinase inhibitor 1 (BKI1) (Jaillais et al. 2011a) and by the botrytis-induced kinase 1 (BIK1) (Lin et al. 2013). Recently, a new negative regulator of BR signaling, BAK1-interacting receptor-like kinase 3 (BIR3), was identified that functions on the level of both BAK1 and BRI1 (Halter et al. 2014b; Imkampe et al. 2017). Imkampe and colleagues (2017) demonstrated via multiple interaction studies that BIR3 forms complexes with BAK1 as well as with BRI1 in the absence of exogenous BR (Figure 1). However, the degree of interaction appears to be different with a higher affinity of BIR3 to BAK1 than to BRI1 (Imkampe et al. 2017). After application of BR, BIR3 is released from BAK1 and BRI1, allowing downstream signaling (Imkampe et al. 2017). This has been substantiated by the interaction study of the extracellular domains (Hohmann et al. 2018), where the ectodomains of BAK1 and BIR3 bind with a stoichiometry of 1:1 and the BL-bound ectodomain of BRI1 ($BRI1^{BL}$) can compete with BIR3 for the interaction with BAK1. Interestingly, the ectodomains of BRI1 and BIR3 do not appear to interact in this essay (Hohmann et al. 2018), suggesting that transmembrane and cytoplasmic domains also play a role in the experimentally observed interactions of the whole proteins (Imkampe et al. 2017).

These experimental data provoke many as yet unsolved questions. (i) Can BRI1 and BAK1 interact in the absence of BR based on their cytoplasmic domains? (ii) Which mechanism(s) avoid(s) unwanted transphosphorylation within the preformed BRI1-BAK1 hetero-oligomer in the absence of BR? (iii) Which role do the cytoplasmic domains play in the interaction of BAK1 and BRI1 with BIR3 and can these interactions provide an explanation for the observed phenotypes of BIR3 and BIR3/BRI1 overexpressing plants?

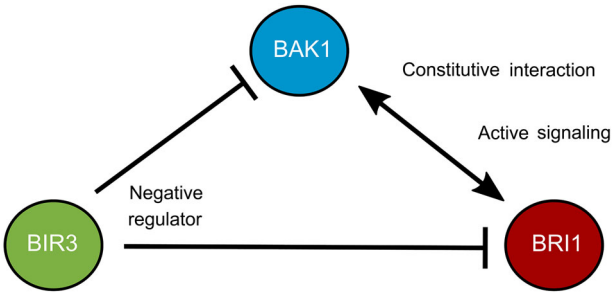

Figure 1. Schematic representation of the known functional interactions between BIR3, BAK1 and BRI1

There is detectable interaction of the full-length proteins of BIR3 and BRI1 as shown by Imkampe et al. (2017) as well as our own experiments. Furthermore, transphosphorylation requires at least the transient interaction of the cytoplasmic domains. Therefore, we employed comparative modeling and molecular docking analyses to analyze the structural and energetic requirements of the potential protein complexes to address how the cytoplasmic domains of BIR3, BAK1 and BRI1 may contribute to the interactions observed for the whole proteins. Our modeling demonstrated that the BAK1/BIR3 interaction is energetically preferred over the BRI1/BIR3 interaction and the BRI1/BAK1 interaction. An analysis of the binding sites provides insight into the molecular reason behind the phenotype of BIR3 and BIR3/BRI1 overexpressing plants (Imkampe et al. 2017).

RESULTS

Comparative modeling and preparation of molecular docking analysis for the study of BAK1, BIR3 and BRI1 structure, interaction and oligomerization

Comparative modeling is commonly used to determine the structure of a target protein of interest based on the structure of a closely related protein (Hilbert et al. 1993). Here, we used the structure of BAK1-interacting receptor-like kinase 2 (BIR2) (PDB ID 4l68) (Blaum et al. 2014) – a negative regulator in microbe-associated molecular pattern signaling (Halter et al. 2014a, 2014b) – as a template for the modeling of the BIR3 structure. The primary structure of BIR2 shares 66% identity with BIR3 in the region of interest (Figure S1). Comparative modeling can not only be used to model structures of closely related proteins, but also to fill the gaps in experimentally determined protein structures, where parts of the protein are too flexible to be structurally defined. These gaps have to be filled by comparative modeling to get a more accurate picture of the complex formation. Even though a structure was available for BRI1 (PDB ID 5lpw) (Bojar et al. 2014), we employed

comparative modeling to fill the gaps in this structure (Webb and Sali 2014) (Figure S2). We evaluated the structures generated by comparative modeling based on their Quality Model Energy Analysis (QMEAN) scores (Benkert et al. 2008, 2011). The structures with the best QMEAN4 (see Materials and Methods) score were used for subsequent docking analyses. In the case of BIR3 we obtained two equivalent structures with different solutions for the unresolved loops in the template structure of BIR2 (Figures 2A, S3A, B). For BAK1, we used the structure published by Cheng et al. (2011) (PDB ID 3tl8) (Figure S4).

To study the protein complex formation within a set of physiological constraints, the diffusional association of the interacting partners was simulated by utilizing the online version of the Simulation of Diffusional Association software (webSDA) (Motiejunas et al. 2008; Yu et al. 2015). SDA has been widely employed to study the complex formation in different systems, for example the cysteine synthase complex from mitochondrial *Arabidopsis thaliana* (Feldman-Salit et al. 2013) or the dynamics of dimerization of human K-Ras guanosine triphosphatases (Sayyed-Ahmad et al. 2016). Here, we applied webSDA to model complexes between the cytoplasmic domains of BAK1, BIR3 and BRI1 as this method allows the specification of physiological parameters such as ion strength and pH. To substantiate our results, we used an additional docking method called ClusPro (Comeau et al. 2004a, b; Kozakov et al. 2006, 2013, 2017), which samples the energetic landscape extensively and clusters the 1,000 complexes with the lowest energy into up to 30 clusters. Unlike webSDA, which computes encountered complexes by rigid body docking, ClusPro includes an additional step to adjust the orientation of flexible side chains to the complex formation. The webserver shows several fields of applications ranging from studying the interactions between acyl carrier proteins (Ye et al. 2014) to characterizing antibodies for tumor necrosis factor receptor 1 (Steeland et al. 2015).

We limited the analyses to the cytoplasmic domains as the kinase domains are the essential parts for intracellularly propagating the signal. While modeling the proteins as a whole would yield the most comprehensive picture – especially when accounting for the differences in environment inside and outside the cell – the transmembrane domains in particular are largely unresolved. Furthermore, the interaction of the extracellular domains of BIR3, BAK1 and BRI1 has already been experimentally studied in great detail (Jaillais et al. 2011b; Santiago et al. 2013; Sun et al. 2013; Bücherl et al. 2013; Hohmann et al. 2017, 2018) and were therefore not part of our analyses.

Energetics of BRI1-BAK1 interaction via their cytoplasmic domains

One step in the early events in BR signaling after hormone binding to the extracellular LRR domain of

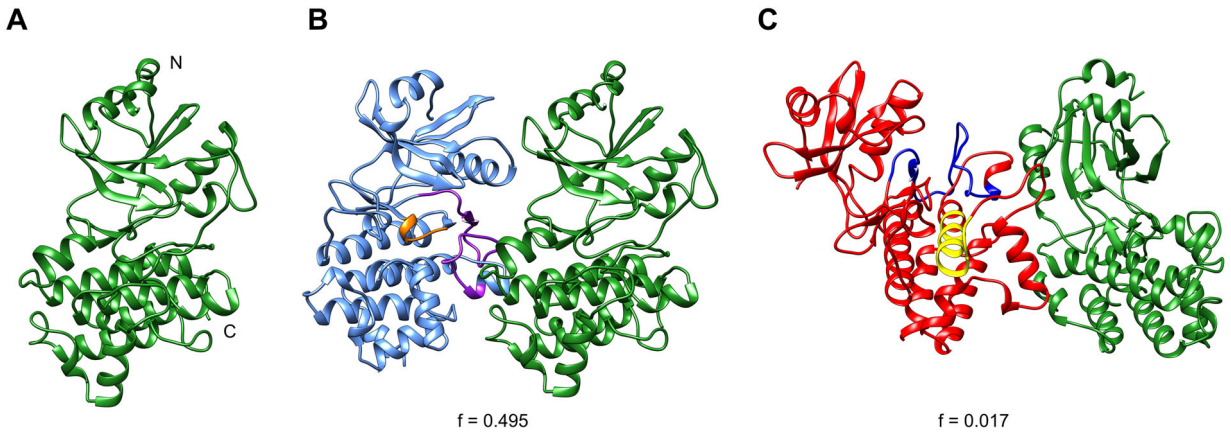

Figure 2. BIR3 interacts with BAK1 and BRI1
(**A**) Modeled structure of BIR3 based on the template of BIR2 (PDB ID 4l68, chain A) (Blaum et al. 2014). Equivalent modeled structure of BIR3 in Figure S3. (**B**) Favored complex between the first BIR3 structure and BAK1 calculated by webSDA. (**C**) Favored complex between BIR3 and BRI1 calculated by webSDA. Color code: BIR3 (green); BAK1 (blue), catalytic domain (orange), activation loop (purple); BRI1 (red): catalytic domain (yellow), activation loop (blue). All structures and complexes are oriented in a way that the membrane would be located above the complex.

BRI1 is the transphosphorylation between BAK1 and BRI1, where both proteins are expected to associate with and act as substrate for each other (Wang et al. 2008). However, this does not exclude the possibility that BRI1 and BAK1 interact via their intracellular cytoplasmic domain in the absence of BR, thus establishing a preformed receptor/co-receptor complex. There is experimental evidence that the kinase domains of BAK1 and BRI1 weakly interact if they are combined *in vitro* (Bojar et al. 2014).

To test whether this is *per se* energetically possible, we ran a molecular docking analysis for the cytoplasmic domains of BAK1 (Figure 3A) and BRI1 (Figure 3B) and analyzed their interaction sites. Here, we primarily relied on webSDA as it allows the specification of ionic strength and pH before simulating potential complexes by Brownian dynamics. By using webSDA we sampled 500 potential complexes between BAK1 and BRI1 and sorted them into 10 representative clusters. For these clusters, we determined the spatial orientation of the cytoplasmic domains and considered only those clusters as feasible that allowed the unhindered continuation of the proteins with the transmembrane domain at the N-terminus and did not interfere with the structurally unresolved C-terminus.

Different docking methods employ different ways of computing the effective binding energies of the complexes. Thus, the respective energy values are difficult to compare when employing several docking approaches. As the number of complexes in each cluster is a measure for the probability of encountering this cluster (Camacho et al. 1999; Kozakov et al. 2013, 2017), we used the relative size of the clusters as a selection criterion. The relative size $f_{cluster}$ was defined as $f_{cluster} = \frac{n_{complexes}}{N_{all\ complexes}}$, where $n_{cluster}$ represents the number of complexes per cluster and $N_{all\ complexes}$ stands for the total number of observed complexes.

The docking analysis of the cytoplasmic domains of BAK1 and BRI1 revealed the complexes depicted in Figure 3C (webSDA) and Figure S5 (ClusPro). These complexes of the cytoplasmic domains suggest that BAK1 can interact with BRI1 by its catalytic site, the activation loop and catalytic domain (Yan et al. 2012), where BRI1 binds to BAK1 via its catalytic motive and the activation loop (Bojar et al. 2014). This observed cluster has an unfavorable energetic landscape: In webSDA this cluster was observed with a frequency of $f_{BRI1,BAK1} = 0.009$. Part of the interaction surface between the cytoplasmic domain of BAK1 and BRI1 is the loop containing D1139. The change of D1139 to A is the underlying cause for the strong loss of function

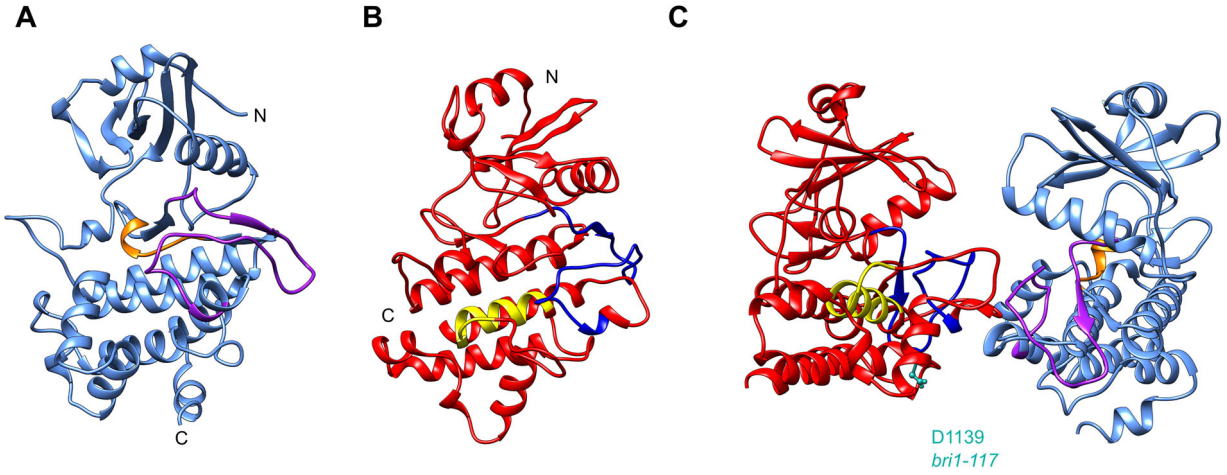

Figure 3. BAK1 interacts with BRI1 by its catalytic domain
(**A, B**) Cytoplasmic domains of BAK1 (A, blue) and BRI1 (B, red). (**A**) Structure of the cytoplasmic domain of BAK1 (blue) (PDB ID 3tl8) (Cheng et al. 2011). Orange: catalytic domain. Purple: activation loop. (**B**) Gap-filled structure of the cytoplasmic domain of BRI1 (red) (based on PDB ID 5lpw) (Bojar et al. 2014). Yellow: catalytic domain. Blue: activation loop. (**C**) Modeled complex of BAK1 and BRI1 by webSDA ($f_{BAK1,BRI1} = 0.009$) D1139 highlighted in cyan. Color code for BAK1 and BRI1 as A and B. All structures are oriented in a way that the membrane would be located above the complex.

phenotype of the bri1-117 mutant (Li and Chory 1997; Friedrichsen 2000).

These data corroborate the experimental data that cytoplasmic domain-mediated BRI1/BAK1 complexes may in principle exist in the absence of the BR ligand in the plasma membrane (Caesar et al. 2011; Bücherl et al. 2013; Hutten et al. 2017) and that BRI1 and BAK1 kinase domains may weakly interact *in vitro* (Bojar et al. 2014). However, the existence of such preformed complexes carries the risk of unwanted BR signaling by coincidental transphosphorylation events.

Energetics of BIR3 interaction with BAK1 and BRI1

Physiological and biochemical experiments have shown that BIR3 acts as a negative regulator of BR signaling by association with both BAK1 and BRI1 (Imkampe et al. 2017). The question remains how this negative regulation is realized on molecular and energetic levels and what the mechanistic consequences might be. Hohmann and colleagues have already demonstrated that the ectodomains of BIR3 and BAK1 interact, which requires $BRI1^{BL}$ to compete with this interaction (Hohmann et al. 2018). However, this study did not observe the interaction of BIR3 and BRI1 based on the respective ectodomains, which suggests that the interaction of the complete proteins is in part due to their transmembrane and cytoplasmic domains (Imkampe et al. 2017). Therefore, we again performed a docking analysis using the cytoplasmic domains of BIR3 in association with BAK1 and BRI1. This analysis revealed an energetically much more favorable interaction between the cytoplasmic domains of BIR3 (Figure 2A) and BAK1 (Figure 3A) compared to the interaction of BAK1 and BRI1, with a relative occurrence of $f_{BAK1,BIR3a} = 0.495$ (Figure 2B and $f_{BAK1,BIR3b} = 0.36$ Figure S3C). Furthermore, we determined that the interaction site of BAK1 and BIR3 includes the catalytic site and the P-loop of BAK1 (Yan et al. 2012), which are then shielded from other prospective interacting partners (e.g. BRI1). More specifically, BIR3 preferentially binds BAK1 and prevents the interaction of BAK1 and BRI1 in the absence of the ligand.

We also analyzed the complex formation between BRI1 and BIR3. The webSDA analysis revealed potential complexes with a relative occurrence of $f_{BRI1,BIR3a} = 0.017$ (Figure 2C and $f_{BRI1,BIR3b} = 0.104$, Figure S3D). The reduced number of complexes per cluster means that encountering this complex is less likely compared to the one between BIR3 and BAK1. The same qualitative behavior can be observed for the docking analysis using ClusPro (Figure S6A–D) although the frequency of the individual complexes varies to a small degree.

To substantiate the differential interaction capacity of BIR3 with BAK1 and BRI1 we carried out a quantitative *in vivo* Förster Resonance Energy Transfer (FRET)-fluorescence lifetime imaging microscopy (FLIM). Full-length BIR3-green fluorescence protein (GFP) (FRET donor fusion) was transiently co-expressed in tobacco (*Nicotiana benthamiana*) leaf epidermal cells together with mCherry fusions of either full-length BAK1 or full-length BRI1 (FRET acceptor fusions).

To determine the background FLIM values, BIR3-GFP was expressed alone. When BIR3-GFP was co-expressed with BAK1-mCherry a strong decrease in the fluorescence lifetime of the donor fusion was observed compared to the lifetime values of BIR3-GFP alone (Figure 4A, B). A significant reduction of the fluorescence lifetime was also observed when BIR3-GFP was co-expressed with BRI1-mCherry (Figure 4). However, the lifetime reduction of BIR3-GFP in the presence of BRI1-mCherry was much less pronounced compared to the changes in the presence of BAK1-mCherry (Figure 4). These results suggest that BIR3 is able to independently associate with both BAK1 and BRI1 and that the probability of encountering these complexes differs significantly between BIR3-GFP with BAK1-mCherry and BIR3-GFP with BRI1-mCherry in living plant cells. Thus, our FRET-FLIM data and the results from Imkampe and colleagues (2017) are in agreement with the computational modeling outcomes.

Energetics of BR-independent BRI1 interaction with BIR3-complexed BAK1

Several groups have reported an interaction between BRI1 and BAK1 in the plasma membrane and co-existence of BAK1 and BRI1 in membrane nanoclusters in the absence of exogenous BR or in BR-depleted cells (Caesar et al. 2011; Bücherl et al. 2013; Hutten et al. 2017). However, based on the broad and constitutive expression of BIR3 in *Arabidopsis* (Imkampe et al. 2017) and our computational results, the interaction between the surface regions in the cytoplasmic domains of BIR3 and BAK1 appears to be too favorable to be interfered by the cytoplasmic domain of BRI1 in the absence of the hormonal ligand. Therefore, BRI1/BAK1 interaction and

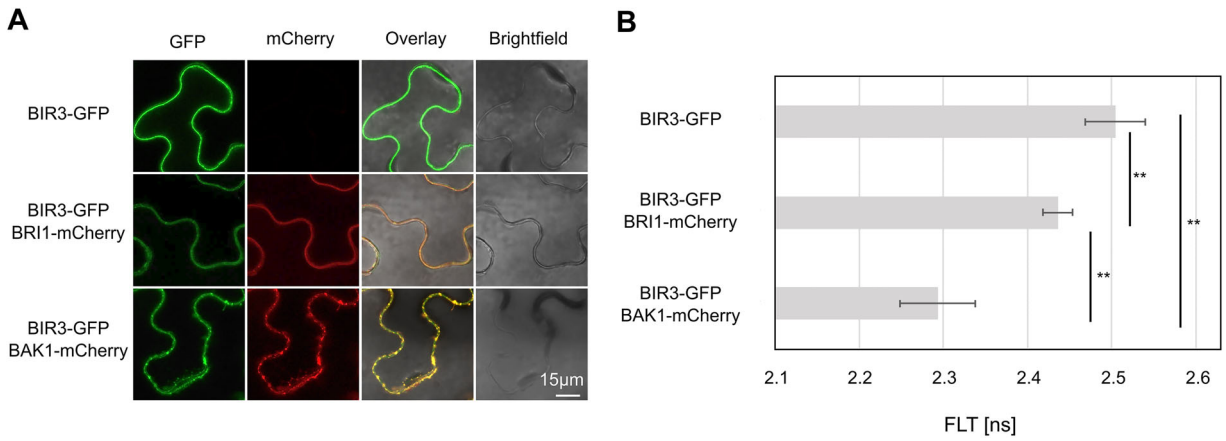

Figure 4. BIR3 co-localizes and differentially associates with BAK1 and BRI1 in the plasma membrane in plant cells
(**A**) Tobacco epidermal leaf cells were transiently transformed with indicated fusion constructs and laser scanning confocal images recorded 3 d after *Agrobacterium* infiltration (representative images are shown). (**B**) Fluorescence lifetime (FLT in ns) of BIR3-GFP alone and co-expressed with either BAK1-mCherry or BRI1-mCherry. Values are means ± *SD* of three different biological replicates and measurements of at least seven cells each. *P*-values were calculated by the Steel-Dwass-Test. ***P*-value was below 0.01.

the existence of preformed BRI1/BAK1 complexes appear to be energetically very unlikely in the absence of BR, when BIR3 is present. Thus, we further tried to elucidate whether the interaction of BAK1 with BIR3 creates new interaction surfaces for BRI1, where the cytoplasmic domain of BRI1 may simultaneously interact with BAK1 and BIR3. As the computation of trimeric complexes is currently not possible using webSDA, we had to rely on ClusPro alone to see if this interaction is possible based on the structures.

Our analysis revealed the formation of several potential complexes where BRI1 binds to BIR3-complexed BAK1 with a frequency in the range of $f_{trimeric} = 0.02–0.044$ (Figures 5, S7, S8 A, B). These computational results open the possibility that a physical association of BRI1 and BAK1 is *per se* energetically possible at a site independent of the one observed for the complex in Figure 3C, even while BAK1 is in interaction with BIR3 (Figure 5). This putative trimeric complex can provide the structural background for the experimentally observed hormone-independent interaction of BRI1 and BAK1 *in planta* (Caesar et al. 2011; Bücherl et al. 2013; Hutten et al. 2017). In these modeled complexes BRI1 cannot access the catalytic center of BAK1 but binds to another site of BAK1 that does not allow unspecific activation of BAK1 and BRI1. This complex would therefore prevent unwanted BL signaling in the absence of the ligand before BIR3 is released.

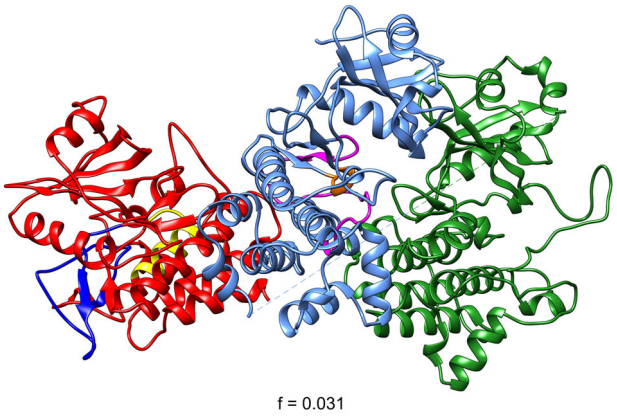

Figure 5. BRI1 interacts with BIR3-complexed BAK1 establishing a potential trimeric complex
This model was computed using ClusPro based on the complex between BIR3 and BAK1 in Figure 2B. The dashed line indicates that BAK1 and BIR3 were entered as a complex in this docking run. Color code: BIR3 (green), BAK1 (blue), catalytic domain (orange), activation loop (purple), BRI1 (red), catalytic domain (yellow), activation loop (blue). The complex is oriented in a way that the membrane would be located above the complex.

DISCUSSION

BRs play a central role in plant growth, development and responses to environmental cues. Therefore, the precise molecular regulation of BR signaling is essential.

Here, we employed comparative modeling and molecular docking analysis for the determination of the structural requirements and energetics of BAK1, BIR3, and BRI1-related protein-protein interaction and oligomerization. We used comparative modeling to generate a structure of BIR3 based on the experimentally determined structure of BIR2 (PDB ID 4l68 chain A) (Blaum et al. 2014) and in order to fill the gaps in the structure of BRI1 (PDB ID 5lpw) (Bojar et al. 2014). While these modeled sections of the protein structures can have a minor effect on the complex formation, we do not expect them to have a notable effect on the orientation of the proteins in the complexes. In fact, we obtained two potential structures for the cytoplasmic domain of BIR3 and ran the docking analysis for both conformations. Some variation between SDA and ClusPro runs occurs since both are sampling methods which calculate a limited number of complexes. Thus, some variations in the number of complexes recorded per cluster and also the average cluster binding energy, especially for the rarer complexes with a less favorable energetic landscape, is to be expected. The complexes we calculated for both structures of BIR3 with BAK1 with both webSDA and ClusPro are close in spatial orientation underlining the validity of our approach (Figure S9). In our selection of feasible complexes, we required a "minimal distance" (definition see Materials and Methods) of the N- and C-terminus of one protein to the nearest amino acid of the other protein(s) in the complex, since all structures used in this study continue at both N- and C-termini. With this "minimal distance" criterion we can be reasonably sure that no immediate clash between N- and C-termini and the other protein occurs.

From an energetical perspective we predict that the cytoplasmic domains of BRI1 and BAK1 are *per se* able to mediate the formation of stable BRI1-BAK1 hetero-oligomers in the absence of BR. Specification of the regions responsible for the interaction would allow coincidental transphosphorylation events between BRI1 and BAK1 in the absence of BR. Interestingly, the computed complexes include the loop containing D1139 in the interaction surface of BRI1 with BAK1. The D1139 to A exchange is the underlying cause of *bri1-117* phenotype that exhibits a strong loss of function phenotype (Li and Chory 1997; Friedrichsen 2000). This region is also involved in the interaction with the negative regulator BKI1, which inhibits the interaction between BRI1 and BAK1 kinase domains (Jaillais et al. 2011a). However, the BRI1-BAK1 interaction in the absence of the ligand would carry the risk of unwanted initiation of BR signaling and explains the requirement for inhibitory mechanisms.

Among the known inhibitory mechanisms (Wang et al. 2005; Jaillais et al 2011a; Lin et al. 2013), the BIR3-related one was of particular interest for us, because it implicated the interaction of BIR3 with both BRI1 and BAK1 (Imkampe et al. 2017). Here, the ectodomains have been shown to play a deciding role in the interaction of BAK1 and BIR3 (Hohmann et al. 2018). However, this does not preclude a role of the cytoplasmic domains in the interactions of the whole proteins, since the experimentally observed interaction of BIR3 and BRI1 (Imkampe et al. 2017) and this study does not appear to be mediated by the ectodomains of these proteins (Hohmann et al. 2018). Our docking analyses indeed predicted the potential of the cytoplasmic domains of BIR3 to associate with BRI1 and BAK1 by using different structural regions on the receptor and co-receptor. The energetic landscape favors the formation of the BIR3-BAK1 complex over the complex consisting of BIR3 and BRI1 – a prediction that was confirmed by quantitative FRET-FLIM studies. As BRI1 and BIR3 share the same preferential binding site on BAK1, BRI1 and BIR3 can in principle compete for interaction with BAK1, which fits the behavior observed for the ectodomains of these proteins. However, it would require a much higher amount of BRI1 in the nanoclusters or the participation of other protein parts or the ligand to shift the equilibrium toward the formation of the BRI1-BAK1 complex.

In the presence of BR, BIR3 has to be released from BAK1 in order to allow the interaction *via* its LRR ectodomain with the LRR ectodomain of $BRI1^{BR}$. This switch places the intracellular kinase domains of BAK1 and BRI1 into the correct position for transphosphorylation to allow initiation of BR signaling. This suggests that the complex binding energy of the $BRI1^{BR}$-BAK1 complex is more negative than the complex binding energy of the BIR3-BAK1 complex, the most stable cytoplasmic complex present in the proposed nanoclusters. Indeed, experiments have demonstrated that $BRI1^{BL}$ can compete with BIR3 for BAK1 complex formation (Hohmann et al. 2018). From a kinetic perspective, the switch of interaction surfaces has to happen rapidly as BR-induced alterations in cell

physiology such as hyperpolarization of the plasma membrane, cell wall expansion (Caesar et al. 2011) and dephosphorylation of BRI1-EMS suppressor (BES1) (He et al. 2002) are observed within a few minutes after BR application.

In our models, BIR3 consistently interacts with BAK1 by the catalytic site and the activation loop of BAK1 when in complex with the co-receptor (Figures 2B, S3C, S6 A,C, S9). Even though there are several less likely complexes, the majority of those show the same inhibitory interaction between BIR3 and BAK1 (Figures S10, S11, S12). This prediction by our computational analyses explains the phenotypes observed in the BIR3 and BIR3/BRI1 overexpression lines (Imkampe et al. 2017). The strong 35S promotor-driven overexpression of BIR3 renders plants insensitive to BR, phenocopies *bri1* null-mutants and prevents BRI1 and BAK1 from interacting (Imkampe et al. 2017). This overexpression caused inhibition, due to the shift in the protein amounts in the nanoclusters, is strong enough to overcome the proposed strong complex binding energy generated by the formation of $BRI1^{BR}$-BAK1 hetero-oligomers. By the overexpression of BRI1 in BIR3-overexpressing plants the additional BRI1 competes with BIR3 at sufficient levels to restore BR signaling as long as the ligand is present to stabilize the interaction of BAK1 and BRI1 (Imkampe et al. 2017).

Interestingly, *bir3* mutants show only a weak BR phenotype (Imkampe et al. 2017). This is considered to be due to a reduced BAK1 protein level in *bir3* mutants, so that less co-receptor molecules are available for $BRI1^{BR}$-BAK1 signaling. It is noteworthy that only 10% of active BRI1-BAK1 complexes are required for saturating BR responses such as in root growth (van Esse et al. 2013). But adding BAK1 by ectopic expression in the background of *bir3* mutants reveals the positive effect of *bir3* mutations on BR signaling (Imkampe et al. 2017) indicating that the BAK1 levels are essential for full responses. Among the native functions of BIR3 are the stabilization of BAK1 and to keep the BRI1-BAK1 hetero-oligomer inactive in the absence of BR or at low BR concentrations, in concert with the other known inhibitory mechanisms (Wang et al. 2005; Jaillais et al. 2011a; Lin et al. 2013). Therefore, the loss of BIR3 function would result in a BR hypersensitive phenotype as described for the *elg* mutant that perturbs interaction of BIRs and BAK1 (Hohmann et al. 2018). Thus, a fine-tuning of the BIR3 protein amount or interaction capability, for example by post-translational modification, would provide an elegant possibility for modulating the BRI1-BAK1 hetero-oligomer for its quantitative response to BR.

Our computational modeling demonstrates that the cytoplasmic domains of BRI1, BAK1 and BIR3 are indeed likely to play a role in the interactions of the whole proteins, providing an explanation for the differential interactions observed for the ectodomains and whole proteins. In line with the interaction of the ectodomains (Hohmann et al. 2018), our analysis shows that BRI1 and BIR3 compete for the overlapping interaction surfaces, but that the interaction between BIR3 and BAK1 is the more favorable one (Figure 6). We further demonstrate that BRI1, BAK1 and BIR3-containing nanoclusters are possible based on our computational simulations. However, further quantitative biochemical and *in planta* spectro-microscopic data are necessary to substantiate this model in the future.

MATERIALS AND METHODS

Comparative modeling

The comparative modeling itself was done using the tool Modeller v9.16 (Webb and Sali 2014) and was utilized to generate a structure for BIR3 as well as filling the gaps in the structure of BRI1. The template structures were obtained from the protein databank (Berman et al. 2000). First, a pairwise alignment was generated between the template structure and the amino acid sequences using the algorithm implemented in Modeller v9.16 (Webb and Sali 2014). In case of BIR3 (At1g27190), the structurally resolved parts of BIR2 (Uniport ID Q9LSI9, PDB ID 4l68, chain A, *Arabidopsis thaliana*) (Blaum et al. 2014) served as a template for the primary structure of BIR3 (Figure S1). For BRI1, the primary structure was aligned with the structurally resolved parts of the cytoplasmic domain (BRI1–Uniprot ID O22476, PDB ID 5lpw, *Arabidopsis thaliana*) (Bojar et al. 2014; Figure S2). Based on these alignments, a set of 20 potential structures was generated for each protein using a resolution of 2Å.

Structure validation

To select the structures for the docking analysis, all 20 potential structures of each protein were evaluated based on their stereochemical quality using the

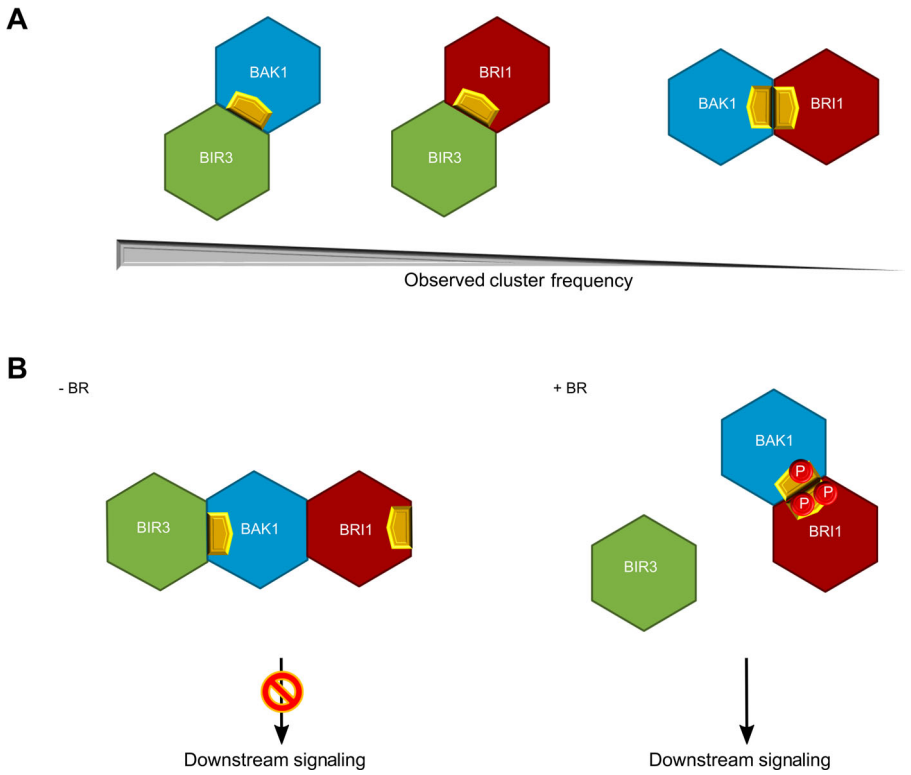

Figure 6. New model of BRI1 complex formation and signaling

(**A**) Updated interaction scheme of BIR3, BAK1 and BRI1 cytoplasmic domains. Catalytic domains are indicated in yellow. The strong interaction of BIR3 and BAK1 prevents BAK1 and BRI1 from interacting in the absence of the ligand. (**B**) Putative trimeric complex in the absence of the hormonal ligand. The catalytic domains of BAK1 and BRI1 do not interact and can therefore not initiate downstream signaling. After the addition of BR and binding to the ectodomain of BRI1, BAK1 is released from the interaction with BIR3 and is available to interact with BRI1, upon which BAK1 and BRI1 phosphorylate (P) each other and induce downstream signaling.

QMEAN4 score (available at https://swissmodel.expasy.org/qmean/) (Benkert et al. 2008, 2011). If two structures had the same QMEAN4 score, both were used for subsequent docking analyses.

Molecular docking analysis by webSDA

The molecular docking analysis regarding the complex formation between BIR3, BAK1 (structure ID 3tl8, chain A) (Cheng et al. 2011) and BRI1 (gap-filled structure based on ID 5lpw) (Bojar et al. 2014) was run using webSDA 1.0, which is available at http://mcm.h-its.org/webSDA of the Heidelberg Institute for Theoretical Studies (Gabdoulline and Wade 1997, 1998; Motiejunas et al. 2008; Yu et al. 2015; Martinez et al. 2015). The webSDA settings were: ionic strength, 150 mmol/L; included interaction terms, electrostatic interaction (Gabdoulline and Wade 1996; Baker et al. 2001), electrostatic desolvation (Elcock et al. 1999), nonpolar desolvation (Gabdoulline and Wade 2009); pH, 7.2; SDA runs, 500; generated unique complexes, 500; generated clusters, 10. The docking between BRI1 and BAK1 was constrained to a 45 Å center-center distance, as no feasible complex was observed in unconstrained docking runs. The docking of BAK1 and BRI1 with BIR3 was left without a distance constraint to get a more complete view of the energetic landscape.

Molecular docking analysis by ClusPro

The molecular docking analyses using ClusPro were run using the webserver available at https://cluspro.bu.edu// (Comeau et al. 2004a, b, Kozakov et al. 2006, 2013, 2017). For BRI1, the gap-filled structure was used. The docking between BRI1 and BAK1 was constrained to a 45 Å center-center distance. The docking between BAK1, BRI1 and BIR3 as well as the docking of BRI1 with BIR3-complexed BAK1 was left without a distance

constraint to get a more complete view of the energetic landscape. Clusters were primarily analyzed based on the scoring by the van der Waals and electrostatic interaction terms to get a measure of the energetic landscape. Only the docking between BAK1 and BRI1 was evaluated based on the balanced scoring function.

Cluster selection

Of the recorded complexes only those with feasible orientations were considered for further analysis. All protein structures used during this analysis were truncated at both N- and C-termini. Therefore, proteins in the complex had to be oriented such that the N-termini could be extended toward the plasma membrane without the C-terminus interfering (e.g. the C-terminus potentially extending into the membrane). Assuming that the extracellular domains are also involved in the interaction between proteins, the N-termini of the proteins have to be oriented in approximately the same direction. Therefore, proteins were not allowed to interact by C-terminal and N-terminal (membrane proximate) domains or by their C-terminal domains along the longitudinal axis. Furthermore, complexes were not allowed to clash with the N- and C-termini of the involved proteins, since the structures used for the docking analysis do not comprise the whole cytoplasmic domain and continue at both N- and C-termini of the modeled structure. More specifically, clashing was considered when N- or C-terminus of a protein was part of the complex interaction surface. Here, we introduce a "minimal distance" criterion for the N- or C-terminus and the other protein that a complex had to fulfill. Based on the computed complexes of our proteins of interest, we sampled the distance between these proteins at the interaction surface as defined by the amino acid backbones (specifically Cα atoms, sample size $n = 100$), which approximately follows a normal distribution (Figure S13A, B). The threshold was set to $\bar{x} + 2\sigma$, where $\bar{x}$ is the mean and σ is the standard deviation of the sample. A N- or C-terminus that was closer to the other protein in the complex than this "minimal distance" criterion was considered to cause a clash and the complex was not considered for further analysis. The threshold of $\bar{x} + 2\sigma$ is expected to cover 97.8% of potential interactions and thus clashes between structurally unresolved N- or C-termini. webSDA computes encountered complexes by rigid body docking and ClusPro has an additional step of adjusting the amino acid side chains, placing the proteins closer to each other in a complex. Therefore, different thresholds were used for both webSDA and ClusPro.

As the number of complexes in each cluster is a measure for the probability of encountering this cluster (Kozakov et al. 2017), we used the relative size of the clusters as selection criterion. The relative size $f_{cluster}$ was defined as $f_{cluster} = \frac{n_{complexes}}{N_{total\ complexes}}$, where $n_{cluster}$ is the number of complexes per cluster and $N_{total\ complexes}$ is the total number of observed complexes. In the case of webSDA, two cluster sizes are available: the number of unique recorded complexes and the total number of complexes observed for the cluster. As a more accurate estimate for the energetic landscape, we used the latter for the computation of the relative cluster size. Complexes were rendered using Chimera (Pettersen et al. 2004).

FRET-FLIM

For FRET-FLIM analysis, the coding sequences of BIR3, BRI1 and BAK1 were expressed as C-terminal fluorophore fusions in pH7FWG2 (GFP) or in pABindmCherry (mCherry) (Karimi et al. 2002; Bleckmann et al. 2010). These binary vectors and p19 as gene silencing suppressor were transformed into *Agrobacterium tumefaciens* strain GV3101 and infiltrated into *Nicotiana benthamiana* leaves. The measurements were performed 2 d after infiltration using the SP8 laser scanning microscope (Leica Microsystems GMBH) with LAS AF and SymPhoTime software as described (Veerabagu et al. 2012). Before the FRET-FLIM measurement, the presence of the fluorophores was detected by using 488 nm or 561 nm lasers for GFP or mCherry excitation, respectively.

The lifetime τ [ns] of either the donor only expressing cells or the donor-acceptor pairs was measured with a pulsed laser as an excitation light source of 470 nm and a repetition rate of 40 MHz (PicoQuant Sepia Multichannel Picosecond Diode Laser, PicoQuant Picoharp 300 TCSPC Module and Picosecond Event Timer). The acquisition was performed until 500 photons in the brightest pixel were reached. To obtain the GFP fluorescence lifetime, data processing was performed with SymPhoTime software and bi-exponential curve fitting, correction for the instrument response function and a fitting range from channel

90 to 1,400. FRET-FLIM data are derived from three different biological replicates and measurements of at least seven cells each. For statistical evaluation, data points were analyzed regarding their variances. As the samples display significantly different variances, a Steel-Dwass test was performed using JMP version 13.1.

ACKNOWLEDGEMENT

We thank the CRC 1101 "Molecular Encoding of Specificity in Plant Processes" of the German Research Foundation and the Klaus Tschira Foundation for funding. We thank Rebecca Wade and Neil Bruce at the Heidelberg Institute for Theoretical Studies (HITS gGmbH) for advice and fruitful discussions. R.G. would like to thank the Schmeil Foundation (Heidelberg) and the Heidelberg Graduate School of Mathematical and Computational Methods for the Sciences (HGS MathComp) for support.

AUTHOR CONTRIBUTIONS

U.K., K.H., B.K., R.G. devised the study. R.G., A.F.S. did the comparative modeling. R.G., A.F.S. did the webSDA analysis. R.G. did the ClusPro analysis. F.W. did the FRET-FLIM measurements. N.G. did the statistical analysis of the FRET-FLIM data. B.K., S.S. contributed to experimental data and discussion. R.G., A.F.S., U.K., K.H. wrote the paper. All authors read and agreed to its contents.

REFERENCES

Baker NA, Sept D, Joseph S, Holst MJ, McCammon JA (2001) Electrostatics of nanosystems: Application to microtubules and the ribosome. **Proc Natl Acad Sci USA** 98: 10037–10041

Belkhadir Y, Jaillais Y (2015) The molecular circuity of brassinosteroid signaling. **New Phytol** 206: 522–540

Benkert P, Biasini M, Schwede T (2011) Toward the estimation of the absolute quality of individual protein structure models. **Bioinformatics** 27: 343–350

Benkert P, Tosatto SCE, Schomburg D (2008) QMEAN: A comprehensive scoring function for model quality assessment. **Proteins Struct Funct Bioinfor** 71: 261–277

Berman HM, Westbrook J, Feng Z, Gilliland G, Bhat TN, Weissig H, Shindyalov IN, Bourne PE (2000) The protein data bank. **Nucleic Acids Res** 28: 235–242

Blaum BS, Mazzotta S, Nöldeke ER, Halter T, Madlung J, Kemmerling B, Stehle T (2014) Structure of the pseudokinase domain of BIR2, a regulator of BAK1-mediated immune signaling in *Arabidopsis*. **J Struct Biol** 186: 112–121

Bleckmann A, Weidtkamp-Peters S, Seidel CAM, Simon R (2010) Stem cell signaling in *Arabidopsis* requires CRN to localize CLV2 to the plasma membrane. **Plant Physiol** 52: 166–176

Bojar D, Martinez J, Santiago J, Rybin V, Bayliss R, Hothorn M (2014) Crystal structures of the phosphorylated BRI1 kinase domain and implications for brassinosteroid signal initiation. **Plant J** 78: 31–43

Bücherl CA, van Esse GW, Kruis A, Luchtenberg J, Westphal AH, Aker J, van Hoek A, Albrecht C, Borst JW, de Vries S (2013) Visualization of BRI1 and BAK1 (SERK3) membrane receptor heterooligomers during brassinosteroid signaling. **Plant Physiol** 162: 1911–1925

Caesar K, Elgass K, Chen Z, Huppenberger P, Witthöft J, Schleifenbaum F, Blatt MR, Oecking C, Harter K (2011) A fast brassinolide-regulated response pathway in the plasma membrane of *Arabidopsis thaliana*. **Plant J** 66: 528–540

Camacho CJ, Weng Z, Vajda S, DeLisi C (1999) Free energy landscapes of encounter complexes in protein-protein association. **Biophys J** 76: 1166–1178

Cheng W, Munkvold KR, Gao H, Mathieu J, Schwizer S, Wang S, Yan YB, Wang J, Martin GB, Chai J (2011) Structural analysis of pseudomonas syringae AvrPtoB bound to host BAK1 reveals two similar kinase-interacting domains in a type III effector. **Cell Host Microbe** 10: 616–626

Clouse SD, Langford M, Mcmorris TC (1996) A brassinosteroid-insensitive mutant in *Arabidopsis thaliana* exhibits multiple defects in growth and development. **Plant Physiol** 11: 671–678

Comeau SR, Gatchell DW, Vajda S, Camacho CJ (2004a) ClusPro: A fully automated algorithm for protein-protein docking. **Nucleic Acids Res** 32: W96–W99

Comeau SR, Gatchell DW, Vajda S, Camacho CJ (2004b) ClusPro: An automated docking and discrimination method for the prediction of protein complexes. **Bioinformatics** 20: 45–50

Elcock AH, Gabdoulline RR, Wade RC, McCammon JA (1999) Computer simulation of protein-protein association kinetics: acetylcholinesterase-fasciculin. **J Mol Biol** 291: 149–162

Feldman-Salit A, Hering S, Messiha HL, Veith N, Cojocaru V, Sieg A, Westerhoff HV, Kreikemeyer B, Wade RC, Fiedler T (2013) Regulation of the activity of lactate dehydrogenases from four lactic acid bacteria. **J Biol Chem** 288: 21295–306

Friedrichsen DM (2000) Brassinosteroid-insensitive-1 is a ubiquitously expressed leucine-rich repeat receptor serine/threonine kinase. **Plant Physiol** 123: 1247–1256

Gabdoulline RR, Wade RC (1996) Effective charges for macromolecules in Solvent. **J Phys Chem** 100: 3868–3878

Gabdoulline RR, Wade RC (1997) Simulation of the diffusional association of barnase and barstar. **Biophys J** 72: 1917–1929

Gabdoulline RR, Wade RC (1998) Brownian dynamics simulation of protein-protein diffusional encounter. **Methods** 14: 329–341

Gabdoulline RR, Wade RC (2009) On the contributions of diffusion and thermal activation to electron transfer between *Phormidium laminosum* plastocyanin and cytochrome *f*: Brownian dynamics simulations with explicit modeling of nonpolar desolvation interactions and electron. **J Am Chem Soc** 131: 9230–9238

Halter T, Imkampe J, Blaum BS, Stehle T, Kemmerling B (2014a) BIR2 affects complex formation of BAK1 with ligand binding receptors in plant defense. **Plant Signal Behav** 9: 1–4

Halter T, Imkampe J, Mazzotta S, Wierzba M, Postel S, Bücherl C, Kiefer C, Stahl M, Chinchilla D, Wang X, Nürnberger T, Zipfel C, Clouse S, Borst JW, Boeren S, de Vries SC, Tax F, Kemmerling B (2014b) The leucine-rich repeat receptor kinase BIR2 is a negative regulator of BAK1 in plant immunity. **Curr Biol** 24: 134–143

He J-X, Gendron JM, Yang Y, Li J, Wang Z-Y (2002) The GSK3-like kinase BIN2 phosphorylates and destabilizes BZR1, a positive regulator of the brassinosteroid signaling pathway in *Arabidopsis*. **Proc Natl Acad Sci USA** 99: 10185–10190

Hilbert M, Böhm G, Jaenicke R (1993) Structural relationships of homologous proteins as a fundamental principle in homology modeling. **Proteins** 17: 138–51

Hohmann U, Lau K, Hothorn M (2017) The structural basis of ligand perception and signal activation by receptor kinases. **Annu Rev Plant Biol** 68: 1–928

Hohmann U, Nicolet J, Moretti A, Hothorn LA, Hothorn M (2018) The SERK3 elongated allele defines a role for BIR ectodomains in brassinosteroid signalling. **Nat Plants** 4: 1–7

Hutten SJ, Hamers DS, Den Toorn MA, van Esse W, Nolles A, Bücherl CA, de Vries SC, Hohlbein J, Borst JW (2017) Visualization of BRI1 and SERK3/BAK1 nanoclusters in *Arabidopsis* roots. **PLoS ONE** 12: e0169905

Imkampe J, Halter T, Huang S, Schulze S, Mazzotta S, Schmidt N, Manstretta R, Postel S, Wierzba M, Yang Y, van Dongen WMAM, Stahl M, Zipfel C, Goshe MB, Clouse S, de Vries SC, Tax F, Wang X, Kemmerling B (2017) The *Arabidopsis* leucine-rich repeat receptor kinase BIR3 has dual functions in the negative regulation of BAK1 receptor complex formation and in stabilization of BAK1. **Plant Cell** 29: 2285–2303

Jaillais Y, Hothorn M, Belkhadir Y, Dabi T, Nimchuck ZL, Meyerowitz EM, Chory J (2011a) Tyrosine phosphorylation controls brassinosteroid receptor activation by triggering membrane release of its kinase inhibitor. **Genes Dev** 25: 232–7

Jaillais Y, Belkhadir Y, Balsemão-Pires E, Dangl JL, Chory J (2011b) Extracellular leucine-rich repeats as a platform for receptor/coreceptor complex formation. **Proc Natl Acad Sci USA** 108: 8503–8507

Karimi M, Inzé D, Depicker A (2002) GATEWAY^{TM} vectors for *Agrobacterium*-mediated plant transformation. **Trends Plant Sci** 7: 193–195

Kozakov D, Beglov D, Bohnuud T, Mottarella SE, Xia B, Hall DR, Vajda S (2013) How good is automated protein docking? **Proteins Struct Funct Bioinfor** 81: 2159–2166

Kozakov D, Brenke R, Comeau SR, Vajda S (2006) PIPER: An FFT-based protein docking program with pairwise potentials. **Proteins Struct Funct Genet** 65: 392–406

Kozakov D, Hall DR, Xia B, Porter KA, Padhorny D, Yueh, C, Beglov D, Vajda S (2017) The ClusPro web server for protein-protein docking. **Nat Protoc** 12: 255–278

Li J, Chory J (1997) A putative leucine-rich repeat receptor kinase involved in brassinosteroid signal transduction. **Cell** 90: 929–938

Li J, Wen J, Lease KA, Doke JT, Tax FE, Walter JC (2002) BAK1, an *Arabidopsis* LRR receptor-like protein kinase, interacts with BRI1 and modulates brassinosteroid signaling. **Cell** 110: 213–222

Lin W, Lu D, Gao X, Jiang S, Ma X, Wang Z, Mengiste T, He P, Shan L (2013) Inverse modulation of plant immune and brassinosteroid signaling pathways by the receptor-like cytoplasmic kinase BIK1. **Proc Natl Acad Sci USA** 110: 12114–12119

Martinez M, Bruce NJ, Romanowska J, Martinez M, Bruche NJ, Romanowska J, Kohk DB, Ozboyaci M, Yu X, Öztürk MA, Richter S, Wade RC (2015) SDA 7: A modular and parallel implementation of the simulation of diffusional association software. **J Comput Chem** 36: 1631–1645

Meng EC, Pettersen EF, Couch GS, Huang CC, Ferrin TE (2006) Tools for integrated s4eqence-structure analysis with UCSF Chimera. **BMC Bioinfor** 7: 339

Motiejunas D, Gabdoulline R, Wang T, Feldman-Salit A, Johann T, Winn PJ, Wade RC (2008) Protein-protein docking by simulating the process of association subject to biochemical constraints. **Proteins Struct Funct Genet** 71: 1955–1969

Müssig C, Fischer S, Altmann T (2002) Brassinosteroid-regulated gene expression. **Plant Physiol** 129: 1241–51

Nakaya M, Tsukaya H, Murakami N, Kato M (2002) Brassinosteroids control the proliferation of leaf cells of *Arabidopsis thaliana*. **Plant Cell Physiol** 43: 239–244

Nam KH, Li J (2002) BRI1/BAK1, a receptor kinase pair mediating brassinosteroid signaling. **Cell** 110: 203–212

Pettersen EF, Goddard TD, Huang CC, Couch GS, Greenblatt DM, Meng EC, Ferrin TE (2004) UCSF Chimera – A visualization system for exploratory research and analysis. **J Comput Chem** 25: 1605–1612

Santiago J, Henzler C, Hothorn M (2013) Molecular mechanism for plant steroid receptor activation by somatic embryogenesis co-receptor kinases. **Science** 341: 889–892

Sayyed-Ahmad A, Cho KJ, Hancock JF, Gorfe AA (2016) Computational equilibrium thermodynamic and kinetic analysis of K-Ras dimerization through an effector binding surface suggests limited functional role. **J Phys Chem B** 120: 8547–8556

Steeland S, Puimège L, Vandenbroucke RE, Van Hauwermeiren F, Haustraete J, Devoogdt N, Hulpiau P, Leroux-Roels G, Laukens D, Meuleman P, De Vos M, Libert C (2015) Generation and characterization of small single domain antibodies inhibiting human tumor necrosis factor receptor 1. **J Biol Chem** 290: 4022–4037

Sun Y, Han Z, Tang J, Hu Z, Chai C, Zhou B, Chai J (2013) Structure reveals that BAK1 as a co-receptor recognizes the BRI1-bound brassinolide. **Cell Res** 23: 1326–1329

van Esse W, van Mourik S, Albrecht C, van Leeuwen J, de Vries S (2013) A mathematical model for the coreceptors SOMATIC EMBRYOGENESIS RECEPTOR-LIKE KINASE1 and SOMATIC EMBRYOGENESIS RECEPTOR-LIKE KINASE3 in BRASSINOSTEROID INSENSITIVE1-mediated signaling. **Plant Physiol** 163: 1472–1481

Veerabagu M, Elgass K, Kirchler T, Huppenberger P, Harter K, Chaban C, Mira-Rodado V (2012) The *Arabidopsis* B-type response regulator 18 homomerizes and positively regulates cytokinin responses. **Plant J** 72: 721–731

Wang X, Kota U, He K, Blackburn K, Li J, Goshe MB, Huber SC, Clouse SD (2008) Sequential transphosphorylation of the BRI1/BAK1 receptor kinase complex impacts early events in brassinosteroid signaling. **Dev Cell** 15: 220–35

Wang X, Li X, Meisenhelder J, Hunter T, Yoshida S, Asami T, Chory J (2005) Autoregulation and homodimerization are involved in the activation of the plant steroid receptor B RI1. **Dev Cell** 8: 855–865

Webb B, Sali A (2014) Comparative protein structure modeling using MODELLER. **Curr Protoc Bioinfor** 47: 5.6.1–5.6.32

Witthöft J, Caesar K, Elgass K, Huppenberger P, Kilian J, Schleifenbaum F, Oecking C, Harter K (2011) The activation of the *Arabidopsis* P-ATPase 1 by the brassinosteroid receptor BRI1 is independent of threonine 948 phosphorylation. **Plant Signal Behav** 6: 1063–1066

Witthöft J, Harter K (2011) Latest news on *Arabidopsis* brassinosteroid perception and signaling. **Front Plant Sci** 2: 58

Yan L, Ma Y, Liu D, Wei X, Sun Y, Chen X, Zhao H, Zhou J, Wang Z, Shui W, Lou Z (2012) Structural basis for the impact of phosphorylation on the activation of plant receptor-like kinase BAK1. **Cell Res** 22: 1304–1308

Ye Z, Musiol EM, Weber T, Williams GJ (2014) Reprogramming acyl carrier protein interactions of an Acyl-CoA promiscuous trans-acyltransferase. **Chem Biol** 21: 636–646

Yu X, Martinez M, Gable AL, Fuller JC, Bruche NJ, Richter S, Wade RC (2015) webSDA: A web server to simulate macromolecular diffusional association. **Nucleic Acids Res** 43: W220–4

SUPPORTING INFORMATION

Additional Supporting Information may be found online in the supporting information tab for this article: http://onlinelibrary.wiley.com/doi/10.1111/jipb.12803/suppinfo

Figure S1. Alignment of the primary structure of BIR3 to the structurally resolved parts of BIR2 (PDB ID 4l68) (Blaum et al. 2014)

Overall, a sequence identity of 66% was determined between the proteins in the region of interest. This alignment was generated using Modeller (Webb and Sali 2014).

Figure S2. Alignment of the primary structure of BRI1 to the structurally resolved parts of BRI1 (PDB ID 5lpw) (Bojar et al. 2014)

This alignment was generated using Modeller (Webb and Sali 2014).

Figure S3. Interactions of the second BIR3 structure with BAK1 and BRI1 computed by webSDA

(**A**) Second computed structure of BIR3. (**B**) Alignment of both BIR3 structures. Differences are highlighted in red. (**C**) BAK1 interacts with BIR3 preferentially by its catalytic domain and its activation loop. (**D**) Complex between BRI1 and the second BIR3 structure covers the catalytic domain. Color code: BIR3 (green), BAK1 (blue), catalytic domain (orange), activation loop (purple), BRI1 (red), catalytic domain (yellow), activation loop (blue). The structures and complexes are oriented in a way that the membrane would be located above the complexes.

Figure S4. Template selection for BAK1

(**A**) BAK1 - PDB ID 3tl8, chain A (Cheng et al. 2011). (**B**) BAK1- PDB ID 3uim (Yan et al. 2012). Arrows indicate gaps in the structure. (**C**) B-Factor of 3tl8. The binding of the inhibitor causes a lower B-Factor in the structure of BAK1 at its binding site. (**D**) B-Factor of 3uim. (**E**) Comparison of 3tl8 and 3uim by alignment. Differences between the structures are highlighted in blue. (**F**) RMSD of the Ca atoms between the two structures. Areas with greater differences are indicated in red. (**G, H**) QMEAN4 scores of 3tl8 (**G**) and 3uim (**H**) (Benkert et al. 2008, 2011). (**I**) Normalized QEMAN4 score depending on the protein size. The positions of 3tl8 and 3uim are indicated by red stars. G–I: Output generated by QMEAN calculations (Benkert et al. 2008, 2011).

Figure S5. Complex computed between BAK1 and BRI1 computed by ClusPro. BRI1 and BAK1 interact by their respective activation loop and catalytic domains (Yan et al. 2012; Bojar et al. 2014)

This complex was obtained using the balanced scoring function of ClusPro as the docking analysis based on van der Waals and electrostatic forces yielded no allowed complex within our set of constraints. Color code: BAK1

(blue), catalytic domain (orange), activation loop (purple), BRI1 (red), catalytic domain (yellow), activation loop (blue), D1139 highlighted in cyan. The complex is oriented in a way that the membrane would be located above the complex.

Figure S6. Complexes between the two structures of BIR3 and BAK1 as well as BRI1 computed by ClusPro

(**A**) Computed complex between BAK1 and the first BIR3 structure. (**B**) Computed complex between BRI1 and the first BIR3 structure. (**C**) Computed complex between BAK1 and the second BIR3 structure. (**D**) Computed complex between BRI1 and the second BIR3 structure. Color code: BIR3 (green), BAK1 (blue), catalytic domain (orange), activation loop (purple), BRI1 (red), catalytic domain (yellow), activation loop (blue). The complexes are oriented in a way that the membrane would be located above the complexes.

Figure S7. Trimeric complex based on the complex of BIR3 with BAK1 (Figure S3C) and BRI1 docking to this complex

The model was computed using ClusPro. The dashed line indicates that BAK1 and BIR3 were entered as a complex in this docking run. Color code: BIR3 (green), BAK1 (blue), catalytic domain (orange), activation loop (purple), BRI1 (red), catalytic domain (yellow), activation loop (blue). All complexes are oriented in a way that the membrane would be located above the complex.

Figure S8. Trimeric complexes based on the complex of BIR3 with BAK1 (Figure S6C) and BRI1 docking to this complex

The models were computed using ClusPro. The dashed line indicates that BAK1 and BIR3 were entered as a complex in the docking runs. Color code: BIR3 (green), BAK1 (blue), catalytic domain (orange), activation loop (purple), BRI1 (red), catalytic domain (yellow), activation loop (blue). All complexes are oriented in a way that the membrane would be located above the complex.

Figure S9. Interaction sites on BAK1 and BIR3 are consistent between BIR3 structures and docking methods. The complexes were alternately aligned to either BIR3 or BAK1 using the MatchMaker tool in Chimera to visualize the interaction site of the respective complex (Meng et al. 2006)

Color code: BIR3 (green), BAK1 (blue), catalytic domain (orange), activation loop (purple).

Figure S10. Additional complexes computed by webSDA

(**A**) Additional complex computed between BAK1 and BIR3 that also inhibits BAK1 activity. (**B–D**) Additional complexes computed for BRI1 and BIR3. (**E**) Additional complex computed for BRI1 and the second BIR3 structure. For this structure, no additional complexes between BAK1 and BIR3 were computed within our set of criteria. Color code: BIR3 (green), BAK1 (blue), catalytic domain (orange), activation loop (purple), BRI1 (red), catalytic domain (yellow), activation loop (blue). The complexes are oriented in a way that the membrane would be located above the complexes.

Figure S11. Additional complexes that were classified as feasible for the first BIR3 structure as computed by ClusPro

(A–N) Several complexes are feasible for the interaction of BIR3 and BAK1. While the majority of these complexes inhibits the activity of BAK1, the majority do not block the catalytic domain or the activation loop of BAK1. (**K**) Second feasible complex recorded for BIR3 and BRI1. Color code: BIR3 (green), BAK1 (blue), catalytic domain (orange), activation loop (purple), BRI1 (red), catalytic domain (yellow), activation loop (blue). All complexes are oriented in a way that the membrane would be located above the complex.

Figure S12. Additional complexes that were classified as feasible for the second BIR3 structure as computed by ClusPro

No complexes were recorded for BRI1 and the second BIR3 structure. Color code: BIR3 (green), BAK1 (blue), catalytic domain (orange), activation loop (purple), BRI1 (red), catalytic domain (yellow), activation loop (blue). All complexes are oriented in a way that the membrane would be located above the complex.

Methods

Figure S13. Distribution of distances between interacting amino acids in the interaction surface of the complexes (sample $n = 100$). The distributions approximately follow a normal distribution

(**A**) Sampled distances of proteins in complexes computed by webSDA with a mean of $\bar{x} = 8.452$ Å and a standard deviation of $\sigma = 1.956$ Å. (**B**) Sampled distances between proteins in complexes computed by ClusPro with a mean of $\bar{x} = 7.185$ Å and a standard deviation of $\sigma = 1.495$ Å. The threshold of $\bar{x} + 2\sigma$ is expected to cover 97.8% of potential interactions and thus clashes between structurally unresolved N- or C-termini.

Scan using WeChat with your smartphone to view JIPB online

Scan with iPhone or iPad to view JIPB online

Supporting Information

Structure selection for BAK1

Three structures of the BAK1 cytosolic domain were available on the Protein Data Bank (Berman et al. 2000; Rose et al. 2017) starting from residue 272 to residue 583, depending on the structure: 3uim and 3ulz (residues 272-321, 327-573) (Yan et al. 2012) (fig. S3 B) and 3tl8 (273-576) (Cheng et al. 2011) (fig. S3 A). All structures have comparable resolutions ranging from 2.2 Å (3uim) to 2.5 Å (3tl8) and 2.6 Å (3ulz).

Based on completeness and structure quality alone, 3tl8 is the best candidate for docking analysis. However, it has been crystallized in the presence of the inhibitor (Cheng et al. 2011). To determine the impact of the binding of the inhibitor on the structure and if it might introduce a bias in the docking analysis, we compared 3uim and 3tl8 in detail.

First, we evaluated the completeness of the structures. In contrast to 3tl8, 3uim contains a gap in the structure from 322 to 326. Furthermore, 3lt8 has three more residues that are structurally resolved at the C-terminal end.

By visualizing the B-factor, which is a measure for the fluctuations of the individual atoms in the structure, we determine the region of BAK1 that is affected by the binding of the inhibitor (fig. S3C, blue). Subsequently, we evaluated the conservation between the structures (fig. S3 E) as well as the root mean square distance (RMSD) of the Cα atoms in the amino acid backbone. Here, the regions with differences between the structures (fig. S3 E, blue; fig. S3 F, white-red) are not in the region where the inhibitor binds to BAK1 in 3tl8.

Last, we checked the structural quality in detail using the QMEAN4 score. The QMEAN4 score evaluates not only the torsion angle over three amino acids, but also the interaction potential of Cβ molecules and the solvation potential. Here, 3uim performs consistently worse than 3tl8 (fig. S3 G, H). Finally, a comparison of the QMEAN4 score with a non-redundant set of PDB structures shows that 3uim has indeed a worse quality not only compared to 3tl8 but also to the reference set. Therefore, we chose 3tl8 for docking analysis.

BAK1 and BRI1 can interact based on their kinase domains

To substantiate the results of the webSDA analyses, we also used the ClusPro sever to compute the different complexes (https://cluspro.org/). Unlike webSDA, which simulates the diffusional association by Brownian dynamics, ClusPro extensively samples the interaction space by computing 70,000 potential complexes. Of these, the 1000 with the lowest scoring

function value are kept and clustered into up to 30 clusters. To compare the information of the energetic landscape, we used the scoring function that combines van der Waals and electrostatic forces. Only if this analysis yielded no allowed complex within our criteria, we also considered the balanced scoring function, which contains a description of the structure compatibility based on the Decoy as a Reference Structure (DARS) (Chuang et al. 2008). While this method was optimized for antigen-antibody and protein-inhibitor complexes, it can still help identifying potential complexes in other situations. However, the power of discriminating between the complexes is poor in these cases (Chuang et al. 2008).

Here, the docking of the cytoplasmic domains of BAK1 and BRI1 yielded a complex very similar to the one computed by webSDA analysis (fig. S4). In particular, the proteins are closer together as ClusPro allows the adjustment of amino acid side chains in an additional step during docking analysis. Notably, the loop containing D1139 is again part of this interaction surface. The fact that we did not see this complex based on electrostatics and van der Waals scoring alone but only in combination with DARS underlines how unfavorable this formation is. However, it is still theoretically possible necessitating the regulatory mechanisms by BKI1, BIK1 and BIR3.

Energetics of BIR3 interacting with BAK1 and BRI1

To confirm the results of the docking by webSDA, we repeated the same docking using ClusPro. Here, we also see that BIR3 preferentially interacts with BAK1 by its catalytic domain and activation loop (fig. S7 A, C). Similar to the results of the webSDA analysis, the docking by ClusPro favors the formation of a complex between BIR3 and BAK1 over a complex between BIR3 and BAK1. As ClusPro relies on extensive sampling of the interaction space instead of simulating the diffusional association by Brownian dynamics, there are some differences in the frequency of the different complexes. Nonetheless, the favored complex between BIR3 and BAK1 appears to be a more favorable interaction than the preferred complex between BIR3 and BRI1 (fig. S7). In addition to the complexes depicted in fig. S7, several other complexes were allowed based on our set of criteria (fig. S8, S9). While some complexes demonstrate BIR3 binding to BAK1 at a different site than the catalytic domain and the activation loop, the majority demonstrate the same inhibitory interaction observed for the most likely complexes. These differences can also be due to the fact that webSDA, unlike ClusPro, allows the specification of physiological parameters such as solvent pH.

BRI1 can interact with BIR3-complexed BAK1

Finally, we also checked if BRI1 can still dock with BAK1 in the complexes computed by ClusPro (see fig. S7 A, C). Here, we docked BRI1 to BIR3-complexed BAK1 without any constraining reaction criteria. We applied the same selection criteria as before (see Materials & Methods) and checked if a feasible complex was among the clusters recorded by ClusPro based on the scoring function based on van der Waals and electrostatic interaction terms.

These docking analysis yielded feasible complexes for only one BIR3 structure (fig. S12 A, B). These complexes occur with a relatively low frequency of $f_{trimeric} = \mathbf{0}.02\,\mathbf{I}\,0.04\mathbf{4}$ showing that this is indeed not a favored interaction. Repeated docking analyses for the other BIR3 structure did not yield any complex that fulfilled all criteria (orientation, membrane accessibility of the N-terminus, minimal distance criterion). Considering the fact of how unfavorable this interaction seems to be based on the complexes that were computed, this is not surprising. Also, the docking analysis allows for more degrees of freedom as the proteins are not anchored to the membrane as they are in reality. Therefore, this allows for complexes that would not be possible under normal circumstances but can occur due to the sampling and filtering process by the docking analysis.

```
position          280       290       300       310       320       330
4l68        GLAQRLRSHKLTQVSLFQKPLVKVKLGDLMAATNNFNSENIIVSTRTGTTYKALLPDGSALAVKH
BIR3        DWIGLLRSHKLVQVTLFQKPIVKIKLGDLMAATNNFSSGNIDVSSRTGVSYKADLPDGSALAVKR
conserved        ****** ** ***** ** ************ * ** ** ***  *** **********

position     340       350       360       370       380       390
4l68        LSTCKLGEREFRYEMNQLWELRHSNLAPLLGFCVVEEEKFLVYKYMSNGTLHSLLDSNR---GEL
BIR3        LSACGFGEKQFRSEMNKLGELRHPNLVPLLGYCVVEDERLLVYKHMVNGTLFSQLHNGGLCDAVL
conserved   ** *  **  ** *** * **** ** **** **** *  **** * **** * *         *

position   400       410       420       430       440       450       460
4l68        DWSTRFRIGLGAARGLAWLHHGCRPPILHQNICSSVILIDEDFDARIIDSGLARLMVP-------
BIR3        DWPTRRAIGVGAAKGLAWLHHGCQPPYLHQFISSNVILLDDDFDARITDYGLAKLVGSRDSNDSS
conserved   ** **  ** *** ********* ** *** * * *** * ****** * *** *

position        470       480       490       500       510           520
4l68        ----DLGEFGYVAPEYSTTMLASLKGDVYGLGVVLLELATGLKAVG---------GSLVDWVKQL
BIR3        FNNGDLGELGYVAPEYSSTMVASLKGDVYGFGIVLLELVTGQKPLSVINGVEGFKGSLVDWVSQY
conserved       **** ******** ** ********* * ***** ** *            ******* *

position       530       540       550       560       570       580       590
4l68        ESSGRIAETFDENIRGKGHDEEISKFVEIALNCVSSRPKERWSMFQAYQSLKAIAEKQGYSFSEQ
BIR3        LGTGRSKDAIDRSICDKGHDEEILQFLKIACSCVVSRPKERPTMIQVYESLKNMADKHG--VSEH
conserved      **     *  *  *******  *  **  ** ******  * * * ***  * * *   **

position           600
4l68        DDDFPLIFDTQ
BIR3        YDEFPLVFNKQ
conserved    * *** *  *
```

Figure S1: Alignment of the primary structure of BIR3 to the structurally resolved parts of BIR2 (PDB ID 4l68) (Blaum et al. 2014). Overall, a sequence identity of 66% was determined between the proteins in the region of interest. This alignment was generated using Modeller (Webb and Sali 2014).

```
position         870       880       890       900       910       920
5lpw           KPLRKLTFADLLQATNGFHNDSLIGSGGFGDVYKAILKDGSAVAIKKLIHVSGQGDREFMAEM
BRI1           KPLRKLTFADLLQATNGFHNDSLIGSGGFGDVYKAILKDGSAVAIKKLIHVSGQGDREFMAEM
conserved      ************************************************************

position      930       940       950       960       970       980       990
5lpw           ETIGKIKHRNLVPLLGYCKVGDERLLVYEFMKYGSLEDVLHDP---GVKLNWSTRRKIAIGSA
BRI1           ETIGKIKHRNLVPLLGYCKVGDERLLVYEFMKYGSLEDVLHDPKKAGVKLNWSTRRKIAIGSA
conserved      ****************************************   ****************

position            1000      1010      1020      1030      1040      1050
5lpw           RGLAFLHHNCSPHIIHRDMKSSNVLLDENLEARVSDFGMARLMSAMDTHLSVSTLAGTPGYVP
BRI1           RGLAFLHHNCSPHIIHRDMKSSNVLLDENLEARVSDFGMARLMSAMDTHLSVSTLAGTPGYVP
conserved      ************************************************************

position         1060      1070      1080      1090      1100      1110
5lpw           PEYYQSFRCSTKGDVYSYGVVLLELLTGKRPT---------LVGWVKQHAKLRISDVFDPELM
BRI1           PEYYQSFRCSTKGDVYSYGVVLLELLTGKRPTDSPDFGDNNLVGWVKQHAKLRISDVFDPELM
conserved      ******************************         **********************

position      1120      1130      1140      1150      1160
5lpw           KEDPALEIELLQHLKVAVACLDDRAWRRPTMVQVMAMFKEIQA
BRI1           KEDPALEIELLQHLKVAVACLDDRAWRRPTMVQVMAMFKEIQA
conserved      ******************************************
```

Figure S2: Alignment of the primary structure of BRI1 to the structurally resolved parts of BRI1 (PDB ID 5lpw) (Bojar et al. 2014). This alignment was generated using Modeller (Webb and Sali 2014).

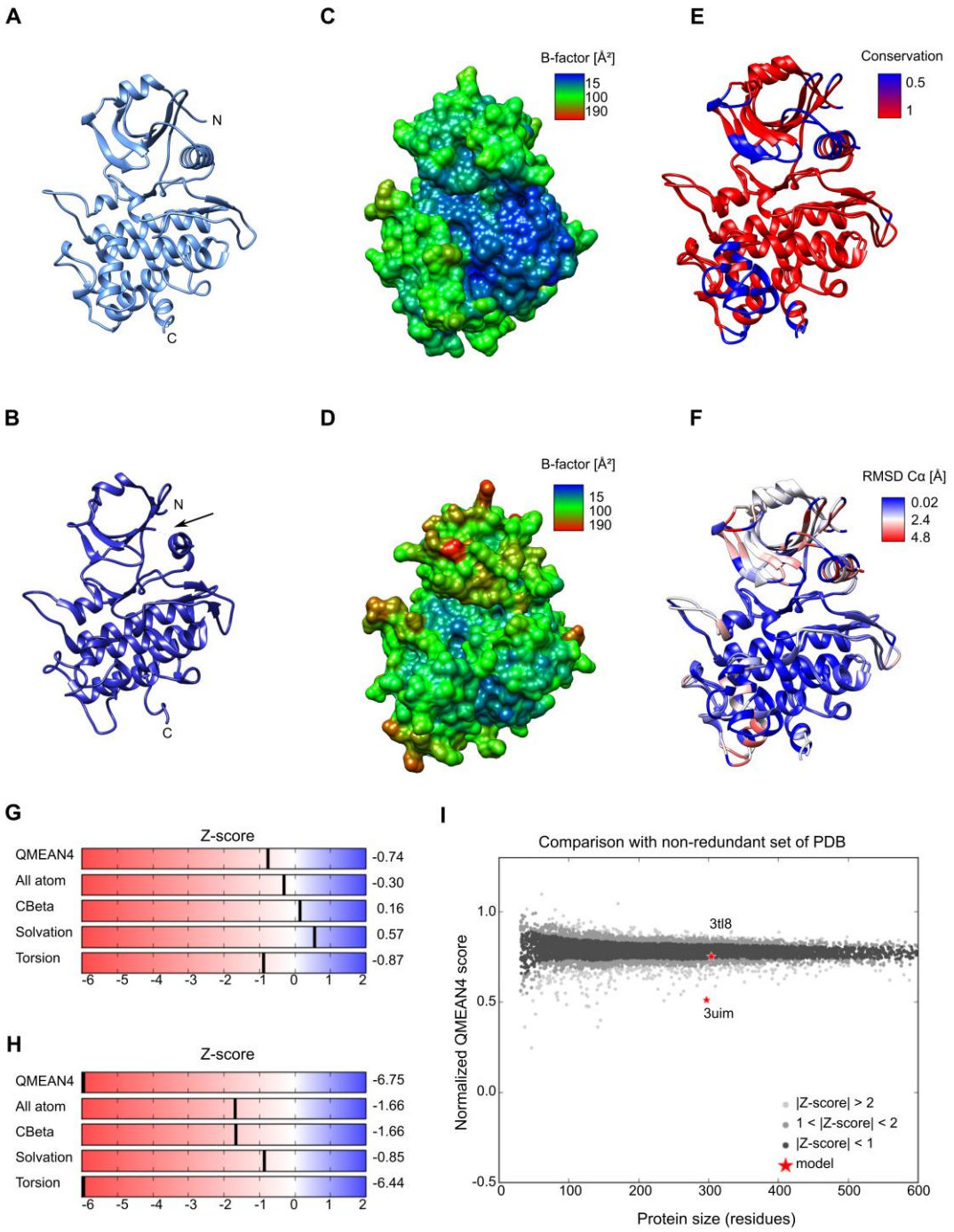

Figure S3: Template selection for BAK1. **A**: BAK1 - PDB ID 3tl8, chain A (Cheng et al. 2011). **B**: BAK1- PDB ID 3uim (Yan2012). Arrows indicate gaps in the structure. **C**: B-Factor of 3tl8. The binding of the inhibitor causes a lower B-Factor in the structure of BAK1 at its binding site. **D**: B-Factor of 3uim. **E:** Comparison of 3tl8 and 3uim by alignment. Differences between the structures are highlighted in blue. **F**: RMSD of the Ca atoms between the two structures. Areas with greater differences are indicated in red. **G, H**: QMEAN4 scores of 3tl8 (G) and 3uim (H) (Benkert et al. 2008, 2011). **I**: Normalized QEMAN4 score depending on the protein size. The position of 3tl8 and 3uim are indicated by red stars. G-I: Output generated by QMEAN calculations (Benkert et al. 2008, 2011).

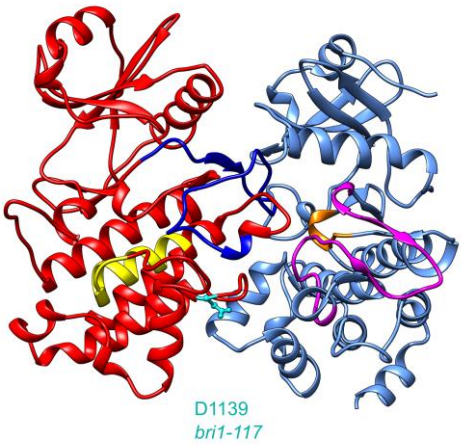

Figure S4: Complex computed between BAK1 and BRI1 computed by ClusPro. BRI1 and BAK1 interact by their respective activation loop and catalytic domains (Yan et al. 2012; Bojar et al. 2014). This complex was obtained using the balanced scoring function of ClusPro as the docking analysis based on van der Waals and electrostatic forces yielded no allowed complex within our set of constraints. Color code: BAK1 (blue), catalytic domain (orange), activation loop (purple); BRI1 (red): catalytic domain (yellow), activation loop (blue), D1139 highlighted in cyan. The complex is oriented in a way that the membrane would be located above the complex.

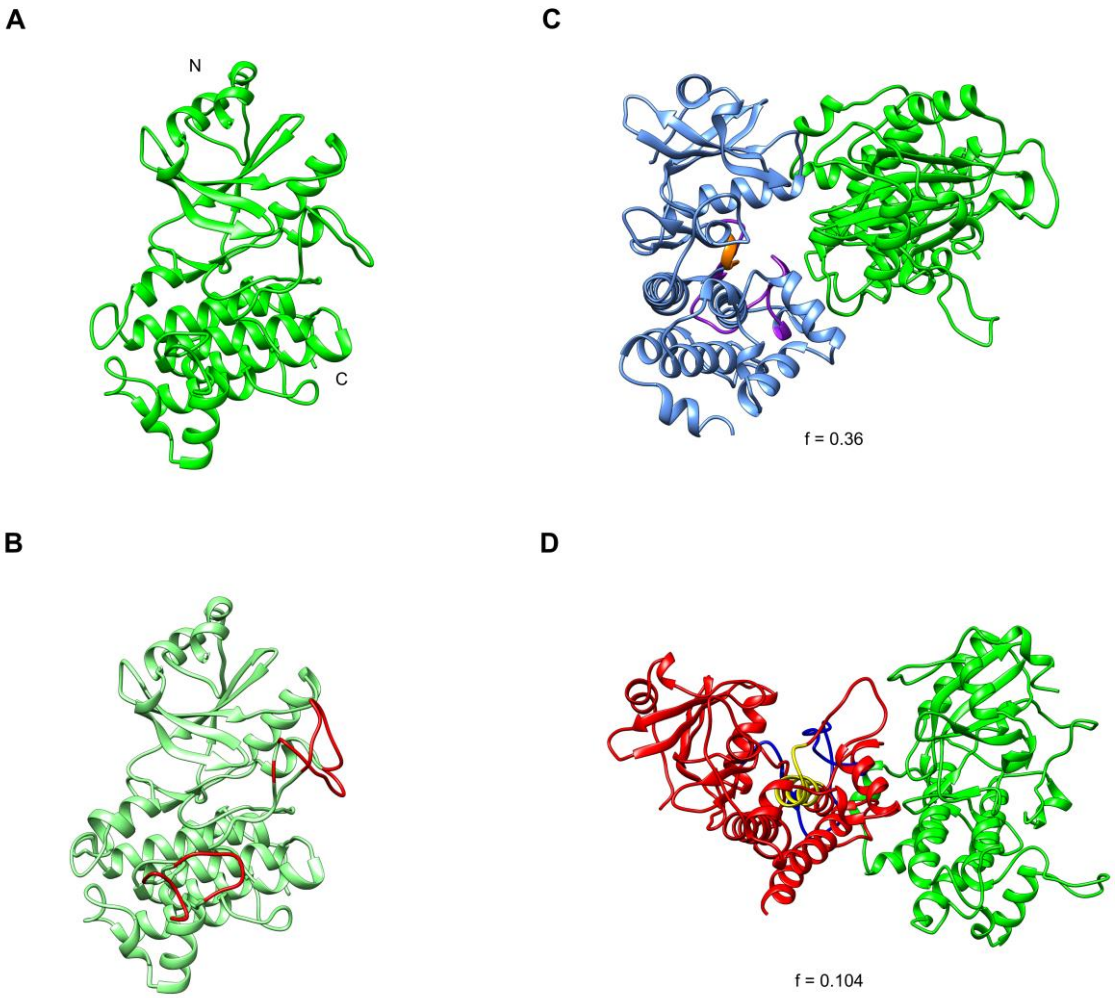

Figure S5: Interactions of the second BIR3 structure with BAK1 and BRI1 computed by webSDA. **A**: Second computed structure of BIR3. **B**: Alignment of both BIR3 structures. Differences are highlighted in red. **C**: BAK1 interacts with BIR3 preferentially by its catalytic domain and its activation loop. **D**: Complex between BRI1 and the second BIR3 structure covers the catalytic domain. Color code: BIR3 (green); BAK1 (blue), catalytic domain (orange), activation loop (purple); BRI1 (red): catalytic domain (yellow), activation loop (blue). The structures and complexes are oriented in a way that the membrane would be located above the complexes.

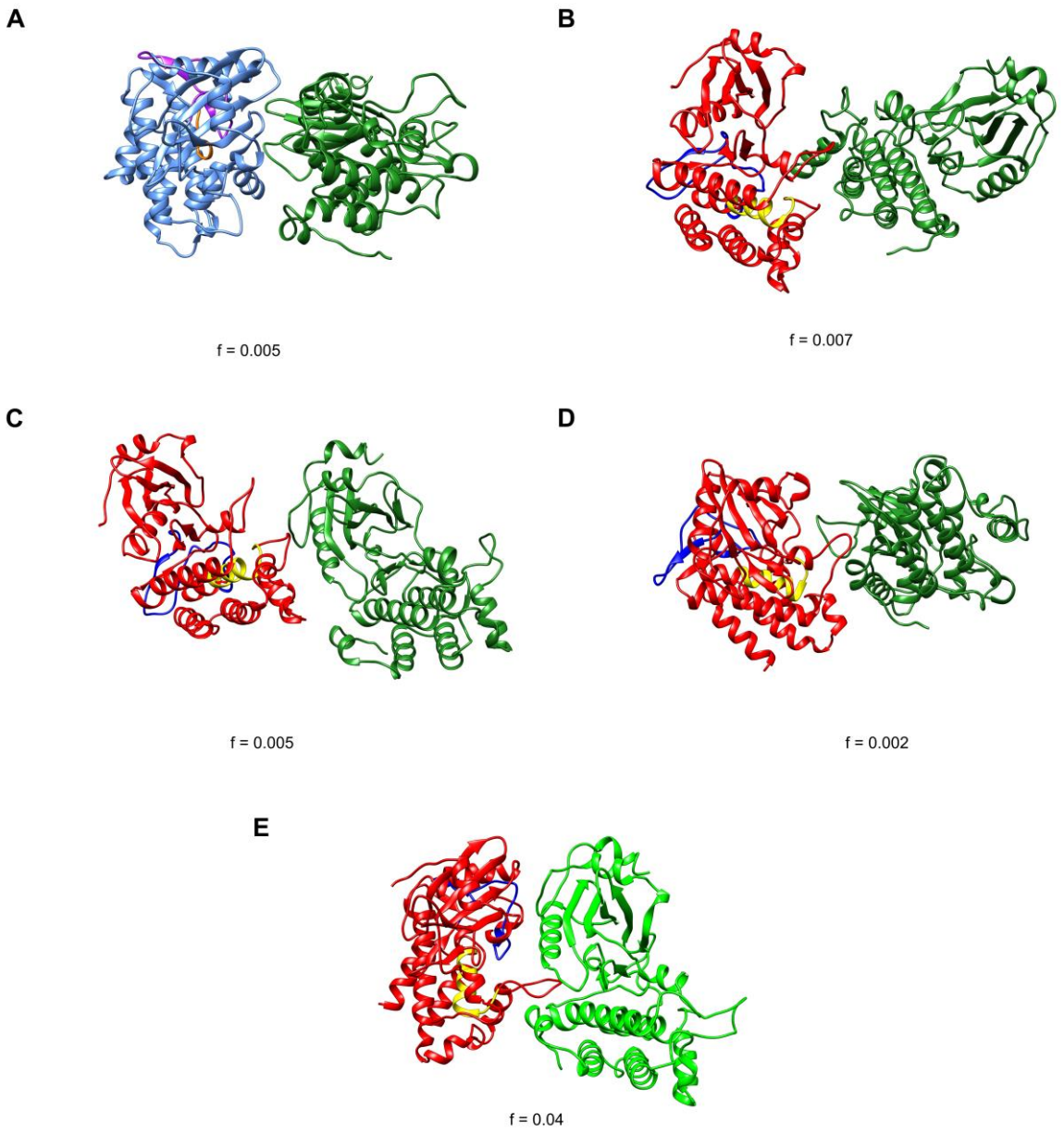

Figure S6: Additional complexes computed by webSDA. **A:** Additional complex computed between BAK1 and BIR3 that also inhibits BAK1 activity. **B-D:** Additional complexes computed for BRI1 and BIR3. **E:** Additional complex computed for BRI1 and the second BIR3 stucture. For this structure, no additional complexes between BAK1 and BIR3 were computed within our set of criteria. Color code: BIR3 (green); BAK1 (blue), catalytic domain (orange), activation loop (purple); BRI1 (red): catalytic domain (yellow), activation loop (blue). The complexes are oriented in a way that the membrane would be located above the complexes.

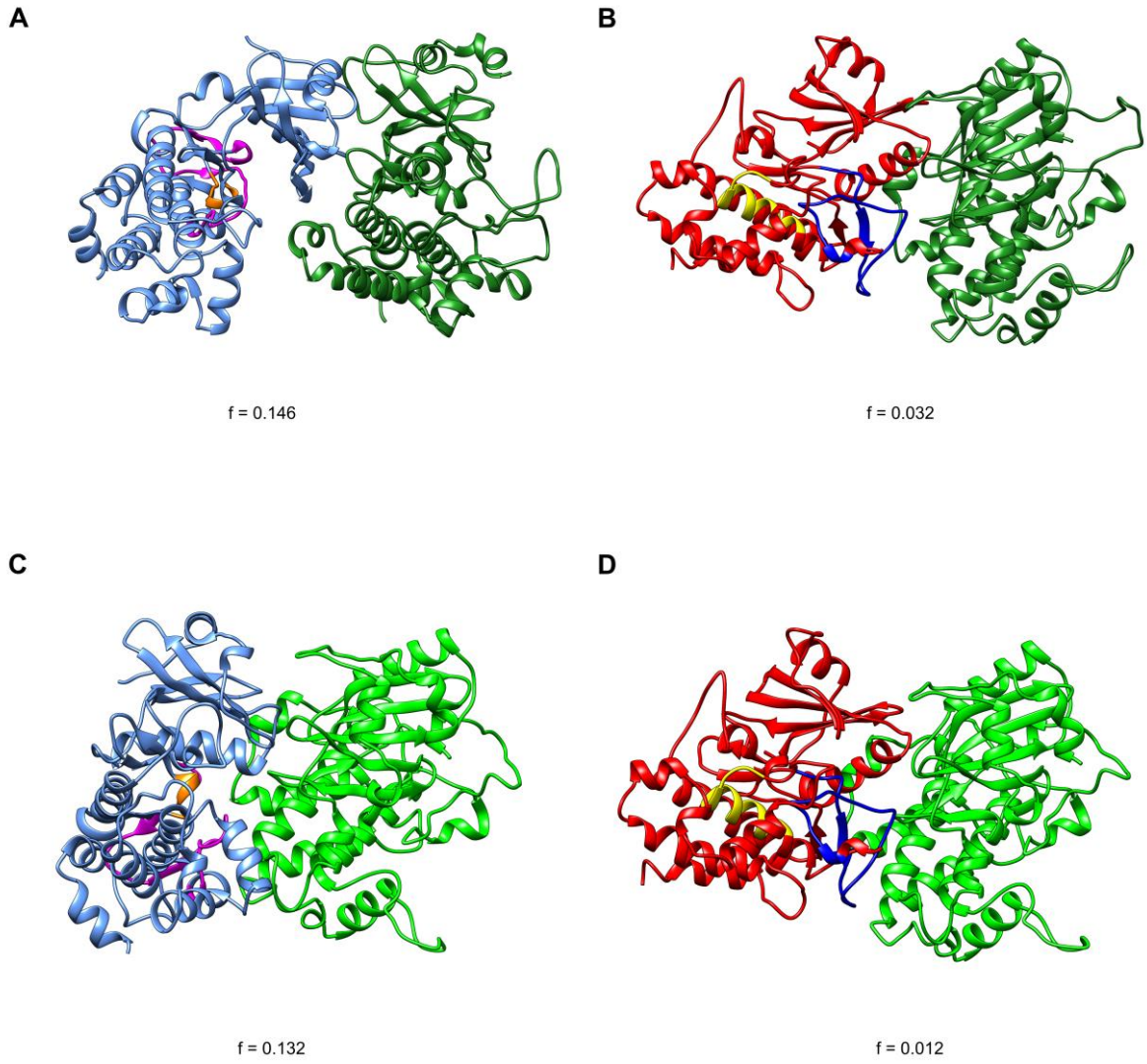

Figure S7: Complexes between the two structures of BIR3 and BAK1 as well as BRI1 computed by ClusPro. **A**: Computed complex between BAK1 and the first BIR3 structure. **B**: Computed complex between BRI1 and the first BIR3 structure. **C**: Computed complex between BAK1 and the second BIR3 structure. **D**: Computed complex between BRI1 and the second BIR3 structure. Color code: BIR3 (green); BAK1 (blue), catalytic domain (orange), activation loop (purple); BRI1 (red): catalytic domain (yellow), activation loop (blue). The complexes are oriented in a way that the membrane would be located above the complexes.

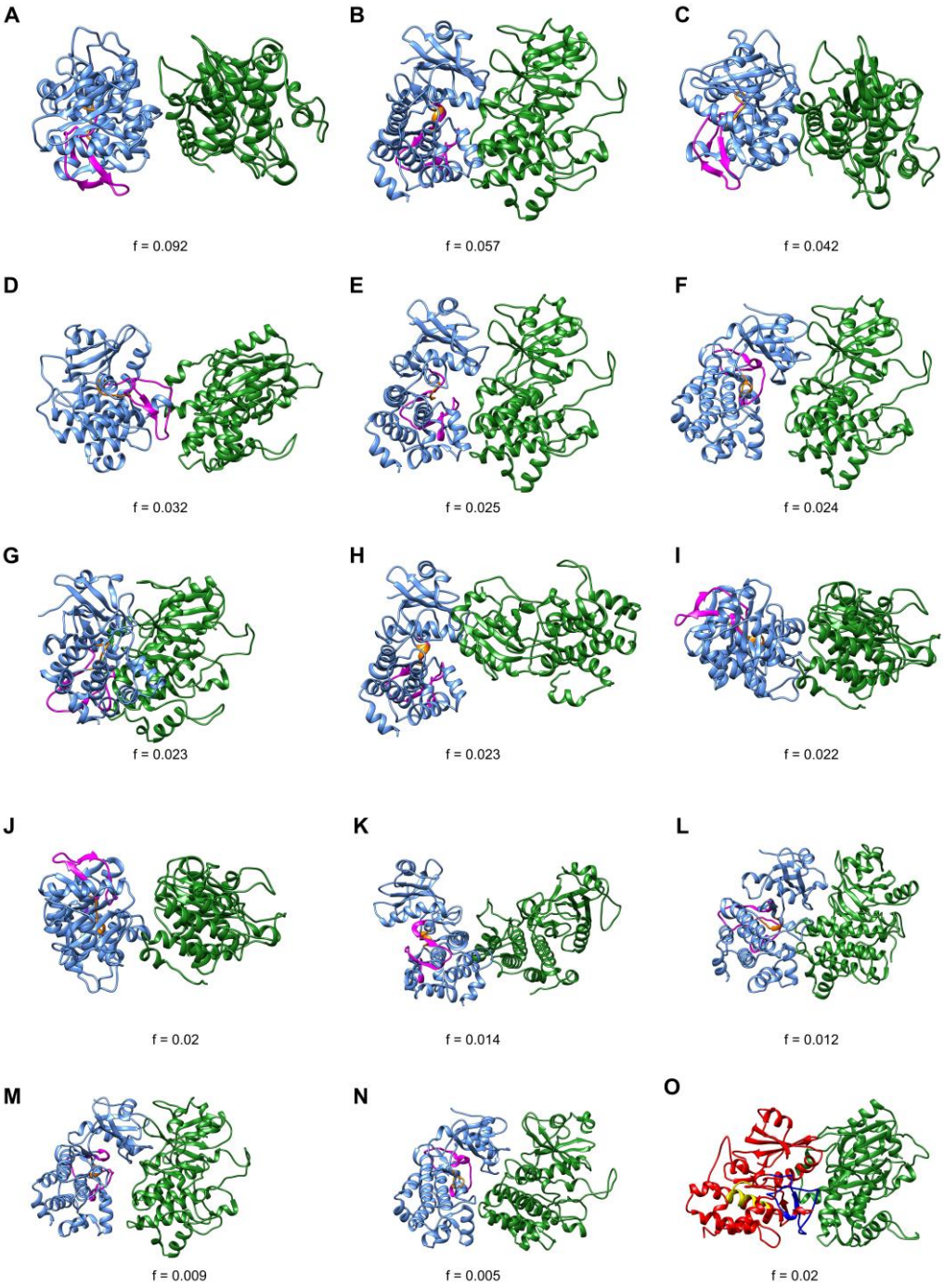

Figure S8: Additional complexes that were classified as feasible for the first BIR3 structure as computed by ClusPro. **A-N:** Several complexes are feasible for the interaction of BIR3 and BAK1. While the majority of these complexes inhibits the activity of BAK1, the majority do not block the catalytic domain or the activation loop of BAK1. **K:** Second feasible complex recorded for BIR3 and BRI1. Color code: BIR3 (green); BAK1 (blue), catalytic domain (orange), activation loop (purple); BRI1 (red): catalytic domain (yellow), activation loop (blue). All complexes are oriented in a way that the membrane would be located above the complex.

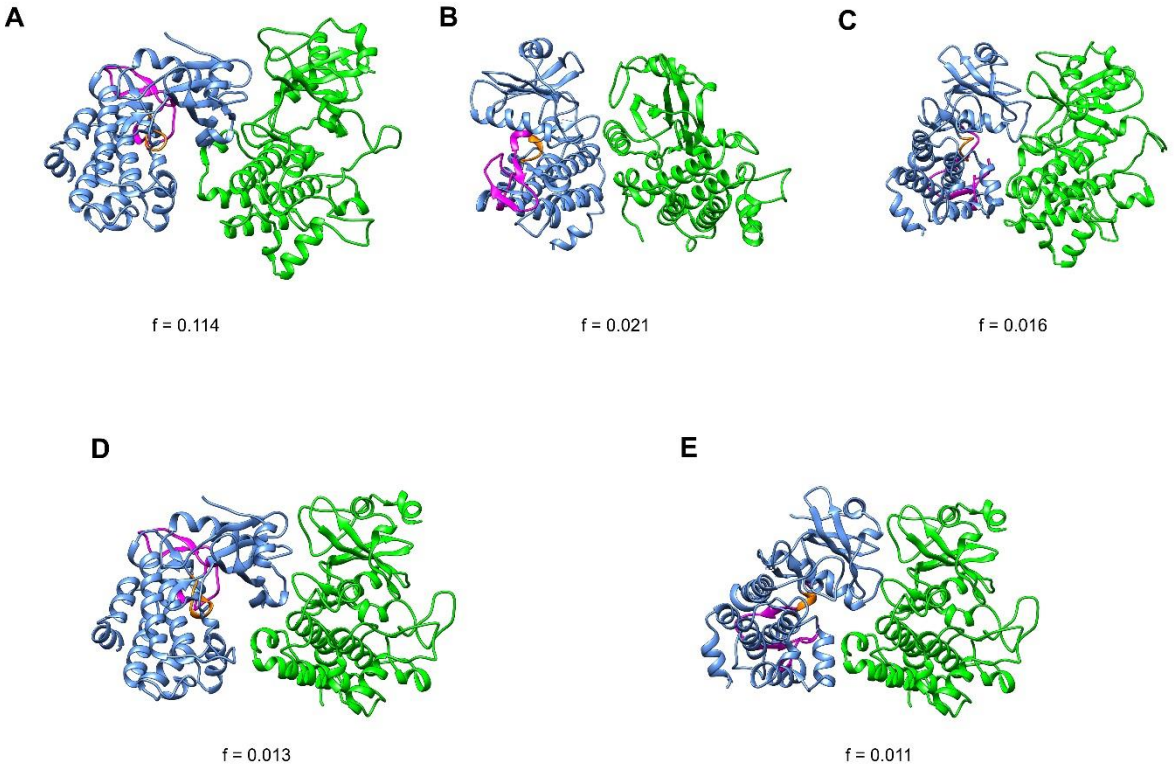

Figure S9: Additional complexes that were classified as feasible for the second BIR3 structure as computed by ClusPro. No complexes were recorded for BRI1 and the second BIR3 structure. Color code: BIR3 (green); BAK1 (blue), catalytic domain (orange), activation loop (purple); BRI1 (red): catalytic domain (yellow), activation loop (blue). All complexes are oriented in a way that the membrane would be located above the complex.

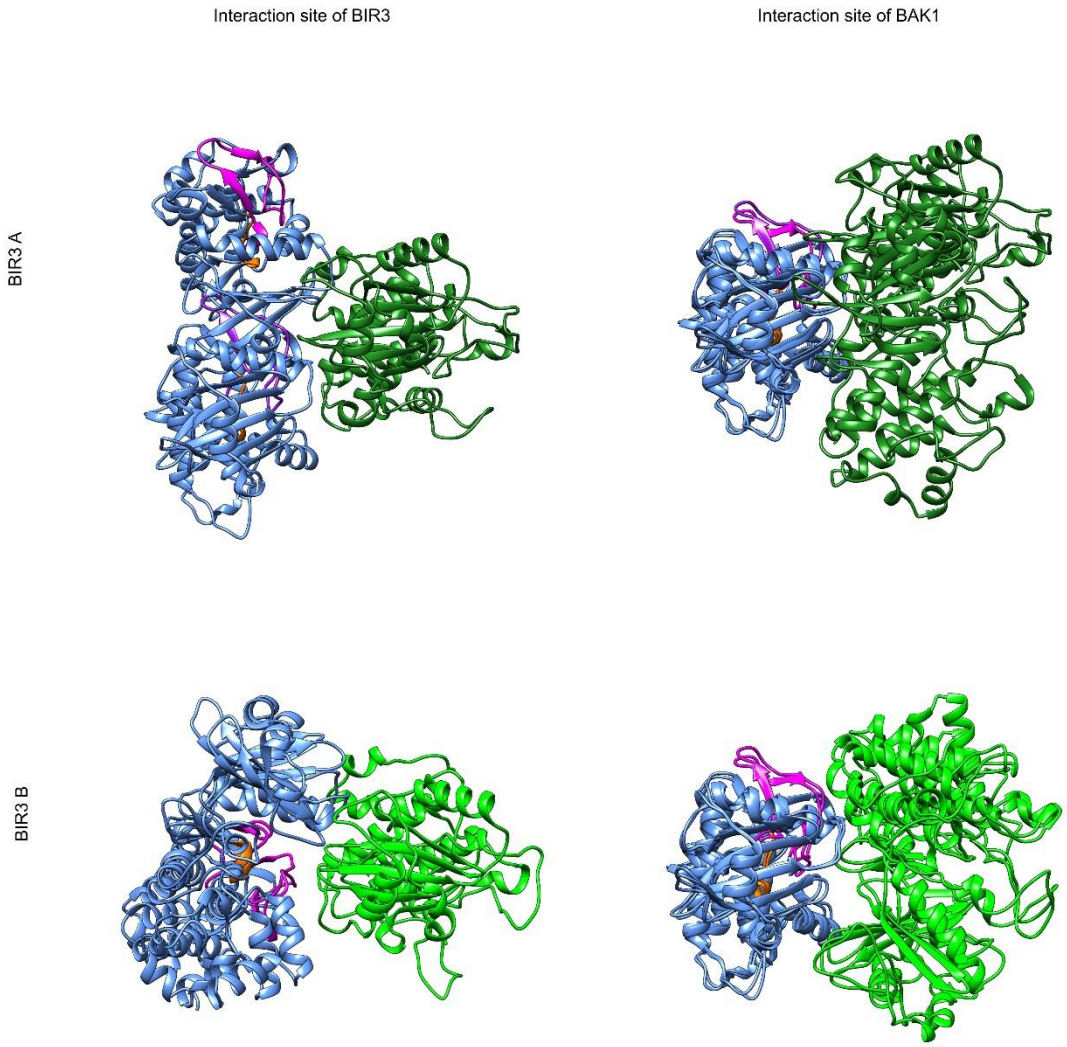

Figure S10: Interaction sites on BAK1 and BIR3 are consistent between BIR3 structures and docking methods. The complexes were alternately aligned to either BIR3 or BAK1 using the MatchMaker tool in Chimera to visualize the interaction site of the respective complex (Meng et al. 2006). Color code: BIR3 (green); BAK1 (blue), catalytic domain (orange), activation loop (purple).

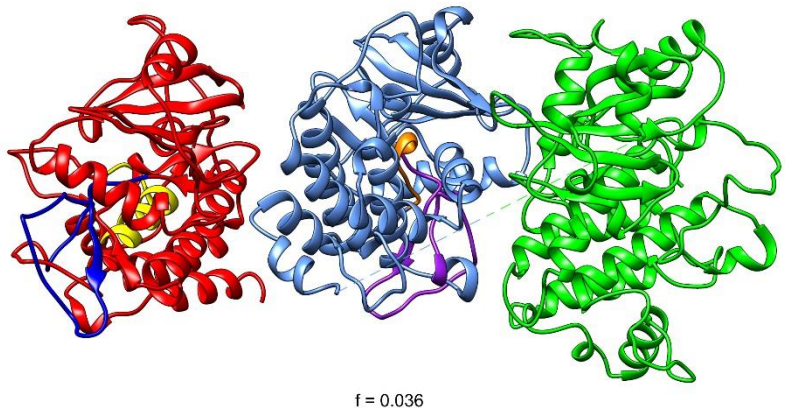

Figure S11: Trimeric complex based on the complex of BIR3 with BAK1 (fig. S5 C) and BRI1 docking to this complex. The model was computed using ClusPro. The dashed line indicates that BAK1 and BIR3 were entered as a complex in this docking run. Color code: BIR3 (green); BAK1 (blue), catalytic domain (orange), activation loop (purple); BRI1 (red): catalytic domain (yellow), activation loop (blue). All complexes are oriented in a way that the membrane would be located above the complex.

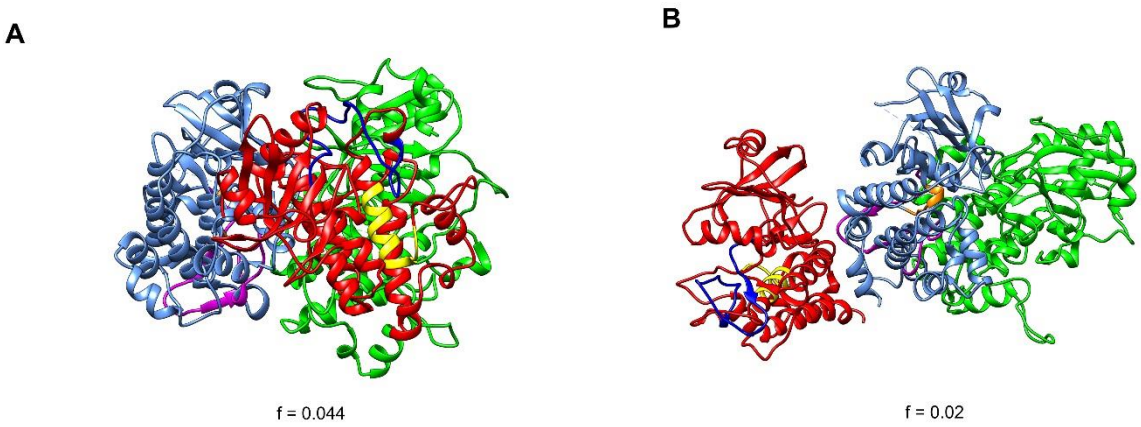

Figure S12: Trimeric complexes based on the complex of BIR3 with BAK1 (fig. S7 C) and BRI1 docking to this complex. The model was computed using ClusPro. The dashed line indicates that BAK1 and BIR3 were entered as a complex in this docking run. Color code: BIR3 (green); BAK1 (blue), catalytic domain (orange), activation loop (purple); BRI1 (red): catalytic domain (yellow), activation loop (blue). All complexes are oriented in a way that the membrane would be located above the complex.

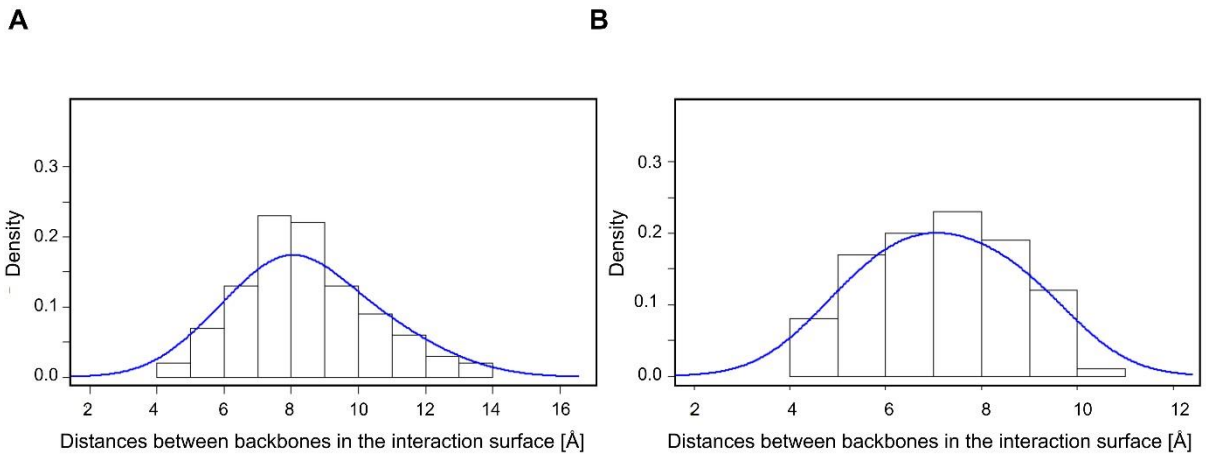

Figure S13: Distribution of distances between interacting amino acids in the interaction surface of the complexes (sample n=100). The distributions approximately follow a normal distribution. **A**: Sampled distances of proteins in complexes computed by webSDA with a mean of $\bar{x}$ = 8.452 Å and a standard deviation of σ = 1.956 Å. **B**: Sampled distances between proteins in complexes computed by ClusPro with a mean of $\bar{x}$ = 7.185 Å and a standard deviation of σ = 1.495 Å. The threshold of $\bar{x} + 2\sigma$ is expected to cover 97.8% of potential interactions and thus clashes between structurally unresolved N- or C-termini.

Supporting References

Benkert P, Biasini M, Schwede T (2011) Toward the estimation of the absolute quality of individual protein structure models. **Bioinformatics** 27:343–350. doi: 10.1093/bioinformatics/btq662

Benkert P, Tosatto SCE, Schomburg D (2008) QMEAN: A comprehensive scoring function for model quality assessment. **Proteins Struct Funct Bioinforma** 71:261–277. doi: 10.1002/prot.21715

Berman HM, Westbrook J, Feng Z, Gilliland G, Bhat TN, Weissig H, Shindyalov IN, Bourne PE (2000) The protein data bank. **Nucleic Acids Res** 28:235–242

Blaum BS, Mazzotta S, Nöldeke ER, Halter T, Madlung J, Kemmerling B, Stehle T (2014) Structure of the pseudokinase domain of BIR2, a regulator of BAK1-mediated immune signaling in Arabidopsis. **J Struct Biol** 186:112–121

Bojar D, Martinez J, Santiago J, Rybin V, Bayliss R, Hothorn M (2014) Crystal structures of the phosphorylated BRI1 kinase domain and implications for brassinosteroid signal initiation. **Plant J** 78:31–43

Cheng W, Munkvold KR, Gao H, Mathieu J, Schwizer S, Wang S, Yan YB, Wang J, Martin GB, Chai J (2011) Structural analysis of pseudomonas syringae AvrPtoB bound to host BAK1 reveals two similar kinase-interacting domains in a type III effector. **Cell Host Microbe** 10:616–626

Chuang G-Y, Kozakov D, Brenke R, Comeau SR, Vajda S (2008) DARS (Decoys As the Reference State) Potentials for Protein-Protein Docking. **Biophys J** 95:4217–4227. doi: 10.1529/BIOPHYSJ.108.135814

Meng EC, Pettersen EF, Couch GS, Huang CC, Ferrin TE (2006) Tools for integrated sequence-structure analysis with UCSF Chimera. **BMC Bioinformatics** 7:339. doi: 10.1186/1471-2105-7-339

Pettersen EF, Goddard TD, Huang CC, Couch GS, Greenblatt DM, Meng EC, Ferrin TE (2004) UCSF Chimera - A visualization system for exploratory research and analysis**. J Comput Chem** 25:1605–1612. doi: 10.1002/jcc.20084

Rose PW, Prlić A, Altunkaya A, Bi C, Bradley AR, Christie CH, Di Costanzo L, Duarte JM, Dutta S, Feng Z, Green RK, Goodsell DS, Hudson B, Kalro T, Lowe R, Peisach E,

Randle C, Rose AS, Shao C, Tao YP, Valasatava Y, Voigt M, Westbrook JD, Woo J, Yang H, Young JY, Zardecki C, Berman HM, Burley SK (2017) The RCSB protein data bank: Integrative view of protein, gene and 3D structural information. **Nucleic Acids Res** 45:D271–D281. doi: 10.1093/nar/gkw1000

Webb B, Sali A (2014) Comparative Protein Structure Modeling Using MODELLER. **Curr Protoc Bioinforma** 47: 5.6.1-5.6.32

Yu X, Martinez M, Gable AL, Fuller JC, Bruce NJ, Richter S, Wade RC (2015) webSDA: a web server to simulate macromolecular diffusional association. **Nucleic Acids Res** 43: W220-4

Yan L, Ma Y, Liu D, Wei X, Sun Y, Chen X, Zhao H, Zhou J, Wang Z, Shui W, Lou Z (2012) Structural basis for the impact of phosphorylation on the activation of plant receptor-like kinase BAK1**. Cell Res** 22:1304–8

A.1.6 The interplay of BR and PSK hormone signalling via RLP44

BRI1 controls vascular cell fate in the *Arabidopsis* root through RLP44 and phytosulfokine signaling

Accepted

This article describes the complex interplay of the brassinosteroid hormone receptor BRASSINOSTEROID INSENSITIVE 1 (BRI1), the RECEPTOR LIKE PROTEIN 44 (RLP44) and the phytosulfokine hormone receptor PHYTOSULFOKINE RECEPTOR 1 (PSKR1) for the determination of the cell fate in the root vasculature of *Arabidopsis thaliana*. RLP44 interacts with both BRI1 and PSKR1 as well as with their mutual co-receptor BRI1-ASSOCIATED KINASE 1 (BAK1). BRI1 mutants show ectopic xylem in procambial position, which is not dependent on classical brassinosteroid signalling, but depends directly on the expression and function of RLP44. Both RLP44 and phytosulfokine signalling is required for the maintenance of procambial cell identity. Phytosulfokine hormone treatment of *rlp44* rescues the former phenotype of ectopic xylem in the position of procambium. Consequently, RLP44 could balance the signalling of brassinosteroid hormone for the proliferation of cells in the vasculature with the phytosulfokine signalling for the maintanance of the procambial identity.

BRI1 controls vascular cell fate in the *Arabidopsis* root through RLP44 and phytosulfokine signaling

Eleonore Holzwart[a], Apolonio Ignacio Huerta[a,1,2], Nina Glöckner[b,1], Borja Garnelo Gómez[a,1], Friederike Wanke[b,1], Sebastian Augustin[a,3], Jana Christin Askani[a], Ann-Kathrin Schürholz[a], Klaus Harter[b], and Sebastian Wolf[a,4]

[a]Department of Cell Biology, Centre for Organismal Studies Heidelberg, Heidelberg University, 69120 Heidelberg, Germany; and [b]Plant Physiology, Center for Plant Molecular Biology (ZMBP), Universität Tübingen, 72076 Tübingen, Germany

Edited by Elliot M. Meyerowitz, HHMI and California Institute of Technology, Pasadena, CA, and approved October 3, 2018 (received for review August 22, 2018)

Multicellularity arose independently in plants and animals, but invariably requires a robust determination and maintenance of cell fate that is adaptive to the environment. This is exemplified by the highly specialized water- and nutrient-conducting cells of the plant vasculature, the organization of which is already prepatterned close to the stem-cell niche, but can be modified according to extrinsic cues. Here, we show that the hormone receptor BRASSINOSTEROID INSENSITIVE 1 (BRI1) is required for root vascular cell-fate maintenance, as BRI1 mutants show ectopic xylem in procambial position. However, this phenotype seems unrelated to canonical brassinosteroid signaling outputs. Instead, BRI1 is required for the expression and function of its interacting partner RECEPTOR-LIKE PROTEIN 44 (RLP44), which, in turn, associates with the receptor for the peptide hormone phytosulfokine (PSK). We show that PSK signaling is required for the maintenance of procambial cell identity and quantitatively controlled by RLP44, which promotes complex formation between the PSK receptor and its coreceptor. Mimicking the loss of RLP44, PSK-related mutants show ectopic xylem in the position of the procambium, whereas *rlp44* is rescued by exogenous PSK. Based on these findings, we propose that RLP44 controls cell fate by connecting BRI1 and PSK signaling, providing a mechanistic framework for the dynamic balancing of signaling mediated by the plethora of plant receptor-like kinases at the plasma membrane.

cell fate | plant development | xylem | brassinosteroids | phytosulfokine

A key function of signaling networks in multicellular organisms is to ensure robust determination and maintenance of cell fate. In plants, extreme specialization is displayed by the cells of the vascular tissues, which are vital for the distribution of water, nutrients, and signaling molecules. Xylem tracheary elements are characterized by lignified secondary cell-wall thickenings that protect against collapse and provide mechanical support for vertical growth. Positioned between xylem and the nutrient-transporting phloem are the cells of the procambium, which give rise to the lateral meristems during secondary growth (1). In *Arabidopsis*, root vascular tissue patterning is set up in the embryo by mutual antagonism of auxin and cytokinin signaling domains (2–5), but can adapt to environmental conditions later in development (6). After xylem precursor cells are displaced from the root meristem, an intricate gene-regulatory network connected to patterning mechanisms mediates differentiation into tracheary elements (7–10). Thus, primary root vascular patterning can be traced back to early specification events in the embryo. In contrast, during secondary growth, (pro)cambial cells adjacent to the existing tracheary elements acquire a xylem cell fate dependent on positional information (11).

Brassinosteroid (BR) hormone signaling (12, 13) is implicated in xylem differentiation and vascular patterning (14, 15). BRs are perceived by BRASSINOSTEROID INSENSITIVE 1 (BRI1) (16), which belongs to the large group of plant receptor-like kinases (RLK) with a leucine-rich repeat (LRR) extracellular domain, a transmembrane domain, and a cytosolic kinase domain related to animal Irak and Pelle kinases (17). Upon ligand binding, BRI1 heterodimerizes with members of the SOMATIC EMBRYOGENESIS RECEPTOR KINASE (SERK) LRR-RLK family such as BRI1-ASSOCIATED KINASE 1 (BAK1) (18, 19) and activates a signaling cascade that negatively regulates BRASSINOSTEROID INSENSITIVE 2 (BIN2) (20), a GSK3-like kinase that phosphorylates the BR-responsive transcription factors BRASSINAZOLE RESISTANT 1 (BZR1) and BRI1 EMS SUPPRESSOR 1 (BES1)/BZR2 (21, 22). Inhibition of BIN2 activity allows BZR1 and BES1 to translocate to the nucleus, where they mediate BR-responsive transcriptional changes (23–25). A so far somewhat enigmatic relationship exists between BR and PHYTOSULFOKINE (PSK) signaling. PSKs are small secreted peptides that have been implicated in a variety of fundamental processes and are perceived by two close relatives of BRI1, PHYTOSULFOKINE RECEPTOR-1 and -2 (26–29). PSK activity depends on proteolytic processing of the precursor peptides, the sulfation of two tyrosine residues in the mature pentapeptide (YIYTQ) by TYROSYLPROTEIN SULFOTRANSFERASE (TPST) (30), and functional BR signaling (31, 32). At present, it is not clear how BR and PSK signaling interact, but the receptors for both growth factors share the requirement for a SERK coreceptor (33, 34).

Recently, we demonstrated that feedback information from the cell wall is integrated with BR signaling at the level of the receptor complex through RECEPTOR-LIKE PROTEIN (RLP) 44 (35).

Significance

Cell-fate determination and cellular behavior in plants rely mainly on positional information and intercellular communication. A plethora of cues are perceived by surface receptors and integrated into an adequate cellular output. Here, we show that the small receptor-like protein RLP44 acts as an intermediary to connect the receptors for two well-known signaling molecules, brassinosteroid and phytosulfokine, to control cell fate in the root vasculature. Furthermore, we show that the brassinosteroid receptor has functions that are independent from the responses to its hormone ligands and reveal that phytosulfokine signaling promotes procambial cell identity. These results provide a mechanistic framework for the integration of multiple signaling pathways at the plasma membrane by shifting associations of receptors in multiprotein complexes.

Author contributions: E.H., K.H., and S.W. designed research; E.H., A.I.H., N.G., B.G.G., F.W., S.A., J.C.A., A.-K.S., and S.W. performed research; E.H., A.I.H., N.G., B.G.G., F.W., S.A., K.H., and S.W. analyzed data; and S.W. wrote the paper.

The authors declare no conflict of interest.

This article is a PNAS Direct Submission.

[1]A.I.H., N.G., B.G.G., and F.W. contributed equally to this work.

[2]Present address: Department of Biology, ETH Zurich, 8092 Zurich, Switzerland.

[3]Present address: Department of Plant Molecular Biology, University of Lausanne, 1015 Lausanne, Switzerland.

[4]To whom correspondence should be addressed. Email: sebastian.wolf@cos.uni-heidelberg.de.

This article contains supporting information online at www.pnas.org/lookup/suppl/doi:10.1073/pnas.1814434115/-/DCSupplemental.

Published online October 30, 2018.

RLP44 is genetically required for the BR-mediated response to cell-wall modification and is sufficient to elevate BR signaling when overexpressed. RLP44 was shown to be in a complex with BRI1 and BAK1. Thus, we hypothesized that RLP44 modulates BR signaling strength in response to cues from the cell wall (35). However, it is not clear whether the RLP44-BR–signaling module plays additional roles in plant physiology (36). Here, we show that RLP44 is required for the maintenance of cell fate in the root vasculature by connecting components of the BR and PSK signaling pathways. RLP44 controls xylem differentiation in a BRI1-dependent manner by directly interacting with PSKR1 and promoting its interaction with BAK1. In addition, the *rlp44* phenotype can be rescued by application of PSK peptide, and mutants affected in PSK signaling show an *rlp44*-like xylem phenotype, suggesting that RLP44 has a positive effect on PSK signaling, which, in turn, promotes procambial identity.

Results

RLP44 Is Expressed in the Developing Root Vasculature. We previously demonstrated that RLP44 is present in a complex with BRI1 and BAK1 and is able to promote BR signaling upon cues from the cell wall or when overexpressed (35). To study the function of RLP44 in more depth, we generated transgenic plants expressing a translational GFP fusion of RLP44 under the control of the *RLP44* promoter (*pRLP44:RLP44-GFP*). These plants displayed elongated, narrow leaf blades and elongated petioles, reminiscent of BRI1-overexpressing plants (Fig. 1 *A* and *B*) (37), as previously observed for RLP44 overexpression (35). We crossed a *pRLP44:RLP44-GFP* line with the *RLP44* loss-of-function mutant *rlp44*^{cnu2} (35), resulting in plants with a wild-type–like appearance (Fig. 1*C*), demonstrating that the fusion protein is functional and confirming that the transgenic RLP44 expression (*SI Appendix*, Fig. S1*A*) is causative for the observed morphological effects. In the root apical meristem of *pRLP44:RLP44-GFP* and *pRLP44:RLP44-GFP* (*rlp44*^{cnu2}), fluorescence was markedly enriched in the stele toward the more mature part of the root (Fig. 1 *D–G* and *SI Appendix*, Fig. S1 *B–E*) in accordance with previously published transcriptome data (37) and β-glucuronidase reporter activity under control of the RLP44 promoter (*SI Appendix*, Fig. S1 *F* and *G*). In the differentiating part of the root stele, RLP44-GFP fluorescence was present in all cell types, including the undifferentiated procambial cells (Fig. 1 *H* and *I* and *SI Appendix*, Fig. S1 *C* and *D*).

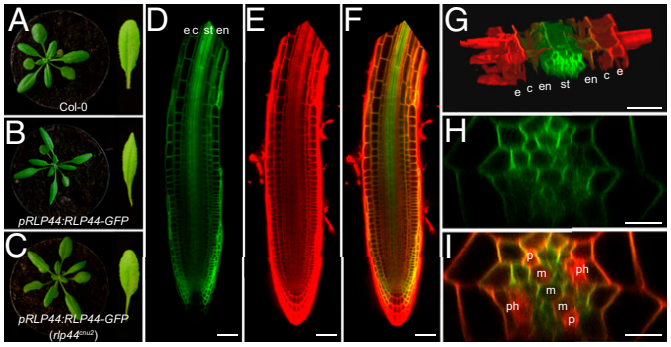

Fig. 1. RLP44 is expressed in the root vascular tissue. (*A*) Col-0. (*B*) *pRLP44:RLP44-GFP* in wild-type background shows a growth phenotype reminiscent of enhanced BR signaling. (*C*) Mutation of endogenous *RLP44* in *pRLP44:RLP44-GFP* (*rlp44*^{cnu2}) reconstitutes wild-type–like phenotype. (*D–F*) *pRLP44:RLP44-GFP* expression (*D*) in root meristem counterstained with propidium iodide (*E*) and merged (*F*). c, cortex; e, epidermis; en, endodermis; st, stele. (Scale bars: 100 μm.) (*G*) Projection of a confocal stack through the differentiation zone before maturation of the casparian strip of a *pRLP44:RLP44-GFP* root showing fluorescence predominantly in the stele. Labeling as in *D*. (*H* and *I*) Optical section through the stele of a *pRLP44:RLP44-GFP*–expressing root in the differentiation zone (*H*), counterstained with propidium iodide (*I*), indicating differentiated phloem (ph) and protoxylem (p) and as-yet-undifferentiated metaxylem (m). (Scale bar: 10 μm.)

RLP44 Controls Xylem Cell Fate. Because our reporter lines suggested expression of RLP44 in the stele, we assessed the role of RLP44 in vascular development. We visualized lignified secondary cell walls in *rlp44* loss-of-function mutants through basic fuchsin staining. Strikingly, we observed supernumerary metaxylem-like cells, frequently outside the primary xylem axis in the position of the procambium (Fig. 2 *A* and *B* and *SI Appendix*, Fig. S2*A*), a phenotype we never observed in wild-type roots. Quantification of metaxylem cells in seedling roots of both *rlp44*^{cnu2} and the T-DNA insertion line *rlp44*-3 6 d after germination showed a significant increase (Fig. 2*C*), suggesting that RLP44 controls xylem cell fate. Expression of *RLP44* under control of its own promoter complemented this phenotype (*SI Appendix*, Fig. S2*B*). Since we had previously identified RLP44 as an activator of BR signaling, we analyzed the root xylem of a number of BR-related mutants spanning a broad range of growth phenotypes. Hypomorphic *bri1* mutants such as *bri1*^{cnu1} (38), *bri1-301* (20), and *bri1-5* (39), the more severe signaling mutant *bin2-1* (20), as well as the BR-deficient biosynthetic mutants *constitutive photomorphogenic dwarf* (*cpd*) (40) and *dwarf4-102* (41) did not show a pronounced increase in xylem cell number (Fig. 2*D* and *SI Appendix*, Fig. S2 *C* and *D*). In sharp contrast, *bri1* null alleles such as a previously characterized T-DNA mutant (termed *bri1-null*) (42) and the *bri1 brl1 brl3* triple mutant (called *bri-triple* from hereon) (43) displayed a marked increase in the number of differentiated xylem cells (Fig. 2*D* and *SI Appendix*, Fig. S3), whereas expression of *BRI1* under the control of its own promoter in *bri1-null* restored wild-type–like xylem (Fig. 2*E*). Taken together, our results show that the xylem differentiation phenotype does not correlate with the severity of BR-deficiency–related growth phenotypes (*SI Appendix*, Fig. S2*E*). This is exemplified by the comparison between *cpd* and *bri1-null*, with *cpd* displaying wild-type–like xylem cell numbers, despite exhibiting a *bri1-null*–like growth phenotype. Thus, the control of xylem cell number requires the presence of both BRI1 and RLP44. To test whether increased levels of BRs in BRI1 loss-of-function mutants (39) contribute to the xylem phenotype, we depleted endogenous BRs in the wild-type and *bri-triple* plants with the BR biosynthesis inhibitor propiconazole (PPZ) (44), rendering wild-type plants indistinguishable from the mutant (*SI Appendix*, Fig. S4*A*). However, metaxylem cell number was not significantly affected in either genotype by PPZ treatment (*SI Appendix*, Fig. S4*B*), despite a slightly elevated number of metaxylem cells in wild type. However, PPZ treatment occasionally led to gaps in the protoxylem (*SI Appendix*, Fig. S4*C*), a phenotype also found in *bri-triple* (Fig. 2*D* and *SI Appendix*, Fig. S3) and in *dwf4-102* (*SI Appendix*, Fig. S4*D*), but not in any other mutant (*SI Appendix*, Fig. S4 *D–F*), suggesting that BR signaling has a role in the maintenance of protoxylem and that the *cpd* mutant is not strictly equivalent to *dwf4-102* for unknown reasons. Conversely, neither root-growth–promoting nor root-growth–inhibiting doses of brassinolide (BL) (*SI Appendix*, Fig. S4*G*) affected xylem cell numbers (*SI Appendix*, Fig. S4*H*). Activating BR signaling downstream of BRI1 by inhibiting BIN2 and other GSK3-like kinases through bikinin treatment (45) partially rescued the short-root phenotype of *bri-triple* (*SI Appendix*, Fig. S5*A*), but did not significantly alter the metaxylem cell number in either mutant or wild type (*SI Appendix*, Fig. S5*B*). This indicates that BRI1, rather than canonical downstream BR-signaling components, is critical for normal xylem cell fate. To assess whether BRI1 kinase activity is required for the control of cell fate, we analyzed *bri1-1* (46, 47), which harbors a point mutation in the kinase domain (A909T) and is expected to prevent adenine nucleotide binding and thus to render the protein kinase dead (48). The *bri1-1* mutant, which is morphologically indistinguishable from the transcriptional knockout *bri1-null*, showed supernumerary xylem cells despite the presence of BRI1 protein (*SI Appendix*, Fig. S5*C*), suggesting that BRI1 kinase activity is required for the control of xylem cell fate.

BRI1 Is Required for Normal RLP44 Expression. To analyze how BRI1 and RLP44 could be linked in the control of xylem cell fate, we investigated *RLP44* expression in BR-related mutants. Interestingly, the expression of *RLP44* was reduced in *bri1-null*, suggesting that

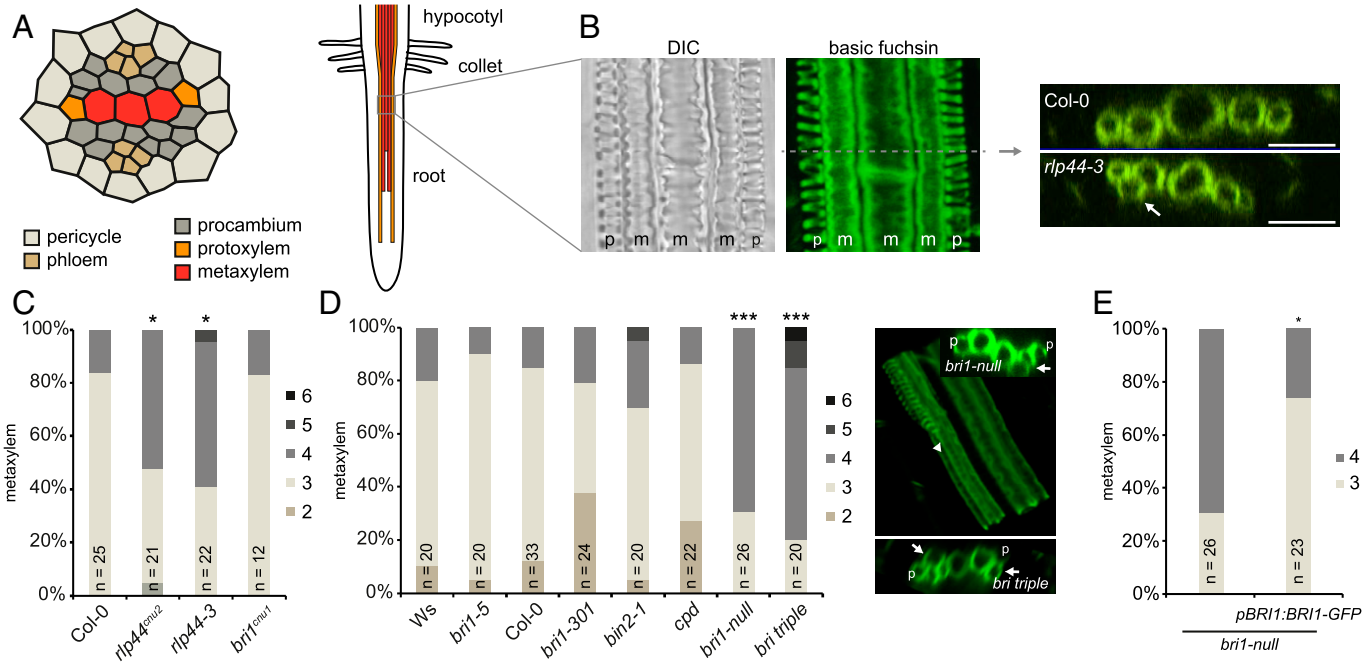

Fig. 2. RLP44 and BRI1 are required for the control of xylem cell fate. (*A*) Overview of xylem differentiation in the *Arabidopsis* root and schematic representation of the stele. Gray square in root schematic indicates point of xylem observation. (*B*) Basic fuchsin staining of 6-d-old *Arabidopsis* root. DIC image shows secondary cell-wall thickenings of protoxylem and metaxylem (*Left*), and basic fuchsin labels lignified secondary cell walls (*Middle*). Confocal stacks allow xylem number quantification of the indicated genotypes in orthogonal view (*Right*). Note ectopic metaxylem in procambial position (arrow). (*Left*) A median plane image. (*Middle*) A maximum projection. (Scale bar: 50 μM.) (*C* and *D*) Frequency of roots with the indicated number of metaxylem cells in *rlp44* and BR-related mutants. *Right* in *D* shows orthogonal view and maximum projection of *bri-triple* root. Note ectopic metaxylem (arrows) and disrupted protoxylem (arrowhead). Asterisks indicate statistically significant difference from Col-0 based on Dunn's post hoc test with Benjamini–Hochberg correction after Kruskal–Wallis modified *U* test (**P* < 0.05; ****P* < 0.001). (*E*) Transgenic expression of *BRI1* under control of its own regulatory 5′ sequence rescues the ectopic xylem phenotype of *bri1-null*.

reduced RLP44 levels could at least partially explain the xylem phenotype of this mutant (*SI Appendix*, Fig. S6 *A* and *B*). Consistent with this notion, uncoupling *RLP44* transcription from BRI1 control through driving the expression of an RLP44 transgene by the 35S promoter could alleviate the *bri1-null* xylem phenotype (*SI Appendix*, Fig. S6*C*), but not its growth defects (*SI Appendix*, Fig. S7), suggesting that BRI1 and RLP44 indeed act in the same pathway regulating xylem cell fate. As *RLP44* expression was only mildly affected in *bri1* hypomorphs, *cpd*, *dwf4-102*, *bin2-1* or by BR depletion (*SI Appendix*, Figs. S6 *A* and *B* and S8 *A*–*C*), BR signaling output-independent control of *RLP44* expression by BRI1 may explain the presence and absence of vascular cell-fate defects in the various BR-related mutants. Conversely, BL or bikinin treatment, as well as BRI1-independent activation of BR-signaling outputs through hyperactive versions of the transcription factors BES1 and BZR1, did not alter *RLP44* transcript levels in an appreciable manner (*SI Appendix*, Fig. S8*A*). These results corroborate previous genome-wide transcriptome analyses showing that expression of *RLP44* is strongly reduced in the null mutant *bri1-116*, but in contrast to that of bona fide BR target genes, is not recovered in the *bri1-116 bzr1-1D* double mutant, which has constitutively activated BR-signaling outputs (24) *SI Appendix*, Fig. S8*D*). In line with this, *RLP44* is not among the experimentally defined targets of BZR1 or BES1 (24, 25). Finally, the limited effects of BR-signaling–related cues on *RLP44* transcript levels are consistent with publicly available transcriptome data (49), *SI Appendix*, Fig. S9). Taken together, our findings indicate that the phenotype of *bri1* loss-of-function mutants is at least partially independent from BR-signaling outputs and suggest that RLP44 exerts its function downstream of BRI1 through other signaling components.

Vascular Cell-Fate Determination by RLP44 and BRI1 Is Independent of BR-Signaling–Mediated Control of Cell Proliferation. We next asked whether the increase in xylem cell number observed in the *rlp44* mutant could be caused by enhanced cell proliferation. In *rlp44-3*, vascular cell number was indistinguishable from wild type in the differentiation zone, suggesting normal meristematic activity (*SI Appendix*, Fig. S10*A*). The *bri1*^{cnu1} mutant, which did not display ectopic xylem cells, showed a significant increase in total vascular cell number (*SI Appendix*, Fig. S10*A*), consistent with the described role of BR signaling in controlling formative cell divisions (50). These results suggest that increased proliferation in the vasculature is not a prerequisite for an increase in metaxylem. In line with this, depletion of BRs by PPZ resulted in a pronounced increase of vascular cell number (*SI Appendix*, Fig. S10 *B* and *C*). When PPZ-treated roots were supplemented with 0.5 nM of BL, both root growth and vascular cell number were fully recovered (*SI Appendix*, Fig. S10 *B* and *C*). A higher dose of 5 nM BL suppressed root growth and led to a strongly decreased vascular cell number (*SI Appendix*, Fig. S10*C*). The *rlp44*^{cnu2} mutant displayed a wild-type–like response to the manipulation of BR levels in terms of cell number (*SI Appendix*, Fig. S10*C*), further supporting the independence of xylem cell fate from BR-signaling–mediated control of cell proliferation. Moreover, the expression domain of the xylem precursor marker *pTMO5:NLS-3xGFP* (51) was unaltered in *rlp44*^{cnu2} root meristems (*SI Appendix*, Fig. S11), suggesting that the acquisition of xylem cell fate in the mutant is a late event occurring outside of the meristem.

RLP44 Controls Xylem Cell Fate by Promoting PSK Signaling. The results described so far suggested that the maintenance of procambial cell identity in the root requires the presence of both BRI1 and RLP44, with RLP44 acting downstream of BRI1. Thus, we speculated that, devoid of a kinase domain, RLP44 is likely required to interact with and influence the activity of another signaling component(s), which, in turn, control(s) xylem cell fate. Interestingly, in addition to BRI1 and its close homologs BRL1, BRL2, and BRL3, the LRR X clade of RLKs harbors the receptors for the peptide growth factor PSK, PSKR1, and -2 (17). As PSK signaling has also been implicated in promoting the

transdifferentiation of *Zinnia elegans* mesophyll cells into tracheary elements (52, 53), depends on functional BR signaling (29), and *BRI1* (14), *PSKR1* (54), *PSK4*, and *PSK5* (*SI Appendix*, Fig. S12*A*) are coexpressed with *RLP44* in the vasculature, we tested the association of RLP44 with PSKR1. Coimmunoprecipitation experiments in *Nicotiana benthamiana* showed that PSKR1-GFP (34) was present in RLP44-RFP (35) immunoprecipitates (Fig. 3*A*). In addition, Foerster resonance energy transfer-fluorescence lifetime imaging microscopy (FRET-FLIM) analysis showed a pronounced reduction in fluorescence lifetime when PSKR1-GFP was coexpressed with RLP44-RFP, suggesting a direct interaction (Fig. 3*B* and *SI Appendix*, Fig. S12*B*), which was not affected by exogenous application of PSK peptide (*SI Appendix*, Fig. S12 *C* and *D*). Supporting a role of PSK signaling in the control of xylem cell fate, the *pskr1-3 pskr2-1* double mutant (54) showed increased metaxylem cell numbers, reminiscent of *rlp44* (Fig. 3*C*). A similar phenotype was observed in the *tpst-1* mutant, which is impaired in the biosynthesis of PSK and other sulfated peptides (Fig. 3*C*) (30, 55). While exogenous PSK had no effect on wild-type xylem, it partially rescued metaxylem cell number in *tpst-1* (*SI Appendix*, Fig. S12*E*) and reverted *rlp44* xylem back to a wild-type pattern (Fig. 3*D*). Consistent with RLP44 acting through PSK signaling, the *pskr1-3 pskr2-1 rlp44*^{cnu2} triple mutant did not show an enhanced phenotype compared with *pskr1-3 pskr2-1* (*SI Appendix*, Fig. S12*F*). In addition, *RLP44* overexpression, which was able to rescue the *bri1-null* metaxylem phenotype (*SI Appendix*, Fig. S6*C*), did not rescue that of *pskr1-3 pskr2-1* (*SI Appendix*, Fig. S12*G*). In accordance with this, *rlp44*^{cnu2} is quantitatively challenged in the root growth response to exogenous PSK (*SI Appendix*, Fig. S12*H*). Similar to RLP44 and in contrast to BR deficiency conditions, PSK-related mutants did not show gaps in the protoxylem (*SI Appendix*, Fig. S12*I*). Taken together, our results suggest that RLP44 acts through PSK receptors and is required to quantitatively control PSK-signaling strength.

RLP44 Promotes the Association of PSKR1/BRI1 and Their Coreceptor. To elucidate how RLP44 might promote PSK signaling, we assessed whether its presence affects the association between PSKR1 and its coreceptor BAK1, both of which also directly interact with RLP44 (Fig. 3) (35). Indeed, more BAK1 was detected in immunoprecipitates of PSKR1-GFP when RLP44-RFP was coexpressed (Fig. 4*A*), suggesting that RLP44 might act as a scaffold in the complex. Supporting this notion, BAK1 levels in immunoprecipitates of PSKR1-GFP were reduced in the *rlp44*^{cnu2} mutant (*SI Appendix*, Fig. S13*A*). Consistent with an essential role of BAK1/SERK3 and other SERKs as coreceptors in PSK signaling (33, 34), the *serk1-3 serk3-1 serk4-1* triple mutant (56) showed increased metaxylem cell numbers (Fig. 4*B*). Because we had previously demonstrated that RLP44 can activate BR signaling upon cues from the cell wall (35), we assessed whether BR-signaling activation by RLP44 might occur through a similar mechanism. RLP44 and BRI1 showed direct interaction in yeast-mating–based split ubiquitin assays (*SI Appendix*, Fig. S13*B*) and FRET-FLIM analysis after transient expression in *N. benthamiana* (Fig. 4*C* and *SI Appendix*, Fig. S13 *C* and *D*). Furthermore, endogenous BRI1 and BAK1 were detected in immunoprecipitates of *RLP44-GFP* expressed under the control of its own promoter in the *rlp44*^{cnu2} mutant background (*SI Appendix*, Fig. S13*E*). Similar to what was observed for PSKR1, the presence of RLP44 increased the association of BRI1 with its coreceptor BAK1 (*SI Appendix*, Fig. S13*F*) in a line that expresses BRI1-mCitrine and BAK1-HA under control of their own promoters in the *bri1-null* background. In summary, our data suggest that RLP44 acts as a scaffold to stabilize the PSKR1-BAK1 and BRI1-BAK1 complexes, respectively. While the interaction between RLP44 and BRI1 might not play a role in the context of vascular cell-fate determination, RLP44 is controlled by BRI1 at the transcriptional level and is required to promote PSK signaling in the vasculature, which, in turn, suppresses the progression from procambial to xylem identity (Fig. 4*D*).

Discussion

RLP44 Controls Vascular Cell Fate Through PSK Signaling. The expanded family of plant RLK proteins and their ligands play central roles in intercellular communication, cell identity maintenance, and the regulation of cell expansion and proliferation (57). Currently, our view of these pathways is evolving to integrate the extensive cross-talk and interdependence of diverse signaling pathways (58). Here, we report that BR and PSK signaling are linked at the level of their plasma membrane receptors through RLP44 and that this signaling module is required to control xylem cell fate. Our genetic and biochemical data support a scenario where PSK-signaling strength is quantitatively controlled by RLP44, which itself is dependent on the presence of BRI1. While we cannot rule out posttranslational control of RLP44 by BRI1, for example, through phosphorylation of the cytoplasmic domain or through a role of BRI1 in the correct receptor complex assembly, this dependency is at least partially based on BRI1-mediated control of *RLP44* expression. More work will be needed to understand how these BRI1-dependent, but apparently BR-signaling output-independent functions, such as the control of *RLP44* expression, are achieved at the molecular level, but the branching of signaling transduction pathways immediately downstream or even at the level of plasma membrane receptor complexes is emerging as a common feature of RLK-dependent signaling (58). BRI1 and PSKR1/2 share the requirement for interaction with SERK coreceptors to form an active, heteromeric signaling complex (33, 34, 59). Consistent with this, the

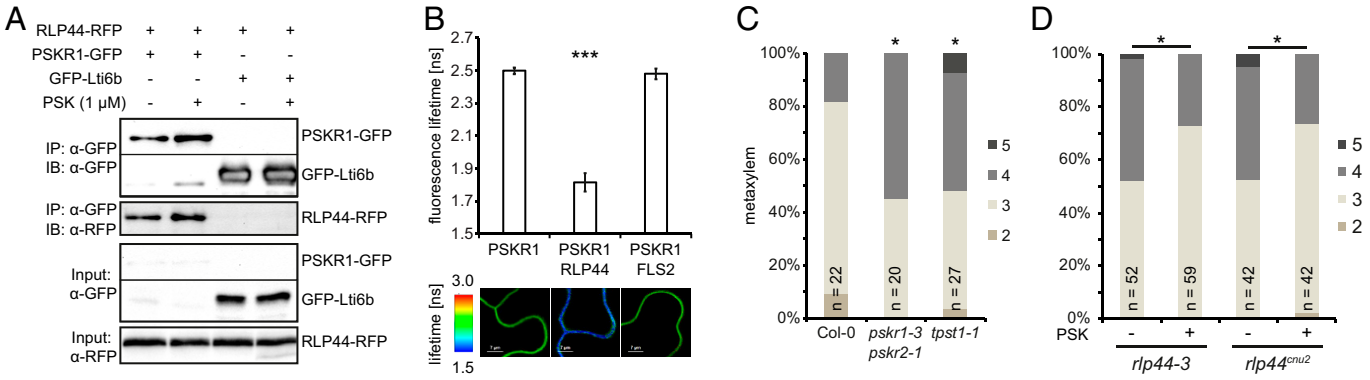

Fig. 3. RLP44 interacts with PSKR1 to promote PSK signaling and procambial identity. (*A*) Coimmunoprecipitation after transient expression in *N. benthamiana* leaves demonstrates the presence of RLP44-RFP in PSKR1-GFP immunoprecipitates. (*B*) FRET-FLIM analysis of the PSKR1-GFP/RLP44-RFP interaction in *N. benthamiana* leaves. Bars denote average of seven to eight measurements ±SD. Asterisks indicate statistically significant difference from PSKR1-GFP and PSKR1-GFP coexpressed with FLS2-RFP according to pairwise *t* test (***$P < 0.001$). (*C*) Quantification of metaxylem cell number in Col-0 and PSK-signaling–related mutants. (*D*) Application of PSK peptide rescues the ectopic xylem phenotype of *rlp44* mutants. Asterisks in *C* and *D* indicate statistically significant difference from Col-0 based on Dunn's post hoc test with Benjamini–Hochberg correction after Kruskal–Wallis modified *U* test (*$P < 0.05$).

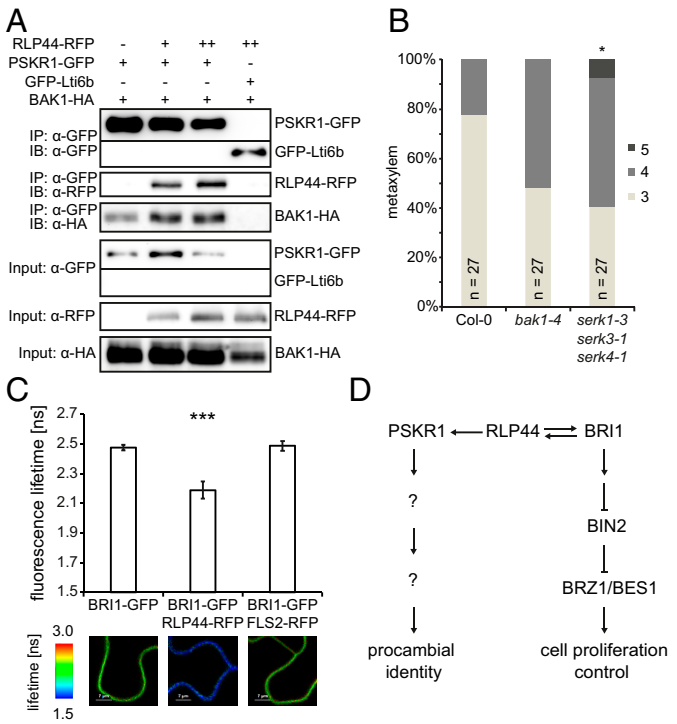

Fig. 4. RLP44 promotes the association of LRR-RLKs and their coreceptor. (*A*) Coimmunoprecipitation analysis after transient expression in *N. benthamiana* leaves demonstrates an increased amount of BAK1-HA in PSKR1-GFP immunoprecipitates in the presence of RLP44-RFP. RLP44 levels were adjusted through increasing the density of Agrobacteria (denoted by + or ++). (*B*) Quantification of metaxylem cell number in *bak1-4* and *triple-serk* mutants. Asterisks in *C* and *D* indicate statistically significant difference from Col-0 based on Dunn's post hoc test with Benjamini–Hochberg correction after Kruskal–Wallis modified *U* test (*$P < 0.05$). (*C*) FRETFLIM analysis of the RLP44-BRI1 interaction in *N. benthamiana* leaves. Bars denote average of six to seven measurements ±SD. Asterisks indicate statistically significant difference from BRI1-GFP and BRI1-GFP coexpressed with FLS2-RFP after pairwise *t* test (***$P <$ 0.001). (*D*) Model of RLP44-mediated activation of PSK and BR signaling. RLP44 is capable of activating both signaling pathways, depending on the conditions, and is under transcriptional control by BRI1. Thus, BRI1 is required for RLP44-mediated control of procambial cell fate through PSK signaling.

presence of RLP44 promoted the interaction between BAK1 and both BRI1 and PSKR1. Which RLK pathway is activated by RLP44 at a given time could depend on the conditions, in line with the initial identification of RLP44 as an essential factor for BR-signaling activation upon challenge of cell-wall integrity (35). These results and our model are in agreement with the emerging theme of dynamic, promiscuous, and flexible interactions of plasma membrane proteins to integrate signaling information and fine-tune cellular responses to external cues (60–62). Interestingly, the mechanism by which RLPs influence signaling seems to differ widely, ranging from direct participation in ligand binding (63, 64), to the control of signaling specificity through blocking access of RLK ligands (64), to the guarding of extracellular proteins targeted by pathogens (65). Here, we propose a scaffolding function of RLP44 for the interaction between PSKR1 and its coreceptor BAK1, expanding the mechanistic diversity of RLPs.

The Role of BR Signaling in Vascular Development. It has been described that BR signaling plays an important role in the development of vascular tissue (14, 15). In addition, it has been reported that BR signaling is kept at low levels in procambial cells of leaf and hypocotyl to prevent their differentiation into xylem cells (66). Our results suggest that, in the primary xylem of the root, BR signaling plays only a minor role in controlling differentiation, in marked contrast to the strong patterning defects of BR signaling and biosynthetic mutants in the shoot (15). Conversely, at least in the root, the presence of BRI1 has a negative effect on xylem cell fate through RLP44- and PSK-signaling–mediated maintenance of procambial identity. Therefore, our results identify a role of BRI1 in root development that is independent of its role as a BR receptor.

PSK Signaling Likely Promotes Procambial Identity. Alongside classical plant hormones, signaling peptides play major roles in plant development and stress responses (67, 68). The sulfated peptide PSK has been implicated diverse processes (26, 68). Here, we propose that PSK signaling controls xylem cell fate through promoting the maintenance of procambial identity. A number of observations support this hypothesis. First, PSK treatment rescued the ectopic xylem phenotype in *rlp44* mutants. Second, PSK-related mutants showed increased xylem differentiation in procambial position, and PSK genes are coexpressed with RLP44 in procambial cells (37). Third, PSK expression is transiently increased before the acquisition of a procambial intermediate state by cells transdifferentiating into tracheary elements (52, 69), which could explain why PSK promotes tracheary element formation in *Z. elegans* only when applied early to the cell culture (52, 53). Finally, PSK signaling promotes callus growth and longevity, in line with a role in the maintenance of cell identity (29). However, it is unclear how PSK signaling affects cellular behavior, in part due to a lack of knowledge about potential downstream targets. To gain a deeper understanding of xylem differentiation, it will be important to unveil how the BRI1-RLP44-PSK–signaling module described here integrates with the fundamental patterning mechanisms and the gene regulatory networks controlling cell fate (2, 8).

Materials and Methods

The sources of mutants used in this study are described in *SI Appendix*, Table S1. Seeds were sterilized with 1.2% NaOCl in 70% ethanol and washed twice with absolute ethanol before being dried under the sterile hood. Plants were grown in 1/2 strength MS medium supplemented with 1% sucrose and 0.9% plant agar. If appropriate, 24 epi-BL, PPZ, or bikinin were added to the medium after sterilization at the indicated concentrations. After a 48- to 72-h incubation in the dark, plants were grown at 23 °C during a 16-h light period.

Details regarding the construction of plasmids and generation of transgenic plants, analysis of xylem and vascular cell number, immunoprecipitation, qRT-PCR, interaction assays, and microscopy are provided in *SI Appendix, Materials and Methods*. Mutants and transgenic lines used in this study are listed in *SI Appendix*, Table S1.

ACKNOWLEDGMENTS. We thank Sigal Savaldi-Goldstein for the *bri*-triple mutant; Michael Hothorn for antisera against BRI1 and BAK1 and mutants; and Karin Schumacher for antiserum against RFP. Research in our laboratories was supported by German Research Foundation (DFG) Grants WO 1660/6-1 (to S.W.) and HA 2146/22-1 and CRC 1101-D02 (to K.H.). S.W. is supported by the DFG through Emmy Noether Programme Grant WO 1660/2.

1. Lucas WJ, et al. (2013) The plant vascular system: Evolution, development and functions. *J Integr Plant Biol* 55:294–388.
2. Bishopp A, et al. (2011) A mutually inhibitory interaction between auxin and cytokinin specifies vascular pattern in roots. *Curr Biol* 21:917–926.
3. De Rybel B, et al. (2014) Plant development. Integration of growth and patterning during vascular tissue formation in Arabidopsis. *Science* 345:1255215.
4. Zhou J, Wang X, Lee JY, Lee JY (2013) Cell-to-cell movement of two interacting AT-hook factors in Arabidopsis root vascular tissue patterning. *Plant Cell* 25: 187–201.
5. Ohashi-Ito K, et al. (2014) A bHLH complex activates vascular cell division via cytokinin action in root apical meristem. *Curr Biol* 24:2053–2058.
6. Ramachandran P, Wang G, Augstein F, de Vries J, Carlsbecker A (2018) Continuous root xylem formation and vascular acclimation to water deficit involves endodermal ABA signalling via miR165. *Development* 145:dev159202.
7. Kubo M, et al. (2005) Transcription switches for protoxylem and metaxylem vessel formation. *Genes Dev* 19:1855–1860.
8. Taylor-Teeples M, et al. (2015) An Arabidopsis gene regulatory network for secondary cell wall synthesis. *Nature* 517:571–575.
9. Carlsbecker A, et al. (2010) Cell signalling by microRNA165/6 directs gene dose-dependent root cell fate. *Nature* 465:316–321.
10. Zhong R, Ye ZH (2015) Secondary cell walls: Biosynthesis, patterned deposition and transcriptional regulation. *Plant Cell Physiol* 56:195–214.

11. Baum SF, Dubrovsky JG, Rost TL (2002) Apical organization and maturation of the cortex and vascular cylinder in Arabidopsis thaliana (Brassicaceae) roots. *Am J Bot* 89: 908–920.
12. Belkhadir Y, Jaillais Y (2015) The molecular circuitry of brassinosteroid signaling. *New Phytol* 206:522–540.
13. Singh AP, Savaldi-Goldstein S (2015) Growth control: Brassinosteroid activity gets context. *J Exp Bot* 66:1123–1132.
14. Caño-Delgado A, et al. (2004) BRL1 and BRL3 are novel brassinosteroid receptors that function in vascular differentiation in Arabidopsis. *Development* 131:5341–5351.
15. Ibañes M, Fàbregas N, Chory J, Caño-Delgado AI (2009) Brassinosteroid signaling and auxin transport are required to establish the periodic pattern of Arabidopsis shoot vascular bundles. *Proc Natl Acad Sci USA* 106:13630–13635.
16. Li J, Chory J (1997) A putative leucine-rich repeat receptor kinase involved in brassinosteroid signal transduction. *Cell* 90:929–938.
17. Shiu SH, Bleecker AB (2001) Receptor-like kinases from Arabidopsis form a monophyletic gene family related to animal receptor kinases. *Proc Natl Acad Sci USA* 98: 10763–10768.
18. Nam KH, Li J (2002) BRI1/BAK1, a receptor kinase pair mediating brassinosteroid signaling. *Cell* 110:203–212.
19. Li J, et al. (2002) BAK1, an Arabidopsis LRR receptor-like protein kinase, interacts with BRI1 and modulates brassinosteroid signaling. *Cell* 110:213–222.
20. Li J, Nam KH (2002) Regulation of brassinosteroid signaling by a GSK3/SHAGGY-like kinase. *Science* 295:1299–1301.
21. Wang ZY, et al. (2002) Nuclear-localized BZR1 mediates brassinosteroid-induced growth and feedback suppression of brassinosteroid biosynthesis. *Dev Cell* 2:505–513.
22. Yin Y, et al. (2002) BES1 accumulates in the nucleus in response to brassinosteroids to regulate gene expression and promote stem elongation. *Cell* 109:181–191.
23. Chaiwanon J, Wang ZY (2015) Spatiotemporal brassinosteroid signaling and antagonism with auxin pattern stem cell dynamics in Arabidopsis roots. *Curr Biol* 25: 1031–1042.
24. Sun Y, et al. (2010) Integration of brassinosteroid signal transduction with the transcription network for plant growth regulation in Arabidopsis. *Dev Cell* 19:765–777.
25. Yu X, et al. (2011) A brassinosteroid transcriptional network revealed by genome-wide identification of BESI target genes in Arabidopsis thaliana. *Plant J* 65:634–646.
26. Sauter M (2015) Phytosulfokine peptide signalling. *J Exp Bot* 66:5161–5169.
27. Amano Y, Tsubouchi H, Shinohara H, Ogawa M, Matsubayashi Y (2007) Tyrosine-sulfated glycopeptide involved in cellular proliferation and expansion in Arabidopsis. *Proc Natl Acad Sci USA* 104:18333–18338.
28. Matsubayashi Y, Ogawa M, Morita A, Sakagami Y (2002) An LRR receptor kinase involved in perception of a peptide plant hormone, phytosulfokine. *Science* 296: 1470–1472.
29. Matsubayashi Y, Ogawa M, Kihara H, Niwa M, Sakagami Y (2006) Disruption and overexpression of Arabidopsis phytosulfokine receptor gene affects cellular longevity and potential for growth. *Plant Physiol* 142:45–53.
30. Komori R, Amano Y, Ogawa-Ohnishi M, Matsubayashi Y (2009) Identification of tyrosylprotein sulfotransferase in Arabidopsis. *Proc Natl Acad Sci USA* 106:15067–15072.
31. Hartmann J, Stührwohldt N, Dahlke RI, Sauter M (2013) Phytosulfokine control of growth occurs in the epidermis, is likely to be non-cell autonomous and is dependent on brassinosteroids. *Plant J* 73:579–590.
32. Heyman J, et al. (2013) ERF115 controls root quiescent center cell division and stem cell replenishment. *Science* 342:860–863.
33. Wang J, et al. (2015) Allosteric receptor activation by the plant peptide hormone phytosulfokine. *Nature* 525:265–268.
34. Ladwig F, et al. (2015) Phytosulfokine regulates growth in Arabidopsis through a response module at the plasma membrane that includes CYCLIC NUCLEOTIDE-GATED CHANNEL17, H+-ATPase, and BAK1. *Plant Cell* 27:1718–1729.
35. Wolf S, et al. (2014) A receptor-like protein mediates the response to pectin modification by activating brassinosteroid signaling. *Proc Natl Acad Sci USA* 111: 15261–15266.
36. Wolf S (2017) Plant cell wall signalling and receptor-like kinases. *Biochem J* 474: 471–492.
37. Brady SM, et al. (2007) A high-resolution root spatiotemporal map reveals dominant expression patterns. *Science* 318:801–806.
38. Wolf S, Mravec J, Greiner S, Mouille G, Höfte H (2012) Plant cell wall homeostasis is mediated by brassinosteroid feedback signaling. *Curr Biol* 22:1732–1737.
39. Noguchi T, et al. (1999) Brassinosteroid-insensitive dwarf mutants of Arabidopsis accumulate brassinosteroids. *Plant Physiol* 121:743–752.
40. Szekeres M, et al. (1996) Brassinosteroids rescue the deficiency of CYP90, a cytochrome P450, controlling cell elongation and de-etiolation in Arabidopsis. *Cell* 85:171–182.
41. Nakamoto D, Ikeura A, Asami T, Yamamoto KT (2006) Inhibition of brassinosteroid biosynthesis by either a dwarf4 mutation or a brassinosteroid biosynthesis inhibitor rescues defects in tropic responses of hypocotyls in the Arabidopsis mutant nonphototropic hypocotyl 4. *Plant Physiol* 141:456–464.
42. Jaillais Y, Belkhadir Y, Balsemão-Pires E, Dangl JL, Chory J (2011) Extracellular leucine-rich repeats as a platform for receptor/coreceptor complex formation. *Proc Natl Acad Sci USA* 108:8503–8507.
43. Vragović K, et al. (2015) Translatome analyses capture of opposing tissue-specific brassinosteroid signals orchestrating root meristem differentiation. *Proc Natl Acad Sci USA* 112:923–928.
44. Hartwig T, et al. (2012) Propiconazole is a specific and accessible brassinosteroid (BR) biosynthesis inhibitor for Arabidopsis and maize. *PLoS One* 7:e36625.
45. De Rybel B, et al. (2009) Chemical inhibition of a subset of Arabidopsis thaliana GSK3-like kinases activates brassinosteroid signaling. *Chem Biol* 16:594–604.
46. Clouse SD, Langford M, McMorris TC (1996) A brassinosteroid-insensitive mutant in Arabidopsis thaliana exhibits multiple defects in growth and development. *Plant Physiol* 111:671–678.
47. Friedrichsen DM, Joazeiro CA, Li J, Hunter T, Chory J (2000) Brassinosteroid-insensitive-1 is a ubiquitously expressed leucine-rich repeat receptor serine/threonine kinase. *Plant Physiol* 123:1247–1256.
48. Bojar D, et al. (2014) Crystal structures of the phosphorylated BRI1 kinase domain and implications for brassinosteroid signal initiation. *Plant J* 78:31–43.
49. Hruz T, et al. (2008) Genevestigator v3: A reference expression database for the meta-analysis of transcriptomes. *Adv Bioinforma* 2008:420747.
50. Kang YH, Breda A, Hardtke CS (2017) Brassinosteroid signaling directs formative cell divisions and protophloem differentiation in Arabidopsis root meristems. *Development* 144:272–280.
51. Schlereth A, et al. (2010) MONOPTEROS controls embryonic root initiation by regulating a mobile transcription factor. *Nature* 464:913–916.
52. Motose H, et al. (2009) Involvement of phytosulfokine in the attenuation of stress response during the transdifferentiation of zinnia mesophyll cells into tracheary elements. *Plant Physiol* 150:437–447.
53. Matsubayashi Y, Takagi L, Omura N, Morita A, Sakagami Y (1999) The endogenous sulfated pentapeptide phytosulfokine-alpha stimulates tracheary element differentiation of isolated mesophyll cells of zinnia. *Plant Physiol* 120:1043–1048.
54. Kutschmar A, et al. (2009) PSK-α promotes root growth in Arabidopsis. *New Phytol* 181:820–831.
55. Matsuzaki Y, Ogawa-Ohnishi M, Mori A, Matsubayashi Y (2010) Secreted peptide signals required for maintenance of root stem cell niche in Arabidopsis. *Science* 329: 1065–1067.
56. Hohmann U, et al. (2018) Mechanistic basis for the activation of plant membrane receptor kinases by SERK-family coreceptors. *Proc Natl Acad Sci USA* 115:3488–3493.
57. De Smet I, Voss U, Jürgens G, Beeckman T (2009) Receptor-like kinases shape the plant. *Nat Cell Biol* 11:1166–1173.
58. Couto D, Zipfel C (2016) Regulation of pattern recognition receptor signalling in plants. *Nat Rev Immunol* 16:537–552.
59. Santiago J, Henzler C, Hothorn M (2013) Molecular mechanism for plant steroid receptor activation by somatic embryogenesis co-receptor kinases. *Science* 341:889–892.
60. Smakowska-Luzan E, et al. (2018) An extracellular network of Arabidopsis leucine-rich repeat receptor kinases. *Nature* 553:342–346.
61. Stegmann M, et al. (2017) The receptor kinase FER is a RALF-regulated scaffold controlling plant immune signaling. *Science* 355:287–289.
62. Gui J, et al. (2016) OsREM4.1 interacts with OsSERK1 to coordinate the interlinking between abscisic acid and brassinosteroid signaling in rice. *Dev Cell* 38:201–213.
63. Albert I, et al. (2015) An RLP23-SOBIR1-BAK1 complex mediates NLP-triggered immunity. *Nat Plants* 1:15140.
64. Lin G, et al. (2017) A receptor-like protein acts as a specificity switch for the regulation of stomatal development. *Genes Dev* 31:927–938.
65. Rooney HC, et al. (2005) Cladosporium Avr2 inhibits tomato Rcr3 protease required for Cf-2-dependent disease resistance. *Science* 308:1783–1786.
66. Kondo Y, et al. (2014) Plant GSK3 proteins regulate xylem cell differentiation downstream of TDIF-TDR signalling. *Nat Commun* 5:3504.
67. Tavormina P, De Coninck B, Nikonorova N, De Smet I, Cammue BP (2015) The plant peptidome: An expanding repertoire of structural features and biological functions. *Plant Cell* 27:2095–2118.
68. Matsubayashi Y (2014) Posttranslationally modified small-peptide signals in plants. *Annu Rev Plant Biol* 65:385–413.
69. Kondo Y, Fujita T, Sugiyama M, Fukuda H (2015) A novel system for xylem cell differentiation in Arabidopsis thaliana. *Mol Plant* 8:612–621.

Supplemental Information

Materials and Methods

Plasmid Construction, Generation of Transgenic plants

Constructs for mating-based split-ubiquitin and FRET-FLIM assays were generated using Gateway technology (Life Technologies). The constructs of RLP44, BAK1 and BRI1 in pMetYC-Dest and pXNubA22-Dest were already described (1). BAK1-HA was generated by recombination of the available BAK1 entry clone (1) with pGWB14 using Gateway technology. Similarly, BRI1-GFP was created using pH7FWG2 (2). The pRLP44-GFP-GUS lines were created using primers RLP44prom_GW_L and RLP44prom_GW_R and destination vector pKGWFS7 (2). PSKR1-GFP was already described in Ladwig et al., 2015 (3). For the FRET-FLIM assays with RLP44 and BRI1, the destination vector pFRETtv-2in1-CC was used (4). For this system, the respective genes had to be cloned into pDONR221 P1P4 and pDONR221 P3P2 using multisite Gateway technology (Life Technologies). FLS2 (at5g46330) ORF was amplified from plasmid DNA under omission of the stop codon with forward primer FLS2_attB1_F and reverse primer FLS2_attB4_R. RLP44 was amplified with RLP44_attb3_F and RLP44_attb2_R omitting the stop codon and BRI1 was amplified with primers BRI1_attB3_F and BRI1_attB2_R. Subsequently, the respective constructs were cloned into the pFRETtv-2in1-CC. We generated the 2in1 constructs RLP44-mTurquoise-FLS2-mVenus and RLP44-mTurquise-BRI1-mVenus. Oligonucleotides are described in Table S1.
All other constructs are based on the GreenGate system (5). For details regarding cloning and constructs please see Table S2. For BRI1 (at4g39400) CDS GreenGate Cloning, three internal BsaI/Eco31I recognition sites were removed through the generation of 4 PCR fragments with following primers BRI1_GGC_1F, BRI1_GGC_1R, BRI1_GGC_2F BRI1_GGC_2R, BRI1_GGC_3F, BRI1_GGC_3R, BRI1_GGC_4F and BRI1_GGC_4R. Subsequently the PCR products of all combinations were gel purified, digested with Eco31I, ligated and continued according to the GreenGate protocol (5).

Genotyping

For genotyping of the *bri1-null* T-DNA insertion line, we used for the wildtype allele BRI1-GK_WT_F and primer BRI1_3'UTR_R. Presence of the T-DNA insertion was assessed with primers GK-o8409 and BRI1_GK-134E10_R. The presence of the *bri1-116* allele in segregating *bri triple* and 35SRLP44-GFP (*bri triple*) seedlings was determined with primers bri1-116_CAPS_F and bri1-116_CAPS_R and subsequent digestion of the PCR product with MssI. For *pskr1-3* mutants, primers SALK_008585_F and SALK_008585_R were used to detect the wildtype allele and primers SALK_008585_F and LBb1.3 were used to detect the T-DNA. For *pskr2-1* mutant, SALK_203857_F and SALK_203857_R were combined for the wildtype allele and SALK_203857_F and LBb1.3 for the T-DNA. Genotyping of *rlp44*^{cnu2} is described in (1).

Analysis of Xylem and Total Vascular Cell Number

For Basic Fuchsin staining, 6 day old seedlings were fixed in methanol for 1-2 hours using 6-well plates with cell strainers and subsequently placed in 10% (w/v) NaOH and incubated for 3-4 hours at 65°C. After removal of the NaOH solution, seedlings were stained in 0.01% basic fuchsin (w/v) in water for five minutes, destained in 70% (v/v) ethanol for 10 minutes, and stored in 50% (v/v) glycerol. Samples were mounted in 50% Glycerol and imaged on a Zeiss LSM 510 or a Leica SP5 using excitation of 514 nm. Fluorescence emission was detected with

a 560 nm long pass filter. Xylem cell type was determined via the patterning of ligninified secondary cell all thickenings from z stacks. For Calcofluor White staining of the cell walls, seedlings were placed in 1 M KOH solution for 6 hours at 37°C. After removal of KOH, seedlings were washed three times in 50 mM Tris-HCl pH 7.5, and with 100 µg/µl Calcofluor white in the same buffer for 1.5 hours on a benchtop shaker. After three washing steps with 50 mM Tris-HCL pH7.5, seedlings were stored in 50% glycerol. Samples were mounted in 50% Glycerol and imaged on a Zeiss LSM 510 using excitation at 405 nm and detection with a 420-480 nm band pass filter.

Immunoprecipitation and Western Blotting

Transient expression was performed in leafs of 4-6 week old *Nicotiana benthamiana* plants through Agrobacteria infiltration (OD_{600} = 1). Two days after transformation, 0,75 g plant material was harvested. PSK was infiltrated 60 min before harvesting. For immunoprecipitation from Arabidopsis, 6 to 9 day old seedlings grown on plates as described were harvested, and up to 1 g plant material was frozen in liquid nitrogen. The following steps were the same for both experimental approaches. The plant material was ground using 2 ml/g of extraction buffer (50mM Tris-HCL pH 7.5, 150 mM NaCl, 10% glycerol, 5 mM EDTA, 1% NP40, 5 mM DTT and 1 % plant protease inhibitor cocktail). The total ground material was spun down for 15 min in a table top centrifuge (max. rpm, 4 °C). 60 µl of the protein extract was taken as the input sample and boiled with 20 µl of 4x SDS-PAGE sample buffer (Roti Load1, Roth) at 95 °C. The remaining protein extract was incubated with GFP-trap or RFP-trap agarose beads. For each sample, 30 µl of beads were equilibrated in 1 ml of the extraction buffer and spun down for 5 min in centrifuge (500 rpm, 4°C). After removal of the supernatant, the protein extract was added to the beads and incubated for 2 hours at 4°C (over-head shaker). After incubation, the beads were washed three times with extraction buffer and the supernatant was discarded. The remaining beads were boiled in 60 µl of 2x SDS-PAGE sample buffer at 95 °C for 5 min. SDS-PAGE gels were self-prepared and for RLP44 detection 12% gels, for BAK1 10% and for BRI1 6 or 7 % gels were used. The same protein quantity was loaded in the SDS-PAGE and after Western blotting probed with the indicated antibodies. Before probing with the antibodies the PVDF membrane (Immobilon-P, Millipore) was blocked for 1 h in 5% BSA in 1 x TBST blocking solution (20 nM Tris-base pH 7.4, 150 mM NaCl, 0.05% Tween). Primary antibodies, mouse anti-GFP (1GFP63, Biolegend, 1:10000), mouse anti-HA (F-7, Santa Cruz Biotechnology, 1:5000), rabbit anti-RFP (1:10000), rabbit anti-BRI1 ((6), 1:5000) and rabbit anti-BAK1 ((6), 1:10000) were diluted in 3 % BSA and incubated with the membrane overnight at 4 °C on a shaker. Membranes were washed 8 x 5 min with 1 X TBST before they were incubated with the secondary antibodies, goat polyclonal anti-rabbit coupled to horseradish peroxidase (Thermo Fisher Scientific, 1:10000) or rabbit polyclonal anti-mouse coupled to horseradish peroxidase (Sigma-Aldrich, 1:10000) diluted in in 3% BSA for 1 hour on gentle agitation on room temperature. Membranes were again washed 8 x 5 min before imaging with an INTAS science imaging device using a chemiluminescence detection kit (Supersignal West Pico, Thermo Fischer Scientific).

Quantitative Reverse Transcription PCR

Total RNA was extracted from roots of 5 day old seedlings. Not more than 100 mg of roots were frozen in liquid nitrogen and RNA was extracted with the GeneMATRIX Universal RNA Purification Kit (EURx/Roboklon) with an additional DNaseI digestion step, either directly on the column (Roboklon DnaseI-RNase free E1345) or subsequently DNase I digestion (DNase I, RNase-free, Thermo Fisher Scientific EN0525) followed by a RNA column clean-up (Roboklon RNA Purification Kit). 1 µg RNA in 5,75 µL RNase free water was used for cDNA synthesis with AMV Reverse Transcriptase Native according the manufacturer's protocol (Roboklon E1372) with RiboLock RNase Inhibitor (Thermo Fisher Scientific EO0381). qPCR reactions were performed in 15 µL volume, of which are 5 µL 1:40 diluted cDNA template in water, 0.3 µL of JumpStartTM Tag DNA Polymerase (Sigma-Aldrich), 1.5 µL appropriate

buffer, 0.3 µM of each forward and reverse primer, 2 µM dNTPs (Sigma-Aldrich), 0.6 mM $MgCl_2$ and 0.15 µL of 1:400 diluted SYBR ® Green I (Sigma-Aldrich) and fill up with H_2O. Gene expression was normalized to housekeeping gene clathrin adaptor subunit (7). Primer sequences are listed in the table. Ct values were measured in the Rotor Gene Q 2plex (Qiagen) and the data was analysed with the 75 Rotor-Gene Q 2plex software and evaluated according to (8) and (9).

Confocal Laser-Scanning Microscopy

Laser lines of 405 nm (Calcofluor White), 488 nm (GFP, FM4-64), 514 nm (YFP, basic fuchsin), or 543 nm (RFP, mCherry, propidium iodide) on a Zeiss LSM 510 Meta and Leica SP5 microscope systems equipped with 25× and 63× water immersion objectives were used for excitation. Fluorescence was recorded between 420 and 480 nm for Calcofluor White, between 530 and 600 nm for YFP, and between 490 and 525 nm for GFP. FM4-64 fluorescence was recorded between 600 nm and 720 nm and propidium iodide was recorded using a 560 nm long pass filter. Images were analyzed with Zeiss Zen software and Fiji. Images were processed with Fiji and Adobe Photoshop CS for figure preparation.

Mating-Based Split-Ubiquitin Assay and FRET-FLIM Analysis

mbSUS and FRET-FLIM were performed as described (1, 10).

Glucuronidase staining

GUS staining was performed as described (11).

Statistical Analysis

The number of samples analyzed for quantifications are indicated in the figures as (n). The significance of difference between samples were determined by One-way ANOVA combined with Tukey's post hoc test, or by Student's t-test. Xylem cell numbers were analyzed using Mann-Whitney U-test or Kruskal-Wallis modified U-test and Dunn's post hoc test with Benjamini-Hochberg correction. QRT-PCR was analysed as described (9), followed by one-way ANOVA.

References

1. Wolf S*, et al.* (2014) A receptor-like protein mediates the response to pectin modification by activating brassinosteroid signaling. *Proc Natl Acad Sci U S A* 111(42):15261-15266.
2. Karimi M, Inze D, & Depicker A (2002) GATEWAY vectors for Agrobacterium-mediated plant transformation. *Trends Plant Sci* 7(5):193-195.
3. Ladwig F*, et al.* (2015) Phytosulfokine Regulates Growth in Arabidopsis through a Response Module at the Plasma Membrane That Includes CYCLIC NUCLEOTIDE-GATED CHANNEL17, H+-ATPase, and BAK1. *Plant Cell* 27(6):1718-1729.
4. Hecker A*, et al.* (2015) Binary 2in1 Vectors Improve in Planta (Co)localization and Dynamic Protein Interaction Studies. *Plant Physiol* 168(3):776-787.
5. Lampropoulos A*, et al.* (2013) GreenGate---a novel, versatile, and efficient cloning system for plant transgenesis. *PLoS One* 8(12):e83043.
6. Bojar D*, et al.* (2014) Crystal structures of the phosphorylated BRI1 kinase domain and implications for brassinosteroid signal initiation. *Plant J* 78(1):31-43.

7. Czechowski T, Stitt M, Altmann T, Udvardi MK, & Scheible WR (2005) Genome-wide identification and testing of superior reference genes for transcript normalization in Arabidopsis. *Plant Physiol* 139(1):5-17.
8. Muller PY, Janovjak H, Miserez AR, & Dobbie Z (2002) Processing of gene expression data generated by quantitative real-time RT-PCR. *Biotechniques* 32(6):1372-1374, 1376, 1378-1379.
9. Rieu I & Powers SJ (2009) Real-time quantitative RT-PCR: design, calculations, and statistics. *Plant Cell* 21(4):1031-1033.
10. Grefen C, Obrdlik P, & Harter K (2009) The determination of protein-protein interactions by the mating-based split-ubiquitin system (mbSUS). *Methods Mol Biol* 479:217-233.
11. Wolf S, Mravec J, Greiner S, Mouille G, & Hofte H (2012) Plant cell wall homeostasis is mediated by brassinosteroid feedback signaling. *Curr Biol* 22(18):1732-1737.
12. Wang ZY*, et al.* (2002) Nuclear-localized BZR1 mediates brassinosteroid-induced growth and feedback suppression of brassinosteroid biosynthesis. *Dev Cell* 2(4):505-513.
13. Hruz T*, et al.* (2008) Genevestigator v3: a reference expression database for the meta-analysis of transcriptomes. *Advances in bioinformatics* 2008:420747.
14. Schlereth A*, et al.* (2010) MONOPTEROS controls embryonic root initiation by regulating a mobile transcription factor. *Nature* 464(7290):913-916.
15. Brady SM*, et al.* (2007) A high-resolution root spatiotemporal map reveals dominant expression patterns. *Science* 318(5851):801-806.
16. Winter D*, et al.* (2007) An "Electronic Fluorescent Pictograph" browser for exploring and analyzing large-scale biological data sets. *PLoS One* 2(8):e718.
17. Matsuzaki Y, Ogawa-Ohnishi M, Mori A, & Matsubayashi Y (2010) Secreted peptide signals required for maintenance of root stem cell niche in Arabidopsis. *Science* 329(5995):1065-1067.
18. Li J & Nam KH (2002) Regulation of brassinosteroid signaling by a GSK3/SHAGGY-like kinase. *Science* 295(5558):1299-1301.
19. Noguchi T*, et al.* (1999) Brassinosteroid-insensitive dwarf mutants of Arabidopsis accumulate brassinosteroids. *Plant Physiol* 121(3):743-752.
20. Jaillais Y, Belkhadir Y, Balsemao-Pires E, Dangl JL, & Chory J (2011) Extracellular leucine-rich repeats as a platform for receptor/coreceptor complex formation. *Proc Natl Acad Sci U S A* 108(20):8503-8507.
21. Vragovic K*, et al.* (2015) Translatome analyses capture of opposing tissue-specific brassinosteroid signals orchestrating root meristem differentiation. *Proc Natl Acad Sci U S A* 112(3):923-928.
22. Szekeres M*, et al.* (1996) Brassinosteroids rescue the deficiency of CYP90, a cytochrome P450, controlling cell elongation and de-etiolation in Arabidopsis. *Cell* 85(2):171-182.
23. Kutschmar A*, et al.* (2009) PSK-alpha promotes root growth in Arabidopsis. *New Phytol* 181(4):820-831.
24. Komori R, Amano Y, Ogawa-Ohnishi M, & Matsubayashi Y (2009) Identification of tyrosylprotein sulfotransferase in Arabidopsis. *Proc Natl Acad Sci U S A* 106(35):15067-15072.

Supplemental Figures and Tables

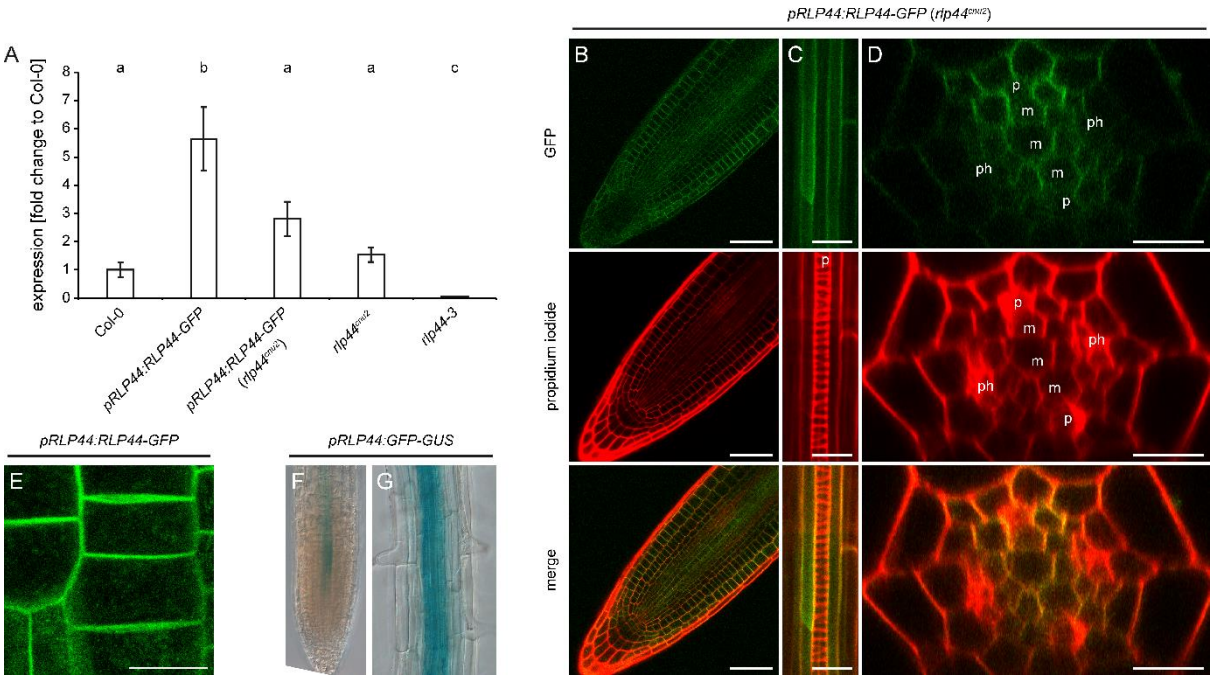

Fig. S1: *RLP44* is expressed in the root vascular tissue. (A) Quantitative Real Time PCR analysis of *RLP44* expression levels in transgenic RLP44-GFP lines and *rlp44* mutants. Note that *rlp44*^{cnu2} carries a point mutation creating a premature stop codon, whereas *rlp44-3* is a T-DNA insertion line (1). Bars denote mean ±SEM of four experiments, letters indicate statistically significant differences based on one-way ANOVA, n = 3. (B) Expression of *RLP44* fused to GFP under control of its own regulatory 5' sequences (*pRLP44:RLP44-GFP*) in the *rlp44*^{cnu2} mutant background. With the exception of the columella, all root meristem cells show GFP fluorescence, but intensity is increased in epidermis, lateral root cap, and vascular precursor cells. Scale bar = 50 µm. (C) Expression of *pRLP44:RLP44-GFP* (*rlp44*^{cnu2}) in differentiating xylem cells. Scale bar = 10 µm. (D) Orthogonal view of a confocal stack recording expression of *pRLP44:RLP44-GFP* in the differentiating vascular tissue of *rlp44*^{cnu2} roots. Note increased fluorescence in procambial cells. Scale bar = 10 µm. Indicated are differentiated phloem (ph), and protoxylem (p), as well as yet undifferentiated metaxylem (m). (E) High magnification image of a root cortex cell expressing pRLP44:RLP44-GFP, showing plasma membrane and intracellular vesicular localization, in agreement with previous observations (1). (F) A reporter line expressing the *uidA* gene under control of the RLP44 promoter displays epidermal and vascular reporter gene activity in the root.

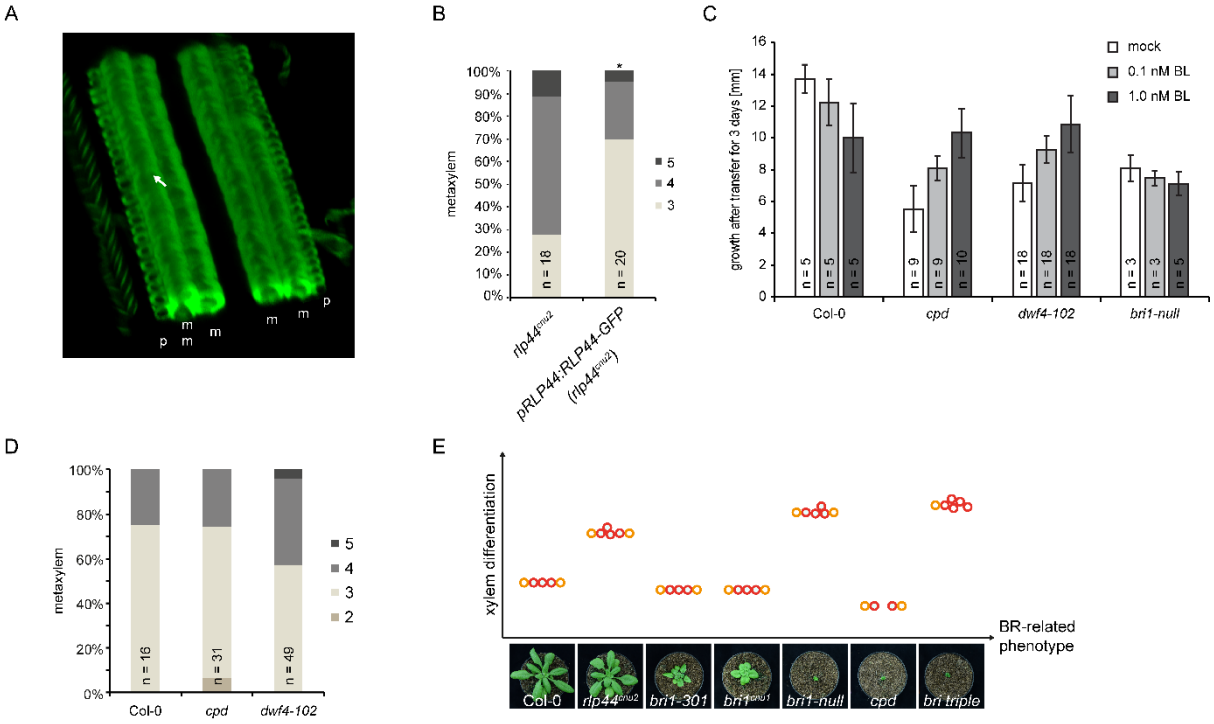

Fig. S2. (A) 3D reconstruction of a stack taken from an *rlp44-3* root indicating ectopic xylem cell (arrow) with pitted metaxylem (m)-like secondary cell wall patterning rather than spiral/annular protoxylem (p) patterning. (B) Expression of *RLP44* under control of its own promoter complements the *rlp44*^{cnu2} xylem phenotype. (C) The BR biosynthetic mutants *cpd* and *dwf4-102* behave similarly in the response to BL, whereas the *bri-null* mutant is insensitive. Bars indicate average growth in mm ± SD after transfer to BL- or DMSO (mock)-containing plates from 4 DAG to 7 DAG. (D) Metaxylem cell number in the *cpd* and *dfw4-102* mutants. (E) Overview over ectopic xylem phenotypes of *rlp44* and BR-related mutants. Note the absence of correlation between severity of BR signalling deficiency (x-axis) and frequency of ectopic xylem phenotype (y-axis). Based on Fig. 2C and D. Bars in (A) and (C) denote frequency of roots with the indicated number of xylem cells. Asterisk indicates statistically significant difference based on Dunn's post-hoc test with Benjamini-Hochberg correction after Kruskal-Wallis modified U-test (*p < 0.05, **p<0.01, ***p<0.001; n.s. = not significant).

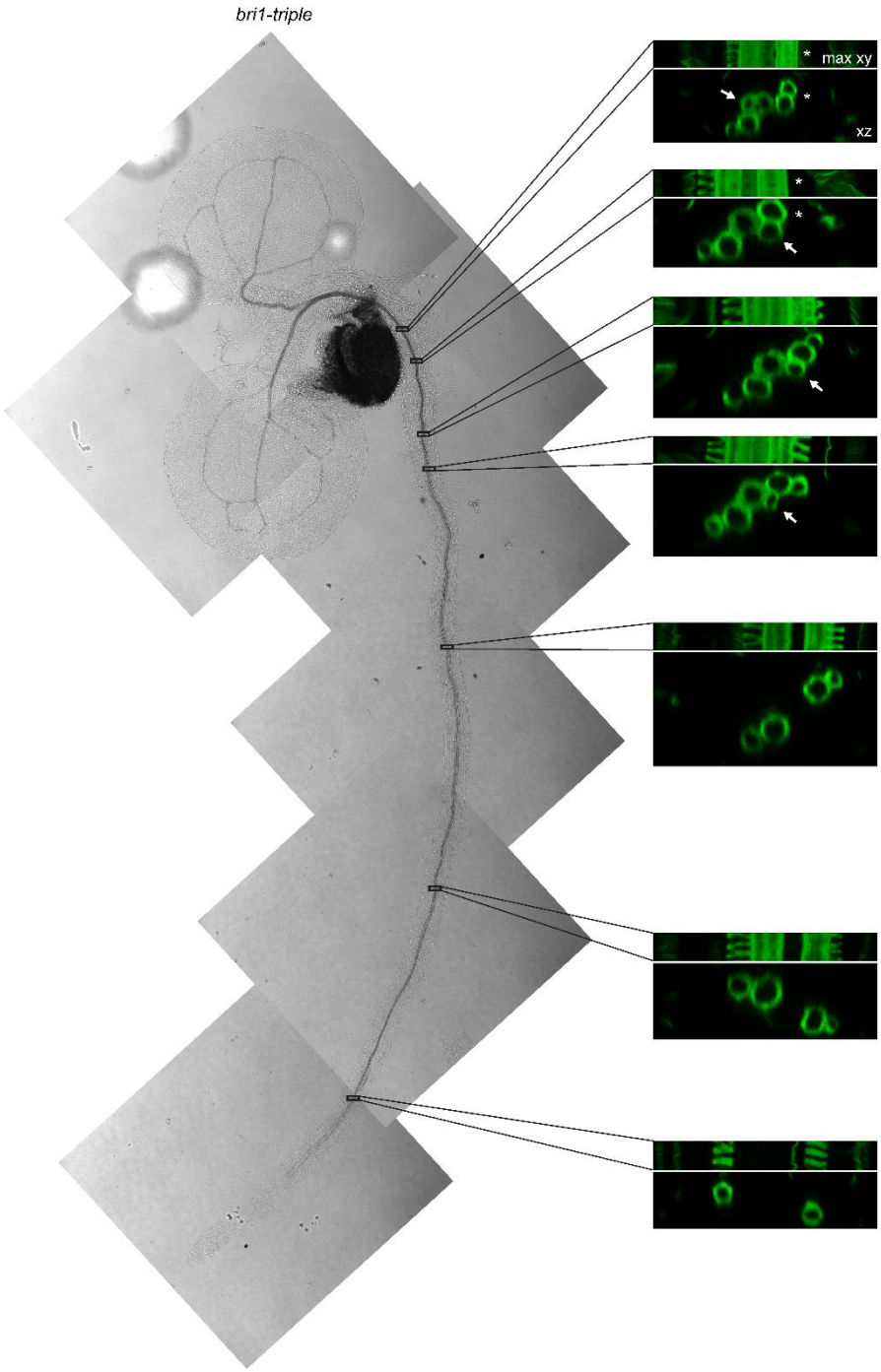

Fig. S3. Overview over xylem phenotype in a 6-day old *bri1-triple* seedling. Approximate imaging position for each stack is indicated. Top Panels are maximum xy projections of the stacks, lower panels show orthogonal xz views. Arrows indicate ectopic metaxylem, asterisks indicate missing protoxylem.

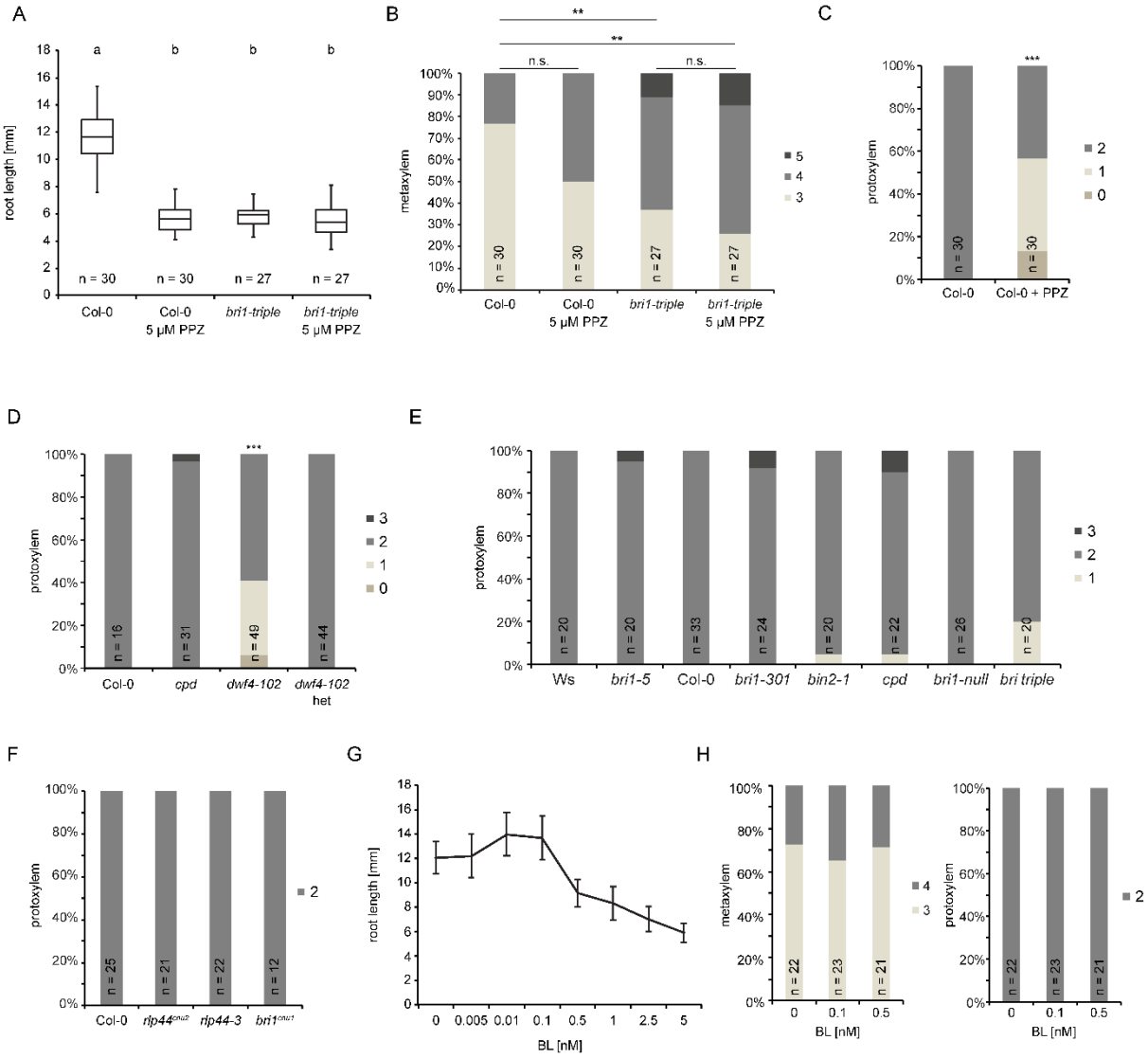

Fig. S4. (A) Depletion of BRs by PPZ treatment leads to *bri-triple*-like growth in the wild type and does not further reduce *bri-triple* root growth. Box plots indicate interquartile range (box), median (bar) and minimum/maximum (whiskers). (B) Metaxylem cell numbers are not significantly altered by depletion of BRs. (C) Depletion of BRs by PPZ treatment results in protoxylem defects. (D) *dwf4-102*, but not *cpd* shows reduced protoxylem cell number. Het = heterozygous and wildtype plants of the segregating *dwf4-102* population (E and F) Protoxylem cell number of genotypes analysed in Fig. 2. (G) Dose-response curve of wildtype root growth in the presence of exogenously supplied BL. (H) Neither a growth promoting, nor a growth inhibiting dose (see (G)) of BL has an effect on metaxylem (left panel) or protoxylem (right panel) cell number. Bars in (B-F, and H) denote frequency of roots with the indicated number of xylem cells. Asterisks indicate statistically significant difference based on Dunn's post-hoc test with Benjamini-Hochberg correction after Kruskal-Wallis modified U-test (**p<0.01, ***p<0.001; n.s. = not significant).

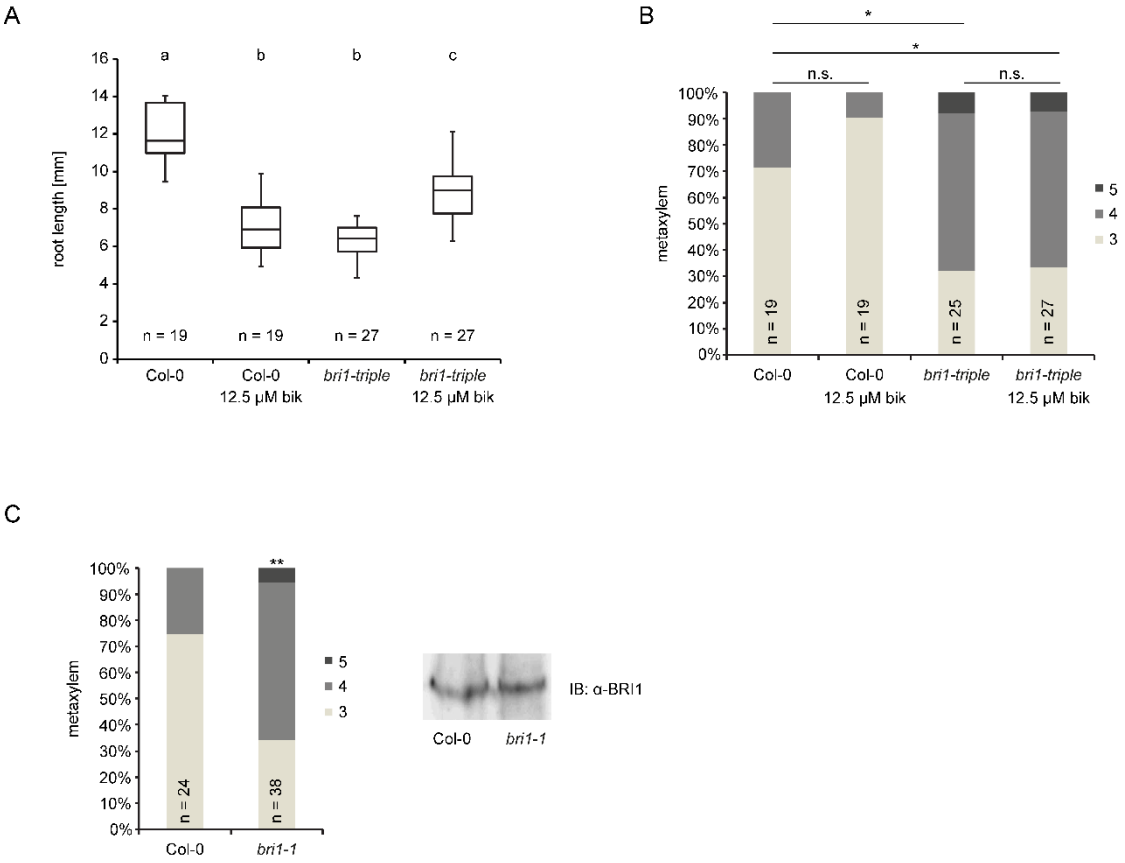

Fig. S5. (A) Root length measurements of Col-0 and *bri-triple* with and without bikinin treatment indicate that 12.5 µM bikinin leads to growth depression in the wildtype, but partially rescues *bri1-triple* root growth. (B) Bikinin treatment has no effect on Col-0 and *bri-triple* metaxylem cell number. (C) Metaxylem cell number is increased in the kinase dead *bri1-1* mutant despite the presence of wild type-like BRI1 protein levels. Left panel shows frequency of metaxylem cell numbers in Col-0 and *bri1-1*, whereas right panel shows a Western Blot developed with antiserum against BRI1 with total protein samples from the same genotypes. Box plots in (A) indicate interquartile range (box), median (bar) and minimum/maximum (whiskers). Bars in (B) and (C) denote frequency of roots with the indicated number of metaxylem cells. Asterisks indicate statistically significant difference based on Dunn's post-hoc test with Benjamini-Hochberg correction after Kruskal-Wallis modified U-test (*$p < 0.05$, **$p<0.01$; n.s. = not significant).

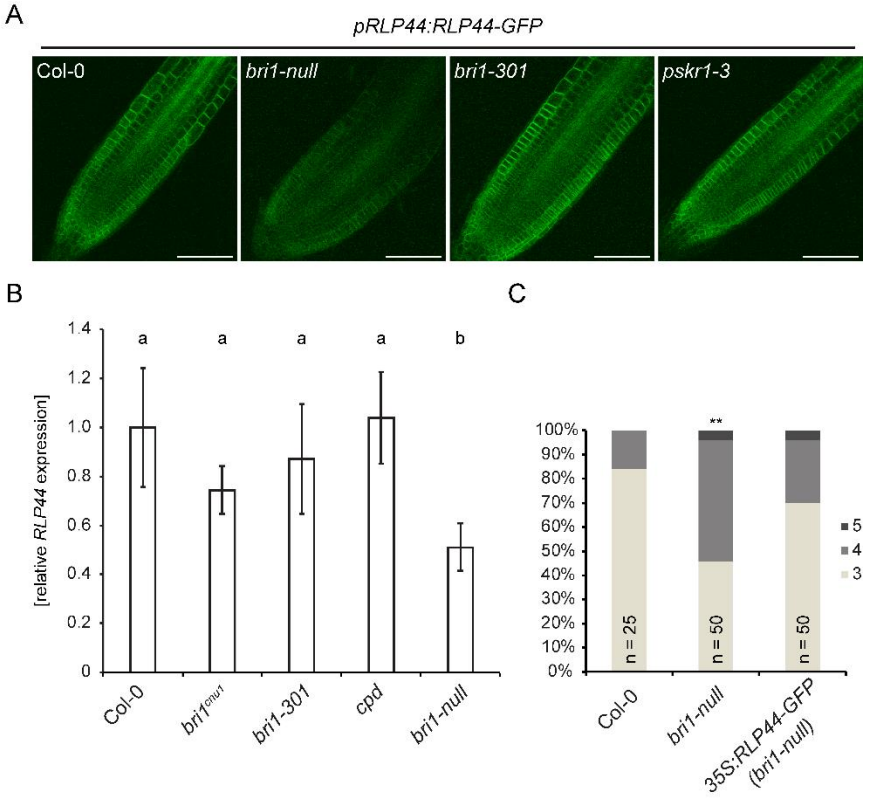

Fig. 6. RLP44 function requires the presence of BRI1 independent of BR signalling strength. (A) Fluorescence intensity derived from RLP44-GFP expressed under control of its own promoter is decreased in the *bri1-null* mutant but largely unaffected in *bri1* hypomorphs and *pskr1-3*. The same *pRLP44:RLP44-GFP* line in Col-0 background was used for crossing with the indicated mutants. (B) QRT-PCR showing reduced steady state levels of RLP44 transcript in roots *of bri1-null*, but not in the biosynthetic mutant *cpd*. Bars denote mean ± SEM of five experiments. Letters indicates statistically significant differences based on one-way ANOVA. (C) Ubiquitous overexpression of *RLP44* rescues the *bri1-null* xylem phenotype. Bars denote frequency of roots with the indicated number of metaxylem cells, asteriska indicate statistically significant difference based on Dunn's post-hoc test with Benjamini-Hochberg correction after Kruskal-Wallis modified U-test **p<0.01).

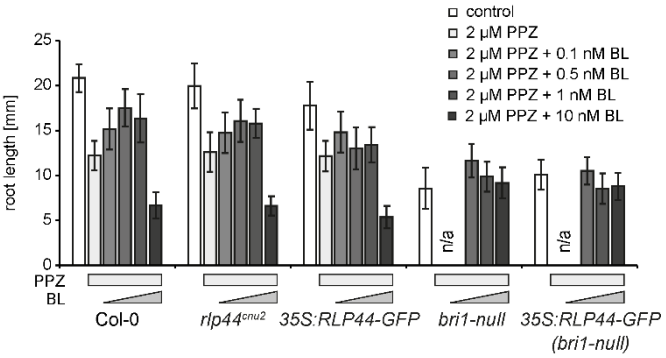

Fig. S7. RLP44 does not promotes BR response *bri1-null*. (A) Response of Col-0, *rlp44*^{cnu2}, *35S:RLP44-GFP*, *bri1-null*, and *35S:RLP44-GFP* (*bri1-null*) to depletion (PPZ) and exogenous supply of brassinosteroids. Bars indicate average root length ± S.D. ($17 < n < 21$). Note that homozygous *bri1-null* mutants are infertile. Therefore, offspring of a heterozygous plant was used and *bri1-null* homozygotes were selected based on phenotype (shorter and thicker root, dark green cotyledons); both genotypes showed the expected 1:3 segregation ratio. Due to the BR deficiency phenotype induced in all plants, PPZ and PPZ + 0.1 nM BL conditions did not allow for confident identification of *bri1-null* mutants.

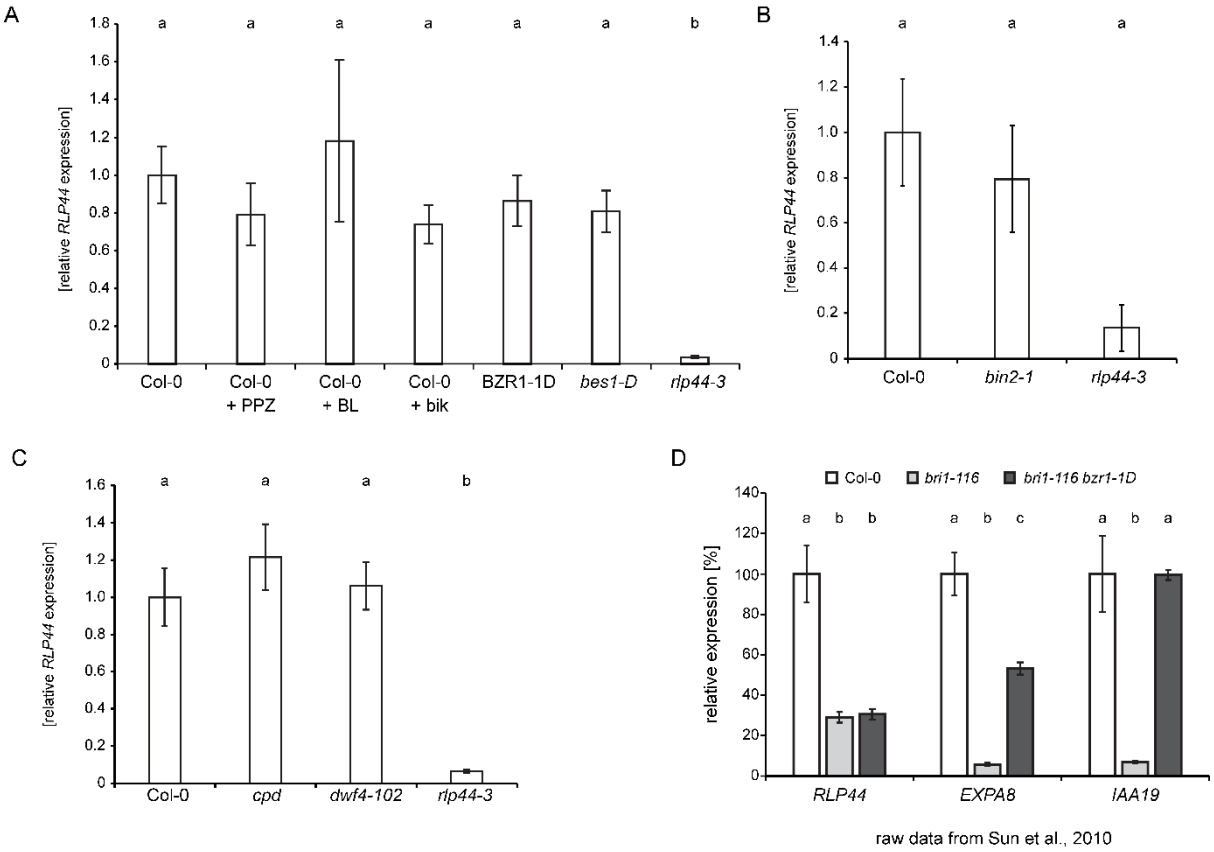

Fig. S8. *RLP44* expression is not affected by BR signalling-related cues. (A-C) QRT-PCR estimation of relative *RLP44* transcript levels upon the indicated treatments and genotypes. Bars denote averages of three biological replicates (two to three technical replicates each) ± SEM. BZR1-1D indicates the *pBZR1:bzr1-1D-CFP* line (12). Letters indicate statistically significant differences based on one-way ANOVA. (D) Re-analysis of published transcriptome data (13) shows that *RLP44* transcript levels are reduced in the null allele *bri1-116* and are not recovered by the constitutively active transcriptions factor *bzr1-1D*, unlike canonical BR target genes such as *EXPA8* and *IAA19*. Bars denote averages of three biological replicates ±SD. Letters indicate statistically significant differences based on one-way ANOVA.

A

Dataset: 21 perturbations from data selection: DATA-AT_AFFY_ATH1-3

Showing 1 measure(s) of 1 gene(s) on selection: AT-0

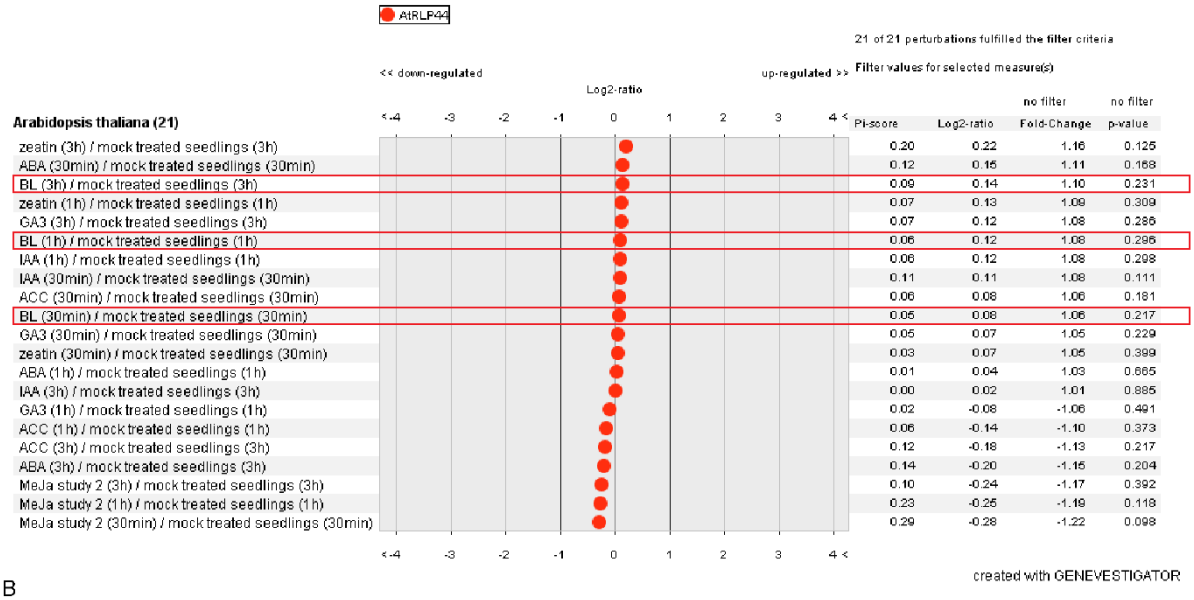

B

Dataset: 5 perturbations from data selection: DATA-AT_mRNASeq_ARABI_GL-4

Showing 1 measure(s) of 1 gene(s) on selection: AT-0

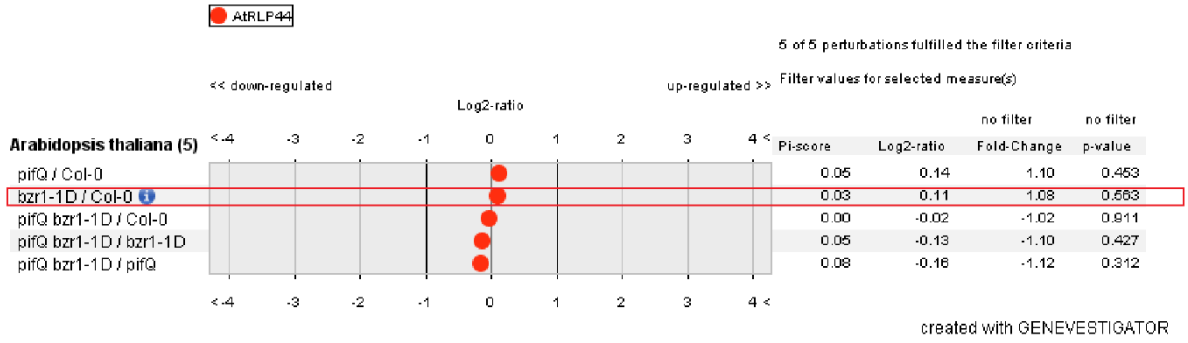

C

Dataset: 18 perturbations from data selection: DATA-AT_AFFY_ATH1-0

Showing 1 measure(s) of 1 gene(s) on selection: AT-0

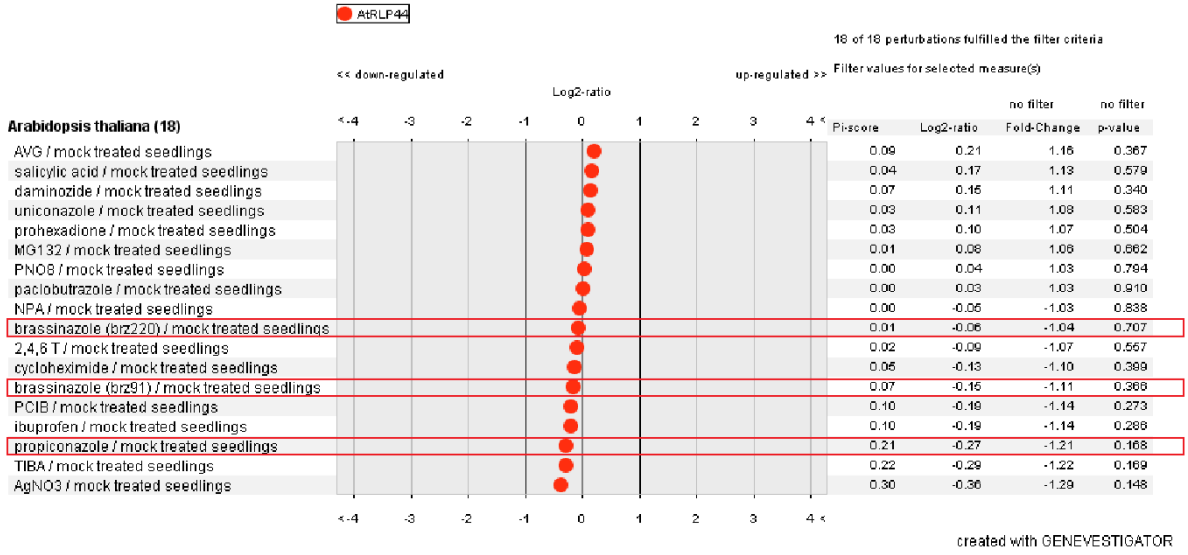

Fig. S9. Publicly available transcriptome datasets (10) suggest limited response of *RLP44* expression to various treatments. BR signalling-related conditions are highlighted.

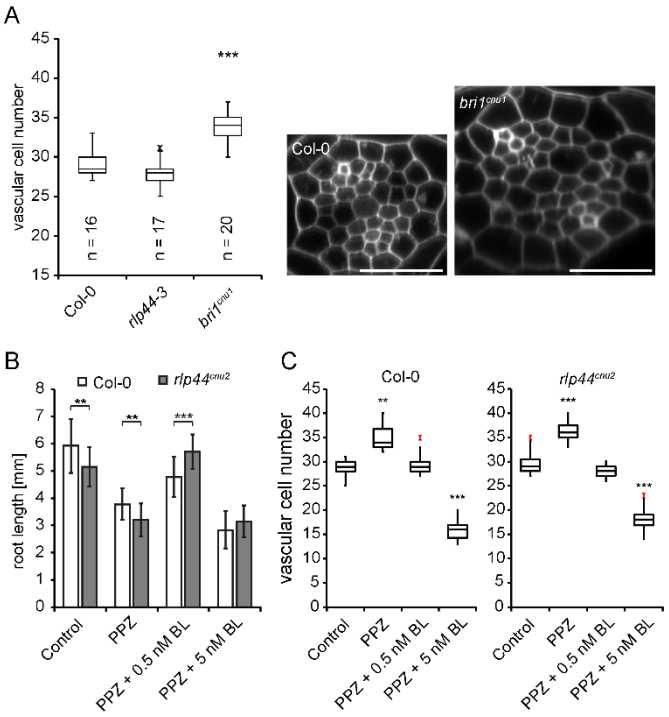

Fig. S10. RLP44 and BRI1 determine vascular cell fate independent of BR signalling-mediated control of cell proliferation. (A) Box-plot quantification of vascular cell number. Asterisks indicate statistically significant difference from Col-0 after pairwise t-test with ***p < 0.001. Optical cross sections of caclofluor white-stained roots were taken in the differentiation zone prior to maturation of the casparian strip. (B) Response of root length to depletion and exogenous addition of brassinosteroids in Col-0 and *rlp44*^{cnu2}. Bars denote mean root length ± SD, n = 14-26. Asterisks denote statistically significant differences after one-way ANOVA and Tukey's post hoc test between Col-0 and *rlp44*^{cnu2} with **p < 0.01 and *** p<0.001. (C) Response of vascular cell number to depletion (PPZ) and exogenous addition of BL in Col-0 and *rlp44*^{cnu2}. Asterisks indicate statistically significant differences from control conditions as determined by two-tailed t test with **p < 0.01 and *** p<0.001. Box plots in (A) and (C) indicate interquartile range (box), median (bar) and minimum/maximum (whiskers).

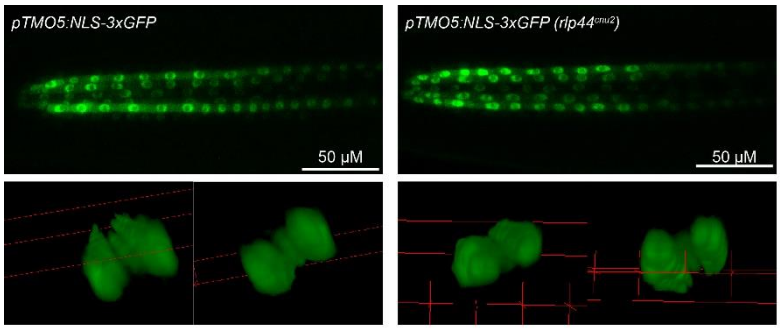

Fig. S11. The expression domain of the xylem precursor marker *pTMO5:NLS-3xGFP* (14) is not altered in *rlp44*^{cnu2} root apical meristems. Upper panels depict median section through root tips showing TMO5-positive cells in the xylem axis. Lower panels depict 3D projections of confocal stacks to visualize absence of TMO5-positive cells outside of the xylem axis.

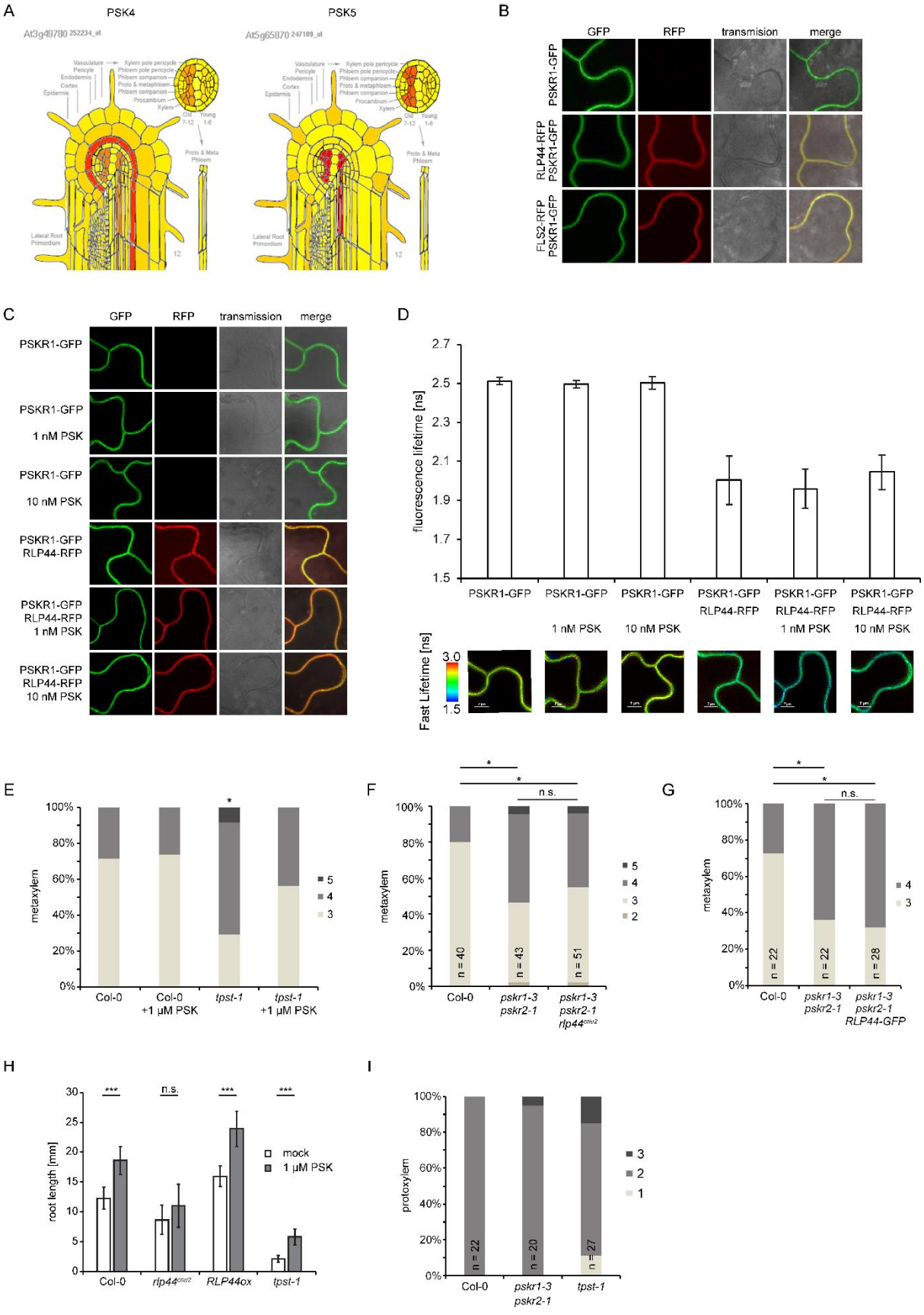

Fig. S12. RLP44 physically and genetically interacts with PSKR1. (A) *PSK* genes are co-expressed with *RLP44* in procambial cells. Tissue-specific expression pattern of *PSK4* and *PSK5* in the root. Data from (15) were analyzed using the eFP browser

(http://bar.utoronto.ca/efp/cgibin/efpWeb.cgi) (16). (B) Representative images of FRET-FLIM experiment analysed in Fig. 3B. (C, D) Interaction of RLP44 and PSKR1 is not modified by exogenous application of PSK. Representative confocal images of *Nicotiana benthamiana* epidermal leaf cells transiently expressing the indicated fusion proteins in the presence or absence of PSK (C) and FRET-FLIM analysis of the RLP44-PSKR1 interaction in the presence or absence of PSK (D) are shown. Bars denote the average of 14 measurements, each ± SD. Micrographs below bars depict fluorescence lifetime heat maps of representative plasma membrane areas used for the FLIM measurements. PSK in the indicated concentrations was applied to the leaf by vacuum infiltration 2 days after *Agrobacterium* transformation. FRET-FLIM measurements were started 15 min after infiltration. Mock treatment was carried out in the identical way but without PSK. (E) Exogenous application of PSK does not alter WT metaxylem cell number, but partially rescues the biosynthetic mutant *tpst-1*. (F) The xylem phenotype in the *pskr1-3 pskr2-1 rlp44*^{cnu2} triple mutant is not enhanced compared to *the pskr1-3 pskr2-1* double mutant. (G) Overexpression of *RLP44* (*p35S:RLP44-GFP*) cannot rescue the *pskr1-3 pskr2-1* mutant. (H) The *rlp44*^{cnu2} mutant is quantitatively challenged in the root growth response to PSK. The growth phenotype of *tpst-1* is only partially rescued by the treatment, in agreement with published data (17), as full recovery requires co-treatment with the sulfated peptide ROOT GROWTH FACTOR1. (I) PSK-related mutants do not show pronounced reduction in protoxylem cell numbers. Bars in (E—G, and I) denote frequency of roots with the indicated number of xylem cells. Asterisk indicates statistically significant difference based on Dunn's post-hoc test with Benjamini-Hochberg correction after Kruskal-Wallis modified U-test (*$p < 0.05$). n.s. = not significant.

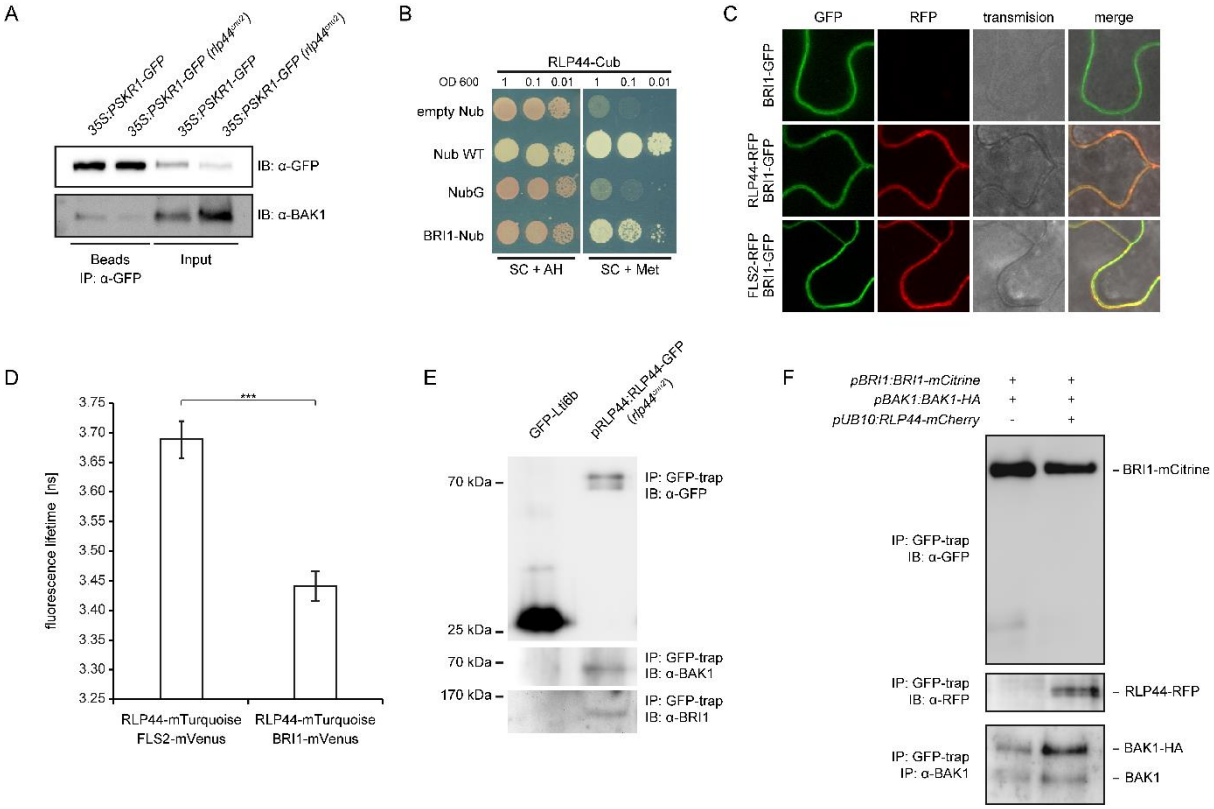

Fig. S13. BRI1 directly interacts with RLP44. (A) Mating-based split-Ubiquitin analysis in yeast reveals direct interaction of RLP44 and BRI1. After mating, presence of RLP44-Cub and BRI1-Nub enables yeast growth under selective conditions (SC + Met). Empty Nub vector and NubG are used as negative controls whereas interaction with WT Nub serves as a positive control. (B) FRET-FLIM analysis of RLP44-mTurquoise and BRI1-mVenus interaction. The related LRR-RLK FLS2 is used as a negative control. Bars indicate mean fluorescence lifetime ± SD (n = 11), asterisks indicate statistical significance according to two-tailed t test with ***p > 0.001. (C) RLP44 is present in BRI1 and BAK1 containing complexes under native expression levels. Immunoprecipitates of RLP44-GFP expressed under control of its own promoter in the *rlp44*^{cnu2} background were probed with antisera raised against BRI1 and BAK1 (6). (D) Presence of RLP44 enhances interaction between BRI1 and BAK1 in a line expressing BRI1-mCitrine and BAK1-HA from their native promoters in the *bri1-null* mutant background.

Table S1: Mutants and transgenic lines used in this study

Mutant/transgenic line	Reference	Acession
rlp44^{cnu2}	(1)	
rlp44-3	(1)	SAIL_596_E12
bri1^{cnu1}	(11)	
bri1-301	(18)	
bri1-5	(19)	
bri1-null	(20)	GK-134E10
bri1-1	(Clouse 1996; Friedrichsen et al., 2000)	
bri triple	(21)	*bri1-116*; SALK_005982 (*brl1*); SALK_006024 (*brl3*)
bin2-1	(18)	
cpd	(22)	
dwf4-102	(Nakamoto et al., 2006)	SALK_020761
pskr1-3 pskr2-1	(23)	
pskr1-3 psy1r1	(24)	
tpst-1	(17)	
pRLP44:RLP44-GFP	This study	
pRLP44:RLP44-GFP (*rlp44^{cnu2}*)	This study	
pRLP44:RLP44-GFP (*bri1-301*)	This study	
pRLP44:RLP44-GFP (*bri1-null*)	This study	
pRLP44:RLP44-GFP (*pskr1-3*)	This study	
35S:RLP44-GFP	(1)	
RLP44ox (35S:RLP44-RFP)	(1)	
35S:RLP44-GFP (bri1-null)	This study	
35S:PSKR1-GFP	(23)	
35S:PSKR1-GFP (rlp44^{cnu2})	This study	
pBRI1:BRI1-GFP (bri1-null)	This study	
pRLP44:GFP-GUS	This study	
pTMO5:NLS-3xGFP	(Schlereth et al. 2010)	
pTMO5:NLS-3xGFP (rlp44^{cnu2})	This study	
pBRI1:BRI1-mCitrine/pBAK1:BAK1:HA (bri1-null)	provided by M.Hothorn	GK-134E10
pBRI1:BRI1-mCitrine/pBAK1:BAK1:HA(pUBQ10:RLP44-mCherry (bri1-null)	This study	GK-134E10

Table S2: Oligonucleotides used in this study

Oligonucleotide	Sequence
BRI1_3'UTR_R	aaacgaaaacattacaaatcc
BRI1-GK_WT_F	AACTATGGCTGAATATGTTAG
GK-o8409	ATATTGACCATCATACTCATTGC
BRI1_ GK-134E10_R	TCGTTCCATTGAAGAGATTGG
RLP44prom_GW_L	GGGGACAAGTTTGTACAAAAAAGCAGGCTtttgcgatatttttggctgtc
RLP44prom_GW_R	GGGGACCACTTTGTACAAGAAAGCTGGGTttttaaattttagagaggtttc
FLS2_attB1_F	GGGGACAAGTTTGTACAAAAAAGCAGGCTATGAAGTTACTCTCAAAGAC
FLS2_attB4_R	GGGGACAACTTTGTATAGAAAAGTTGGGTGtAACTTCTCGATCCTCGTTACG
RLP44_attb2_R	GGGGACCACTTTGTACAAGAAAGCTGGGTtGTAATCAGGCATAGATTGAC
RLP44_attb3_F	GGGGACAACTTTGTATAATAAAGTTGATGACAAGGAGTCACCGGTTAC
BRI1_attB2_R	GGGACCACTTTGTACAAGAAAGCTGGGTtTAATTTTCCTTCAGGAACTTCTT
BRI1_attB3_F	GGGGACAACTTTGTATAATAAAGTTGATGAAGACTTTTTCAAGCTTCTT
BRI1_GGC_1F	AACAGGTCTCAGGCTCATGAAGACTTTTTCAAGCTTCT
BRI1_GGC_1R	AACAGGTCTCaATCACACGCGCCGGAGAGAAAGTCAG
BRI1_GGC_2F	aacaGGTCTCaTGATACACTCACTGGaCTCGATCTCTCTGGA
BRI1_GGC_2R	aacaGGTCTCaGAGtCCAGGATTGTTCAAGAA
BRI1_GGC_3F	aacaGGTCTCaACTCTGTGGTTATCCTCTT
BRI1_GGC_3R	aacaggTCTCaGGCCTCCTTCCATGAGATCT
BRI1_GGC_4F	aacaGGTCTCaGgCCAGCGTCCCTTGCTGGT
BRI1_GGC_4R	AACAGGTCTCACTGATAATTTTCCTTCAGGAACTTC
at5G46630_cod_F	TCGATTGCTTGGTTTGGAAGAT
at5G46630_cod_R	GCACTTAGCGTGGACTCTGTTTGC
RLP44_cod2_F	TCAGATTCCGCAGCAATTAG
RLP44_cod2_R	TCCTGCAACGGATAACCATA
SALK_008585_F	CTCGCTTTCTGGTATGACGAG
SALK_008585_R	TCCGAAACTATACACATCGCC
SALK_203857_F	TTCTTAGACTGTTTGGCTCGG
SALK_203857_R	GCGTTACAAACATGCAACAAG
LBb1.3	ATTTTGCCGATTTCGGAAC

Table S3. Overview of constructs generated with GreenGate cloning (Lampropoulos et al., 2013) and the primers used to generate modules, where appropriate.

pSW362	**pRLP44:RLP44-GFP**		
pSW299	RLP44 (at3g49750) promoter	AACAGGTCT**C**AACCTtttgcgatatttttggctgtc	AACAGGTCTCATGTTttttaaattttagagaggtttc
pGGB003	B-Dummy	Lampropoulos et al., 2013	
pSW334	RLP44 (at3g49750) CDS	AACAGGTCTCAGGCTCAATGACAAGGAGTCACCGGTTA	AACAGGTCTCACTGAGTAATCAGGCATAGATTGAC
pGGD001	GFP	Lampropoulos et al., 2013	
pGGE009	UBQ10 terminator	Lampropoulos et al., 2013	
pGGF001	pMAS::BastaR::tMAS	Lampropoulos et al., 2013	
pGGZ0001	destination vector	Lampropoulos et al., 2013	
pSW420	**pBRI1:BRI1-GFP**		
pSW379	BRI1(AT4G39400) promoter	AACAGGTCTCAACCTgatcttccttctttatttg	AACAGGTCTCATGTTttctcaagagtttgtgagag
pGGB003	B-Dummy	Lampropoulos et al., 2013	
pSW380	BRI1(AT4G39400) CDS	AACAGGTCTCAGGCTCATGAAGACTTTTTCAAGCTTC	AACAGGTCTCACTGATAATTTTCCTTCAGGAACTTC
pGGD001	GFP	Lampropoulos et al., 2013	
pGGE009	UBQ10 terminator	Lampropoulos et al., 2013	
pGGF001	pMAS::BastaR::tMAS	Lampropoulos et al., 2013	
pGGZ001	destination vector	Lampropoulos et al., 2013	
pSW375	**pUBQ10:RLP44-mCherry**		
pGGA006	UBQ10 (At4g05320)		
pGGB003	B-Dummy	Lampropoulos et al., 2013	
pSW334	RLP44 (at3g49750) CDS	AACAGGTCTCAGGCTCAATGACAAGGAGTCACCGGTTA	AACAGGTCTCACTGAGTAATCAGGCATAGATTGAC
pGGD003	Linker mCherry	Lampropoulos et al., 2013	
pGGE009	UBQ10 terminator	Lampropoulos et al., 2013	
pGGF005	pUBQ10::HygR::tOCS	Lampropoulos et al., 2013	
pGGZ001	destination vector	Lampropoulos et al., 2013	

A.2 Manipulation of signalling during pathogen infection and signalling integration for the transition to flowering

A.2.1 The dual role of ABCG36 for auxin and immune responses

Regulation of ABCG36/PEN3/PDR8 during *Fusarium oxysporum* infection involves the LRR receptor-like kinase, ALK1

In preparation

This article describes the role of the ATP BINDING CASETTE (ABC) transporter type G 36 (ABCG36), which is regulated by the AUXIN-INDUCED LRR KINASE (ALK1). ABCG36 specifically transports indol-3-butyric acid (IBA), an auxin variant or precurser that promotes lateral root formation. Both the ascomycete *Fusarium oxysporum* and treatment with IBA specifically alters the expression and polarity of ABCG36 in the *Arabidopsis* root. Also, both treatments affect the phospho-state of serine residue number 825 of ALK1. This manipulation of the plant transporter could facilitate the colonization by the pathogen.

Title page

Regulation of ABCG36/PEN3/PDR8 during *Fusarium oxysporum* infection involves the LRR receptor-like kinase, ALK1

Bibek Aryal[1], John Huynh[1], Zehan Hu[1], Jerôme Schneuwly[1], Martin Di Donato[1], Yoichiro Fukao[2,4], Silke Lehmann[1,5], Santiago Alejandro[7], Jutta Ludwig-Müller[3], Nina Glöckner[6], Michael Hothorn[7], Jörn Dengjel[1], Klaus Harter[6], Enrico Martinoia[8], Jean-Pierre Métraux[1] and Markus Geisler[1,9]

[1] University of Fribourg, Department of Biology, Fribourg, Switzerland
[2] Plant Global Education Project, Graduate School of Biological Sciences, Nara Institute of Science and Technology, Ikoma, Nara 630-0192, Japan
[3] Institut für Botanik, Technische Universität Dresden, Zellescher Weg 20b, 01062 Dresden, Germany
[4] present address: Department of Bioinfomatics, Ritsumeikan University, Shiga, Japan.
[5] present address: School of Life Sciences, University of Warwick, Gibbet Hill, CV4 7AL, Coventry, England
[6] Zentrum für Molekularbiologie der Pflanzen, Pflanzenphysiologie, Universität Tübingen, Auf der Morgenstelle 32, 72076 Tübingen, Germany
[7] Structural Plant Biology Laboratory, Department of Botany and Plant Biology Sciences III, University of Geneva, 30 Quai E. Ansermet, 1211 Geneva, Switzerland
[8] Institute for Plant and Microbial Biology, Zollikerstrasse 107, 8008 Zurich, Switzerland
[9] to whom correspondence should be addressed: markus.geisler@unifr.ch

Abstract
The PDR-type ABCG transporter, ABCG36/PDR8/PEN3, is thought to be implicated in the export of a few structurally unrelated substrates, including the auxin precursor, indole-3-acetic acid (IBA), although clear-cut transport proof is lacking. An outward facing, lateral root location for ABCG36 fuelled speculations that it might secrete IBA into the rizhosphere critical for plant-microbe interaction.
Here we provide strong evidence that ABCG36 catalyses the export of IBA - but not of IAA - over the plasma membrane. ABCG36 functions redundantly with closely related isoform ABCG37 in a negative control of acropetal IBA transport in roots, which might be dampened by concerted, lateral IBA export. Interestingly, ABCG36 expression and polarity is specifically distorted upon *F. oxysporum* root infection, which can be phenocopied by IBA treatments. In order to identify a controlling element for this event, we identified the leucin-rich repeat receptor-like kinase, Auxin-induced LRR Kinase 1 (ALK1), as a functional ABCG36 interactor. Co-expression in tobacco and analyses of the *alk1* mutant revealed a functional impact of ALK1 on ABCG36 transport activity. Phosphorylation of S825 activates ABCG36 transport activity, which is dependent on ALK1 and reduced by IBA treatment and *F. oxysporum* infection. A common function of ABCG36 and ALK1 in the same defense pathway is supported by enhanced susceptibility found for both *ABCG36* and *ALK1* mutant alleles.
Our findings identify a novel mode of ABC transporter regulation by a LRR receptor-like kinase and contribute to our understanding of this module during auxin-controlled plant-pathogen interaction.

Introduction

Pleiotropic drug resistance (PDR) ABC transporters belong to the ABCG family of ATP-Binding Cassette (ABC) transporters and are limited to plants and fungi (Kang et al. 2010; Kretzschmar et al. 2012; Strader and Bartel 2009). Plant PDRs have been assigned to several biotic and abiotic stress responses: for example, tobacco PDR1 was identified as exporter of the antifungal terpenoid, sclareol (Jasinski et al. 2001), while PDR5 is induced by the defense hormone, jasmonic acid, and wounding and plays a role in herbicide resistance (Bienert et al. 2012). The PDR, Leaf Rust Resistance34, confers durable, race-specific resistance to multiple fungal pathogens in wheat (Krattinger et al. 2009), while Petunia PDR1 was shown to export the hormone, strigolactone, in the context of arbuscular mycorrhizal establishment (Kretzschmar et al. 2012).
Mutant alleles of *ABCG36/PDR8/PEN3* (hereafter referred to as ABCG36) were shown to display altered responses to diverse pathogens (Kobae et al. 2006; Stein et al. 2006), decreased extracellular accumulation of flg22-induced callose (Clay et al. 2009) and hyper-accumulation of flg22- or pathogen-elicited indole glucosinolate derrivates of the PEN2 pathway (Bednarek et al. 2009; Clay et al. 2009). On the other hand, *abcg36* was also found to own an increased sensitivity to heavy metals (Kim et al. 2007). Moreover, *abcg36* alleles hyper-accumulate IBA and are hypersensitive to IBA (Lu et al. 2015; Strader and Bartel 2009), which was initially explained by overlapping functions of exported phytochemicals in plant development and plant defense (Bednarek et al. 2009).
Finally, the close ABCG36 homolog, ABCG37/PDR9/PIS1, was shown to confer resistance to auxinic herbicides (Ito and Gray 2006) and to transport auxinic compounds, including IBA 2.4-D but not IAA (Ruzicka et al. 2010). On the other hand, members of the PIN and ABCB families of IAA transporters do not transport IBA (Ruzicka et al. 2010), which indicates an independent evolution of auxin substrate specificities on distinct transporter classes.

A striking feature of ABCG36 is its focal accumulation at the site of leaf pathogen entry, where it is thought to export defence compounds over the plasma membrane (Stein et al. 2006; Xin et al. 2013). In the root, ABCG36 is predominantly laterally localized at outermost root plasma membrane domains (Langowski et al. 2010; Ruzicka et al. 2010). Lateral trafficking is not well-understood, however, recent work has established that ABCG36 trafficking does not require known components of the apical-basal targeting machinery (Langowski et al. 2010; Underwood and Somerville 2013; Xin et al. 2013) but is dependent on ACTIN7 that fulfils a generic role in auxin transporter secretion (Mao et al. 2016; Zhu et al. 2016)
On these lateral domains that were defined as the root-soil interface (Langowski et al. 2010; Ruzicka et al. 2010), ABCG36 was shown to widely co-localize with ABCG37 and was thus suggested to act redundantly in mediating root auxin homeostasis (Ruzicka et al. 2010). Both *ABCG36* and *ABCG37* were thus identified in chemical genetic screens for hypersensitivity toward auxinic compounds and auxin transport inhibitors, such as IBA and NPA, respectively. However, it is currently unclear if IBA, widely used by gardeners for lateral root induction, is an active auxin itself or acts as an auxin precursor that is

transformed into IAA by peroxisomal β-oxidation (Ludwig-Muller 2007; Strader and Bartel 2011).

Remarkably, pathogens have developed strategies to manipulate plant auxin signaling and transport in order to induce root architecture changes (such as increasing the root surface), which is beneficial to root colonization. The best known example is the production of auxin (and cytokinin) essential for *A. tumefaciens* virulence (Spaepen and Vanderleyden 2011). Other examples are truffles that influence root morphogenesis by auxin (Splivallo et al. 2009). Moreover, IAA produced by plant growth promoting rhizobia has been shown to alter the auxin homeostasis inside the plants by interfering with plant long-range auxin transport (van Noorden et al. 2006). A second potentially related strategy seems to lie in the interference with plant hormone transporters (Grunewald et al. 2009). Arabidopsis plants expressing the RXLR effector, PSE1, from the oomycete *P. parasitica* show increased susceptibility but also auxin related phenotypes most likely caused by altered expression of PIN4 and PIN7 (Evangelisti et al. 2013). Some microorganisms (including plant symbionts) produce themselves IBA, which has led to the concept that ABCG36/ABCG37-dependent transport of IBA mediates interactions between the root and the soil microflora (Ruzicka et al. 2010).

These data indicate that root microbes are able to manipulate auxin gradients by interfering with auxin transporters. However, a mechanistic investigation of transporter targets and involved regulatory components in the root has not yet been provided. Here we show that ABCG36 expression and polarity is specifically distorted upon *F. oxysporum* root infection, which can be phenocopied by IBA treatments. Moreover, we identify the leucin-rich repeat (LRR) receptor-like kinase, Auxin-induced LRR Kinase 1 (ALK1), as a regulator of ABCG36 transport activity. Phosphorylation of relevant, ALK1-specific phosphor-sites is likewise reduced by *F. oxysporum* and IBA treatments suggesting that underlying mechanisms are interconnected.

Results

ABCG36 is involved in some but not all auxin-controlled developmental programs that are partially shared with ABCG37

Originally, the *ABCG36* allele, *pdr8-115/abcg36-6*, was isolated in a mutant screen for mutants that were able to restore IBA but not IAA responsiveness to auxin signaling mutants (Strader and Bartel 2009). In the following, individual mutant alleles of *ABCG36* have been tested for their sensitivity toward IBA using root growth as read-out. Using different technical setups this assay revealed mixed reports: while *abcg36-1*, *abcg36-2*, *abcg36-3*, *abcg36-4* and *abcg36-6* were found hypersensitive (Lu et al. 2015; Ruzicka et al. 2010; Strader and Bartel 2011), the mutant allele, *abcg36-5*, was not (Lu et al. 2015). Moreover, for the *abcg37-2/pdr9-2* allele, normal and hypersensitivity toward IBA, as well as a redundant function with ABCG36 were reported (Ruzicka et al. 2010).

Therefore, we reanalyzed a well-established set of *ABCG36* and *ABCG37* single and double mutant lines for their ability to elongate their roots after transfer on IBA plates as described in Ito and Gray (2006). Results indicated that *abcg36-4/pen3-4* was hypersensitive in comparison with WT as shown before (Lu et al. 2015; Strader and Bartel 2009), while *abcg37-2/pdr9-2* was not, with the exception for low IBA concentrations (Fig. 1A). The latter is in agreement with a former report (Ito and Gray 2006) that likewise employed also a transfer of seedlings onto IBA medium, while apparently growth on IBA produces different results (Ruzicka et al. 2010). This is apparently also true for the reported functional redundancy between ABCG36 and ABCG37 (Ruzicka et al. 2010) that was not found using the same double mutant lines.

As a second developmental parameter, we measured the lateral root (LR) number of the same set of lines used above after transfer on IBA, found previously to result in increased LR production for *abcg36-2* (Strader and Bartel 2009). As expected, low concentrations of IBA increased LR numbers but *abcg36* and *abcg37* alleles were hyper-responsive toward IBA, while no significant difference was found on solvent control (Fig. 1B). Interestingly, in contrast to primary root development, LR development revealed a high degree of functional redundancy between ABCG36 and ABCG37 found already at 1 µM IBA.

As a third parameter of auxin controlled development, we measured root gravitropism for the same mutant set, which to our knowledge has not been analyzed in this respect. Interestingly, all loss-of-function alleles revealed WT-like root bending (Suppl. Fig. 1). Also all mutant lines showed similar sensitivities toward the non-competitive auxin transport inhibitor, N-1-naphylphtalamic acid (NPA) that efficiently blocks IAA-controlled root gravitropism (Bailly et al. 2008). As a positive control, we included the *abcg37-1/pdr9-1* allele, which was characterized as an *ABCG37* gain-of-function mutant (Ito and Gray 2006), providing NPA resistance by NPA export (Ito and Gray 2006; Ruzicka et al. 2010). In agreement, root bending of the *abcg37-1/pdr9-1* allele was significantly less affected by NPA.

In summary, these data support an individual involvement of ABCG36 in some auxin-controlled developmental programs that are partially shared with ABCG37, as illustrated by LR production. However, root gravitropism data suggest that ABCG36 (and ABCG37) is not involved in all auxin-controlled cell elongation processes. The finding that *abcg* mutant roots bend like Wt might indicate that both transporters are not sensitive to NPA.

ABCG36 and ABCG37 have an impact on auxin signaling and accumulation

Results from above indicate that IBA interferes via ABCG36 (and ABCG37) with root developmental programs that are thought to be controlled by the native auxin, IAA. This supports a scenario in that IBA would not act independently but as a precursor for IAA (Ludwig-Muller 2007; Woodward and Bartel 2005). In agreement, recently hyper-sensitivity of *abcg37/pis1* to IBA had been correlated with increased induction of the auxin-responsive element, DR5:GFP known to be not activated by IBA itself (Ruzicka et al. 2010).

Like shown for *abcg37/pis1* based on quantification of DR5:GFP expression, auxin signaling was not different in *abcg36* and *abcg36 abcg37* compared to wild-type on control media (Fig. 2A-B). However, like for *abcg37* application of IBA led to significantly higher reporter activation in *abcg36* compared to the wild-type. Interestingly, this effect was reverted in the *abcb36 abcg37* double mutant (Fig. 2A-B) arguing for compensating roles of both transporters in the columella.

In order to provide more direct evidence for an involvement of ABCG36 (and ABCG37) in IBA/IAA homeostasis and to dissect IBA and IAA - but also ABCG36,37 - functionalities, we analyzed free IBA and IAA levels from entire roots and shoots of Arabidopsis seedlings by GC-MS. Both roots and shoots of *abcb36* and *abcg37* single and double mutants contained significantly less IBA than the wild-type most likely caused by defect IBA distribution (Fig. 2C). Interestingly, IAA levels in *abcb36* and *abcb36 abcg37* roots, but not in those of *abcg37*, were also reduced. It is important to note that indirect and direct IAA quantifications obtained by the DR5:GFP reporter (no difference under control conditions) and GC-MS (reduced IAA), respectively, are not essentially in conflict because the DR5:GFP is a maximum reporter of the columella, which does not reflect IAA levels in the mature root. However, these data support on one hand that ABCG36 has an impact on both IBA and IAA levels (the latter verifying DR5:GFP data) but on the other that ABCG36 has a dominant role in root IAA homeostasis. The opposite is found for the shoot where ABCG36 and ABCG37 seem to function redundantly in IAA homeostasis.

In summary, this data set uncovers that ABCG36 and ABCG37 have an impact on root and shoot IAA and IBA homeostasis but that their individual impact is tissue-specific.

ABCG36 functions as an exporter of IBA and is involved in its polar distribution

Recently, by means of heterologous expression in yeast and HeLa cells and polar Arabidopsis root transport measurements, ABCG37 was unambiguously shown to function as transporter of IBA, 2.4-D and NPA but not IAA (Ito and Gray 2006; Ruzicka et al. 2010). For *abcg36* alleles, increased accumulation and reduced efflux from entire root tips were measured but no direct transport data, especially in the absence of plant-specific factors have been provided.

In order to demonstrate such a transport activity that is supported by functional redundancy with ABCG37 (Figs. 1-2), we functionally expressed ABCG36 in the heterologous hosts, baker's yeast and tobacco. ABCG36 (and ABCG37) expressing yeast revealed significantly reduced IBA and 2.4-D retention, assayed in parallel by double isotope labeling (Fig. 3A). Reduced retention argues together with a predominant PM localization of ABCG36 (not shown) for an export activity. Recently using an identical

approach ABCG37 was shown to function as ER importer in yeast (Ruzicka et al. 2010); discrepancies between these localizations for ABCG37 are currently not known. However, *N. benthamiana* transfection resulted in expression of ABCG36 on the PM (Fig. 5B-C), which greatly enhanced IBA and 2.4-D export from prepared protoplasts, although differences to vector control were only significant for 2.4-D (Fig. 3B).
Also stable Arabidopsis lines over-expressing ABCG36 (Kim et al. 2007) and ABCG37-GFP (Ruzicka et al. 2010) exported significantly more IBA and 2.4-D (Fig. 3C) but not IAA (Suppl. Fig. 2), indicating that both transporters own overlapping substrate specificities. In agreement, T-DNA insertion, null alleles of ABCG36, *abcg36-3*, *abcg36-4*, *abcg36-7*, previously shown to express no functional ABCG36 protein (Lu et al. 2015), reveal significantly reduced IBA and 2.4-D export (Fig. 3D).
Previous work has established that in roots, both IBA and IAA move in two distinct polarities with similar transport rates (Rashotte et al. 2003). Quantification of directional IBA distributions revealed that acropetal (root-ward) transport is significantly enhanced in *abcg36, abcg37* and *abcg36 abcg37* mutant roots, although significantly differences were only found with the double mutant (Fig. 3E). This effect is specific as it was not found with IAA assayed in parallel. Basipetal (shoot-ward) transport rates were likewise significantly enhanced in *abcg36* and *abcbg36 abcbg37* but not in *abcg37* roots, indicating a selective contribution of ABCG37 in these streams. No significant difference for basipetal transport in *abcg37* roots is in conflict with a recent report revealing reduced IBA transport using columella-applied radiotracers (Ruzicka et al. 2010). In this context it is important mentioning that basipetal IAA transport profiles resemble remarkably those of IBA, although both ABCG transporters were shown to not transport IAA (Suppl. Fig. 2). Therefore, we believe that differences in basipetal IAA transport for *abcg36* might be caused by IBA to IAA conversion during the elevated time-frame that is technically necessary for measuring this directionality. IBA to IAA conversion in Arabidopsis roots has been shown to be effective even 2h after application (Ruzicka et al. 2010).
Enhanced transport rates for transporter loss-of-function mutations are counter-intuitive at first place. A possible explanation is that in light of the strict lateral, outward-facing distribution for ABCG36 (Fig. 4, Suppl. Fig. 4, (Strader and Bartel 2009)) and ABCG37 (Ruzicka et al. 2010), both transporters function in excluding IBA from the apical-basal transport stream; loss-of-function would thus result in enhanced polar IBA transport (see Suppl. Fig. 7). Altogether, this dataset clearly demonstrates that ABCG36 acts like ABCG37 as an IBA exporter and is involved in the regulation of its polar distribution by the not yet identified apical-basal transport machinery.

IBA treatment and *Fusarium oxysporum* root infection alter ABCG36 expression and polarity

Numerous ABC transporters, including plant hormone transporters (Kretzschmar et al. 2011), have been shown to be up-regulated by their own substrates. IBA treatments drastically up-regulated ABCG36 expression in the root (Fig. 4A, C). Remarkably, IBA treatments led also to ABCG36 expression in non-epidermal cell files, like the cortex and the stele. Moreover, in all cells ABCG36 loses its lateral polarity and owns widely a non-polar PM distribution. Like for polar IBA distribution by ABCG36, this effect was specific to IBA because IAA had no effect.

ABCG36/PEN3 was shown to accumulate at the site of leaf pathogen entry (Stein et al. 2006; Xin et al. 2013) but the effect of pathogen infection on root location has not been tested yet. In order to do so, we employed a hydroponic-based *Fusarium oxysporum* system, a well-characterized root-penetrating pathogen previously shown to interfere with Arabidopsis auxin signalling and transport in a tissue-specific manner (Kidd et al. 2011). Moreover, it was recently shown that genetic or pharmacolocaigal alteration of polar auxin transport increased resistance to *F. oxysporum* (Kidd et al. 2011). In analogy to IBA treatments, *F. oxysporum* infection likewise but even stronger altered ABCG36 abundance and polarity (Fig. 4B-C). A similar effect was also found for ABCG37 even when expressed constitutively (Suppl. Fig. 3A) but not for H^+-ATPase isoform, AHA2, or auxin exporter, ABCB1 (Fig. 4B-C). A quantification of ABCG36-GFP signals revealed a ca. 3-4 and 10-fold up-regulation in the epidermis and stele by *F. oxysporum*, respectively (Suppl. Fig. 3C). Up-regulation by *F. oxysporum* infection is independent of transcription as revealed by real-time PCR analyses of *ABCG36,37* transcripts (Suppl. Fig. 3D): while typical wounding markers, like transcription factors MYB51 and WRKY11, were up-regulated this was not the case for *ABCG36,37* transcripts or *AHA2* or *NIP5;1*, employed as negative control. The fact that both ABCG36 and ABCG37 both are up-regulated by *F. oxysporum* infection independent of their individual promoters further supported the concept that *F. oxysporum* infection interferes with ABCG36 on the post-transcriptional level.

ABCG36 co-localizes and interacts with the LRR receptor-like kinase, ALK1, *in planta.*

Equally altered expression on the post-transcriptional level caused by IBA treatment or *F. oxysporum* infection suggested the existence of an - potentially even common - controlling module. In order to identify such regulatory components, we employed a co-immunoprecipitation approach followed by tandem mass spectrometry (MS-MS) analyses similar to Henrichs et al. (2012) and Zhu et al. (2016) but using whole ABCG36-GFP (PEN3:PEN3-GFP) seedlings as starting material. Three independent co-immunoprecipitation/MS-MS analyses identified a short list of 9 common, putative ABCG36 interacting proteins (Suppl. Table 2). This contained a high degree of proteins previously shown to directly or indirectly have an impact on ABCG36 function, such as ACTIN7 (Mao et al. 2016) or ABCG37 (Strader and Bartel 2009). Further, it showed a remarkable enrichment in kinases of different subfamilies, including LysM receptor kinase, Chitin elicitor receptor kinase 1 (CERK1) and Proline extensin-like receptor kinase 1 (PERK1) shown function as chitin receptor (Miya et al. 2007) and to be rapidly induced by wounding (Silva and Goring 2002). This made them primary candidates for such a proposed regulatory impact on ABCG36 because based on several phosphor-proteomic approaches, ABCG36 was shown to be phosphorylated by a range of biotic and abiotic stimuli (Benschop et al. 2007; Chen et al. 2010; Niittyla et al. 2007; Nuhse et al. 2007; Nuhse et al. 2004).

However, we selected the leucine-rich repeat receptor-like kinase (LRR-RLK), At3g02880, for further analyses based on the following: At3g02880 was previously pulled-down as an ABCG36/PEN3 interacting protein (Campe et al. 2016), was predicted to reside on the PM and auto-phosphorylation was found to be stimulated by auxin (Chen et al. 2010). Therefore, it will be referred to in the following as Auxin-stimulated LRR Kinase 1, ALK1.

In order to sustain a functional interaction on the PM, we co-transfected ABCG36-GFP (PEN3:PEN3-GFP) and ALK1-mCherry (35S:ALK1-mCherry) in leaves of *N. benthamiana.* Confocal imaging revealed that ABCG36-GFP and ALK1-mCherry co-localize on the PM of tobacco pavement cells (Fig. 5A, C). Interestingly, enhanced ABCG36-GFP and ALK1-mCherry signals and co-localization was found in the necks of these pavement cells (Fig. 5B). Co-immunoprecipitation analyses using microsomes prepared from co-transfected *N. benthamiana* leaves allowed to detect ALK1-mCherry in the elution fraction using ABCG36-GFP but not free GFP as a bait (Suppl. Fig. 4D).

ABCG36-GFP and ALK1-mCherry widely co-localize in the columella and epidermis of Arabidopsis roots as was found by crossing of stable Arabidopsis PEN3:PEN3-GFP and 35S:ALK1-mCherry lines (Fig. 5A). A subcellular co-residence on PMs of these tissues was hardened by separation of total microsomes prepared from PEN3:PEN3-GFP/35S:ALK1-mCherry seedlings by linear sucrose gradient fractionation. ABCG36-GFP-positive bands perfectly co-sediment in these gradients with PM marker PIP1 (Suppl. Fig. 4B; REF).

FRET-FLIM analysis of ABCG36-GFP (PEN3:PEN3-GFP)-ALK1-mCherry (35S:ALK1-mCherry) interaction in *N. benthamiana* pavement cells after *A. tumefaciens*-mediated co-transfection resulted in reduced fluorescence lifetime for the ABCG36-GFP/ALK1-mCherry pair compared to the donor (ABCG36-GFP) alone. This is an indicative for a very close proximity of both partners (< 10 nm) that is interpreted as a physical interaction.

Taken together, co-localization and FRET-FLIM analyses in tobacco and Arabidopsis, respectively, strongly support a physical interaction between ABCG36 and ALK1 on the PM.

IBA transport by ABCG36 is controlled by the LRR receptor-like kinase, ALK1

Physical interaction on one hand (Fig. 5), as well as phosphor-proteomics-based indication for ABCG36 phosphorylation, a well-known mode of ABC transporter regulation REF prompted us to investigate the impact of ALK1 on ABCG36 transport activity. Co-expression of ALK1 and ABCG36 in yeast significantly enhanced IBA (and 2.4-D) retention arguing for reduced export by ABCG36 (Fig. 6A). Unfortunately, a similar - in the case of 2.4-D significant - inhibitory effect was also found for expression of ALK1 in the absence of ABCB36 shedding doubt on the specificity of the regulatory impact of ALK1. A plausible explanation is that ALK1 interferes with background auxin export activity most-likely provided by yeast endogenous, PM-based PDR-type ABC transporters, such as PDR5, Ste6 and Yor1 (Balzi and Goffeau 1995). In order to avoid background issues caused by high PDR presence, we quantified ABCG36-mediated auxin efflux upon ALK1 co-expression in the tobacco system, where ALK1 expression alone had no effect on IBA and 2.4-D export (Fig. 6B). Here, ALK1 co-expression strikingly reduced ABCG36-catalyzed auxin export and this inhibitory impact was dependent on ALK1 kinase activity: a putative kinase-dead mutant version ($ALK1^{D488N}$) or a truncated version of ALK1 ($ALK1^{trunc}$) lacking the entire kinase domain (cut-off after aa 286) were unable to inhibit ABCG36 (Fig. 6B). Importantly, co-expression with ALK1 (or the unspecific control, AHA2) in this tobacco system did not alter significantly expression or location of ABCG36 (Fig. 5C).

These heterologously generated data were substantiated *in planta*, where a negative regulatory impact of ALK1 was expected to result in enhanced auxin efflux for the *alk1*

mutant. In agreement, the Arabidopsis *alk1-2* mutant allele exported significantly more IBA but not IAA than the wild-type (Fig. 6C), indicating that the inhibitory effect of ALK1 on ABCG36 transport activity is substrate-specific. In analogy to tobacco co-expression, loss-of-ALK1 function did not significantly change ABCG36 expression (Suppl. Fig. 4A-C) as could be revealed by crosses between *ABCBG36-GFP/PEN3:PEN3-GFP* and *alk1-2* lines. Interestingly, the *alk1-2* mutant showed also an inverse behavior to *abcg36 abcg37* mutant roots in acropetal IBA transport (Fig. 3E). In line with an inhibitory action for ALK1 and a lateral, epidermal removal of IBA by ABCG36/37, absence of ALK1 would lead to enhanced export of IBA out of the root, which would dampen polar IBA streams. Also this regulatory effect was not found for IAA and in basipetal IBA transport arguing for a specific involvement of ALK1 in regulation of acropetal IBA streams.

Remarkably, *alk1-2* was also lacking the hyper-sensitivity of the *abcg36* mutant upon IBA treatments visualized using the DR5:GFP responsive element (Fig. 2A-B). This might be in analogy to above explained again by ABCG36-mediated reduced acropetal IBA streams (Fig. 3E) reducing columella IBA levels for IAA conversion, and thus leading to reduced DR5:GFP expression.

In order to further underline the specificity of ALK1 action on ABCG36, we tested the lysin motif (LysM) receptor kinase, CERK1, that was shown also to co-purify with ABCG36-GFP (Suppl. Table 2) and to function as part of the cell surface chitin receptor transmitting immune signals to an MAPK cascade (Miya et al. 2007; Yamada et al. 2016). CERK1 co-expression in yeast had no effect on ABCG36 IBA and 2.4-D transport activity (Suppl. Fig. 5A). We included in these analyses also the FKBP42, TWISTED DWARF1 (TWD1) for the two ratios: 1. TWD1 was shown to perfectly co-localize on lateral outward-facing PM domains with ABCG36 (Wang et al. 2013), and 2. *TWD1* (At3g21640) was found to lie directly up-stream of *CERK1* (At3g21630) on chromosome 3 (Suppl. Fig. 5B). However, neither TWD1 alone or in combination with CERK1 had a significant effect on ABCG36 transport activity (Suppl. Fig. 5A). An indirect involvement of CERK1 is also unlikely because the *cerk1-2* mutant allele revealed wild-type IBA responsiveness (Fig. 2A-B) and wild-type IBA levels in the root (Fig. 2C).

In summary, this subset of data indicates that ALK1 negatively regulates ABCG36-mediated IBA transport in an action that requires its kinase activity. While this obviously enhances efflux from isolated, non-polar *alk1* cells (Fig. 6C), the opposite is found for acropetal IBA transport in the tissue context, where ABCG36 has apparently a role in dampening polar IBA streams (see Suppl. Fig. 7).

Phosphorylation of S825 is responsible for ALK1-mediated activation of ABCG36 transport activity

In order to identify ALK1-specific phosphorylation sites on ABCG36 that are both of relevance for transport regulation we employed quantitative phosphor-proteomics. In order to determine the number of ALK1-specific sites, we co-transfected ABCG36 in *N. benthamiana* with active ALK1-mCherry or with the inactive versions of ALK1, ALK1^{D488N} or ALK1^{trunc}, respectively. This differential MS approach in that phosphor-sites detected also with ALK1^{D488N} or ALK1^{trunc} were considered as unspecific, revealed 18 putative ALK1-specific phosphorylation sites that cluster essentially over the entire ABCG36

sequence (results not shown). Quantitative MS analyses of ABCG36 phosphor-sites that were significantly reduced in *alk1* in comparison to Wt enabled us to substantially narrow down the number to two ALK1-specific sites: S823 and S825 (Fig. 7B and Suppl. Table 3). Interestingly, S825 phosphorylation was also significantly down-regulated by both IBA treatment and *F. oxysporum* infection, while S823 phosphorylation was only reduced by IBA treatment. The fact that IBA treatment and *F. oxysporum* infection were previously shown to both up-regulated ABCG36 expression (Fig. 4), made S825 our prime candidate for further functional analysis.

In order to test the impact of S825 phosphorylation, we expressed the phosphor-mimicry version S825D of ABCBG36 in yeast and quantified IBA/2.4-D transport. Interestingly, $ABCG36^{S825D}$ yeast exported significantly more IBA/2.4-D leading to a net export in comparison to Wt ABCB36 (Fig. 7C). The same effect was found also for $ABCG36^{S844D}$ but not for $ABCG36^{S841D}$ or $ABCG36^{S37D}$ that were all not reproducibly identified in our phosphor-proteomics (Suppl. Table 3). In summary, we conclude that S825 (beside other cluster 2 phosphorylation sites) is most likely phosphorylated by ALK1 leading to activation of ABCG36 transport activity.

Mutations in *ABCG36* and *ALK1* increase *F. oxysporum* susceptibility accompanied by reduced salicylic acid and camalexin production

Likewise reduced S825 phosphorylation in *alk1* and by *F. oxysporum* infection suggests that ALK1 and ABCG36 might function in the same pathway for pathogen resistance. In order to address this, we challenged available *abcg36/pen3* and *alk1* alleles by soil infection with *F. oxysporum*. As shown previously, *abcg36-4* (Mao et al. 2017) but also all other tested *abcg36* alleles revealed increased infection susceptibility compared to infected Wt indicated by a higher number of disease leaf symptoms, like chlorosis and necrosis (Fig. 8A-B). Interestingly, a similar degree of increased infection symptoms was also found for *alk1-2* and complementation of *abcg36-4* and *alk1-2* with *35S:ABCG36* and *35S:ALK1-mCherry*, respectively, rescued these mutant phenotypes (Fig. 8A-B). Increased disease symptoms correlated well with the quantification of fungal biomass analyzed by Q-PCR of leaf material: *abcg36* and *alk1* alleles revealed increased fungal development, which was again rescued by *ABCG36* and *ALK1* complementation (Fig. 8D). Root infection resulted in strongly reduced plant biomass and *abcg36* (but not *alk1*) alleles revealed overall an even stronger reduction in plant fresh weight, which was again rescued by *35S:ABCG36* (Suppl. Fig. 7). In contrast, inhibition of root elongation and root fungal progression upon *F. oxysporum* infection was independent of ABCG36 and ALK1 (Suppl. Fig. 7 B-C), suggesting that roots are not limiting for fungal infection of the shoot.

Salicylic acid (SA) is known to reduce *F. oxysporum* disease susceptibility (Diener and Ausubel 2005), and recently *ABCG36* null alleles were shown to hyper-accumulate free and total SA in response to infection with the powdery-mildew, *G. orontii* (SA; (Lu et al. 2015)). In our pathosystem, *F. oxysporum* infection led as well to strong induction of total (Fig. 8D) and free SA induction in Wt (Suppl. Fig. 7), however, in contrast to the host-adapted fungus, *G. orontii*, *F. oxysporum* challenge resulted in significantly reduced total (but not free; Suppl. Fig. 7D) SA in most null *abcg36* alleles and also in *alk1-2*, while again *35S:ALK1-mCherry* was able to rescue this mutant phenotype. The same trend was also found for induction of the phytoalexin, camalexin, that is essential for Arabidopsis

resistance to several necrotrophic fungi (Nawrath and Metraux 1999): the 10-fold induction found for Wt was reduced to below 5-fold for *abcg36* and *alk1* alleles.
Taken together, these data point to a common function of ABCG36 and ALK1 in disease resistance toward the root-penetrating fungus, *F. oxysporum*. Interestingly, in all our infection analyses, a mutant allele of *BAK1*, a LRR receptor-like protein kinase, that appears to function as co-receptor in development and immunity (Kim et al. 2013), was not behaving different from Wt. This exclude a mechanistic involvement of BAK1 in this pathway an underlines the specificity of ALK1 action on ABCG36.

Discussion

ABCG36 is an IBA exporter negatively regulating root-ward IBA transport

The current work enhances the portfolio of ABCG36 substrates by the putative auxin precursor, IBA. This has been established by heterologous expression in non-plant and plant systems, as well as by analyses of Arabidopsis *ABCG36* gain- and loss-of-function mutant lines (Fig. 3). As reported for ABCG37, ABCG36 seems thus to transport a few structurally unrelated substances (Lu et al. 2015) in analogy to yeast PDR orthologs (Balzi and Goffeau 1995; Golin et al. 2007). Interestingly, in this substrate category, ABCG36 (like ABCG37) seems to be specific for a few auxinic compounds, such as IBA and 2.4-D, but does for example not transport the major native auxin, IAA (Suppl. Fig. 2), which differs from IBA only by 2 carbons. A key to this interesting phenomenon is given eventually by the recent analyses of two ABCG36 alleles, *abcb36-5* and *abcg36-6*, that are each apparently uncoupled toward one substrate, a so far not yet identified indole glycosinolate derivate and IBA, respectively (Lu et al. 2015).

A careful analysis of polar auxin transport roots in *abcg* mutant alleles revealed that ABCG36 seems to function redundantly with ABCG37 in dampening root acropetal IBA (but not IAA) transport (Fig. 3F), which might be caused by concerted, lateral IBA export out of the root (see Suppl. Fig. 7). ABCG36 (but not ABCG37) seems to negatively control also basipetal IBA transport (Fig. 3E) but a similar impact was also found for IAA, which is at first place difficult to understand, especially in light of the exclusion of IAA as a substrate. However, identification of the facultative IAA im/exporter, ABCB4, as ABCG36 interacting protein (Suppl. Table 2) might suggest a functional interaction between IAA and IBA transport systems, despite their known exclusive substrate specificities (Rashotte et al. 2003; Ruzicka et al. 2010).

Loss-of-*ABCG36* function leads to hyper-sensitivity toward IBA, which affects important developmental programs, such as root elongation or LR production (Fig. 1). Currently it is unclear if this is a primary auxinic effect of IBA itself (Ludwig-Muller 2007) or caused by peroxisomal IBA to IAA conversion (Strader and Bartel 2011). Analyses of IAA-responsive, DR5:GFP expression indicates that the latter might be the case because, like for *abcg37* (Ruzicka et al. 2010), also *abcg36* roots revealed highly enhanced DR5:GFP expression upon IBA treatment compared to the wild-type.

Are ABCG36 and ABCG37 acting redundant?

Both ABCG36 and ABCG37 function as IBA exporter on overlapping lateral, outward-facing PM domain in the root epidermis. Both *abcg37* (Ruzicka et al. 2010) and *abcg36* (Fig. 2A-B) mutant roots are hypersensitive to IBA, suggesting functional redundancy. As discussed above, lateral root development supports functional redundancy between ABCG36 and ABCG37 (Fig. 1A), while primary root elongation does not. Obviously these developmental programs are both under control of local IAA maxima (Casimiro et al. 2003), however, these are thought to be active at the elongation zone or the mature root, respectively. Interestingly, redundancy of ABCG36/37 transport directionalities correlates with the origin and location of local auxin maxima: both root elongation and basipetal auxin transport, thought to be the primary cause of a local root tip auxin maximum REF, are only dependent on ABCG36 but not on ABCG37 (Figs. 3F, 1A). Contrarily, lateral root

development, which is thought to be initiated by a shoot-derived (acropetal) auxin maximum (Casimiro et al. 2003; Schlicht et al. 2013) is like acropetal IBA root transport apparently provided by both ABCG36 and ABCG37 (Figs. 1B, 3E).
Interestingly, quantification of auxin responses and free IBA in *abcb36 abcg37* roots (Fig. 2), revealed a certain degree of compensation of individual single-mutant phenotypes. In light of an overall redundant function in IBA transport this is not easy to understand. An important finding in this respect might be that ABCG37 was pulled-down as interactor of ABCG36 (Suppl. Table 2). An appealing scenario is therefore that ABCG36 and ABCG37 itself functionally interact, which might explain both the discrepancies found during compensatory and redundant function. The impact of ABC-ABC transporter interaction is currently still unclear but has been recently supported by uncovering the ABC transporter interactome in yeast (Snider et al. 2013).

A novel mode of ABC transporter regulation by the LRR receptor-like kinase, ALK1
ALK1 was isolated as an ABCG36 interactor by co-immunoprecipitation and interaction was substantiated by *in planta* co-locations and FRET-FLIM analyses in tobacco (Fig. 5). Co-expression in tobacco revealed a functional (inhibitory) impact of ALK1 on ABCG36 transport activity (Fig. 6), which was independent of ABCG36 expression or location (Suppl. Fig. 4). By means of quantitative phosphor-proteomics we identified S825 as a functional key residue that is most-likely phosphorylated by ALK1 and that highly enhances ABCG36 transport activity (Fig. 7). S844 (but not S37 and S841) phosphor-mimicry has the same impact on ABCG36 transport, however, currently it is unclear if these residues are also phosphorylated by ALK1. These opposite effects of ALK1 on ABCG36 activity might seem at first surprising, however, one should keep in mind that for many ABC transporters, including members of the PDR family, positive and negative effects on transport activity have been documented (Aryal et al. 2015). The most-simple explanation is therefore that ALK1 phosphorylates ABCG36 at another phosphorylation site(s), and that this event has the potential to overwrite the activating effect of S825 phosphorylation (red pathway in Suppl. Fig. 7).
Functional regulation of ABCG36 by ALK1 phosphorylation was further hardened by characterization of the *alk1* mutant. In agreement with an ABCG36 activation in *alk1*, *alk1* roots showed no IBA hypersensitivity (Fig. 2A-B) but decreased acropetal IBA transport (Fig. 3E), while protoplast assays revealed enhanced cellular IBA efflux (Fig. 6C).
Further proof for a common function for ABCG36 and ALK1 in the same pathway comes from infection analyses that revealed increased disease susceptibility and fungal biomass for *abcg36* and *alk1* alleles on one hand and reduced total SA and camalexin reduction on the other caused by root infection with *F. oxysporum*. Importantly, these mutant phenotypes were rescued by *ABCG36* and *ALK1* complementation (Fig. 8). The importance of ABCG36 phosphorylation for defense against the powdery mildew pathogen, *Blumeria graminis* f.sp. *hordei*, was recently demonstrated, however, amongst the tested ABCG phosphor-sites of cluster 1 and 2 (Fig. 7), only S40A and S45A mutations failed to restore *Blumeria* penetration resistance (Underwood and Somerville 2017). Both phosphor-sites were also significantly reduced upon *F. oxysporum* infection (Suppl. Table 3), however, based on our data an involvement of ALK1 is unlikely (Fig. 7).

Regulation of plant (Christie et al. 2011; Henrichs et al. 2012) and non-plant ABC transporters by protein kinases is an evolutionary conserved module (Aryal et al. 2015). However, this is to our knowledge the first description of ABC transporter regulation by a receptor-like kinase. For members of other transporter classes, a regulatory impact by receptor kinases has been described: the LRR receptor kinase, PSY1R, serves as a receptor for the peptide growth hormone, PSY1, and activates AHA2 by protein phosphorylation (Fuglsang et al. 2014).

Is ABCG36 regulation by IBA and *F. oxysporum* mechanistically coupled via ALK1?

IBA treatment and *F. oxysporum* infection resulted likewise in reduced phosphorylation of S825 (and S45) of ABCG36, however, only the effect on S825 seems to be mediated by ALK1 (Fig. 7), suggesting a mechanistic coupling. *F. oxysporum* is known to trigger tissue-specific regulation of auxin transport and signaling genes (Lyons et al. 2015) affecting auxin homeostasis (Kidd et al. 2011). This is underlined by up-regulation of DR5 expression in the root by *Fusarium* infection (Suppl. Fig. 3B, (Kidd et al. 2011)). On the other hand, chemical or genetic alteration of polar auxin transport conferred increased resistance to *Fusarium* infection, indicating that *F. oxysporum* requires components of transport to efficiently colonize the plant root.

In light of these findings, it is tempting to speculate that *Fusarium* itself, known to produce auxins (including IAA, (Kidd et al. 2011)), manipulates ABCG36 expression by IBA secretion (see green pathway in Suppl. Fig. 7). Although IBA production has to our knowledge not been shown for *F. oxysporum*, it is widely distributed among fungi (Ludwig-Muller 2015).

On the other hand, sequence alignments revealed that the apoplastic LRR domain of ALK1 is probably too short in order to function as a receptor. Therefore, ALK1 more likely functions as a co-receptor trans-phosphorylating ABCG36 upon activation by a so far not yet identified receptor. Good candidates for such a receptor might be members of the receptor-like kinase families that co-purified with ABCG36 and ALK1, like CERK1 or PERK1. CERK1 itself, however is a less likely candidate because DR5:GFP responsiveness upon IBA treatment was not different from wild-type (Fig. 2). A search for the receptor transducing IBA secretion and/or *Fusarium* infection via ALK1 onto ABCG36 is ongoing.

Remarkably, IBA treatment and *F. oxysporum* infection resulted beside down-regulation of S825 phosphorylation also similarly in specific ABCG36 up-regulation (Fig. 4; blue pathway in Suppl. Fig. 7), suggesting that a similar regulatory module is employed as for ABCG36 phosphorylation (see blue pathway in Suppl. Fig. 7). While we do not yet have any experimental support that *F. oxysporum* uses IBA excretion, a direct involvement of ALK1 is unlikely because ABCG36 expression and polarity if unchanged in *alk1* (Suppl. Fig. 4).

Material and Methods

Plant Material and Phenotypic Analyses

The following *Arabidopsis thaliana* lines in ecotype Columbia (Col WT) were used: *abcg36-4 (pen3-4)* (Stein et al., 2006), *abcg37-2 (pdr9-2)* (Ito & Gray, 2006), *abcg36-4 abcg37-2 (pen3-4 pdr9-2)* (Ruzicka et al., 2010), *cerk1-2* (Miya et al., 2007), *alk1-1* (GABI-Kat-689A02), *35S:ABCG37-GFP* (Ruzicka et al., 2010), *ABCG36:ABCG36-GFP (PEN3:PEN3-GFP)* (Stein et al., 2006), *AHA2:AHA2-GFP* (Fuglsang et al., 2014), *ABCB1:ABCB1-GFP* (Mravec et al., 2008). For *35S:ALK1-YFP*, ALK1 cDNA was amplified by using ALK1-s (5`-AT GAA GTA TAA GCG TAA GC-3`) and ALK1-dir-as (5`-TGG AAC GTT CTC TTC TTT CTT TCT C-3`) primers and inserted into the pCR8/GW/TOPO vector, which was recombined into Gateway destination vector pBIN19-YFP. For *35S:ALK1-mcherry,* ALK1 cDNA was amplified using primers ALK1-dir-s (5`-CAC CAT GAA GTA TAA GCG TAA GCT AAG C-3`) and ALK1-dir-as (5`- GTC GGA TAC AGG ATT TGG GGA G-3`) primers. Similarly, for 35S:ALK1^{trunc}-mcherry, ALK1 cDNA was amplified by using ALK1-dir-s and ALK1-dir^{trunc}-as (5`-TGG AAC GTT CTC TTC TTT CTT TCT C-3`) primers, cloned into the pENTR/D-TOPO® vector followed by a recombination into pEG101-mcherry and transformation into *alk1-2* mutant by floral dipping.

DR5:GFP previously described in (Ruzicka et al., 2010) was crossed into *abcg36-4 abcg37-2, alk1-2* and *cerk1-2* and isogenic, homozygous lines for the transgene in the F3 generations were used for further analyses. The same strategy was used for crossing of *ABCG36:ABCG36-GFP into alk1-2* and *35S:ALK1-mcherry* respectively. *35S:ABCG36 Arabidopsis* lines were constructed by transforming *35S:PDR8* (Kim et al., 2006) into *pen3-4* mutant.

Seedlings were generally grown on vertical plates containing 0.5 Murashige and Skoog media, 1% sucrose, and 0.75% phytoagar in the dark or at 16 h (long day) light per day. Developmental parameters, such as primary root lengths, lateral root number and root gravitropism were quantified by microscopy as described in (Ruzicka et al., 2010). All experiments were performed at least in triplicate with 30 to 40 seedlings per each experiment.

Yeast work

ABCG36, ABCG37, ALK1, CERK1 and TWD1 were expressed from shuttle vectors pYES2NT/C-ABCG36, pNEV-ABCG37-HA (Ruzicka et al. 2010), pGPD-ALK1-GFP, pGPD-CERK1-HA and pRS314CUP-TWD1 (Bouchard et al. 2006) in WT strain JK93da (Hemenway and Heitman 1996). cDNA of ABCG36 was PCR-amplified and inserted into BamHI/ XhoI sites of pYES2NT/C-ABCG36. ALK1 cDNA was amplified using primers ALK1-s (AT GAA GTA TAA GCG TAA GCT AAG C-3`) and ALK1-as (5`- GTC GGA TAC AGG ATT TGG GGA G-3`), CERK1 cDNA was amplified by using CERK1-s (ATG AAG CTA AAG ATT TCT CT AAT C-3`) and CERK-as (5`-CCG GCC GGA CAT AAG ACT GAC-3`) was inserted into pCR8/GW/TOPO® vector. Thus formed ALK1, CERK1 cDNA from pCR8/GW/TOPO® was recombined with yeast Gateway shuttle vectors, pGPD:GFP and pGPD:HA (Plant Systems Biology, Ghent University), to give pGPD:ALK1-GFP and pGPD:CERK1-HA, respectively. Yeast IBA/2.4-D transport was performed as described

(Kim et al. 2010). Putative phosphorylation sites in ABCG36 were mutated by site-directed mutagenesis (QuikChange Lightning Site-Directed Mutagenesis Kit, Agilent).
Relative export from yeast is calculated from retained radioactivity as follows: (radioactivity in the yeast at time t=10 min.) - (radioactivity in the yeast at time t=0)) * (100%)/ (radioactivity in the yeast at t=0 min.); presented are mean values from 4 independent experiments.

Affinity purification of ABCG36-GFP interacting proteins and mass spectrometric analysis
Co-immunoprecipitation analyses were carried out in triplicate as described recently using anti-GFP MicroBeads (Miltenyi Biotec, Germany; (Henrichs et al. 2012)) except that bands of interest were size-selected by silver stain and manually cut out of the gel prior to trypsin digest. LC-MS/MS analyses were performed by using an LTQ-Orbitrap XL-HTC-PAL system. MS/MS spectra were analyzed using the MASCOT server (version 2.2) searching the TAIR10 database (The Arabidopsis Information Resource). The MASCOT search parameters were as follows: set off the threshold at 0.05 in the ion-score cut off, peptide tolerance at 10 ppm, MS/MS tolerance at ± 0.8Da, peptide charge of 2+ or 3+, trypsin as enzyme allowing up to one missed cleavage, carboxymethylation on cysteines as a fixed modification and oxidation on methionine as a variable modification. Mascot identified vector control proteins were subtracted manually from ABCG36-GFP proteins, and proteins were sorted according to their appearance in triple experiments (identified counts) and listed according to their score (Supplementary Table 1).

Protein phosphorylation analyses by LC-MS/MS
For *in-planta* phosphorylation analyses, 35S:ABCG36 was co-transfected in *N. benthamiana* leaves with *35S:ALK1, 35S:ALK1*^{D488N} and *35S:ALK1*^{trunc} as described above. As alternative approach, Arabidopsis *ABCG36:ABCG36-GFP* lines were used after auxin treatment or *Fusarium* infection. As starting material either total microsomes REF or ABCG36-GFP bands manually cut from Commassie-stained gels after immunoprecipitation using anti-GFP MicroBeads (Miltenyi Biotec, Germany). Total microsomes were loaded on 50 kDa horizontal cut-off filters (Vivacon 500, 50,000 MWCO Hydrosart) for buffer exchange. Trypsin digest was processed by FASP protocol overnight; phoshopeptides were enriched by TiO_2 affinity beads.
Samples were fractionated by LC-MS/MS using a nanoscale–HPLC on an EASY-nLC 1000 Liquid Chromatograph connected online to a Q-Executive hybrid quadrupole-Orbitrap mass spectrometer (Thermo Scientific). Peptides were separated over a linear gradient from 10-30% ACN in 0.5% acetic acid with a flow rate of 250 nl/min. All full-scan acquisition was done in the FT-MS part of the MS in the range from m/z 350-2000 with an automatic gain control target value of 10^6 and at resolution 75,000 at m/z 400. MS acquisition was done in data-dependent mode to sequentially perform MS/MS on the ten most intense ions in the full scan (Top10) in the HCD cell using the following parameters. AGC target value: 5,000. Ion selection thresholds: 1000 counts and a maximum fill time of 100 ms. Wide-band activation was enabled with an activation q = 0.25 applied for 30 ms at a normalized collision energy of 25%. Singly charged and ions with unassigned charge state were excluded from MS/MS. Dynamic exclusion was applied to reject ions from repeated MS/MS selection for 45 s.

All recorded LC-MS/MS raw files were processed together in MaxQuant version 1.4.1.2 with default parameters using the UniProt *Arabidopsis thaliana* database. Search parameters were a mass accuracy thresholds of 0.5 (MS/MS) and 20 ppm (precursor), Trypsin/P+DP as protease, maximum three missed cleavages, carbamidomethylation (C) as fixed modification and oxidation (M), phosphorylation (STY) and protein N-terminal acetylation as variable modifications. MaxQuant was used to filter the identifications for a FDR below 1% for peptides, sites and proteins using forward-decoy searching. Match between runs were enabled with a retention time window of 2 min. Phosphosites with localization probabilities $\geq$0.75 (class I sites) were used for bioinformatics analyses.

Confocal laser scanning and FRET-FLIM lifetime imaging

For confocal laser scanning microscopy work, a SP5 Lycia confocal laser microscope was used. Various confocal settings were set to record the emission of GFP (excitation 488 nm, emission 500–550 nm) and RFP (excitation 561 nm, emission 600-680 nm). Distribution of ABCG36-GFP expression in the root was quantified with a self-written plug-in by creating a mask for whole roots using the fluorescence image by local contrast enhancement (CLAHE), followed by setting auto threshold (Huang method) to segment the root and perform a binary morphological operation. This step is followed by constructing inner and outer region of interest using distance ratio and finally measuring signal ratio in Fiji.

For FRET analysis, binary vectors *ABCG36:ABCG36-GFP*, *35S:ALK1-mCherry* and *AHA2:AHA2-RFP* and *p19* as gene-silencing suppressor were transformed into *Agrobacterium tumefaciens* strain GV3101 and infiltrated into *Nicotiana benthamiana* leaves. The measurements were performed 3 dai using a SP8 laser scanning microscope (Leica Microsystems) with LAS-AF and SymPhoTime software as described (Veerabagu et al. 2012). Before FRET-FLIM measurement, the presence of the fluorophores was detected using 488- or 561-nm lasers for GFP or RFP excitation, respectively. The lifetime τ [ns] of either the donor only expressing cells or the donor-acceptor pairs was measured with a pulsed laser as an excitation light source of 473 nm and a repetition rate of 40 MHz (PicoQuant Sepia multichannel picosecond diode laser, PicoQuant Picoharp 300 TCSPC module, and Picosecond event timer). The acquisition was performed until 1000 photons in the brightest pixel were reached. To obtain the GFP fluorescence lifetime, data processing was performed with SymPhoTime software and mono-exponential curve fitting, correction for the instrument response function, and a fitting range from channel 90 to 1400.

Plant auxin transport

Simultaneous ^{3}H-IBA , ^{14}C-2.4-D or ^{14}C-IAA export from *Arabidopsis* and *N. benthamiana* mesophyll protoplasts was analyzed as described (Henrichs et al. 2012). *N. benthamiana* mesophyll protoplasts were measured 4 days after agrobacterium-mediated co-transfection of combinations of *35S:ABCG36* with *35S:ALK1-YFP*, *35S:ALK1^{D488N}-mCherry* and 35S:ALK1^{trunc}*-mCherry*. Relative export from protoplasts is calculated from exported radioactivity as follows: (radioactivity in the protoplasts at time t = x min.) - (radioactivity in the protoplasts at time t = 0)) * (100%)/ (radioactivity in the protoplasts at t

= 0 min.); presented are mean values from 4 independent experiments. Root acropetal and basipetal PAT measurements were performed as described (Lewis and Muday, 2009).

In planta analysis of salicylic acid, camalexin and auxin contents and responses

Endogenous free IBA and IAA were quantified from shoot and root segments of 9 dag Arabidopsis seedlings by using gas chromatography-mass spectrometry (GC-MS) as described in (Leljak-Levanic et al. 2010). Methylation was performed by adding equal sample amounts of a 1:10 diluted solution (in diethylether) of trimethylsilyldiazomethane solution (Sigma-Aldrich) for 30 min at room temperature. The mixture was then evaporated and resuspended in 50 mL of ethyl acetate for GC-MS analysis. Data are means of four independent lots of 30–50 seedlings each, and equivalent to ca. 100 mg root shoot material, respectively.

Homozygous generations of *Arabidopsis abcg36-4, abcg36-4 abcg37-2, cerk1-2* and *alk1-2* expressing DR5:GFP were obtained by crossing with DR5:GFP lines (Ottenschlager et al. 2003). Seedlings were grown vertically for 5 dag and for 4h on 5 uM IBA plates and analyzed by confocal laser-scanning microscopy.

Free and conjugated salicylic acid and camalexin were extracted according to (Nawrath and Metraux 1999). For HPLC analysis, the organic phase was evaporated and re-suspended in methanol:water:acetic acid (60:39:1). Separation was performed using a reverse phase column (Supelco Discovery HS-C18, 25 mm x 4 mm x 5µm) with a water:methanol gradient (initial phase 2 min at 40 % methanol followed by a ramp from 40 % methanol to 100 % methanol within 18 min) and a flow rate of 0.9 ml/min.

Fusarium oxysporum root infection assays

Fusarium oxysporum f. sp. Conglutinas, strain 699 (ATCC 58110) was grown as described in (Mao et al. 2017). Hydroponic infection assays were conducted as in (Poncini et al. 2017). In short, seeds were surface-sterilized and placed in batches of 10 in 12-well plates onto a foam disk floating on 3 ml of liquid basal medium. The 12-well plates were sealed with medical tape and placed in a growth chamber under a photoperiod of 10h of light (100 µmol m^{-2} s^{-1}) and a day/ night temperature of 24°C/ 22°C at 60% relative humidity. ABCG36 localization, infection rate and transcript expression was analyzed 48h post infection. For fungal progression analyses, 3 dpi seedling roots grown in hydroponics were stained for 2 min. in 1% Evans blue, and washed three times in distilled water. Measures of infected roots were performed with a digital caliper under a binocular.

For plate infection assays, 1µl droplets of the *F. oxysporum* supspension (10^5 conidia/ml) were applied 2 mm under the root tips of 4 dag seedlings and root elongation was monitored 2 dpi. *F. oxysporum* root infection assays in soil were performed as reported in (Mao et al. 2017) In short, 3-week-old *Arabidopsis thaliana* plants were infected by pipetting 10 ml conidia suspension (10^7 conidia/ml) directly into the soil contained in a 125 ml plastic pot harboring a single plant. Fresh-weight and disease sensitivity scores were obtained by measuring rosette weight and by observing chlorotic and necrotic symptoms scored at a scale from 1-10 as number of affected leaves per plant, respectively, two weeks after inoculation. 15-30 plants were employed per genotype per experiments in each of three independent experiments (n = 3).

Real-time PCR analyses

Total RNA from plants infected with *F. oxysporum* were isolated by using TRIZOL reagent (Roth, Germany). First strand cDNA synthesis from DNAse-treated RNA (New England Biolabs) was performed with the Omniscript RT kit (Qiagen, Hilden Germany) according to the manufacturer guidelines. qPCR reaction was operated by using the SensiMix SYBR® from Bioline (www.bioline.com) and a Magnetic Induction Cycler (Bio Molecular Systems) using primers listed in Table S2. The PCR condition included initial denaturation cycle for 10 min at 95°C followed by 45 cycles of denaturation for 20s, annealing for 20s at 59°C, extension for 20s at 72°C. Data were analyzed with the software micPCR vers. 1.4.0. Expression of target genes were normalized to the *RHIP1* reference gene ((Czechowski et al. 2005). Three biological replicates (with three technical replicates for each experiment) were performed for each time point after infection.

For quantification of fungal biomass, two weeks after soil inoculation, 3 to 4 leaves of independent plants were frozen in liquid nitrogen and DNA was extracted with the peqGOLD Plant DNA Mini Kit (www.vwr.com). As external standard, the DIG2 plasmid was added into the lysis buffer at early stage of the extraction, which was amplified by using RT_PRA2M primers. *F. oxysporum* DNA was detected using fw Foxy_F2 and rv Fus_EF2 primers, respectively.

Data Analysis

Data were statistically analyzed using Prism 7.0a (GraphPad Software, San Diego, CA) and the R software package of the Comprehensive R Archive Network (CRAN) (http://cran.r-project.org).

Acknowledgments

We would like thank L. Charrier for excellent technical assistance, B. Egger and F. Meyenhofer for help with confocal imaging and quantification of root GFP signals, A. Fuglsang for *AHA2:AHA2-GFP* lines, J. Friml for *35S:ABCG37-GFP*, *abcg36-s/pdr9-2*, *abcg36-4/pen3-4, and abcg37-2/pdr9-2* lines, B. Underwood for *PEN3:PEN3-GFP* plasmid construct and *PEN3* serine mutant lines and R. Rohr and L.-F. Bersier for help with statistical analyses. This work was supported by grants from the Swiss National Funds, the Pool de Recherche of the University of Fribourg, the Novartis Foundation and the ESA (all to MG).

Author contribution

MG and BA designed research; BA, JH, JS, YF, MD, SL and ZH, JLM, and MH performed research; SA, EM and JPM provided unpublished material or methods; AB, YF, ZH, JH, JLM, KH, MH, JD, and MG analyzed data; MG wrote the manuscript.

Conflict of interest

The authors declare that they have no conflict of interest.

Abbreviations

NPA, 1-*N*-naphthylphthalamic acid; IBA, indole-3-butyric acid; IAA, indole-3-acetic acid; PAT, polar auxin transport; ABCG, ATP-binding cassette protein subfamily G; PDR, Pleiotropic drug resistance; ABCB, ATP-binding cassette protein subfamily B; PIN, pin-formed; dag, day(s) after germination; dai, day(s) after infection; WT, wild-type; MS, mass spectrometry.

Figure Legends

Figure 1: ABCG36 and ABCG37 contribute differently to root growth

(A) For root length elongation assays, 5 dag seedlings were transferred to solvent control or indicated IBA plates, and root elongation was judged after 24h.

(B) Quantification of lateral root numbers of seedlings grown for 12 dags on indicated IBA concentrations or solvant control plates

Significant differences (unpaired *t* test with Welch's correction, $p < 0.05$) between wild-type and mutant alleles with 'a' (means ± SE; n = 4 sets of 20 seedlings each).

Figure 2: Auxin responses and quantification of free IBA and IAA.

(A-B) Root auxin responses visualized by the auxin-responsive element in the columella of 5 dag seedlings grown on solvent (DMSO) or 5 µM IBA (**B,** quantification of **A**). Significant differences (unpaired *t* test with Welch's correction, $p < 0.05$) to wild-type or to solvent controls are indicated by 'a' and 'b', significant, while differences between IBA-treated wild-type and mutant alleles by 'c' (mean ± SE; n ≥ 20 images). Bar, 20 µm.

(C) Free IBA is reduced in *abcg36,37* roots and shoots. Significant differences (unpaired *t* test with Welch's correction, $p < 0.05$) between wild type and mutant alleles are indicated by 'a' (mean ± SE; n =4).

Figure 3: ABCG36 transports the native and synthetic auxins, IBA and 2.4-D, but not IAA.

(A) Yeast expressing ABCG or ABCG37 retain significantly less IBA and 2.4-D indicating higher export.

(B) Analyses of auxin export from *N. benthamiana* protoplasts after transfection with ABCG36.

(C) Efflux of IBA and 2.4-D from *ABCG36* and *ABCG37* gain-of-function (35S:ABCG36/ABCG37) protoplasts.

(D) Efflux of IBA and 2.4-D from *ABCG36* loss-of-function protoplasts.

(E-F) Acropetal (**E**, root-ward) and basipetal (**F**, shoot-ward) root transport of ^{3}H-IAA and ^{14}C-IAA assayed in parallel.

Significant differences (unpaired *t* test with Welch's correction, $p < 0.05$) between wild type and mutant alleles are indicated by asterisks (mean ± SE; n ≥ 4 transport experiments generated from independent yeast transformations or tobacco transfections).

Figure 4: Root infection and IBA treatments specifically alter ABCG36 expression and polarity

(A) ABCG36-GFP (PEN3:PEN3-GFP) was imaged 48h after IBA or IAA (1 µM) treatment in comparison with the solvent control (control). Bar, 50 µm.

(B) ABCG36-GFP (PEN3:PEN3-GFP), AHA2-GFP (AHA2:AHA2-GFP) and ABCB1-GFP (ABCB1:ABCB1-GFP) was imaged 48h after *F. oxysporum* (Fox) infection in comparison with buffer control (control). Bars, 50 µm.

(C) Quantification of GFP intensities in **B**. Significant differences (unpaired *t* test with Welch's correction, $p < 0.05$) between to solvent are indicated by an 'a' (mean ± SE; $n \geq 50$ images). nd, not done.

Figure 5: ABCG36 co-localizes and interacts with ALK1 *in planta.*
(A) ABCG36-GFP (PEN3:PEN3-GFP) and ALK1-mCherry (35S:ALK1-mCherry) co-localize on the PM of *N. benthamiana* pavement cells after *A. tumefaciens*-mediated co-transfection. Asterisks mark enhanced signals and co-localization in the necks of cells. Bar, 100 µm.
(B) ABCG36-GFP (PEN3:PEN3-GFP) and ALK1-mCherry (35S:ALK1-mCherry) co-localize in the columella and epidermis of Arabidopsis roots. Bar, 50 µm.
(C) Confocal imaging of ABCG36-GFP (PEN3:PEN3-GFP) with ALK1-mCherry (35S:ALK1-mCherry) or AHA2-GFP (AHA2:AHA2-GFP) in *N. benthamiana* pavement cells after *A. tumefaciens*-mediated co-transfection used for FRET-FLIM analyses in **D**. Bar, 10 µm.
(D) FRET-FLIM analysis of ABCG36-GFP (PEN3:PEN3-GFP)-ALK1-mCherry (35S:ALK1-mCherry) interaction in *N. benthamiana* pavement cells after *A. tumefaciens*-mediated co-transfection. Note significantly reduced fluorescence lifetime for the ABCG36-GFP/ALK1-mCherry pair compared to the donor (ABCG36-GFP) alone, not found with ABCG36-GFP/AHA2-RFP, indicating a close proximity. Significant differences (unpaired *t* test with Welch's correction, $p < 0.05$) between infiltrations are indicated by 'a' (mean ± SE; $n \geq 50$ images).

Figure 6: ALK1 inhibits ABCG36-mediated auxin efflux activity.
(A) ALK1 inhibits significantly ABCG36-mediated IBA but not 2.4-D export in yeast, determined as increase of auxin retention. Note inhibitory effect caused by expression of ALK1 alone in comparison to vector control indicating an inhibitory effect on yeast endogenous transporters.
(B) ALK1 significantly inhibits ABCG36-mediated IBA and 2.4-D export from *N. benthamiana* protoplasts after co-transfection, while a mutated, inactive ALK1 ($ALK1^{D488N}$-mCherry) or a kinase-truncated version of ALK1 ($ALK1^{trunc}$-mCherry) has no significant effect.
(C) Efflux of IBA but not of IAA from *alk1-2* loss-of-function protoplasts is enhanced.
Significant differences (unpaired *t* test with Welch's correction, $p < 0.05$) to vector control or to wild type are indicated by 'a' (mean ± SE; $n \geq 4$ independent transformations/ transfections or protoplast preparations).

Figure 7: Identification of ALK1-specific phosphorylation sites on ABCBG36.
(A) Proteomically supported phosphorylation sites identified in this study align with previously classified clusters in cytosolic stretches prior to NBD1 and NBD2. Phosphorylation sites that were shown to be ALK1-specific are colored green, those that were identified here but are not unambiguously ALK1-specific are in blue, while residues that were here not identified but characterized previously (Underwood and Somerville 2017) are colored in red. NBD, nucleotide binding domain; TMD, transmembrane domain.

(B) Mean abundance of indicated ABCG36 phosphosites identified by MS analyses of Arabidopsis Wt solvent control (control), *alk1-2*, or Wt treated with IBA (10 uM) or infected with *F. oxysporum*. Significant differences (unpaired *t* test with Welch's correction, $p < 0.05$) to Wt solvent control is indicated by asterisks (mean ± SE; n = 3 independent treatments and MS analyses).
(C) Phosphormimicry of S825 and S844 significantly enhances ABCG36-mediated IBA and 2.4-D export in yeast. Significant differences (unpaired *t* test with Welch's correction, $p < 0.05$) between vector control/ABCG36 and ABCG36/mutant versions of ABCG36 are indicated by 'a' and 'b', respectively (mean ± SE; n ≥ 4 transport experiments generated from independent yeast transformations or tobacco transfections).

Figure 8: Mutations in *ABCG36* and *ALK1* increase *F. oxysporum* susceptibility accompanied by reduced salicylic acid and camalexin induction
(A-B) 5-week-old plants grown on soil without (control) or with *F. oxysporum* treatment (FOX) after 3 weeks. Note the increased number of chlorotic and necrotic leaves (**A**) and increased disease sensitivity (**B**) in *abcg36/pen3* and *alk1* alleles. Significant differences (unpaired *t* test with Welch's correction, $p < 0.0001$) to infected wild type are indicated by 'a' (mean ± SE; n = 3 independent infections).
(C) Fungal biomass of soil-infected plants quantified by Q-PCR of leaf material. Significant differences between means ± SE (n = 3 independent infections; F test to compare variances) to infected wild-type are indicated by 'a' ($p<0.0001$) or 'b' ($p<0.005$).
(D-E) HPLC quantification of total salicylic acid and camalexin from soil-infected and non-infected leaves. Significant differences (unpaired *t* test with Welch's correction, $p < 0.05$) to wild type inductions (infected/ non-infected) are indicated by 'a' (mean ± SE; n ≥ 7 HPLC analyses).

References

Aryal, B., Laurent, C. and Geisler, M. (2015) Learning from each other: ABC transporter regulation by protein phosphorylation in plant and mammalian systems. *Biochem Soc Trans* 43: 966-974.

Bailly, A., Sovero, V., Vincenzetti, V., Santelia, D., Bartnik, D., Koenig, B.W., et al. (2008) Modulation of P-glycoproteins by auxin transport inhibitors is mediated by interaction with immunophilins. *J Biol Chem* 283: 21817-21826.

Balzi, E. and Goffeau, A. (1995) Yeast multidrug resistance: the PDR network. *J Bioenerg Biomembr* 27: 71-76.

Bednarek, P., Pislewska-Bednarek, M., Svatos, A., Schneider, B., Doubsky, J., Mansurova, M., et al. (2009) A glucosinolate metabolism pathway in living plant cells mediates broad-spectrum antifungal defense. *Science* 323: 101-106.

Benschop, J.J., Mohammed, S., O'Flaherty, M., Heck, A.J., Slijper, M. and Menke, F.L. (2007) Quantitative phosphoproteomics of early elicitor signaling in Arabidopsis. *Mol Cell Proteomics* 6: 1198-1214.

Bienert, M.D., Siegmund, S.E., Drozak, A., Trombik, T., Bultreys, A., Baldwin, I.T., et al. (2012) A pleiotropic drug resistance transporter in Nicotiana tabacum is involved in defense against the herbivore Manduca sexta. *The Plant journal : for cell and molecular biology* 72: 745-757.

Bouchard, R., Bailly, A., Blakeslee, J.J., Oehring, S.C., Vincenzetti, V., Lee, O.R., et al. (2006) Immunophilin-like TWISTED DWARF1 modulates auxin efflux activities of Arabidopsis P-glycoproteins. *J Biol Chem* 281: 30603-30612.

Campe, R., Langenbach, C., Leissing, F., Popescu, G.V., Popescu, S.C., Goellner, K., et al. (2016) ABC transporter PEN3/PDR8/ABCG36 interacts with calmodulin that, like PEN3, is required for Arabidopsis nonhost resistance. *New Phytol* 209: 294-306.

Casimiro, I., Beeckman, T., Graham, N., Bhalerao, R., Zhang, H.M., Casero, P., et al. (2003) Dissecting Arabidopsis lateral root development. *Trends in Plant Science* 8: 165-171.

Chen, Y., Hoehenwarter, W. and Weckwerth, W. (2010) Comparative analysis of phytohormone-responsive phosphoproteins in Arabidopsis thaliana using TiO2-phosphopeptide enrichment and mass accuracy precursor alignment. *The Plant journal : for cell and molecular biology* 63: 1-17.

Christie, J.M., Yang, H., Richter, G.L., Sullivan, S., Thomson, C.E., Lin, J., et al. (2011) phot1 inhibition of ABCB19 primes lateral auxin fluxes in the shoot apex required for phototropism. *PLoS Biol* 9: e1001076.

Clay, N.K., Adio, A.M., Denoux, C., Jander, G. and Ausubel, F.M. (2009) Glucosinolate

metabolites required for an Arabidopsis innate immune response. *Science* 323: 95-101.

Czechowski, T., Stitt, M., Altmann, T., Udvardi, M.K. and Scheible, W.R. (2005) Genome-wide identification and testing of superior reference genes for transcript normalization in Arabidopsis. *Plant Physiol* 139: 5-17.

Diener, A.C. and Ausubel, F.M. (2005) RESISTANCE TO FUSARIUM OXYSPORUM 1, a dominant Arabidopsis disease-resistance gene, is not race specific. *Genetics* 171: 305-321.

Evangelisti, E., Govetto, B., Minet-Kebdani, N., Kuhn, M.L., Attard, A., Ponchet, M., et al. (2013) The Phytophthora parasitica RXLR effector penetration-specific effector 1 favours Arabidopsis thaliana infection by interfering with auxin physiology. *The New phytologist* 199: 476-489.

Fuglsang, A.T., Kristensen, A., Cuin, T.A., Schulze, W.X., Persson, J., Thuesen, K.H., et al. (2014) Receptor kinase-mediated control of primary active proton pumping at the plasma membrane. *Plant J* 80: 951-964.

Golin, J., Ambudkar, S.V. and May, L. (2007) The yeast Pdr5p multidrug transporter: how does it recognize so many substrates? *Biochem Biophys Res Commun* 356: 1-5.

Grunewald, W., Cannoot, B., Friml, J. and Gheysen, G. (2009) Parasitic nematodes modulate PIN-mediated auxin transport to facilitate infection. *PLoS Pathog* 5: e1000266.

Hemenway, C.S. and Heitman, J. (1996) Immunosuppressant target protein FKBP12 is required for P-glycoprotein function in yeast. *J Biol Chem* 271: 18527-18534.

Henrichs, S., Wang, B., Fukao, Y., Zhu, J., Charrier, L., Bailly, A., et al. (2012) Regulation of ABCB1/PGP1-catalysed auxin transport by linker phosphorylation. *EMBO J* 31: 2965-2980.

Ito, H. and Gray, W.M. (2006) A gain-of-function mutation in the Arabidopsis pleiotropic drug resistance transporter PDR9 confers resistance to auxinic herbicides. *Plant Physiol* 142: 63-74.

Jasinski, M., Stukkens, Y., Degand, H., Purnelle, B., Marchand-Brynaert, J. and Boutry, M. (2001) A plant plasma membrane ATP binding cassette-type transporter is involved in antifungal terpenoid secretion. *Plant Cell* 13: 1095-1107.

Kang, J., Hwang, J.U., Lee, M., Kim, Y.Y., Assmann, S.M., Martinoia, E., et al. (2010) PDR-type ABC transporter mediates cellular uptake of the phytohormone abscisic acid. *Proc Natl Acad Sci U S A* 107: 2355-2360.

Kidd, B.N., Kadoo, N.Y., Dombrecht, B., Tekeoglu, M., Gardiner, D.M., Thatcher, L.F., et al. (2011) Auxin signaling and transport promote susceptibility to the root-infecting fungal pathogen Fusarium oxysporum in Arabidopsis. *Mol Plant Microbe Interact* 24: 733-748.

Kim, B.H., Kim, S.Y. and Nam, K.H. (2013) Assessing the diverse functions of BAK1 and its homologs in arabidopsis, beyond BR signaling and PTI responses. *Mol Cells* 35: 7-16.

Kim, D.Y., Bovet, L., Maeshima, M., Martinoia, E. and Lee, Y. (2007) The ABC transporter AtPDR8 is a cadmium extrusion pump conferring heavy metal resistance. *Plant J* 50: 207-218.

Kim, J.Y., Henrichs, S., Bailly, A., Vincenzetti, V., Sovero, V., Mancuso, S., et al. (2010) Identification of an ABCB/P-glycoprotein-specific inhibitor of auxin transport by chemical genomics. *J Biol Chem* 285: 23309-23317.

Kobae, Y., Sekino, T., Yoshioka, H., Nakagawa, T., Martinoia, E. and Maeshima, M. (2006) Loss of AtPDR8, a plasma membrane ABC transporter of Arabidopsis thaliana, causes hypersensitive cell death upon pathogen infection. *Plant Cell Physiol* 47: 309-318.

Krattinger, S.G., Lagudah, E.S., Spielmeyer, W., Singh, R.P., Huerta-Espino, J., McFadden, H., et al. (2009) A putative ABC transporter confers durable resistance to multiple fungal pathogens in wheat. *Science* 323: 1360-1363.

Kretzschmar, T., Burla, B., Lee, Y., Martinoia, E. and Nagy, R. (2011) Functions of ABC transporters in plants. *Essays Biochem* 50: 145-160.

Kretzschmar, T., Kohlen, W., Sasse, J., Borghi, L., Schlegel, M., Bachelier, J.B., et al. (2012) A petunia ABC protein controls strigolactone-dependent symbiotic signalling and branching. *Nature* 483: 341-344.

Langowski, L., Ruzicka, K., Naramoto, S., Kleine-Vehn, J. and Friml, J. (2010) Trafficking to the outer polar domain defines the root-soil interface. *Curr Biol* 20: 904-908.

Leljak-Levanic, D., Jezic, M., Cesar, V., Ludwig-Muller, J., Lepedus, H., Mladinic, M., et al. (2010) Biochemical and epigenetic changes in phytoplasma-recovered periwinkle after indole-3-butyric acid treatment. *J Appl Microbiol* 109: 2069-2078.

Lu, X., Dittgen, J., Pislewska-Bednarek, M., Molina, A., Schneider, B., Svatos, A., et al. (2015) Mutant Allele-Specific Uncoupling of PENETRATION3 Functions Reveals Engagement of the ATP-Binding Cassette Transporter in Distinct Tryptophan Metabolic Pathways. *Plant Physiol* 168: 814-827.

Ludwig-Muller, J. (2007) Indole-3-butyric acid synthesis in ecotypes and mutants of Arabidopsis thaliana under different growth conditions. *J Plant Physiol* 164: 47-59.

Ludwig-Muller, J. (2015) Bacteria and fungi controlling plant growth by manipulating auxin: balance between development and defense. *J Plant Physiol* 172: 4-12.

Lyons, R., Stiller, J., Powell, J., Rusu, A., Manners, J.M. and Kazan, K. (2015) Fusarium oxysporum triggers tissue-specific transcriptional reprogramming in Arabidopsis thaliana. *PloS one* 10: e0121902.

Mao, H., Aryal, B., Langenecker, T., Hagmann, J., Geisler, M. and Grebe, M. (2017) Arabidopsis BTB/POZ protein-dependent PENETRATION3 trafficking and disease susceptibility. *Nat Plants* 3: 854-858.

Mao, H., Nakamura, M., Viotti, C. and Grebe, M. (2016) A framework for lateral membrane trafficking and polar tethering of the PEN3 ATP-binding cassette transporter. *Plant Physiol*.

Miya, A., Albert, P., Shinya, T., Desaki, Y., Ichimura, K., Shirasu, K., et al. (2007) CERK1, a LysM receptor kinase, is essential for chitin elicitor signaling in Arabidopsis. *Proc Natl Acad Sci U S A* 104: 19613-19618.

Nawrath, C. and Metraux, J.P. (1999) Salicylic acid induction-deficient mutants of Arabidopsis express PR-2 and PR-5 and accumulate high levels of camalexin after pathogen inoculation. *Plant Cell* 11: 1393-1404.

Niittyla, T., Fuglsang, A.T., Palmgren, M.G., Frommer, W.B. and Schulze, W.X. (2007) Temporal analysis of sucrose-induced phosphorylation changes in plasma membrane proteins of Arabidopsis. *Mol Cell Proteomics* 6: 1711-1726.

Nuhse, T.S., Bottrill, A.R., Jones, A.M. and Peck, S.C. (2007) Quantitative phosphoproteomic analysis of plasma membrane proteins reveals regulatory mechanisms of plant innate immune responses. *Plant J* 51: 931-940.

Nuhse, T.S., Stensballe, A., Jensen, O.N. and Peck, S.C. (2004) Phosphoproteomics of the Arabidopsis plasma membrane and a new phosphorylation site database. *Plant Cell* 16: 2394-2405.

Ottenschlager, I., Wolff, P., Wolverton, C., Bhalerao, R.P., Sandberg, G., Ishikawa, H., et al. (2003) Gravity-regulated differential auxin transport from columella to lateral root cap cells. *Proc Natl Acad Sci U S A* 100: 2987-2991.

Poncini, L., Wyrsch, I., Denervaud Tendon, V., Vorley, T., Boller, T., Geldner, N., et al. (2017) In roots of Arabidopsis thaliana, the damage-associated molecular pattern AtPep1 is a stronger elicitor of immune signalling than flg22 or the chitin heptamer. *PLoS One* 12: e0185808.

Rashotte, A.M., Poupart, J., Waddell, C.S. and Muday, G.K. (2003) Transport of the two natural auxins, indole-3-butyric acid and indole-3-acetic acid, in Arabidopsis. *Plant Physiol* 133: 761-772.

Ruzicka, K., Strader, L.C., Bailly, A., Yang, H., Blakeslee, J., Langowski, L., et al. (2010) Arabidopsis PIS1 encodes the ABCG37 transporter of auxinic compounds including the auxin precursor indole-3-butyric acid. *Proc Natl Acad Sci U S A* 107: 10749-10753.

Schlicht, M., Ludwig-Muller, J., Burbach, C., Volkmann, D. and Baluska, F. (2013) Indole-3-butyric acid induces lateral root formation via peroxisome-derived indole-3-acetic acid and nitric oxide. *New Phytol* 200: 473-482.

Silva, N.F. and Goring, D.R. (2002) The proline-rich, extensin-like receptor kinase-1 (PERK1) gene is rapidly induced by wounding. *Plant Mol Biol* 50: 667-685.

Snider, J., Hanif, A., Lee, M.E., Jin, K., Yu, A.R., Graham, C., et al. (2013) Mapping the functional yeast ABC transporter interactome. *Nat Chem Biol* 9: 565-572.

Spaepen, S. and Vanderleyden, J. (2011) Auxin and plant-microbe interactions. *Cold Spring Harb Perspect Biol* 3.

Splivallo, R., Fischer, U., Gobel, C., Feussner, I. and Karlovsky, P. (2009) Truffles regulate plant root morphogenesis via the production of auxin and ethylene. *Plant physiology* 150: 2018-2029.

Stein, M., Dittgen, J., Sanchez-Rodriguez, C., Hou, B.H., Molina, A., Schulze-Lefert, P., et al. (2006) Arabidopsis PEN3/PDR8, an ATP binding cassette transporter, contributes to nonhost resistance to inappropriate pathogens that enter by direct penetration. *Plant Cell* 18: 731-746.

Strader, L.C. and Bartel, B. (2009) The Arabidopsis PLEIOTROPIC DRUG RESISTANCE8/ABCG36 ATP binding cassette transporter modulates sensitivity to the auxin precursor indole-3-butyric acid. *Plant Cell* 21: 1992-2007.

Strader, L.C. and Bartel, B. (2011) Transport and metabolism of the endogenous auxin precursor indole-3-butyric acid. *Mol Plant* 4: 477-486.

Underwood, W. and Somerville, S.C. (2013) Perception of conserved pathogen elicitors at the plasma membrane leads to relocalization of the Arabidopsis PEN3 transporter. *Proc Natl Acad Sci U S A* 110: 12492-12497.

Underwood, W. and Somerville, S.C. (2017) Phosphorylation is required for the pathogen defense function of the Arabidopsis PEN3 ABC transporter. *Plant Signal Behav* 12: e1379644.

van Noorden, G.E., Ross, J.J., Reid, J.B., Rolfe, B.G. and Mathesius, U. (2006) Defective long-distance auxin transport regulation in the Medicago truncatula super numeric nodules mutant. *Plant Physiol* 140: 1494-1506.

Veerabagu, M., Elgass, K., Kirchler, T., Huppenberger, P., Harter, K., Chaban, C., et al. (2012) The Arabidopsis B-type response regulator 18 homomerizes and positively regulates cytokinin responses. *Plant J* 72: 721-731.

Wang, B., Bailly, A., Zwiewka, M., Henrichs, S., Azzarello, E., Mancuso, S., et al. (2013) Arabidopsis TWISTED DWARF1 functionally interacts with auxin exporter ABCB1 on the root plasma membrane. *Plant Cell* 25: 202-214.

Woodward, A.W. and Bartel, B. (2005) Auxin: regulation, action, and interaction. *Ann Bot (Lond)* 95: 707-735.

Xin, X.F., Nomura, K., Underwood, W. and He, S.Y. (2013) Induction and suppression of PEN3 focal accumulation during Pseudomonas syringae pv. tomato DC3000 infection of Arabidopsis. *Mol Plant Microbe Interact* 26: 861-867.

Yamada, K., Yamaguchi, K., Shirakawa, T., Nakagami, H., Mine, A., Ishikawa, K., et al. (2016) The Arabidopsis CERK1-associated kinase PBL27 connects chitin perception to MAPK activation. *EMBO J* 35: 2468-2483.

Zhu, J., Bailly, A., Zwiewka, M., Sovero, V., Di Donato, M., Ge, P., et al. (2016) TWISTED DWARF1 Mediates the Action of Auxin Transport Inhibitors on Actin Cytoskeleton Dynamics. *Plant Cell* 28: 930-948.

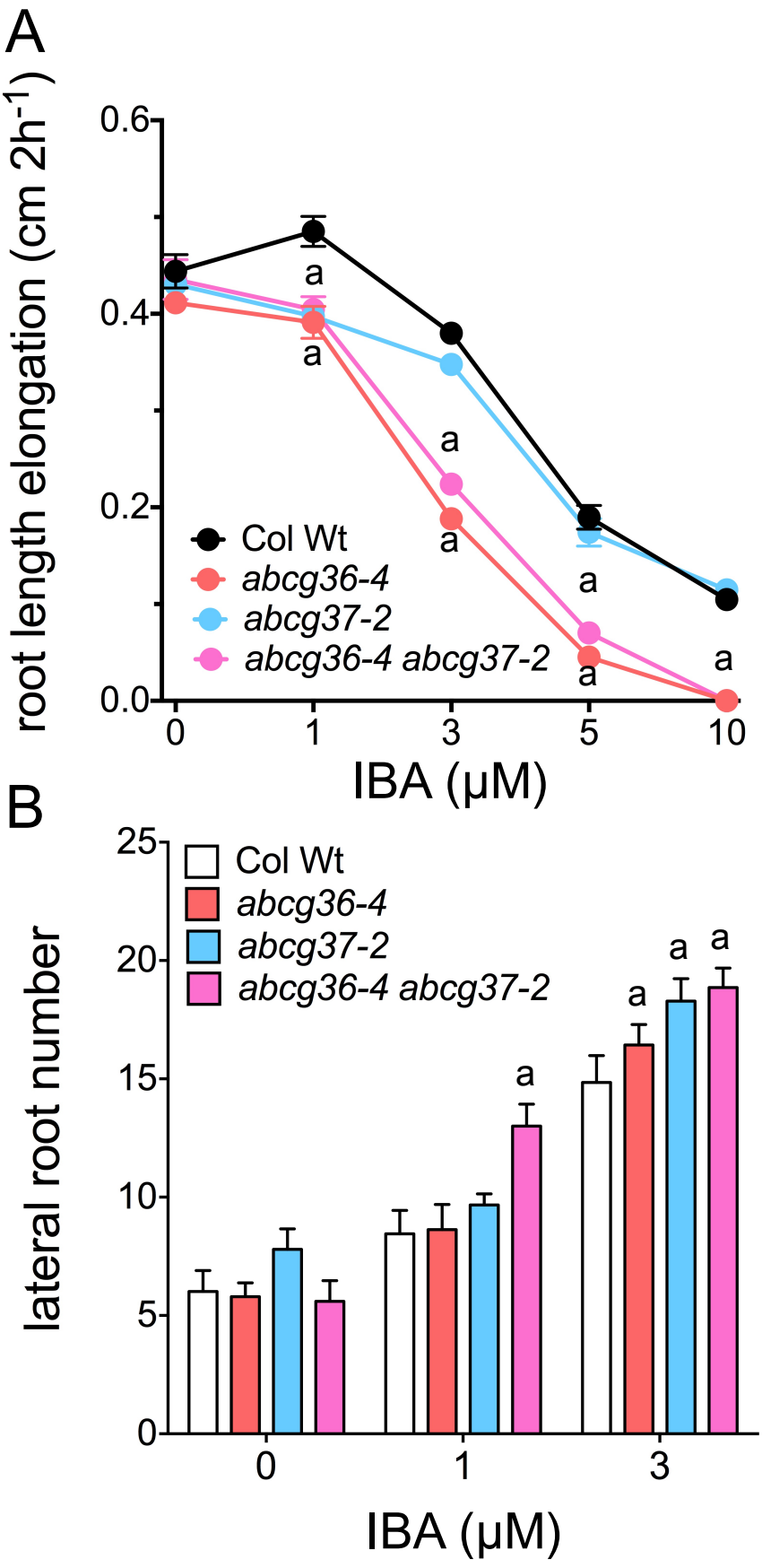

Aryal et al_Fig. 1

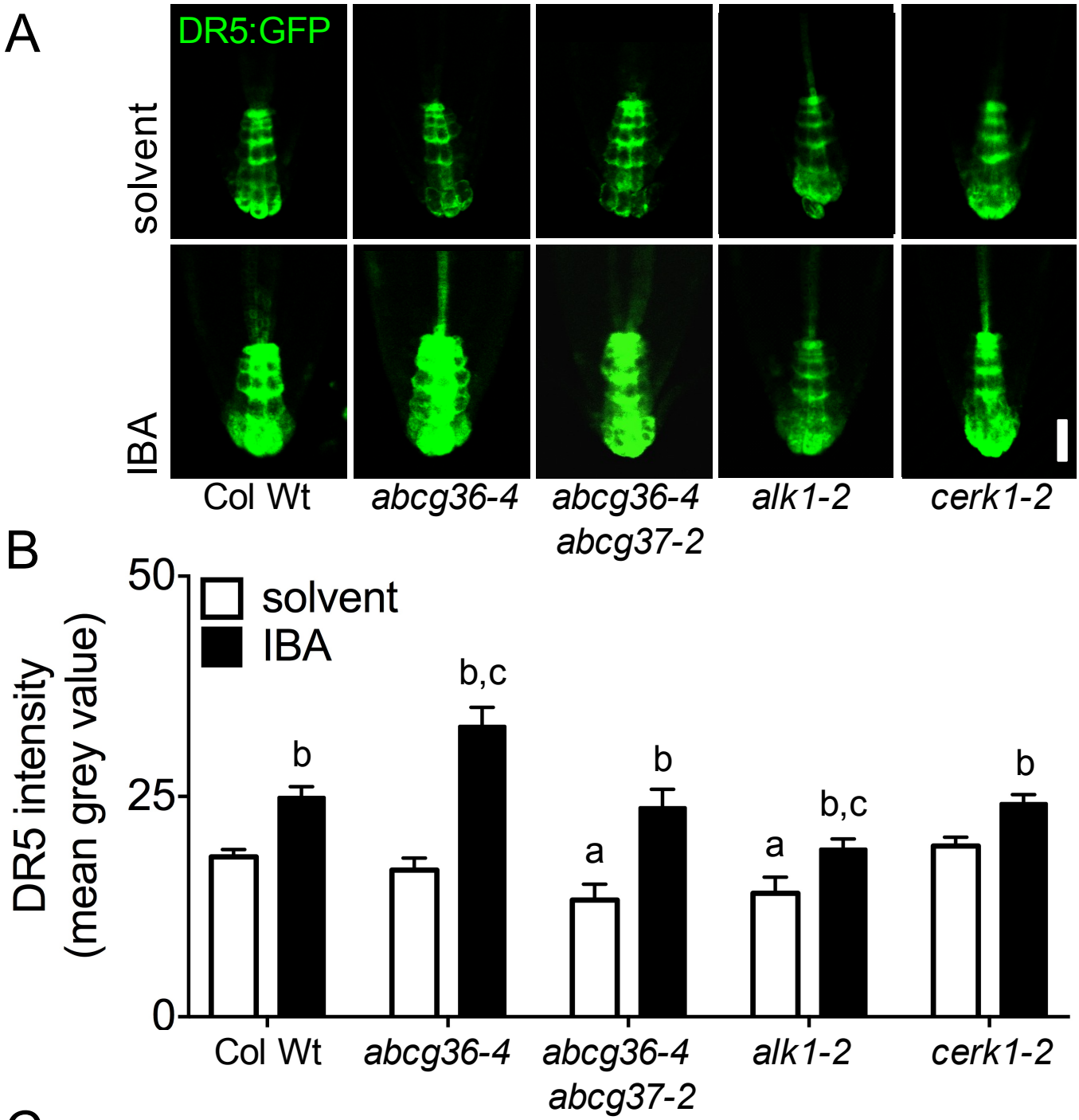

Aryal et al_Fig. 2

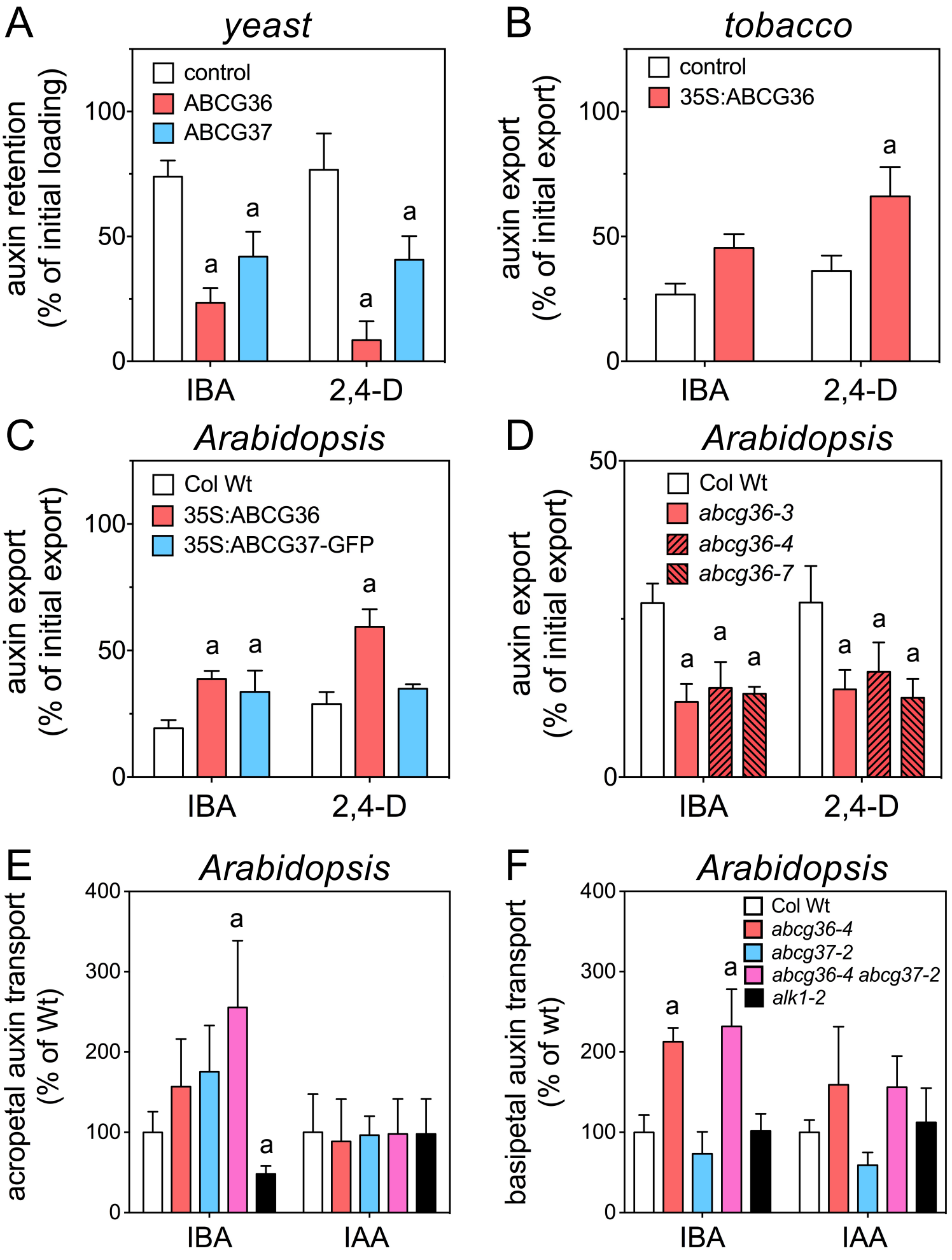

Aryal et al_Fig. 3

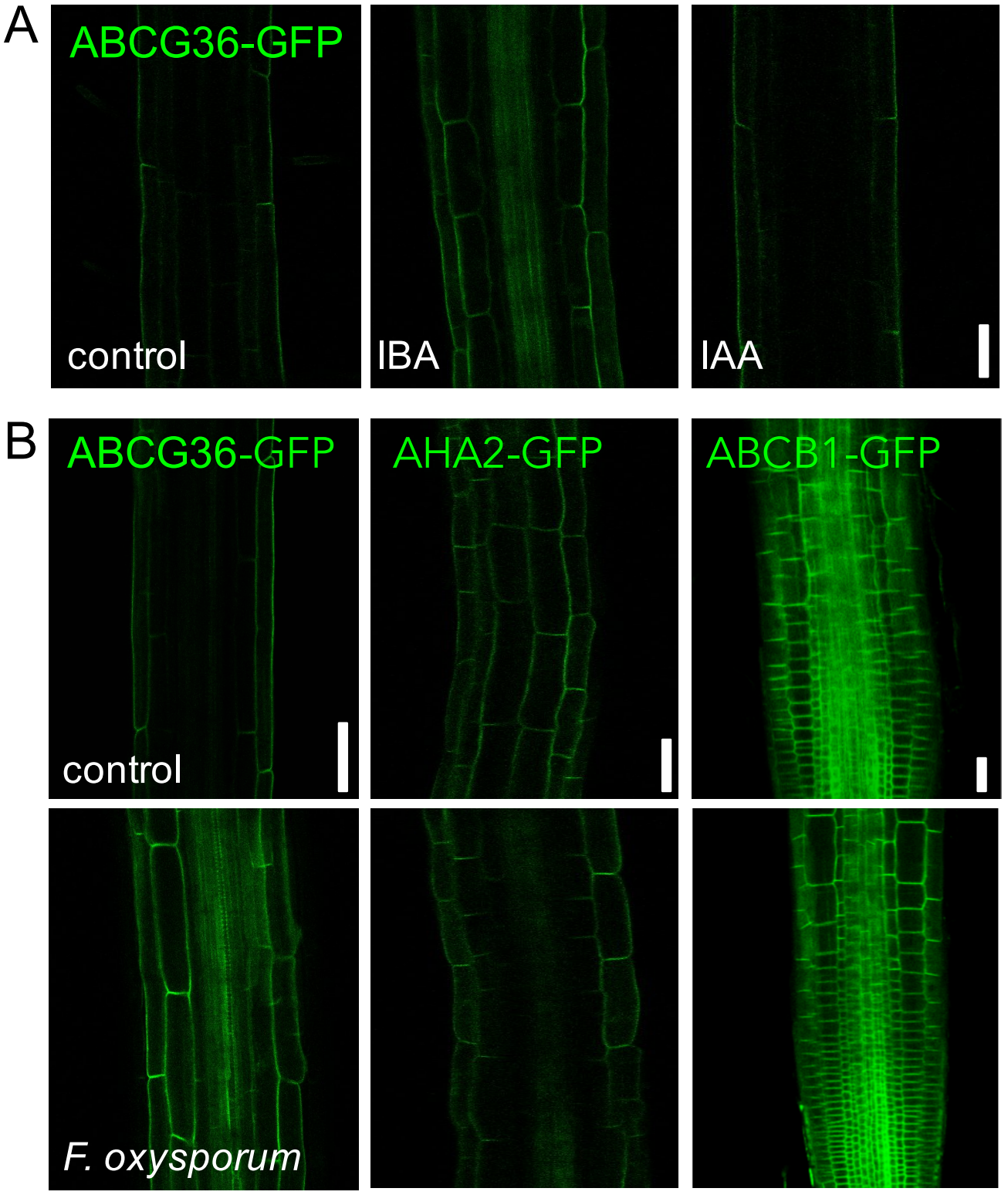

Aryal et al. Fig. 4

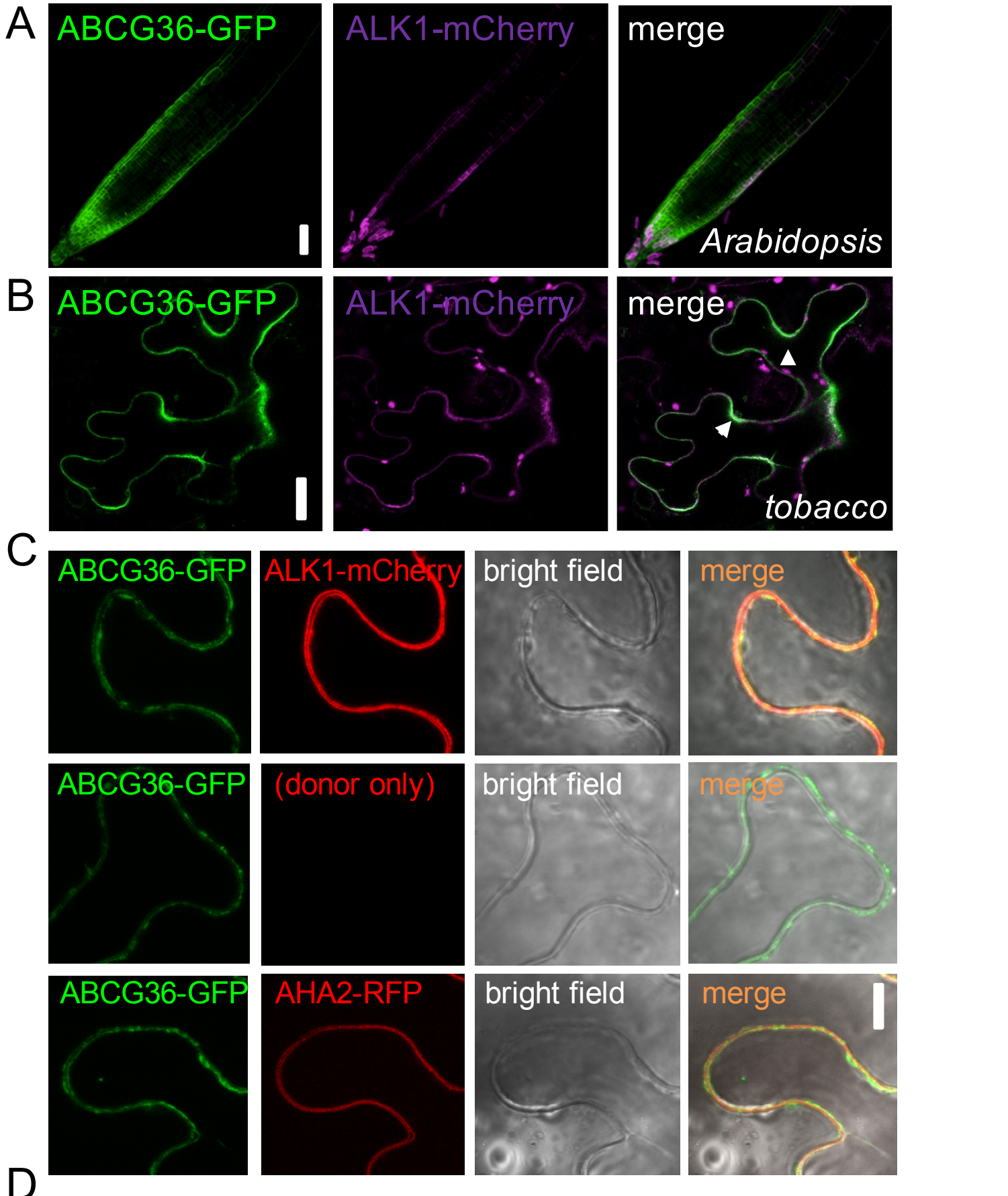

Aryal et al. Fig. 5

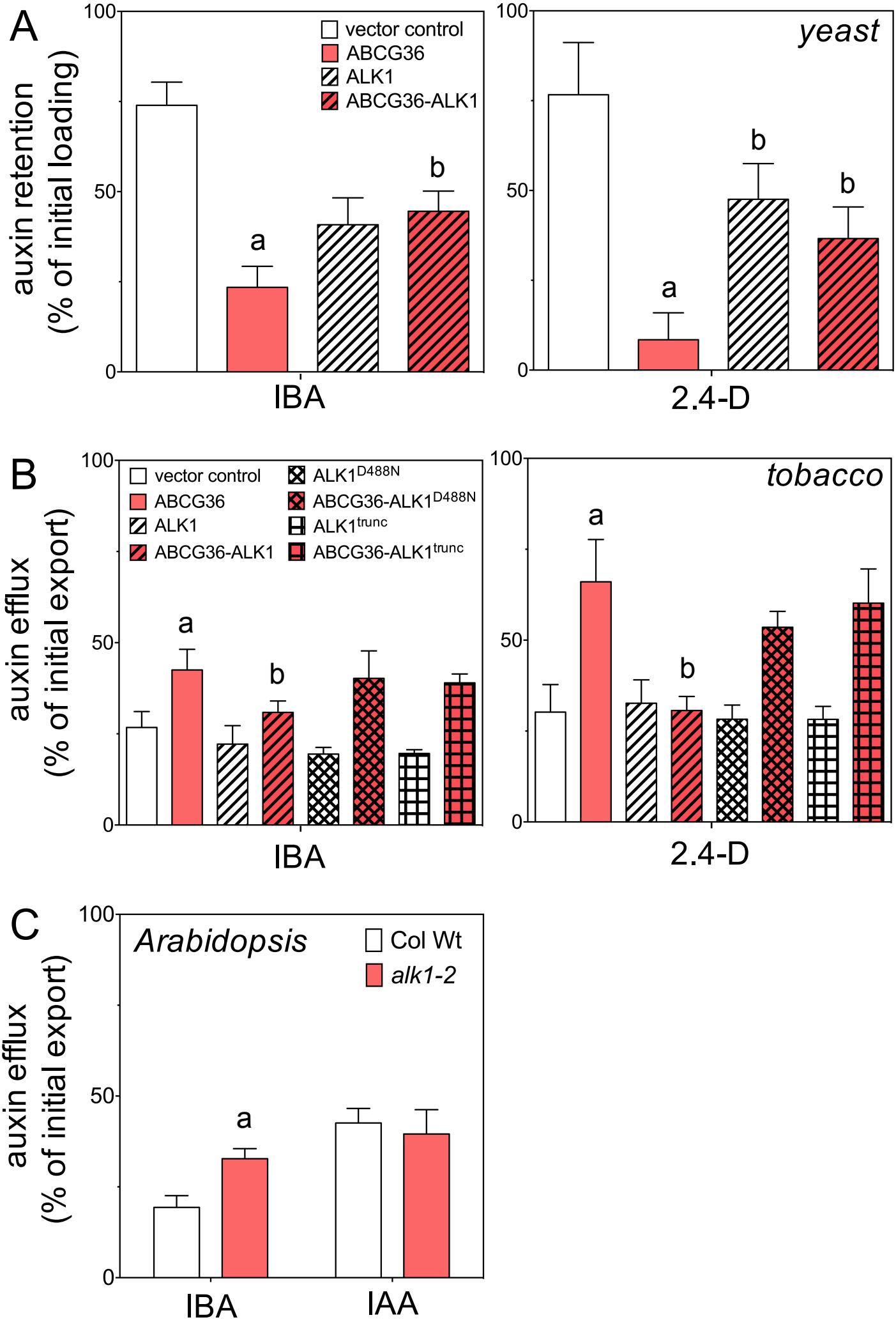

Aryal et al. Fig. 6

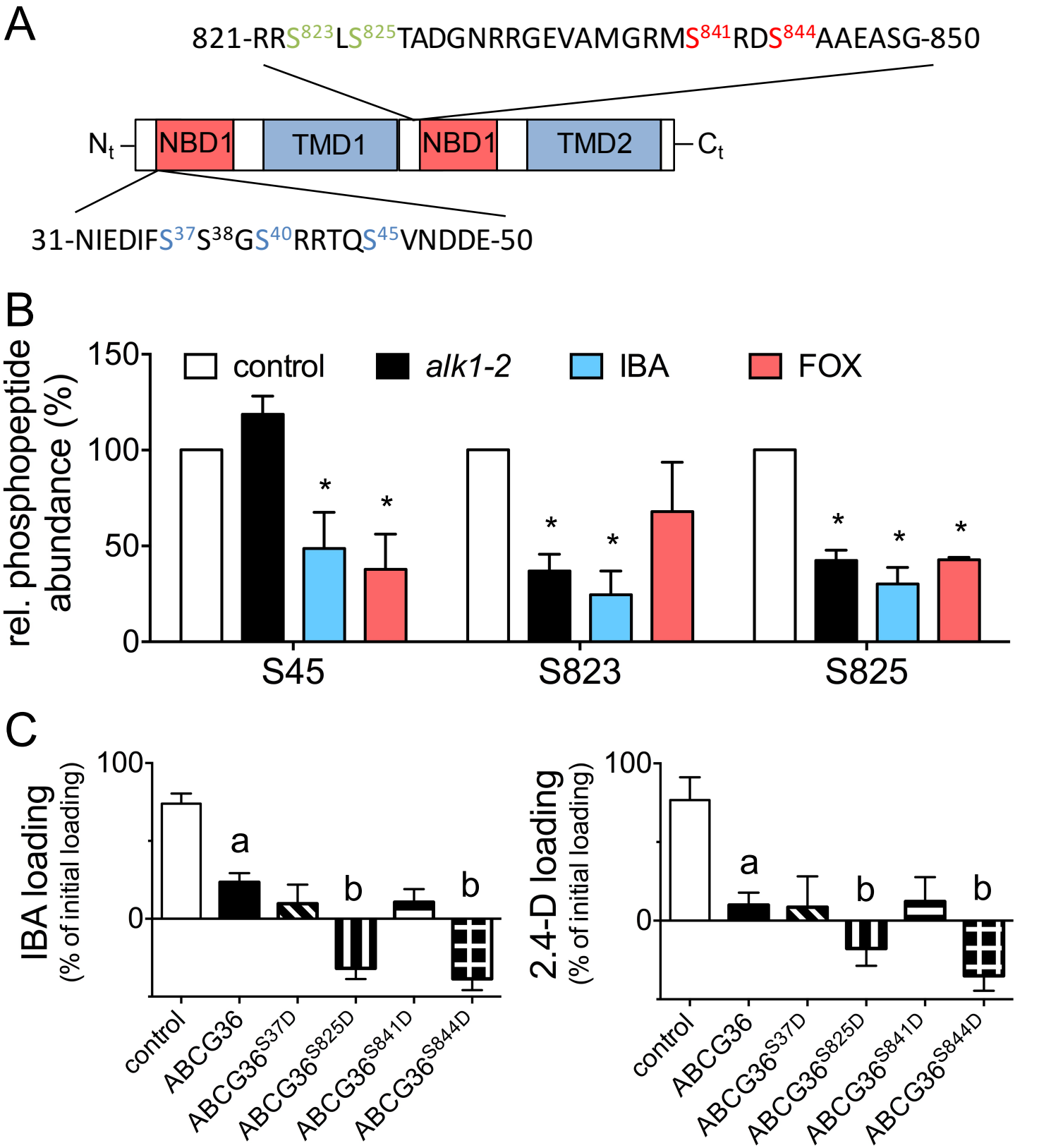

Aryal et al. Fig. 7

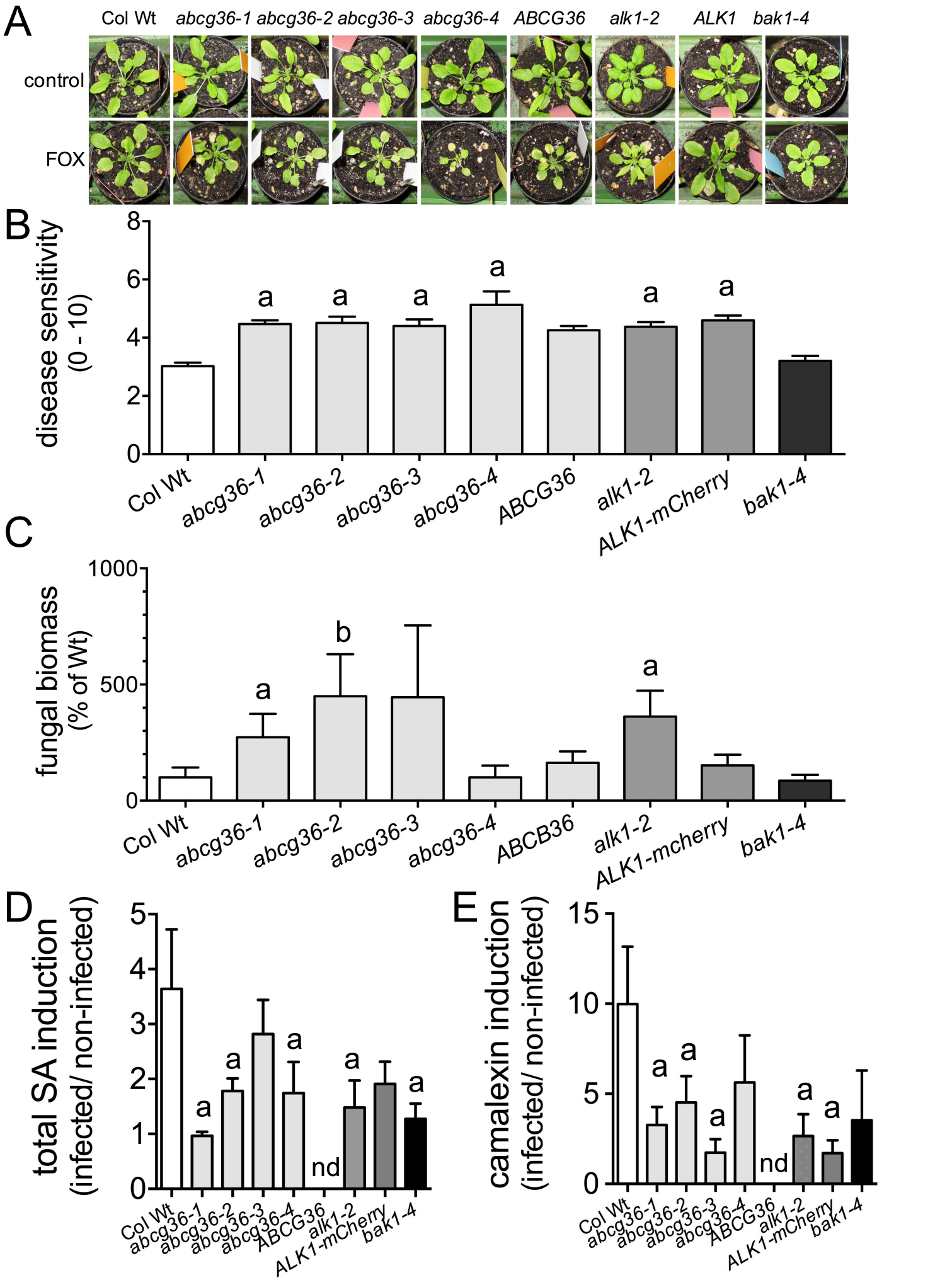

Aryal et al. Fig. 8

Supplementary Figures

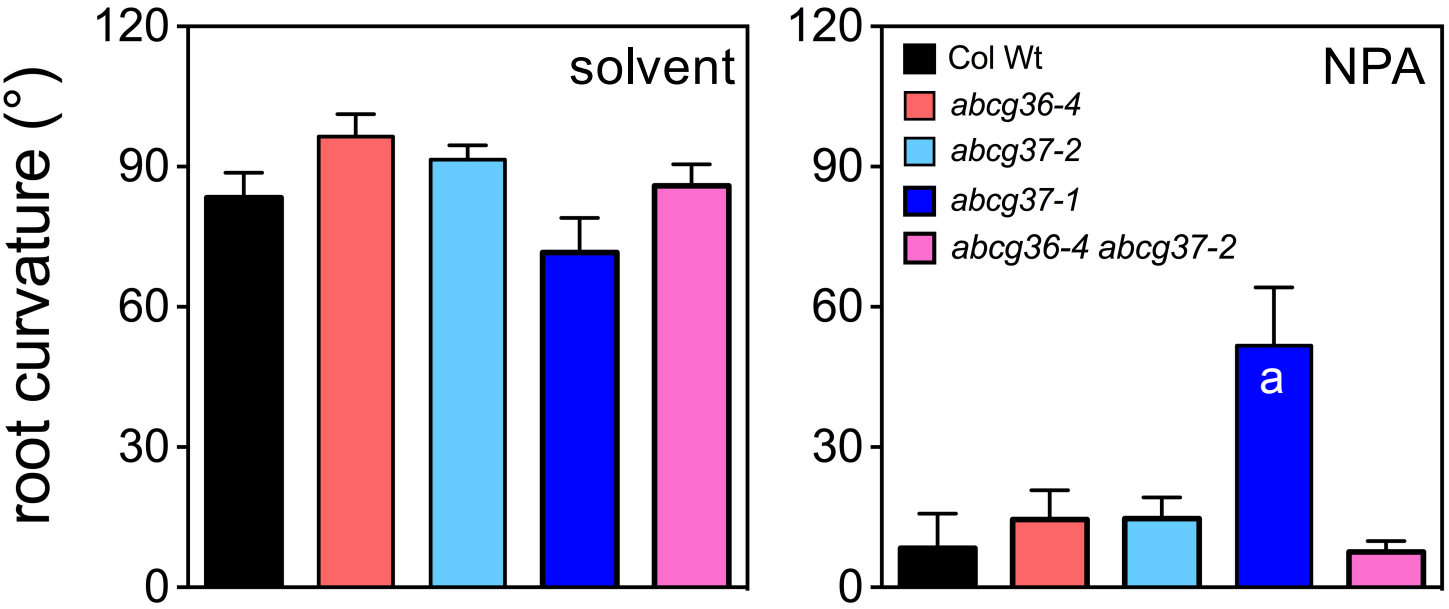

Supplementary Figure 1: ABCG36 and ABCG37 do not have a significant impact on root bending

For root length elongation assays, 5 dag seedlings were transferred to solvent control or NPA (10 µM) plates, and root bending angles was judged after 12h in the dark. Significant differences (unpaired *t* test with Welch's correction, $p < 0.05$) between wild-type and mutant alleles are marked with 'a' (means ± SE; n = 4 sets of 20 seedlings each).

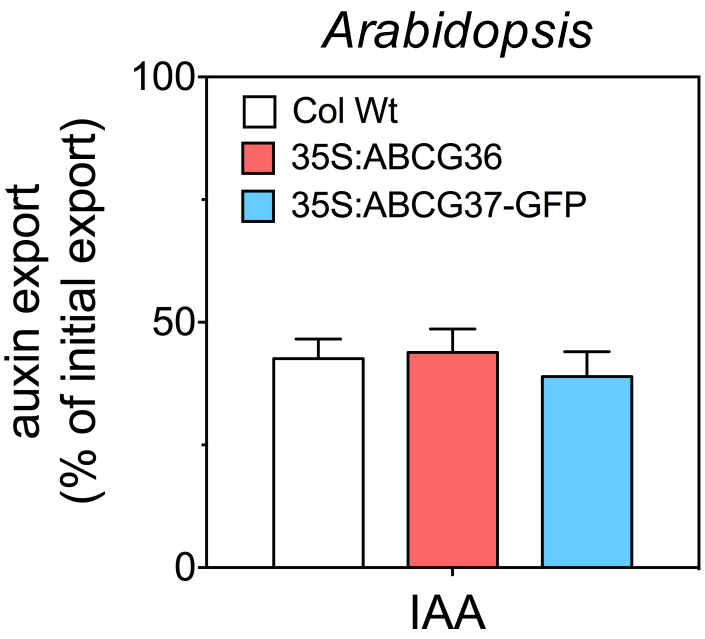

Supplementary Figure 2: Neither ABCG36 nor ABCG37 transport IAA.
Efflux of IAA from protoplasts prepared from stable Arabidopsis *ABCG36* and *ABCG37* gain-of-function (35S:ABCG36/ABCG37-GFP) lines. Significant differences (unpaired *t* test with Welch's correction, $p < 0.05$) between wild type and mutant alleles are indicated by an 'a' (mean ± SE; $n \geq 4$ independent protoplast preparations).

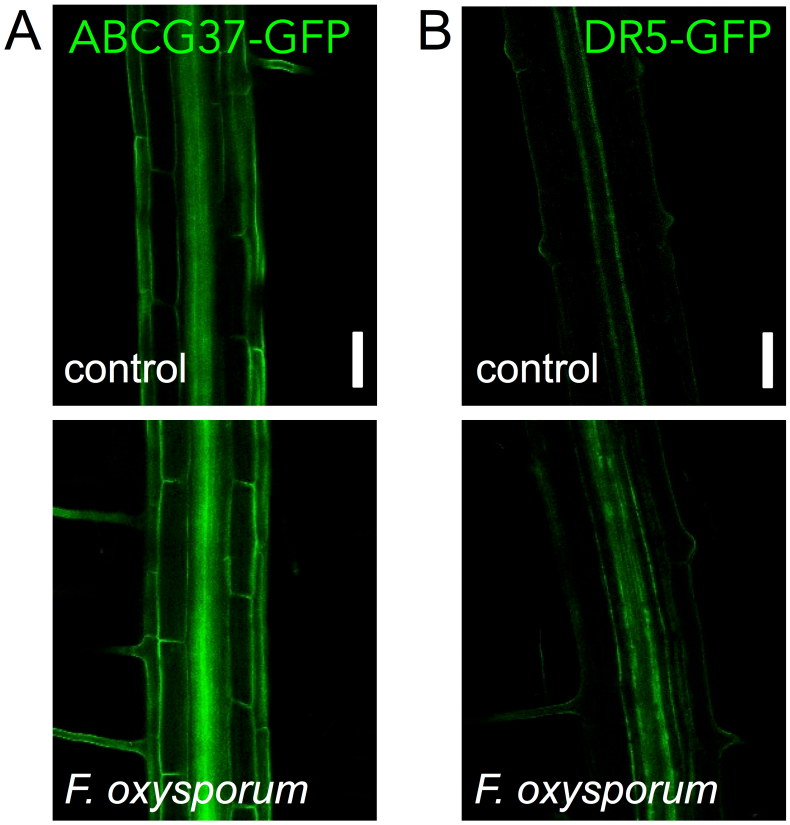

C

	GFP intensity mock	GFP intensity Fox
left epidermis	21.05	77.89
stele	4.66	42.59
right epidermis	20.85	60.72
mean (left + right epidermis)	20.95	69.31
epidermis/ stele (ratio)	4.5	1.63

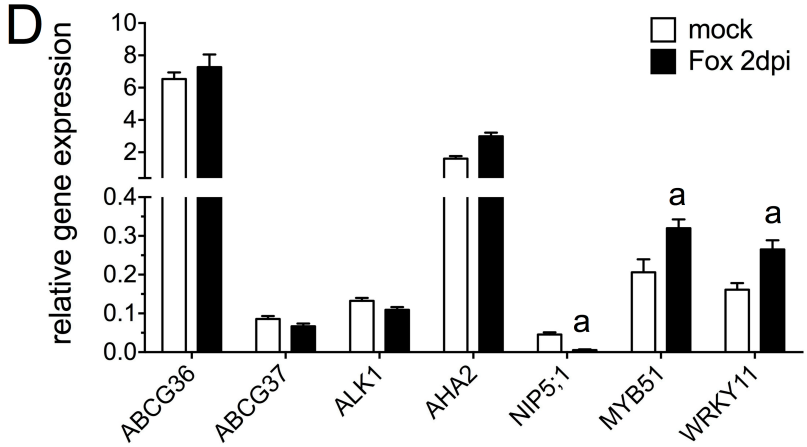

Supplementary Figure 3: *Fusarium* root infection up-regulates ABCG37 expression and auxin responses.

(A) ABCG37-GFP (35S:ABCG37-GFP) was imaged 48h after *F. oxysporum* infection in comparison with buffer control (control). Bars, 100 µm.

(B) Root auxin responses visualized by imaging the auxin-responsive element DR5-GFP in the ro ot 48h after *F. oxysporum* infection in comparison with buffer control (control). Bars, 100 µm.

(C) Quantification of local ABCG36-GFP intensities 48h after *F. oxysporum* infection (Fox) in comparison with buffer control (mock). Epidermal and stele GFP signals were quantified using a self-written Fiji plug-in (for details, see Methods).

(D) Quantification of relative root expression of indicated gene transcripts upon *F. oxysporum* infection. Significant differences (unpaired *t* test with Welch's correction, $p < 0.05$) between *Fusarium* infected roots (Fox) and non-infected roots (mock) are indicated by 'a' (mean ± SE; n =3).

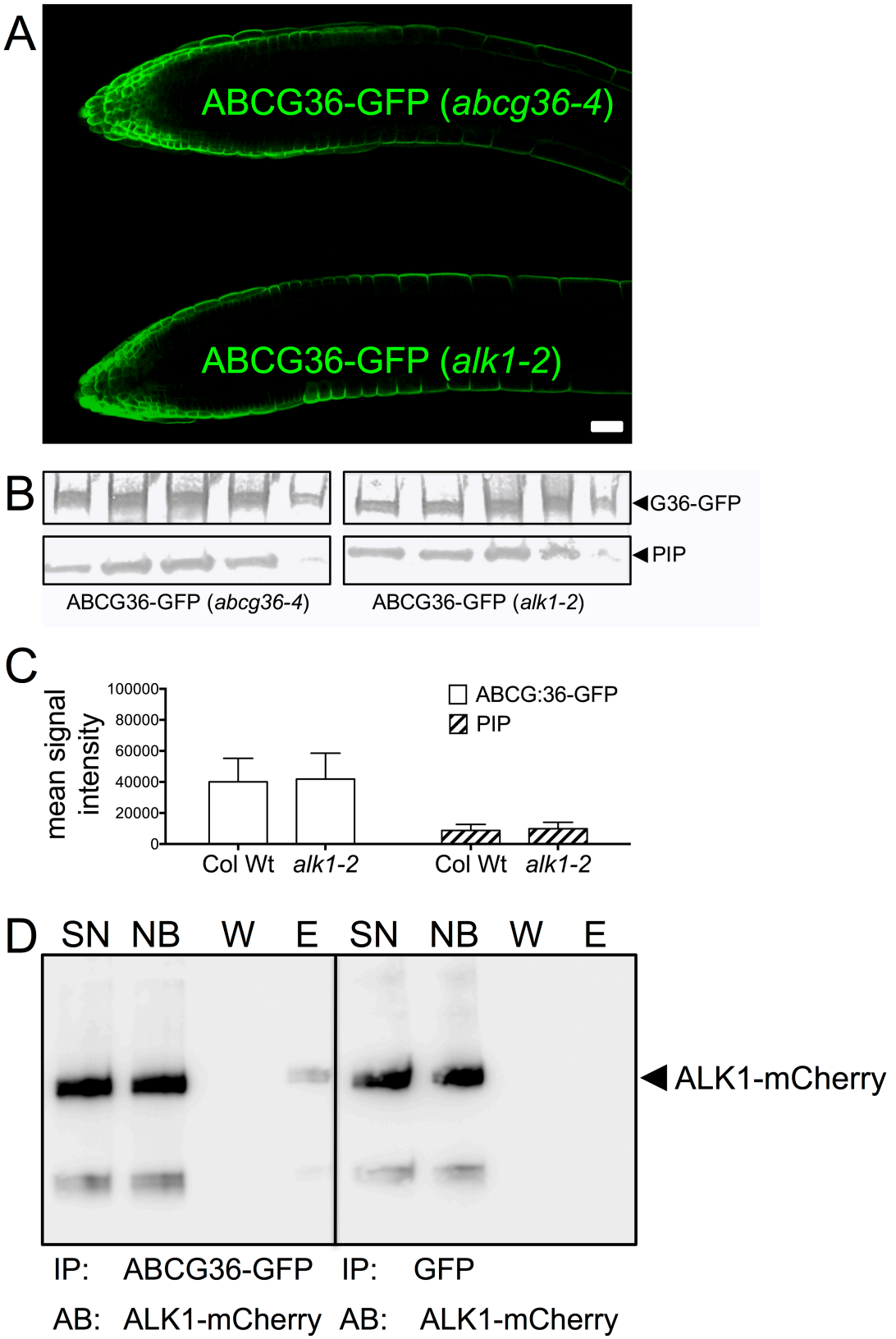

Supplementary Figure 4: ALK1 does not alter ABCG36-GFP expression and location.
(A) ABCG36-GFP (PEN3:PEN3-GFP) expression and location is not significantly altered in roots of *alk1-2* compared to the complemented mutant line (*abcg36-4*). Bar, 100 µm.
(B-C) ABCG36-GFP (PEN3:PEN3-GFP) expression is not significantly altered in seedling of *alk 1-2* compared to the complemented mutant line (*abcg36-4*) based on Western analyses of PM-fr actions isolated by linear sucrose gradient fractionation. PM fractions were determined by emplo ying the PM marker aquaporin, PIP1 (Kammerloher et al. 1994). ABCG36-GFP and PIP1 bands of three independent Western blots were quantified and revealed no significant differences betw een complemented line (Col Wt) and *alk1-2* (**C**).
(D) Co-immunoprecipitation (IP) of ABCG36-GFP (PEN3:PEN3-GFP) or free GFP after co-transfection with ALK1-mCherry (35S:ALK1-mCherry) in *N. benthamiana*. Note that band of the expected size of roughly 100 kDa for ALK1-mCherry is found in the elution (E) for the IP with ABCG36-GFP but not with free GFP.

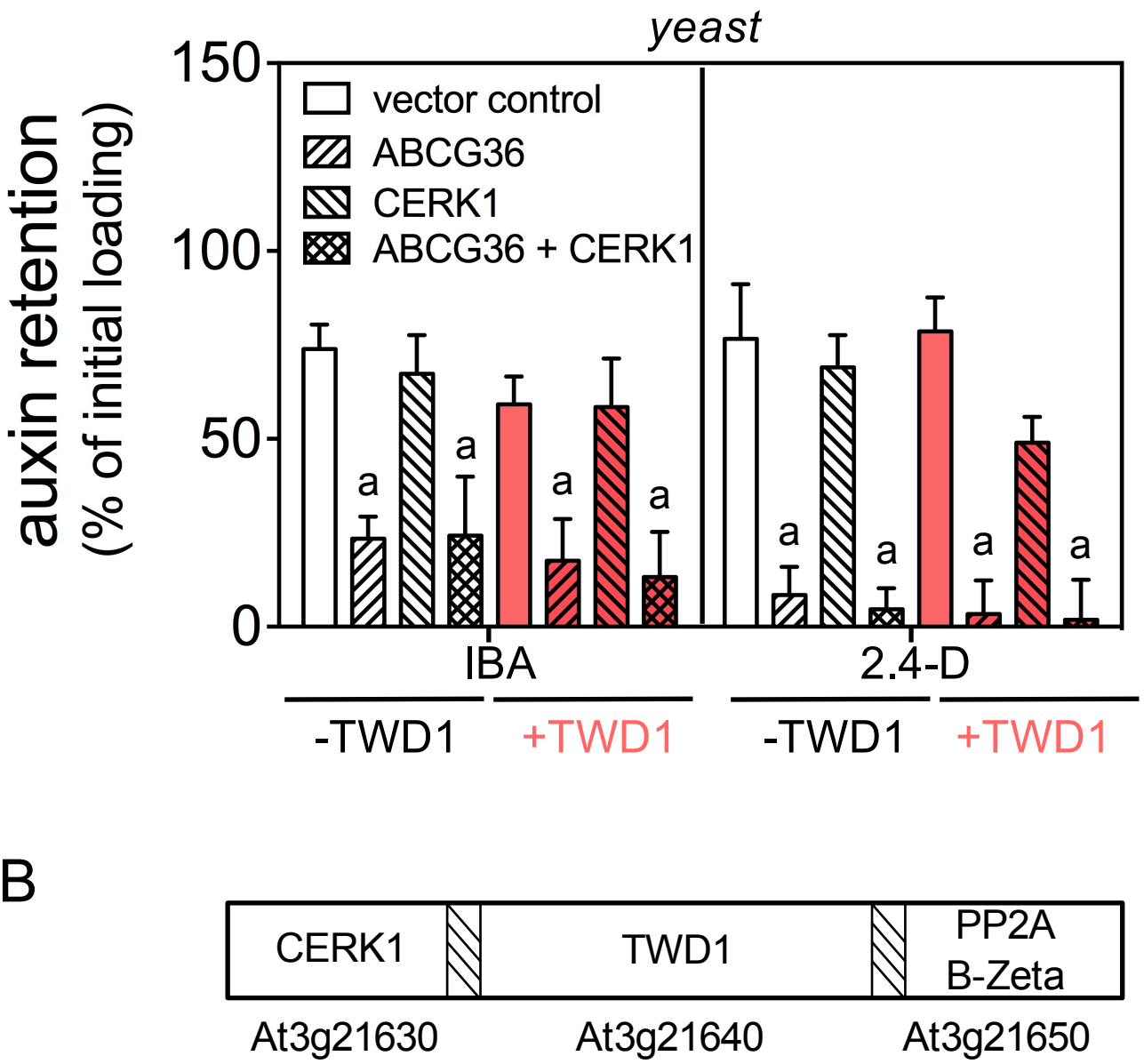

B

Supplementary Figure 5: Co-expression of CERK1 with or without TWD1 does not alter ABCG36-mediated auxin efflux

(A) Neither co-expression of CERK1 or TWD1 nor triple expression with CERK1 and TWD1 significantly effected ABCG36-mediated IBA or 2.4-D export in yeast, determined as increase of auxin retention. Significant differences (unpaired *t* test with Welch's correction, $p < 0.05$) to vector control or ABCB36 are indicated by 'a' and 'b', respectively (mean ± SE; $n \geq 6$ independent transformations).

(B) CERK1 (At3g21630) is a down-stream gene of TWD1 (At3g21640) on chromosome 3. Information taken from TAIR (https://www.arabidopsis.org).

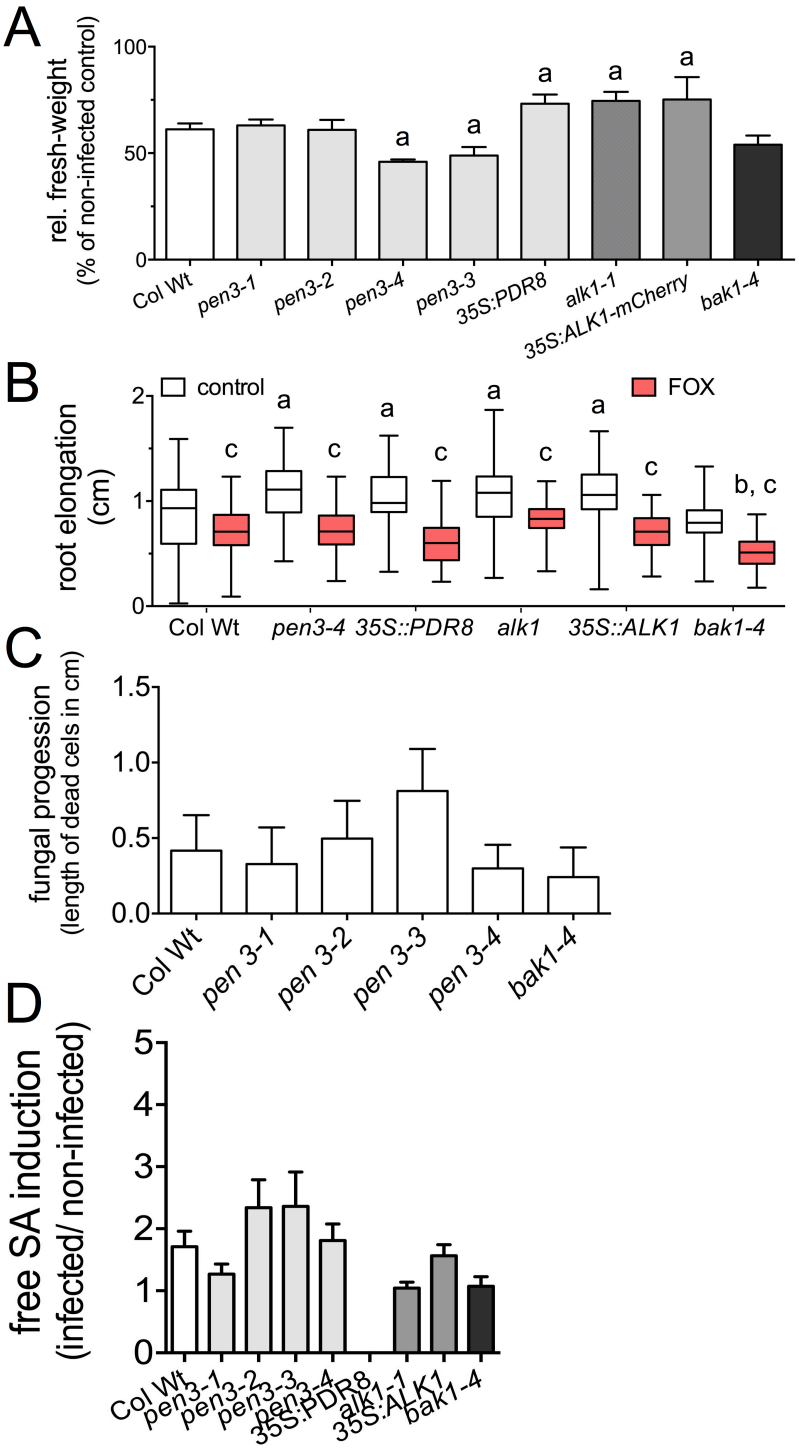

Supplementary Figure 6: Mutations in *ABCG36* and *ALK1* reduce plant fresh-weight but have no significant effect on inhibition of root elongation by *F. oxysporum*, fungal progression and free salicylic acid induction.

(A) Leaf fresh weight of soil-infected plants. Significant differences between means ± SE (n = 3 independent infections; unpaired *t* test with Welch's correction, $p < 0.05$) to non-infected wild-type (set to 100%) are indicated by 'a'.

(B) Arabidopsis seedlings were infected on plate 4 dag with *F. oxysporum* (FOX) and root elongation was monitored 48 hpi. Significant differences (unpaired *t* test with Welch's correction, $p < 0.0001$) to Wt control, infected Wt or non-infected control are indicated by 'a', 'b' or 'c' (mean ± SE; n = 3 independent infections).

(C) Fungal progression of 3 dpi seedling roots was monitored by Evans blue stain (means ± SE; n = 3 independent infections).

(D) HPLC quantification of free salicylic acid from soil-infected and non-infected leaves (mean ± SE; n ≥ 7 HPLC analyses).

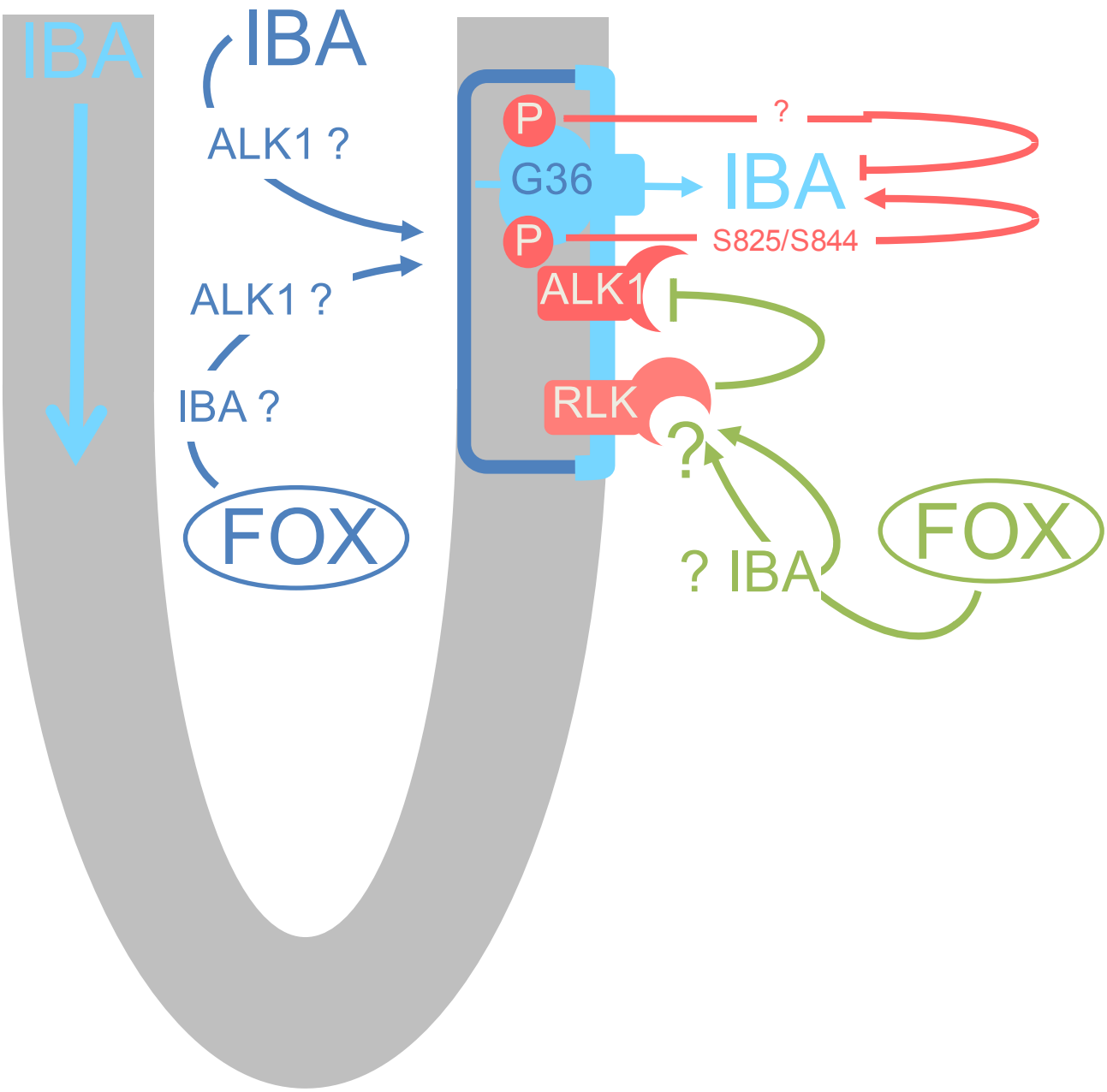

Supplementary Figure 7: Putative model on the role of ABCG36 in polar transport of IBA and the regulatory impact of ALK1 on ABCG36 transport activity.
The current work suggests that ABCG36 contributes to the root-ward (acropetal) transport of IBA, which seems to be shared by ABCG37. Lateral, outward-facing PM expression in the root epidermis suggests lateral IBA excretion into the rhizosphere.
The LRR receptor-like kinase, ALK1, has a regulatory impact on ABCG36 IBA export activity (**red pathway**) that is dependent on its kinase activity. S825 and S844 have been identified as key residues that promote IBA export activity of ABCG36. However, co-expression with ALK1 results in ABCG36 transport inhibition suggesting the presence of so far unknown phosphorylation site(s) that have a negative impact.
Fusarium oxysporum root infection (**FOX**) and IBA (**IBA**) treatments likewise reduce ABCG36 phosphorylation via ALK1 (**green pathway**), suggesting the existence of a putative second LRR receptor-like kinase (**RLK**) might act as a receptor for a so far not identified ligand. The identity of this ligand as well as an involvement of IBA during *Fusarium* infection is currently unknown. *Fusarium oxysporum* (**FOX**) root infection and IBA treatments both alter ABCG36 expression and location (**blue pathway**), however, if this pathway employs the same ALK1 module is currently unknown.

target name	acc. number	primer sequences
ABCG36	*At1g59870*	fw: CAT GGA CCG TGT ATG GAG TG rev: AGA CGG TGA AAG CGA TGA GTG
ABCG37	*At3g53480*	fw: TTG CGA TGT TCC TCG TCT C rev: GAG TGT CCA AGA CGT TGG TG
ALK1	*At3g02880*	fw: AAC CGT ATT GAT GGC TAC CG rev: ACC CAT CTC GGC AAA TCT AC
AHA2	*At4g30190*	fw: GGC ACT TGC TCA AAG GAC AC rev: GCT TCA CGA CTG ATT CCA C
NIP5;1	*At4g10380*	fw: ATT GGC AGG TAT AGC CGT TG rev: GTA GAC CGC TGC ACC AGA TAT G
MYB51	*At1g18570*	fw: CTA CAA GTG TTT CCG TTG ACT CTG AA rev: ACG AAA TTA TCG CAG TAC ATT ACA GGA
WRKY11	*At4g31550*	fw: CCC ACG TGG TTA CTA CAA GTG C rev: TGG ATC ATC TAA TGC TCG TTC CAC
RHIP1 *(house-keeping gene)*	*At4g26410*	fw: GAG CTG AAG TGG CTT CCA TGA C rev: GGT CCG ACA TAC CCA TGA TCC
PRA2M *(DIG2 plasmid)*	-	fw: CGT CGT CCA TTA CTT TTC ACG rev: GTT TCT GTT CGC GGT AGA GC
F. oxysporum	-	fw: GCA GTC ACT AAC CAT TCA A rev: GGA (G/A)GT ACC AGT (G/C)A TCA TGT T

Supplementary Table 1: Forward (fw) and reverse (rev) primers used for real-time PCR analyses in this study.

acc. no.	name	putative function
At1g04820	TUBA4 (tubulin alpha-4 chain)	cytoskeleton
At5g09810	ACTIN7	cytoskeleton
At2g47000	ABCB4/ MDR4/ PGP4	facult. IAA ex/ importer
At3g53480	**ABCG37**	**exporter of auxinic compounds**
At1g13320	PP2A A3 (protein phosphatase 2A subunit A3)	put. protein phosphatase regulator
At1g51830	serine/threonine protein kinase	put. protein kinase
At3g02880	**LRR receptor-like kinase (ALK1)**	**put. LRR protein kinase, IAA-induced**
At1g13320	**CERK1 (Chitin elicitor receptor kinase 1)**	**LysM receptor kinase**
At3g24550	PERK1 (Proline extensin-like receptor kinase 1)	Prolin-extensin-like receptor kinase

Supplementary Table 2: ABCG36 interacting proteins identified by co-immunoprecipitation followed by MS/MS analyses using ABCG36-GFP as bait. MASCOT-identified vector control proteins (free GFP) were subtracted manually from ABCG36-GFP-interacting proteins and hits from three independent co-IP/MS analyses were grouped according to their putative function. 9 putative ABCG36 interactors were identified in all 3 co-IPs. Relevant proteins for this study are marked in bold.

A.2.2 *Flower-in-flower*, a novel LEAFY allele

The striking flower-in-flower phenotype of *Arabidopsis thaliana* Nossen (No-0) is caused by a novel LEAFY allele

Submitted

This article describes a novel mutation in LEAFY (LFY), a trancriptional regulator that promotes the transition to flowering. During the vegetative growth phase, LFY expression increases in the newly formed leaves until a certain threshold is reached and thus initiates flowering. Additionally, functional LFY is involved in the floral meristem development by activation of the ABC patterning factor APETALA3. The *flower-in-flower fif* phenotype is cauesed by a cysteine-to-tyrosine exchange in the α1-helix of the LFY DNA-binding domain. LFY^{FIF} can not bind to the DNA anymore, but is still able to form homotypic (LFY-LFY, LFY^{FIF}-LFY^{FIF}) and heterotypic (LFY-LFY^{FIF}) homomers. Consequently, the non-binding LFY^{FIF} protein can additionally titrate functional, DNA-binding LFY proteins away. This model provides an explanation for the observed dominant-negativ effect on the plant morphology.

The striking *flower-in-flower* phenotype of *Arabidopsis thaliana* Nossen (No-0) is caused by a novel *LEAFY* allele

Anne Mohrholz[1], Hequan Sun[2], Nina Glöckner[1], Sabine Hummel[1], Üner Kolukisaoglu[1], Korbinian Schneeberger[2], Klaus Harter[1*]

[1]*Department of Plant Physiology, Center for Plant Molecular Biology, Universität Tübingen, 72076 Tübingen, Germany*

[2] *Department of Plant Developmental Biology, Max Planck Institute for Plant Breeding Research, 50829 Cologne, Germany*

*For correspondence (e-mail Klaus.harter@zmbp.uni-tuebingen.de)

Summary

The transition to reproduction is a crucial step in the life cycle of any organism. In *Arabidopsis thaliana* the establishment of reproductive growth can be divided into two phases: In the first phase, cauline leaves with axillary meristems are formed and internode elongation begins. In the second phase, lateral meristems develop into flowers with defined organs. Floral shoots are usually determinate and suppress the development of lateral shoots. Here, we describe a *Ds* transposon insertion mutant in the Nossen (No-0) accession with severe defects in floral development and flower morphology. The most striking aspect is the outgrowth of stems from the axillary bracts of the primary flower carrying terminal secondary flowers. Therefore, we named this mutant *flower-in-flower* (*fif*). However, the insertion of the transposon in the annotated gene is not responsible for the *fif* phenotype. By means of classical and genome sequencing-based mapping, the mutation responsible for the *fif*

phenotype was found to be in the *LEAFY* (*LFY*) gene. The mutation, a G-to-A exchange in the second exon of *LFY*, creates a novel *lfy* allele and causes a cysteine-to-tyrosine exchange in the α1-helix of the LFY DNA-binding domain. Whereas subcellular localization and homomerization are not affected, the DNA-binding of LFY^{FIF} is abolished. We propose that the amino acid exchange interferes with the cooperative binding of LFY to its target DNA. To generate the strong *fif* phenotype, LFY^{FIF} may act dominant-negatively by either forming non-binding LFY/LFY^{FIF} heteromers or by titrating out the interaction partners, required for LFY function as transcription factor.

Keywords: *Arabidopsis thaliana*, floral development, flower morphology, *Ds* transposon, classical/sequencing-based mapping, *LEAFY*, DNA-binding

Significant Statement: The *fif* phenotype of *Arabidopsis thaliana* No-0 is caused by a novel allele of the *LEAFY* gene

Introduction

The development of flowers is indispensable for the reproductive success of angiosperm plants. During vegetative growth, the shoot apical meristem (SAM) develops leaves and/or branches, the latter with their own SAMs. After the switch to reproductive growth, the apical meristems give rise to flowers. Floral development differs crucially from vegetative shoot growth, as the flower possesses several types of organs of which the number, arrangement and morphology are species-specific. Furthermore, the development of lateral shoots is inhibited in flowers and floral shoots are determinate after the last reproductive organs have been initiated (Piñeiro

and Coupland, 1998; Ma, 1998; Pidkowich *et al.*, 1999). Thus, the coordination of complex molecular processes is necessary for successful floral development.

There has been significant progress in recent years towards understanding the molecular mechanisms underlying flower formation. Central to this was the identification and cloning of the genes that initiate and maintain floral development in plant species, including *Arabidopsis thaliana*. The most intriguing discovery was the *Arabidopsis* loss-of-function mutants with structures that are intermediate between floral and vegetative shoots. The cloning of the corresponding genes revealed the existence of the master regulators required for the floral initiation process (FLIP). To date, five FLIP regulatory master genes are known: *LEAFY* (*LFY*), *APETALA1* (*AP1*), *CAULIFLOWER* (*CAL*), *APETALA2* (*AP2*) and *UNUSUAL FLORAL ORGANS* (*UFO*) (Pidkowich *et al.*, 1999). *LFY* and *AP1* play a primary role in initiating the floral program, as the corresponding loss-of-function mutants do not generate shoots with floral characteristics and the ectopic expression of either gene induces precocious flower formation (Irish and Sussex, 1990; Huala and Sussex, 1992; Bowman *et al.*, 1993). Based on its amino acid similarity and expression characteristics *CAL* appears to be functionally redundant to *AP1* (Kempin *et al.*, 1995). *LFY*, *AP1* and *CAL* encode for transcription factors and are expressed predominantly in floral primordia (Weigel *et al.*, 1992; Mandel *et al.*, 1992; Kempin *et al.*, 1995).

During plant vegetative growth, *LFY* expression increases in newly formed leaves until a certain threshold is reached (Bowmann *et al.*, 1993). LFY then induces the expression of *AP1*/*CAL* genes by binding to the *AP1*/*CAL* promoters. Through their mutual transcriptional up-regulation, LFY and AP1/CAL cooperate to cause the floral transition (Blazquez *et al.*, 2006). Once the floral meristem is established, the FLIP gene functions govern its spatial patterning by inducing the expression of the floral homeotic *ABC* genes, such as *AP2*, *AP3*, *Pistillata* (*PI*) and *AGAMOUS* (*AG*). The

ABC gene functions in turn control the identity of the stereotypically arranged *Arabidopsis* floral organs (Coen and Meyerowitz, 1991; Lohmann and Weigel, 2002). In the course of our study of the influence of abiotic stress on flower symmetry, we searched for novel insertion mutants with defects in floral development or morphology in different *Arabidopsis thaliana* accessions. We focused on genes that had not yet been linked to flowering. A *Ds* transposon insertion mutant, which developed secondary inflorescences with partially aberrant flowers, was identified in the No-0 accession . The wild-type allele of the gene carrying the *Ds* transposon codes for a cystein/histidine-rich C1 domain protein (Shinya *et al.*, 2007; Miwa *et al.*, 2008). However, a thorough genetic analysis revealed that the transposon-inserted allele is not the cause of the observed floral phenotype. Using classical mapping and mapping-by-sequencing, we eventually found a novel mutant allele of *LFY* to be responsible for the aberrant floral development and flower morphology and determined the molecular reason for LFY malfunction.

Results

The *flower-in-flower* (*fif*) transposon insertion line displays a novel flower phenotype

In order to identify novel *Arabidopsis thaliana* mutants with defects in flowering we screened the RIKEN Arabidopsis Phenome Information Database (RAPID; Kuromori *et al.*, 2006). RAPID also covers a *Ds* transposon mutant collection in the *Arabidopsis* Nossen-0 (No-0) background (Ito *et al.*, 2002; Kuromori *et al.*, 2004). We identified a transposon-tagged line (15-3794-1), which developed secondary inflorescences with partially aberrant flowers (Fig. 1a). Because of this phenotype, we named this novel *Arabidopsis* mutant *flower-in-flow*er (*fif*).

As shown in Figure 1c and d, wild-type *Arabidopsis* flowers does not have bracts but consist of four concentric rings of 4 sepals, 4 petals, 6 stamens and 2 fused carpels. In contrast, the primary flower of the *fif* mutant had bracts as well as sepals but the petals were incompletely developed or entirely missing (Fig. 1b, e). In addition, there were either no stamens or the stamens displaying an aberrant development (Fig. 1b, e). Furthermore, there were more than 2 carpels per flower, which were not or only partially overgrown and did not establish fertile ovaries. Most obvious, however, was the outgrowth of stems from the axillary meristems of the bracts, which carried terminal secondary flowers. A few secondary *fif* flowers showed a wild-type-like phenotype and were, thus, fertile (Fig. 1b, e).

Furthermore, the *fif* mutant plant displayed a bushy habitus compared to wild-type No-0 (Fig. 2a, b). This bushy appearance was due to an enhanced number of stem-born side branches compared to wild-type No-0, whereas the number of rosette-born side shoots was the same in *fif* and wild-type No-0 plants (Fig. 2c). In addition, *fif* mutant plant exhibited delayed flowering compared to wild-type No-0 (Fig. 2a, b).

The transposon insertion is not responsible for the *fif* phenotype

According to the RIKEN RAPID and our own genotyping results, the *Ds* transposon was located in the second exon of the gene *At1g20990* that codes for a putative cysteine/histidine-rich C1 domain protein with an as yet unknown function. To validate the causal relationship between the *fif* phenotype and the *Ds* transposon insertion, we analysed an independent insertion mutant in the *Arabidopsis thaliana* Col-0 background, which exhibited a T-DNA insertion in the promoter region of *At1g20990* (SALK_073291; Alonso *et al.*, 2003). However, homozygous mutant plants of this line showed no aberrant phenotype compared to wild-type (Col-0) with respect to floral development, flower morphology, flowering time and growth habitus.

This observation raised doubts as to whether there is a functional link between the *Ds* transposon insertion and the *fif* mutant phenotype. We therefore performed a (co-) segregation analysis by backcrossing the *fif* mutant with wild-type No-0 in both directions (♀*fif* x ♂No-0, ♀No-0 x ♂*fif*). Irrespective of the direction, the crosses were successful as demonstrated by PCR on genomic DNA extracted from F1 plants using *Ds* transposon- and *At1g20990*-specific primers (Figure S1). All tested F1 plants were heterozygous for the *Ds* transposon and wild-type *At1g20990* and displayed wild-type floral organs and growth habiti (Figure S1). Therefore, the mutation that causes the *fif* phenotype is recessive. Next, six F1 plants were self-fertilized and 20 to 30 progenies each analysed for their pheno- and genotypes. As shown in figure 3, around one quarter of the F2 plants displayed the *fif* phenotype indicating that it is caused by a single mutant gene. Intriguingly, our genotyping results showed that the *Ds* transposon insertion did not co-segregate with the *fif* phenotype: 29 % of the *fif* phenotype-displaying plants did not contain the transposon, an additional 49% contained the transposon insertion only heterozygously (Figure 3). These results prove that the *Ds* insertion into the *At1g20990* locus does not cause the *fif* phenotype.

The *fif* phenotype is caused by a novel allele of *LEAFY (LFY)*

To identify the mutant locus genetically responsible for the *fif* phenotype, we combined a classical mapping (Neff *et al.*, 2002; Kover *et al.*, 2009; Pacurar *et al.*, 2012) with a mapping-by-sequencing approach (James *et al.*, 2013; Schneeberger, 2014). To establish a mapping population, *fif* mutant plants (No-0) were crossed in both direction with plants of the Col-0 accession. Irrespective of the crossing direction, all the F1 plant displayed a wild-type phenotype (Figure S2a). Eight F1 plants were self-fertilized and 1582 F2 plants characterized phenotypically. In

accordance with the self-crossing results described above, around 25 % of the F2 plants (437 of the 1582) showed the *fif* phenotype (Figure S2b). Leaf material was harvested from 425 of the 437 F2 plants in groups of 15 to 20 individuals; in addition leaf material from 200 F2 plants was collected individually. Genomic DNA was extracted and used for classical mapping. Using chromosome-specific INsertion and DELetion (INDEL) markers (Pacurar *et al.*, 2012) the mutant locus was mapped to the q-arm of chromosome 5 (Figure 4a). Two additional INDEL markers and two Single Nucleotide Polymorphism (SNP) based Derived Cleaved Amplified Polymorphic Sequences (dCAP) markers (Kover *et al.*, 2009; Neff *et al.*, 2002) limited the Quantitative Trait Locus (QTL) responsible for the *fif* phenotype to the terminal end of chromosome 5´s q-arm (Figure 4b, dCAP S5-24: 99% No-0).

To establish the exact localization of the mutant locus, we deep-sequenced the total genome of 245 homozygous *fif* mutant plants derived from the *fif* (No-0) x WT (Col-0) crosses described above, and determined the frequencies of No-0 and Col-0 alleles along the chromosomes. Whereas the heterozygous distribution of No-0 and Col-0 sequences was found to be equal with respect to chromosomes 1 to 4 (Figure S3a-d), there was a very significant deviation towards No-0 sequences at the terminal end of chromosome 5 (Figure 5a). A detailed examination of this 300 kb stretch revealed 100 % identity with the No-0 sequence (Figure 5b). This sequence stretch conformed with the QTL identified by classical mapping.

A detailed comparison of the *fif* and wild-type No-0 sequence in this 300 kb stretch revealed a single SNP, which did not result in a silent mutation but caused a change in a codon. This SNP was also found in all the 143 individually tested *fif* mutant plants and reflected a single guanine-to-adenine exchange in the second exon of the *LEAFY* (*LFY*) gene (*At5g61850*, Figure 5c). This mutation caused a cysteine-to-tyrosine amino acid exchange at position 263 in the DNA-binding domain of the LFY

protein (Figure 5d). To prove that this point mutation causes the *fif* phenotype, we transformed the *fif* mutant (No-0) with constructs expressing LFY-GFP or LFY^{FIF}-GFP under the control of the *35S* promoter. Whereas the expression of LFY-GFP complemented the *fif* mutant phenotype almost completely, there was no complementation with LFY^{FIF}-GFP (Figure S4).

LFY^{FIF} impairs DNA-binding capability but shows wild-type intracellular localization and homomerization

Having identified a new *LFY* allele to be responsible for the *fif* phenotype, we next analysed the putative consequences of the Cys263-to-Tyr exchange for LFY protein properties at molecular and cell biological levels.

To test a putative alteration in subcellular localization, C-terminal GFP fusions of wild-type LFY and the mutant LFY version (LFY^{FIF}) were expressed under the control of the *Arabidopsis ubiquitin 10* (*UBQ10*) promoter in transiently transformed *Nicotiana benthamiana* epidermal leaf cells. The functionality of C- (and N-terminal) GFP fusions of LFY was previously shown by the genetic complementation of the *lfy-12* mutant phenotype (Wu *et al.*, 2003). As shown in figure 6a, LFY-GFP and LFY^{FIF}-GFP localised to the cytoplasm and the nucleus in a similar manner. The observed fluorescence pattern of LFY-GFP and LFY^{FIF}-GFP is in accordance with the pattern previously reported for their expression in tobacco epidermal leaf cells (Siriwardana and Lamb, 2012b).

Next, we tested by *in vivo* FRET-FLIM whether LFY protein-protein interaction, here especially LFY homomerization (Sirwardana and Lamb, 2012a), was altered. To do so, C-terminal GFP fusions (FRET donor) and C-terminal RFP fusions (FRET acceptor) were transiently expressed, either individually (donor only) or in combination in *N. benthamiana* epidermal leaf cells and the fluorescence lifetime of

the donor fusion was measured. As shown in figure 6b, the fluorescence lifetimes of LFY-GFP and LFY^{FIF}-GFP were similar in the absence of the acceptor fusions. However, the lifetimes of LFY-GFP and LFY^{FIF}-GFP decreased significantly when they were co-expressed with either LFY-RFP or LFY^{FIF}-RFP demonstrating homotypic (LFY-LFY, LFY^{FIF}-LFY^{FIF}) and heterotypic (LFY-LFY^{FIF}) homomerization *in planta* (Figure 6b). In addition, there was no significant difference in the interaction of the homotypic and heterotypic homomers (Figure 6b).

The Cys263-to-Tyr exchange is located in the first α-helix of the LFY DNA-binding domain (Figure 5d). We, therefore, used a quantitative DNA-protein interaction ELISA approach (qDPI-ELISA; Fischer, Böser *et al.*, 2016) to test whether the mutation interferes with the DNA-binding capability of LFY *in vitro*. We expressed N-terminally GFP-tagged full-length LFY, as well as full-length LFY^{FIF} and GFP, in *E. coli* independently and applied the crude extracts containing the fusion proteins or GFP, in identical amounts, based on the GFP fluorescence and western-blotting, to ELISA plates in two dilutions. The plates were covered with double-stranded (ds) DNA oligonucleotides representing either the LFY-binding sequence of the *AP1* promoter (*pAP1*), a mutated *pAP1* version (*pAP1m*) that is not recognized by LFY (Winter *et al.*, 2011) a random sequence without any similarity to the LFY binding motif (*C28M12*), or were uncovered. The DNA-binding efficiency of the proteins was recorded by determining the GFP fluorescence of the bound proteins (Fischer, Böser *et al.*, 2016). GFP-LFY exhibited a specific binding to *pAP1* and no binding to any other oligonucleotide or to the oligonucleotide-free ELISA plate (Figure 7). In contrast, GFP-LFY^{FIF}, like GFP or the *E. coli* crude extract without recombinant protein, was unable to recognize *pAP1* or any other oligonucleotide (Figure 7). To exclude the possibility that the Cys263-to-Tyr exchange may alter the DNA-binding specificity we used a DPI-ELISA based approach to screen a dsDNA oligonucleotide

library reflecting 4096 randomized DNA hexamers (Brand *et al.*, 2013a, b) with GFP-LFY- and GFP-LFY^{FIF}-containing *E.coli* extracts. Whereas a DNA-binding consensus sequence was obtained for GFP-LFY (5´-GGGC-3´/3´-CCCG-5`), there was no DNA-binding of GFP-LFY^{FIF} to any oligonucleotide in the library.

Discussion

In our search for novel floral genes in *Arabidopsis thaliana* we identified the *fif* Ds transposon insertion mutant in the No-0 accession in the RIKEN RAPID collection (Ito *et al.*, 2002; Kuromori *et al.*, 2004). *fif* mutant plants display a novel floral phenotype and inflorescence architecture, as they develop aberrant and infertile primary flowers in combination with short stems that emerge from vegetative meristems in the axillars of the bracts and carry fertile secondary flowers.

The *Ds* transposon insertion in the genome of the *fif* mutant was annotated to gene *At1g20990*, which encodes a cysteine/histidine-rich C1 domain protein. However, as demonstrated by our genetic analysis, the *Ds* transposon insertion into the *At1g20990* locus is not the cause of the *fif* phenotype. Obviously, another mutant locus generated somewhere else in the genome, most likely during transposon movement, is responsible for the *fif* phenotype. Using combined classical and genome sequencing-based mapping approaches, the causal mutation for the *fif* phenotype was found to be in the *LFY* gene. The mutation is a single G-to-A exchange in the second exon of *LFY*, creating the novel, recessive *lfy* allele. The mutation causes a Cys-to-Tyr exchange at position 263 in the LFY^{FIF} amino acid sequence.

The cell biological analysis of LFY-GFP and LFY^{FIF}-GFP revealed an intracellular localization in the cytoplasm and nucleus of tobacco epidermal leaf cells identical to that previously reported for LFY-GFP (Siriwardana and Lamb, 2012a). Thus, a mis-

localisation cannot be the cause of the LFY^{FIF} malfunction. In addition, as shown by quantitative FRET-FLIM interaction studies the mutation does not interfere with the homomerization capacity of LFY. Especially the latter result was to be expected as the domain essential for homomerization is located at the N-terminus of LFY (amino acid 46 to 127; Siriwardana and Lamb, 2012a).

However, our quantitative DPI-ELISA assay demonstrated that, in contrast to LFY-GFP, LFY^{FIF}-GFP lost its capacity to bind to its DNA target, as it is present, for instance, in the *AP1* promoter (Winter *et al.*, 2011). Furthermore, the DPI-ELISA based approach for the determination of putative alterations in binding specificity did not reveal any DNA-binding activity for LFY^{FIF}-GFP.

According to the available crystal structure of the DNA-bound dimer, Cys263 is well conserved between the LFY homologs of many plant species but has never previously been reported to be crucial for DNA-binding (Hames *et al.*, 2008). Intriguingly, Cys263 does not contribute to the physical contact of LFY with DNA; however, the α1-helix, in which Cys263 is positioned, participates in the cooperative DNA-binding of LFY, as it facilitates the establishment and stabilization of the DNA-binding domains in the minor and major grove of DNA (Hames *et al.*, 2008). Therefore, the change of the relatively small Cys to the bulky, aromatic Tyr might prevent the folding of the α1-helix and thereby strongly restrict the cooperative binding of LFY to its target DNA.

The total failure of LFY^{FIF} to bind to DNA explains the strong floral phenotype of especially the primary flowers. LFY is one of the master regulators in the FLIP of *Arabidopsis* (and other plant species) and controls, together with other factors and *via* a complex regulatory network, the spatiotemporal expression of downstream FLIP genes and also of the homeotic flower genes required for flower organ formation. Although only a single amino acid exchange is affected, LFY^{FIF} mirrors in principle

the flower phenotype of known strong *lfy* alleles. However, of the more than 15 described *lfy* alleles (Weigel *et al.*, 1992), the six alleles that show such a strong floral phenotype produce shortened LFY polypeptides caused by either premature stop codons (*lfy-1*, *lfy-6*, *lfy-7*, *lfy-8*, *lfy-11*) or a non-sense frame shift C-terminal of Gln196 (*lfy-15*). Hence, the strong phenotype of the *fif* allele needs a different explanation: LFY^{FIF} may act dominant-negatively by either forming non-functional heteromers with wild-type LFY, which cannot longer bind to DNA, or by titrating out interaction partners required for LFY function (Siriwardana and Lamb, 2012b). However, as long as sufficient wild-type LFY is present in heterozygous plants, the *fif* mutant shows recessive inheritance.

The failure of LFY^{FIF} to bind to DNA is also explains the bushy growth architecture of the *fif* mutant. It has recently been shown (Chahtane *et al.*, 2013) that mutations in *lfy* can cause the emergence of axillary meristems instead of floral meristems resulting in an enhanced number of side branches. In addition, the ectopic expression of a nearly full-length LFY version with weaker *in vitro* DNA-binding capacity and dramatically reduced *in vivo* transcriptional activity [$LFY_{HARA(\Delta 40)}$] in the Col-0 accession causes a bushy phenotype similar to that of the No-0 *fif* mutant (Chahtane *et al.*, 2013). Interestingly, the His387-to-Ala and Arg390-to-Ala in $LFY_{HARA(\Delta 40)}$ are also mooted to interfere with the cooperative binding of LFY to its target DNA as well. Taken together, our data demonstrate the general importance of Cys263 for LFY function not only in floral development but also in axillary meristem outgrowth in *Arabidopsis*.

Most intriguingly, the *fif* floral phenotype appears to be specific for the No-0 accession, as, to our knowledge, it has never been reported for the Col-0 or any other accession. However, the *fif* phenotype also becomes also manifest in the Col-0 accession when the *fif* locus of No-0 is transferred to Col-0. This phenomenon might

be explained by differences in the spatio-temporal transcriptional activity of the No-0 and Col-0 *LFY* loci during vegetative meristem and floral development. Therefore, the *fif* phenotype may only be visible in other accessions such as Col-0 when the No-0 locus is artificially introduced into them and drives LFY^{FIF} accumulation.

Experimental procedures

Plant material

Seeds of the homozygous *Ds* transposon insertion line 15-3794-1 and the corresponding wild-type accession (No-0) were obtained from the RIKEN *Arabidopsis* Phenome Information database (RAPID; Kuromori *et al.*, 2006). Seeds of the homozygous T-DNA insertion line Salk_073291 and the corresponding wild-type accession (Col-0) were obtained from the Nottingham *Arabidopsis* Stock Centre (NASC; Alonso *et al.*, 2003).

Plasmid construction

Using gene-specific primers [sense (S): 5´-caccATGGATCCTGAAGGTTTCACG-3´, antisense (A): 5´-GAAACGCAAGTCGTCGCCG-3´) the cDNA of *LFY* was amplified from pSST14 (gift Jan Lohmann, University of Heidelberg, Germany) and cloned in pENTR™/D-TOPO®. Site-directed mutagenesis (SDM) was performed to produce the *fif* cDNA using the following primers (S: 5´-CTGTTCCACTTGTACGAACAATaCCGTGAGTTCCTTCTTCAG-3´, A: 5´-CTGAAGAAGGAACTCACGGtATTGTTCGTACAAGTGGAACAG-3´). With Gateway™ LR Clonase™ II Enzyme mix the *LFY* cDNA was inserted into pUGT1-Dest (A. Hahn, unpublished) and pB7RWG2-Dest (Karimi *et al.*, 2002) for plant expression and into pET-Dest42GFP (Fischer, Böser *et al.*, 2016) for *E. coli* expression.

Classical mapping and mapping by genome sequencing

Genetic mapping was accomplished using 100 phenotypic *fif* plants collected from a F2 population derived from a cross between *fif* (No-0) and Col-0. The mapping strategy and the molecular markers used to identify the causal locus were described by Păcurar *et al.* (2012). After mapping of the chromosome arm and next-generation sequencing (NGS, see below) the point mutation was confirmed by derived cleaved-amplified polymorphic sequence primers designed by using the dCAPS Finder 2.0 software (Neff, Turk and Kalishman, 2002). One or two mismatches were introduced in one of the used primer to incorporate an allele-specific restriction site into the PCR product. After amplification, the PCR products were digested (enzymes from Thermo Scientific) following the manufacturer's recommendations and separated on a 4% agarose gel. All used markers are listed in table S1.

NGS mapping was performed using a pool of 425 phenotypic *fif* plants from the crossing described above. A pool of 40 wild-type No-0 plants was sequenced to generate a genome-wide marker list and to mine the *fif* genome for acquired mutations. Isolation of genomic DNA was performed in groups up to 20 plants using the DNeasy® Plant Mini Kit (QIAGEN) following the manufacturer's recommendations. DNA concentration was determined with the use of NanoDrop ND-1000 and the whole pool composed by using 100 µg DNA of each group. Sequencing was performed at the Max Planck-Genome-Centre Cologne by a HiSeq2500 (Illumina) Sequencer producing ~35.000.000 read-pairs for each pool. Short reads of both pools were respectively aligned against the Col-0 reference sequence (TAIR10) and SNPs were called using *shore* pipeline (version v0.8) with *GenomeMapper* (version v0.4.4s) with default parameters (Ossowski *et al.*, 2008; Schneeberger *et al.*, 2009a). Genome-wide SNP markers were defined with filtering for sequencing coverage and allele frequency using *SHOREmap* (version 3.0, Sun *et*

al., 2015; Schneeberger *et al.*, 2009b; Schneeberger, 2014). Sliding window-based estimation of allele frequencies of the Nos allele in the pooled F2 samples and identification of a mapping interval were performed with *SHOREmap* (version 3.0) using default parameters. Comparison of the consensus calls of both pools in the 300 kb mapping interval revealed the mutation in *LFY*.

Localization and FRET-FLIM studies

The indicated constructs and p19 as gene silencing suppressor were transformed into *Agrobacterium tumefaciens* strain GV3101 and infiltrated into *Nicotiana benthamiana* leaves. The localization of the fusion proteins was performed 3 days after infiltration using 488 nm or 561 nm lasers for GFP or RFP excitation, respectively, at the SP8 laser scanning microscope (Leica Microsystems GMBH) with LAS AF and SymPhoTime software using a 63x/1.20 water immersion objective (Ladwig *et al.*, 2015). FLIM data were derived from measurements of at least 20 probes for each fusion protein combination. To excite LFY-GFP and LFY^{FIF}-GFP for FLIM experiments, a 470 nm pulsed laser (LDH-P-C-470) was used, and the corresponding emission was detected with a SMD Emission SPFLIM PMT from 495 to 545 nm by time-correlated single-photon counting using a Picoharp 300 module (PicoQuant). Each time-correlated single-photon counting histogram was reconvoluted with the corresponding instrument response function and fitted against a monoexponential decay function for donor-only samples and a biexponential decay function for the other samples to unravel the GFP fluorescence lifetime of each probe. The average GFP fluorescence lifetimes as well as the standard error values were calculated using Microsoft Excel 2013. To test for homogenity of variance Levene's test ($df=5/140$, $F=26.298$, $p < 0.0001$) was used and statistical significance

was calculated by a two-tailed, all-pair Kruskal-Wallis test followed by a Steel-Dwass *post hoc* correction using JMP version 12.2.0 (Ohmi *et al.*, 2016).

qDPI-ELISA, DPI-ELISA based screening and western blotting

qDPI-ELISA was performed using *E.coli* crude extracts containing GFP-tagged LFY or LFY^{FIF}, GFP alone or no fluorescent protein according to Fischer, Böser *et al.* (2016). The sequences of the 5´-biotinylated dsDNA oligonucleotides *AP1*, *mAP1* and *C28M12* used for the immobilization on Streptavidin-coated 384 well microtiter plate are displayed in table S2. Before addition to the microtiter plate, the equal content of GFP-tagged fusion protein in the crude extracts was adjusted according to the GFP fluorescence using a fluorescence reader (TECAN Safire).

The DPI-ELISA based specificity screening, using a dsDNA oligo array on a 384 well microtiter plate covering all possible 4096 hexanucleotide DNA motifs was performed as described previously (Brand *et al.* 2013a, b).

Acknowledgements

The authors would like to thank J. Lohmann (Universität Heidelberg, Germany) for the *LFY* cDNA, M. Fischer for technical support, J. Schröter and G. Huber for support in plant cultivation, F. de Courcy for proofreading the manuscript and the members of the multidisciplinary graduate school “Morphological Variability of Organisms under Environmental Stress” for discussion. This work was supported by a grant of the Ministerium für Wissenschaft, Forschung und Kunst Baden-Württemberg to A. Mohrholz.

Supporting information

Additional Supporting Information is found in the on-line version of this article.

References

Alonso, J.M., Stepanova, A.N., Leisse, T.J., Kim, C.J., Chen, H., Shinn, P., Stevenson, D.K., Zimmerman, J., Barajas, P., Cheuk, R., Gadrinab, C., Heller, C., Jeske, A., Koesema, E., Meyers, C.C., Parker, H., Prednis, L., Ansari, Y., Choy, N., Deen, H., Geralt, M., Hazari, N., Hom, E., Karnes, M., Mulholland, C., Ndubaku, R., Schmidt, I., Guzman, P., Aguilar-Henonin, L., Schmid, M., Weigel, D., Carter, D.E., Marchand, T., Risseeuw, E., Brogden, D., Zeko, A., Crosby, W.L., Berry, C.C. and Ecker, J.R. (2003) Genome-wide insertional mutagenesis of Arabidopsis thaliana. *Science*, **301**, 653-657.

Blazquez, M.A., Ferrandiz, C., Madueno, F. and Parcy, F. (2006) How floral meristems are built. *Plant Mol Biol*, **60**, 855-870.

Bowman, J.L., Alvarez, J., Weigel, D., Meyerowitz, E.M. and Smyth, D.R. (1993) Control of flower development in Arabidopsis thaliana by APETALA1 and interacting genes. *Development*, **119**, 721-743.

Brand, L.H., Henneges, C., Schussler, A., Kolukisaoglu, H.U., Koch, G., Wallmeroth, N., Hecker, A., Thurow, K., Zell, A., Harter, K. and Wanke, D. (2013a) Screening for protein-DNA interactions by automatable DNA-protein interaction ELISA. *PLoS One*, **8**, e75177.

Brand, L.H., Fischer, N.M., Harter, K., Kohlbacher, O. and Wanke, D. (2013b) Elucidating the evolutionary conserved DNA-binding specificities of WRKY transcription factors by molecular dynamics and in vitro binding assays. *Nucleic Acids Res*, **41**, 9764-9778.

Chahtane, H., Vachon, G., Le Masson, M., Thevenon, E., Perigon, S., Mihajlovic, N., Kalinina, A., Michard, R., Moyroud, E., Monniaux, M., Sayou, C., Grbic, V., Parcy, F. and Tichtinsky, G. (2013) A variant of LEAFY reveals its capacity to stimulate meristem development by inducing RAX1. *Plant J*, **74**, 678-689.

Coen, E.S. and Meyerowitz, E.M. (1991) The war of the whorls: genetic interactions controlling flower development. *Nature*, **353**, 31-37.

Fischer, S.M., Böser, A., Hirsch, J.P. and Wanke, D. (2016) Quantitative Analysis of Protein-DNA Interaction by qDPI-ELISA. *Methods Mol Biol*, **1482**, 49-66.

Hames, C., Ptchelkine, D., Grimm, C., Thevenon, E., Moyroud, E., Gerard, F., Martiel, J.L., Benlloch, R., Parcy, F. and Muller, C.W. (2008) Structural basis for LEAFY floral switch function and similarity with helix-turn-helix proteins. *EMBO J*, **27**, 2628-2637.

Huala, E. and Sussex, I.M. (1992) Leafy Interacts with Floral Homeotic Genes to Regulate Arabidopsis Floral Development. *Plant Cell*, **4**, 901-913.

Irish, V.F. and Sussex, I.M. (1990) Function of the Apetala-1 Gene during Arabidopsis Floral Development. *Plant Cell*, **2**, 741-753.

Ito, T., Motohashi, R., Kuromori, T., Mizukado, S., Sakurai, T., Kanahara, H., Seki, M. and Shinozaki, K. (2002) A new resource of locally transposed Dissociation elements for screening gene-knockout lines in silico on the Arabidopsis genome. *Plant Physiol*, **129**, 1695-1699.

James, G.V., Patel, V., Nordstrom, K.J.V., Klasen, J.R., Salome, P.A., Weigel, D. and Schneeberger, K. (2013) User guide for mapping-by-sequencing in Arabidopsis. *Genome Biol*, **14**.

Karimi, M., Inze, D. and Depicker, A. (2002) GATEWAY vectors for Agrobacterium-mediated plant transformation. *Trends Plant Sci*, **7**, 193-195.

Kempin, S.A., Savidge, B. and Yanofsky, M.F. (1995) Molecular-Basis of the Cauliflower Phenotype in Arabidopsis. *Science*, **267**, 522-525.

Kover, P.X., Valdar, W., Trakalo, J., Scarcelli, N., Ehrenreich, I.M., Purugganan, M.D., Durrant, C. and Mott, R. (2009) A Multiparent Advanced Generation Inter-Cross to fine-map quantitative traits in Arabidopsis thaliana. *PLoS genetics*, **5**, e1000551.

Kuromori, T., Hirayama, T., Kiyosue, Y., Takabe, H., Mizukado, S., Sakurai, T., Akiyama, K., Kamiya, A., Ito, T. and Shinozaki, K. (2004) A collection of 11 800 single-copy Ds transposon insertion lines in Arabidopsis. *Plant J*, **37**, 897-905.

Kuromori, T., Wada, T., Kamiya, A., Yuguchi, M., Yokouchi, T., Imura, Y., Takabe, H., Sakurai, T., Akiyama, K., Hirayama, T., Okada, K. and Shinozaki, K. (2006) A trial of phenome analysis using 4000 Ds-insertional mutants in gene-coding regions of Arabidopsis. *Plant J*, **47**, 640-651.

Ladwig, F., Dahlke, R.I., Stuhrwohldt, N., Hartmann, J., Harter, K. and Sauter, M. (2015) Phytosulfokine Regulates Growth in Arabidopsis through a Response Module at the Plasma Membrane That Includes CYCLIC NUCLEOTIDE-GATED CHANNEL17, H+-ATPase, and BAK1. *Plant Cell*, **27**, 1718-1729.

Lohmann, J.U. and Weigel, D. (2002) Building beauty: the genetic control of floral patterning. *Dev Cell*, **2**, 135-142.

Ma, H. (1998) To be, or not to be, a flower--control of floral meristem identity. *Trends Genet*, **14**, 26-32.

Mandel, M.A., Gustafsonbrown, C., Savidge, B. and Yanofsky, M.F. (1992) Molecular Characterization of the Arabidopsis Floral Homeotic Gene Apetala1. *Nature*, **360**, 273-277.

Miwa, H., Betsuyaku, S., Iwamoto, K., Kinoshita, A., Fukuda, H. and Sawa, S. (2008) The Receptor-Like Kinase SOL2 Mediates CLE Signaling in Arabidopsis. *Plant Cell Physiol*, **49**, 1752-1757.

Neff, M.M., Turk, E. and Kalishman, M. (2002) Web-based primer design for single nucleotide polymorphism analysis. *Trends Genet*, **18**, 613-615.

Ohmi, Y., Ise, W., Harazono, A., Takakura, D., Fukuyama, H., Baba, Y., Narazaki, M., Shoda, H., Takahashi, N., Ohkawa, Y., Ji, S., Sugiyama, F., Fujio, K., Kumanogoh, A., Yamamoto, K., Kawasaki, N., Kurosaki, T., Takahashi, Y. and Furukawa, K. (2016) Sialylation converts arthritogenic IgG into inhibitors of collagen-induced arthritis. *Nature Communications*, **7**, 11205.

Ossowski, S., Schneeberger, K., Clark, R.M., Lanz, C., Warthmann, N. *et al*. (2008) Sequencing of natural strains of *Arabidopsis thaliana* with short reads. *Genome Research*, **18**, 2024-2033.

Pacurar, D.I., Pacurar, M.L., Street, N., Bussell, J.D., Pop, T.I., Gutierrez, L. and Bellini, C. (2012) A collection of INDEL markers for map-based cloning in seven Arabidopsis accessions. *Journal of experimental botany*, **63**, 2491-2501.

Pidkowich, M.S., Klenz, J.E. and Haughn, G.W. (1999) The making of a flower: control of floral meristem identity in IT>Arabidopsis/IT>. *Trends Plant Sci*, **4**, 64-70.

Pineiro, M. and Coupland, G. (1998) The control of flowering time and floral identity in Arabidopsis. *Plant Physiol*, **117**, 1-8.

Schneeberger, K. (2014) Using next-generation sequencing to isolate mutant genes from forward genetic screens. *Nat Rev Genet*, **15**, 662-676.

Schneeberger, K., Hagmann, J., Ossowski, S., Warthmann, N., Gessing, S. *et al.* (2009a) Simulataneous alignment of short reads against multiple genomes. *Genome Biology*, **10**, R98.

Schneeberger, K., Ossowski, S., Lanz, C., Juul, T., Petersen A.H., Nielsen K.L., Jørgensen, J.E., Weigel D. and Andersen S.U. (2009b) SHOREmap: simultaneous mapping and mutation identification by deep sequencing. *Nature Methods*, **6**, 550-1.

Shinya, T., Galis, I., Narisawa, T., Sasaki, M., Fukuda, H., Matsuoka, H., Saito, M. and Matsuoka, K. (2007) Comprehensive analysis of glucan elicitor-regulated gene expression in tobacco BY-2 cells reveals a novel MYB transcription factor involved in the regulation of phenylpropanoid metabolism. *Plant Cell Physiol*, **48**, 1404-1413.

Siriwardana, N.S. and Lamb, R.S. (2012a) A conserved domain in the N-terminus is important for LEAFY dimerization and function in Arabidopsis thaliana. *Plant J*, **71**, 736-749.

Siriwardana, N.S. and Lamb, R.S. (2012b) The poetry of reproduction: the role of LEAFY in Arabidopsis thaliana flower formation. *Int J Dev Biol*, **56**, 207-221.

Sun, H.Q. and Schneeberger, K. (2015) SHOREmap v3.0: fast and accurate identification of causal mutaitons from forward genetic screens. *Methods Mol. Biol.*, **1284**, 381-95.

Weigel, D., Alvarez, J., Smyth, D.R., Yanofsky, M.F. and Meyerowitz, E.M. (1992) LEAFY controls floral meristem identity in Arabidopsis. *Cell*, **69**, 843-859.

Winter, C.M., Austin, R.S., Blanvillain-Baufume, S., Reback, M.A., Monniaux, M., Wu, M.F., Sang, Y., Yamaguchi, A., Yamaguchi, N., Parker, J.E., Parcy, F., Jensen, S.T., Li, H. and Wagner, D. (2011) LEAFY target genes reveal floral regulatory logic, cis motifs, and a link to biotic stimulus response. *Dev Cell*, **20**, 430-443.

Wu, X., Dinneny, J.R., Crawford, K.M., Rhee, Y., Citovsky, V., Zambryski, P.C. and Weigel, D. (2003) Modes of intercellular transcription factor movement in the Arabidopsis apex. *Development*, **130**, 3735-3745.

Figure legends

Figure 1. Flower phenotype of the *Arabidopsis thaliana* (No-0) *flower-in-flower* (*fif*) mutant. (a) Overview over representative *fif* mutant "inflorescence" displaying different flower types 1 to 4. (b) Floral organs of the primary *fif* flower (1) and different secondary *fif* flowers (2-4). (c) Flower of the wild-type No-0 accession. (d-e) Flower diagram of the wild-type No-0 flower (d) and the primary flower of the *fif* mutant (e). (f) Primary flowers of the *fif* mutant with stems that outgrow from axillary bract meristems (red arrow heads) and carry secondary flowers. Size bar: 1 mm.

Figure 2. Growth habitus and degree of branching of wild-type No-0 and *fif* mutant plants. (a-b) Overview over the growth habitus and magnification of the inflorescence of 6.5-weeks old wild-type No-0 (a) and *fif* (b) plants, grown side-by-side in the greenhouse. Size bar: 1.0 cm. (c) Number of rosette-born side branches and stem-born side branches of wild-type No-0 (white bars) and *fif* (black bars) plants. Error bars indicate the standard deviation of the mean (n_{No-0} = 33, n_{fif} = 25, ***: $p = 2x10^{-23}$).

Figure 3. Segregation of the floral phenotype and the Ds transposon insertion within the combined F_2 population of (♀*fif* x ♂No-0) and (♀No-0 x ♂*fif*) backcrosses. (a) Distribution of F_2 plants, showing either the wild-type (78.4 %) or the *fif* floral phenotype (21.6 %). (b) Distribution of the transposon insertions within the plants of the F_2 population that displayed the *fif* floral phenotype. White circle outcut: no transposon insertion (29.2 %), striped outcut: heterozygous for the Ds transposon insertion (45.8 %), black outcut: homozygous for the Ds transposon insertion (25.0 %).

Figure 4. INDEL marker- and SNP-based dCAP marker-associated containment of the *fif* locus using a mapping population generated by a cross of the *fif* mutant (No-0) with wild-type Col-0. (a) Schematic representation of the 5 *A. thaliana* chromosomes (sizes in MB) and the localization of the chromosome-specific INDEL markers initially used for mapping (codes above blue lines). (b) Schematic representation of the q-arm of chromosome 5 and the localization of INDEL (codes above the blue lines) and SNP-based dCAP markers (codes above red lines) used for fine mapping.
The pie charts show the distribution of the No-0 and Col-0 genotypes for each chromosome (a) and the q-arm of chromosome 5 (b). White circular outcut: homozygous for Col-0, striped outcut: heterozygous for Col/No-0, black outcut: homozygous for No-0; red dot: localization of the centromere.

Figure 5. Identification of the *fif*-related SNP in the second exon of the *LEAFY* (*LFY*) locus on chromosome 5 by genome sequencing of a mapping population generated by a cross of the *fif* mutant (No-0) with wild-type Col-0. (a) Allele frequency analysis of the Nos genotype within chromosome 5 of the recombinant mutant pool . Each red circle refers to a SNP marker distinguishing the Nos and Col genotypes. The blue line refers to a 200 kb sliding window analysis of the allele frequencies. The brown line and blue box highlight the estimated mapping intervals (x-axis: genomic location; y-axis: Nos allele frequency). (b) Like (a), but only showing the 300 kb mapping interval. (c) Exon-intron organization of the *LFY* locus with the *fif*-related SNP marked by an arrow. Exons are shown as grey boxes and introns as exons connecting lines. (d) Sequence of the *LFY* gene showing the *fif* SNP (G to A exchange, red) and the resulting amino acid exchange (C to Y, red) within the DNA-binding domain of the LFY protein. Green boxes: β-sheets; blue boxes: α-helices (according to Hames et al., 2008).

Figure 6. Comparative analysis of the intracellular localization and homomerization capacity of LFY and LFY^{FIF}. (a) Confocal fluorescence images of transiently transformed *Nicotiana benthamina* epidermal leaf cells expressing LFY-GFP and LFY^{FIF}-RFP in the same cell. Size bar: 5 µm. (b) FRET-FLIM analysis of the homo- and heterotypic interaction of LFY and LFY^{FIF}. LFY-GFP or LFY^{FIF}-GFP were expressed either alone or together with the indicated RFP fusions and the fluorescence lifetime of the GFP fusions measured in nucleus. A reduction of the GFP fluorescence lifetime indicates interaction. The data are presented in Box-and-Whisker plots including the median (thick line), the upper and lower quartile (+/- 25%, white boxes), the maximum and minimum (dottet line) and outlier points (n > 20, each). The variance was analyzed by a Levene test and statistical significance was determined with an all-pair, two-sided Kruskal-Walles test followed by an all-pair Steel-Dwass test (**: $p < 0.01$; ***: $p < 0.001$).

Figure 7. Comparative analysis of the *in vitro* DNA-binding capacity of LFY and LFY^{FIF} using a GFP-fluorescence-based DPI-ELISA approach. GFP-LFY and GFP-LFYFIF were expressed in *E.coli*. After extraction, crude extracts containing either no recombinant protein (w/o protein) or, based on GFP fluorescence, equal amounts of GFP or GFP fusion protein were added to ELISA plates covered with either the double-stranded (ds) DNA oligonucleotide *pAP1*, which contains a LFY recognition site, an altered version of *pAP1* (*pAP1m*), in which the recognition site was mutated, a dsDNA oligonucleotide unrelated to the *pAP1* and *pAP1m* sequences (*C28M12*) or without any DNA-oligonucleotide. The amount of DNA-bound fusion protein was detected by reading out the GFP fluorescence. The crude extract was either used undiluted (black bars) or in a 1:4 dilution (grey bars). Error bars indicate the standard deviation of the mean (n = 3) and asteriks statistically significant differences to the

background fluorescence (dotted horizontal line), determined by two-sided t-test (*: $p < 0.05$; **: $p < 0.01$).

The inlet shows a Western-blot of the crude extracts using a GFP polyclonal antiserum for detection of GFP, GFP-LFY and GFP-LFY^{FIF} as well as a Coomassie stain as loading control.

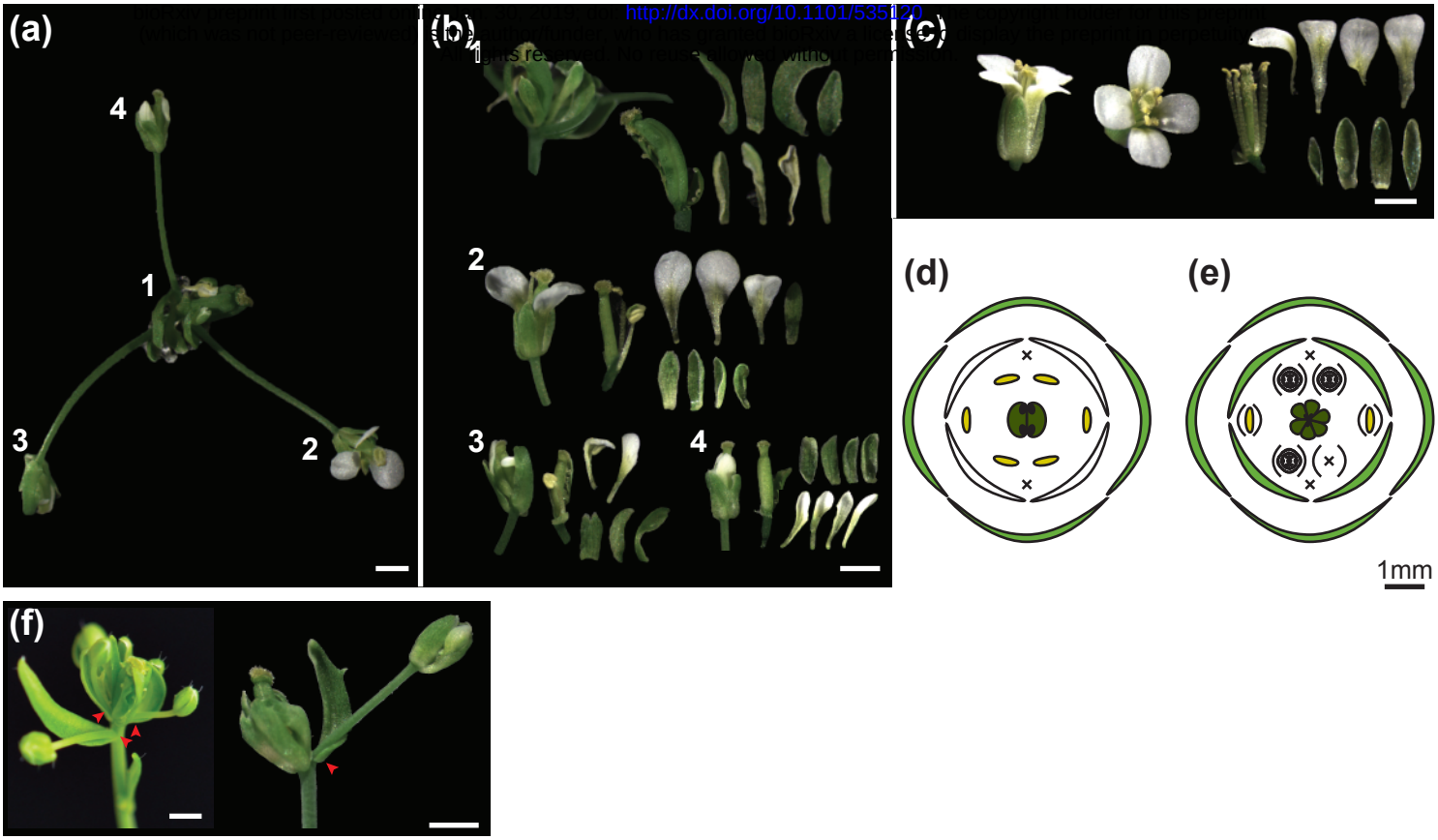

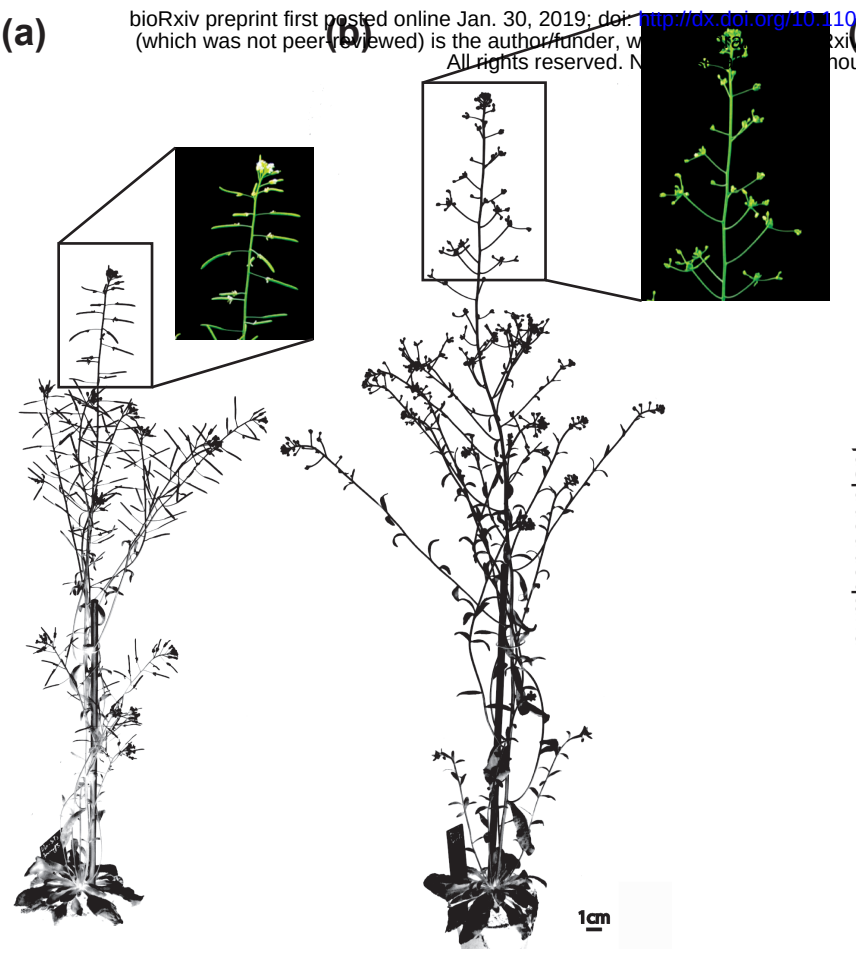

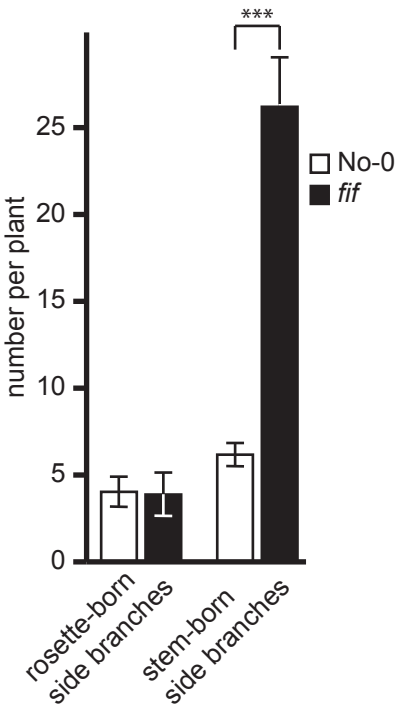

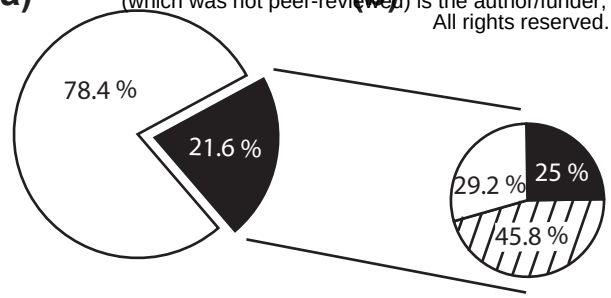

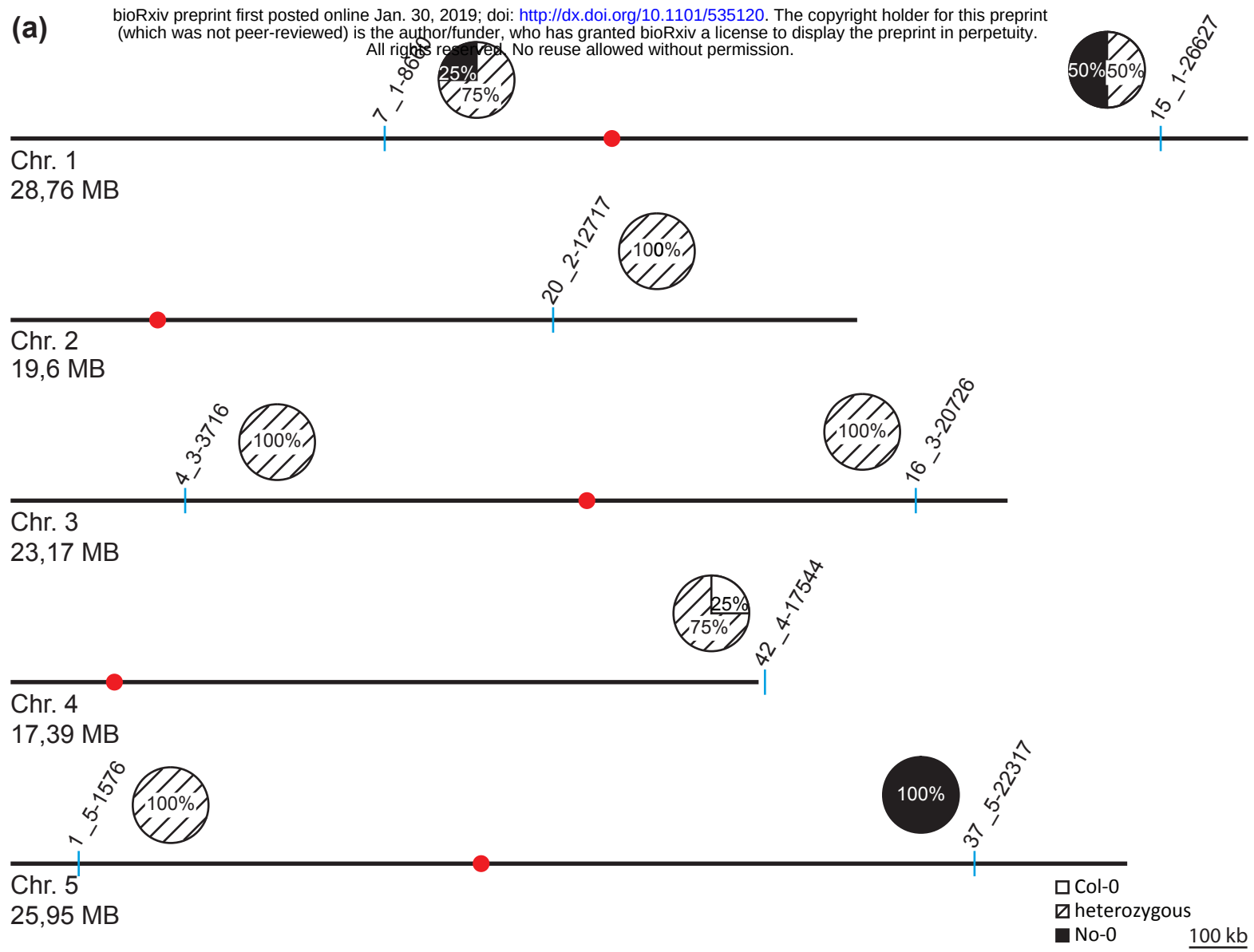

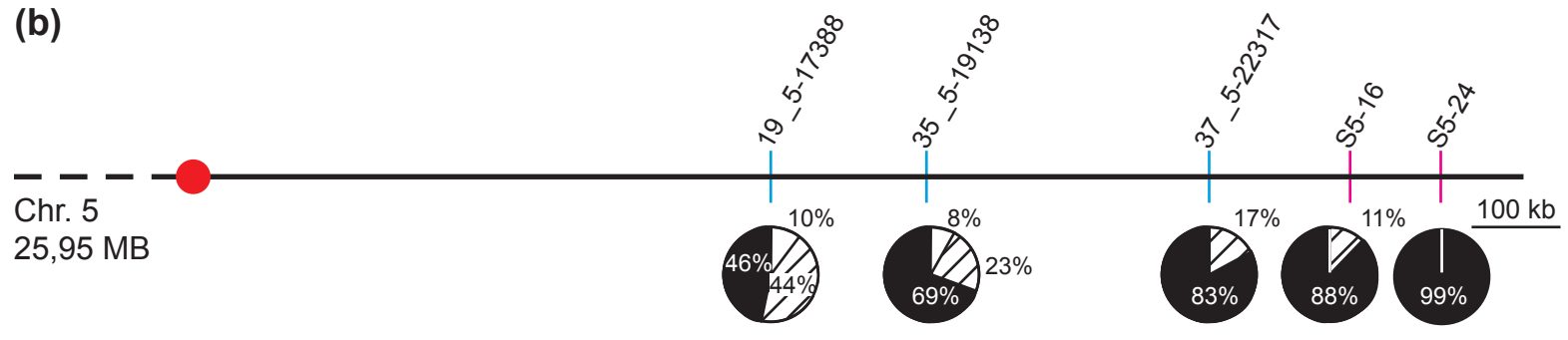

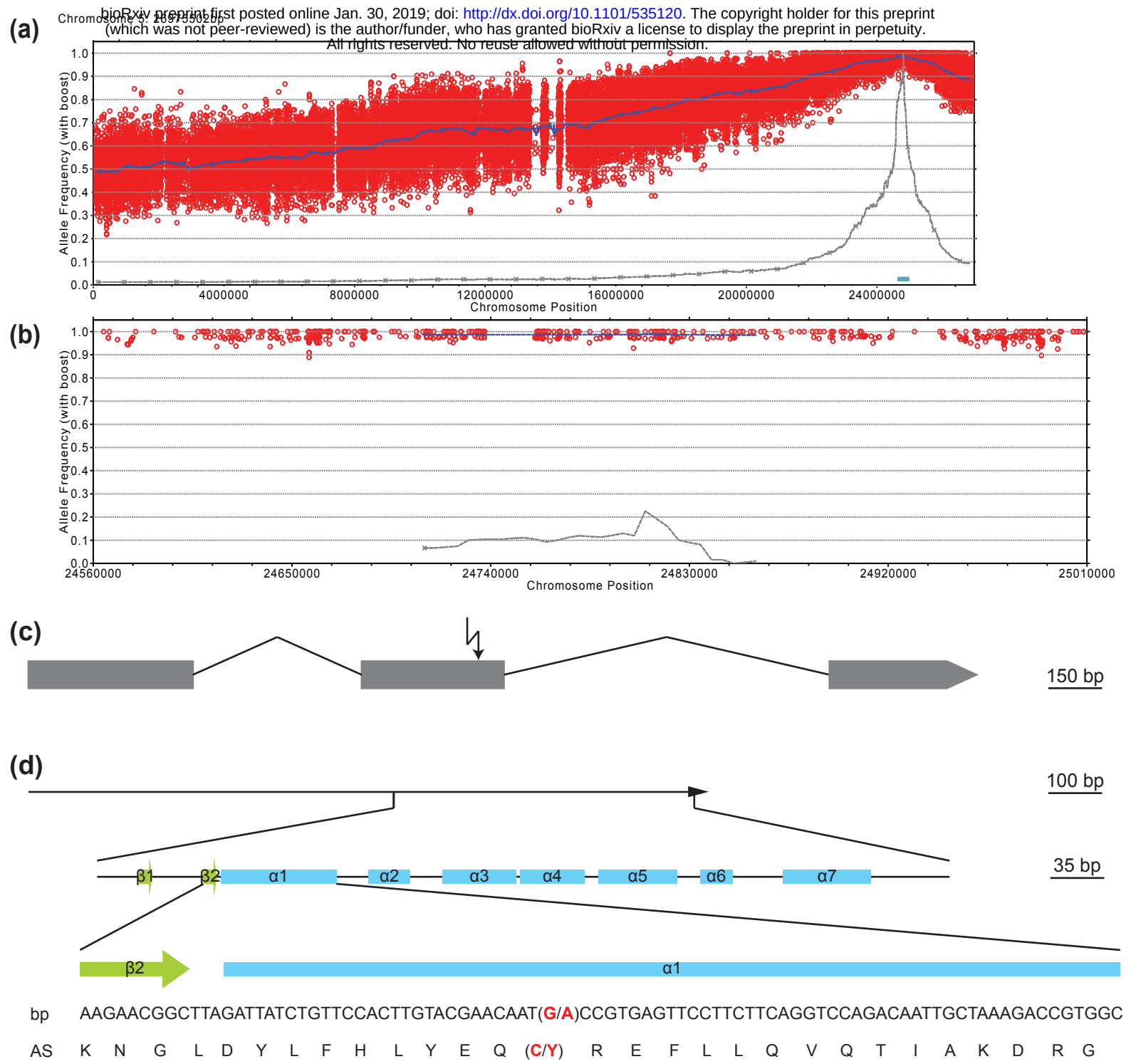

bp AAGAACGGCTTAGATTATCTGTTCCACTTGTACGAACAAT(G/A)CCGTGAGTTCCTTCTTCAGGTCCAGACAATTGCTAAAGACCGTGGC

AS K N G L D Y L F H L Y E Q (C/Y) R E F L L Q V Q T I A K D R G

(a)

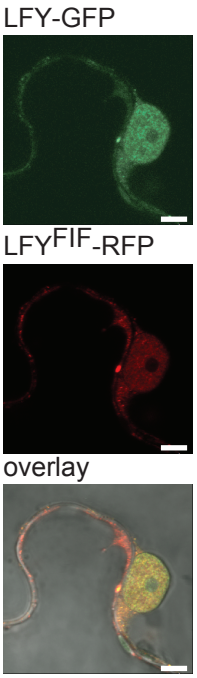

(b)

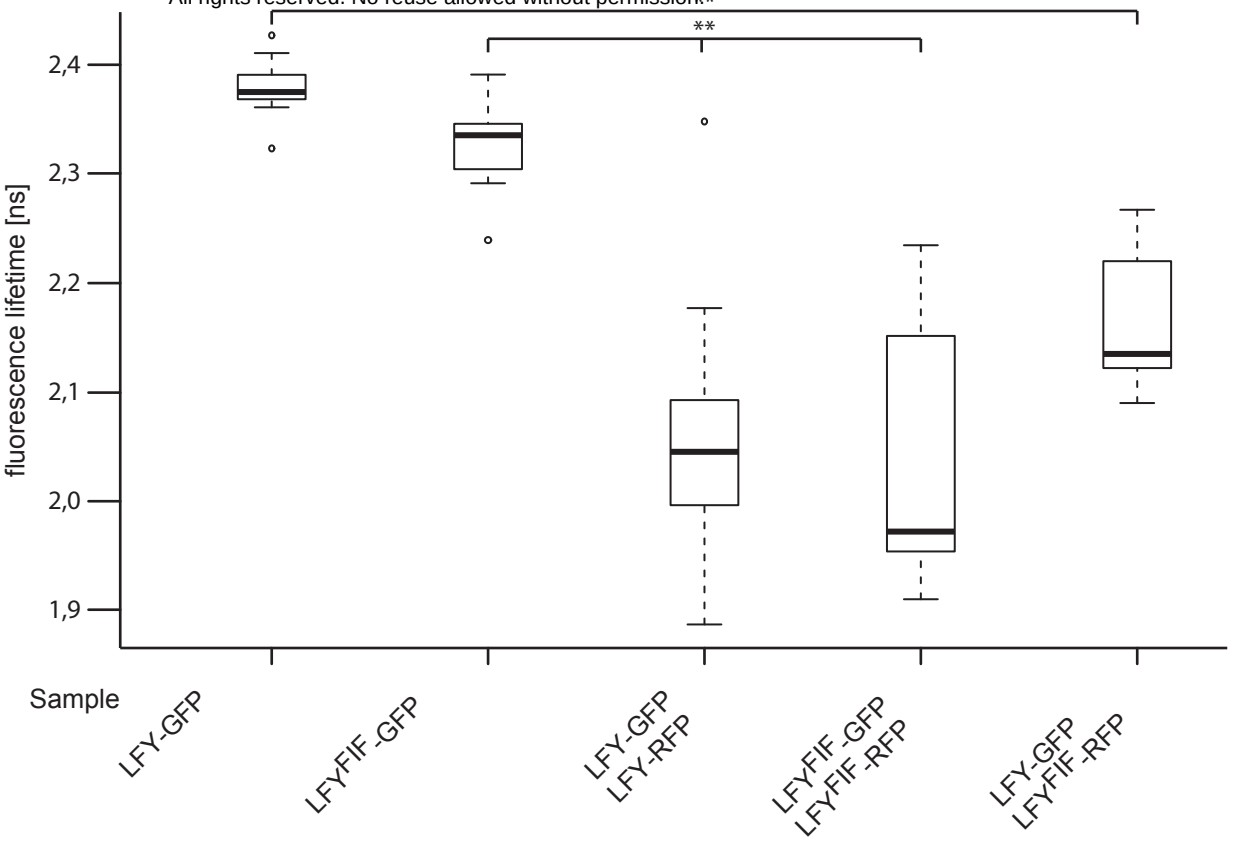

Bar (C) 5µm

Nichtparametrische Vergleiche für alle Paare mittels Dunn-Methode für gemeinsame Ränge
* signifikant <0,05
** hoch signifikant <0,01
*** Höchst signifikant <0,001

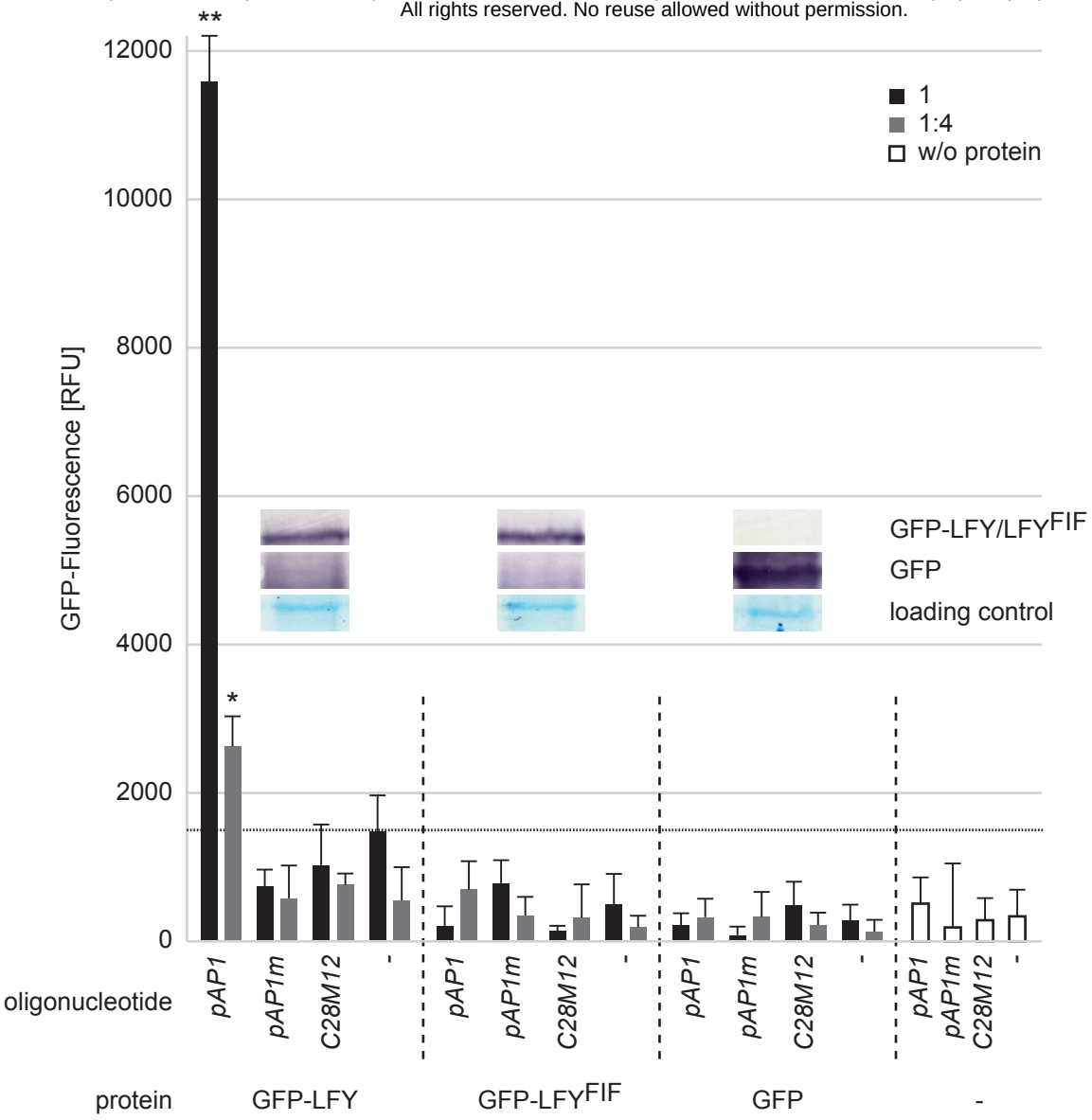

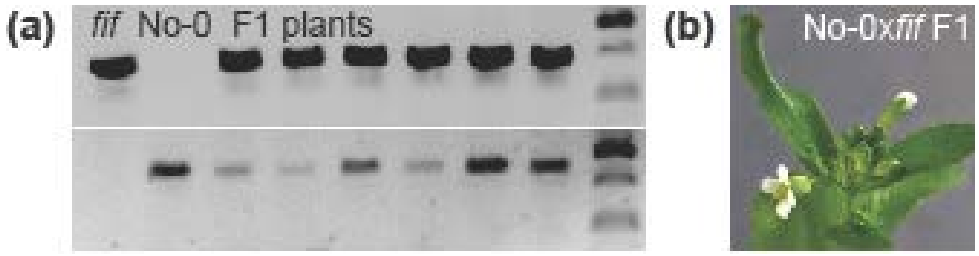

Figure S1. Proof of the successful backcross of the *fif* mutant with wild-type No-0. **(a)** Genotyping PCR analysis of F1 plant material using a primer pair (sense: 5´-CGTGAAACTCAAGGCATTCTCTACTTC -3´; antisense: 5´-CGATTTCGACTTTAACCCGACCGG -3´) specifically amplifying the Ds transposon (upper row) and a primer pair (sense: see above; antisense: 5´-CGTACGTAGAACAACAGAGAATAAGC-3´) specifically amplifying the wild-type genomic region (lower row). **(b)** Representative image of the inflorescence and flower phenotype of F1 plants generated by the cross of the *fif* mutant with wild-type No-0 (♀No-0 x ♂*fif*). The reciprocal cross (♀*fif* x ♂No-0) provided the identical the results.

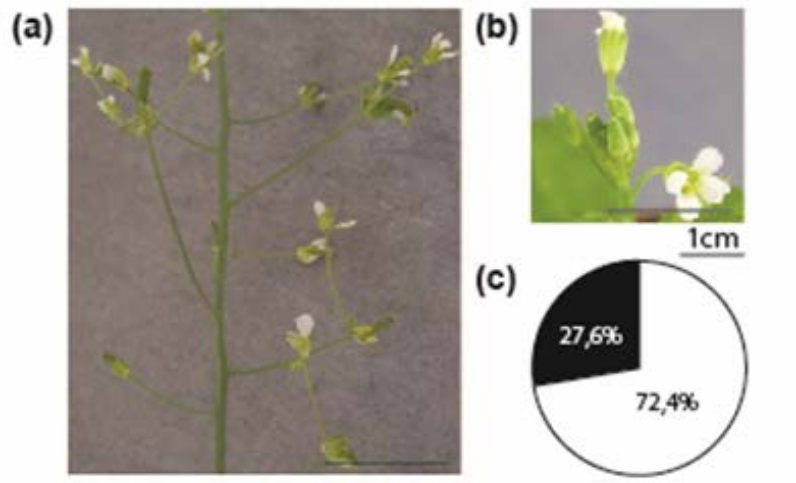

Figure S2. Distribution of the *fif* phenotype in the outcrossed F2 mapping population derived from plants of a F1 population generated by crosses of the *fif* mutant (No-0) with wild-type Col-0 (♀No-0 x ♂*fif*, ♀*fif* x ♂No-0). Representative images of the inflorescence of an outcrossed *fif* mutant **(a)** and wild-type individual **(b)**. **(c)** Distribution of plants showing either the *fif* mutant or wild-type floral phenotype within the outcrossed F2 mapping population. White circle outcut: plants with wild-type phenotype (72.4 %), black outcut: plants *fif* phenotype (27.6 %).Proof of the successful backcross of the *fif* mutant with wild-type No-0.

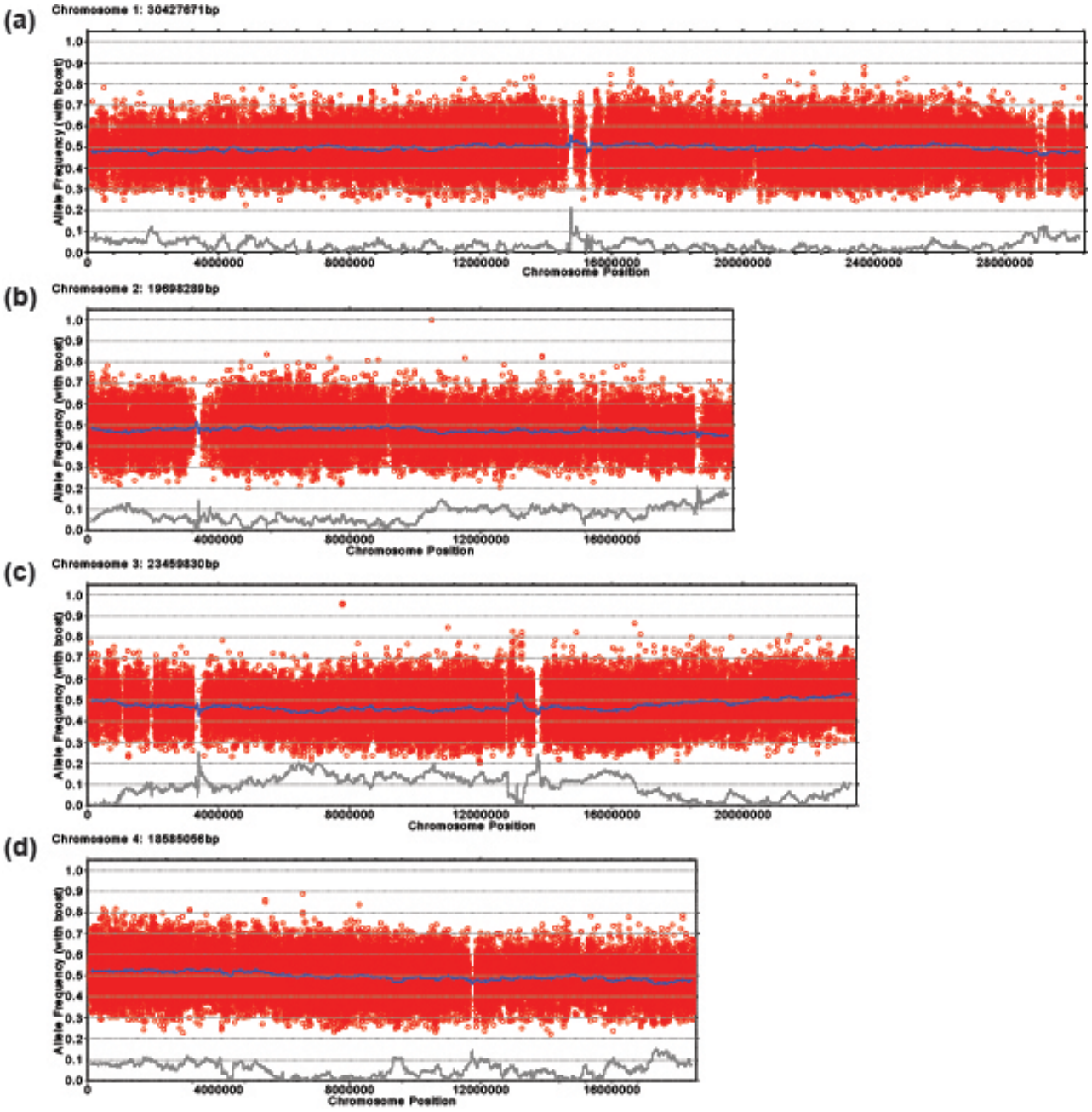

Figure S3. Allele frequency analysis of the Nos-0 allele within the recombinant mutant pool (unlinked chromosomes). Each red circle refers to a SNP marker distinguishing the Nos and Col genotypes. The blue line refers to a 200 kb sliding window analysis of the allele frequencies. The brown line would highlight potential mapping intervals (x-axis: genomic location; y-axis: Nos-0 allele frequency). **(a)** Chromosome 1. **(b)** Chromosome 2. **(c)** Chromosome 3. **(d)** Chromosome 4.

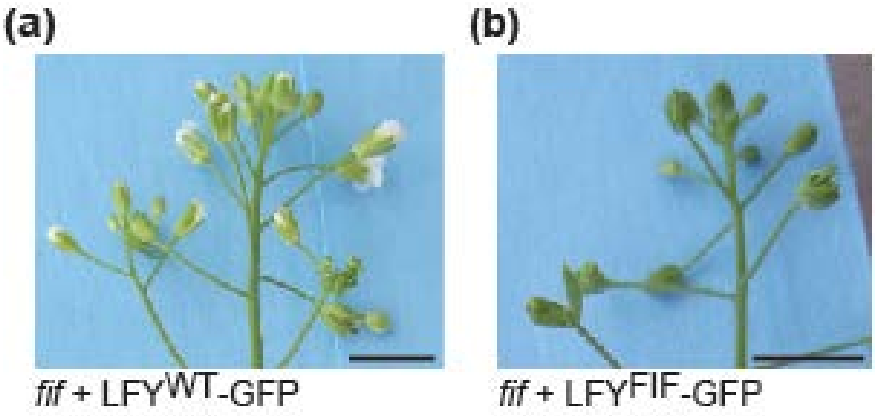

Figure S4. Complementation analysis of the *fif* mutant phenotype. *fif* mutant plants were transformed with binary constructs expressing, under the control of the UBQ10 promoter, either wild-type LFY-GFP or LFY^{FIF}-GFP. Whereas the expression of LFY-GFP almost fully complements the *fif* floral phenotype of the mutant **(a)**, no complementation was observed for the expression of LFY^{FIF}-GFP **(b)**.

Name		Sequence	Marker Type		bp *Col-0*	bp *No-0*
7_1-8660	S	GCGGCACAACCTAAATGAAA	INDEL		189	168
	A	TGCATGCAATTATCACGTATG				
15_1-26627	S	GCAATTCATCAGCAGGAGGT	INDEL		245	261
	A	ATCAGGGAGCAAAATGCAAG				
20_2-12717	S	AAAATGGGGCCTAATACGTTG	INDEL		403	~180
	A	CAAAGGAAACACCTGCATCA				
4_3-3716	S	TAATGGTGGCCCAATCTCAT	INDEL		1482	613
	A	AATTCCAAATGGAGCCACAA				
16_3-20726	S	GGGCCCATTTCAACTAAGGA	INDEL		149	~160
	A	TCTCACAAGCCCAGTAAAAACT				
42_4-17544	S	CACCATTGACATTTGATGCAC	INDEL		214	234
	A	CCGTAGCTCCATTGGCTTAT				
1_5-1576	S	CAGCTCCGACGATGATGATA	INDEL		363	~420
	A	TGGAGTAATTGTTCCTTCACAAA				
37_5-22317	S	GCATTGAAATAGTGTTTTTAACCAAA	INDEL		132	152
	A	TGTTGGTTGCCACCTTATCA				
19_5-17388	S	TTTTGCAAGTCCGTAGTCAATG	INDEL		110	121
	A	TTTGGTTTTGGAATTTCTTTTG				
35_5-19138	S	AACTCATGCAATGCGACATC	INDEL		182	164
	A	CCCGTCCATGATCTGTTTCT				
37_5-22317	S	GCATTGAAATAGTGTTTTTAACCAAA	INDEL		132	152
	A	TGTTGGTTGCCACCTTATCA				
				Enzyme		
S5-16	S	CACGAGAGATACCTGCAAAACAG	dCAP	DraII	160	134+26
	A	CAAACGCTTTTGAAATCATGGGT**C**C				
S5-24	S	GTAATACACAACAATGGGGAG	dCAP	Esp3I	244+43+26	287+26
	A	CATATTCGAGTTCTGATGCACAC				
5-LFY	S	TATCTGTTCCACTTGTACGAA**GT**AT	dCAP	AccI	150	129+21
	A	CATAAATTTCAAGATAATGAACGGTC				
5-LFY#2	S	TATCTGTTCCACTTGTACGAA**GC**AT	dCAP	SphI	129+21	150
	A	Same as 5-LFY				

Table S1 Names and sequences of the INDEL and dCAP primers. Bold and underlined: introduced mismatches to incorporate an ecotype specific restriction site in the PCR product

Name			sequence
pAP1	SA	Bio-	aaaaaGAAGGACCAGTGGTCCGTACaaaaa tttttGTACGGACCACTGGTCCTTCttttt
pAP1m	SA	Bio-	aaaaaGAAGGAAAAGTAATCCGTACaaaaa tttttGTACGGATTACTTTTCCTTCttttt
C28M12	SA	Bio-	aaaaaaTTTATACTTGATCATaaCTTaaaa ttttAAGttATGATCAAGTATAAAttttt

Table S2 Sequences of the dsDNA oligonucleotides used in the DPI-ELISA.

A.2.3 UV-B dependent repression of flowering by RUP2

Arabidopsis RUP2 represses UVR8-mediated flowering in noninductive photoperiods

Accepted

This article describes the signalling events that lead to the UV-B light dependent transition from vegetative growth to the reproductive state of *Arabidopsis*. The transition to flowering is only possible in long day conditions and the UV-B dependent transition depends on the UV-B photoreceptor UV RESISTANCE LOCUS 8 (UVR8). The repression of flowering during noninductive photoperiods (short day) is mediated by REPRESSOR OF UV-B PHOTOMORPHOGENESIS 2 (RUP2), which can directly interact with the key activator of flowering CONSTANS (CO). It involves the repression of CO, which in turn supresses the transcription of the florigen FLOWERING LOCUS T (FT).

Arabidopsis RUP2 represses UVR8-mediated flowering in noninductive photoperiods

Adriana B. Arongaus,[1] Song Chen,[1] Marie Pireyre,[1] Nina Glöckner,[2] Vinicius C. Galvão,[3] Andreas Albert,[4] J. Barbro Winkler,[4] Christian Fankhauser,[3] Klaus Harter,[2] and Roman Ulm[1,5]

[1]Department of Botany and Plant Biology, Section of Biology, Faculty of Sciences, University of Geneva, 1211 Geneva 4, Switzerland; [2]Department of Plant Physiology, Center for Plant Molecular Biology (ZMBP), University of Tübingen, 72076 Tübingen, Germany; [3]Center for Integrative Genomics, Faculty of Biology and Medicine, University of Lausanne, 1015 Lausanne, Switzerland; [4]Research Unit Environmental Simulation, Helmholtz Zentrum München, 85764 Neuherberg, Germany; [5]Institute of Genetics and Genomics of Geneva (iGE3), University of Geneva, 1211 Geneva 4, Switzerland

Plants have evolved complex photoreceptor-controlled mechanisms to sense and respond to seasonal changes in day length. This ability allows plants to optimally time the transition from vegetative growth to flowering. UV-B is an important part intrinsic to sunlight; however, whether and how it affects photoperiodic flowering has remained elusive. Here, we report that, in the presence of UV-B, genetic mutation of *REPRESSOR OF UV-B PHOTOMORPHOGENESIS 2* (*RUP2*) renders the facultative long day plant *Arabidopsis thaliana* a day-neutral plant and that this phenotype is dependent on the UV RESISTANCE LOCUS 8 (UVR8) UV-B photoreceptor. We provide evidence that the floral repression activity of RUP2 involves direct interaction with CONSTANS, repression of this key activator of flowering, and suppression of *FLOWERING LOCUS T* transcription. RUP2 therefore functions as an essential repressor of UVR8-mediated induction of flowering under noninductive short day conditions and thus provides a crucial mechanism of photoperiodic flowering control.

[*Keywords*: sun simulator; plant–environment interaction; photoperiodism; flowering; UV-B photoreceptor; UVR8; *Arabidopsis*]

Supplemental material is available for this article.

Received July 5, 2018; revised version accepted August 17, 2018.

Timely and synchronous flowering is important to optimize pollination and allow seed maturation during favorable environmental conditions. In addition to being adaptive traits for plants in natural environments, synchronous flowering and maximal seed yields are also crucial in horticulture and agricultural production systems. In recent decades, the genetic pathways and regulatory proteins that promote flowering in response to changes in day length (photoperiod) were largely defined in the model species *Arabidopsis thaliana*, a facultative long day (LD) plant (i.e., flowers early in LDs but will eventually also flower under short days [SDs]) (Song et al. 2015). Photoperiodic flowering in *Arabidopsis* is due to the suppression of flowering in SDs, which is released under LD conditions. Flowering under inductive LD photoperiods is activated by the CONSTANS (CO) transcription factor, a master regulator of *FLOWERING LOCUS T* (*FT*) expression (Putterill et al. 1995; Samach et al. 2000; Turck et al. 2008; Andres and Coupland 2012; Song et al. 2015). FT is a major component of the florigen, a systemic signal that moves through the vasculature from the leaves into the apical meristem, where it induces flowering in response to the inductive photoperiod (Wigge et al. 2005; Corbesier et al. 2007; Jaeger and Wigge 2007; Mathieu et al. 2007; Turck et al. 2008; Song et al. 2015). Regulation of CO activity is complex and takes place at many different levels (Romera-Branchat et al. 2014; Song et al. 2015; Shim et al. 2017). A prominent component of this regulation under noninductive SD conditions is CO ubiquitination during the night period by the CONSTITUTIVELY PHOTOMORPHOGENIC 1 (COP1)–SUPPRESSOR OF PHYTOCHROME A-105 (SPA) E3 ubiquitin ligase complex followed by degradation in the 26S proteasome (Laubinger et al. 2006; Jang et al. 2008; Liu et al. 2008). Consistently, *cop1* and *spa1* plants flower early under SD conditions compared with wild type (McNellis et al. 1994; Laubinger et al. 2006). In LDs, the COP1–SPA complex is inhibited during the day period by cryptochrome 2 (cry2), which is required for early flowering under these conditions (Guo

Corresponding author: roman.ulm@unige.ch
Article published online ahead of print. Article and publication date are online at http://www.genesdev.org/cgi/doi/10.1101/gad.318592.118. Freely available online through the *Genes & Development* Open Access option.

et al. 1998; Zuo et al. 2011). COP1 is also a well-known molecular player directly interacting with the UV-B photoreceptor UV RESISTANCE LOCUS 8 (UVR8) (Favory et al. 2009; Rizzini et al. 2011; Cloix et al. 2012; Yin et al. 2015; Jenkins 2017; Podolec and Ulm 2018). However, despite this and the fact that UV-B is an intrinsic part of sunlight, our molecular understanding of photoperiodic flowering regulation in *Arabidopsis* is basically based on growth chamber experiments in the absence of UV-B. Thus, the role of UVR8 signaling in photoperiodic control of flowering time has not been investigated previously.

The seven-bladed β-propeller protein UVR8 forms homodimers in the absence of UV-B (Favory et al. 2009; Rizzini et al. 2011). UVR8 monomerizes upon UV-B absorption by specific intrinsic tryptophan residues, which is followed by interaction with COP1 (Favory et al. 2009; Rizzini et al. 2011). As a result of this UV-B-dependent interaction, the COP1 target protein ELONGATED HYPOCOTYL 5 (HY5) is stabilized (Favory et al. 2009; Huang et al. 2013; Binkert et al. 2014). HY5 is a bZIP transcription factor that plays a central role in light signaling (Lau and Deng 2012), including UVR8-mediated UV-B signaling (Ulm et al. 2004; Brown et al. 2005; Stracke et al. 2010; Binkert et al. 2014). The UVR8 photocycle involves negative feedback regulation by REPRESSOR OF UV-B PHOTOMORPHOGENESIS 1 (RUP1) and RUP2, which are UVR8-interacting proteins that facilitate the ground state reversion of UVR8 via redimerization (Gruber et al. 2010; Heijde and Ulm 2013). RUP1 and RUP2 act largely redundantly for all UV-B responses characterized to date, and their role is to establish UVR8 homodimer/monomer equilibrium under diurnal conditions (Gruber et al. 2010; Heijde and Ulm 2013; Findlay and Jenkins 2016). A recent report has suggested that an apparently UV-B-independent role of RUP1 and RUP2 in flowering time regulation exists (note that EARLY FLOWERING BY OVEREXPRESSION 1 [EFO1] = RUP1 and EFO2 = RUP2) (Wang et al. 2011). However, the underlying molecular mechanism and the role of RUP1 and RUP2 in photoperiodic flowering regulation have remained enigmatic. Here we report how RUP2 functions as a key repressor of UVR8-mediated induction of flowering through regulation of CO activity and that this function is crucial to distinguish noninductive SDs from inductive LDs, thus enabling photoperiodic flowering.

Results

RUP2 is a repressor of flowering under SD conditions containing UV-B

Flowering time regulation in natural ecological settings is complex and often distinct from that under laboratory conditions (Weinig et al. 2002; Wilczek et al. 2009; Brachi et al. 2010). UV-B is an important part of the sunlight spectrum that is usually lacking in controlled growth chamber environments. To better understand the potential roles of UV-B and RUP1/RUP2 in the regulation of flowering, we grew wild-type, *rup1*, *rup2*, and *rup1 rup2* plants under LD (16-h/8-h light/dark) and SD (8-h/16-h light/dark) conditions. In contrast to a previous report (Wang et al. 2011), the flowering time and leaf number at flowering for *rup2* as well as *rup1 rup2* were comparable with those in wild type under standard laboratory growth conditions; i.e., in the absence of UV-B (LD – UV and SD – UV) (Fig. 1A–E). Strikingly, however, *rup2* as well as *rup1 rup2* flowered much earlier than wild type in SDs in the presence of UV-B (SD + UV) (Fig. 1A–C). This early flowering phenotype was specific to *rup2*, as *rup1* flowered similarly to wild type (Fig. 1A–C). Moreover, the early flowering phenotype of *rup2* and *rup1 rup2* in SD + UV was indistinguishable and, importantly, dependent on the UV-B photoreceptor UVR8, as *rup2 uvr8* and *rup1 rup2 uvr8* plants flowered as late as wild type and *uvr8* (Fig. 1F,G; Supplemental Fig. S1). Of note, the striking early flowering phenotype of *rup2* under SD + UV was rescued by transgenic expression of the genomic *RUP2* locus with an ~1.5-kb promoter region (*rup2-1/Pro$_{RUP2}$:RUP2*) and was also observed in *rup2-2* plants carrying a different T-DNA insertion in *RUP2* than *rup2-1* (Supplemental Fig. S2). Under LD conditions, the flowering phenotype of *rup1*, *rup2*, and *rup1 rup2* was not different from that of wild type in both the absence and presence of UV-B (Fig. 1D,E). In fact, *rup2* plants under SD + UV flowered with as few leaves as wild type and *rup2* under LD conditions (Fig. 1B,D), indicating that *RUP2* mutation rendered *Arabidopsis* from a facultative LD to a day-neutral plant. We conclude that RUP2 is essential to inhibit flowering under noninductive SD conditions, specifically in the presence of UV-B perceived by the UVR8 photoreceptor.

We further tested whether RUP2 overexpression represses flowering under LD conditions. However, RUP2 overexpression plants flowered as early as wild-type plants in both LD – UV and LD + UV (Supplemental Fig. S3A,B) despite strongly elevated RUP2 levels (Supplemental Fig. S3C). It should be noted that RUP2 overexpression is associated with a strong UV-B hyposensitive phenotype, resembling the "UV-B blindness" of *uvr8*-null mutants (Gruber et al. 2010). We thus conclude that RUP2 overexpression cannot repress flowering under LD conditions. However, blocking UVR8 activation precludes analysis of a distinct effect of RUP2 overexpression on the UVR8-induced flowering pathway. Moreover, in contrast to the results in a previous study (Wang et al. 2011), we did not observe an early flowering phenotype for the RUP2 overexpression line in SDs (Supplemental Fig. S3D,E).

It has been shown previously that UVR8 overexpression lines at the seedling stage display a UV-B phenotype enhanced similarly to *rup2* and *rup1 rup2* (Favory et al. 2009; Gruber et al. 2010). To test whether overactivation of the UV-B signaling pathway leads to early flowering under SD + UV, we used an established UVR8 overexpression line (Favory et al. 2009). As expected, the UVR8 overexpression line displayed a similar morphology in response to UV-B exposure compared with that of *rup2*, such as smaller rosettes (Supplemental Fig. S4A). However, UVR8 overexpression did not affect the flowering time in comparison with that in wild type (Supplemental Fig. S4B,C). It is of note that UVR8 overexpression was associated with strongly enhanced RUP2 levels (Supplemental

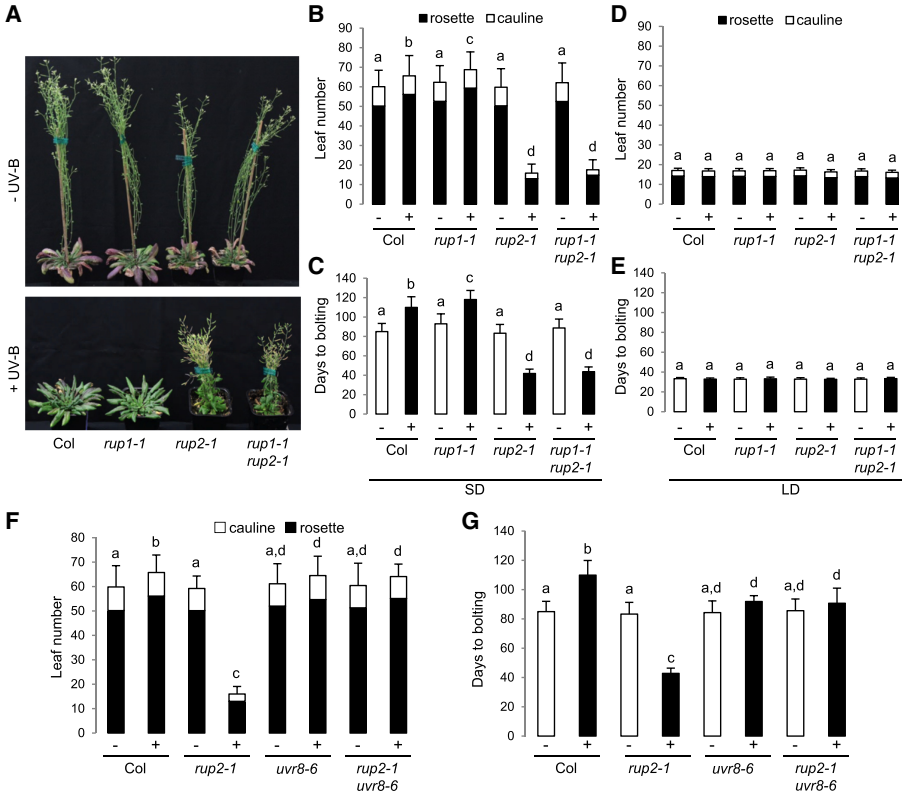

Figure 1. *rup2* flowers early in SDs with UV-B, which is dependent on the UVR8 photoreceptor. (*A*) Representative images of 100-d-old wild-type (Col), *rup1-1*, *rup2-1*, and *rup1-1 rup2-1 Arabidopsis* plants grown with (+) or without (−) UV-B. (*B–E*) Quantification of flowering time of wild-type (Col), *rup1-1*, *rup2-1*, and *rup1-1 rup2-1* plants grown in SDs (*B*,*C*) and LDs (*D*,*E*) with (+) or without (−) UV-B. (*F*,*G*) Quantification of flowering time of wild-type (Col), *rup2-1*, *uvr8-6*, and *rup2-1 uvr8-6* plants grown in SDs with (+) or without (−) UV-B. The flowering time is represented by total leaf number (rosette and cauline leaves; *B*,*D*,*F*) and days to bolting (*C*,*E*,*G*). Error bars represent standard deviation. $n = 30$. Shared letters indicate no statistically significant difference in the means. $P > 0.05$.

Fig. S4D). Our data suggest that overactivation of the UVR8 signaling pathway is not sufficient to induce early flowering, likely due to the balancing effect of elevated RUP2 activity as a repressor of flowering.

We further tested the importance of RUP2 repression of early flowering in SD + UV in sun simulators that allow growth under a natural spectral balance from ultraviolet to infrared (Thiel et al. 1996). Under these more realistic irradiation conditions, *rup2* plants maintained an early flowering phenotype, which is in contrast to that of wild-type, *rup1*, *uvr8*, and *rup2 uvr8* plants (Fig. 2), thus confirming and further strengthening the results generated using plants grown in growth chambers containing UV-B. Therefore, we conclude that a major role of RUP2 concerns the repression of UVR8-induced flowering in SD + UV, which is an activity crucial for photoperiodic flowering under natural irradiation conditions, including UV-B.

RUP2 interacts with CO

To better understand the role of RUP2 as a repressor of flowering, we performed a yeast two-hybrid screen, which identified the B-box proteins CO-LIKE 1 (COL1)/BBX2, COL2/BBX3, and COL5/BBX6 as RUP2-interacting partners (Supplemental Fig. S5). As *rup2* shows an early flowering phenotype (Fig. 1) and the COL family members are highly related to the eponymous key flowering time regulator CO/BBX1 (Putterill et al. 1995; Khanna et al. 2009), we assessed the direct interaction between RUP2 and CO in yeast. Indeed, yeast two-hybrid growth assays indicated that RUP2 interacts with full-length CO (Fig. 3A). In contrast to the CO–COP1 interaction (Fig. 3A; Liu et al. 2008), the N-terminal 183 amino acids of CO are sufficient for the interaction with RUP2, whereas the C-terminal CCT domain of CO is not required for interaction with RUP2 (Fig. 3A).

CO was found to be highly unstable in protein extracts, which precluded coimmunoprecipitation experiments. We thus resorted to Förster resonance energy transfer (FRET)-fluorescence lifetime imaging microscopy (FLIM) as a cell biological assay for protein–protein association in transiently transformed *Nicotiana benthamiana* epidermal leaf cells. First, we observed that RUP1-GFP and RUP2-GFP localized to the nucleus in a diffuse manner when expressed alone or together with an NLS-mCherry but aggregated in nuclear speckles when coexpressed with CO-mCherry (Fig. 3B). Further supporting CO–RUP interaction in yeast, our in planta FRET-FLIM analysis

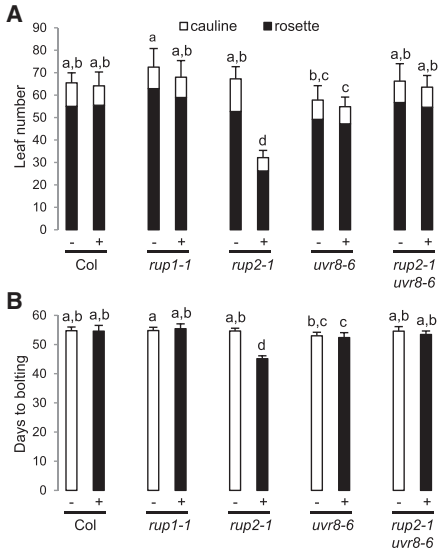

Figure 2. *rup2-1* flowers early under realistic irradiation conditions in a sun simulator. Quantification of flowering time of wild-type (Col), *rup1-1*, *rup2-1*, *uvr8-6*, and *rup2-1 uvr8-6* plants grown in SDs with (+) or without (−) UV. The flowering time is represented by total leaf number (rosette and cauline leaves; *A*) and days to bolting (*B*). Error bars represent standard deviation. $n = 20$. Shared letters indicate no statistically significant difference in the means. $P > 0.05$.

detected highly significant changes in the lifetime of the donor RUP1-GFP and RUP2-GFP fusions in the nucleus when coexpressed with CO-mCherry (Fig. 3C). In contrast, we did not observe significant GFP fluorophore lifetime changes when RUP1-GFP and RUP2-GFP were expressed alone or with NLS-mCherry (Fig. 3C). We thus conclude that RUP1 and RUP2 are closely associated with the key flowering regulator CO in plant cells.

Early flowering of rup2 *in SD + UV depends on the flowering time regulator CO and its target, FT*

Our finding that RUP2 interacts with CO suggests that *rup2* early flowering may depend on CO activity. Indeed, the early flowering phenotype of *rup2* in SD + UV was completely suppressed in *rup2 co* double mutants (Fig. 4). CO is an activator of *FT* expression that encodes the florigen FT, a major positive regulator of flowering time (Turck et al. 2008). In agreement with the *rup2* early flowering phenotype under SD + UV, *FT* expression was indeed up-regulated in *rup2* and *rup1 rup2* compared with that in wild-type, *rup1*, and *rup1 rup2 uvr8* plants (Fig. 5A). Furthermore, *FT* promoter-driven GUS expression (*Pro$_{FT}$:GUS*) in the leaf vasculature under SD + UV was enhanced in the *rup2* background in comparison with that in wild-type, *uvr8*, and *rup2 uvr8* backgrounds (Fig. 5B). Our findings suggest that *rup2* early flowering depends on enhanced CO-regulated *FT* expression and thus FT activity. Indeed, the early flowering phenotype of *rup2* under SD + UV was completely suppressed in *rup2 ft* double mutants (Fig. 5C–E). We thus conclude that *FT* expression is deregulated in *rup2* due to enhanced CO activity and that active FT is required for early flowering of *rup2* under SD + UV.

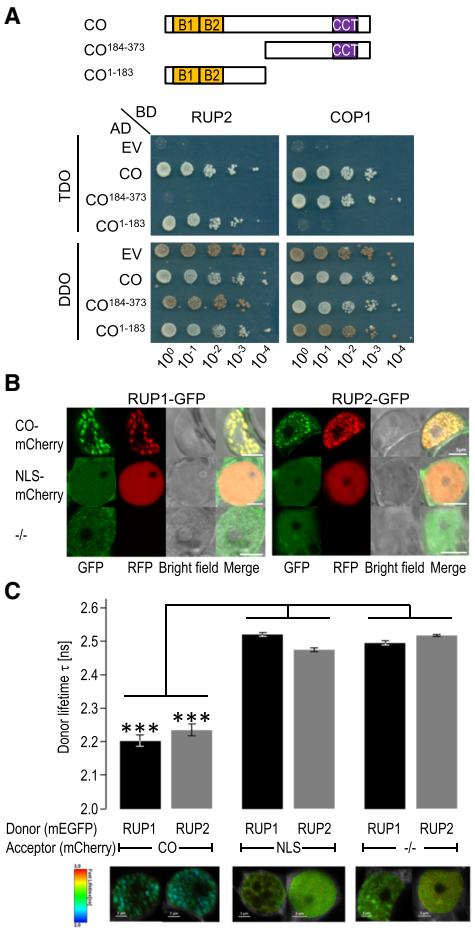

Figure 3. RUP1 and RUP2 interact with CO. (*A*) Interaction of RUP1 and RUP2 with CO in a yeast two-hybrid growth assay. (*Top*) Schematic representation of full-length and truncated CO used in interaction analysis. (*Bottom*) Tenfold serial dilutions of transformed yeast spotted on SD/−Trp/−Leu (DDO; nonselective for interaction) and SD/−Trp/−Leu/−His (TDO; selective) plates. (AD) Activation domain; (BD) binding domain; (EV) empty vector. (*B*) Colocalization analysis of RUP1-mEGFP and RUP2-mEGFP with either CO-mCherry or NLS-mCherry or without a mCherry fusion protein (−/−) in transiently transformed *Nicotiana benthamiana* epidermal leaf cells. Shown are confocal images in the GFP and RFP channel as well as the corresponding bright-field and merged images. Bars, 5 µm. (*C*) Fluorescence lifetime imaging microscopy (FLIM) analyses comparing the different Förster resonance energy transfer (FRET) pairs. (*Top*) FLIM measurements of transiently transformed *N. benthamiana* epidermal leaf cells expressing RUP1-mEGFP or RUP2-mEGFP donors in the presence of CO-mCherry or NLS-mCherry acceptor fusion or without a mCherry acceptor (−/−). Error bars indicate standard deviation. $n \geq 20$. (***) $P \leq 0.001$, a significant difference. (*Bottom*) Heat maps of representative nuclei used for FLIM measurements. Donor lifetimes of RUP1-mEGFP and RUP2-mEGFP are color-coded according to the scale at the *left*.

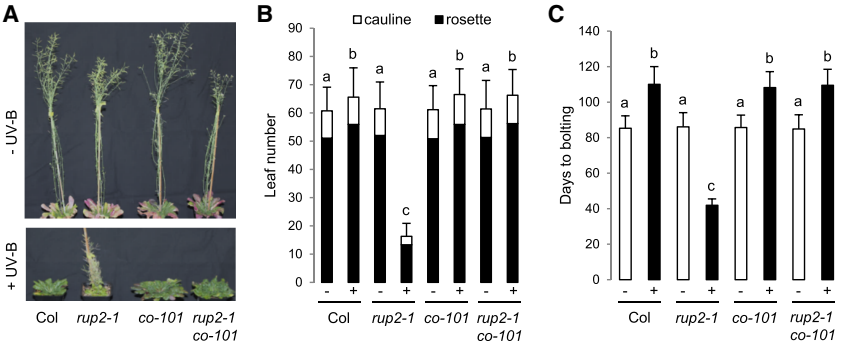

Figure 4. Early flowering of *rup2* in SDs supplemented with UV-B depends on the key flowering regulator CO. (*A*) Representative images of 100-d-old wild-type (Col), *rup2-1*, *co-101*, and *rup2-1 co-101 Arabidopsis* plants grown with (+) or without (–) UV-B. (*B*,*C*) Quantification of flowering time of wild-type (Col), *rup2-1*, *co-101*, and *rup2-1 co-101* plants grown in SD with (+) or without (–) UV-B. The flowering time is represented by total leaf number (rosette and cauline leaves; *B*) and days to bolting (*C*). Error bars represent standard deviation. $n = 21$. Shared letters indicate no statistically significant difference in the means. $P > 0.05$.

RUP2 represses CO binding to the FT *promoter*

Our findings that mutation of RUP2 affects flowering in a CO-dependent manner and that RUP2 interacts with CO suggest that RUP2 may regulate CO post-transcriptionally. In agreement, the expression pattern of *CO* was not altered in *rup2* compared with that in wild type during a 24-h time course under SD + UV conditions, excluding any effect on the diurnal regulation of *CO* mRNA levels (Fig. 6A,B). As endogenous CO levels have never been detected in wild type, we expressed a Pro_{35S}*:3HA-CO* transgene in *rup2* plants. As described before (Song et al. 2012), HA-tagged CO was detectable on protein immunoblots, and its expression in a wild-type background resulted in accelerated flowering in SDs (Fig. 6C–E). This effect was also detectable in the *rup2* mutant background, thus strongly diminishing the effect of *RUP2* mutation on flowering time under SD + UV (Fig. 6C,D). Although this caveat has to be taken into consideration, regulation of diurnal protein dynamics of overexpressed HA-CO was not affected by *RUP2* loss of function when compared with wild-type (Fig. 6E). We further tested whether RUP2 has an effect on CO activity. CO associates with CO-responsive elements (COREs; with CCACA core motif) located at –220 and –161 base pairs relative to the start codon that are essential for CO-mediated *FT* activation (Tiwari et al. 2010; Song et al. 2012; Bu et al. 2014; Gnesutta et al. 2017). Indeed, chromatin immunoprecipitation (ChIP) assays of HA-CO showed specific and strongly enhanced binding to the *FT* promoter region in close vicinity to the CORE sequences ($Pro_{FT\text{-}100}$ fragment) in *rup2*/3HA-CO compared with that in the wild-type background (Col/3HA-CO) in plants grown under UV-B (Fig. 6F). The specificity of the ChIP data was demonstrated by the negative controls provided by the nontransgenic Col wild type as well as by a distal *FT* promoter region ($Pro_{FT\text{-}1185}$ fragment) not bound by CO (Fig. 6F; Song et al. 2012; Bu et al. 2014). In agreement with enhanced CO activity and thus *FT* expression, transient transcription activity assays revealed enhanced *FT* promoter activation by CO in protoplasts deficient of RUP2 compared with those with wild-type RUP2 (Fig. 6G). We thus conclude that RUP2 represses CO activity on *FT* expression by interfering with its *FT* promoter-binding capacity.

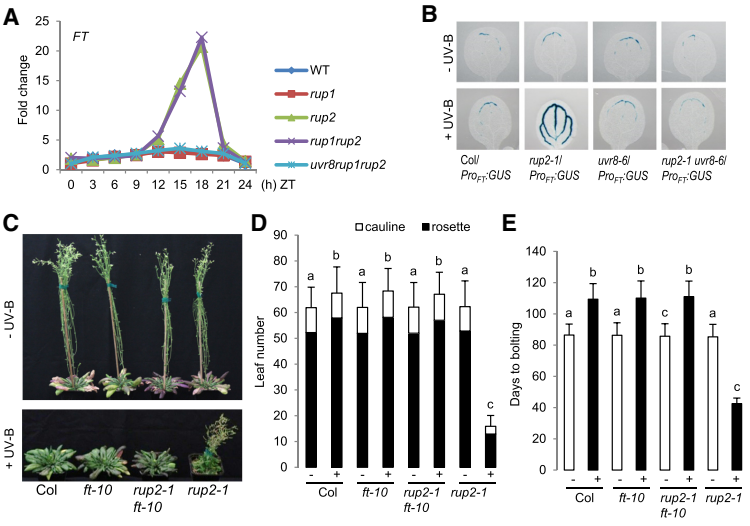

Figure 5. Early flowering of *rup2* in SDs with UV-B depends on the florigen FT. (*A*) Quantitative RT–PCR (qRT–PCR) analysis of *FT* expression in 30-d-old wild-type, *rup1-1*, *rup2-1*, *rup1-1 rup2-1*, and *uvr8-6 rup1-1 rup2-1* plants grown under SD + UV on soil. Samples were collected every 3 h; a representative experiment is shown. (ZT) Zeitgeber time; (ZT0) lights on; (ZT8) lights off. (*B*) GUS assays representing *FT* promoter activity in 5-d-old wild-type (Col/Pro_{FT}*:GUS*), *rup2-1*/Pro_{FT}*:GUS*, *uvr8-6*/Pro_{FT}*:GUS*, and *rup2-1 uvr8-6*/Pro_{FT}*:GUS* seedlings grown in SDs with (+) or without (–) UV-B. (*C*) Representative images of 100-d-old wild-type (Col), *ft-10*, *rup2-1 ft-10*, and *rup2-1 Arabidopsis* plants grown with (+) or without (–) UV-B. (*D*,*E*) Quantification of flowering time of wild-type (Col), *ft-10*, *rup2-1 ft-10*, and *rup2-1* plants grown in SDs with (+) or without (–) UV-B. The flowering time is represented by total leaf number (rosette and cauline leaves; *D*) and days to bolting (*E*). Error bars represent standard deviation. $n = 21$. Shared letters indicate no statistically significant difference in the means. $P > 0.05$.

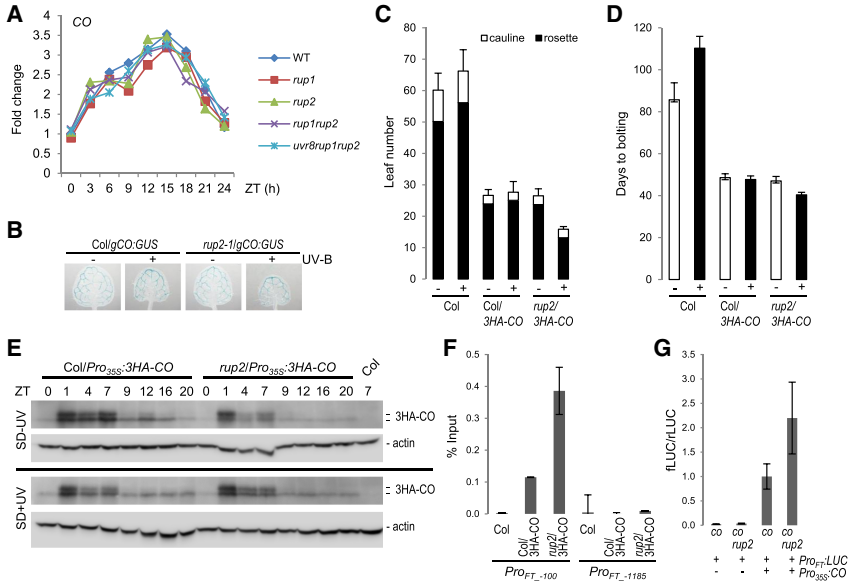

Figure 6. RUP2 represses CO binding to the *FT* promoter and inhibits CO-mediated *FT* expression. (*A*) qRT–PCR analysis of *CO* expression in 30-d-old wild-type, *rup1-1*, *rup2-1*, *rup1-1 rup2-1*, and *uvr8-6 rup1-1 rup2-1* plants grown under SD + UV on soil. Samples were collected every 3 h; a representative experiment is shown. (ZT) Zeitgeber time; (ZT0) lights on; (ZT8) lights off. (*B*) GUS assays representing *CO* promoter activity in 5-d-old wild-type (Col/*gCO:GUS*) and *rup2-1/gCO:GUS* seedlings grown in SDs with (+) or without (−) UV-B. (*C*,*D*) Quantification of flowering time of wild-type (Col), Col/*Pro*$_{35S}$*:3HA-CO*, and *rup2-1*/*Pro*$_{35S}$*:3HA-CO* plants grown in SDs with (+) or without (−) UV-B. The flowering time is represented by total leaf number (rosette and cauline leaves; *C*) and days to bolting (*D*). Error bars represent standard deviation. $n = 16$. (*E*) RUP2 does not affect the diurnal regulation of CO stability in *Pro*$_{35S}$*:3HA-CO* overexpression lines. Immunoblot analysis of 3HA-CO protein level at the indicated Zeitgeber time in 10-d-old Col/*Pro*$_{35S}$*:3HA-CO* and *rup2*/*Pro*$_{35S}$*: 3HA-CO* plants grown in the absence (SD − UV; *top* panel) or presence (SD + UV; *bottom* panel) of UV-B. Actin levels are shown as a loading control; wild type (Col) at ZT7 was added as a control sample for anti-HA specificity. (*F*) HA-CO ChIP-qPCR using 12-d-old wild type (Col), Col/*Pro*$_{35S}$*:3HA-CO*, and *rup2*/*Pro*$_{35S}$*:3HA-CO* seedlings grown in SD + UV (ZT8). The numbers of the analyzed DNA fragments indicate the positions of the 5′ base pair of the amplicon relative to the translation start site. ChIP efficiency of DNA associated with HA-CO is presented as the percentage recovered from the total input DNA (% Input). A representative experiment is shown; error bars represent standard deviation of three technical replicates. (*G*) Relative LUC activity of protoplasts isolated from *co-101* and *co-101 rup2-1* plants growing under SD + UV. After protoplast transfection with *Pro*$_{FT}$*:fLUC* and *Pro*$_{35S}$*:CO*, chemiluminescence was measured at ZT3–ZT4. Error bars represent standard deviation of four independent experiments, each consisting of at least two independent protoplast transfections.

Discussion

Seasonal patterns of flowering are of great importance for the reproductive success of many plants in natural ecosystems as well as in horticulture and agricultural production systems. The impact of day length on flowering has been studied since the discovery of photoperiodism in 1920 (Garner and Allard 1920). In recent decades, the genetic pathways and regulatory proteins that promote flowering in response to photoperiod were largely defined in the model species *A. thaliana* (Turck et al. 2008; Andres and Coupland 2012; Song et al. 2015). However, most of the work was and still is performed in growth chambers whose light spectrum does not include UV-B, an intrinsic portion of sunlight. Here, using controlled growth environments containing UV-B, we identified and characterized the unanticipated role of RUP2 in photoperiodic flowering control as a crucial repressor of CO activity associated with UVR8-inducible flowering in SDs. RUP2-mediated prevention of flowering thus contributes to the perception of day length by allowing discrimination of SDs from LDs in the presence of UV-B.

CO is a B-box family transcriptional regulator that is a key activator of flowering by inducing *FT* expression. Thus, the activity of CO is regulated at many levels, including transcription, phosphorylation status, protein stability, and activity (Romera-Branchat et al. 2014; Song et al. 2015; Shim et al. 2017). Under inductive LD conditions, CO accumulates toward the end of the day, forming a complex with the histone-fold domain containing dimeric B and C subunits of nuclear factor Y (NF-Y) (Ben-Naim et al. 2006; Wenkel et al. 2006; Jang et al. 2008; Gnesutta et al. 2017). The CCT domain of CO within the heterotrimeric NF–CO complex conveys binding specificity to the CORE in the *FT* promoter, thereby promoting *FT* expression near dusk (Gnesutta et al. 2017). Here, we provide evidence that RUP2 is a major repressor of CO activity under noninductive SD + UV conditions, since *rup2* plants flower very early under SD + UV conditions. Moreover, as this early flowering phenotype is suppressed in *rup2 uvr8* and *rup2 co* double mutants, it is thus UVR8- and CO-dependent. RUP2 apparently does not affect *CO* transcription or CO protein levels, but its repressive activity involves direct interaction with CO. Indeed, CO transcriptional activity is repressed by RUP2, and this effect is detectable at the level of reduced *FT* expression, *FT* promoter activity in transient reporter assays, and CO association with the *FT* promoter in ChIP assays. Interestingly, several CO-interacting proteins were described recently as negative regulators of CO transcriptional activity, acting through recruitment of TOPLESS repressor proteins or through inhibition of CO binding to target genes (Wang et al. 2014, 2016; Nguyen et al. 2015; Zhang et al. 2015; Graeff et al. 2016; Xu et al. 2016; Ordonez-Herrera et al. 2018), the latter of which is similar to our findings for RUP2 activity. It is interesting to note that RUP2 binds

to the N-terminal part of CO, which is comprised of two tandem B-box domains. This interaction could directly affect binding of CO to target promoters. Alternately, this interaction may facilitate the binding of a presently unknown repressor of CO and/or may prevent interaction with a positive regulatory interaction partner by blocking the interaction site.

If RUP2 is a general repressor of CO activity in the absence of UV-B, we would expect delayed flowering in RUP2 overexpression lines particularly under LD – UV conditions and early flowering in *rup2* plants in SD – UV. Previous work has suggested that overexpression of *RUP2*/*EFO2* results in early flowering in both SDs and LDs (Wang et al. 2011), a phenotype that we, however, did not observe in our experimental conditions using lines for which RUP2 overexpression was clearly confirmed by immunoblot analysis. Furthermore, we did not observe delayed flowering of RUP2 overexpression lines in LD – UV or early flowering of *rup2* in SD – UV. This suggests that RUP2 affects photoperiodic flowering very specifically for a distinct UVR8-induced CO activation mechanism. As CO–FT regulation is largely localized to phloem companion cells in the leaf vasculature (Takada and Goto 2003; Turck et al. 2008; Song et al. 2015), the tissue specificity of UVR8 and RUP2 activity in the regulation of flowering remains to be determined as well as the exact mechanism by which UVR8 activates CO.

Interpretation of the lack of a RUP2 overexpression effect in LD + UV is complicated due to the fact that UVR8 activity is fully repressed by RUP2 overexpression (Gruber et al. 2010; Heijde and Ulm 2013). Indeed, RUP2 overexpression lines mimic the phenotype of *uvr8*-null mutants, and, indeed, no UVR8 monomers and no physiological response were detected in these lines upon UV-B treatment (Gruber et al. 2010; Heijde and Ulm 2013). It is thus clear that UVR8-mediated activation of flowering is impaired at the level of photoreceptor regulation in RUP2 overexpression lines, and an independent effect on CO activity cannot be investigated, as no UVR8-mediated signaling occurs with RUP2 overexpression. Notwithstanding this, it is of note that the role of RUP2 in flowering time regulation seems independent of its role in the regulation of UVR8 activity. This is particularly highlighted by the fact that UVR8 overexpression plants do not show early flowering, although they display a UV-B hypersensitivity similar to that in *rup2*, as determined by the rosette phenotype. This is further supported by the interaction of RUP2 with CO and its effect on CO transcriptional activity and *FT* promoter binding.

It is noteworthy that wild type developed slower and flowered later under SD + UV than under SD – UV conditions (e.g., Figs. 1, 4A–C, 5C–E), which is in agreement with a recent report (Dotto et al. 2018). Interestingly, this delayed flowering was partially UVR8-dependent (Fig. 1F,G; Supplemental Fig. S1) and has been linked previously to the age pathway of flowering (Dotto et al. 2018). The potential interplay between the effects of UVR8 signaling on the age and photoperiod pathways remains to be determined; however, it is clear that the effect of RUP2 mutation on the photoperiodic pathway overrides the potential effect of UVR8 hyperactivity in *rup2* on the age pathway. Moreover, it is of note that the delay in flowering under UV-B was not detectable in the sun simulator experiment, but the repressor function of RUP2 clearly was (Fig. 2).

Seasonal responses of flowering time assessed in field trials are not always as anticipated based on experiments performed under laboratory conditions (Weinig et al. 2002; Wilczek et al. 2009; Brachi et al. 2010; Andres and Coupland 2012). In part, the absence of UV-B in most laboratory experiments may contribute to this phenomenon; however, such a notion needs to be experimentally further verified. Independent of this, we show that RUP2 loss of function renders the facultative LD species *A. thaliana* into a day-neutral plant in the presence of UV-B, suggesting that RUP2 is required for flowering time regulation by day length under natural conditions. Thus, although UV-B seems to play a rather minor role in *Arabidopsis* wild-type flowering, loss of RUP2 exposes an existing UVR8-activated pathway that can efficiently promote flowering in noninductive SDs. It is intriguing to speculate why wild-type *Arabidopsis* has a pathway to flower in response to UV-B but apparently does not make use of it. A possibility is that the *Arabidopsis rup2* mutant revealed a UVR8 flowering pathway that is indeed active in other plant species but repressed in *Arabidopsis* as a (facultative) LD plant. Alternatively, it remains to be investigated whether RUP2 may integrate other environmental factors to regulate flowering in the field under sunlight, with its intrinsic UV-B. For example, it can be envisaged that RUP2 degradation may be a potent inducer of flowering in noninductive photoperiods, a possibility that deserves further investigation.

Materials and methods

Plant material and growth conditions

The mutants and overexpression lines used in this study were in the *A. thaliana* Columbia (Col) accession and were described previously as follows: *uvr8-6* (Favory et al. 2009), *rup1-1*, *rup2-1*, *rup2-1*/*Pro$_{35S}$:RUP2* (Gruber et al. 2010), *cop1-4* (Deng et al. 1992), *ft-10* (Yoo et al. 2005), *co-101* (Takada and Goto 2003), and *Pro$_{35S}$:3HA-CO* line #7 (Song et al. 2012). *rup2-2* (SALK_139836) (Alonso et al. 2003) was characterized in this study (Supplemental Fig. S6). The GUS reporter lines used were *Pro$_{FT}$:GUS* (Takada and Goto 2003), which was introgressed into *rup2-1*, *uvr8-6*, and *rup2-1 uvr8-6* mutants by genetic crossing, and *gCO:GUS* (Takada and Goto 2003), which was introgressed into *rup2-1*. The *RUP2* (At5g23730) genomic locus, including an ~1.5-kb promoter region, was amplified with primers RUP2pFW (5′-GGGG*ACAAGTTTGTACAAAAAAGCAG GCT*TCCACGTATGACTCGTCCTTACTTTGC-3′; the *att*B1 site is in italic, and the gene-specific sequence is underlined) and RUP2pREV (5′-GGGG*ACCACTTTGTACAAGAAAGCTG GGT*CATGAAAACAGAGTAATGACTGTTG C-3′; the *att*B2 site is in italic, and the gene-specific sequence is underlined), cloned into pDONR207 using Gateway technology (Invitrogen), and sequenced to confirm the integrity of the cloned fragment. The genomic clone was inserted into the binary destination vector pMDC163 (Curtis and Grossniklaus 2003). *rup2-1* plants were transformed by *Agrobacterium* using the floral dip method (Clough and Bent 1998).

For flowering time experiments, quantitative RT–PCR (qRT–PCR), GUS reporter assays, and transient expression assays, seeds were stratified for 2 d at 4°C in the dark, and plants were grown with a day/night temperature cycle of 22°C/18°C in GroBanks (CLF Plant Climatics) with Philips Master TL-D 58W/840 white light fluorescent tubes (120 µmol m^{-2} s^{-1}, measured with a LI-250 light meter; LI-COR Biosciences) supplemented or not with UV-B from Philips TL40W/01RS narrowband UV-B tubes (0.07 mW cm^{-2}; measured with a VLX-3W ultraviolet light meter equipped with a CX-312 sensor; Vilber Lourmat). Plants were grown under 8-h/16-h light/dark SD or 16-h/8-h light/dark LD conditions, as indicated.

For immunoblot analysis, ChIP, hypocotyl length measurement, and anthocyanin quantification, seeds were surface-sterilized with 70% ethanol and 0.005% Tween 20 and plated on half-strength MS medium (Duchefa) containing 1% sucrose and 0.8% agar. For hypocotyl length measurement and anthocyanin quantification, seedlings were grown as described previously (Oravecz et al. 2006; Favory et al. 2009). For immunoblot analysis, qRT–PCR, and ChIP, seedlings were grown in GroBanks under SD − UV or SD + UV conditions, as indicated.

A sun simulator of the Research Unit Environmental Simulation at the Helmhotz Zentrum München (Thiel et al. 1996) was used to study flowering time regulation under conditions simulating natural light and UV radiation conditions. The condition of the treatment in the sun simulator was similar to that described previously (Favory et al. 2009; Gruber et al. 2010; González Besteiro et al. 2011) with an 8-h day period with mean photosynthetically active radiation (PAR; 400–700 nm) of 600 µmol m^{-2} s^{-1} and 6 h of UV-B irradiance with a biologically effective radiation of 308 mW m^{-2} (weighted by the generalized plant action spectrum [Caldwell 1971] and normalized at 300 nm) (Supplemental Fig. S7). Controls were grown excluding the entire UV radiation spectrum. The temperature was maintained at 23°C during the day and 18°C at night. The relative humidity was kept constant at 60%.

PCR genotyping of mutants and isolation of double mutants

Single mutants were crossed, and the double mutants were identified by PCR genotyping in the F2 generation. *rup1-1*, *rup2-1*, and *uvr8-6* were genotyped as described previously (Gruber et al. 2010). *co-101, ft-10*, and *rup2-2* were genotyped as follows: *co-101*: CO101_LP (5′-AGCTCCCACACCATCAAACTTACTACATC-3′) + CO101_RP (5′-AGTCCATACTCGAGTTGTAATCCA-3′) = 0.6 kb for wild type, and CO101_LP + T-DNA primer LB3 (5′-TAGCATCTGAATTTCATAACCAATCTCGATACAC-3′) = 0.45 kb for *co-101*; *ft-10* (GABI_290E08): FT10_LP (5′-ATATTGATGAATCTCTGTTGTGG-3′) + FT10_RP (5′-AGGGTTGCTAGGACTTGGAACA-3′) = 0.3 kb for wild type, and T-DNA primer 8474 (5′-ATAATAACGCTGCGGACATCTACATTTT-3′) + FT_RP = 0.5 kb for *ft-10*; and *rup2-2* (SALK_139836): RUP2_SALK_139836_LP (5′-TGTTTCGGTGTTACCATTACG-3′) + RUP2_SALK_139836_RP (5′-TCGGATCCCATACTTGCATAG-3′) = 1.0 kb for wild type, and T-DNA primer LBb1.3 (5′-ATTTTGCCGATTTCGGAAC-3′) + RUP2_SALK_139836_RP = 0.5 kb for *rup2-2*.

Immunoblot analysis

Proteins were extracted in 50 mM Na-phosphate (pH 7.4), 150 mM NaCl, 10% glycerol, 5 mM EDTA, 1 mM DTT, 0.1% Triton X-100, 50 µM MG132, 2 mM Na_3VO_4, 2 mM NaF, and 1% (v/v) protease inhibitor mixture for plant extracts (Sigma-Aldrich, P9599). For immunoblot analysis, total cellular proteins were separated by electrophoresis in 10% (w/v) SDS–polyacrylamide gels and transferred to PVDF membranes according to the manufacturer's instructions (iBlot dry blotting system, Thermofisher Scientific).

Rabbit polyclonal antibodies were generated against synthetic peptides derived from the RUP2 protein sequence [amino acids 1–15 + C: MNTLHPHKQQQEQAQC; anti-RUP2$^{(1-15)}$] and were affinity-purified against the peptide (Eurogentec). Anti-RUP2$^{(1-15)}$, anti-UVR8$^{(426-440)}$ (Favory et al. 2009), anti-HA.11 (BioLegend, 901513), and anti-actin (Sigma-Aldrich, A0480) were used as primary antibodies. Horseradish peroxidase (HRP)-conjugated anti-rabbit and anti-mouse immunoglobulins (Dako A/S) were used as the secondary antibodies. Chemiluminescent signals were generated with the ECL Plus Western detection kit and revealed with an ImageQuant LAS 4000 mini-CCD camera system (GE Healthcare).

Yeast two-hybrid interaction assays

A yeast two-hybrid screen was performed using RUP2 as bait fused to the GAL4-binding domain (Matchmaker Gold yeast two-hybrid system, Clontech). The screen was carried out following the standard protocol suggested by the manufacturer.

Arabidopsis RUP1-coding (At5g52250) and *RUP2*-coding sequences were cloned into yeast two-hybrid plasmid containing a DNA-binding domain (pGBKT7-GW) (Yin et al. 2015), and *CO* was cloned into plasmid containing an activation domain (pGADT7-GW). Bait and prey constructs were transformed into *Saccharomyces cerevisiae* strain Y2H Gold and Y187, respectively. To quantify protein–protein interaction, using CPRG as a substrate, yeast growth was carried out directly on the plates as described before (Rizzini et al. 2011), and the assay was performed according to the protocol described in the yeast protocol handbook from Clontech (version PR973283). The lacZ β-galactosidase activity is expressed as Miller units.

Anthocyanin extraction and measurement

Arabidopsis seedlings were grown for 4 d under low narrowband UV-B fields with the appropriated cutoff filters, as described previously (Oravecz et al. 2006; Favory et al. 2009). Fifty milligrams of seedlings was harvested from agar plates and immediately frozen in liquid nitrogen. Sample tissues were processed for 10 sec using a Silamat S5 mixer (Ivoclar Vivadent). Two-hundred-fifty microliters of acidic methanol (1% [w/v] HCl) was added to each sample that was homogenized and placed in an overhead shaker for 1 h at 4°C as described before (Yin et al. 2012). Samples were centrifuged at 14,000 rpm for 1 min, and the supernatant was used to quantify anthocyanin content in a spectrophotometer at 535 and 650 nm. Values are reported as A530 −0.25 (A657) per gram of fresh weight.

Hypocotyl length

Four-day-old *Arabidopsis* seedlings were grown in the appropriate light conditions, and their hypocotyl lengths were measured (n > 30) using ImageJ software as described previously (Oravecz et al. 2006).

Statistical analysis of flowering time experiments

ANOVA with post-hoc Tukey HSD statistical analyses were performed using the R software package. The means and standard deviations were derived from replicated independent biological

samples unless stated otherwise. Shared letters indicate no statistically significant difference in the means ($P > 0.05$).

Confocal laser scanning microscopy (CLSM) and FLIM analyses

For CLSM and FLIM analyses, the binary 2in1 vectors were used (Hecker et al. 2015). The coding sequences of *RUP1* or *RUP2* were cloned into the donor plasmid (mEGFP), while *CO* was cloned into acceptor plasmid (mCherry) using the MultiSite Gateway Technology (Invitrogen). mCherry fused to an NLS was used as a negative control. These constructs were transformed into *Agrobacterium tumefaciens* strain GV3101 and infiltrated into *N. benthamiana* leaves as described previously (Hecker et al. 2015). Leaves were subjected to CLSM and FLIM analyses 1–2 d after infiltration.

The measurements were performed as described previously (Hecker et al. 2015). Briefly, all CLSM and FLIM measurements were performed using a Leica TCS SP8 confocal microscope (Leica Microsystems) equipped with a FLIM unit (PicoQuant). Images were acquired using a 63×/1.20 water immersion objective. For the excitation and emission of fluorescent proteins, the following settings were used: mEGFP at excitation 488 nm and emission 495–530 nm; and mCherry at excitation 561 nm and emission 580–630 nm.

FLIM data were derived from measurements of at least 20 nuclei for each fusion protein combination. To excite RUP1-mEGFP and RUP2-mEGFP for FLIM experiments, a 470-nm pulsed laser (LDH-P-C-470) was used, and the corresponding emission was detected with a SMD emission SPFLIM PMT 495–545 nm by time-correlated single-photon counting using a Picoharp 300 module (PicoQuant). Each time-correlated single-photon counting histogram was reconvoluted with the corresponding instrument response function and fitted against a monoexponential decay function for donor-only samples and a biexponential decay function for the other samples to unravel the mEGFP fluorescence lifetime of each nucleus.

The average mEGFP fluorescence lifetimes as well as the standard error values were calculated using Microsoft Excel 2013. Statistical analysis was performed with JMP (version 12.2.0). To test for homogeneity of variance, Levene's test ($df = 5/140$, $F = 26.298$, $P < 0.0001$) was used, and statistical significance was calculated by a two-tailed all-pair Kruskal-Wallis test followed by a Steel-Dwass post hoc correction.

GUS staining

Arabidopsis leaves were fixed in 90% acetone for 30 min. After washing three times in ice-cold water, plant tissues were incubated with staining buffer (0.5 mg/mL 5-bromo-4-chromo-3-indolyl-β-d-glucuronide [X-Glc], 10 mM EDTA, 0.5 mM ferricyanide, 0.5 mM ferrocyanide, 0.1% Triton X-100 in phosphate buffer) for 5 min at 4°C followed by incubation at 37°C. After removal of staining solution, tissue was cleared by successive washes with 75% ethanol. Samples were mounted in glycerol and analyzed using a stereomicroscope (Leica MZ16, Leica Microsystems AG) or a differential interference contrast (DIC) microscope (Zeiss Axioscope II, Carl Zeiss AG, or Nikon Eclipse 80i, Nikon AG).

qRT–PCR

Arabidopsis total RNA was isolated with the plant RNeasy kit according to the manufacturer's instructions (Qiagen), followed by DNase I treatment. In order to inactivate DNase I, 20 mM EDTA was added, and samples were incubated for 10 min at 65°C. Synthesis of the first strand of cDNA was performed using the TaqMan reverse transcription reagent kit according to the manufacturer's standard protocol (Thermofisher Scientific). Each qRT–PCR reaction was composed of cDNA synthesized with a 1:1 mixture of oligo(dT) primers and random hexamers from 25 ng of total RNA. PCR reactions were performed using the ABsolute qPCR Rox mix kit (ABgene) and a QuantStudio 5 real-time PCR system (Thermofisher Scientific). The following primers were used: for *CO* (At5g15840), CO_qRT_fw (5′-CCTCAGGGACTC ACTACAACG-3′) and CO_qRT_rv (5′-TCTTGGGTGTGAAGC TGTTG-3′), and for *FT* (At1g65480), FT_qRT_fw (5′-CCAAGA GTTGAGATTGGTGGA-3′) and FT_qRT_rv (5′-ATTGCCAA AGGTTGTTCCAG-3′). The levels of expression of 18S and *UBQ10* (Czechowski et al. 2005) were used to normalize the concentrations of the various mRNA samples in which gene expression was analyzed using qbasePLUS real-time PCR data analysis software version 2.4 (Biogazelle). Each reaction was performed in technical triplicates; data shown are representative of at least two independent biological repetitions.

ChIP

Samples were cross-linked in 3% formaldehyde solution in PBS, and cross-linking was quenched with 0.2 M glycine. Nucleus enrichment was performed as described (Fiil et al. 2008). Samples were sonicated in lysis buffer (50 mM Tris-HCL at pH8, 10 mM EDTA, 1% SDS) and further processed as described (Stracke et al. 2010; Binkert et al. 2014). The chromatin was immunoprecipitated with anti-HA antibody (ChIP-grade; Abcam, ab9110) overnight at 4°C, after which cross-linking was reversed for 2 h at 85°C. DNA was purified using QIAquick PCR purification kit (Qiagen) before analysis with a QuantStudio 5 real-time PCR system (Thermofisher Scientific) and the following primer sets: Pro_{FT_-100}-Fw (5′-AGAGGGTTCATGCCTATGATA C-3′), Pro_{FT_-100}-Rv (5′-CTTTGATCTTGAACAAACAGGTG-3′) (Bu et al. 2014), Pro_{FT_-1185}-Fw (5′-TTATCCTGGTCGTGCAAATG-3′), and Pro_{FT_-1185}-Rv (5′-CAAGCGGCCATATTATGGAA-3′) (Song et al. 2012). qPCR data were analyzed according to the percentage of input method (Haring et al. 2007). Each reaction was performed in technical triplicates; data shown are representative of three independent biological repetitions.

Transient expression assays in protoplasts

For the Pro_{FT}*:fLUC* reporter construct, the *FT* promoter region (−1 to −5722) was amplified with primers oVCG-475 (5′-CCCCC *CTCGAG*GTCGACATTTGCTGAACAAAAATCTATT-3′; the XhoI site is in italic, and the gene-specific sequence is underlined) and oVCG-476 (5′-GGTG*GCGGCCGC*TCTAGCTTTGATCTT GAACAAACAGGTG-3′; the NotI site is in italic, and the gene-specific sequence is underlined) from the BAC clone F5I14 and cloned into pGREENII 0800-LUC XhoI/NotI restriction sites (Hellens et al. 2005).

Protoplasts were isolated from 4 to 8-wk-old *co-101* and *rup2-1 co-101* plants growing under SD + UV. Expanded leaves were harvested, and protoplasts were prepared as described previously (Wu et al. 2009). Each protoplast transfection was performed with 5 µg of Pro_{FT}*:fLUC* and Pro_{35S}*:CO* plasmids and incubated overnight in darkness at 21°C. Luciferase assay was performed with the dual-luciferase reporter assay system (Promega) at Zeitgeber time (ZT) 3–4 (ZT0 = lights on, ZT8 = lights off) following the manufacturer's instructions and a GloMax 96 Microplate Luminometer (Promega). Relative luciferase activity corresponds to normalized firefly/Renilla ratio.

Acknowledgments

We thank Takato Imaizumi and Koji Goto for providing plant material, Christopher Grefen for the binary 2in1 vectors, Hongtao Liu for the pGREENII 0800-LUC construct, Rodrigo S. Reis for technical assistance with protoplast transient expression assays, Isabelle Fleury for contributing some of the crosses, Stefanie Mühlhans for excellent technical assistance in sun simulator experiments, and Michael Hothorn for helpful comments on the manuscript. This work was supported by the University of Geneva, the Swiss National Science Foundation (grant nos. 31003A_175774 to R.U., and CRSII3_154438 to R.U. and C.F.), the European Research Council (ERC) under the European Union's Seventh Framework Programme (grant no. 310539 to R. U.), and the German Research Foundation (grant CRC 1101-D02 to K.H.). V.C.G. was supported by an EMBO long-term fellowship (ALTF 293-2013).

Author contributions: A.B.A. and R.U. conceived and designed the study. A.B.A. performed all of the experiments reported here except for the following: N.G. and K.H. contributed the FRET-FLIM data (Fig. 3B,C), A.A. and J.B.W. contributed the sun simulator data (Fig. 2; Supplemental Fig. S7), M.P. contributed the ChIP data (Fig. 6F), S.C. contributed the protein immunoblots (Fig. 6E; Supplemental Figs. S3C, S4D), and V.C.G. and C.F. contributed the transient expression assays in protoplasts (Fig. 6G). R.U. supervised the research, and A.B.A. and R.U. wrote the manuscript with input from all authors.

References

Alonso JM, Stepanova AN, Leisse TJ, Kim CJ, Chen H, Shinn P, Stevenson DK, Zimmerman J, Barajas P, Cheuk R, et al. 2003. Genome-wide insertional mutagenesis of *Arabidopsis thaliana*. *Science* **301:** 653–657.

Andres F, Coupland G. 2012. The genetic basis of flowering responses to seasonal cues. *Nat Rev Genet* **13:** 627–639.

Ben-Naim O, Eshed R, Parnis A, Teper-Bamnolker P, Shalit A, Coupland G, Samach A, Lifschitz E. 2006. The CCAAT binding factor can mediate interactions between CONSTANS-like proteins and DNA. *Plant J* **46:** 462–476.

Binkert M, Kozma-Bognar L, Terecskei K, De Veylder L, Nagy F, Ulm R. 2014. UV-B-responsive association of the *Arabidopsis* bZIP transcription factor ELONGATED HYPOCOTYL5 with target genes, including its own promoter. *Plant Cell* **26:** 4200–4213.

Brachi B, Faure N, Horton M, Flahauw E, Vazquez A, Nordborg M, Bergelson J, Cuguen J, Roux F. 2010. Linkage and association mapping of *Arabidopsis thaliana* flowering time in nature. *PLoS Genet* **6:** e1000940.

Brown BA, Cloix C, Jiang GH, Kaiserli E, Herzyk P, Kliebenstein DJ, Jenkins GI. 2005. A UV-B-specific signaling component orchestrates plant UV protection. *Proc Natl Acad Sci* **102:** 18225–18230.

Bu Z, Yu Y, Li Z, Liu Y, Jiang W, Huang Y, Dong AW. 2014. Regulation of *Arabidopsis* flowering by the histone mark readers MRG1/2 via interaction with CONSTANS to modulate *FT* expression. *PLoS Genet* **10:** e1004617.

Caldwell MM. 1971. Solar UV irradiation and the growth and development of higher plants. In *Photophysiology* (ed. Giese AC), pp. 131–177. Academic Press, New York.

Cloix C, Kaiserli E, Heilmann M, Baxter KJ, Brown BA, O'Hara A, Smith BO, Christie JM, Jenkins GI. 2012. C-terminal region of the UV-B photoreceptor UVR8 initiates signaling through interaction with the COP1 protein. *Proc Natl Acad Sci* **109:** 16366–16370.

Clough SJ, Bent AF. 1998. Floral dip: a simplified method for *Agrobacterium*-mediated transformation of *Arabidopsis thaliana*. *Plant J* **16:** 735–743.

Corbesier L, Vincent C, Jang S, Fornara F, Fan Q, Searle I, Giakountis A, Farrona S, Gissot L, Turnbull C, et al. 2007. FT protein movement contributes to long-distance signaling in floral induction of *Arabidopsis*. *Science* **316:** 1030–1033.

Curtis MD, Grossniklaus U. 2003. A gateway cloning vector set for high-throughput functional analysis of genes in planta. *Plant Physiol* **133:** 462–469.

Czechowski T, Stitt M, Altmann T, Udvardi MK, Scheible WR. 2005. Genome-wide identification and testing of superior reference genes for transcript normalization in *Arabidopsis*. *Plant Physiol* **139:** 5–17.

Deng XW, Matsui M, Wei N, Wagner D, Chu AM, Feldmann KA, Quail PH. 1992. COP1, an *Arabidopsis* regulatory gene, encodes a protein with both a zinc-binding motif and a Gβ homologous domain. *Cell* **71:** 791–801.

Dotto M, Gomez MS, Soto MS, Casati P. 2018. UV-B radiation delays flowering time through changes in the PRC2 complex activity and miR156 levels in *Arabidopsis thaliana*. *Plant Cell Environ* **41:** 1394–1406.

Favory JJ, Stec A, Gruber H, Rizzini L, Oravecz A, Funk M, Albert A, Cloix C, Jenkins GI, Oakeley EJ, et al. 2009. Interaction of COP1 and UVR8 regulates UV-B-induced photomorphogenesis and stress acclimation in *Arabidopsis*. *EMBO J* **28:** 591–601.

Fiil BK, Qiu JL, Petersen K, Petersen M, Mundy J. 2008. Coimmunoprecipitation (co-IP) of nuclear proteins and chromatin immunoprecipitation (ChIP) from *Arabidopsis*. *CSH Protoc* **2008:** pdb prot5049.

Findlay KM, Jenkins GI. 2016. Regulation of UVR8 photoreceptor dimer/monomer photo-equilibrium in *Arabidopsis* plants grown under photoperiodic conditions. *Plant Cell Environ* **39:** 1706–1714.

Garner WW, Allard HA. 1920. Effect of the relative length of day and night and other factors of the environment on growth and reproduction in plants. *J Agric Res* **18:** 553–606.

Gnesutta N, Kumimoto RW, Swain S, Chiara M, Siriwardana C, Horner DS, Holt BF III, Mantovani R. 2017. CONSTANS imparts DNA sequence specificity to the histone fold NF-YB/NF-YC dimer. *Plant Cell* **29:** 1516–1532.

González Besteiro MA, Bartels S, Albert A, Ulm R. 2011. *Arabidopsis* MAP kinase phosphatase 1 and its target MAP kinases 3 and 6 antagonistically determine UV-B stress tolerance, independent of the UVR8 photoreceptor pathway. *Plant J* **68:** 727–737.

Graeff M, Straub D, Eguen T, Dolde U, Rodrigues V, Brandt R, Wenkel S. 2016. MicroProtein-mediated recruitment of CONSTANS into a TOPLESS trimeric complex represses flowering in *Arabidopsis*. *PLoS Genet* **12:** e1005959.

Gruber H, Heijde M, Heller W, Albert A, Seidlitz HK, Ulm R. 2010. Negative feedback regulation of UV-B-induced photomorphogenesis and stress acclimation in *Arabidopsis*. *Proc Natl Acad Sci* **107:** 20132–20137.

Guo H, Yang H, Mockler TC, Lin C. 1998. Regulation of flowering time by *Arabidopsis* photoreceptors. *Science* **279:** 1360–1363.

Haring M, Offermann S, Danker T, Horst I, Peterhansel C, Stam M. 2007. Chromatin immunoprecipitation: optimization, quantitative analysis and data normalization. *Plant Methods* **3:** 11.

Hecker A, Wallmeroth N, Peter S, Blatt MR, Harter K, Grefen C. 2015. Binary 2in1 vectors improve in planta (co)localization and dynamic protein interaction studies. *Plant Physiol* **168:** 776–787.

Heijde M, Ulm R. 2013. Reversion of the *Arabidopsis* UV-B photoreceptor UVR8 to the homodimeric ground state. *Proc Natl Acad Sci* **110:** 1113–1118.

Hellens RP, Allan AC, Friel EN, Bolitho K, Grafton K, Templeton MD, Karunairetnam S, Gleave AP, Laing WA. 2005. Transient expression vectors for functional genomics, quantification of promoter activity and RNA silencing in plants. *Plant Methods* **1:** 13.

Huang X, Ouyang X, Yang P, Lau OS, Chen L, Wei N, Deng XW. 2013. Conversion from CUL4-based COP1–SPA E3 apparatus to UVR8–COP1–SPA complexes underlies a distinct biochemical function of COP1 under UV-B. *Proc Natl Acad Sci* **110:** 16669–16674.

Jaeger KE, Wigge PA. 2007. FT protein acts as a long-range signal in *Arabidopsis*. *Curr Biol* **17:** 1050–1054.

Jang S, Marchal V, Panigrahi KC, Wenkel S, Soppe W, Deng XW, Valverde F, Coupland G. 2008. *Arabidopsis* COP1 shapes the temporal pattern of CO accumulation conferring a photoperiodic flowering response. *EMBO J* **27:** 1277–1288.

Jenkins GI. 2017. Photomorphogenic responses to ultraviolet-B light. *Plant Cell Environ* **40:** 2544–2557.

Khanna R, Kronmiller B, Maszle DR, Coupland G, Holm M, Mizuno T, Wu SH. 2009. The *Arabidopsis* B-box zinc finger family. *Plant Cell* **21:** 3416–3420.

Lau OS, Deng XW. 2012. The photomorphogenic repressors COP1 and DET1: 20 years later. *Trends Plant Sci* **17:** 584–593.

Laubinger S, Marchal V, Gentilhomme J, Wenkel S, Adrian J, Jang S, Kulajta C, Braun H, Coupland G, Hoecker U. 2006. *Arabidopsis* SPA proteins regulate photoperiodic flowering and interact with the floral inducer CONSTANS to regulate its stability. *Development* **133:** 3213–3222.

Liu LJ, Zhang YC, Li QH, Sang Y, Mao J, Lian HL, Wang L, Yang HQ. 2008. COP1-mediated ubiquitination of CONSTANS is implicated in cryptochrome regulation of flowering in *Arabidopsis*. *Plant Cell* **20:** 292–306.

Mathieu J, Warthmann N, Kuttner F, Schmid M. 2007. Export of FT protein from phloem companion cells is sufficient for floral induction in *Arabidopsis*. *Curr Biol* **17:** 1055–1060.

McNellis TW, von Arnim AG, Araki T, Komeda Y, Misera S, Deng XW. 1994. Genetic and molecular analysis of an allelic series of *cop1* mutants suggests functional roles for the multiple protein domains. *Plant Cell* **6:** 487–500.

Nguyen KT, Park J, Park E, Lee I, Choi G. 2015. The *Arabidopsis* RING domain protein BOI inhibits flowering via CO-dependent and CO-independent mechanisms. *Mol Plant* **8:** 1725–1736.

Oravecz A, Baumann A, Mate Z, Brzezinska A, Molinier J, Oakeley EJ, Adam E, Schafer E, Nagy F, Ulm R. 2006. CONSTITUTIVELY PHOTOMORPHOGENIC1 is required for the UV-B response in *Arabidopsis*. *Plant Cell* **18:** 1975–1990.

Ordonez-Herrera N, Trimborn L, Menje M, Henschel M, Robers L, Kaufholdt D, Hansch R, Adrian J, Ponnu J, Hoecker U. 2018. The transcription factor COL12 is a substrate of the COP1/SPA E3 ligase and regulates flowering time and plant architecture. *Plant Physiol* **176:** 1327–1340.

Podolec R, Ulm R. 2018. Photoreceptor-mediated regulation of the COP1/SPA E3 ubiquitin ligase. *Curr Opin Plant Biol* **45:** 18–25.

Putterill J, Robson F, Lee K, Simon R, Coupland G. 1995. The CONSTANS gene of *Arabidopsis* promotes flowering and encodes a protein showing similarities to zinc finger transcription factors. *Cell* **80:** 847–857.

Rizzini L, Favory JJ, Cloix C, Faggionato D, O'Hara A, Kaiserli E, Baumeister R, Schafer E, Nagy F, Jenkins GI, et al. 2011. Perception of UV-B by the *Arabidopsis* UVR8 protein. *Science* **332:** 103–106.

Romera-Branchat M, Andres F, Coupland G. 2014. Flowering responses to seasonal cues: what's new? *Curr Opin Plant Biol* **21:** 120–127.

Samach A, Onouchi H, Gold SE, Ditta GS, Schwarz-Sommer Z, Yanofsky MF, Coupland G. 2000. Distinct roles of CONSTANS target genes in reproductive development of *Arabidopsis*. *Science* **288:** 1613–1616.

Shim JS, Kubota A, Imaizumi T. 2017. Circadian clock and photoperiodic flowering in *Arabidopsis*: CONSTANS is a hub for signal integration. *Plant Physiol* **173:** 5–15.

Song YH, Smith RW, To BJ, Millar AJ, Imaizumi T. 2012. FKF1 conveys timing information for CONSTANS stabilization in photoperiodic flowering. *Science* **336:** 1045–1049.

Song YH, Shim JS, Kinmonth-Schultz HA, Imaizumi T. 2015. Photoperiodic flowering: time measurement mechanisms in leaves. *Annu Rev Plant Biol* **66:** 441–464.

Stracke R, Favory JJ, Gruber H, Bartelniewoehner L, Bartels S, Binkert M, Funk M, Weisshaar B, Ulm R. 2010. The *Arabidopsis* bZIP transcription factor HY5 regulates expression of the PFG1/MYB12 gene in response to light and ultraviolet-B radiation. *Plant Cell Environ* **33:** 88–103.

Takada S, Goto K. 2003. TERMINAL FLOWER2, an *Arabidopsis* homolog of HETEROCHROMATIN PROTEIN1, counteracts the activation of *FLOWERING LOCUS T* by CONSTANS in the vascular tissues of leaves to regulate flowering time. *Plant Cell* **15:** 2856–2865.

Thiel S, Döhring T, Köfferlein M, Kosak A, Martin P, Seidlitz HK. 1996. A phytotron for plant stress research: how far can artificial lighting compare to natural sunlight? *J Plant Physiol* **148:** 456–463.

Tiwari SB, Shen Y, Chang HC, Hou Y, Harris A, Ma SF, McPartland M, Hymus GJ, Adam L, Marion C, et al. 2010. The flowering time regulator CONSTANS is recruited to the *FLOWERING LOCUS T* promoter via a unique cis-element. *New Phytol* **187:** 57–66.

Turck F, Fornara F, Coupland G. 2008. Regulation and identity of florigen: FLOWERING LOCUS T moves center stage. *Annu Rev Plant Biol* **59:** 573–594.

Ulm R, Baumann A, Oravecz A, Mate Z, Adam E, Oakeley EJ, Schafer E, Nagy F. 2004. Genome-wide analysis of gene expression reveals function of the bZIP transcription factor HY5 in the UV-B response of *Arabidopsis*. *Proc Natl Acad Sci* **101:** 1397–1402.

Wang W, Yang D, Feldmann KA. 2011. EFO1 and EFO2, encoding putative WD-domain proteins, have overlapping and distinct roles in the regulation of vegetative development and flowering of *Arabidopsis*. *J Exp Bot* **62:** 1077–1088.

Wang CQ, Guthrie C, Sarmast MK, Dehesh K. 2014. BBX19 interacts with CONSTANS to repress *FLOWERING LOCUS T* transcription, defining a flowering time checkpoint in *Arabidopsis*. *Plant Cell* **26:** 3589–3602.

Wang H, Pan J, Li Y, Lou D, Hu Y, Yu D. 2016. The DELLA–CONSTANS transcription factor cascade integrates gibberellic acid and photoperiod signaling to regulate flowering. *Plant Physiol* **172:** 479–488.

Weinig C, Ungerer MC, Dorn LA, Kane NC, Toyonaga Y, Halldorsdottir SS, Mackay TF, Purugganan MD, Schmitt J. 2002. Novel loci control variation in reproductive timing in *Arabidopsis thaliana* in natural environments. *Genetics* **162:** 1875–1884.

Wenkel S, Turck F, Singer K, Gissot L, Le Gourrierec J, Samach A, Coupland G. 2006. CONSTANS and the CCAAT box binding complex share a functionally important domain and interact

to regulate flowering of *Arabidopsis*. *Plant Cell* **18:** 2971–2984.

Wigge PA, Kim MC, Jaeger KE, Busch W, Schmid M, Lohmann JU, Weigel D. 2005. Integration of spatial and temporal information during floral induction in *Arabidopsis*. *Science* **309:** 1056–1059.

Wilczek AM, Roe JL, Knapp MC, Cooper MD, Lopez-Gallego C, Martin LJ, Muir CD, Sim S, Walker A, Anderson J, et al. 2009. Effects of genetic perturbation on seasonal life history plasticity. *Science* **323:** 930–934.

Wu FH, Shen SC, Lee LY, Lee SH, Chan MT, Lin CS. 2009. Tape–*Arabidopsis* sandwich—a simpler *Arabidopsis* protoplast isolation method. *Plant Methods* **5:** 16.

Xu F, Li T, Xu PB, Li L, Du SS, Lian HL, Yang HQ. 2016. DELLA proteins physically interact with CONSTANS to regulate flowering under long days in *Arabidopsis*. *FEBS Lett* **590:** 541–549.

Yin R, Messner B, Faus-Kessler T, Hoffmann T, Schwab W, Hajirezaei MR, von Saint Paul V, Heller W, Schaffner AR. 2012. Feedback inhibition of the general phenylpropanoid and flavonol biosynthetic pathways upon a compromised flavonol-3-O-glycosylation. *J Exp Bot* **63:** 2465–2478.

Yin R, Arongaus AB, Binkert M, Ulm R. 2015. Two distinct domains of the UVR8 photoreceptor interact with COP1 to initiate UV-B signaling in *Arabidopsis*. *Plant Cell* **27:** 202–213.

Yoo SK, Chung KS, Kim J, Lee JH, Hong SM, Yoo SJ, Yoo SY, Lee JS, Ahn JH. 2005. *CONSTANS* activates *SUPPRESSOR OF OVEREXPRESSION OF CONSTANS 1* through *FLOWERING LOCUS T* to promote flowering in *Arabidopsis*. *Plant Physiol* **139:** 770–778.

Zhang B, Wang L, Zeng L, Zhang C, Ma H. 2015. *Arabidopsis* TOE proteins convey a photoperiodic signal to antagonize CONSTANS and regulate flowering time. *Genes Dev* **29:** 975–987.

Zuo Z, Liu H, Liu B, Liu X, Lin C. 2011. Blue light-dependent interaction of CRY2 with SPA1 regulates COP1 activity and floral initiation in *Arabidopsis*. *Curr Biol* **21:** 841–847.

Arabidopsis RUP2 represses UVR8-mediated flowering in noninductive photoperiods

Adriana B. Arongaus, Song Chen, Marie Pireyre, et al.

Genes Dev. published online September 25, 2018
Access the most recent version at doi:10.1101/gad.318592.118

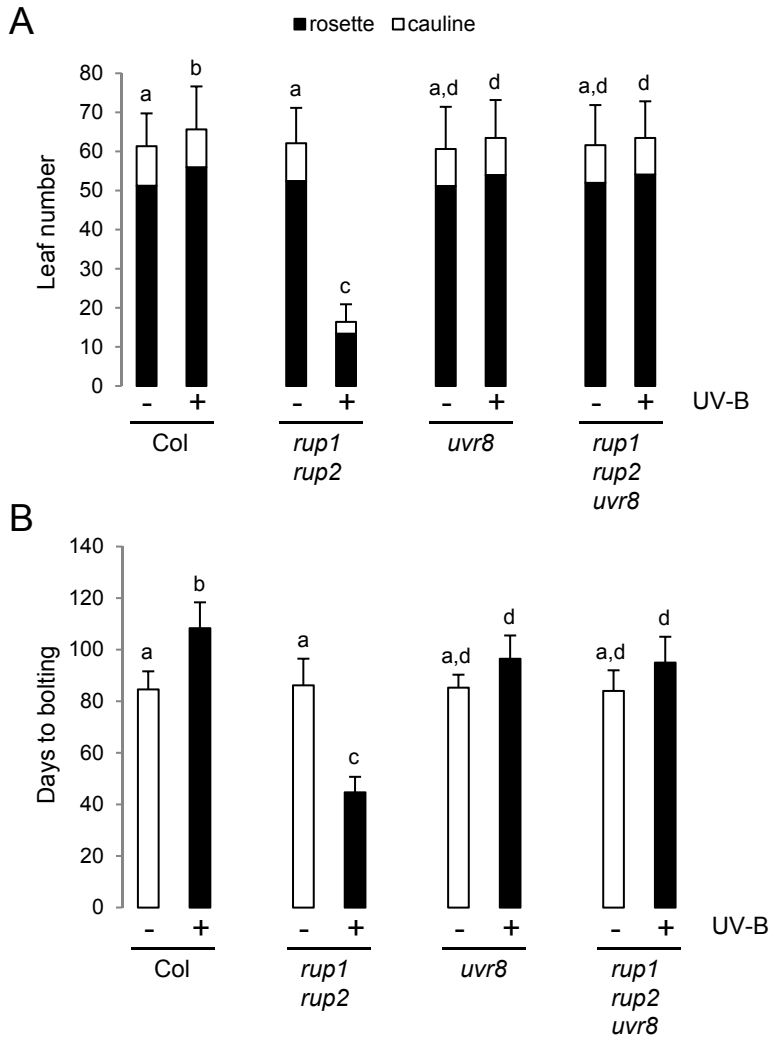

Figure S1. Early flowering of *rup1 rup2* double mutants in SD with UV-B is suppressed by UVR8 mutation. (*A*,*B*) Quantification of flowering time of wild-type (Col), *uvr8-6*, *rup1-1 rup2-1*, and *rup1-1 rup2-1 uvr8-6* plants grown in SD with (+) or without (-) UV-B. The flowering time is represented by total leaf number (rosette and cauline leaves; *A*) and days to bolting (*B*). Error bars represent SD (n = 30); shared letters indicate no statistically significant difference in the means ($P > 0.05$).

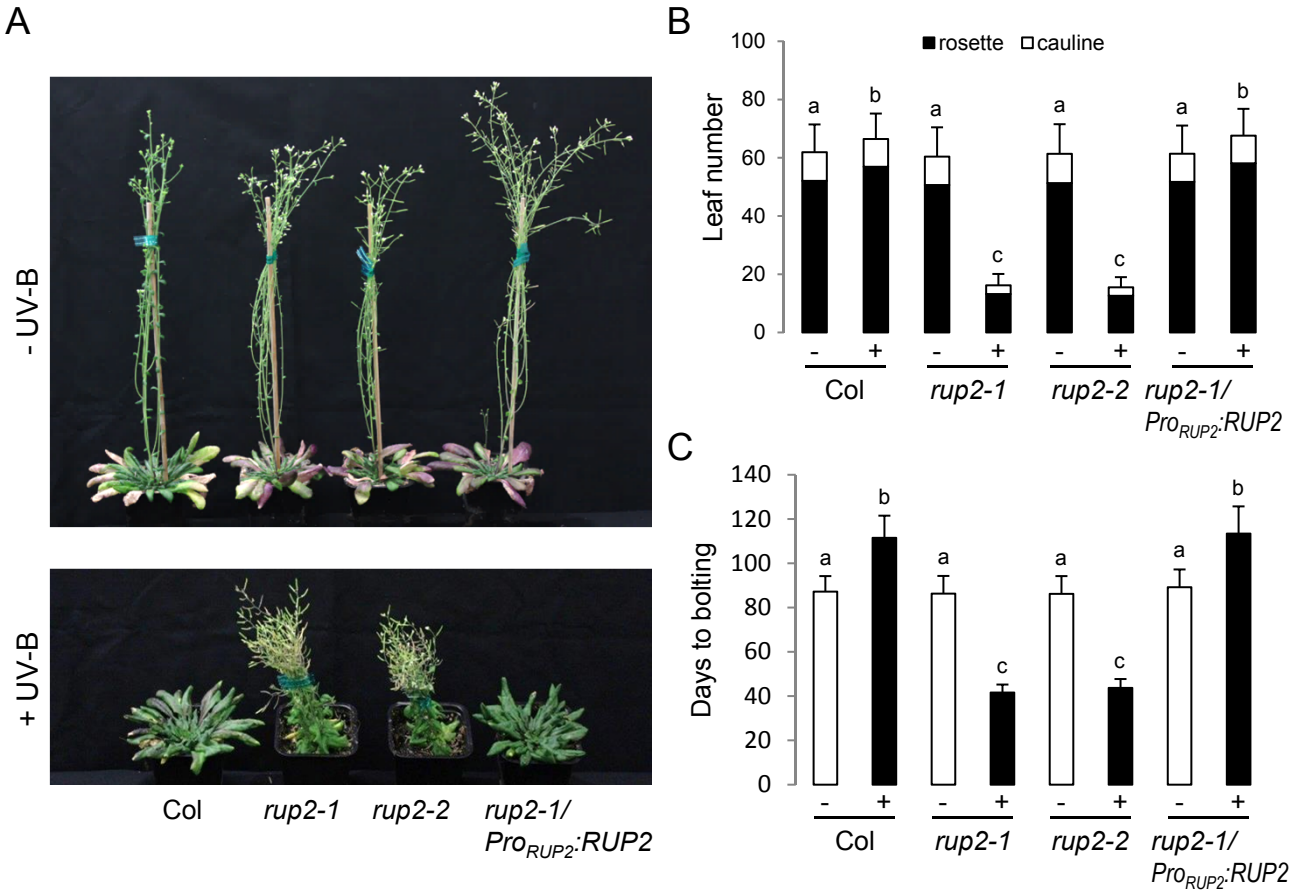

Figure S2. The novel *rup2-2* mutant allele flowers early in SD with UV-B and transgenic expression of *RUP2* complements the *rup2-1* early flowering phenotype. (*A*) Representative images of 100-d-old wild-type (Col), *rup2-1*, *rup2-2*, and *rup2-1*/*Pro*$_{RUP2}$*:RUP2 Arabidopsis* plants grown with (+UV-B) or without (-UV-B) UV-B (note that the *rup2-1* +UV-B plant is identical to the one shown in Fig. 1A, as from the same experiment). (*B*,*C*) Quantification of flowering time of wild-type (Col), *rup2-1*, *rup2-2*, and *rup2-1*/*Pro*$_{RUP2}$*:RUP2* plants grown in SD with (+) or without (-) UV-B. The flowering time is represented by total leaf number (rosette and cauline leaves; *B*) and days to bolting (*C*). Error bars represent SD (n = 30); shared letters indicate no statistically significant difference in the means ($P > 0.05$).

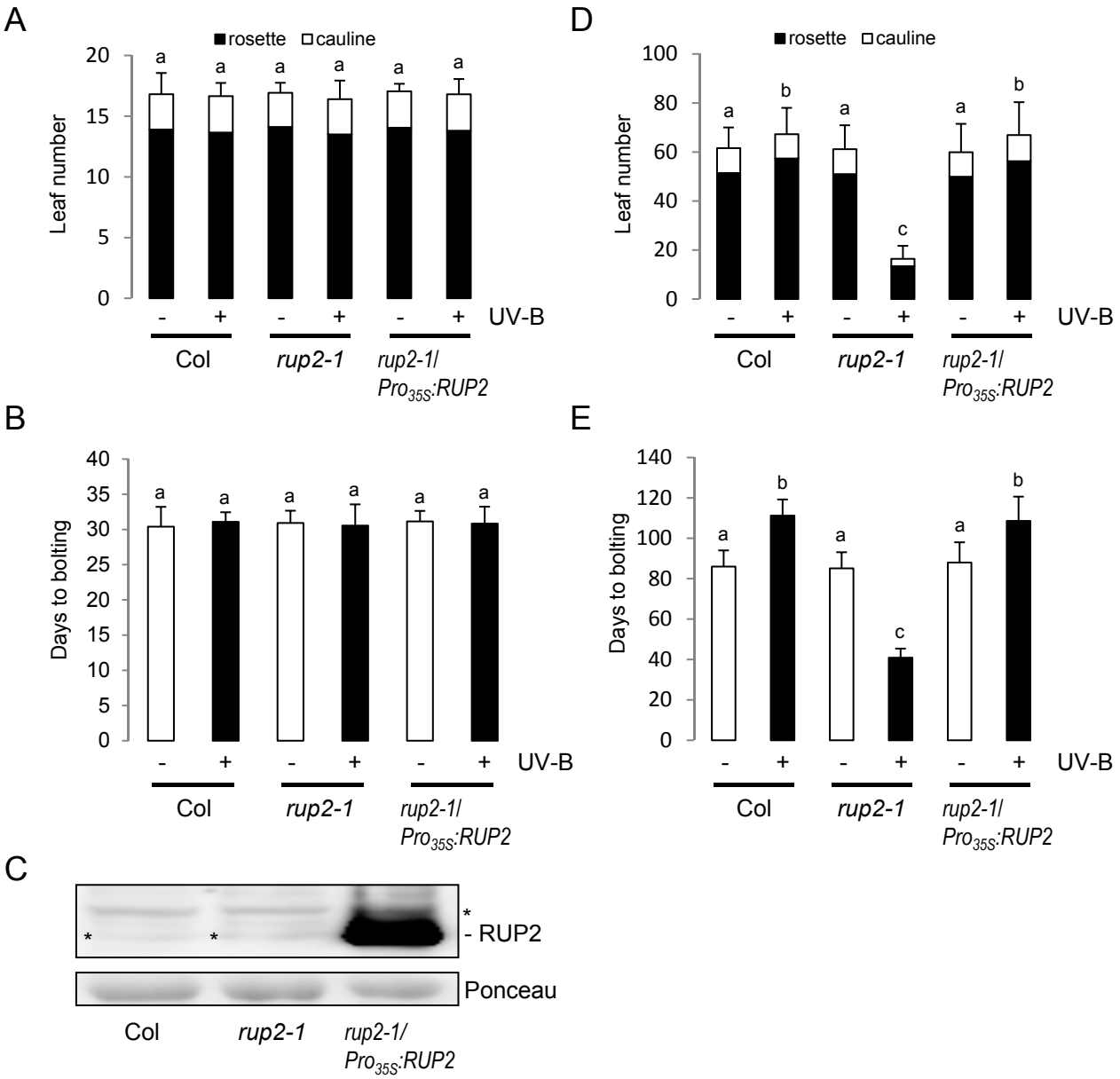

Figure S3. *RUP2* overexpression does not affect the flowering time in LD, independent of the absence or presence of UV-B. (*A,B*) Quantification of flowering time of WT (Col), *rup2-1*, and *rup2-1*/*Pro*$_{35S}$*:RUP2* plants grown in LD with (+) or without (-) UV-B. The flowering time is represented by total leaf number (rosette and cauline leaves; A) and days to bolting. Error bars represent SD (n = 30). (*C*) Immunoblot analysis of RUP2 levels in the *rup2-1*/*Pro*$_{35S}$*:RUP2* overexpression line compared to that in WT (Col) and *rup2-1*. Asterisks indicate nonspecific cross-reacting bands. The membrane was stained with Ponceau S as a loading control. (*D,E*) Quantification of flowering time of WT (Col), *rup2-1*, and *rup2-1*/*Pro*$_{35S}$*:RUP2* plants grown in SD with (+) or without (-) UV-B. The flowering time is represented by total leaf number (rosette and cauline leaves; *D*) and days to bolting (*E*). Error bars represent SD (n = 24).

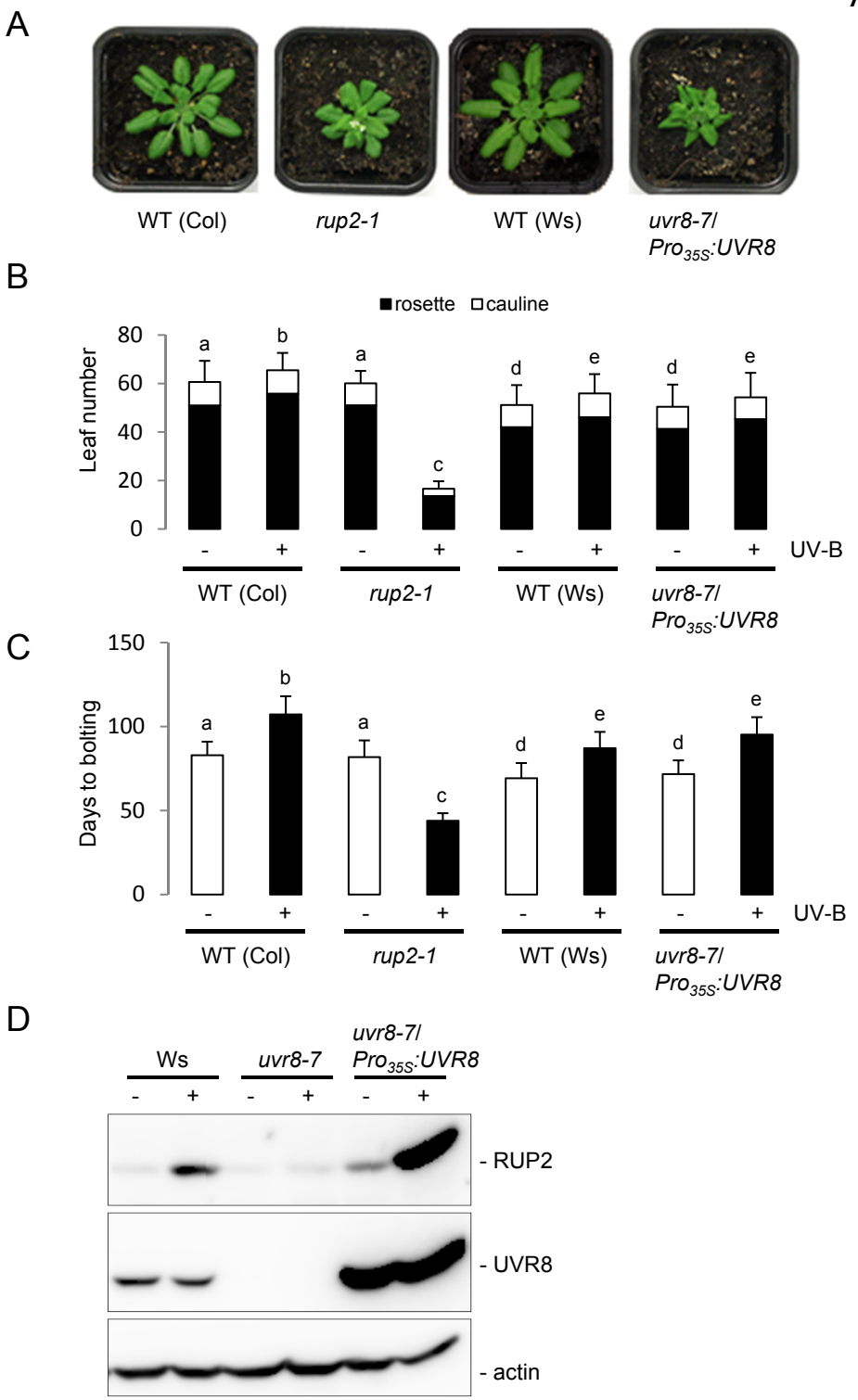

Figure S4. Overexpression of UVR8 results in UV-B hypersensitivity but not in an early flowering phenotype under SD+UV. (*A*) Representative images of 45-d-old WT (Col and Ws), *rup2-1*, and *uvr8-7*/*Pro*$_{35S}$*:UVR8* plants grown under SD+UV. (*B*,*C*) Quantification of flowering time of WT (Col and Ws), *rup2-1*, and *uvr8-7*/*Pro*$_{35S}$*:UVR8* plants grown in SD with (+) or without (-) UV-B. The flowering time is represented by total leaf number (rosette and cauline leaves; *B*) and days to bolting (*C*). Error bars represent SD (n = 30); shared letters indicate no statistically significant difference in the means ($P > 0.05$). (*D*) Immunoblot analysis of RUP2 and UVR8 protein levels in 4-d-old wild-type (Ws), *uvr8-7*, and *uvr8-7*/*Pro*$_{35S}$*:UVR8* seedlings grown in the absence (-) or presence (+) of UV-B. Actin levels are shown as a loading control.

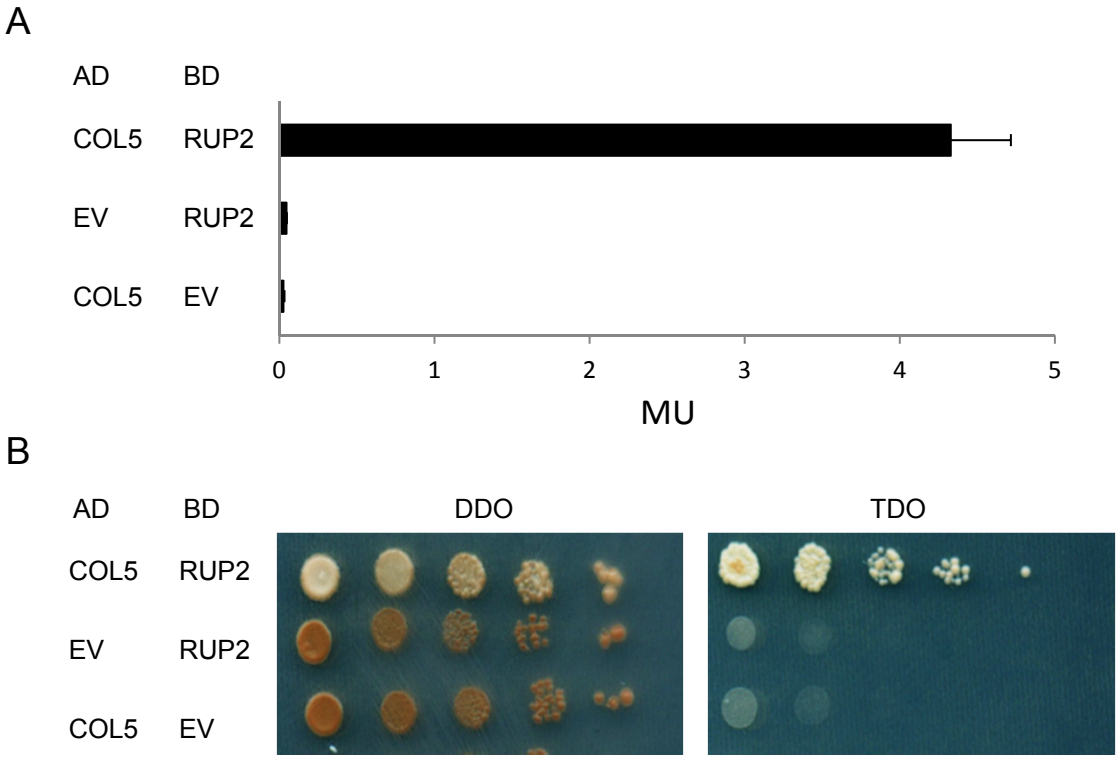

Figure S5. RUP2 interacts with COL5/BBX6 in yeast. (*A*,*B*) Quantitative β-galactosidase yeast two-hybrid activity assay (*A*) and growth assay of 10-fold serial dilutions on DDO (nonselective for interaction) and TDO (selective) plates (*B*). AD: activation domain; BD: binding domain; EV: empty vector; MU, Miller units; DDO, SD/-Trp/-Leu; TDO, SD/-Trp/-Leu/-His. Means and SEM from three biological replicates are shown.

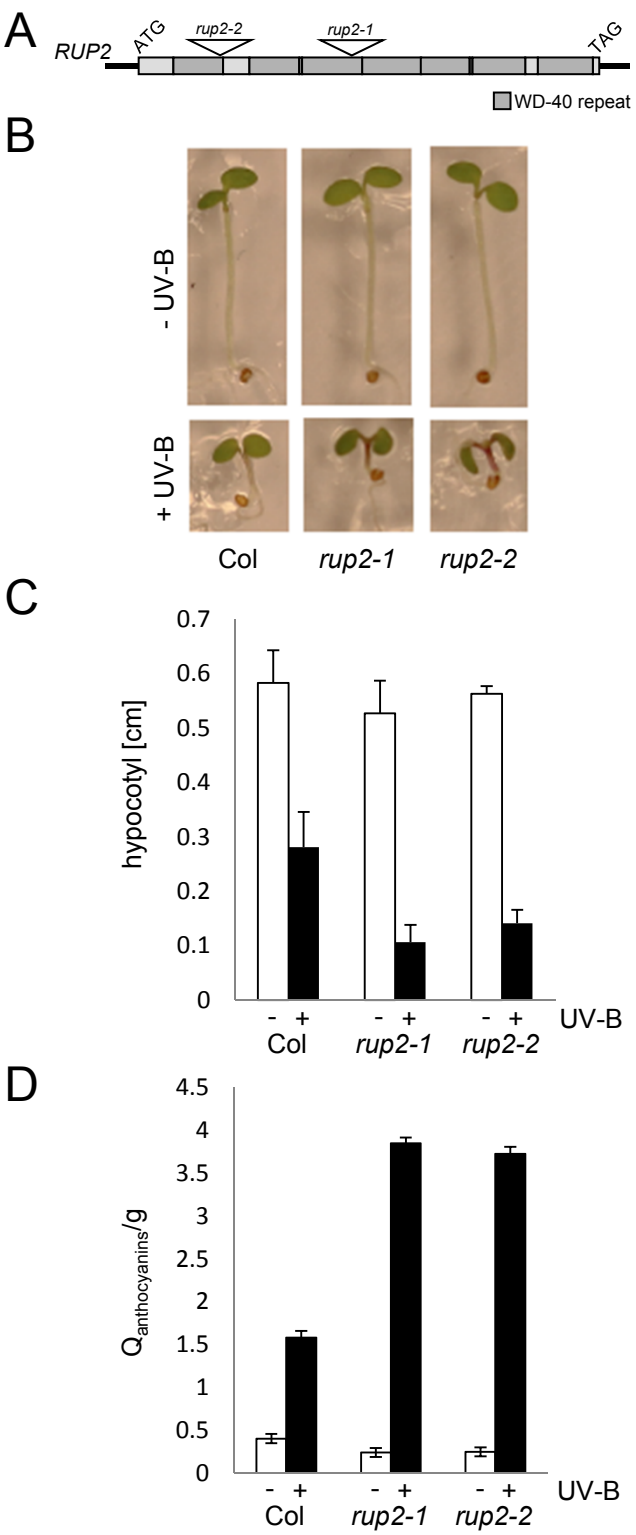

Figure S6. The *rup2-2* mutant allele confers UV-B hypersensitivity, similar to *rup2-1*. (*A*) Structure of *RUP2*, and the approximate locations of T-DNA insertions in *rup2-1* and *rup2-2*. (*B*) Representative images showing the UV-B inhibition of hypocotyl length and elevated anthocyanin content (dark red pigmentation) in 4-d-old WT (Col), *rup2-1*, and *rup2-2* seedlings when compared to seedlings grown in weak-white light devoid of UV-B. (*C*) Hypocotyl length measurements of 4-d-old seedlings grown with (+) or without (-) UV-B. Error bars indicate SEM ($n = 30$). (*D*) Anthocyanin level of 4-d-old *Arabidopsis* seedlings grown with (+) or without (-) UV-B. Data shown are the mean values of three independent biological replicates. Error bars represent SD ($n = 3$).

A

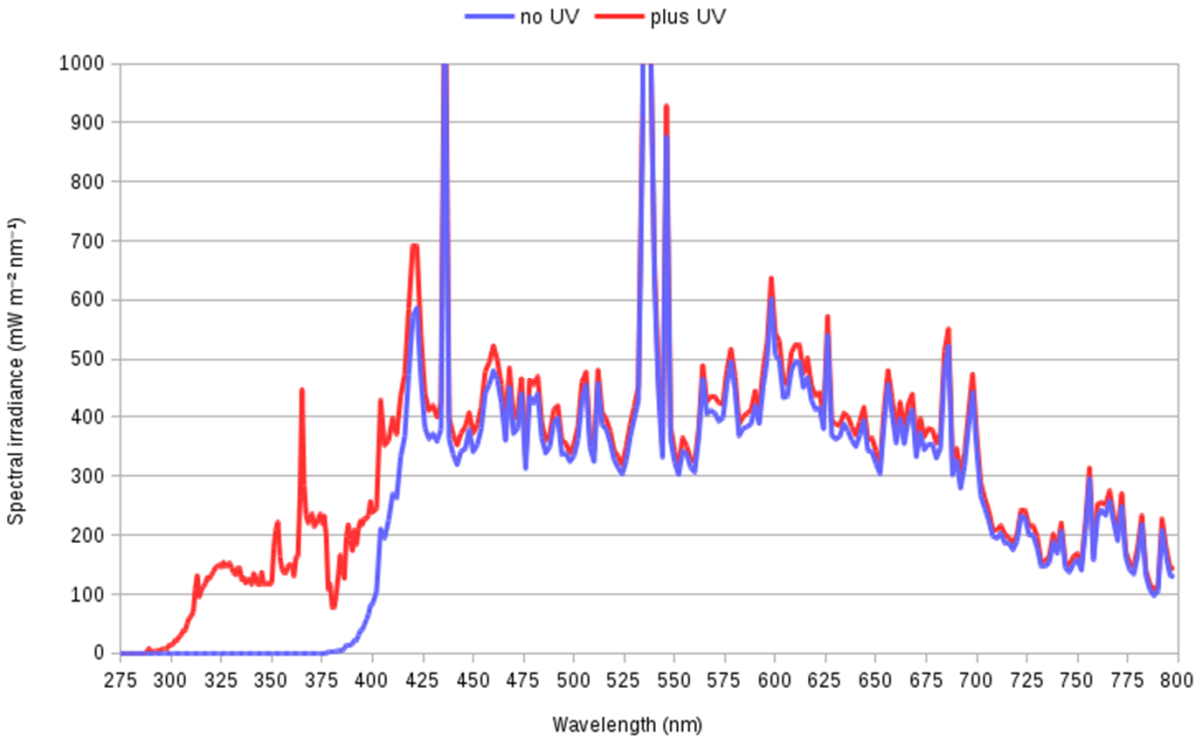

B

	-UV	+UV
PAR (µmol m^{-2} s^{-1})	580	600
UV-B_{BE} (mW m^{-2})	< 0.1	308
UV-C (W m^{-2})	< 1e-04	< 1e-04
UV-B (W m^{-2})	< 1e-04	0.91
UV-B (µmol m^{-2} s^{-1})	< 1e-03	2.34
UV-A (W m^{-2})	0.59	14.14
UV-A (µmol m^{-2} s^{-1})	1.5	42.6

Figure S7. Irradiance conditions in the sun simulator. (*A*) Spectral irradiances of the study in the sun simulator for control and UV treatment. (*B*) Determined values from spectroradiometric measurements of the irradiance condition in the sun simulator. UV-B_{BE}: biologically effective UV-B radiation, normalized at 300 nm (Caldwell 1971).

A.3 Other

A.3.1 Autofluorescence in confocal laser scanning microscopy for spectroscopy

Morphology of hindwing veins in the shield bug *Graphosoma italicum* (Heteroptera: Pentatomidae)

Accepted

This article describes the use of confocal laser scanning microscopy (CLSM) as spectroscopic method to unravel the spatial organization of elastic and rigid tissue of the wing. Together with light- and electron microscopy, mechanical adaptations were found, that enhance the reliability and durability of the mechanically stressed wing veins. The understanding of the minimally neccessary components for a functional wing can serve as bionic model for leight weight construction in architecture.

Arthropod Structure & Development 47 (2018) 375–390

Contents lists available at ScienceDirect

Arthropod Structure & Development

journal homepage: www.elsevier.com/locate/asd

Morphology of hindwing veins in the shield bug *Graphosoma italicum* (Heteroptera: Pentatomidae)

Paavo Bergmann [a, b, *, 1], Sandra Richter [c], Nina Glöckner [c], Oliver Betz [b]

[a] Electron Microscopy Center, Biology, University of Konstanz, Germany
[b] Evolutionary Biology of Invertebrates, Institute of Evolution and Ecology, University of Tübingen, Germany
[c] Center for Plant Molecular Biology, University of Tübingen, Germany

ARTICLE INFO

Article history:
Received 29 January 2018
Accepted 19 April 2018
Available online 3 May 2018

Keywords:
Chitin
Composite
Cuticle
Resilin
Tube

ABSTRACT

Light, fluorescence, and electron microscopy were applied to cross sections and -breakage and whole-mount preparations of the anterior hindwing vein of the shield bug *Graphosoma italicum*. These analyses were complemented by investigations of the basal part of the forewing Corium and Clavus. The integration of structural, histological, and fluorescence data revealed a complex arrangement of both rigid and elastic structures in the wall of wing veins and provided insights into the constitution of transition zones between rigid and elastic regions. Beneath the exocuticular layers, which are continuous with the dorsal and ventral cuticle of the wing membrane, the lumen of the veins is encompassed by a mesocuticular layer, an internal circular exocuticular layer, and an internal longitudinal endocuticular layer. Separate parallel lumina within the anterior longitudinal vein of the hindwing, arranged side-by-side rostro-caudally, suggest that several veins have fused in the phylogenetic context of vein reduction in the pentatomid hindwing. Gradual structural transition zones and resilin enrichment between sclerotized layers of the vein wall and along the edges of the claval furrow are interpreted as mechanical adaptations to enhance the reliability and durability of the mechanically stressed wing veins.

1. Introduction

The wing veins of insects serve multiple functions. In a mechanical context, they act as load bearing struts and stiffening rods that form a functional aerofoil as a lightweight durable flying apparatus, together with the delicate wing membrane. They also play an important role in enhancing fracture toughness of the wing by their ability to stop crack propagation (Dirks and Taylor, 2012; Rajabi et al., 2015a). In a physiological context, they accommodate the nerves, tracheae, and hemolymph flow, all of which supply the wing area including its sensilla. According to the much-cited paranotal hypothesis (Müller, 1873, but see also Bruce and Patel, 2018), the wing develops as a duplicature of the thoracic body wall, i.e., an epidermal fold, covered on both the dorsal and ventral sides by cuticle. After the secretion of the cuticular wing membrane, the epidermal cells retract along the tracheae (Woodworth, 1906; Weber, 1933), followed by the bonding of the cuticular layers of the wing membrane. With respect to the true veins, the cuticle bulges out around the path of the tracheae and accompanying nerves to enclose the lumen of the true vein, which hence consists of two opposing half-circles of dorsal and ventral cuticle. Recent analyses in damselflies and dragonflies have shown that load-bearing veins can exhibit complex patterns of cuticle arrangement. Appel et al. (2015) and Rajabi et al. (2016b) have demonstrated that wing veins consist of multiple layers of cuticle with various degrees of sclerotization, fiber arrangement, and resilin content correlated with their different mechanical properties. These findings have helped to explain the passively controlled wing deformability. Such passive deformability has been shown to improve the flight performance of insects (Jongerius and Lentink, 2010; Marrocco et al., 2010; Rajabi et al., 2011, 2016b; Ren et al., 2013; Sivasankaran et al., 2016; Sun and Bhushan, 2012; Wootton, 1992). During flight, the insect wing is only operated at its base to control both its up-/downstroke and forward-/backward movement. At rest, the entire wing can be folded back on top of the abdomen in

* Corresponding author. Electron microscopy centre, Department of Biology, Konstanz University, room M615, D-78457, Konstanz, Germany.
E-mail address: paavo.bergmann@uni-konstanz.de (P. Bergmann).
[1] Permanent address: Electron Microscopy Center, Department of Biology, University of Konstanz, Germany.

https://doi.org/10.1016/j.asd.2018.04.004
1467-8039/

neopteran insects. Folding also reduces both wing breadth and length, and the total surface area of the wings is thus decreased up to tenfold. All these movements are remotely operated by muscles that attach at the wing base, including the pteralia. Their action on wing folding and unfolding is supported by defined folds and flexion lines in combination with localized patches of the highly elastic protein resilin (e.g., Haas, 2000; Haas et al., 2000a, 2000b). Resilin microjoints at crossing wing veins (e.g., Rajabi et al., 2015b) and resilin layers within the vein wall itself (Appel et al., 2015) prevent excessive bending of the cross veins and reduce the stress concentration in the joint. In flies, resilin has also been detected at the proximal end of the wing, where it might reduce the risk of breakage near the wing hinge during flapping (Lehmann et al., 2011; for a review of the distribution and role of resilin in insect flight systems, see Michels et al., 2016). Increasing evidence supports the view that insect wings should not be considered as rigid flat plates but rather as passively deformable aerofoils, whose 3D shape during flight largely results from the aeroelastic behavior of the wing cuticle itself, and from inertia forces, entailing lift- and drag-modulating aerodynamic effects (e.g., Lehmann et al., 2011). The overall wing stiffness might be largely influenced by the distribution of resilin across the wing, i.e., resilin must be considered as a key element in the formation of flexible wings (Appel et al., 2015; Donoughe et al., 2011; Rajabi et al., 2016a). All these features make insect wings reversibly deformable planar lightweight structures that are able to withstand complex loading regimes and both span- and chordwise-directed deformations comprising torsion, bending, and camber change without losing shape (Ha et al., 2013). They successfully reconcile conflicting properties such as (1) the deformability required for wing folding and (2) the strength necessary for flying, whereby primarily supporting areas, e.g., wing veins or thickened zones of the wing membrane, and deformable areas, e.g., flat membranes with weakened cross veins, can be distinguished across the wing. In particular, insect wings need to show a high resistance toward local buckling during compression, plastic deformation, fatigue cracking and crack propagation during tension, and fracture in order to maintain their performance (Dirks and Taylor, 2012; Rajabi et al., 2016c, 2017a).

Insect wings have become important concept generators in the field of biomimetics (e.g., Born et al., 2017; Ha et al., 2014; Lehmann, 2004; Nguyen et al., 2010a, 2010b; Schieber et al., 2017; Shang et al., 2009; Sivasankaran et al., 2016; Sun and Bhushan, 2012; Wu et al., 2011). For example, they have been used in the development of flapping-wing aerial vehicles and façade-shading devices. Their various folding patterns and mechanisms, especially the wing folding patterns of Dermaptera and Coleoptera, have received much attention in the past (e.g., Danforth and Michener, 1988; Deiters et al., 2016; Fedorenko, 2009; Forbes, 1924; Gorb, 1998; Haas, 2006, 2000, 1994, Haas et al., 2011, 2000a, 2000b; Haas and Beutel, 2001; Haas and Kukalova-Peck, 2001; Haas and Wootton, 1996; Hammond, 1979; Hörnschemeyer, 1998; Kaufmann, 1960; Kleinow, 1966; Muhammad et al., 2009, 2010).

In the current contribution, we focus on the ultramorpholgy of selected wing veins of the so-called "minstrel bug", *Graphosoma italicum lineatum* (O.F. MÜLLER, 1766), a member of the family of Pentatomidae (shield bugs). The wing veins of heteropterans have received less attention by functional morphologists, except for taxonomic examinations and determinations of wing vein homologies. However, their reduced venation pattern (Weber, 1930) makes heteropterans interesting concept generators for possible biomimetic applications, as the reduced complexity lends itself more amenable to technical adaptation. Additionally, the folding pattern of the hind wings of Pentatomidae incorporates model cases for all critical structures, i.e., rigid, pliable, and elastic regions, straight and curved bending zones, and bifurcating bending zones with bending in opposite directions. In spite of being large and heavy insects, pentatomids have a small wing area in relation to their body weight compared with other insects, which results in high wing loads. Pentatomids are also active fliers with good flight performance (Lee and Leskey, 2015; Wiman et al., 2015), spuring interest in the system also in terms of its reliability and durability. In Heteroptera, the wings have a reduced venation, and the fore- and hind wings are coupled in flight with a peculiar cuticular apparatus situated close to the distal end of the leading true wing vein ("cd" in Fig. 1) (Schneider and Bohne, as cited in: Betts, 1986; Goodwyn and Gorb, 2004; Weber, 1930). The forewing consists basally of two sclerites, i.e., the Clavus and the Corium, which are connected by a flexible bending line, the claval furrow ("Cl", "Cr", "cf" in Figs. 1 and 7a). A second flexible line, the "median flexion line" *sensu* Betts (1986) intersects the Corium ("mfl" in Fig. 1). Distally, a membranous field with multiple corrugations forms the tip of the wing ("mp" in Fig. 1). In the hind wing, most veins are represented as thickened stripes of solid cuticle ("thickened ridge-and-basin type" *sensu* Betts (1986), called "false veins" in this publication). In these bugs, true veins that incorporate a lumen with nerves and tracheae are restricted to five straight unbranched structures (Fig. 1, designated "SRM", "Ca", "A1", "A2", "A3" following the suggestion of Betts (1986)), whereby neither of them spans the full wing length. The longest and widest of the true veins is the most anterior and ends in the "stigma", i.e., a special region of the wing just caudal to the wing-coupling device ("St", "cd" in Fig. 1). At the stigma, the most anterior vein is visibly widened (white asterisk in Fig. 1). Phylogenetic analyses of the venation pattern in various families of true bugs have led to the hypothesis that this vein represents a fusion of three major wing veins, i.e., the subcosta, the radius, and the media, in Pentatomidae (Betts, 1986). Hence, we will refer to this structure as the "SRM vein" throughout this publication. Distally, the SRM branches into two cuticular ridges ("cr" in Fig. 5e, f) and a solid "false" vein ("fv" in Fig. 5a). This "false" vein connects to two other "false" veins ("fv" in Fig. 1) at the stigma to support the distal third of the hind wing.

In an interdisciplinary biomimetic project involving insect wings as concept generators for façade shading, we have recently studied the transition zones between the wing areas of various elastic properties in this bug, which exhibits the flexagon pattern of wing folding (Born et al., 2017; Schieber et al., 2017). We found substantial structural differentiation between the ventral and dorsal cuticle layers of the wing membrane. The variation of the number and density of the fiber layers appears to be the principal source of differentiation of the mechanical properties of false veins, membrane fields, and bending zones, whereby the transitions between these structures are gradual (Schieber et al., 2017).

In the present study, we focus on the ultrastructure of both the composition and the fiber arrangement of rigid structures in the wings of *G. italicum*. In the fore wing, the sclerite fields and the coupling device ("cd" in Fig. 1) have been analyzed in whole-mount preparations and by SEM imaging (Figs. 2a and 7a, b). The true veins (Fig. 2b), with special emphasis on the distal part of the SRM vein (Figs. 3–7), the stigma, and the coupling device (Fig. 7c), have been analyzed in the hind wing. Our results reveal a complex structure of the vein walls and principally show a greater resemblance to the structure of dragonfly wing veins (Appel et al., 2015) than to the traditional model, i.e., opposing convexities of the dorsal and ventral cuticle of the wing encompassing the trachea (Snodgrass, 1935; Weber, 1933). A selection of regions of interest was undertaken in order to provide an overview of the constitution of the key elements involved in wing coupling and in the withstanding of mechanical stresses during folding/unfolding and wingbeat cycles. Additional ultrastructural investigations

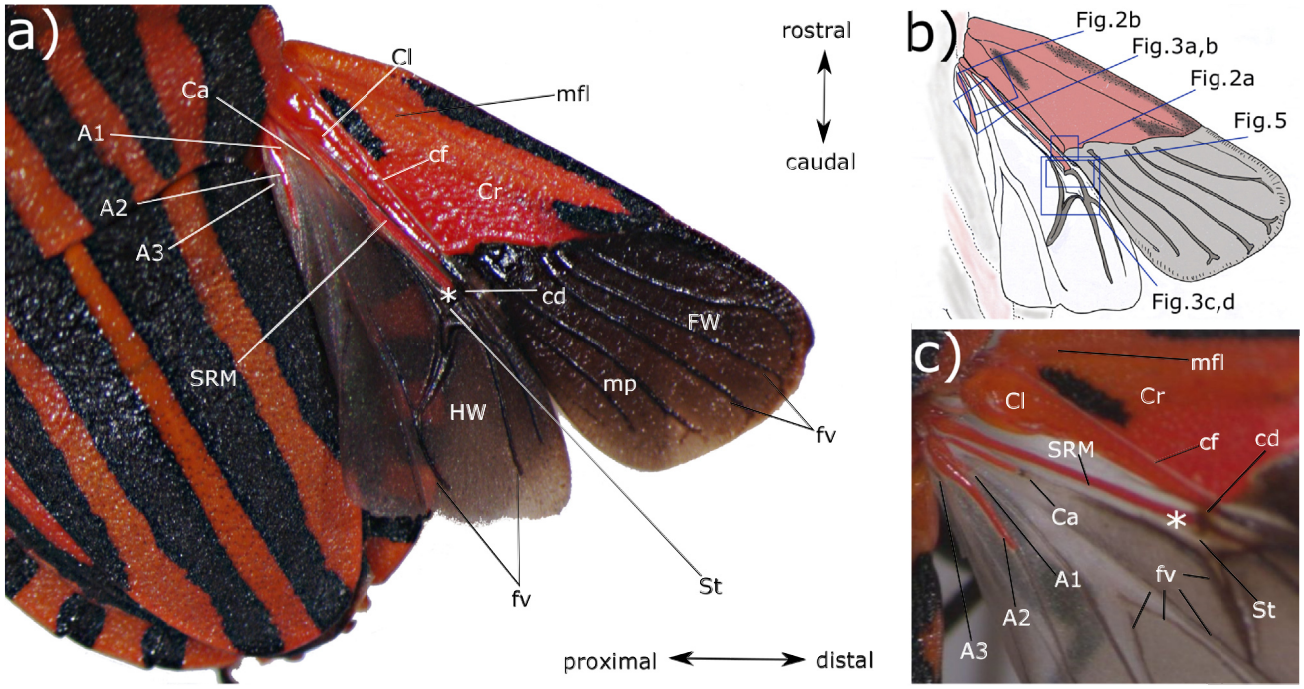

Fig. 1. a) Photographic image of the partially extended right wing of *Graphosoma italicum*. Dorsal aspect. Detail of the image shown in Schieber et al. (2017) (there: Fig. 1) Fore and hind wings are coupled. Bioinspiration & Biomimetics by IOP Publishing. Reproduced with permission of IOP Publishing in the format. Order Detail ID: 70945350, Journal/magazine via Copyright Clearance Center. b) Schematic drawing with indications of the anatomical regions from which the detailed micrographs were taken. c) Basal portion of the coupled forewing and hindwing, artificially extended. Abbreviations: A1-3: Analis 1-3; Ca: Cubitus anterior; cd: coupling device at which the leading edge of the hindwing is attached to the trailing edge of the forewing; cf: claval furrow after Betts (1986); Cl: Clavus; Cr: Corium; fv: false veins; FW: forewing; HW: hindwing; mMfl: median flexion line of the Corium; mp: membranous part of the forewing; SRM: fused Subcosta + Radius + Media vein after Betts (1986); St: stigma at the distal end of the hollow part of the SRM vein. White asterisk: distal end of the SRM vein, just posterior to the coupling device and at the stigma.

were carried out on the SRM vein to elucidate the unusual structure of this longest and largest vein, which connects the wing base to the coupling device, and is most prominently involved in stabilizing the hindwing during all three key active mechanical functions of the hind wing, i.e., wing coupling, folding/unfolding, and wing beating during flight. Because of these aspects, and its favourable scaling relations, the SRM vein is also the most promising candidate as a concept generator for biomimetic applications. Furthermore, the occurrence of multiple lumina within the SRM vein, in combination with the analysis of the fiber arrangement, corroborates the hypothesis that the leading vein of the hind wing in *G. italicum* is a composite vein developed from the fusion of three former wing veins.

Our study is aimed at elucidating the mechanical construction of the wings of *G. italicum* with special emphasis on the distribution of sclerotized material, resilin, and transition zones between rigid and pliable structures. In particular, we have sought fresh data on the overall cross sectional shape, the dimension of the wing veins, and its pattern of cuticle differentiation (cf., Banerjee, 1988).

2. Materials and methods

2.1. Wholemount preparations

In the course of this study, wings of the minstrel bug *Graphosma italicum* were subjected to various investigations regarding their structural composition.

For the forewing, whole wings of freshly killed specimens were prepared on glass slides and embedded in either glycerol, purified water, or Entellan for wide-field epifluorescence microscopy (WFM) of the ventral side of the posterior edge, including the Clavus, Corium, part of the coupling device, and claval furrow (Fig. 2a). Confocal laser scanning fluorescence analysis proved to have no additional benefit with regard to forewing preparations, because the penetration depth of the laser was limited to superficial imaging by the thick sclerotized cuticle and the abundant pigmentation of the sclerotized parts. Additional forewings were broken and cut into pieces and mounted for scanning electron microscopy (SEM; see below) of the Corium and Clavus, including the cubitus anterior and analis 1 veins, and of the claval furrow (Fig. 7a, b).

With respect to the hindwing, whole wings of freshly killed specimens were prepared on glass slides and embedded in either glycerol, purified water, or Entellan for fluorescence microscopy of the basal portions of the SRM, cubitus anterior, and analis 1-3 vein and of the anterior edge in the region of and including the stigma and coupling device (Figs. 2b, 3, 5a).

Preparations of the hindwings were also embedded in epoxy resin (see below), and a series of both semithin and ultrathin cross sections were produced of the SRM vein and the adjacent anterior edge of the hindwing from a distance of ~200 μm basal of the coupling device toward the false veins just distal of the stigma (Fig. 5). These sections were investigated by WFM and confocal laser scanning fluorescence microscopy (CLSM), conventional light microscopy, and transmission electron microscopy (TEM) (Figs. 4–6).

Additional hindwings were broken and cut into pieces and mounted for SEM (see below) of the SRM vein, coupling device, and stigma (Fig. 7c, d).

2.2. Scanning electron microscopy (SEM)

Fore- and hindwings were dehydrated, critical-point dried by using a K850X critical-point dryer (Quorum technologies, Laughton, UK), and broken/cut into small segments that were then placed on aluminum SEM stubs and sputter-coated with gold/palladium in

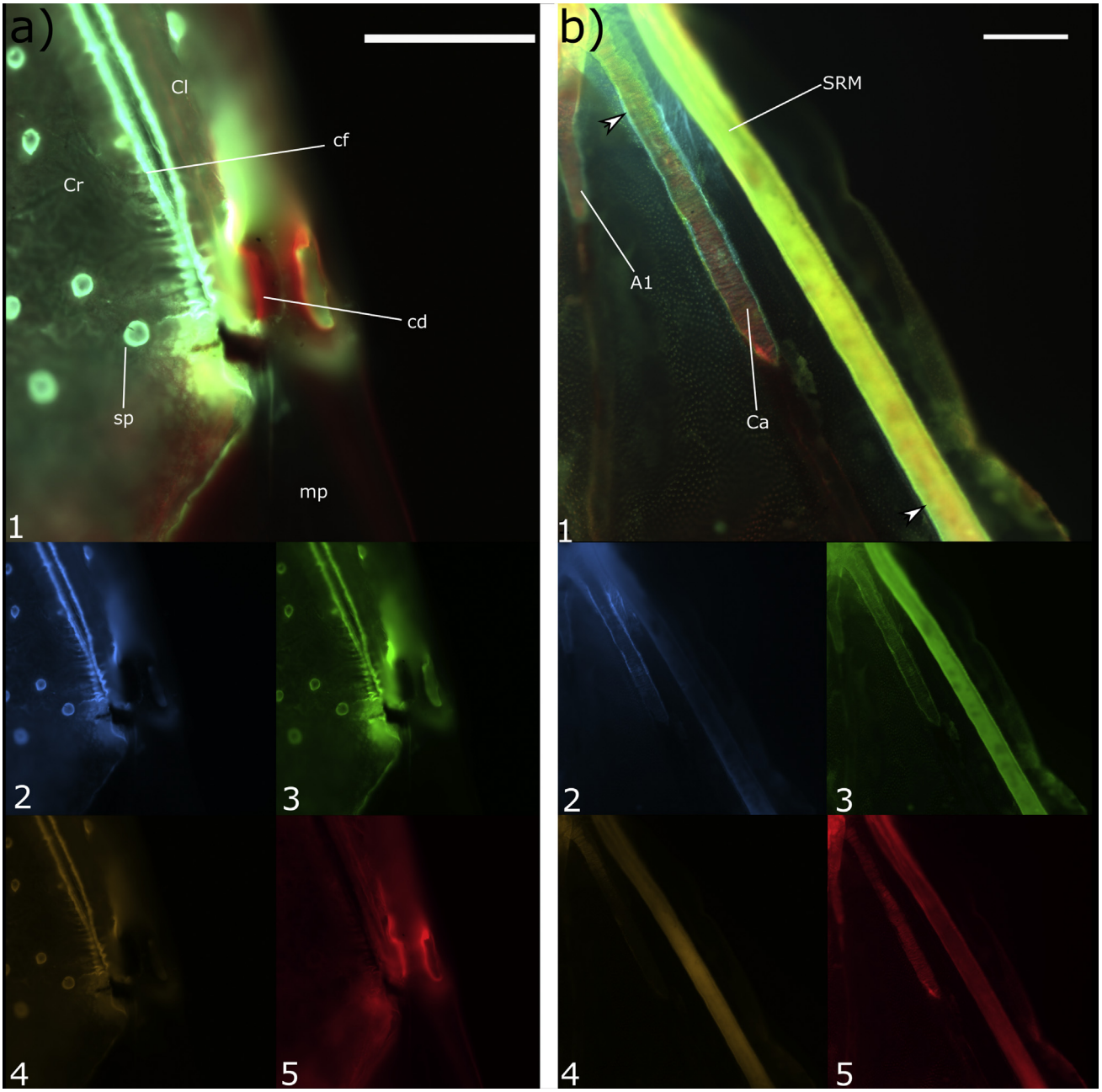

Fig. 2. a) Wide-field epifluorescence microscopy (WFM) image of the coupling device at the forewing. Ventral aspect. DAPI (2), Atto488 (3), Cy3 (4) and Cy5 (5) channels shown separately and as a composite image (top image (1)). Strong sclerotization of the cuticular clamp that catches the edge of the hindwing. Short-wavelengths are restricted to the edges of the claval furrow and the pits of setae. Scale bar: 200 μm. b) WFM image (dorsal aspect) of the basal portion of the four major wing veins of the hind wing. DAPI (2), Atto488 (3), Cy3 (4) and Cy5 (5) channels shown separately and as a composite image (top image (1)). Resilin fluorescence is visible at the base of the veins and as narrow stripes along the vein edges (arrowhead). Sclerotin fluorescence (red) is distributed over the vein proper. Scale bar: 200 μm. Abbreviations: A1: Analis 1; Ca: Cubitus anterior; cd: coupling device at which the leading edge of the hindwing is attached to the trailing edge of the forewing; cf: claval furrow after Betts (1986); Cl: Clavus; Cr: Corium; mp: membranous part of the forewing; sp: setae pits; SRM: fused Subcosta + Radius + Media vein after Betts (1986).

a K550X sputter coater (Quorum technologies, Laughton, UK). Digital images were recorded with a scanning electron microscope (Zeiss EVO L15: Oberkochen, Germany).

2.3. Light microscopy/transmission electron microscopy (TEM)

Wings were fixed in a modified Karnovsky's solution, post-fixed with osmium tetroxide, dehydrated in a graded ethanol series including *en-bloc* staining with uranyl acetate, and embedded in SPURR's low viscosity epoxy resin. After polymerization, semithin (500 nm) and ultrathin (50 nm) sections were cut perpendicularly to the wing plane, at right angles to the SRM vein (for a detailed description of the protocol, see Schieber et al., 2017).

Ultrathin sections were post-stained with uranyl acetate and lead citrate according to Venable and Coggeshall (1965). TEM images were recorded on MACO EMS plate negative films by using a Siemens Elmiskop 1A (Siemens & Halske, Berlin, Germany) or a Philips/FEI Tecnai10 (FEI systems, Eindhoven, The Netherlands) electron microscope equipped with a Megavision III digital camera or on Ilford TF4 black and white 120 mm roll film by means of a Zeiss EM109 TEM (Zeiss, Oberkochen, Germany). The developed negatives were digitized by using an EPSON V750 scanner, and

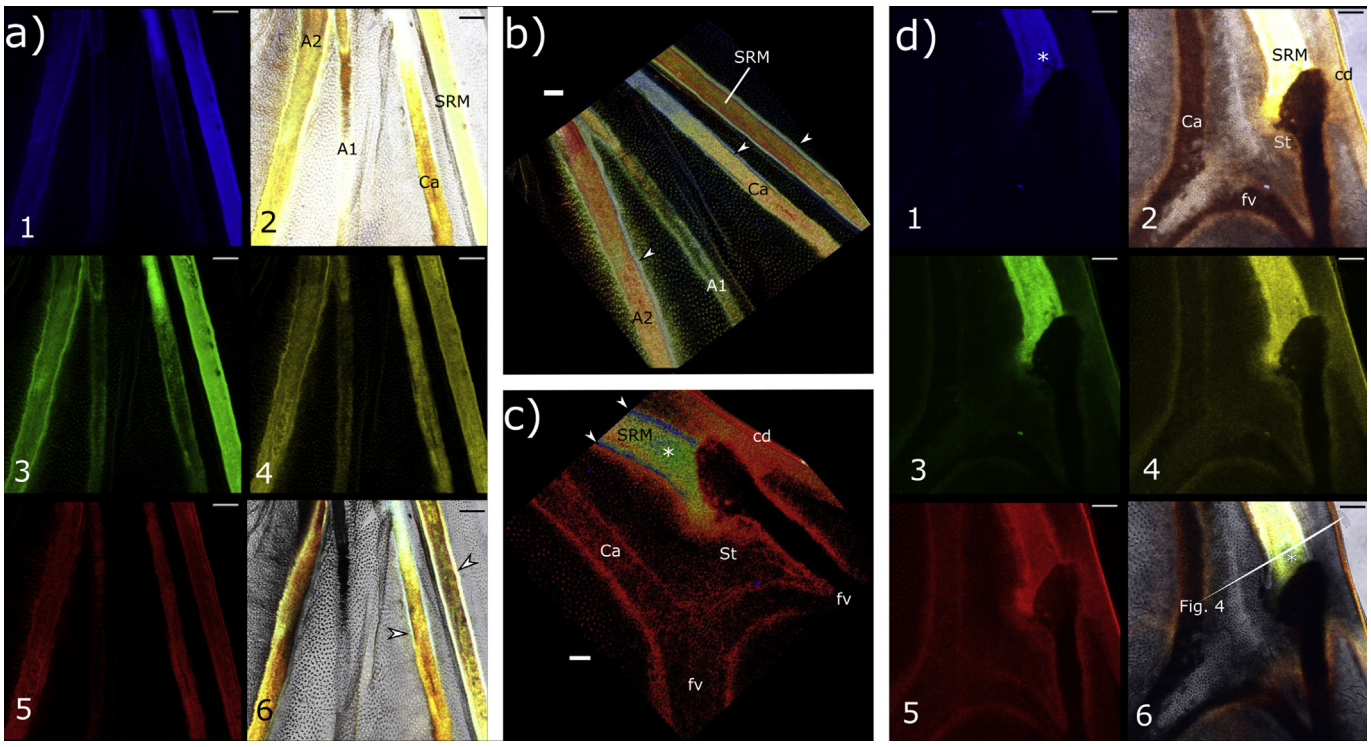

Fig. 3. Representation of confocal laser scanning microscopy (CLSM) data obtained from the hindwing of *Graphosoma italicum*. Dorsal aspects. For subfigures a) & d): Channels are depicted separately as maximum projection. (1) 412–484 nm, (3) 496–568 nm, (4) 569–636 nm, (5) 642–708 nm. Top right image (2) represents a composite of all channels superimposed on a differential interference contrast (DIC) image. Bottom right image (6) shows a composite of one representative z-layer. White arrowheads refer to sources of short-wavelength autofluorescence along the wing veins. a) z-stack recording of the basal portion of the four major wing veins, i.e., fused Subcosta + Radius + Media, Cubitus anterior, Analis 1, and Analis 2. Scale bar: 100 μm. b) Volume rendering of the CLSM dataset, obtained with Drishti software. Dorsal aspect. Short-wavelength signal (blue, green) concentrated along the edges of the veins and on the dorsal surface, and long-wavelengths (amber, red) in the vein wall, corroborating WFM analysis. The top (dorsal) layer of the z-stack is inside the SRM and A1 veins; thus, these veins are represented as longitudinal cuts. Scale bar:100 μm. c) Equivalent representation of a CLSM z-stack recording from the stigma of the hindwing. Short-wavelength signal from the distal end of the SRM vein, with blue fluorescence concentrated laterally. Long-wavelength indicating sclerotization of the edge of the wing at the coupling device and of the false veins extending from the stigma. Note that black pigmentation along the false veins masks the fluorescence signal resulting in a shadowcast-like appearance of the false veins. Scale bar:100 μm. d) z-stack recording from the stigma of the hindwing, with an indication of the approximate plane of section of the semithin section presented in Fig. 4 (white line "Fig. 4". Note: different individual). Scale bar: 100 μm. Abbreviations: A1, A2: Analis 1, Analis 2; Ca: Cubitus anterior; cd: coupling device at which the leading edge of the hindwing is attached to the trailing edge of the forewing; fv: false veins SRM: fused Subcosta + Radius + Media vein after Betts (1986); St: stigma at the distal end of the hollow part of the SRM vein.

digital images were processed with GIMP 2.8.10 (The GIMP team, www.gimp.org) for brightness, contrast, and tonal values to give maximum clarity of structural detail.

Semithin sections were placed on gelatin-coated glass slides and subjected to various staining regimes at regular intervals. The sections were either left unstained and mounted in Entellan for differential interference contrast or fluorescence analysis or were stained with one of the following methods. All sections were softend by exposure to ethanol fumes for 1 h at room temperature, followed by de-osmification in 20% hydrogen peroxide at room temperature.

Staining

(1) AZAN staining for the differentiation of exo-, meso-, and endocuticle:

Staining with 0.1% azocarmine in 1% acetic acid, 30 min at 60 °C, followed by 2 h at 37 °C rinsing with demineralised water 3x dipping into 0.1% aniline in pure ethanol 3x dipping into 0.1% acetic acid in pure ethanol 5% phosphotungstic acid, 90 min at room temperature rinsing with demineralised water. Staining with 0.5% aniline blue, 2% Orange G, and 8% acetic acid in distilled water. Start at room temperature and immediately transfer vial to 60 °C water bath for 22min rinsing with distilled water 3x dipping in pure ethanol.

(2) ferric hematoxylin, and then counter staining with xylidin red for the analysis of tissue- and resilin-containing cuticular regions:

Staining with stock solution of hematoxylin according to Delafield for 5 h at 50 °C rinsing in running tap water for 20 min. Staining with 0.5% xylidine red in 1% acetic acid for 3 min at 50 °C rinsing in distilled water. All chemicals supplied by Merck (Darmstadt). Stained slides were dried in air and by Rotihistol treatment and were mounted in Engelbrechts xylene-free embedding medium. Images were recorded by using a Zeiss Axioplan light microscope with a Nikon D7100 digital camera for conventional light microscopy.

2.4. Fluorescence microscopy

Fluorescence analysis was performed on whole-mount preparations and on unstained semithin sections. Both sample types were air-dried and mounted in Entellan (Merck, Darmstadt).

Wide-field epifluorescence microscopy (WFM) was performed on an epifluorescence microscope (Zeiss Imager M.2, Zeiss, Oberkochen, Germany). Images of cuticular autofluorescence were recorded for 4–5 channels by using Plan-Apochromat objectives, and with filter sets for DAPI (excitation: 359–371 nm, emission: 397–409), Atto 488 (excitation 450–490 nm, emission: 500–550), Cy3 (excitation: 538–562 nm, emission: 570–640 nm), and Cy 5 (excitation: 625–633 nm, emission: 665–715), as these were shown to collect signals conveniently from key cuticular components, namely resilin, arthropodin, and sclerotin, respectively (Michels and Gorb, 2012).

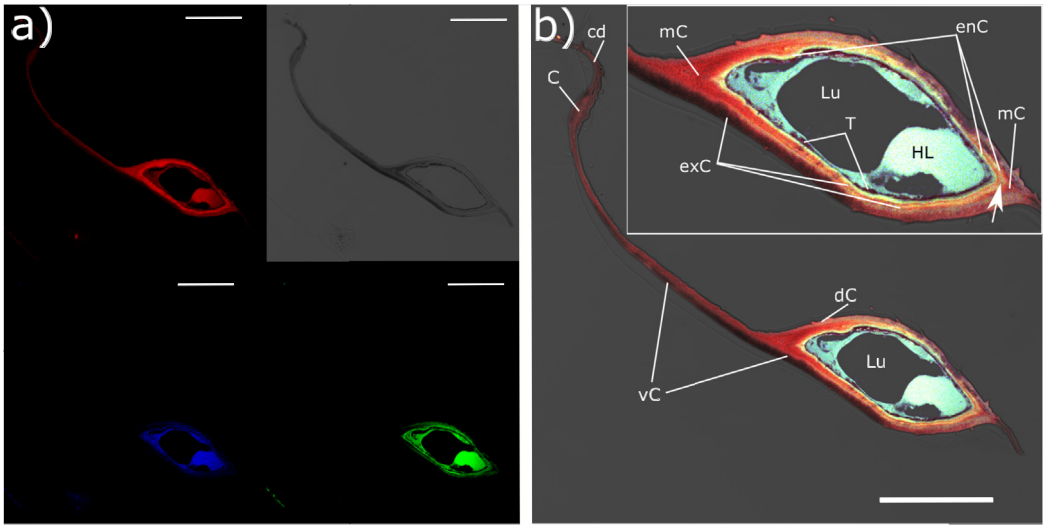

Fig. 4. Confocal laser scanning microscopy (CLSM) recording of an unstained 0.5-μm semithin section taken perpendicularly from the rostral edge of the hindwing of *Graphospoma italicum*, at the proximal end of the hindwing part of the coupling device (indicated in Fig. 5). a) Three fluorescence channels (top left: 423–476 nm, bottom left: 567–552 nm, bottom right: 595–677 nm) and differential interference contrast (DIC) image (top right), shown separately. b) Composite image. Short-wavelength signal concentrated around the lumen, between the dorsal and ventral cuticle, and in an internal circular layer of cuticle. Long-wavelengths from the dorsal and ventral cuticle, especially the ventral cuticle and an internal circular layer of cuticle. The leading edge of the hindwing with the coupling device is strongly sclerotized in both the ventral and the dorsal cuticles. Strong autofluorescence of aldehyde-fixed hemolymph. Scale bars: 100 μm. Abbreviations: C: Costa; cd: coupling device; dC: dorsal cuticle; enC: endocuticle; exC: exocuticle; HL: hemolymph; Lu: Lumen of the SRM vein; mC: mesocuticle; T: epidermal tissue; vC: ventral cuticle.

CLSM data were recorded on a CLSM Leica SP8 AOBS (Leica microsystems, Wetzlar, Germany). Excitation and emission settings were chosen equivalent to the filter settings used in WFM with slight adjustments for maximum clarity, with the exception of the blue channel recording resilin fluorescence. For this channel, the 405 nm diode laser of the SP8 was used for excitation, and hence a detector window for slightly longer wavelengths (412–484 nm) was employed for emission recording, according to extant literature (Michels and Gorb, 2012). We used a HC PL Fluotar 10x/0.30 dry objective, a pinhole of 999.32mAU (70.7 μm) at 580 nm, and either HyD or PMT detectors (see supplement for detailed data on equipment settings for each fluorescence image from both WFM and CLSM imaging).

Whole-mount preparations were recorded by CLSM as z-stacks with 25 layers. Of these, 3D renderings of the fluorescence signal were obtained by splitting the image channels and saving each channel as a gray-value image sequence by using bioformats (Linkert et al., 2010) in Fiji (Rueden et al., 2017; Schindelin et al., 2012). The resulting image sequences of each channel were processed as a volume dataset, and all channel volumes were rendered as a 4-volume project with colorfields according to the original LUTs by using the Drishti program (Limaye, 2006). As no quantitative analysis was performed, all images were adjusted to show the spatial segregation of emission wavelength with maximal clarity.

3. Results

3.1. Wide-field epifluorescence microscopy (WFM) of whole-mount preparations (Figs. 2 and 5a)

3.1.1. Forewing

Autofluorescence imaging of the ventral side of the posterior edge of the forewing (Fig. 2a) reveals that the clamp-like anterior portion (situated at the forewing) of the coupling device (cd in Fig. 1) is thoroughly sclerotized, as indicated by autofluorescence at long (red) wavelengths (Fig. 2a$_5$). In contrast, structures that require mobility for their function, e.g., the base of putatively mechanoreceptive setae and the edges of the claval furrow, exhibit strong autofluorescence at short (blue) wavelength, indicating the presence of resilin (Fig. 2a$_2$).

3.1.2. Hindwing

The veins appear as broad stripes of strong auto-fluorescence because of their thickened cuticle in comparison to the wing membrane (Fig. 2b). Whereas mid-wavelength auto-fluorescence (500–650 nm, Fig. 2b$_3$) is distributed evenly over the structure, both short (390–420 nm, blue, Fig. 2b$_2$) and long (660–720 nm, red, Fig. 2b$_5$) wavelength auto-fluorescence signals exhibit spatial segregation (Fig. 2b). Long-wavelength auto-fluorescence (red) is concentrated in broad stripes along the middle of the veins (Fig. 2b$_5$), especially along the second vein (CA), and at the proximal thickenings of the true veins, whereas their lateral rims are accompanied on either side by narrow stripes of short-wavelength (blue) auto-fluorescence (arrowhead in Fig. 2b$_1$). This is especially apparent in the second wing vein, which almost lacks middle-wavelength auto-fluorescence. In this vein, sharply defined bands of strong blue auto-fluorescence are connected by faint perpendicular lines, which appear to be superimposed on the red auto-fluorescence of the vein proper. In general, mid-wavelength fluorescence tends to thin out from proximal to distal faster than both short- and long-wavelength fluorescence signals. Stronger red autofluorescence is also detectable in the coupling device, the wing membrane between the coupling device and the end of the SRM vein, and in the false veins adjacent to the end of the SRM vein and the stigma (Fig. 5a). The distal end of the SRM vein also exhibits an overall increase in short-wavelength autofluorescence (Fig. 5a).

3.2. Confocal laser scanning (CLSM) of whole-mount preparations of the hindwing (Fig. 3)

In the hind wing, resilin fluorescence can be detected as longitudinal stripes within the wall of the true veins (indicated by white arrowheads in Fig. 3a, b, c; compare Fig. 2b). A patch of enhanced resilin signal is situated at the end of the SRM (white asterisk in Figs. 1 and 3c and d, 5a), adjacent to the sclerotized wing coupling device ("cd" in Figs. 1 and 3c, d, 5a). In its distal

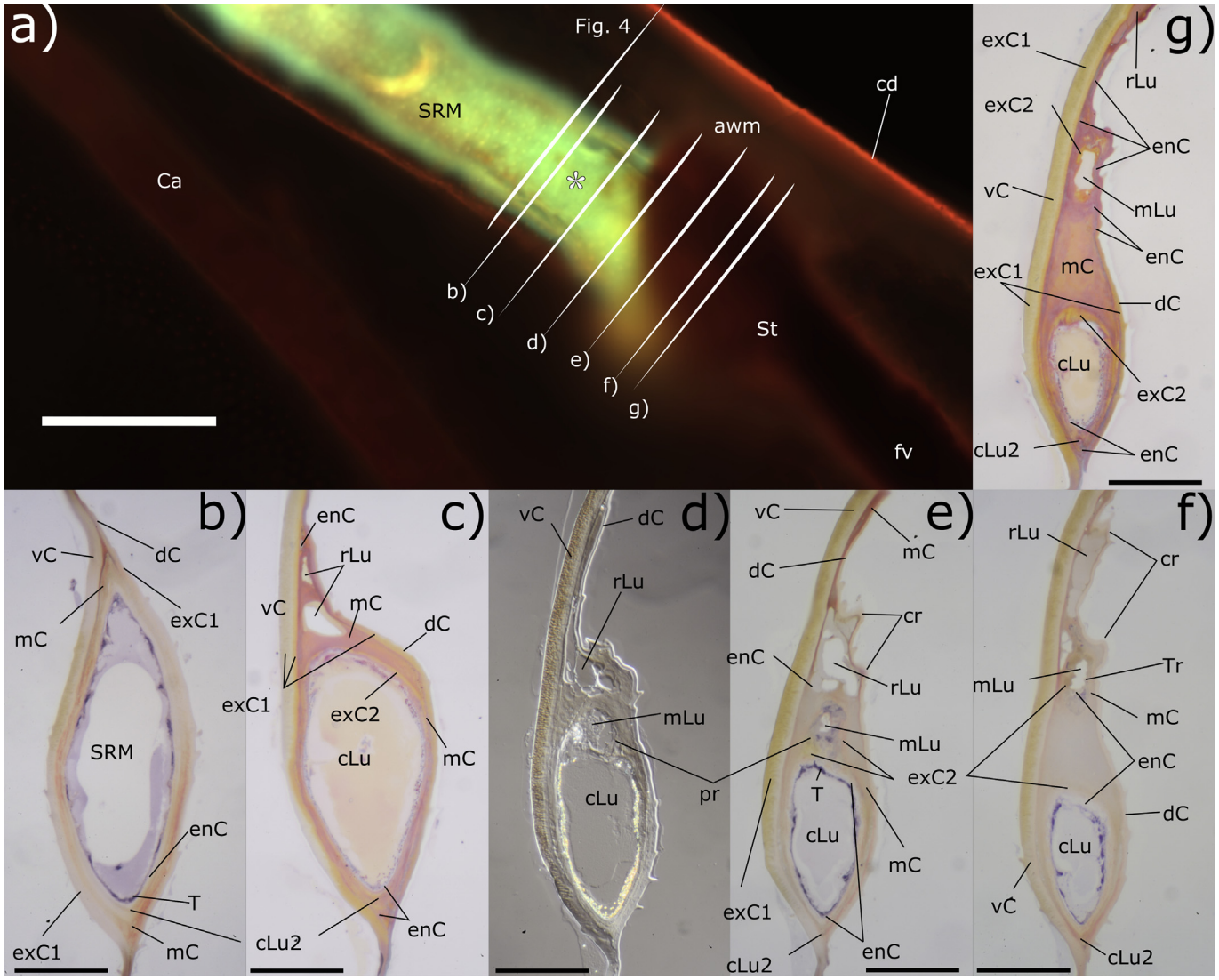

Fig. 5. Serial sections from the distal end of the SRM vein in the hindwing of *Graphosoma italicum*. a) Wide-field epifluorescence microscopy (WFM) composite image of the region around the distal end of the SRM vein in the hindwing. Dorsal aspect. Distribution of various wavelengths is equivalent to CLSM recordings. Approximate locations of perpendicular sections depicted in b) – g), and Fig. 4 are indicated. Note that serial sections were obtained from a different specimen. Scale bar: 200 μm. b)-g): 0.5-μm semithin sections from SPURR-embedded specimens. Images of perpendicular sections are arranged so that the anterior direction (toward the coupling device) is at the top, the posterior direction (toward the cubitus anterior vein) is at the bottom; ventral is at the left, and dorsal is at the right of each image. The ventral cuticle of the wing membrane is thicker than the dorsal one, but both cuticles are of comparable thickness around the vein. Near the distal end, the ventral cuticle becomes thicker and more strongly sclerotized, whereas the dorsal cuticle becomes thinner and less sclerotized, approaching the situation in the wing membrane (cf. Schieber et al. 2017). Separate lumina become apparent toward the distal end of SRM. The rostral lumen appears as hollow spaces with blind ends in the mesocuticle, whereas the middle lumen branches off from the largest (caudal) lumen. These two lumina have an epithelial lining and a sheet of exocuticle separating them from the surrounding mesocuticle and from each other. The rostral lumen extends into the dorsal wing ridges (see "cr" in Figs. 5e, 5f, 6c) that continue as the false veins of the distal part of the wing. b), e), f): Staining: hematoxylin – xylidin red. Tissue of epidermis violet, exocuticle amber (unstained), mesocuticle reddish, endocuticle pale. Resilin presence in the mesocuticle indicated by light sky-blue tinge. c), g): AZAN-staining. Exocuticle yellow, mesocuticle red, endocuticle blue. d) Unstained section imaged with differential interference contrast (DIC). Scale bars: 50 μm. Abbreviations: awm: anterior wing membrane; Ca: Cubitus anterior vein; cd: coupling device; cLu: central lumen of the SRM vein; cLu2: small caudal lumen of the SRM vein; cr: cuticular ridges; dC: dorsal cuticle; enC: endocuticle; exC1: exocuticle, continous with the wing membrane; exC2: exocuticle of the internal circular layer; fv: false veins; mC: mesocuticle; mLu: middle lumen of the distal SRM vein; pr: protrusion of the internal cuticular layers from the principal lumen "cLu", housing the branching-off "mLu"; rLu: rostral lumen of the distal SRM vein; SRM: fused Subcosta + Radius + Media vein after Betts (1986); St: stigma at the distal end of the hollow part of the SRM vein; T: tissue remnants of the epidermis; Tr: trachea; vC: ventral cuticle.

third, the SRM shows the same pattern as the cubitus anterior, but at the distal end of the SRM, the blue fluorescence (Fig. 3a$_1$, d) becomes stronger toward a bulbous distal inflation at the stigma, where the false veins extend (Fig. 3d$_{1,2,6}$). The long-wavelength (red) autofluorescence signal (bottom left channel in Fig. 3a$_5$, d$_5$) is concentrated along the surface of the major veins (Fig. 3a$_{2,5,6}$, b), at the leading edge of the wing in the region of the coupling device and the specialized membrane between the coupling device and the SRM vein (Fig. 3d$_{2,5,6}$, d, 4, 5), and in the false veins fanning out from the distal edge of the first vein (Fig. 3c, d$_{2,5,6}$), at the stigma posterior of the coupling device (Fig. 3c, d). In general, most recordings corroborate the results yielded by WFM (compare Figs. 2b and 5a) but with the added benefit of the 3D localization of cuticular regions at enhanced resolution and sensitivity for regions of weak signal. The red sclerotin signal is localized at the surface of the wing veins in 3D-renderings of z-stack data (Fig. 3b, c), whereas the blue resilin signal is situated deeper in the vein wall, around the lumen.

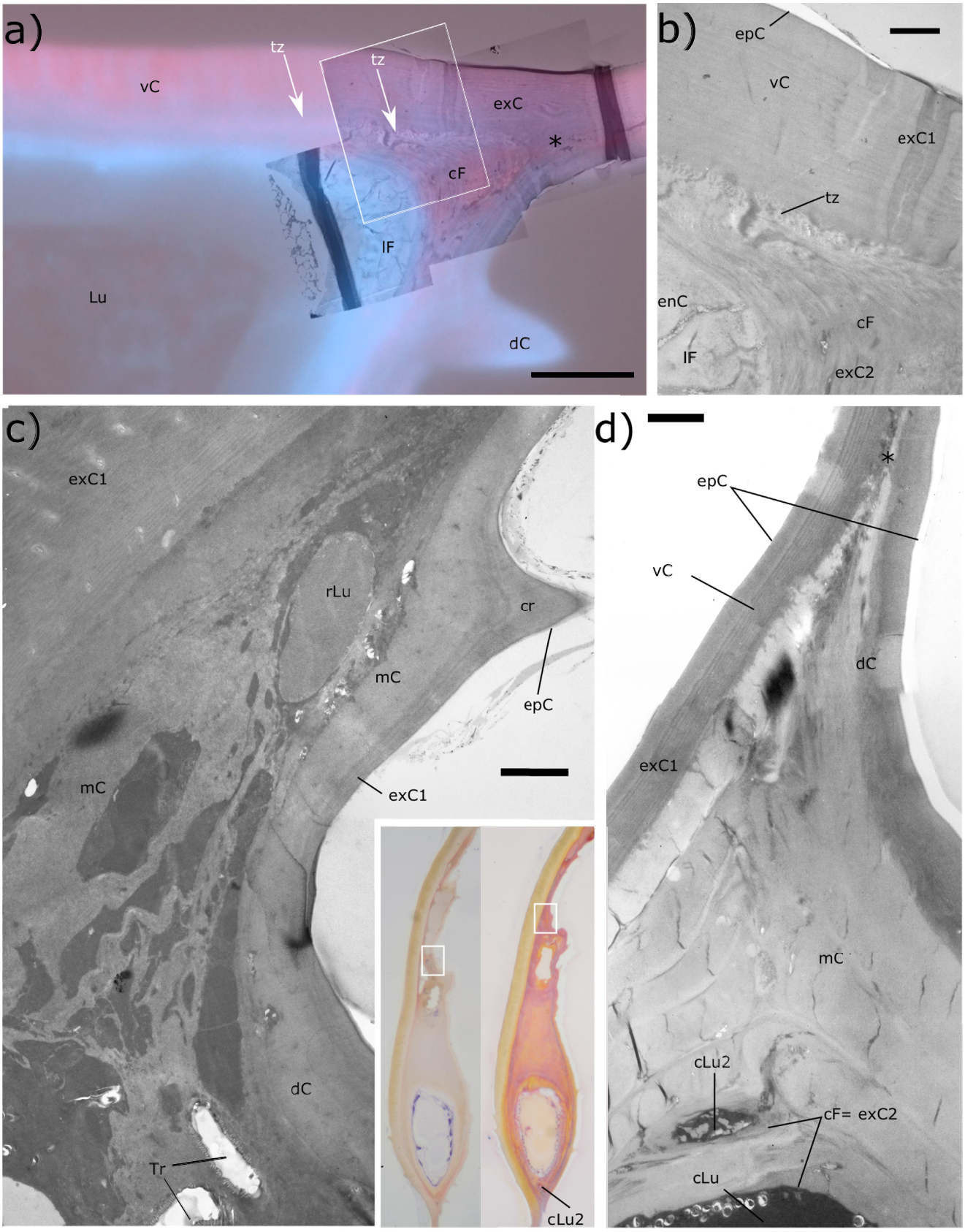

Fig. 6. Ultrastructural analysis of chitin fiber arrangement in the wall of the SRM vein in the hindwing of *Graphosoma italicum*. a) Stitched transmission electron microscopic (TEM) images superimposed on a WFM recording of an adjacent semithin section, taken perpendicularly through the SRM vein, from a different sample than the one shown in Fig. 5b)–g). The plane of sectioning is situated approximately between Fig. 5b) and c). Only DAPI staining and the Cy5 channel are shown. Short-wavelengths (blue, DAPI channel) from dorsal cuticle, internal longitudinal fibers, and intermediate layer. Long-wavelengths (red, Cy5 channel) from ventral cuticle and circular layer. White box: position of image 6b). Scale bar:

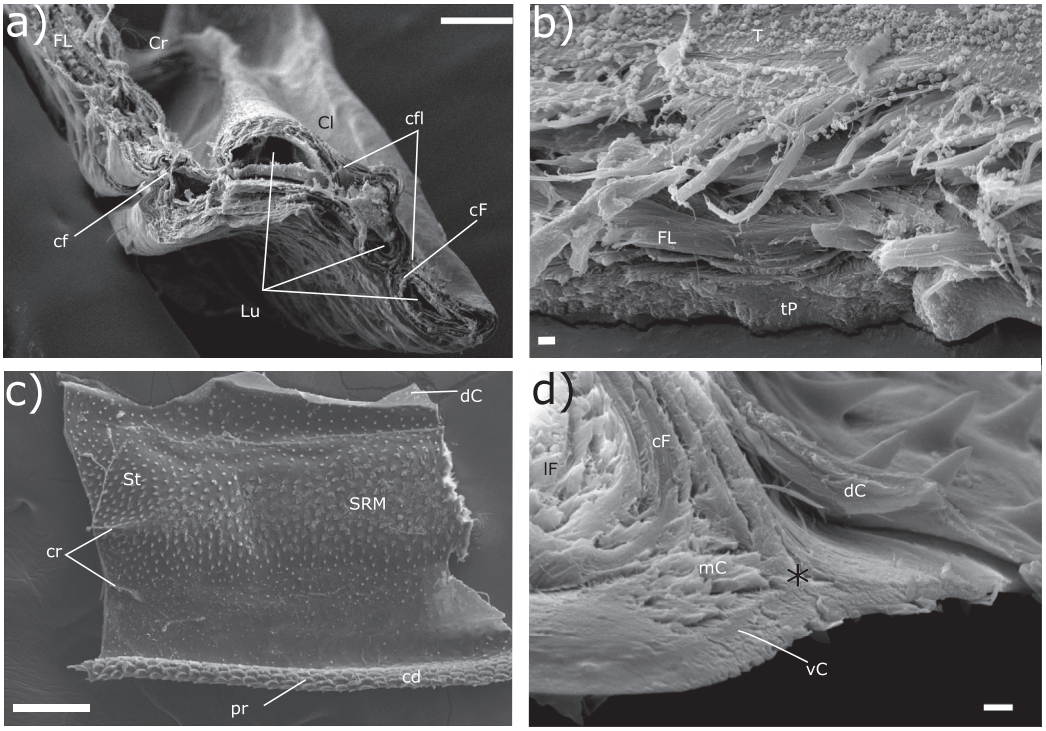

Fig. 7. Scanning electron microscopic images of parts of the wings of *Graphosoma italicum*, manually broken after critical-point drying. a) - b) forewing; c) - d) hindwing. a) Edge of breakage through Corium, Clavus, and claval furrow. Sclerites with massive layers of chitin fibers. Circularly arranged fibers around vein lumen in the sclerites sandwiched between continous layers. Layers narrow and apparently become more flexible around the claval furrow. Scale bar: 100 μ. b) Detail: Edge of a break through the ventral cuticle of the Clavus. Twisted-plywood texture on the outside (bottom), followed by massive layers of alternately arranged chitin fibers; note organic debris as tissue remnants on the inner surface. Scale bar: 2 μm. c) Region of the stigma, dorsal aspect. Surface protuberances that might form a friction-enhancing structure at the coupling device. Dorsal cuticle broken free in the wing membrane. Apparent thickness difference from that of ventral cuticle. Scale bar: 100 μm. d) Perpendicular cut through the caudal edge of the SRM vein. Dorsal and ventral cuticles with twisted-plywood texture. Layers become markedly thicker in the triangular mesocuticular region between the split cuticles. Beneath this region, note a layer of exclusively circular chitin fibers followed by a layer of longitudinal fibers. Scale bar: 2 μm. Abbreviations: cd: coupling device; cf: claval furrow; cF: circular fibers; cfl: continuous fiber layers; Cl: Clavus; Cr: Corium; cr: cuticular ridges; dC: dorsal cuticle; FL: fiber layers; lF: longitudinal fiber layers; Lu: lumen of vein; mC: mesocuticle; pr: protuberances on the coupling device; SRM: fused Subcosta + Radius + Media vein after Betts (1986); St: stigma at the distal end of the hollow part of the SRM vein; T: tissue remnants of the epidermis; tP: "twisted-plywood" - arrangement of chitin fiber layers in the exocuticle of the ventral cuticle; vC: ventral cuticle.

3.3. Confocal laser scanning (CLSM) of semithin sections from the hindwing (Fig. 4)

Cross sections of true veins from the region of the proximal end of the coupling device (position indicated by white line and "Fig. 4" in Figs. 3 and 5) revealed an unexpectedly complex pattern: the vein is built by dorsal and ventral wing cuticle bulging out convexly. In the region of the vein, the dorsal and ventral cuticles exhibit an enhanced red sclerotin signal ("dC","vC" in Fig. 4b). A thick circular layer of strong sclerotin fluorescence separated by a thin transition zone lies between these cuticle layers ("mC" in Fig. 4b). Inside this circular layer, a third innermost layer adjacent to the lumen shows no sclerotin fluorescence but is the primary source of a blue fluorescence signal ("enC" in Fig. 4b, inset). This layer is thickened along the caudal and rostral edge of the vein. Additional sources of blue autofluorescence are small chevron-shaped regions between the split dorsal and ventral cuticles at the caudal edge of the SRM vein, above the internal circular layer of exocuticle (white arrow in Fig. 4b (inset), 6a). The middle-wavelength auto-fluorescence signals are more evenly distributed across the cross section area. The wing membrane anterior of the SRM vein, in the region of and including the coupling device, is strongly sclerotized in both cuticle layers (Fig. 4b). A hollow space between the dorsal and ventral cuticles just posterior of the coupling device can be interpreted as a remnant of the costa vein ("C" in Fig. 4b).

3.4. Light microscopy (Fig. 5)

Semithin cross sections of the SRM vein (Fig. 5b–g) revealed its principal construction and indicated a complex differentiation of sclerotized material in the true veins. The dorsal and the ventral cuticle of the wing bulge out and enclose a lumen lined with epithelium ("T" in Fig. 5b, e). Hematoxylin-xylidin red staining

5 μm. b) Detail: single TEM image from the stitched image used for a). Ventral cuticle shows striation typical for helicoidally stacked "twisted plywood" -texture of chitin fibers. Inwardly, a diffuse layer of loosely arranged chitin fibers connects to a layer of dense, circularly arranged fibers. A layer of longitudinally arranged fibers follows toward the lumen. Scale bar: 1 μm. c) Stitched TEM image from the rostral edge of the SRM vein from the same sample (region between Fig. 5f) and g)). Exocuticles with twisted-plywood texture, lumina and tracheae embedded in mesocuticle with loosely arranged strips of chitin fibers and irregular voids of seemingly fiber-less arthropodin. Inset: white box indicates approximate region of the image in closely neighboring preceding (left) and following (right) semithin section. Scale bar: 2 μm. d) Stitched TEM image from the caudal edge of the SRM vein, slightly basal of Fig. 5b). Sections are taken at a 30° angle to the long axis of the SRM vein. Outer exocuticle with twisted-plywood texture. Mesocuticle with massive layers of medium density. A second lumen is visible next to the principle lumen. Both lumina contain tissue remnants and are separated by layers of circularly arranged, chitin fibers around each lumen. Scale bar: 2 μm. Abbreviations: cF: circularly arranged fibers; cLu: central lumen of the SRM vein; cLu2: small caudal lumen of the SRM vein; cr: cuticular ridge; dC: dorsal cuticle; enC: endocuticle; epC: epicuticle; exC1: exocuticle continous with the wing membrane; exC2: exocuticle of the internal circular layer; IF: longitudinally arranged fibers; rLu: rostral lumen; mC: mesocuticle; Tr: trachea; tz: transition zone between exC1 and exC2; vC: ventral cuticle.

(Fig. 5 b, e, f), AZAN staining (Fig. 5c, g) or the imaging of unstained sections with differential interference contrast (Fig. 5d) all demonstrate the striated appearance of both cuticles, indicative of a twisted-plywood arrangement of the chitin fiber layers. The two cuticles are of comparable thickness. The ventral cuticle, which is generally thicker and also shows a striated texture in the wing membrane, is visibly more sclerotized. The dorsal cuticle and the deeper layers of the ventral cuticle exhibit the yellow tinge that is characteristic of exocuticle ("exC1" in Fig. 5b, c, e–g) in AZAN staining. Where the cuticles split to encompass the lumen of the vein, AZAN staining results in small patches of blue staining, indicating endocuticular components ("enC" in Fig. 5b, c, e–g). Beneath this, chevron-shaped regions of diffuse texture appear in perpendicular sections. These regions exhibit mixed red and yellow staining with AZAN, indicative of mesocuticular properties ("mC" in Fig. 5c, g), and a light blue shade underlying pale reddish color following hematoxylin-xylidin red staining suggesting the presence of resilin among the cuticular proteins ("mC" in Fig. 5b, e, f). These diffuse regions at the rostral and caudal edge of the vein are connected both dorsally and ventrally by thin layers of diffuse texture-less cuticle that stains red with AZAN and xylidin red ("mC" in Fig. 5c). Further below a layer is found with faint striations encompassing the lumen. It stains amber with xylidin red and predominantly yellow with AZAN indicating a composition similar to that of exocuticle ("exC2" in Fig. 5b, c, e–g). A thin layer of only lightly staining, featureless cuticle lies between this circular layer and the epithelium of the vein lumen. The faint blueish coloring following both hematoxylin-xylidin red and AZAN staining suggests its endocuticular nature and the presence of resilin ("enC" in Fig. 5b, c, e–g). Further distally, toward the stigma, the diffuse mesocuticular region enlarges, especially at the rostral edge of the vein, where a series of round hollow spaces or rostral lumina ("rLu" in Fig. 5c–g) appear. Further distally, these spaces protrude toward ridges of the dorsal cuticle ("cr" in Fig. 5e–f, 7c), which continue into the false veins of the distal part of the wing ("fv" in Figs. 1 and 5a). Distal to the origin of these hollow spaces, a protrusion of the inner circular layer of exocuticle ("pr" in Fig. 5d and e) emerges into the diffuse region. This protrusion is circular in cross section and encompasses a lumen with remnants of epithelial cells ("mLu" in Fig. 5d–g). Oblique sectioning angles to the lumen reveal a corrugated wall typical for tracheae ("Tr" in Fig. 5f). The circular layer of exocuticular material surrounding this lumen ("exC2" in Fig. 5c, e–g) is clearly distinguishable from the surrounding diffuse mesocuticle. It continues into a second set of ridges of the dorsal cuticle ("cr" in Fig. 5f, 7 c). The remnants of the principal lumen with their double circular layer of cuticle and including the epithelial lining bend slightly caudally before ending in a rounded dead end, where the vein continues into the thickened cuticular ridges of the false veins emerging from the stigma ("fv" in Fig. 3c and d, white asterisk in Fig. 5a). The tip of the hollow part of the SRM vein with its extended diffuse layer of endo- and mesocuticle (Fig. 5d–g) and at least three separate lumina indicates its origin as a composite vein (Fig. 5c–g). The anterior wing membrane between the SRM vein and the coupling device is strongly sclerotized ("awm" in Fig. 5a).

3.5. Transmission electron microscopy (TEM) (Fig. 6)

The walls of the large composite vein SRM in the hindwing incorporate a complex fiber arrangement. The dorsal and ventral surfaces of the vein consist of the dorsal and ventral wing cuticles, respectively. The wing cuticles are the original cuticle layers covering the surface of the body wall duplicature that develops into the wing (see Introduction). Both the dorsal and the ventral cuticles increase both in their thickness and in the number of layers of helicoidally stacked fiber layers in the region of the vein (Fig. 6b–d), as was also indicated by light microscopy (Fig. 5b–g). The original wing cuticles only form the outermost layer of the vein structure. Beneath them and separated by a narrow transition zone (white arrows in Fig. 4b; "tz" and white arrows in Fig. 6a), which is most prominent as chevron-shaped regions at the anterior and posterior edges of the vein between the ventral and dorsal cuticle (black asterisks in Fig. 6a, d), a massive layer of loosely packed fiber layers develops that is not apparent in the wing membrane and that becomes dominated by circularly arranged fibers toward the lumen of the vein ("cF" in Fig. 6a, b, d). Underneath this zone and most prominent along the borders of the vein toward the wing membrane, we have found large electron translucent bundles of loosely packed fibers running longitudinally along the vein ("lF" in Fig. 6a and b). Ultrathin sections cut in alternation with sections for light microscopy reveal that the pattern of wavelength segregation in auto-fluorescence analysis coincides with a complex spatial arrangement of fiber architecture in the cuticle of the wing vein (Fig. 6a). The superimposition of the adjacent semithin sections examined by fluorescence microscopy and the stitched images of ultrathin sections examined by TEM have revealed this innermost layer and the diffuse transition zone ("tz" in Fig. 6a) to be the principal source of blue auto-fluorescence, whereas the red auto-fluorescence is concentrated in the circular and the twisted-plywood layers of the apical region of the wing vein wall (Fig. 6a). In regions toward the distal end of the lumen of the large composite vein, where separate lumina are discernible (Fig. 5c–g), each lumen including tissue remnants seems to lie within its own separate zone of circularly arranged fibers ("cF" in Fig. 6a, b, d). At the distal end of the principal lumen, the mass of mesocuticular material beneath the layered wing membrane cuticles and between the lumina exhibits a diffuse fiber arrangement ("mC" in Fig. 6c) reminiscent of the transition zone between the outer exocuticle ("exC1" in Fig. 6) and the circular layer ("tz" in Fig. 6a, b). Several tracheoles with ctenidia can be observed in this region ("Tr" in Fig. 6c). Along the caudal edge of the vein, the mesocuticular zone is arranged in several distinct layers of low density ("mC" in Fig. 6d). TEM has further revealed a third, very narrow, tissue-filled lumen ("cLu2" in Fig. 5b, c, e-g, 6d) surrounded by circularly arranged fibers along the caudal edge of the SRM vein.

3.6. Scanning electron microscopy (SEM) (Fig. 7)

3.6.1. Forewing

Cross sections of the forewing show the basic construction of the wing as two cuticles, consisting of continuous fiber layers ("cfl" in Fig. 7a) encompassing veins, as marked by the presence of tracheae, encompassed by circular fiber layers ("cF" in Fig. 7a). The thickened exocuticle exhibits a differentiated pattern of fibers. Beneath the multiple, thin, helicoidally stacked layers reminiscent of the "twisted-plywood" structure of the hind wing membrane cuticles ("tP" in Fig. 7b), several thick layers of uniformly oriented chitin fibers are stacked at intervals separated by thinner fiber layers with a perpendicular orientation ("FL" in Fig. 7a and b).

The claval furrow ("cf" in Figs. 1 and 7a) is formed by a reduction of the thickness of all the involved fiber layers into thin sheets that are not as rigidly bound together as they are in the sclerites (Clavus and Corium).

3.6.2. Hindwing

Preparations of hind wing material with deliberately broken edges enabled the analysis of both the external and the internal features of the region around the distal end of the SRM vein (Fig. 7c). Scale-like protuberances ("pr" in Fig. 7c) mark the coupling device ("cd" in Fig. 7c) at the leading edge of the hindwing.

Two cuticular ridges lead distally from the end of the SRM vein ("cr" in Fig. 7c, compare Fig. 5e–g), whereas the voluminous bulge of the part of the SRM containing the caudal lumen ("cLu" in Fig. 5c–g) bends slightly caudally toward the stigma ("St" in Fig. 7c). Where the dorsal and ventral cuticles are broken separately in the region of the wing membrane, the dorsal cuticle ("dC" in Fig. 7c) can be seen to be much thinner and more flexible than the ventral cuticle.

Roughly broken edges of hind wing veins permit insights into the 3D arrangement of the fibrous material in the wing (Fig. 7d). Where the dorsal and ventral cuticles (each consisting of densely stacked thin layers of chitin fibers) split at the edge of the SRM vein (black asterisk in Fig. 7d), a region of loosely arranged, layered mesocuticle ("mC" in Fig. 7d) with chevron-shaped cross sections appears above a thick layer of circularly arranged chitin fibers encompassing the vein lumen ("cF" in Fig. 7d). Beneath this layer, the lumen is further encircled by a layer of less dense, longitudinally arranged fiber bundles ("lF" in Fig. 7d).

4. Discussion

4.1. General aspects

Insect wings have been the subject of numerous functional morphological and material scientific studies (e.g., Wootton, 1992), and yet one aspect has hitherto been neglected, i.e., the organization of the transition zone between hard and soft cuticles as exemplified by the embedding of sclerotized wing veins into the softer wing membrane. From a technical (biomimetic) point of view, the composition of the transition zones between rigid and pliable regions is of great functional importance, as abrupt changes in properties can potentially lead to high mechanical stresses and hence to the reduced reliability and durability of the structures. Such considerations are not only relevant for technical applications, e.g., in terms of deployable shading devices in architecture (Schieber et al., 2017), but also for considerations of the proper functioning of integrative biological structures such as insect wings, which are exposed to various mechanical stresses. To gain insights into the (ultra)structural organization of the cuticle of the wing veins and their transition to the wing membrane in the "minstrel bug" *Graphosoma italicum*, we have combined various light, fluorescence, and electron microscopic techniques to elucidate the distribution of differently sclerotized cuticle types, of resilin, and of the particular fiber architecture in these structures. Generally, a stronger degree of sclerotization (Figs. 1–5) and a denser packing of chitin fibers (Fig. 6) characterize the exocuticle as opposed to the underlying endocuticle, and, correspondingly, rigid cuticular regions (sclerites, veins, leading wing edge) are generally characterized by a higher proportion of exocuticle as opposed to pliable regions (membranes between veins in the wing plane, folding regions) (compare Figs. 2a, 3 and 4). We expected to find gradual (not abrupt) transitions between soft and hard cuticle.

4.2. Distribution of rigid, pliable, and elastic components

4.2.1. Forewing

In the forewing, the Corium and Clavus represent sclerotized rigid plates (cf. Fig. 1). The wing cuticle in the region of the Corium and Clavus consists of a zone of thin, helicoidally arranged, fiber layers, reminiscent of exocuticle ("tP" in Fig. 7b), underlain with several thick layers of chitin fiber bundles of alternating direction ("FL" in Fig. 7a, b). This arrangement of chitin fibers in thickened cuticular structures has also been reported in other arthropods, e.g., the elytra of beetles (van de Kamp et al., 2016; van de Kamp and Greven, 2010), and therefore probably represents an adaptation for withstanding large external forces in anatomical structures that serve a protective role. In the Pentatomidae, this capacity is largely served by the scutellum, but the scutellum might be a phylogenetically young development, and thus, the forewing still bears its characteristics as a protective cover (Wootton, 1992). As we have not undertaken any serial sectioning of the forewing, and as the opacity of the rigid plates hinders 3D-autofluorescence analysis by CLSM, we are unable to decide with certainty whether the thick alternating fiber layers have mesocuticular properties or represent a differently arranged exocuticular layer. A mesocuticular constitution of the major part of the Corium and Clavus is likely, as most of the autofluorescence signal recorded by WFM is in the mid-to short-wavelength range, and the forewing portion of the wing coupling device can easily be identified as a strongly sclerotized structure by its enhanced long-wavelength autofluorescence compared with its surroundings ("cd" in Fig. 2b). Enclosed between the thickened wing cuticles of the Corium and Clavus are the forewing veins that are surrounded by several thick circular fiber layers ("cfl" in Fig. 7a). This pattern resembles the situation found in Coleoptera (van de Kamp et al., 2016; van de Kamp and Greven, 2010).

Mobility is provided by a sharply defined line of thinned-out pliable membrane, namely the claval furrow ("cf" in Fig. 7a). This furrow is apparently not achieved by a reduction of the number of cuticular fiber layers, but by a strong reduction of the thickness of each layer (Fig. 7a). Mobility and fluorescence properties indicate that the claval furrow and the adjacent edges of the Clavus and Corium are dominated by endocuticular material.

4.2.2. Hindwing

The hindwing of Heteroptera consists mainly of pliable membrane, with the exception of the mainly longitudinal veins (e.g., Betts, 1986; Wootton, 1992), and a region of sclerotized membrane that lies between the coupling device and the SRM vein, and that may control coupling and/or transduce forces between the coupling device and the SRM vein during wing folding and flight (Figs. 3 and 4). Former investigations in *G. italicum* have corroborated the assertions of Wootton (1992) that the wing membrane does not entirely consist of epicuticle but also contains procuticular material throughout (Schieber et al., 2017). Differentiation between the false veins and various regions of the wing membrane exists between the dorsal and ventral cuticles with regard to the amount of exocuticle and the extent of resilin enrichment (Schieber et al., 2017). In the present study, we have focused on the constitution of the longitudinal true veins of the hindwing and on the ultramorphology of the wall of the most anterior longitudinal true vein in *G. italicum*, i.e., the SRM vein.

In the SRM vein, the helicoidally stacked exocuticle of the wing membrane cuticles is underlain by a mesocuticular zone of variable thickness (white arrow in Fig. 4; "tz" and white arrows in Fig. 6a) with a diffuse arrangement of small strands of chitin fibers. Traces of blue AZAN staining ("enC" in Fig. 5g) and a lack of red autofluorescence ("enC" in Fig. 4b) indicate a fine layer of unsclerotized endocuticle between the external exocuticle and internal mesocuticle. The mesocuticle is very thin in the middle of the dorsal and ventral walls of the vein but is wider toward its rostral lateral edge, where it widens distally in the direction of a diffuse zone housing the rostral lumina (cf. "rLu" in Fig. 5). This zone exhibits red autofluorescence indicating sclerotization (Fig. 4) but also light blue hematoxylin staining indicating the possible presence of resilin (Fig. 5e and f). Moreover, at the caudal edge of SRM, the mesocuticle extends a few micrometers between the dorsal and the ventral cuticles, thereby providing a chevron-shaped appearance in perpendicular cross sections (white arrow in Fig. 4b, white arrows, black asterisk in Fig. 6a, d). This layer exhibits shorter wavelength autofluorescence,

indicating less sclerotization, in its deeper layers, but only at the caudal edge of the vein, where CLSM imaging has revealed several alternating layers of stronger and weaker sclerotization (cf. Fig. 4b). Beneath it, a second layer of sclerotized exocuticle (cf., "exC2" in Figs. 5 and 6) shows a circular arrangement of chitin fibers. Under this layer and surrounding the epithelium lining the lumen of the vein, we find a layer of unsclerotized endocuticle that contains bundles of longitudinally arranged chitin fibers. Similar to the above-mentioned mesocuticular layer, this layer is also thinner along the dorsal and ventral walls of the vein and thicker at its lateral edges. Between the distal end of the SRM vein and the part of the coupling device at its anterior edge of the hindwing, the ventral cuticle is heavily sclerotized, forming a rigid connection between the wing coupling device and the vein. The resulting construction of the vein is that of a laterally flattened tube with multilayered walls (Fig. 8a). Hard layers containing heliciodally stacked, chitin fibers or fibers enclosing the lumen in a circular fashion alternate with soft layers in which the chitin fibers are diffuse and longitudinally arranged. Generally, soft and elastic (resilin-bearing) components are more concentrated toward the center, as opposed to the surface. Moreover, the layering is more pronounced with a greater proportion of soft material toward the caudal edge of the vein, as opposed to the rostral edge (Figs. 4b and 8b).

4.3. Transition zones between hard and soft cuticle components

Few studies have addressed the ultrastructure of the transition zones in the hinges of insect wings. In the longitudinal flexion line of the orthopteran wing, Banerjee (1988) found considerably larger microfibrils of continuously helicoidal architecture. Ruangchai et al. (2013) combined various electron microscopic techniques and Raman spectroscopic imaging to study the structure and composition of the joint head cuticle of the isopod *Porcellio scaber* with emphasis on the transition zone toward the arthrodial membrane; this zone was demonstrated to deviate from the main head region showing an especially thick epicuticle and a parallel fiber orientation. For dragonfly wings, Appel et al. (2015) revealed a slightly simplified cuticular layering in the transition zone between the veins and the membrane. Dragonflies and damselflies are also known for their incorporation of resilin in vein joints in which defined mobility between adjacent rigid structures is necessary (Appel and Gorb, 2011, 2012; Donoughe et al., 2011; Gorb, 1999; Marrocco et al., 2010).

In the following, two types of transition zones between hard and soft cuticular structures in the SRM vein of the hindwing of *G. italicum* and their constitution are discussed together with their possible functions and the combined effect on the mechanical system of the hindwing.

4.3.1. Vertical transitions between cuticular layers

With respect to the distribution of resilin, as indicated by its short-wavelength (blue) autofluorescence, we have found that its content is enhanced in the innermost, longitudinally arranged, endocuticular layer of the vein wall and in the soft mesocuticular layers between the internal ("exC2" in Figs. 5, 6 and 8) and external ("exC1" in Figs. 5, 6 and 8) sclerotized exocuticular layers. Resilin-dominated endocuticle has also been observed in other load-bearing cuticular structures of insects, e.g. in the wing veins of dragonflies (Appel et al., 2015; Rajabi et al., 2016c) and tibiae of stick insects (Schmitt et al., 2018).

Fiber directionality and density do not change abruptly between the mesocuticular layer and either of the exocuticular layers (tz in Fig. 6b). However, inside the circularly arranged exocuticle, an abrupt transition of cuticular properties occurs between the inner exocuticular layer and an internal layer of resilin-containing endocuticle with longitudinally arranged chitin fibers ("lF" in Fig. 6a, b).

Possibly, the separate layers of resilin-rich material found in the wall of the SRM vein serve different mechanical functions in a situation that resembles that reported in dragonflies and damselflies (Appel et al., 2015): The innermost layer that incorporates longitudinal fiber bundles within unsclerotized resilin-rich endocuticular material presumably cannot contribute to the function of the transition zone between vein and membrane, as it is separated from the outer exocuticle which is continous with the wing membrane, by a circularly closed, sclerotized internal layer of exocuticle. The internal, longitudinally arranged, resilin-rich endocuticle most probably controls the bending stiffness and bending elasticity of the vein spanwise along the entire length of the tubular portion of the vein, and might be involved in elastic energy storage during wing beats and in folding and unfolding cycles. A similar mechanical function has been described for the dragonfly longitudinal vein, which shares some structural similarities (Appel et al., 2015) to the bug vein studied here. A different function can be envisioned for the mesocuticular layer between the internal, circularly arranged, exocuticular layer ("exC2" in Figs. 5, 6 and 8) and the outer exocuticle ("exC1" in Figs, 5,6,8) and between the converging cuticles at the lateral edges of the vein. This layer, which is characterized by a diffuse fiber arrangement with gradual changes in density and directionality, is by definition and by its staining properties and autofluorescence, less densely sclerotized than the exocuticle.

4.3.2. Lateral transitions of overall wing stiffness

4.3.2.1. Forewing. In the forewing, the stiffness gradient between the thick rigid plates of the Corium and Clavus and the pliable membrane strip of the claval furrow is very steep. The claval furrow resembles a U-shaped trough in cross-section (Fig. 7a). Notable in the forewing is the concentration of short-wavelength fluorescence signals indicating an enhanced resilin content along the edges of the claval furrow ("cf" in Fig. 2a). Two feasible functions of these resilin cushions are (1) the storage of elastic energy to reverse the bending along the furrow, as initiated by transient external forces and (2) the prevention of wear and tear by elastically cushioning peak stretching forces perpendicular to the direction of the furrow. The cushions might also reduce compression forces at the edges of the furrow, where these edges touch in the event of larger bending angles.

4.3.2.2. Hindwing. In the hindwing, the wing area mainly consists of soft membrane material that is supported by the wing veins, which act as stiffening rods or support beams during wing folding and unfolding and wing beat (Wootton, 1992). In the following, we address the way that the lateral transition between the relatively stiff veins and the relatively pliable membrane is constructed. The hollow tube of the vein is formed by the two wing cuticles of the wing membrane (dC, vC in Fig. 8) progressively bulging out to form the vein. The transition of the cuticular characteristics of the cuticles from the wing membrane toward the vein wall is gradual. The ventral cuticle of the SRM vein retains its composition of mainly exocuticular, helicoidally stacked, fiber layers and only gradually gains more layers and general thickness toward the midline of the vein. The dorsal cuticle, which is only weakly sclerotized and exhibits unlayered mesocuticular characteristics and enhanced resilin content in the wing membrane (Schieber et al., 2017), gradually increases in thickness and has a layered exocuticular appearance in the SRM vein, resembling that of the ventral cuticle. Both cuticles are approximately of equal thickness in the midline of the veins (Fig. 5b–c). Near the distal end of the

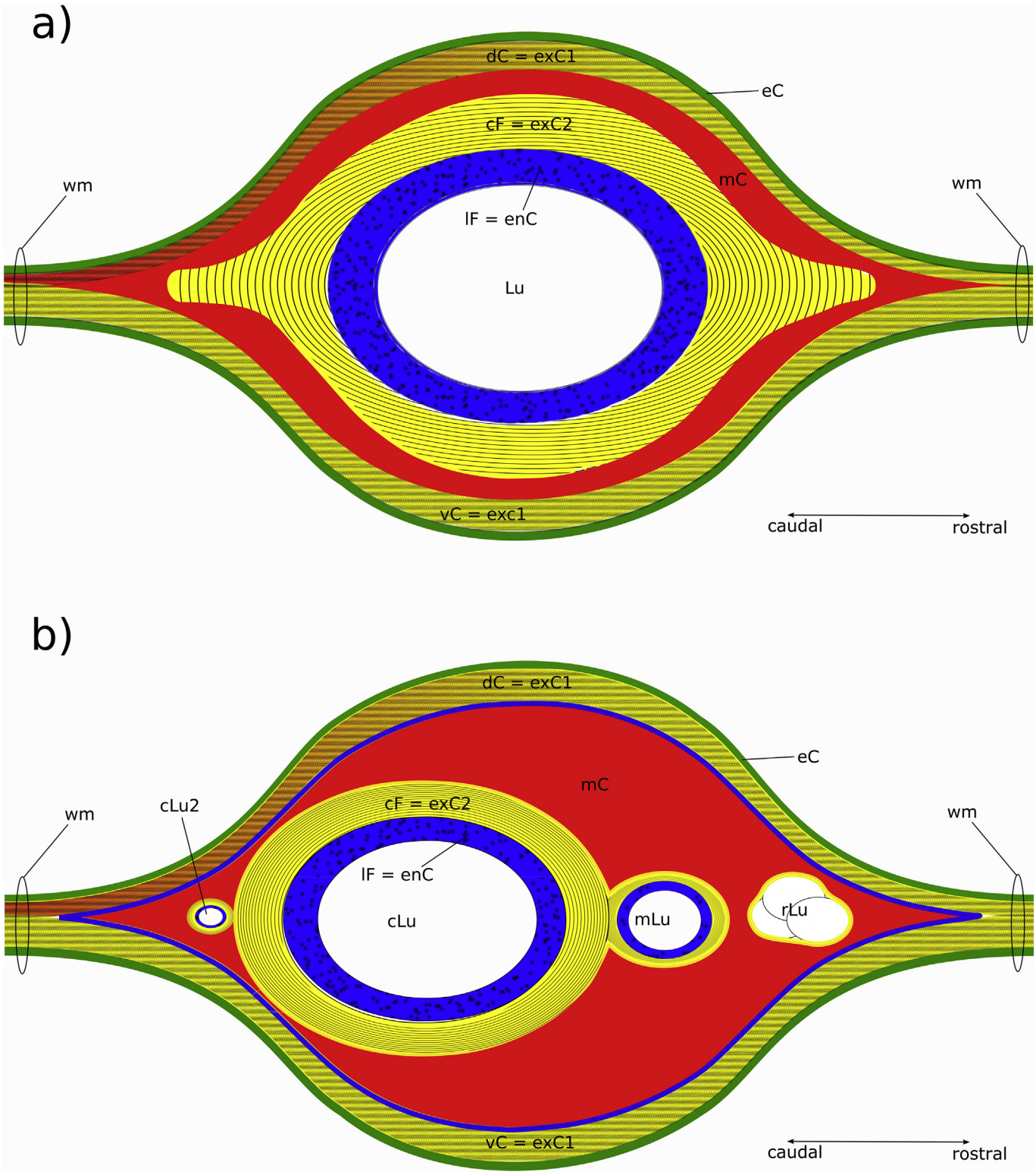

Fig. 8. Representation of the constitution of a cross section of the SRM hindwing vein of *G. italicum*. Color scheme: Green: epicuticle; yellow: exocuticle; red: mesocuticle, blue: endocuticle. Resilin content, as indicated by analysis of autofluorescence, is enhanced in the mesocuticular (red) region, and is strongly enhanced in the endocuticular (blue) region. Colour shading of the dorsal cuticle from red to yellow (left to right) depicts the increasing sclerotization of the dorsal cuticle from the wing membrane posterior to the SRM vein over the dorsal part of the SRM vein towards the anterior wing membrane between the SRM vein and the coupling device at the leading wing edge of the hindwing. a) Principal constitution of the wing vein wall. b) Differentiated situation toward the distal end of the SRM vein, containing several lumina. Abbreviations: cF: circularly arranged fibers; cLu: central lumen; cLu2: small caudal lumen; dC: dorsal cuticle; eC: epicuticle, enC: endocuticle; exC1: outer layer of exocuticle, exC2: internal layer of exocuticle; lF: longitudinally arranged fibers; mC: mesocuticle; mLu: middle lumen; rLu: rostral lumen; vC: ventral cuticle; wm: wing membrane.

SRM vein, the dorsal cuticle gradually becomes thinner once again (Fig. 5d–g, 8). The strongly sclerotized region of the ventral cuticle connecting the distal end of the SRM vein to the coupling device (cf. Fig. 4), begins as a thin superficial layer approximately at the ventral midline of the vein, and gradually gains thickness toward the distal end of the vein and the rostral edge of the hindwing (Fig. 5b–g). Moreover, in their longitudinal direction, the true veins in the hindwing of *G. italicum* exhibit a gradual change in properties (Fig. 2b). The central part of the vein is supported by an additional internal layer of sclerotized cuticle forming a closed ring in perpendicular cross sections (exC2 in Fig. 8a). The space outside of the ring, beneath the diverging cuticles, is filled with a softer mesocuticular material that gradually tapers out toward the wing membrane (mC in Fig. 8a). Thus, summarizing, we have established three structural mechanisms responsible for the overall variation of stiffness of the total cuticular material combined between the vein and its surrounding membrane: (1) the variation in the overall thickness of cuticular material, (2) the variation in the degree of sclerotization of the exocuticular material of the wing cuticles, and (3) the variation in the proportion of sclerotized *versus* unsclerotized cuticle over the total thickness of cuticle. Interestingly, the SRM of *G. italicum*, contrary to many insect wing veins experiencing bending forces, is laterally flattened instead of compressed (Wootton, 1992). This might further lead to soft bending characteristics and to shallower gradients in bending characteristics between vein and membrane. Although the overall stiffness varies greatly between the veins and the surrounding membrane, all changes in mechanical properties are organized in a gradual manner on one to several levels of organization, and thus abrupt changes are seemingly avoided. Gradual changes in cuticle properties as a common rule in insects have also been suggested by simulation studies approximating cuticle behaviour with finite element models (Rajabi et al., 2017b).

The apparent similarities in the complex construction of wing vein walls, incorporating several hard and soft layers with the addition of resilin in internal layers (Figs. 5 and 8), to the situation found in the distantly related dragonflies and damselflies (Appel et al., 2015) might be an indication that we are dealing with a more general (ultra)structural organization of wing veins. Such a system might form a mechanical adaptation of mechanically stressed longitudinal veins in flapping systems with high wing loads (Appel et al., 2015). The presence of resilin along flexion lines in the forewing (Fig. 2a) might prevent damage from shear forces and fatigue breakage, where repeated load shifts at small bending radii are required.

4.4. Developmental formation of the SRM vein wall

Although generally corroborating the notion of Betts (1986), that the SRM vein (cf., SRM in Fig. 1) of the pentatomid hind wing is a composite vein that incorporates several principal veins fused together, our results nonetheless pose additional questions. The presence of several elongated hollow spaces in the distal part of the SRM vein (Fig. 5) supports the view of a composite nature of the vein. If all these separate lumina are counted as remnants of former individual veins, as many as five veins might have become incorporated into the composite vein. However, only one of the smaller lumina ("mLu" in Fig. 5d–g) exhibits a connection to the principal lumen of the SRM vein. Three lumina ("mLu", "cLu" and "cLu2" in Figs. 5, 6 and 8b) share the characteristics of cellular content, tracheal structures, and a separate layer of circularly arranged cuticle, reducing the minimum number of fused veins to three. "cLu2" is very narrow, being discernible with certainty only in ultrathin sections investigated by TEM, and its possible connection with the principal lumen ("cLu") of the SRM vein could not be demonstrated during the course of this study. The rostral hollow spaces designated as the "rostral lumina" ("rLu" in Figs. 5, 6 and 8b) do not exhibit cellular or tracheal content, nor a delimitation by circularly arranged cuticular fiber layers. Whether the differences in complexity between the rostral and the middle and caudal lumina reflect different degrees of reduction attributable to fusion events at different phylogenetic stages, or whether the most anteriorly situated hollow spaces ("rLu" in Figs. 5 and 8b) without connection to the other lumina or circular cuticle layers are unrelated to wing veins and represent differentiations of the stigma of mechanical or other physiological adaptive value cannot be answered at present with certainty.

Our results suggest that, upon retraction of the epidermal cells from the wing proper, a second phase of cuticle secretion of cells situated in the position of true veins commences. Enclosed between the dorsal and the ventral SRM cuticle layers that are continuous with the dorsal and ventral cuticles of the wing membrane ("Flügellamellen" or "wing lamellae" *sensu* Weber, 1930, p. 138), additional procuticular material exists in the region of the SRM: a circular layer of chitin fibers forming a ring around the innermost layer of longitudinally arranged fibers ("lF = enC" in Fig. 8). This arrangement is explained easily only if, first, the circularly ("cF = exC2 in Fig. 8) and, then, the longitudinally arranged fiber layers ("lF = enC" in Fig. 8) are secreted by epidermal cells forming a closed hollow tube inside the vein. As no cell remnants are discernible outside of the circular layer, the simplest explanation is that the secretion of the circular and the longitudinal layer takes place after the wing membrane cuticles are secreted, and that the epidermal cells have receded by this time into the vein cavity. According to this view, the diffuse mesocuticular layer (mC in Fig. 8) that connects the helicoidally stacked, dorsal and ventral layers and the circularly arranged internal layer might be a secretion product of receding epidermal cells between the two major periods of cuticle secretion, i.e., that of the wing membranes and that of the internal layers of the vein walls.

4.5. Methodological considerations

We have demonstrated that AZAN staining is an informative tool for the study of cuticle differentiation, even in epoxy-embedded osmificated material prepared for TEM imaging, although the protocol needs to be adjusted with respect to times, concentrations, and temperatures. Softening of the sections by ethanol fumes and de-osmification by hydrogen peroxide prior to staining improves the staining process.

In addition, auto-fluorescence analyses of unstained semithin sections of TEM-prepared material has proved to be a valuable tool, provided that a mounting medium with sufficiently low auto-fluorescence is used, and that the equipment is sensitive enough to record the weak signal from the thin sections. CLSM analysis of auto-fluorescence is especially suited for examining the spatial arrangement of the cuticular components, as tunable detectors permit better interpretations of the emission signal spectrum in comparison with WFM analyses. CLSM-recorded datasets of z-stacks from whole-mount preparations offer further possibilities for 3D rendering to assess the spatial distribution of various emission sources (Michels and Gorb, 2012).

In combination with histological stains and EM techniques to reveal the ultrastructural fiber arrangement, these methods allow a comprehensive assessment of the cuticle composition. Especially for the localization of resilin, the combination of several methods is

useful, as no method, i.e., neither autofluorescence nor staining or ultrastructural aspects, provide unequivocal evidence for the presence of resilin in histological sections (Michels and Gorb, 2012). Purified chitin, for instance, has a peak fluorescence emission at around 450 nm (Azofeifa et al., 2012) and thus can give a significant signal in commonly used blue detection channels but is characterized in TEM images by visibly fibrous, high-contrast textures as opposed to the featureless electron-lucent aspect of resilin. Thus, the coincidence of short-wavelength autofluorescence, light-blue hematoxylin stain, and electron-lucent cuticular regions in correlative analyses provides reasonable circumstantial evidence for the occurrence of resilin (Fig. 6a and b).

In terms of the distinction between endo-, meso-, and exocuticular regions, we need to consider that the sclerotization of arthropodin into sclerotin results in a shift of the autofluorescence emission to longer (red) wavelengths. Hence, the analysis of red autofluorescence (Figs. 2–4, 5a, 6a) in comparison with histological staining (Fig. 5b–g) and the ultrastructural investigation of the density and directionality of chitin fibers (Figs. 6 and 7) permits greater accuracy in localizing these different cuticle types (Figs. 3 and 4).

5. Conclusion

A multi-method approach for analyzing the structure and spatial differentiation of the wing vein wall in the minstrel bug, *Graphosoma italicum* (Pentatomidae), was undertaken, combining (1) various types of histological staining on serial sections, (2) autofluorescence analysis of whole-mount preparations and semithin sections of embedded material, (3) TEM analysis of ultrathin sections, and (4) SEM studies of break-and-cut preparations. This combination of complementary methods was sucessful in comprehensively revealing the complex layered structure of the wall of the SRM vein in the bug hindwing. Several branching and clearly separated lumina in this vein corroborate its composite nature from several principle veins. The structural constitution of the wing vein wall is characterized by gradual transition zones between wing membrane and vein wall, a flexible connection between external and internal rigid layers, and an internal layer of elastic material with longitudinal directionality. Resilin was detected in both forewing and hindwing structures that require repeated mobility between rigid elements further supporting the view that resilin forms an integral component of the mechanical system of insect wings.

In the future, the applied morphological techniques might become further complemented by macro-scanning ion conductance microscopy (SICM) to conduct large-scale mappings of the material properties (e.g. elastic modulus) across entire wings (Schierbaum et al., 2018).

Acknowledgments

The authors are grateful to the Baden-Württemberg Foundation for funding our research work as part of the project BIAG 'Bio-inspired adaptive facade shading systems'. York-Dieter Stierhof and Lorenz Henneberg (Center for Plant Molecular Biology, University of Tübingen) provided access to WFM equipment and excellent advice. Monika Meinert provided expert SEM assistance. Stefan Fischer suggested a successful contrast-enhancing fixation protocol and assisted with photography, embedding procedures and data handling. Peter Wenk provided valuable insight and staining protocols for resilin. Theresa Jones corrected the English. We are indepted to an anonymous reviewer for valuable comments that greatly helped to improve the quality of the manuscript.

Appendix A. Supplementary data

Supplementary data related to this article can be found at https://doi.org/10.1016/j.asd.2018.04.004.

References

Appel, E., Gorb, S.N., 2011. Resilin-bearing wing vein joints in the dragonfly *Epiophlebia superstes*. Bioinspir. Biomim 6 (046006). https://doi.org/10.1088/1748-3182/6/4/046006.

Appel, E., Gorb, S.N., 2012. Resilin in dragonfly wings. Mitt Dtsch Ges Allg Angew Ent 18, 81–85.

Appel, E., Heepe, L., Lin, C.-P., Gorb, S.N., 2015. Ultrastructure of dragonfly wing veins: composite structure of fibrous material supplemented by resilin. J. Anat. 227, 561–582. https://doi.org/10.1111/joa.12362.

Azofeifa, D.E., Arguedas, H.J., Vargas, W.E., 2012. Optical properties of chitin and chitosan biopolymers with application to structural color analysis. Opt. Mater. 35, 175–183. https://doi.org/10.1016/j.optmat.2012.07.024.

Banerjee, S., 1988. Organisation of wing cuticle in *Locusta migratoria* linnaeus, *Tropidacris cristata* linnaeus and *Romalea microptera* beauvais (Orthoptera : Acrididae). Int. J. Insect Morphol. Embryol 17, 313–326. https://doi.org/10.1016/0020-7322(88)90012-8.

Betts, C.R., 1986. The comparative morphology of the wings and axillae of selected Heteroptera. J. Zool. 1, 255–282. https://doi.org/10.1111/j.1096-3642.1986.tb00639.x.

Born, L., Körner, A., Schieber, G., Westermeier, A.S., Poppinga, S., Sachse, R., Bergmann, P., Betz, O., Bischoff, M., Speck, T., Knippers, J., Milwich, M., Gresser, G.T., 2017. Fiber-reinforced plastics with locally adapted stiffness for bio-inspired hingeless, deployable architectural systems. Key Eng. Mater. 742, 689–696. https://doi.org/10.4028/www.scientific.net/KEM.742.689.

Bruce, H.S., Patel, N.H., 2018. Insect wings and body wall evolved from ancient leg segments. bioRxiv 244541. https://doi.org/10.1101/244541.

Danforth, B.N., Michener, C.D., 1988. Wing folding in the hymenoptera. Ann. Entomol. Soc. Am. 81, 342–349. https://doi.org/10.1093/aesa/81.2.342.

Deiters, J., Kowalczyk, W., Seidl, T., 2016. Simultaneous optimisation of earwig hindwings for flight and folding. Biol. Open 5, 638–644. https://doi.org/10.1242/bio.016527.

Dirks, J.-H., Taylor, D., 2012. Veins improve fracture toughness of insect wings. PLoS One 7 e43411.

Donoughe, S., Crall, J.D., Merz, R.A., Combes, S.A., 2011. Resilin in dragonfly and damselfly wings and its implications for wing flexibility. J. Morphol. 272, 1409–1421. https://doi.org/10.1002/jmor.10992.

Fedorenko, D.N., 2009. Evolution of the beetle hind wing, with special reference to folding (Insecta, Coleoptera), first ed. Pensoft Publishers, Geo Milev Str. 13a, Sofia 1111, Bulgaria info@pensoft.net www.pensoft.net. Sofia - Moscow.

Forbes, W.T.M., 1924. How a beetle folds its wings. Psyche J. Entomol 31, 254–258. https://doi.org/10.1155/1924/68247.

Goodwyn, P.J.P., Gorb, S.N., 2004. Frictional properties of contacting surfaces in the hemelytra-hindwing locking mechanism in the bug *Coreus marginatus*. J. Comp. Physiol. 190, 575–580. https://doi.org/10.1007/s00359-004-0520-9.

Gorb, S.N., 1998. Frictional surfaces of the elytra-to-body arresting mechanism in tenebrionid beetles (Coleoptera : Tenebrionidae) : design of co-opted fields of microtrichia and cuticle ultrastructure. Int. J. Insect Morphol. Embryol 27, 205–225. https://doi.org/10.1016/S0020-7322(98)00013-0.

Gorb, S.N., 1999. Serial elastic elements in the damselfly wing: mobile vein joints contain resilin. Naturwissenschaften 86, 552–555. https://doi.org/10.1007/s001140050674.

Ha, N.S., Truong, Q.T., Goo, N.S., Park, H.C., 2013. Biomechanical properties of insect wings: the stress stiffening effects on the asymmetric bending of the *Allomyrina dichotoma* beetle's hind wing. PLoS One 8, e80689. https://doi.org/10.1371/journal.pone.0080689.

Ha, N.S., Truong, Q.T., Phan, H.V., Goo, N.S., Park, H.C., 2014. Structural characteristics of *Allomyrina dichotoma* beetle's hind wings for flapping wing micro air vehicle. J. Bionic Eng 11, 226–235. https://doi.org/10.1016/S1672-6529(14)60038-X.

Haas, F., 2000. Geometry and Mechanics of Hind-wing Folding in Dermaptera and Coleoptera (Master of Philosophy)1994, University of Exeter; Exeter. Haas F., Wing folding in insects: a natural, deployable structure. In: Pellegrino, S., Guest, S.D. (Eds.), IUTAM-IASS Symposium on Deployable Structures: Theory and Applications, Solid Mechanics and its Applications. Springer, Netherlands, pp. 137–142. https://doi.org/10.1007/978-94-015-9514-8_15.

Haas, F., 2006. Evidence from folding and functional lines of wings on inter-ordinal relationships in Pterygota. Arthropod Syst. Phylogeny 64, 149–158.

Haas, F., Beutel, R.G., 2001. Wing folding and the functional morphology of the wing base in Coleoptera. Zoology 104, 123–141. https://doi.org/10.1078/0944-2006-00017.

Haas, F., Gorb, S., Blickhan, R., 2000a. The function of resilin in beetle wings. Proc. R. Soc. Lond. B Biol. Sci. 267, 1375–1381. https://doi.org/10.1098/rspb.2000.1153.

Haas, F., Gorb, S., Wootton, R., 2000b. Elastic joints in dermapteran hind wings: materials and wing folding. Arthropod Struct. Dev. 29, 137–146. https://doi.org/10.1016/S1467-8039(00)00025-6.

Haas, F., Kukalova-Peck, J., 2001. Dermaptera hindwing structure and folding: new evidence for familial, ordinal and superordinal relationships within Neoptera (Insecta). Eur. J. Entomol. 98, 445–509. https://doi.org/10.14411/eje.2001.065.

Haas, F., Tan Chek Hwen, J., Bun Tang, B., 2011. New evidence on the mechanics of wing unfolding in Dermaptera (Insecta). Arthropod Syst. Phylogeny 70, 95–105.
Haas, F., Wootton, R.J., 1996. Two basic mechanisms in insect wing folding. Proc. R. Soc. Lond. B Biol. Sci. 263, 1651–1658. https://doi.org/10.1098/rspb.1996.0241.
Hammond, P.M., 1979. Wing-folding mechanisms of beetles, with special reference to investigations of adephagan phylogeny (Coleoptera). In: Carabid Beetles: Their Evolution, Natural History, and Classification. Proceedings of the 1. International Symposium of Carabidology, pp. 113–180. https://doi.org/10.1007/978-94-009-9628-1_7.
Hörnschemayer, T., 1998. Morphologie und Evolution des Flügelgelenks der Coleoptera und Neuropteridae (Inaugural-Dissertation). Georg-August-Universität, Göttingen.
Jongerius, S.R., Lentink, D., 2010. Structural analysis of a dragonfly wing. Exp. Mech. 50, 1323–1334. https://doi.org/10.1007/s11340-010-9411-x.
Kaufmann, T., 1960. Faltungsmechanismen der Flügel bei einigen Coleopteren (Doctoral). Ludwig-Maximilians-Universität, München.
Kleinow, W., 1966. Untersuchungen zum Flügelmechanismus der Dermapteren. Z. Für Morphol. Ökol. Tiere 56, 363–416. https://doi.org/10.1007/BF00442290.
Lee, D.-H., Leskey, T., 2015. Flight behavior of foraging and overwintering brown marmorated stink bug, Halyomorpha halys (Hemiptera: Pentatomidae). Bull. Entomol. Res. 105 https://doi.org/10.1017/S0007485315000462.
Lehmann, F.-O., 2004. Aerial locomotion in flies and robots: kinematic control and aerodynamics of oscillating wings. Arthropod Struct. Dev. 33, 331–345. https://doi.org/10.1016/j.asd.2004.05.003. Arthropod Locomotion Systems: from Biological Materials and Systems to Robotics.
Lehmann, F.-O., Gorb, S., Nasir, N., Schützner, P., 2011. Elastic deformation and energy loss of flapping fly wings. J. Exp. Biol. 214, 2949–2961. https://doi.org/10.1242/jeb.045351.
Limaye, A., 2006. Drishti - Volume Exploration and Presentation Tool. Presented at the Vis 2006. Baltimore.
Linkert, M., Rueden, C.T., Allan, C., Burel, J.-M., Moore, W., Patterson, A., Loranger, B., Moore, J., Neves, C., MacDonald, D., Tarkowska, A., Sticco, C., Hill, E., Rossner, M., Eliceiri, K.W., Swedlow, J.R., 2010. Metadata matters: access to image data in the real world. J. Cell Biol. 189, 777–782. https://doi.org/10.1083/jcb.201004104.
Marrocco, J., Demasi, L., Venkataraman, S., 2010. Investigating the structural dynamics implication of flexible resilin joints on dragonfly wings. Acsess Proc 1–6.
Michels, J., Appel, E., Gorb, S.N., 2016. Functional diversity of resilin in Arthropoda. Beilstein J. Nanotechnol. 7, 1241–1259. https://doi.org/10.3762/bjnano.7.115.
Michels, J., Gorb, S.N., 2012. Detailed three-dimensional visualization of resilin in the exoskeleton of arthropods using confocal laser scanning microscopy. J. Microsc. 245, 1–16. https://doi.org/10.1111/j.1365-2818.2011.03523.x.
Müller, F., 1873. Beiträge zur Kenntniss der Termiten. Jena. Z. Naturw 7, 333–358, 451-463.
Muhammad, A., Nguyen, Q.V., Park, H.C., Hwang, D.Y., Byun, D., Goo, N.S., 2010. Improvement of artificial foldable wing models by mimicking the unfolding/folding mechanism of a beetle hind wing. J. Bionic Eng 7, 134–141. https://doi.org/10.1016/S1672-6529(09)60185-2.
Muhammad, A., Park, H.C., Hwang, D.Y., Byun, D., Goo, N.S., 2009. Mimicking unfolding motion of a beetle hind wing. Chin. Sci. Bull. 54, 2416–2424. https://doi.org/10.1007/s11434-009-0242-z.
Nguyen, Q.V., Park, H.C., Goo, N.S., Byun, D., 2010a. Characteristics of a beetle's free flight and a flapping-wing system that mimics beetle flight. J. Bionic Eng 7, 77–86. https://doi.org/10.1016/S1672-6529(09)60195-5.
Nguyen, Q.V., Truong, Q.T., Park, H.C., Goo, N.S., Byun, D., 2010b. Measurement of force produced by an insect-mimicking flappingwing system. J. Bionic Eng 7 (Supplement), S94–S102. https://doi.org/10.1016/S1672-6529(09)60222-5.
Rajabi, H., A, D., A, S., D, T., J.-H, D., 2015a. Numerical investigation of insect wing fracture behaviour. J. Biomech. 48, 89–94.
Rajabi, H., Bazargan, P., Pourbabaei, A., Eshghi, S., Darvizeh, A., Gorb, S.N., Taylor, D., Dirks, J.-H., 2017a. Wing cross veins: an efficient biomechanical strategy to mitigate fatigue failure of insect cuticle. Biomech. Model. Mechanobiol 16, 1947–1955.
Rajabi, H., Ghoroubi, N., Darvizeh, A., Appel, E., Gorb, S.N., 2016a. Effects of multiple vein microjoints on the mechanical behaviour of dragonfly wings: numerical modelling. R. Soc. Open Sci 3, 150610.
Rajabi, H., Ghoroubi, N., Darvizeh, A., Dirks, J.-H., Appel, E., Gorb, S.N., 2015b. A comparative study of the effects of vein-joints on the mechanical behaviour of insect wings: I. Single joints. Bioinspir. Biomim 10, 056003.
Rajabi, H., Jafarpour, M., Darvizeh, A., Dirks, J.-H., Gorb, S.N., 2017b. Stiffness distribution in insect cuticle: a continuous or a discontinuous profile? J. R. Soc. Interface 14, 20170310.
Rajabi, H., Moghadami, M., Darvizeh, A., 2011. Investigation of microstructure, natural frequencies and vibration modes of dragonfly wing. J. Bionic Eng 8, 165–173.
Rajabi, H., Shafiei, A., Darvizeh, A., Dirks, J.-H., Appel, E., Gorb, S.N., 2016b. Effect of microstructure on the mechanical and damping behaviour of dragonfly wing veins. R. Soc. Open Sci. 3. Online. https://www.ncbi.nlm.nih.gov/pmc/articles/PMC4785991/.
Rajabi, H., Shafiei, A., Darvizeh, A., Gorb, S.N., 2016c. Resilin microjoints: a smart design strategy to avoid failure in dragonfly wings. Sci. Rep. 6, 39039.
Ren, H., Wang, X., Li, X., Chen, Y., 2013. Effects of dragonfly wing structure on the dynamic performances. J. Bionic Eng 10, 28–38. https://doi.org/10.1016/S1672-6529(13)60196-1.
Ruangchai, S., Reisecker, C., Hild, S., Ziegler, A., 2013. The architecture of the joint head cuticle and its transition to the arthrodial membrane in the terrestrial crustacean *Porcellio scaber*. J. Struct. Biol. 182, 22–35. https://doi.org/10.1016/j.jsb.2013.01.009.
Rueden, C.T., Schindelin, J., Hiner, M.C., DeZonia, B.E., Walter, A.E., Arena, E.T., Eliceiri, K.W., 2017. ImageJ2: ImageJ for the next generation of scientific image data. BMC Bioinf. 18 (529) https://doi.org/10.1186/s12859-017-1934-z.
Schieber, G., Born, L., Bergmann, P., Körner, A.H., Mader, A., Saffarian, S., Betz, O., Milwich, M., Gresser, G., Knippers, J., 2017. Hindwings of insects as concept generator for hingeless foldable shading systems. Bioinspir. Biomim 13. https://doi.org/10.1088/1748-3190/aa979c.
Schierbaum, N., Hack, M., Betz, O., Schäffer, T.E., 2018. Macro-SICM: a scanning ion conductance microscope for large-range imaging. Analyt. Chem. 90 (8), 5048–5054.
Schindelin, J., Arganda-Carreras, I., Frise, E., Kaynig, V., Longair, M., Pietzsch, T., Preibisch, S., Rueden, C., Saalfeld, S., Schmid, B., Tinevez, J.-Y., White, D.J., Hartenstein, V., Eliceiri, K., Tomancak, P., Cardona, A., 2012. Fiji: an open-source platform for biological-image analysis. Nat. Meth. 9, 676–682. https://doi.org/10.1038/nmeth.2019.
Schmitt, M., Büscher, T.H., Gorb, S.N., Rajabi, H., 2018. How does a slender tibia resist buckling? Effect of material, structural and geometric characteristics on buckling behaviour of the hindleg tibia in stick insect postembryonic development. J. Exp. Biol 221, jeb173047.
Shang, J.K., Combes, S.A., Finio, B.M., Wood, R.J., 2009. Artificial insect wings of diverse morphology for flapping-wing micro air vehicles. Bioinsp Biomim 4, 1–6.
Sivasankaran, P.N., Ward, T.A., Viyapuri, R., Johan, M.R., 2016. Static strength analysis of dragonfly inspired wings for biomimetic micro aerial vehicles. Chin. J. Aeronaut. 29, 411–423. https://doi.org/10.1016/j.cja.2016.02.007.
Snodgrass, R.E., 1935. Principles of Insect Morphology. Macgraw-Hill Book Company, Inc, New York.
Sun, J., Bhushan, B., 2012. The structure and mechanical properties of dragonfly wings and their role on flyability. Comptes Rendus Mécanique 340, 3–17. https://doi.org/10.1016/j.crme.2011.11.003. Biomimetic flow control.
van de Kamp, T., Greven, H., 2010. On the architecture of beetle elytra. Entomol. heute 22, 191–204.
van de Kamp, T., Riedel, A., Greven, H., 2016. Micromorphology of the elytral cuticle of beetles, with an emphasis on weevils (Coleoptera: Curculionoidea). Arthropod Struct. Dev. 45, 14–22. https://doi.org/10.1016/j.asd.2015.10.002.
Venable, J.H., Coggeshall, R., 1965. A simplified lead citrate stain for use in electron microscopy. J. Cell Biol. 25, 407–408.
Weber, H., 1930. Biologie der Hemipteren, eine Naturgeschichte der Schnabelkerfe. J. Springer, Berlin.
Weber, H., 1933. Lehrbuch der Entomologie. Verlag von Gustav Fischer.
Wiman, N.G., Walton, V.M., Shearer, P.W., Rondon, S.I., Lee, J.C., 2015. Factors affecting flight capacity of brown marmorated stink bug, *Halyomorpha halys* (Hemiptera: Pentatomidae). J. Pest Sci 88, 37–47. https://doi.org/10.1007/s10340-014-0582-6.
Woodworth, C.W., 1906. The wing veins of insects. W.W. Shannon, Supt. State Printing, Sacramento.
Wootton, R.J., 1992. Functional morphology of insect wings. Annu. Rev. Entomol. 37, 113–140. https://doi.org/10.1146/annurev.en.37.010192.000553.
Wu, P., Stanford, B.K., Sallstrom, E., Ukeiley, L., Ifju, P.G., 2011. Structural dynamics and aerodynamics measurements of biologically inspired flexible flapping wings. Bioinspir. Biomim 6 (016009). https://doi.org/10.1088/1748-3182/6/1/016009.

B List of abbreviations

Biology

ABCG36	ATP BINDING CASETTE type G 36
ALK1	AUXIN-INDUCED LRR KINASE 1
BAK1	BRI1-ASSOCIATED KINASE 1
BL	Brassinolide, the most active form of brassinosteroid hormones
BR	Brassinosteroid hormone
BRI1	BRASSINOSTEROID INSENSITIVE 1
BIK1	BOTRYTIS-INDUCED KINASE 1
BIR3	BAK1-INTERACTING RECEPTOR-LIKE KINASE 3
BKI1	BRI1 KINASE INHIBITOR 1
CNGC17	CYCLIC NUCLEOTIDE GATED CHANNEL 17
CO	CONSTANS
COP1	CONSTITUTIVELY PHOTOMORPHOGENIC 1
EFR	EF-Tu RECEPTOR
FER	FERONIA
EGCG	Epigallocatechin gallate
FLS2	FLAGELLIN SENSING 2
FT	FLOWERING LOCUS T
HG	Homogalacturonan
LFY	LEAFY
LRR	LEUCIN-RICH REPEAT
LRR-RLK	LEUCIN-RICH REPEAT RECEPTOR-LIKE KINASE
PEN3	PENETRATION RESISTANCE gene 3
PM	Plasma membrane
PME	PECTIN METHYESTERASE
PDR	PLEIOTROPIC DRUG RESISTANCE
PSKR1	PHYTOSULFOKINE RECEPTOR 1
RLK	RECEPTOR-LIKE KINASE
RLP	RECEPTOR LIKE PROTEIN
RLP44	RECEPTOR LIKE PROTEIN 44
RUP1/2	REPRESSOR OF UV-B PHOTOMORPHOGENESIS 2
SERK3	SOMATIC EMBRYOGENESIS RECEPTOR-LIKE KINASE 3 (= BAK1)

FRET-FLIM and formula

FRET	Förster resonance energy transfer
FLIM	Fluorescence lifetime imaging
FLT	Fluorescence lifetime (of the donor fluorophore) (= τ)
E_{FRET}	FRET efficiency
D	Donor fluorophore in FRET applications, here: mTurquoise 2 (mTRQ2)
A / A1	Acceptor fluorophore in FRET applications, here: mVenus (mVEN)
A2	Acceptor fluorophore 2 in FRET applications, here: mRFP
MSD	Mean square displacement $MSD = 4D(t_{lag})^{\alpha}$ - D: diffusion coefficient, t_{lag}: lag time α: coefficient
ODE	Ordinary differential equation
R_0	Förster distance
κ^2	Dipole orientation factor
n	Refractive index (or sample number)
X-Y-Z	Sequence indicates respective fluorophore fusions in three-fluorophore FRET-FLIM, namely X-mTurquoise2, Y-mVenus and Z-mRFP

Microscopy and assays

CLSM	Confocal laser scanning microscopy

CO-IP	Co-immunoprecipitation
COPASI	Software application for simulation & analysis of biochemical networks
DPI-ELISA	DNA-protein interaction enzyme-linked immunosorbent assay
HPTS	8-Hydroxypyrene-1,3,6-trisulfonic acid trisodium salt
MβCD	Methyl-beta-cyclodectran
MFIS	Multiparameter fluorescence imaging spectroscopy
PALM	Photoactivated localization microscopy
STED	Stimulated Emission Depletion
TIRF	Total internal reflection fluorescence microscopy
VAEM	Variable angle epifluorescence microscopy (special form of TIRF)
mbSUS	mating-based split-ubiquitin assay (protein-protein interaction assay)
MIFE	Microelectrode ion flux measurement

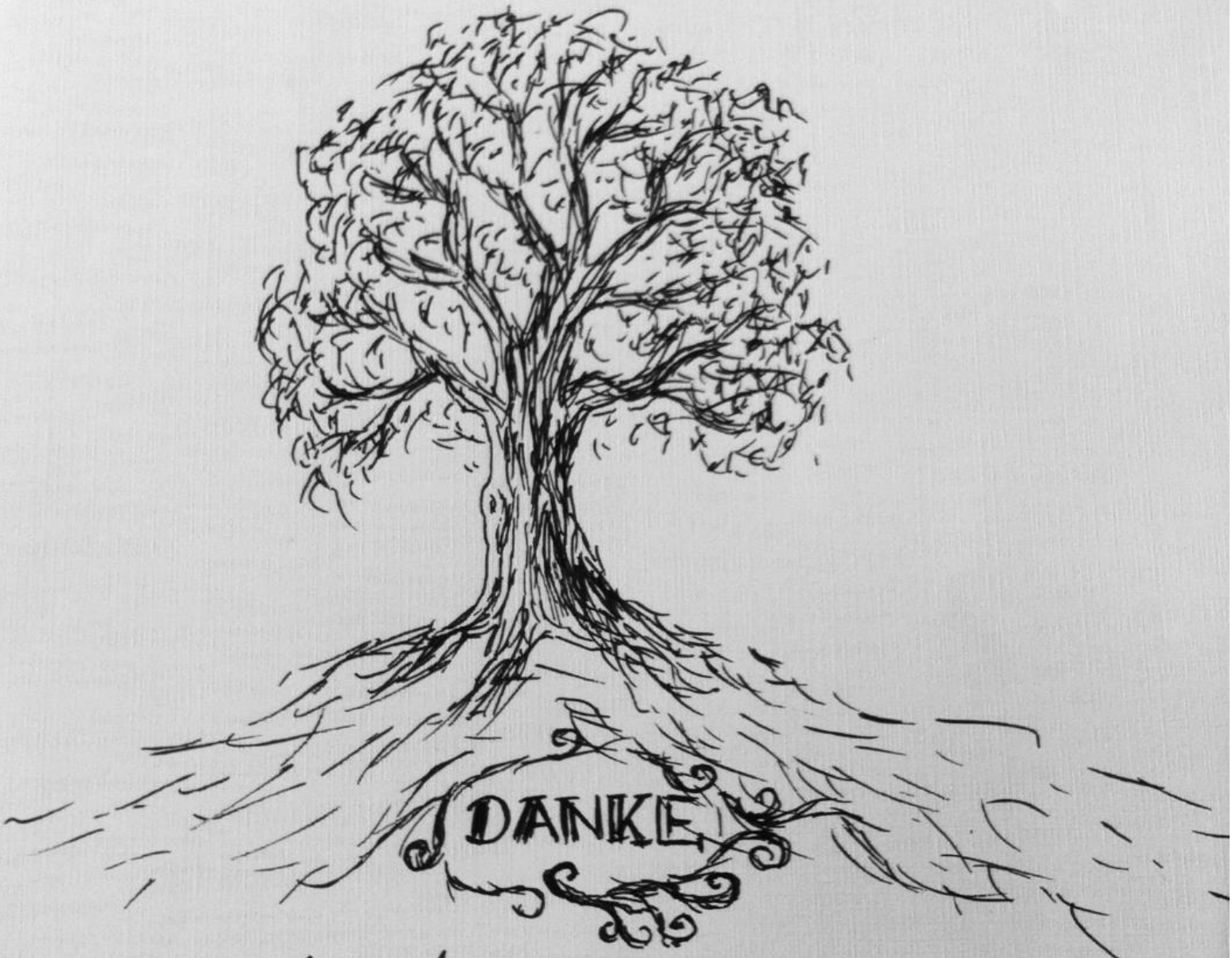

Ich habe vielen zu Danken, die mich
auf meinem Weg bis hier her unterstützt,
ermutigt, angestachelt und zum Lachen
gebracht haben, wenn mir mal gar
nicht zum Lachen war; danke dafür!*
Danke für Gespräche, Rat und Kaffee
in der dunklen Stunden, aber noch
viel mehr für all die gute Zeit

Klaus, vielen Dank dass du mich stets unterstützt und ermutigt hast, mit Rat und Tat zur Seite warst und so viele tolle, spannenden Sachen ermöglicht hast! Insbesondere seien genannt, dass ich einfach die Informatik-Vorlesung besuchen durfte, der Spectroscopy-Workshop, Tasmanien, wirklich tolle Konferenzen und dass ich eigene Ideen verfolgen durfte. Danke für das stets offene Ohr, den ehrlichen Umgang und die konstruktiven und netten Gespräche!
Üner, danke dass du mich durch die Master-Arbeit hinweg und auch während der Promotion unterstützt sowie ehrlich und kritisch mit mir diskutiert hast! Das war manchmal ganz schön hart, hat mich und die Arbeit aber weiter gebracht!
Friederike, danke für deine Unterstützung, Diskussionen, das Feedback, das offene Ohr und das viele Lachen! Der gute Kaffee! Mit dir im Labor ist gute Laune und eine produktive Stimmung garantiert! Mit dir kann man spannende Dinge ausprobieren und dabei Spaß haben!
Kooperationspartnern, danke für die guten Gespräche und Diskussionen, die Scherzchen und dass wir immer mit einander Reden konnten, **danke** für alles (besonders auch in dieser letzten Zeit) und ich hoffe ich hab Eure Daten gut und voll in Eurem Sinne vertreten, nach Alphabet **Eli, Ruth, Zok!**
Christopher Grefen und **Thilo Stehle** für die interessierten und kritischen Rückfragen während der Committee-Meetings! Ganz wichtig, den HiWis, Laborpraktikanten und Bacheloranden möchte ich herzlich danken! In der Reihenfolge in der Ihr da wart: **Marius, Yannick, Victoriya, Rosa, Leander**! Auch seien genannt **Amelie** und **Xuan** Alle, die mir viele Labordinge erst beigebracht haben: **Hoines, Anne, Andy, Luise**; **AG Müller** mit **Steffi, Richi, Doro, Elli, Arvid**! Danke für Euer Zeit nehmen und dass wir immer noch schnacken können! **AG Pimpel**, **RG Bennett**, especially **Daniela** and **Antonia**! **RG Shabala**, especially **Joe** (real life saver!) and **Nana**!

Allen Freunden im ZMBP, der ganzen Pflanzenphys, dem Labor mit **Bay 6 7 8**: **Angela**, **Anne**, **Claudi**, **Fredi**, **Juan**, **Leander**, **Nata**, **Rebecca**, **Stefan**, **Thomas**, **Danke für die gemeinsame Zeit!**

Insbesondere **Michael Fitz** für Rat und Hilfe, Diskussion und nette Gespräche! **Sandra Richter** für Hilfe und stets guten Rat! **Hauke** für Western-Ratschläge! **Die Happy Hour Crew** insbesondere **Hut**!

Natalie, seit dem Master-Studium sind wir beide an der Uni und in der Freizeit stets zusammen unterwegs! Der Nano-Kurs, Kaffee, Konferenzen und in allen Lebenslagen! In dem Zuge der Master-Jahrgang, **Flo**, danke für viele Gespräche über unsere jeweilige Forschung, Korrektur lesen, quatschen; **Anna**, **Melli**, **Phillipp**, **Arvid.**

Puuh gleich geht's zum Druck also viel kürzer als ihr es verdient –
Im Bachelor jeden Tag gesehen, alles zusammen erlebt, alle Höhen und Tiefen, **Marine! Benni! Hannah! Oleg wir vergessen dich niemals, Max! Jan und Vicky und Daniel**! Die Herrenrunde, ich bin wirklich froh Euch zu haben, danke für die tolle Zeit, für Besuche und Lachen und einfach für einander da sein **Michael, Frank, David**! **Suszanna**, danke für die Kaffeemaschine, sie hat sehr geholfen!
Chloe, you are an amazing friend and I am so glad to have you in my life! Thank you for your support and laughs and idle chats! **Dieter Hahn**, danke dass wir über Musik und Bücher, Bilder und Gedichte und einfach alles reden können. Ich verdanke die viel! **Patrick, Maritta, Michi und Alex, Holger**! Viele Spaziergänge, reden, Besuche und einfach zusammen sein! **Vera, Helen Anne**! Seit frühesten Tagen. Danke dass es immer so ist, als ob keine Zeit vergangen ist. Danke für die Unterstützung und Kraft in allen Lebenslagen! **Petra** und **Jens**! Ich kenne dich seit eigentlich immer, zusammen groß werden. **Lilly** und **Alina** sind einfach ganz wunderbar und ich freue mich immer wenn wir uns sehen. Schön, dass es dich gibt!
Momo, ich bin so froh dich zu haben, ich weiß nicht mehr zu sagen als dass du mich wirklich glücklich machst. Danke für deine Geduld und die Unterstützung, besonders in der beschwerlichen Zeit am Schluss. Du bedeutest mir die Welt.
Auch **Birgit und Horst** für guten Rat und für schöne Abende und Tage!

Onkel Stefan und **Tante Klara** für Eure Hilfe, **Onkel Jürgen und Tante Bärbel**, danke dass ihr mich immer auf den Boden zurückholt, Kaffees und Pizza Calzone, dass wir viel lachen und reden können! **Omas und Opas**, insbesondere mein Mutlanger Opa, **Julian**, du hast mich immer unterstützt, danke besonders auch für die letzte Zeit, ich bin so froh dich zu haben ich hoffe ich kann das gleiche für dich tun und **Mama und Papa**. Danke dass ich studieren und promovieren konnte und ihr mich immer unterstützt habt, ohne Euch hätte ich das nicht geschafft.

Danke!